# Experimental studies on the thermodynamics and kinetics of coexisting olivine, silicate melt, and vapor

Thesis by

Lee Michael Saper

In Partial Fulfillment of the Requirements for

the degree of

Doctor of Philosophy

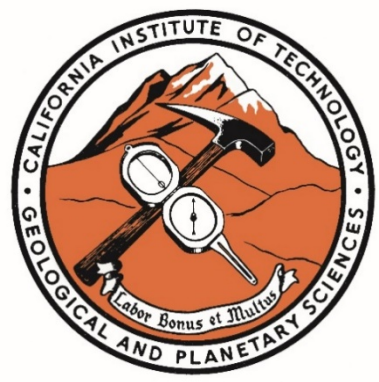


CALIFORNIA INSTITUTE OF TECHNOLOGY

Pasadena, California

2022

(Defended Monday, August 9, 2021)

Lee Michael Saper
ORCID: 0000-0002-3995-9986

**Acknowledgements**

I would like to thank Ed Stolper, my thesis advisor, for being eternally curious, optimistic, and inquisitive about my research ideas and experiments, and for continuing to push me towards achieving higher levels of scholarship, attention to detail, and open-mindedness. I am grateful for the time that you have spent carefully combing through manuscript revisions, and for our weekly conversations that spanned the gamut of research, world events, how to cut your own hair, and general philosophy of science and of life. It has been a pleasure.

Thank you to all of the members of my thesis committee for your guidance: Paul Asimow, John Eiler, and Claire Bucholz. I feel incredibly fortunate to have been able to exchange ideas with each of you, take your courses, work with you as a teaching assistant, and go on fantastic field trips together including to Catalina Island and to Alaska. I will of course always cherish all of the knowledge dropped in our weekly Petrology Reading Group.

I have to specially thank Mike Baker for training me as an experimental petrologist and for providing a level of dedication and guidance in the lab that I am extremely lucky to have had as a graduate student. Thank you for being patient with me through all of our conversations and e-mails about the nitty gritty experimental details, and for managing to keep the furnaces up and running when I needed them most. I am truly grateful for your dedication and the time you spent helping me in the lab.

Thank you to Chi Ma, for welcoming me as the graduate assistant to the division analytical facility and for helping me gain a much deeper understanding of our analytical instruments.

I would also like to thank Frank Richter for many insightful conversations and for your guidance in research, your commitment to quantitative rigor, and for your perspectives on academia. You have become a great friend and I look forward to continuing our chats.

Thank you to the Caltech GPS community, to my fellow Pit Members of 2015, and to the GPS staff and faculty; you have made my graduate experience meaningful and enjoyable. Thank you to Cambrian Explosion, the GPS intramural soccer team, and to my pickup soccer friends for keeping me active and in shape and for being great friends outside of lab.

Thank you to my family, my mother and father, Shelley and Steve, my brother Dan, and sister-in-law Jen for supporting me all of this time despite not quite being sure what I actually do in lab every day.

Lastly, thank you to my incredible wife, Michelle, for uprooting from San Diego and moving with me to Los Angeles in 2015, for being there for me through all of the stress and challenges that cropped up at every step of the journey, for putting up with days and nights where I was out in the field and had no cell service, for being my best friend and partner, and for providing me with the companionship, support, and love, that was necessary for me to make it through the Ph.D.

## Abstract

This thesis focuses on experiments run in 1 atm gas-mixing furnaces exploring the thermodynamics and kinetics of coexisting olivine, silicate melt, and vapor. Chapter 1 provides a high-level introduction and summary of the results for each of the following chapters. Chapter 2 and Chapter 3 both involve experiments run on natural olivines containing melt inclusions. Chapter 2 describes a set of homogenization and cooling rate experiments designed to characterize chemical zonation that develops across melt inclusions during cooling. A diffusion model for MgO in the inclusion liquid was calibrated based on these experiments and then used to calculate the syneruptive cooling rates of lavas on Earth and on Mars based on comparison of the model to experimental and natural diffusion profiles in melt inclusions. Chapter 3 presents the first co-determined measurements of S and Fe oxidation state in experimental silicate melts that were equilibrated with the oxygen fugacity of a gas-mixing furnace. The use of melt inclusions as sulfur-bearing experimental vessels is explored, as are implications for interpreting room temperature measurements of the oxidation state of multivalent elements. A set of natural melt inclusions are used as a case study to demonstrate that the temperature-dependence of sulfur-iron electron exchange in basaltic liquids is either weak or leads to the conversion of ferric iron to ferrous iron during cooling. Chapter 4 presents a new parameterization of the composition-dependence of the olivine-liquid Fe-Mg exchange coefficient, $K_D^{ol/liq}{}_{,Fe2+-Mg}$, based on experiments at low oxygen fugacity where corrections for $Fe^{3+}$ are minor. A quantitative thermodynamic model is fit to the data, showing that the $K_D$ is a function of the Si, Al, Ti, Na+K contents of the liquid as well as olivine composition. Models of $K_D^{ol/liq}{}_{,Fe2+-Mg}$ that do not incorporate liquid compositional variables cannot account for the variability of $K_D$ (~0.22-0.38) observed at low oxygen fugacity in a compilation of high-quality literature experiments. Lastly, in Appendix 1, the published version of *Richter, Saper, et al. (2021), GCA 295* is included. For this chapter, I contributed MELTS calculations (Ghiorso & Sack 1995; Smith & Asimow 2005) which were used to model crystallization processes and to set boundary conditions for models elemental and isotopic diffusion of Mg and Li in lunar olivines and martian olivines and augites. The combined elemental and isotopic diffusion profiles were used to discriminate between zoning formed due to crystallization from that due to diffusion.

## Published Content and Contributions

**Saper, L.,** Stolper, E.M. (2020) Controlled cooling-rate experiments on olivine-hosted melt inclusions: chemical diffusion and quantification of eruptive cooling-rates on Hawai‘i and Mars. *Geochemistry, Geophysics, Geosystems*, 21, doi: 10.1029/2019GC008772

L. Saper conducted the experiments, analyzed the experimental and natural samples, wrote the multicomponent diffusion model, and wrote the manuscript.

Richter, F., **Saper, L.**, Villeneuve, J., Chaussidon, M., Watson, B.E., Davis, A.M., Mendybaev, R.A., Simon, S.S (2021) Reassessing the thermal history of martian meteorite Shergotty and lunar mare basalt Apollo 15555 using kinetic isotope fractionation of zoned minerals. *Geochimica et Cosmochimica Acta*, 295, doi: 10.1016/j.gca.2020.11.002

L. Saper contributed calculations from the MELTS thermodynamic model and contributed towards writing sections on zoning due to crystallization and differentiation. Permission from F. Richter was granted to include the work in this thesis.

**Table of Contents**

**List of Figures**

**Chapter 2** **Page**

**List of Figures**

**Chapter 3** **Page**



**Chapter 4**

**List of Figures**

**Chapter 4 (con't)** **Page**



**Appendix 1**

## List of Figures

**Appendix 1 (con't)** **Page**



## List of Tables

**Chapter 2** **Page**



**Chapter 3** **Page**

**List of Tables**

**Chapter 4**



**Chapter 5** **Page**

*Chapter 1*

# Introduction

Lee M. Saper

Olivine is the predominant mineral phase in the Earth's upper mantle and is the primary liquidus phase during crystallization of most mafic melts that occur on Earth as well as on other rocky bodies in the solar system (BVSP, 1981). Consequently, it is one of the most widely studied mineral phases in petrology and an extraordinary amount of effort has been dedicated to documenting its occurrence and chemical variability in nature, and to experimental studies which explore its thermodynamics and kinetic properties of diffusion, conductivity, and rheology. Despite vast amounts of experimental data on olivine our understanding of some basic properties, such as the systematics of partitioning of its major components $Fe^{2+}$ and Mg between olivine and liquid, are still not fully parameterized for the range of complex compositions and conditions found in nature.

This thesis describes high-temperature experimental studies performed during my Ph.D. that involved olivine, liquid, and a vapor phase. Chapter 2 and Chapter 3 report the results of experiments in 1 atm gas-mixing furnaces that used natural olivines containing roughly spherical pockets of glass quenched from trapped melts, called melt inclusions, as experimental vessels. It has been demonstrated experimentally that over relatively short timescales of hours to days at temperatures where basaltic liquids are molten, the mobility of hydrogen-bearing defects in olivine is sufficiently fast (see Ferriss et al. 2018 for a recent review) that water and oxygen fugacity ($fO_2$) can be rapidly equilibrated across olivines (e.g., Gaetani et al. 2012, Bucholz et al. 2013). When gases such as $H_2$ and $CO_2$ or CO and $CO_2$ are mixed in known proportions at constant T they fix the $fO_2$; in a 1 atm gas-mixing furnaces these mixtures are flowed over samples suspended in hot portions of the furnace tube, which allows for precise and accurate control of T and $fO_2$. Experiments that utilize olivine-hosted melt inclusions as experimental containers provide a method whereby

olivine-saturated silicate melts, containing natural abundances of major, minor, trace, and some volatile elements, can be subjected to a range of T-$fO_2$ conditions. The use of natural olivine-hosted melt inclusions as containers avoids some of the drawbacks of traditional methods used for studying the petrology of silicate melts, including the issue of Fe-loss for experiments hung on metal wire loops (e.g. Grove 1981; Borisov & Jones 1999) and the challenge of maintaining high sulfur contents that, over certain intervals of $fO_2$, are otherwise inaccessible by flowing S-bearing gas mixes directly over melts at 1 atm (e.g. Nash et al. 2019).

Melt inclusions themselves are the subject of intense study due to their potential to preserve melt compositions that were coeval with crystallization of their host phase. Melt inclusions often differ in composition from host lavas and other more differentiated rocks that have undergone fractionation, crystallization, and degassing processes, from which the melt inclusions were shielded by their crystal containers (e.g. Roedder 1979). Yet numerous processes can modify the composition and properties of melt inclusions after they are trapped by their host phase, and there is an entire subfield dedicated to untangling the various ways in which melt inclusions can be compromised, using modeling or experimental homogenization techniques to attempt to reconstruct the compositions of the initially trapped melts (e.g. Danyushevsky et al. 2002, Schiano et al. 2016). Recently, it was shown that over the timescales of eruption, crystallization of olivine on the interior walls of melt inclusions can induce diffusive fractionation of liuid composition that may reach the centers of olivine-hosted melt inclusions (Newcombe et al. 2014). As a result, depending on the cooling rate during eruption glassy inclusions with identical pre-eruptive thermal and chemical histories can have divergent compositions.

The experiments described in Chapter 2 follow from the study of Newcombe et al. 2014, who measured diffusion profiles across natural olivine-hosted melt inclusions, by equilibrating olivines with melt inclusions in a 1 atm furnace and subjecting them to different cooling rates. For both Chapters 2 and 3 the starting materials were Mauna Loa deroved olivine sands from Papakōlea, Hawai‘i that were sorted and hand-picked for spherical melt inclusions ≥75 μm in diameter. These experiments demonstrated that experimental cooling generates diffusion profiles that are analogous to those documented in Newcombe et al. (2014), and that the compositions of melt inclusions are susceptible to modification by diffusion during eruption. A quantitative diffusion model for the inclusion liquid was developed and calibrated based on the experimental results. Because the inclusion liquids are complex multicomponent mixtures, melt inclusions are finite, and temperature was variable, modeling was done using a finite-element approach with a diffusion coefficient for MgO that was dependent on T, and on melt composition. The cooling rates that resulted in the best fit between the modeled and measured diffusion profiles in experimental melt inclusions were typically within ±10% of the known experimental cooling rates. The inverse approach was also used to quantify the cooling rates of lavas at Papakōlea, Hawai’i and on Mars (using the meteorite Yamato 980459) by measuring diffusion profiles across glassy melt inclusions. The results from Papakōlea show cooling rates that ranged from ~50 °C/hr to 11,800 °C/hr; the lowest cooling rate demonstrates that olivine-hosted melt inclusions can cool metastably down to low T while only crystallizing olivine on the inclusion walls (Roedder 1992). The cooling rates measured in melt inclusions from Yamato 980459 (85-1047 °C/hr) are consistent with the

interpretation that it was cooled rapidly at or near the Martian surface (Head & Hammer 2016).

Chapter 3 explores in further detail the use of olivine-hosted melt inclusions as experimental containers for melts that contain high sulfur contents, which can be equilibrated with the precisely controlled $fO_2$ of a mixed gas furnace atmosphere. The importance of sulfur is in part due to its potential effect (e.g., Metrich et al. 2009, Jugo et al. 2010) on the ratio of ferric to ferrous iron ($Fe^{3+}/Fe^{2+}$) in silicate melts. This ratio is widely used to infer variations of $fO_2$ because Fe is the most abundant multivalent element in basaltic melts over the range of natural $fO_2$ levels. Because sulfur exists predominantly as either $S^{2-}$ or $S^{6+}$ in silicate melts (e.g. Wallace & Carmichael 1994; Metrich et al. 2009; Jugo et al. 2010; Klimm et al. 2012), and thus requires eight electrons to convert between oxidation states, it plays a disproportionate role in redox chemistry compared the much more abundant Fe, whose oxidation states only differ by one electron. For example, at $fO_2$ ~FMQ (the fayalite-magnetite-quartz buffer) the concentration of $Fe^{3+}$ in the basaltic liquids can be on order $8\times[S^{2-}]$ (e.g., FeO* = 10 wt% and $Fe^{3+}/Fe^{T} = 0.125$ imply $[Fe^{3+}]$ = 9,700 ppm, whereas at sulfide saturation [S] ~1000 ppm). If the kinetics of electron transfer are rapid (e.g. Berry et al. 2003) and there is a strong temperature dependence to electron exchange between Fe and S (e.g. that inferred by Nash et al. 2019), reactions involving electron transfer between Fe and S can modify the relative abundances of the oxidized and reduced species of both elements during cooling. This raises questions about whether room T measurements of the oxidation state of multivalent elements in silicate glasses are representative of that which was present at high T in the corresponding liquids. The attributes described above for olivine-hosted melt inclusion experiments make it a

promising technique for exploring Fe-S electron exchange, including its temperature dependence (isothermal experiments) and its kinetics (cooling-rate experiments).

The co-determined measurements of $Fe^{3+}/Fe^{2+}$ and $S^{6+}/S^{2-}$ using synchrotron micro-X-ray absorption near-edge structure spectroscopy (XANES) reported in Chapter 3 represent the first determinations of the oxidation states of both Fe and S in experimental basaltic glasses that have been left for >10 minutes (Head et al. 2018) to equilibrate with the $fO_2$ of a gas-mixing furnace. There is some uncertainty about whether equilibrium was attained between the $fO_2$ of the externally imposed furnace gases and that recorded within the melt inclusions in these preliminary 24 hr experiments, the details of which are covered in Chapter 3. More experiments are required to make definitive conclusions about the temperature-dependence and kinetics of Fe-S electron exchange in silicate melts, however several important lessons can be learned from these preliminary experiments and they provide a template for further exploration. It is shown that previous determinations of the relationship between $fO_2$, T, and $S^{6+}/S^{2-}$ are polluted by uncertainties in models that relate $fO_2$, T, $Fe^{3+}/Fe^{2+}$, and melt composition, leading to significant inaccuracies in placing the transition from sulfide to sulfate in silicate melts as a function of $fO_2$. This transition takes place over a range in $fO_2$ of ~2 orders of magnitude, whereas experimental determinations of the sulfide to sulfate transition that do not have independent and direct knowledge of $fO_2$ have an uncertainty of 1.4 log units in $fO_2$ solely due to the choice of Fe oxybarometers). In natural samples the $fO_2$ is not known directly, nor is the cooling rate, and so it is tricky to use these data to populate thermodynamic models of $fO_2$ vs. oxidation state and difficult to interpret their high T histories and the degree to which they were modified during cooling. Using the approach described in Chapter 2, a constraint can be

placed on cooling rate for glassy olivine-hosted melt inclusions, and two examples were selected from Papakōlea, Hawai‘i: one inclusion that was rapidly cooled (~8000 °C/hr) and a second which was slowly cooled (~55 °C/hr) during eruption. XANES measurements of the slowly cooled melt inclusion show that all S (154 ppm) is present as $S^{6+}$, and it is demonstrated in Chapter 3 that this is incompatible with models that infer a strong temperature dependence to Fe-S redox equilibria. Such models result in the consumption of $S^{6+}$ and the concomitant oxidation of $Fe^{3+}$ during cooling (e.g., Nash et al. 2019). These results suggest that either the temperature dependence is small (O'Neill 2021), or that it proceeds in the opposite direction to lower the $Fe^{3+}/Fe^{2+}$ (and sympathetically raise the $S^{6+}/S^{2-}$) during cooling, which would be consistent with in-situ XANES measurements of the T-dependence of Cr-Fe electron transfer in silicate melts (Berry et al. 2003).

Chapter 4 describes a set of Re wire loop experiments exploring compositional-dependence of the olivine-liquid $Fe^{2+}$-Mg exchange coefficient at low $fO_2$ where corrections for $Fe^{3+}$ are minimal. The olivine-liquid exchange coefficient, $K_{D,Fe2+-Mg}$, has been shown to be a function of melt and olivine composition, as well as, T, P, and $fO_2$ (see the Introduction of Chapter 4 for a comprehensive list). In addition, the $Fe^{3+}/Fe^{2+}$ of melts is also a function of composition, T, P, and, explicitly, $fO_2$. Because many of the existing parameterizations of the $K_{D,Fe2+-Mg}$ utilize experiments run at $fO_2$ where $Fe^{3+}$ contents are not negligible, it is difficult to deconvolve the effects of these variables on Fe oxidation state from those on the $K_{D,Fe2+-Mg}$. Routine electron microprobe measurements report all Fe in glasses as FeO*, and in order to calculate $K_{D,Fe2+-Mg}$, an Fe oxybarometry model has to be employed to calculate the fraction of $Fe^{3+}$ present at a particular $fO_2$. As noted above and in recent reviews of these various models (e.g. Matzen et al. 2011; Putirka 2016;

Borisov et al. 2018), this presents a significant source of uncertainty. The alternative is to run experiments at sufficiently low $fO_2$ such that corrections for $Fe^{3+}$ are (e.g., at the experimental conditions described in Chapter 4, the fraction of $Fe^{3+}$ is expected to be <4% and, at Fe metal saturation $Fe^{3+}/Fe^{T} < 2.6\%$, Bowen & Schraier 1935). There exists plentiful experimental data under these conditions, but the majority of these studies used relatively exotic model compositions of lunar, Martian, and asteroidal melts because such low $fO_2$ levels are much more likely in igneous processes on other planetary bodies. Therefore, the goal of Chapter 4 was to parameterize the composition-dependence of the $K_{D,Fe2+-Mg}$ at low $fO_2$ using bulk compositions that are representative of those found on Earth.

The results of the Re wire loop experiments are largely in agreement with previous parameterizations of the $K_{D,Fe2+-Mg}$ (Ford et al. 1983; Toplis et al. 2005), and suggest significant effects of liquid composition due to $SiO_2$, $TiO_2$, $Al_2O_3$, $Na_2O$, and $K_2O$, as well as olivine composition. It is shown algebraically that given sufficient knowledge of individual element partition coefficients, the olivine composition can be expressed in terms of FeO or MgO in the liquid. The results show that olivine composition alone (Blundy et al. 2020) can only account for variations in the $K_{D,Fe2+-Mg}$ over a narrow range of liquid compositions, and that parameters based on $TiO_2$, and alkali content are required to describe the variability in $K_{D,Fe2+-Mg}$ observed at low $fO_2$, particularly when extended to include experiments run on exotic planetary compositions. A refined database of experiments with olivine-liquid pairs run at low pressures and at $fO_2$ no greater than 0.5 log units above the iron-wüstite buffer is presented; experiments were filtered for mass balance and for the quality of analytical measurements including olivine stoichiometry. These experiments, along with the new Re loop experiments, were combined to calibrate a

quantitative and thermodynamic model of the effect of T, melt, and olivine composition on the $K_{D,Fe2+-Mg}$. This knowledge is required for accurately modeling crystallization and melting processes involving olivine, which are important for understanding the genesis of primitive mantle melts and for reconstructing mantle potential temperatures on Earth and on other planetary bodies (e.g. Herzberg & O'Hara 2002; Filiberto et al. 2011; Putirka 2016).

Finally, in Appendix 1 a paper on which I was second author is included (Richter & Saper, et al. 2021), which looked at coupled elemental and isotopic profiles in zoned minerals from Mars and from the moon to place constraints on the thermal evolution of their host rocks. Mg and Li profiles in olivines and pyroxenes were used as case studies to demonstrate how the elemental zoning and kinetic isotopic fractionation profiles can be used in tandem to discriminate between zoning formed due to crystallization and differentiation, the degree to which this zoning was modified by diffusion, or whether zoning is due entirely to diffusion. My main contribution to this paper was running alphaMELTS (Smith & Asimow 2005) models to constrain the expected zoning profiles due to crystallization and differentiation, and to define temperature-dependent boundary conditions between the growing crystal and the surrounding melt for elemental and isotopic diffusion modelling.

## 1.1. References

BVSP 1981. *Basaltic Volcanism on the Terrestrial* Planets. New York: Pergamon Press. P1286

Berry, A.J, Shelley, J.M.G., Foran, G.J., O'Neill, H.S.C., Scott, D.R. (2003). A furnace design for XANES spectroscopy of silicate melts under controlled oxygen fugacities and temperatures to 1773K. *Journal of Synchotron Radiation*, 10, p.332-335

Blundy, J., Melekhova, E., Ziberna, L., Humphreys, M.C.S., Cerantola, V., Brooker, R.A., McCammon, C.A., Pichavant, M., Ulmer, P. (2020). Effect of redox on Fe-Mg-Mn exchange between olivine and melt and an oxybarometer for basalts. *Contributions to Mineralogy and Petrology*. 175:103

Borisov, A.A., Jones, J.H. (1999). An evaluation of Re, as an alternative to Pt, for the 1 bar loop technique: an experimental study at 1400 °C. *American Mineralogist*, 84, p.1528-1534

Borisov, A.A., Behrens, H., Holtz, F. (2018). Ferric/ferrous ratio in silicate melts: a new model for 1 atm data with special emphasis on the effects of melt composition. *Contributions to Mineralogy and Petrology*, 173:98

Bowen, N.L., Schraier, J.F. (1935). The system MgO-FeO-$SiO_2$. *American Journal of Science*, s.5-29, 170, p.151-217

Bucholz, C.E., Gaetani, G.A., Behn, M.D., & Shimizu, N. (2013). Post-entrapment modification of volatiles and oxygen fugacity in olivine-hosted melt inclusions. *Earth and Planetary Science Letters*, 374, p.145-155

Danyushevsky, L.V., McNeill, A.W., & Sobolev, A.V. (2002a). Experimental and petrological studies of melt inclusions in phenocrysts from mantle-derived magmas: an overview of techniques, advantages and complications. *Chemical Geology*, 183, p.5-24,

Ferriss, E., Plank, T., Newcombe, M., Walker, D., & Hauri, E. (2018). Rates of dehydration of olivines from San Carlos and Kīlauea Iki. *Geochimica et Cosmochimica Acta*, 242, p.165-190

Filiberto, J., Dasgupta, R. (2011). $Fe^{2+}$-Mg partitioning between olivine and basaltic melts: applications to genesis of olivine-phyric shergottites and conditions of melting in the Martian interior. *Earth and Planetary Science Letters*, 304(3-4), p.527-537

First, E., Hammer, J. (2016). Igneous cooling history of olivine-phyric shergottite Yamato 980459 constrained by dynamic crystallization experiments. *Meteoritics & Planetary Science,* 51(7) p.1233-1255

Ford, C.E., Russell, D.G., Craven, J.A., Fisk, M.R. (1983). Olivine-liquid equilibria: temperature, pressure, and composition dependence of the crystal/liquid cation partition coefficients for Mg, $Fe^{2+}$, Ca and Mn. *Journal of Petrology*, 24(3), p.256-266

Gaetani, G.A., O'Leary, J.A., Shimizu, N., Bucholz, C.E., & Newville, M. (2012). Rapid reequilibration of H2O and oxygen fugacity in olivine-hosted melt inclusions. *Geology*, 40(10), p.915-918

Grove, T.L. (1981). Use of FePt alloys to eliminate the iron loss problem in 1 atmosphere gas mixing experiments: theoretical and practical considerations. *Contributions to Mineralogy and Petrology*, 78, p.298-304

Head, E., Lanzirotti, A., Newville, M., & Sutton, S. (2018). Vanadium, sulfur, and iron valances in melt inclusions as a window into magmatic processes: a case study at Nyamuragira volcano, Africa. *Geochimica et Cosmochimica Acta*, 226, p.149-173

Herzberg, C., O'Hara, M.J. (2002). Plume-associated ultramafic magmas of Phanerozoic age. *Journal of Petrology*, 43(10), p.1857-1883

Jugo, P.J., Wilke, M., & Botcharnikov, R.E. (2010). Sulfur K-edge XANES analysis of natural and synthetic glasses: implications for S speciation and S content as function of oxygen fugacity. *Geochimica et Cosmochimica Acta*, 74(20), p.5926-5938

Klimm, K., Kohn, S.C., & Botcharnikov, R.E. (2012). The dissolution mechanism of Sulphur in hydrous silicate melts. II: Solubility and speciation of Sulphur in hydrous silicate melts as a function of $fO_2$. *Chemical Geology*, 322-323, p.250-26

Matzen, A.K., Baker, M.B., Beckett, J.R., & Stolper, E.M. (2011). Fe-Mg partitioning between olivine and high-magnesian melts and the nature of Hawaiian parental liquids. *Journal of Petrology*, 52(7:8), p.1243-1263

Metrich, N., Berry, A.J., O'Neill, H.S.C., & Susini, J. (2009) The oxidation state of sulfur in synthetic and natural glasses determined by X-ray absorption spectroscopy. *Geochimica et Cosmochimica Acta*, 73, p.2382-2399

Nash, W.M., Smythe, D.J., & Wood, B.J. (2019). Compositional and temperature effects on sulfur speciation and solubility in silicate melts. *Earth and Planetary Science Letters*, 507, p.187-198

Newcombe ME, Brett A, Beckett JR, Baker MB, Newman S, Guan Y, Eiler JM, Stolper EM (2017) Solubility of water in lunar basalt at low pH2O. Geochimica et Cosmochimica Acta 200 p.330-352

O'Neill, H.S.C. (2021). Comment on "Compositional and temperature effects on sulfur speciation and solubility in silicate melts" by Nash et al. [Earth Planet. Sci. Lett. 507 (2019) 187-198]. *Earth and Planetary Science Letters*, 560, 116843

Richter, F., Saper, L., Villeneuve, J., Chaussidon, M., Watson, B.E., Davis, A.M., Mendybaev, R.A., Simon, S.S (2021) Reassessing the thermal history of martian meteorite Shergotty and lunar mare basalt Apollo 15555 using kinetic isotope fractionation of zoned minerals. *Geochimica et Cosmochimica Acta*, 295

Roedder, E. (1979). Origin and significant of magmatic inclusions. *Bulletin of Mineralogy*, 102, p.487-510

Roedder, E., (1992). Fluid inclusions. *Encyclopedia of Physical Science and Technology, Third Edition, Volume 6*, Academic Press

Schiavi, F., Provost, A., Schiano, P., & Cluzel, N. (2016). P-V-T-X evolution of olivine-hosted melt inclusions during high-temperature homogenization treatment. *Geochimica et Cosmochimica Acta,* 172, p.1-21

Smith, P.M., & Asimow, P.D. (2005). Adiabat 1ph: A new public front-end to the MELTS, pMELTS, and pHMELTS models. Geochemistry Geosphysics Geosystems 6, art. no. Q02004m

Toplis, M.J. (2005). The thermodynamics of iron and magnesium partitioning between olivine and liquid: criteria for assessing and predicting equilibrium in natural and experimental systems. *Contributions to Mineralogy and Petrology*, 149, p.22-39

Wallace, P.J., & Carmichael, I.S.E. (1994). S speciation in submarine basaltic glasses as determined by measurements of SKα X-ray wavelength shifts. *American Mineralogist*, 79, p.161-167

*Chapter 2*

# Controlled cooling rate experiments on olivine-hosted melt inclusions: chemical diffusion and the cooling rates of lavas on Hawai‘i and Mars

Lee M. Saper

Edward M. Stolper

## 1 Abstract

Controlled cooling-rate experiments were conducted on olivine-hosted melt inclusions to characterize the development of compositional zoning observed in natural inclusions. All of the experimentally cooled inclusions are zoned due to olivine crystallization on the inclusion wall and diffusive exchange between the boundary layer adjacent to the growing olivine and the inclusion centers. Experimentally cooled inclusions are characterized by lower MgO and FeO, and higher $SiO_2$, $Al_2O_3$, $Na_2O$ (and other incompatible oxides) near the inclusion wall relative to the inclusion center. The compositions at the centers of inclusions are susceptible to modification by diffusion, particularly for small inclusions and those subjected to low cooling rates. Uphill diffusion is evident in every oxide and is recognized by local extrema along a diffusion profile. CaO exhibits the most extreme manifestation of uphill diffusion, and a model attributes the diffusion behavior in CaO to solution nonideality in the boundary layer liquid. MgO profiles from experimentally cooled inclusions were fit with a diffusion model by varying the cooling rate. The cooling rate which resulted in the best-fit was always within a factor of two and typically within ±10% of the experimental cooling rates, which ranged from 70–50,000 °C/hr. The model was applied to MgO profiles across natural glassy olivine-hosted melt inclusions from Hawai‘i and the shergottite Yamato 980459. Cooling rates from zoned melt inclusions in Yamato 980459 range from 85–1047 °C/hr (mean = 383±43 °C/hr, 1σ, n=8), and support the hypothesis that the sample erupted at or near the Martian surface.

## 2 Introduction

Efforts to analyze the compositions of glass inclusions in natural crystals at high spatial resolution have demonstrated that concentration gradients are preserved near the

interface between the glass and its host (e.g., Anderson, 1974; Goodrich, 2001; Danyushevsky et al.. 2002b; Mercier, 2009; Colin et al., 2012; Newcombe et al., 2014; Manzini et al., 2017; Drignon et al., 2019). These concentration gradients are interpreted as having been generated by diffusive relaxation of a compositional boundary layer in the liquid that forms as the host mineral crystallizes on the inclusion wall during cooling (Albarède & Bottinga, 1972; Watson, 1982; Zhang, 1989; Danyushevsky et al., 2000; Newcombe et al., 2014). As the host phase crystallizes from the melt inclusion, the adjacent liquid becomes progressively depleted in components that are compatible in the host phase (e.g., MgO and FeO in olivine) and enriched in incompatible components that are excluded from the growing crystal. Compositional zoning develops from continuous diffusive exchange between the evolving liquid at the boundary with the host phase and the liquid in the center of the melt inclusion. Zonation is preserved in glass inclusions that are cooled sufficiently rapidly such that the concentration gradients generated during cooling do not have time to homogenize by diffusion.

Newcombe et al. (2014) developed a model for the evolution of one-dimensional diffusion profiles in olivine-saturated spherical melt inclusions during cooling. By varying the cooling history, the authors fit this model to MgO concentration profiles measured in natural inclusions. Best-fit cooling histories assuming constant cooling rates for inclusions from the Siqueros Fracture Zone (subaqueous MORB: cooling rates of 400–4200 °C/hr) and from the Galapagos Islands plume (subaerial: 4400–12,700 °C/hr, and subaqueous: 155 °C/hr and 4400 °C/hr) overlap with the range of eruptive cooling rates for terrestrial lavas calculated by independent methods such as enthalpy relaxation speedometry in basaltic

glasses (e.g., Wilding 2000; Nichols et al., 2009) and $H_2O$ speciation kinetics in rhyolitic glasses (Xu & Zhang, 2002).

In this paper, we report the results of a series of 1-atm controlled cooling experiments conducted on olivine-hosted melt inclusions to explore the cooling rate dependent evolution of compositional zoning and to test the accuracy of determining cooling rates by inverting observed concentration gradients in MgO. The experiments support the interpretation that the zonation observed in melt inclusions is generated during syneruptive cooling of the host magma by the competing effects of the crystallization of olivine on the inclusion wall and diffusive exchange between melt at this boundary and in the interior of the melt inclusion. Subject to various assumptions (Section 4), the model olivine-inclusion system can be used to retrieve cooling rates that accurately recover the measured cooling rates of the experiments conducted over ~3 orders of magnitude to within a factor of 2 or better (typically within ±10%). We conclude that because melt inclusions are common, microprobe analyses are routine, and diffusion in the liquid is rapid relative to that in solids, compositional zonation at melt-crystal boundaries has potential as a tool for quantifying the late-stage thermal histories of rapidly cooled geologic samples.

## 3 Methods

### 3.1 Sample selection

Olivine-rich sand was collected by M.B. Baker from Papakōlea Beach (Pu'u Mahana), ~3 miles northeast of South Point, Hawai'i (18°56'N, 155°38'W). The sands are remnants of 28 kyr wave-eroded olivine basalt flows and ash beds (Rubin et al., 1987), interpreted to be either a littoral cone (Stearns & Macdonald, 1947) or a primary ash vent (Walker, 1992) on the southern flank of Mauna Loa. Olivine grains 1–3 mm in largest

dimension containing roughly spherical, glassy melt inclusions were separated from beach detritus under an optical microscope. Glassy inclusions are typically 100–150 μm in largest dimension and up to 250 μm across. Olivines that contained at least one roughly spherical inclusion ≥75 μm across were selected as starting materials for use in experiments. In transmitted light, glassy inclusions were orange-brown and translucent (Figure 1), but occasionally were clouded by clusters of olivine and pyroxene crystals. When such crystalline phases exceeded ca. several volume percent, an inclusion was rejected as a potential sample.

Similarly, olivine crystals that had obvious alteration features (e.g., surface oxidation, etch pits, pervasive cracks, etc.) were discarded. The glassy inclusions chosen for the experiments all contained an exsolved vapor bubble and minor (less than a few volume percent) Cr-Al-rich spinel, recognized as opaque octahedra usually attached to the inclusion wall or vapor bubble. Small, roughly spherical sulfide blebs (<5 μm diameter) were observed in a few natural inclusions, usually at the inclusion wall.

In total, 55 olivine grains containing one or more suitable melt inclusions were used in experiments and subsequently recovered and quantitatively analyzed. Optical photomicrographs of a typical inclusion taken through the host olivine suspended in isopropanol before and after an experiment are shown in Figure 1. An additional 10 inclusion-bearing olivines were not reheated (hereafter referred to as *natural* as opposed to *experimental*); these were studied to characterize the zoning profiles in naturally occurring olivine and glass compositions for comparison with experimentally treated samples. Experimental inclusions are labeled according to the scheme H#X#, where the first number corresponds to the experiment (e.g., H2X) and the second to a particular olivine grain (e.g.,

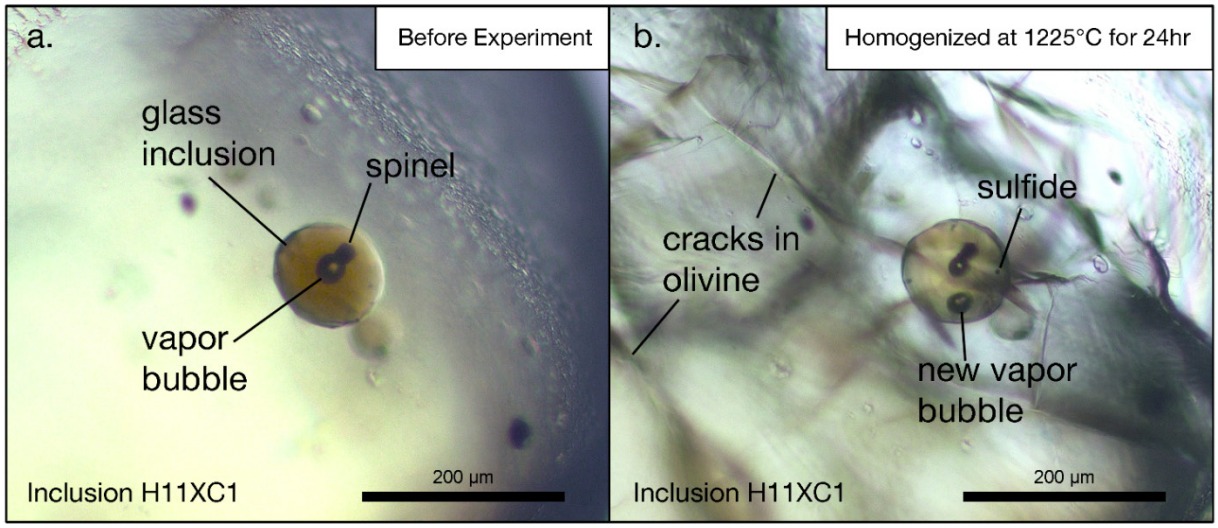


**Figure 1.** Optical photomicrographs (10x magnification) of an olivine-hosted glass inclusion (H11XC1) prior to (**a**) and after (**b**) experimental homogenization, photographed through an unpolished olivine grain suspended in isopropanol. The glass inclusion is the circular orange-brown feature, which initially contains a vapor bubble and spinel crystal (**a**). Note that in this sample, after an isothermal hold at 1225°C for 24 hours at an $fO_2$ of FMQ-1.15, a second vapor bubble formed; the original bubble has shrunk in size but remains in contact with the spinel at approximately the same location as prior to heating (**b**). Opaque spherules of immiscible sulfide liquid are also visible in (**b**). The shape and size of the glass inclusion did not change at this scale of observation after experimental treatment. The experimentally homogenized olivine grain is pervasively cracked due to thermal contraction upon quenching. Scale bar is 200 µm.

H2X1, H2X2, etc.). If more than one inclusion was analyzed in a single olivine grain, then they are distinguished by adding "_#" to the label (e.g., inclusions H5X4_1 and H5X4_2). Homogenized inclusions are indicated by the letters XC in the sample name, e.g., H10XC1. Natural inclusions from Papakōlea Beach are labeled HIGS#.

In addition to the ten natural melt inclusions from Papakōlea Beach, one melt inclusion in each of four olivines from sand in the Kīlauea Iki crater were also studied (labeled KIO#), as were eight melt inclusions in five olivines from a polished thin section of the Yamato 980459 (Y980459) shergottite meteorite (labeled Y98MI#), on loan from the Japanese National Institute for Polar Research. The Kīlauea Iki melt inclusions are petrographically similar from the Papakōlea samples, and the melt inclusions from Y984059 are described in more detail in Section 6.2.

### 3.2 Experimental procedures

Homogenization and cooling experiments were run in a 1-atm Deltech vertical gas-mixing furnace. Two or three MgO buckets (drilled to a depth of ~3.5 mm), each containing 3–6 olivine grains, were suspended in the furnace hotspot from an MgO rod with 0.127 mm Pt hanging wire, adjacent to a Type-S thermocouple. This thermocouple was calibrated at the melting point of gold. In most experiments, the buckets were gradually lowered into the hotspot and held isothermally at 1225 ºC for 24 hr in order to homogenize the melt inclusions and to equilibrate the inclusions with the $fO_2$ of the furnace gas (Gaetani et al. 2012; Bucholz et al. 2013). One set of experiments, H10X, was homogenized at 1260 °C for 24 hr. Temperature was monitored and recorded manually throughout the isothermal heating period and then recorded digitally during cooling using a temperature logger (Omega UTC-USB, one measurement per second) connected to the Type-S thermocouple. For all experiments,

after 24 hr of homogenization, one of the olivine-bearing buckets was drop-quenched into water by fusing the Pt hanging wire.

Immediately after quenching the first bucket, cooling was initiated and the remaining buckets were subjected to a controlled temperature (T) vs. time (t) history. For cooling rates of 70–1570 °C/hr (six experiments), linear cooling to a set point of 800 °C was programmed using a Eurotherm controller attached to a Type B thermocouple near the furnace elements. For most experiments, the cooling olivine-bearing buckets were drop-quenched in water when the thermocouple adjacent to the sample read 1000 °C. To monitor time- and temperature-dependent changes in the experiments during cooling, two sets of experiments (H2X at 1570 °C/hr and H11X at 466 °C/hr) were quenched at multiple temperatures between 1225 °C and 1000 °C (H2X) or 900 °C (H11X). Due to a limit on how fast the furnace can reject heat, cooling rates ≥1600 °C/hr were achieved in two sets of experiments (H4X and H9X) by manually displacing downward the rod on which the olivine-bearing buckets were suspended, such that the samples moved out of the furnace hotspot into a cooler part of the furnace in less than 2 seconds. In order to monitor temperature during cooling using this displacement method, a Type S thermocouple was placed inside an empty MgO bucket and attached to the same rod that carried the olivine container so they moved out of the hotspot in tandem (see Supplementary Figure S1 for a schematic diagram of the experimental setup). For the two experiments cooled using this displacement method, the temperatures at the displaced position were 415 °C (H4X) and 930 °C (H9X). The cooling olivine-bearing buckets in the displacement experiments were quenched in water when the digital thermocouple output read 1000 °C. Finally, the experiment held at 1260 °C for 24 hr, H10X, did not cool on a single linear t-T path as did all the others, but rather was broken into

two cooling segments: 1260 °C to 1134 °C at 93 °C/hr and 1134 °C to 1000 °C at 859 °C/hr. Table 1 details the experimental run conditions for all of the experiments. Thermocouple data from the experiments are shown in Figure 2 and described in more detail in Section 3.1.

Oxygen fugacity was controlled using an $H_2$-$CO_2$ gas mixture that was calibrated with an $Y_2O_3$-stabilized $ZrO_2$ oxygen sensor. For all runs, the gas mixture was fixed (14% $H_2$ and 86% $CO_2$, by volume) such that the $fO_2$ at the temperature of the hotspot during the 24 hr homogenization step at 1225 °C was ΔFMQ = -1.15±0.07 ($\log_{10}$ relative to fayalite-magnetite-quartz (ß) buffer (FMQ); Frost 1991). Note that experiment H10X, which was homogenized at 1260 °C was run under the slightly more reducing conditions of ΔFMQ = -1.34 (Table 1). The uncertainty in the measured $fO_2$ is ~0.05 log units based on bracketing the Fe→FeO reaction in the furnace and monitoring emf fluctuations of the oxygen sensor during the isothermal homogenization step. During cooling from 1225 °C, the mixing ratio of the gas was unchanged, resulting in a progressive decrease in the furnace $fO_2$ to ΔFMQ = -1.8 at 1000 °C based on monitoring of the oxygen sensor; this is slightly more reducing than the expected change in $fO_2$ to ΔFMQ = -1.6 if the $H_2$-$CO_2$ gas maintained equilibrium down to 1000 °C (Beckett & Mendybaev, 1997). The $fO_2$ for the experiments was chosen to be within the range of calculated $fO_2$ values based on wet chemically determined $Fe^{3+}/Fe^{2+}$ of glasses from Mauna Loa lava flows (ΔFMQ = -2.5 to +1, with 10 of 15 samples within 0.5 log units of ΔFMQ = -1; Rhodes & Vollinger, 2005).

After the completion of the experiments, Dr. Mary Peterson measured one doubly polished experimental inclusion homogenized at 1225 °C and quenched in water, and two unheated Papakōlea inclusions using Fe X-ray absorption near edge structure spectroscopy (XANES) at the Advanced Photon Source, Argonne National Laboratory. One additional

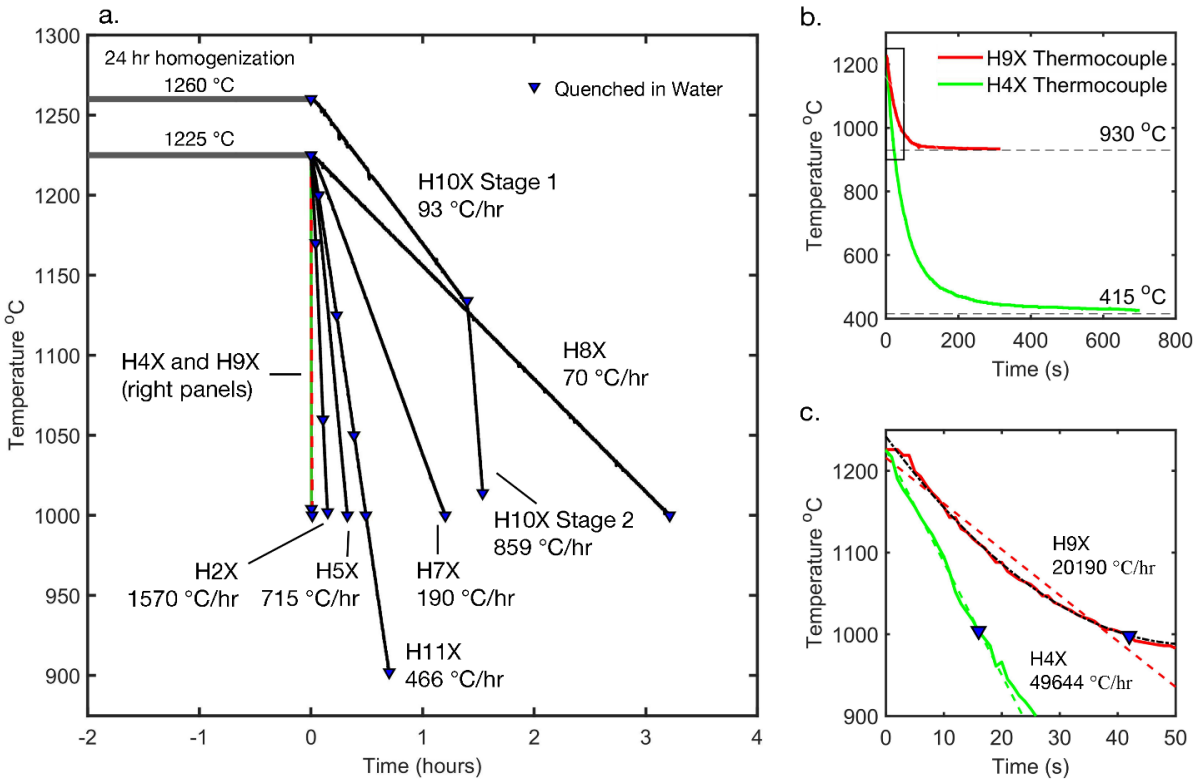


**Figure 2.** (**a**) Digitally logged Type-S thermocouple measurements from cooling experiments. Time = 0 on the x-axis corresponds to the initiation of cooling. Thick solid grey lines indicate the homogenization conditions (7 sets of experiments at 1225 °C, and one set (H10X) at 1260 °C), which extend to minus 24 hours prior to the onset of cooling (Time = 0) for all experiments. Blue triangles indicate temperatures along the cooling paths at which a bucket of olivine was drop-quenched into water. Note that H10X, the experiment homogenized at 1260 °C has two linear cooling stages. The reported cooling rates (°C/hr) are linear best-fits to the thermocouple data for $t \geq 0$. The colored lines indicate experiments H9X and H4X, which are shown in the panels on the right side of the figure. (**b**) Thermocouple measurements from the two fastest cooling rate experiments, H9X and H4X, which were cooled using the displacement method (See Section 2.2). The dashed lines indicate the temperature in the furnace after displacement of the MgO rod containing the experimental samples. The black rectangle shows the extent of panel **c**. (**c**) Initial 50 seconds of cooling during the displacement method for experiments H9X (red line) and H4X (green line). Blue triangles indicate temperatures along the cooling paths at which a bucket of olivine was drop-quenched into water. The dashed red and green lines are linear fits to the thermocouple data from t = 0 until the time and temperature of the drop-quench, and the corresponding rates are 20,190 °C/hr (H9X) 49,644 °C /hr (H4X). The dashed black line is a 2$^{nd}$ order polynomial fit to the H9X thermocouple data, which is a better approximation than the linear fit but intersects t = 0 at 1242 °C, which is well above the actual homogenization temperature of 1225 °C. For the purposes of this paper we adopt the linear fit to the H9X thermocouple data.

***Table 1 - Experimental Conditions***

| Name | Homog Temp °C | Quench Temp °C (n)[a] | Stage 1 (°C/hr) | Stage 2 (°C/hr) | Cooling method[b] | emf[c] | $\log_{10}fO2$ (bars) | ΔFMQ[d] |
|---|---|---|---|---|---|---|---|---|
| H2X | 1225 | 1225 (1), 1160 (2), 1070 (2), 1000 (5) | 1570 | - | T.C. Controlled | -682 | -9.18 | -1.16 |
| H4X | 1225 | 1000 (5) | 49640 | - | Displacement | -682 | -9.18 | -1.16 |
| H5X | 1225 | 1225 (2), 1000 (4) | 715 | - | T.C. Controlled | -682 | -9.18 | -1.16 |
| H7X | 1225 | 1225 (2), 1000 (3) | 190 | - | T.C. Controlled | -680 | -9.15 | -1.13 |
| H8X | 1225 | 1225 (1), 1000 (3) | 70 | - | T.C. Controlled | -680 | -9.15 | -1.13 |
| H9X | 1225 | 1000 (4) | 20190 | - | Displacement | -681 | -9.16 | -1.15 |
| H10X | 1260 | 1260 (3), 1134 (3), 1016 (3) | 93 | 859 | T.C. Controlled | -667 | -8.98 | -1.34 |
| H11X | 1225 | 1225 (1), 1200 (2), 1125 (2), 1050 (2), 1000 (2), 900 (2) | 466 | - | T.C. Controlled | -682 | -9.18 | -1.16 |

[a] n = number of olivine grains recovered and polished to expose melt inclusions.

[b] See section 2.2 for details.

[c] Measured with $Y_2O_3$-stabilized $ZrO_2$ oxygen sensor in furnace.

[d] Frost (1991)

experimental inclusion and two unheated Papakōlea inclusions were measured in a second XANES session by Dr. Maryjo Brounce (see the supplement of Brounce et al. 2017 for details of XANES methods and data reduction). The four unheated Papakōlea inclusions, each with two analyses at the inclusion centers, yielded $Fe^{3+}/Fe_{Total}$ ranging from 0.16–0.17 (inclusion HIGS21) to 0.20 (inclusion HIGS14) (Supplementary Table 1). This ratio of ferric to total iron in the Papakōlea glass compositions corresponds to ΔFMQ = +0.2 to +0.6 (Kress & Carmichael, 1991), which is considerably more oxidizing than the $fO_2$ of the gas mixture used in the heating/cooling experiments. The two experimentally homogenized inclusions (H7XC1 and H11XC1) were each measured twice with XANES and yielded $Fe^{3+}/Fe_{Total}$ of 0.06–0.07 and 0.07, respectively, which corresponds to a range of ΔFMQ = -1.7 to -2.3 at 1225 °C based on Kress and Carmichael (1991). The $Fe^{3+}/Fe_{Total}$ ratios of the homogenized melt inclusions decreased significantly during the 24 hr homogenization step, suggesting that the inclusions were in communication with the gas mixture outside their olivine hosts during the homogenization step of the experiments. However, at 0.06–0.07, their measured $Fe^{3+}/Fe_{Total}$ ratios are lower than the values of ~0.10 that would be expected based on the Kress and Carmichael model if the melt inclusion had equilibrated with the gas mixture in the furnace. This difference may be an artifact related to the accuracy of the measurement at low $Fe^{3+}$ contents, or perhaps due to the fact that Kress and Carmichael and the other available parameterizations of $fO_2$ vs. $Fe^{3+}/Fe^{2+}$ were calibrated with sulfur-free liquids. Preliminary XANES data on homogenization experiments at higher $fO_2$ indicate that the measured $Fe^{3+}$ is systematically lower than that predicted by Kress and Carmichael (1991), but when plotted as $\log_{10}(Fe^{3+}/Fe^{2+})$ vs $\log_{10}(fO_2)$ the data have the predicted slope of 0.2. In any case, the decrease in $Fe^{3+}/Fe_{Total}$ during the experiments from values of 0.16–0.19 based

on the XANES analyses of unheated Papakōlea glass inclusions to the lower values in the experimentally homogenized inclusions ($Fe^{3+}/Fe_{Total}$ = 0.06–0.07) is consistent with the $fO_2$ of the experimentally heated inclusions having changed by interaction with the furnace atmosphere across the olivine host during the 24-hour homogenization period (Gaetani et al. 2012, Bucholz et al. 2013). It is unlikely that during the controlled cooling phase of the experiments the changing $fO_2$ of the furnace was transmitted through the olivine to the melt inclusions due to the relatively short durations of cooling (Figure 2) and the exponential decrease in diffusivities with decreasing temperature (Bucholz et al., 2013).

To determine $H_2O$ contents, one doubly-polished experimentally homogenized inclusion (H7XC1) and four doubly-polished natural inclusions samples were measured using Fourier-Transform Infrared Spectroscopy (FTIR) (Supplementary Figure S2, Supplementary Table 1). Based on the intensity of the absorbance at 3550 $cm^{-1}$, a molar absorptivity of 63.8 L $mol^{-1}$ $cm^{-1}$ (Mercier, 2010), and an approximate glass density of 2.7 g $cm^3$, the natural glassy olivine-hosted melt inclusions from Papakōlea contain 0.10–0.27 wt % $H_2O$ (n = 4; 2-3 measurements per inclusion, 2σ = 0.02–0.04 wt %), within the range of published values for unheated Mauna Loa olivine-hosted melt inclusions (Sobolev et al., 2000; Hauri, 2002; Wallace et al., 2015). The single experimentally homogenized inclusion H7XC1 we measured has a water content of 383–388 ppm, suggesting that the inclusion lost most of its water during the isothermal homogenization step. This value is higher than but on the same order as the calculated solubility of ~250 ppm $H_2O$ in anorthite-diopside liquid at the $pH_2O$ (≈ 0.12 bars) of the furnace atmosphere at the experimental conditions (Newcombe et al., 2017).

### 3.3 Sample analysis

For electron microprobe analysis, the olivine grains were mounted in epoxy and ground down using alumina papers to expose the largest melt inclusion (if there were multiple inclusions) near its center. When the target melt inclusion center was maximally exposed, several other inclusions were often partially exposed, including in a few cases an additional relatively large melt inclusion as much as several

tens of micrometers across. The sample surface was then polished with increasingly fine diamond powder from to 2 to 0.25 μm grit, cleaned with ethanol, and carbon coated.

Concentration profiles of major and minor oxides were measured in both natural and experimentally treated melt inclusions along transects extending from the enclosing host olivine on one side of an inclusion, across its center, and then back out into the olivine on the opposite side using Caltech's JEOL JXA-8200 electron microprobe. Transects were selected to avoid vapor bubbles, spinel, and sulfide exposed on the polished surface, although in some cases the transects passed close to them. The electron beam was focused to <1 μm and analyses were spaced 1.5–2 μm apart with a 10 nA beam current and 15 kV accelerating voltage. Backscattered electron images were acquired of all the inclusions that we studied; a subset of the images of experimentally heated and cooled inclusions is shown in Figure 3, including for each inclusion the locations of the microprobe traverses shown in Figures 7, 8, and 13.

Quantitative wavelength-dispersive analyses (WDS) were done by measuring standards (listed in Table 2), periodically analyzing secondary glass standards, and correcting data using a modified ZAF procedure (Armstrong, 1988). Secondary glass standards (USGS BHVO-2g and BIR-1g) were analyzed three times before and after each microprobe traverse

to account for instrumental drift, however this information was not used for data correction. To assess accuracy, the analyses of the secondary glass standards from fifteen analytical sessions were averaged to determine the percent (relative) deviations from preferred reference values compiled in the GeoReM database (Jochum et al., 2006): +2.87 % for $SiO_2$, -5.95 % for $TiO_2$, -1.65 % for $Al_2O_3$, -2.19 % for FeO, -0.28 % for MgO, -0.63 % for CaO, -5.66 % for $Na_2O$, -14.46 % for $K_2O$, +5.78 % for MnO, and +12.65 % for $P_2O_5$. As a measure of intra-session accuracy, 30 replicate analyses of BIR-1g in a single session gave standard deviations relative to the mean of 0.28 % for $SiO_2$, 3.8 % for $TiO_2$, 0.98 % for $Al_2O_3$, 0.98 % for FeO, 1.02 % for MgO, 0.47 % for CaO, 2.78 % for $Na_2O$, 39.68 % for $K_2O$, 9.65 % for MnO, and 54.96 % for $P_2O_5$.

*Figure 3 is on the following page.*

**Figure 3.** Backscattered electron images of experimental olivine and glass inclusions. The glass inclusions in panels **b**, and **c** have vapor bubbles exposed at the polished surface. Bright phases in the inclusions include both sulfides (panels **b**, **c**, and **d**) and Cr-Al spinel (panels **b** and **f**). Contraction cracks are visible in all of the panels, and sometimes penetrate into the glass inclusion. The natural inclusions (not pictured here) look essentially the same as the experimental samples (e.g., see Figure 1a), except for the higher crack density in the experimental olivine. Thick translucent lines show the locations of high spatial resolution microprobe traverses (point beam analyses separated by 1.5–2 μm increments), which are shown in Figures 7, 8, and 13 from the same samples in the same 2x3 grid order. Crack-filling bright residue (e.g., panel **e**) is metal contamination from polishing.

**Figure 3** – Caption on previous page.

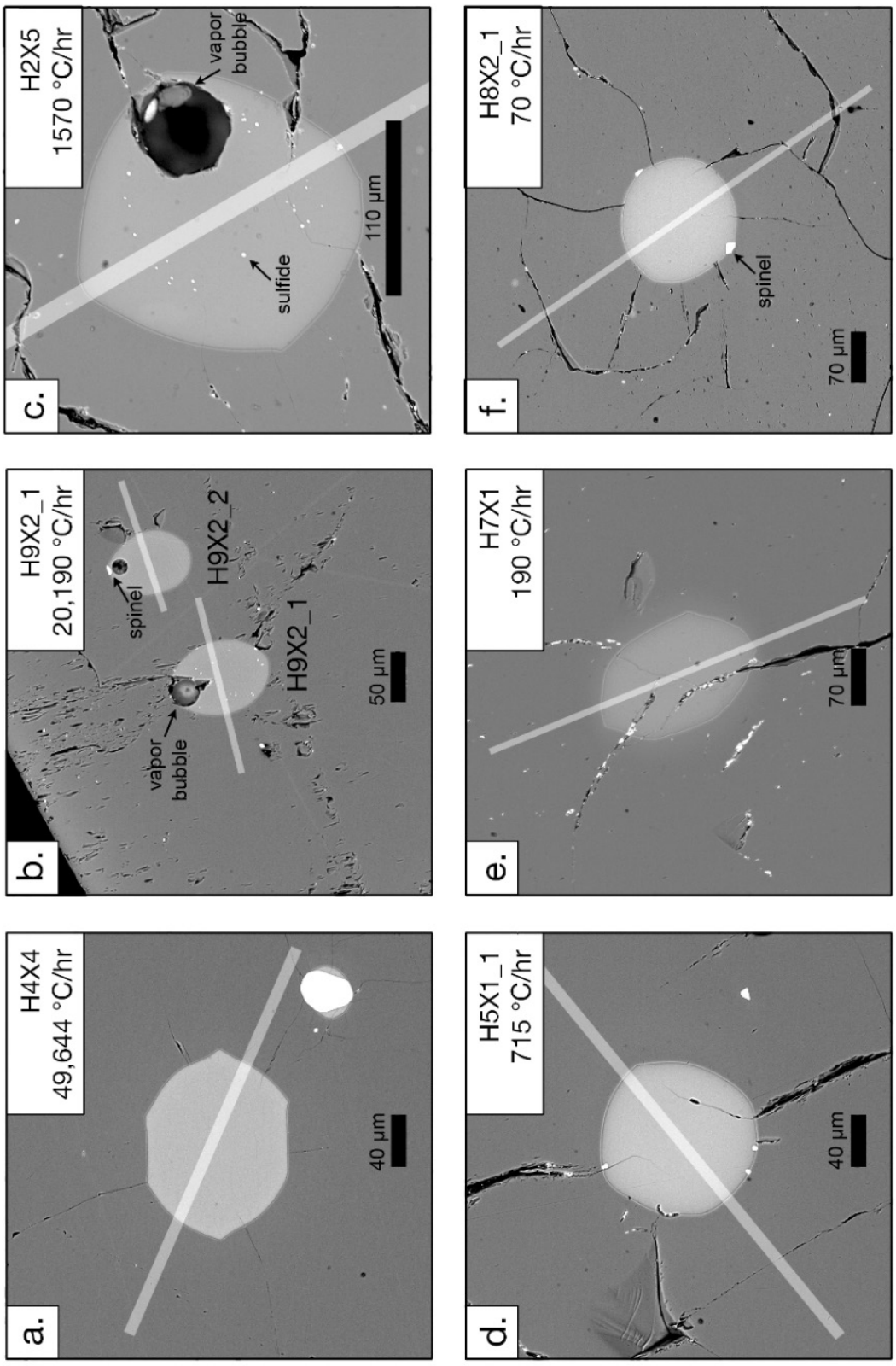

***Table 2 -*** *Compositions of far-field olivine and homogenized glass[a] measured by electron microprobe[b]*

| | Papakōlea Olivine (n=65), wt% (1σ) | Homogenized Glass[c] (n=8), wt% (1σ) | Standard |
|---|---|---|---|
| $SiO_2$ | 40.99 (0.61) | 53.23 (0.40) | VG2 basaltic glass |
| $TiO_2$ | 0.02 (0.01) | 2.14 (0.12) | Synthetic $TiO_2$ |
| $Al_2O_3$ | 0.04 (0.04) | 14.05 (0.35) | Synthetic Anorthite |
| FeO | 11.31 (1.13) | 7.66 (0.79) | Synthetic Fayalite |
| MgO | 47.16 (1.13) | 9.01 (0.13) | Shankland Forsterite |
| CaO | 0.21 (0.01) | 10.52 (0.19) | Synthetic Anorthite |
| $Na_2O$ | 0.007 (0.01) | 2.42 (0.20) | Amelia Albite |
| $K_2O$ | [c] | 0.33 (0.03) | Asbestos Microcline |
| MnO | 0.15 (0.02) | 0.13 (0.01) | Synthetic Tephroite |
| $P_2O_5$ | 0.03 (0.02) | 0.28 (0.06) | Durango Apatite |
| Fo% | 88.45 (1.72) | | |
| Totals | 99.92 (0.50) | 99.81 (0.23) | |

[a] 1225°C for 24 hrs,1 atm,$fO_2$ QFM-1

[b] Beam conditions: 15 kV accelerating voltage, 10 nA beam current, 1 μm beam size, 20s peak counting times, 10s on backgrounds

[c] Below detection limit of 0.008 wt%

# 4 Results

## 4.1 Natural olivine and glass inclusions (unheated)

Compositions were measured for ten unheated olivines from Papakōlea, Hawai‘i and their melt inclusions in order to establish the compositional range of olivines and melt inclusions in the starting materials. These samples provide a baseline for comparison with experimentally treated olivines and glass inclusions, which could not be exposed and measured prior to the experiments. For an individual grain, the olivine composition was defined by averaging ten analyses from the end of a microprobe traverse that was >150 μm away from a melt inclusion and at least 50 μm from the crystal edge. These analyses are referred to as the "far-field" olivine, which typically define compositional plateaus in the olivines (unless the host olivine was zoned) and are not strongly influenced by the presence of a melt inclusion (see Section 3.5 for details on zoning in olivine around the inclusions). The average of the mean forsterite contents (Fo = 100 x MgO/(MgO+FeO)) of the measured far-field olivine analyses is $Fo_{87.8\ (\pm 1.9)}$ (n = 10 olivine, where the number in the parentheses is 2σ of the distribution of means). When compared with previously published compositions for Mauna Loa olivine, the Papakōlea compositions overlap with the previous analyses (Supplementary Figure S3), and are concentrated near the forsteritic end of the range. We note here that the average far-field olivine composition of the experimentally treated population ($Fo_{88.9\ (\pm 1.7)}$ (n = 55), yellow squares in Supplementary Figure S3) is indistinguishable from the unheated olivine. Table 2 lists the average far-field olivine composition of the 65 analyzed olivines from Papakōlea, which includes the 10 natural and 55 experimental samples.

All of the natural glass inclusions are zoned. Near the inclusion wall, MgO and FeO are low and $SiO_2$, $Al_2O_3$, $Na_2O$, and $K_2O$ are high relative to the inclusion center (Figure 4ab). CaO was observed to be either high (Figure 4a) or low (Figure 4b) adjacent

to the inclusion wall, a phenomenon that has been attributed to uphill diffusion in the liquid (Newcombe et al., 2014) and is discussed in detail in Section 5. In five of the natural inclusions, there is a broad compositional plateau across the inclusion center and a narrow zone affected by diffusion near the inclusion wall (see sample HIGS9, Figure 4a), whereas in the remaining five, some or all of the oxide profiles are zoned across the entire inclusion (for example, MgO in sample HIGS6, Figure 4b). A bulk composition was calculated for each inclusion by approximating the inclusion as a sphere and numerically integrating each oxide profile across the inclusion. Corresponding average glass compositions (n = 10) span the following ranges: $SiO_2$ = 52–55 wt%, $TiO_2$ = 1.8–2.3 wt%, $Al_2O_3$ = 12–15 wt%, FeO* = 5.8–9.4 wt%, MgO = 6.2–7.2 wt%, $Na_2O$ = 1.9–2.4 wt%, $K_2O$ = 0.2–0.4 wt%, MnO = 0.11–0.16 wt%, and $P_2O_5$ = 0.1–0.3 wt %. The compositional zonation in the natural unheated glassy melt inclusions is discussed in more detail in Section 6.

### 4.2 Temperature-time paths of cooling experiments

Temperature was recorded during cooling using a digital logger attached to the Type-S thermocouple placed next to the olivine in the furnace hotspot (Figure 2). We chose to fit the temperature-time curves with lines (including each of the two roughly linear cooling segments in experiment H10X), and with the exception of experiment H9X (Figure 2c), the linear approximations fit the data with $r^2 > 0.9935$. As described in Section 2.2, experiments H4X and H9X were manually displaced from the hot spot in order to achieve high cooling rates. Because these two samples were displaced into a colder spot in the furnace, the measured thermal histories follow asymptotic temperature-time paths (Figure 2b), compared to the approximately linear cooling paths in the more slowly cooled experiments in which cooling was imposed by the Type-B control thermocouple (Figure 2a). For experiment H4X, the total duration of cooling was only

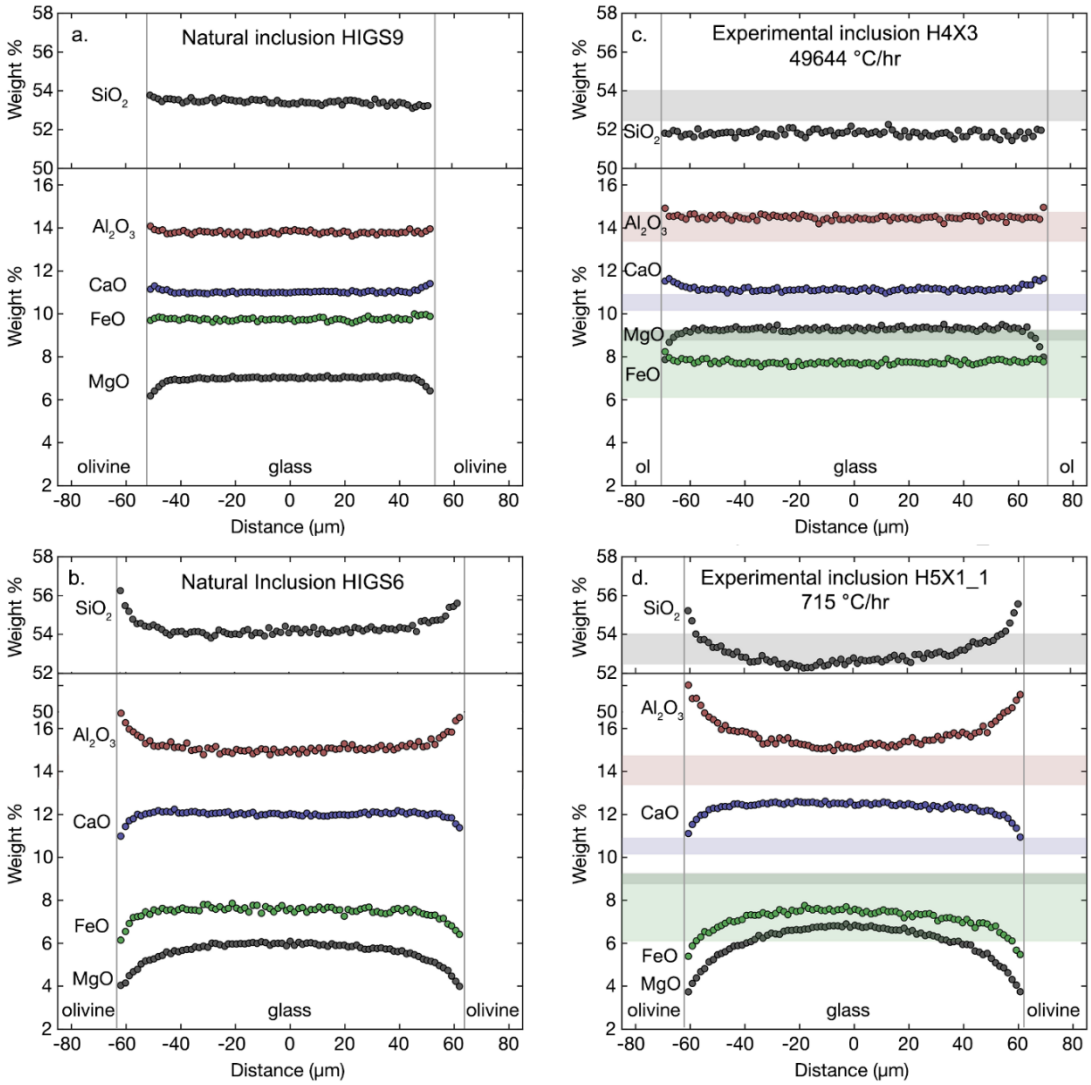


**Figure 4.** Microprobe traverses across selected natural unheated inclusions (left column, a and b) and experimentally homogenized and cooled inclusions (right column, c and d) from Papakolea, Hawaii. Shaded rectangles in c and d show the 2σ range about the mean value measured for each oxide across all inclusions experimentally homogenized at 1225 °C and quenched in water (Table 2, the values exclude liquid near the inclusion wall influenced by quench crystallization, see Section 3.4.1, Figure 5). Vertical grey bars indicate the boundary between glass (interior to the lines) and olivine (exterior to the lines). The x-axis is radial distance in micrometers relative to the center of the glass inclusion.

16 seconds and sufficiently rapid such that the cooling path from 1225 °C to 1000 °C corresponded to the steep initial limb of the asymptotic cooling curve, which is nearly linear (Figure 2c, $r^2 = 0.9935$, giving a linear rate of 49,644 °C/hr). In experiment H9X, the temperature-time curve between 1225 °C and 1000 °C has more curvature, and a parabolic fit ($r^2 = 0.9986$) is a better approximation than linear ($r^2 = 0.9642$). However, the best-fit polynomial curve intersects t = 0 at 1242 °C, which is well above the actual homogenization temperature of 1225 °C. For the purposes of the paper, for experiment H9X we use the best-fit linear rate of 20,190 °C/hr (Figure 2c). The best-fit linear cooling rates for each experiment is shown in Figure 2 and listed in Table 2.

### 4.3 Textural description of experimental samples

Olivine grains recovered from the experiments were first examined in transmitted light using an optical microscope. Cracks were pervasive in many experimentally quenched olivine grains, making individual inclusions difficult to see and photograph in transmitted light. Based on examination of the quenched samples in reflected light and in back-scattered electron imaging, cracks sometimes penetrated partially into the inclusions (e.g., Figure 3ade) suggesting that they were glassy prior to crack propagation, consistent with the fact that no melt was observed to have penetrated cracks in the olivine. These cracks probably formed due to contraction by thermal shock during the rapid drop-quench from high temperatures into room temperature water.

Optical images of samples taken before and after experimental homogenization do not show any significant change in inclusion volume or in its location within the olivine grain (Figure 1). A vapor bubble was present in every natural inclusion prior to the experiments, as well as in the inclusions quenched after the homogenization for 24 hr at 1225 °C or 1260 °C. The vapor bubbles did not change position or size significantly during the experiments, although rarely a second vapor bubble formed and the original

bubble shrank (e.g., Figure 1). Spinel crystals present inside the inclusions prior to experiments were not observed to change size or location during the experiment.

Opaque spherules are present in the experimentally heated inclusions and were determined by WDS to be sulfides of composition $Fe_{28-54}Cu_{1-4}Ni_{7-32}S_{21-36}$ (n = 6). Such sulfide blebs are found in at least one inclusion in 80% of the experimental olivines and are often spatially associated with the inclusion wall and vapor bubble (Figure 3c). Comparison of images of the inclusions before and after the experiments demonstrate that most (but not all) of these blebs formed during reheating. The formation of immiscible sulfide liquids is consistent with the reduced experimental conditions (ΔFMQ ≈ -1) which stabilizes $Fe^{2+}$ and $S^{2-}$ in the liquid relative to the more oxidized starting materials (ΔFMQ = +0.2 - +0.6) leading to sulfide oversaturation and precipitation of an FeS phase (Fincham & Richardson, 1954, O'Neill & Mavrogenes, 2002, Nash et al., 2019). Three out of twelve unheated Papakōlea olivines have one or two visible sulfide blebs in melt inclusions; the natural inclusions had fewer and larger sulfides than most of the experiments, and they do not seem to be associated with the vapor bubble. Some olivines contain multiple melt inclusions, some of which have sulfides and others that do not (e.g., H9X2_1 and H9X2_2 in Figure 3b); in these cases, the sulfide-bearing inclusions have higher total S ( e.g., 705–830 ppm in H9X2_1) compared to the sulfide-free inclusions ( e.g., 541–670 ppm in H9X2_2) (Note that S was measured three times at the center of each inclusion with a 5 μm beam under the same conditions as described in Section 2.3). The radii of 268 sulfides in experimental inclusions were measured in backscattered electron images, and they have a mean radius of 1 μm and a maximum of 4.6 μm. The four inclusions with the largest sulfides have a smaller number of blebs than other inclusions (three or less).

## 4.4 Compositional zonation in experimental inclusions

### 4.4.1 **Homogenized and quenched inclusions (not subjected to controlled cooling)**

In the liquid at 1225°C, the time scale for homogenization of the slowest diffusing species (e.g., $Al_2O_3$; Zhang, 2010; Guo & Zhang, 2016) is on the order of 100 minutes for the largest (~125 μm radius) inclusion we have studied, and the 24-hour isothermal heating was expected to be sufficiently long to relax any preexisting compositional gradients in the inclusions. This is corroborated by the representative microprobe profiles of homogenized inclusions shown in Figure 5, which demonstrate that after the 24-hr heating step, the glass compositions are homogeneous within the analytical uncertainty of the electron microprobe measurements. In some inclusions, particularly those homogenized and quenched from 1260 °C (Figure 5cd), microprobe analyses within 3 μm of the inclusion wall were affected by growth of olivine during the quench from high temperature and show the incipient development of a diffusion profile. Also shown in Figure 5 are the averages of the homogeneous glass compositions in all of the analyzed melt inclusions held at either 1225°C or 1260°C for 24 hr; the colored bands for each element represent ±2σ of these averages over all analyzed homogenized inclusions for each element (Table 2; the few points nearest the olivine that were affected by quench crystallization were discarded when determining these averages). The offsets of the colored bands relative to the data points for the individual profiles shown illustrates the variability of the homogenized glass compositions.

To assess whether local equilibrium between the olivine and melt was achieved during the 24-hr homogenization step, the $K_{D,Fe2+-Mg} = (Fe^{2+}/Mg)_{olivine}/(Fe^{2+}/Mg)_{liquid}$ was calculated for homogenized inclusions. $Fe^{2+}$ in the melt was calculated from the electron microprobe-measured total iron content and either the XANES-measured mean ratio of

$Fe^{3+}/Fe_{Total}$ of 0.07 or assuming $Fe^{3+}/Fe_{Total}$ = 0.10, which is the prediction based on Kress and Carmichael (1991) for a basalt in equilibrium with the furnace gas at ΔFMQ = -1.15 at either 1225 °C or 1260 °C. Taking the plateau FeO*/MgO of the homogenized inclusions and the olivine measured adjacent to the inclusion wall gives $K_{D,Fe\text{-}Mg}$ = 0.298–0.337 or 0.308–0.350 (n = 10 inclusion-olivine pairs) respectively, for the two assumptions for $Fe^{3+}/Fe_{Total}$ in the melt. These olivine-liquid $K_{D,Fe\text{-}Mg}$ values fall between estimates for natural melts from Kīlauea where $Fe^{3+}/Fe_{Total}$ was measured with XANES (0.280±0.06(2σ), Helz et al., 2016) and experimentally determined values for Hawaiian liquids (0.345±0.018(2σ), Matzen et al., 2011), consistent with local Fe/Mg equilibrium having been achieved between olivine on the inclusion wall and the coexisting liquid during the homogenization step.

#### 4.4.2 **Homogenized and cooled inclusions**

After the 24-hr homogenization step, one bucket of olivines was quenched, and the remaining olivine-bearing buckets were cooled at 70 to 50,000 °C/hr and then drop-quenched into water. Overall, the shapes and magnitudes of compositional gradients recorded in oxide concentration profiles from the experiments (right column in Figure 4) closely resemble those in natural samples from the Papakōlea flows (left column in Figure 4) and from the Galapagos Islands and Siqueros Fracture Zone (Newcombe et al., 2014). For example, in the most rapidly cooled inclusions (such as H4X3, cooled at ~50,000 °C/hr; Figure 4c), a boundary layer formed in the melt that is depleted in MgO and FeO (compatible oxides in olivine that are extracted from the melt during crystallization on the inclusion wall) and enriched in $SiO_2$, $Al_2O_3$, and CaO (relatively incompatible oxides that are excluded from the crystallizing olivine). The width of the boundary layer differs from oxide to oxide, reflecting their diffusivities in the melt (Newcombe et al., 2014), and the boundary layers terminate at compositional plateaus

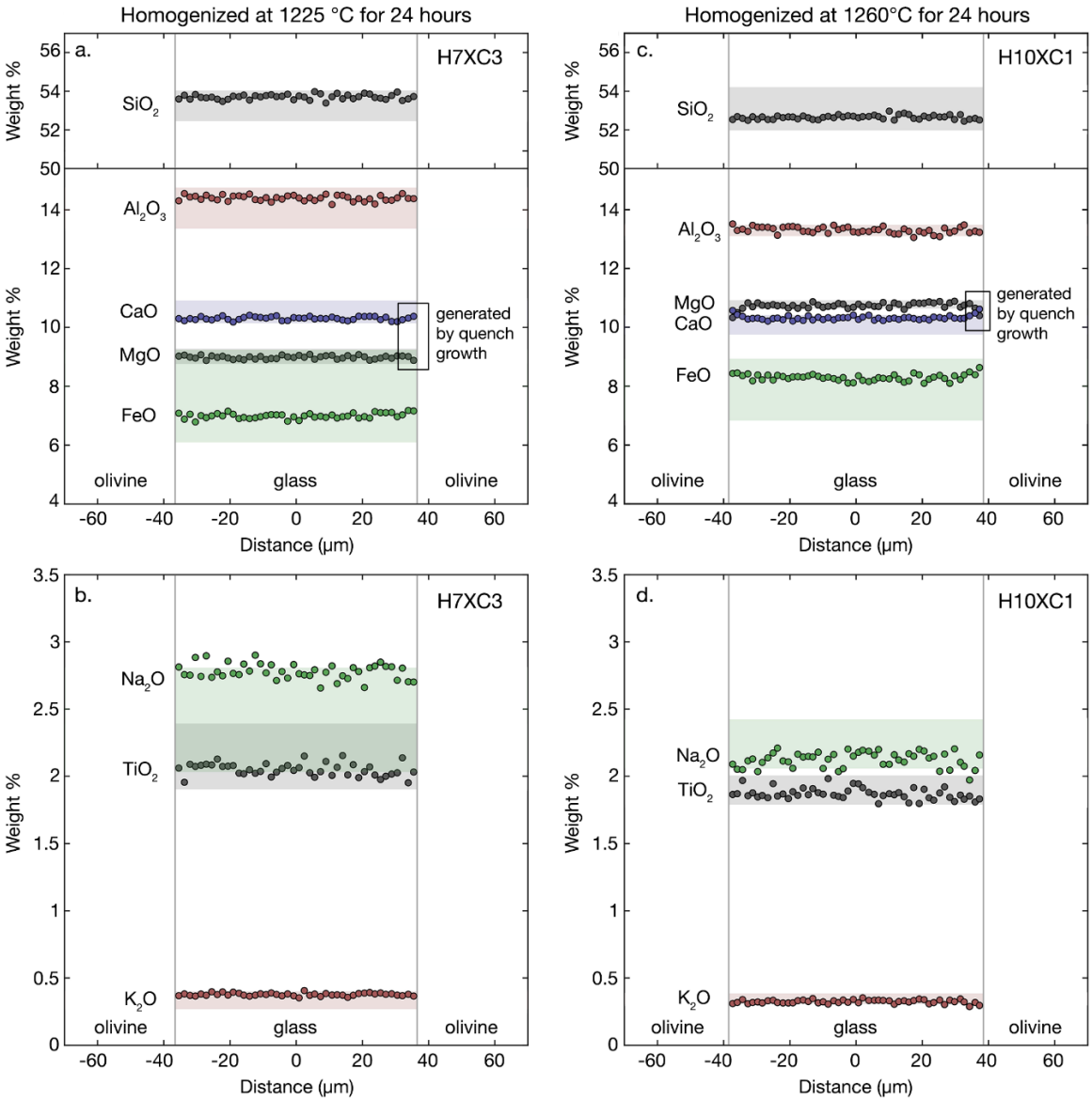


**Figure 5.** Microprobe traverses across experimentally homogenized olivine-hosted glass inclusions (i.e., not subjected to cooling after homogenization). Left column (panels a and b) show microprobe data (filled circles) from inclusion H7XC3, which was homogenized at 1225 °C for 24 hours; right column (panels c and d) show data from H10XC1, which was homogenized at 1260 °C for 24 hours. Shaded rectangles show the 2σ range about the mean value measured for each oxide across all inclusions homogenized at a particular temperature and drop-quenched in water (Table 2, n = 11 at 1225 °C, n = 3 at 1260 °C). Vertical grey lines indicate the boundary between glass and olivine. The black rectangles on the right side of the CaO and MgO profiles in panels a and c highlight the 2–3 data points adjacent to the olivine boundary that have been affected by olivine growth during quenching; these points were omitted when calculating the average composition of homogenized inclusions listed in Table 2. In total, melt inclusions in 11 olivine crystals were homogenized at 1225°C and then quenched and recovered, and 3 at 1260°C from experiment H10X).

established during the homogenization step. In natural sample HIGS9 (Figure 4b), a similar boundary layer is observed that is narrow relative to the inclusion radius, suggesting that it also experienced relatively rapid cooling. For experimental inclusions cooled at lower rates, the boundary layers are wider than for more rapidly cooled samples (compare Figure 4c and 4d). For example, in experimentally cooled inclusion H5X1_1 (Figure 4c, 715 °C/hr), the boundary layer generated by olivine crystallization on the inclusion wall reached the inclusion center, leading to lower FeO and MgO and higher $SiO_2$ and $Al_2O_3$ contents across the entire inclusion relative to the initially homogeneous composition, and to an absence of a plateau in the inclusion center. In some natural inclusions such as HIGS6 (Figure 4b), the profile shapes suggest a similarly prolonged cooling history that led to the formation of wider zones relative to that in HIGS9 (Figure 4a). Note that for both the rapidly and slowly cooled samples, the concentration profiles of the oxides that have higher concentrations in olivine than in the liquid (e.g., FeO and MgO) are concave down, whereas for most oxides with lower concentrations in olivine than in the liquid (e.g., $SiO_2$, $Al_2O_3$, $TiO_2$, $Na_2O$, $K_2O$, see Supplement Section 3), the profiles are concave up. However, although CaO is incompatible in olivine and its concentration profile is concave up in the rapidly cooled experimental inclusions (Figure 4, top row), in the slowly cooled samples CaO is depleted near the olivine wall whereas the inclusion center is enriched relative to the initial homogenized melt composition (i.e., it has a concave down profile similar to FeO and MgO despite the average CaO increasing in the liquid during cooling; Figures 4b and 4d). This anomalous CaO behavior, which was previously described in natural samples by Newcombe et al. (2014), is also observed in the natural Papakōlea and Kīlauea Iki inclusions and will be discussed in more detail in Sections 5 and 6.

Experiment H11X was cooled at 466 °C/hr after homogenization at 1225 °C and quenched at successively lower temperatures between 1200 °C and 900 °C. A temperature series of MgO concentration profiles across melt inclusions from these experiments demonstrate the systematic development and evolution of compositional zoning during cooling (Figure 6). Because MgO in the liquid reflects the progressive extraction of olivine and is used as the basis for modeling in Section 4, for emphasis and clarity it is the only oxide shown in Figure 6 (and Figure 7), but Supplement Section 3 includes plots similar to Figures 6 and 7 for the other oxides. Initially homogeneous at 1225 °C (Figure 6a), by 1200 °C (Figure 6b) sufficient olivine crystallization and diffusion had occurred over the 216 seconds since cooling began for the MgO-depleted boundary layer adjacent to the olivine to have reached the inclusion center such that the central MgO contents were lowered relative to the initial value of 9.01±0.26(2σ) wt% established during the homogenization step. With continued cooling, the MgO content of the liquid analyzed at the olivine-melt interface continually decreased as olivine was progressively extracted by crystallization on the inclusion wall, and the evolving boundary melt continued to exchange via diffusion with the inclusion interior. At lower temperatures (Figure 6d-6f), while MgO continued to decrease in the interface liquid with progressive olivine crystallization, diffusive exchange with the interior of the inclusion slowed because of decreasing temperature, resulting in steepening of the concentration profiles near the inclusion wall, and leaving the inclusion centers relatively unchanged. FeO is similarly concave down and progressively depleted in the interface liquid, whereas the relatively incompatible elements (e.g., $SiO_2$, $Al_2O_3$; but notably not CaO) show the opposite behavior, with interface melt concentrations increased relative to the starting liquid compositions and concave up diffusion profiles (e.g., Figure 4, and see Supplement Section 3). As emphasized by Newcombe et al. (2014), compositional zoning across melt

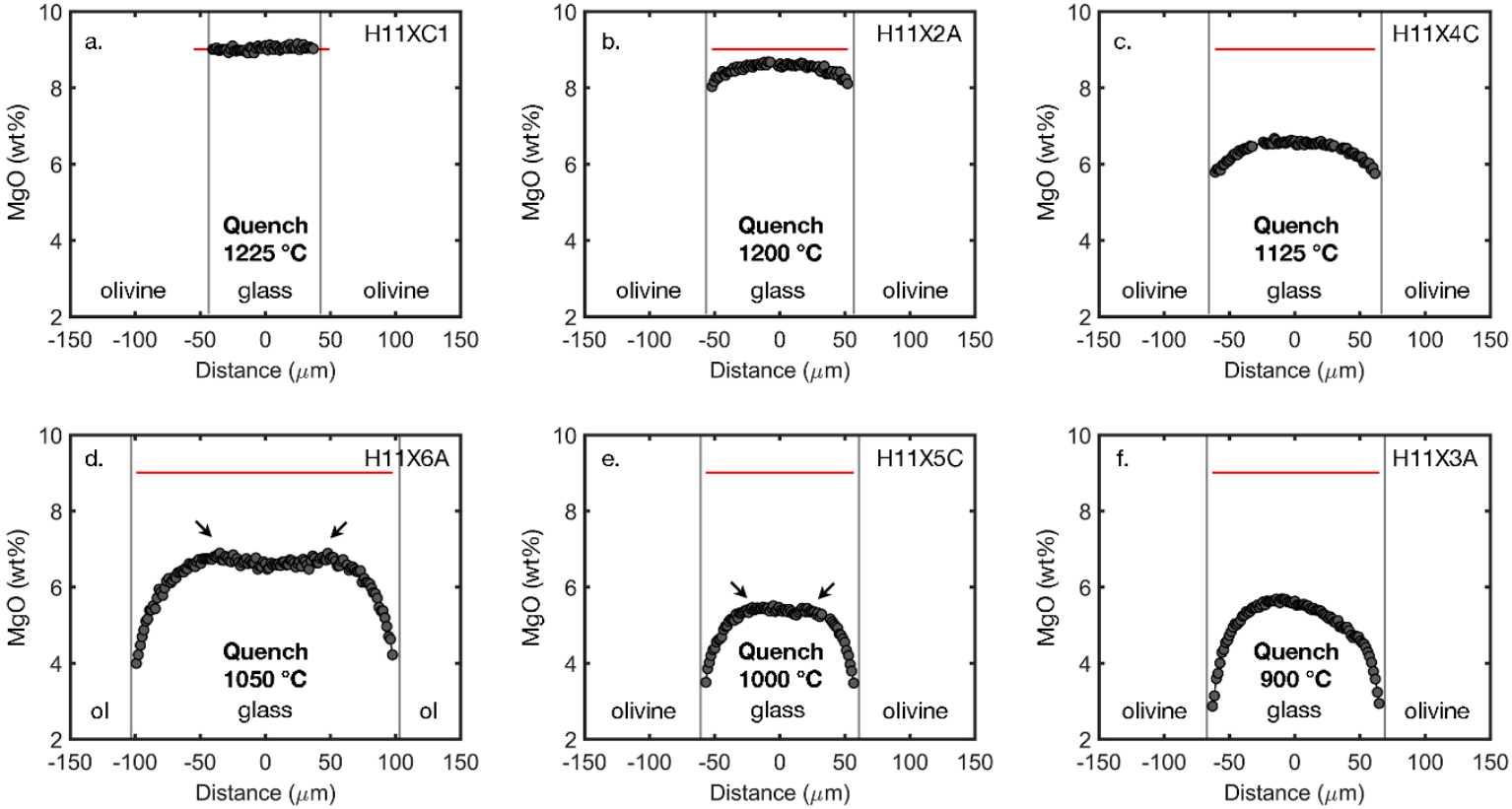


**Figure 6.** MgO profiles across olivine-hosted glass inclusions from experiment H11X, which were held at 1225 °C for 24 hours, cooled at 466 °C/hr, and quenched at different temperatures between 1225 and 900 °C. Each panel corresponds to an inclusion quenched at a different temperature along the cooling path (Figure 2); the quench temperature is indicated in bold text. The horizontal red lines correspond to the mean MgO contents (~9 wt%, Table 2) of glasses homogenized at 1225 °C, and indicates the approximate MgO profile prior to the initiation of cooling (e.g. panel (a) shows an inclusion from experiment H11X (also depicted in Figure 1) that was homogenized and quenched prior to cooling). Vertical grey bars indicate the boundary between glass and olivine. Arrows in panels d and e show possible manifestations of multicomponent effects: local maxima in inclusion H11X6A, a central plateau in inclusion H11X5C at an MgO contents much lower than that established during the homogenization step.

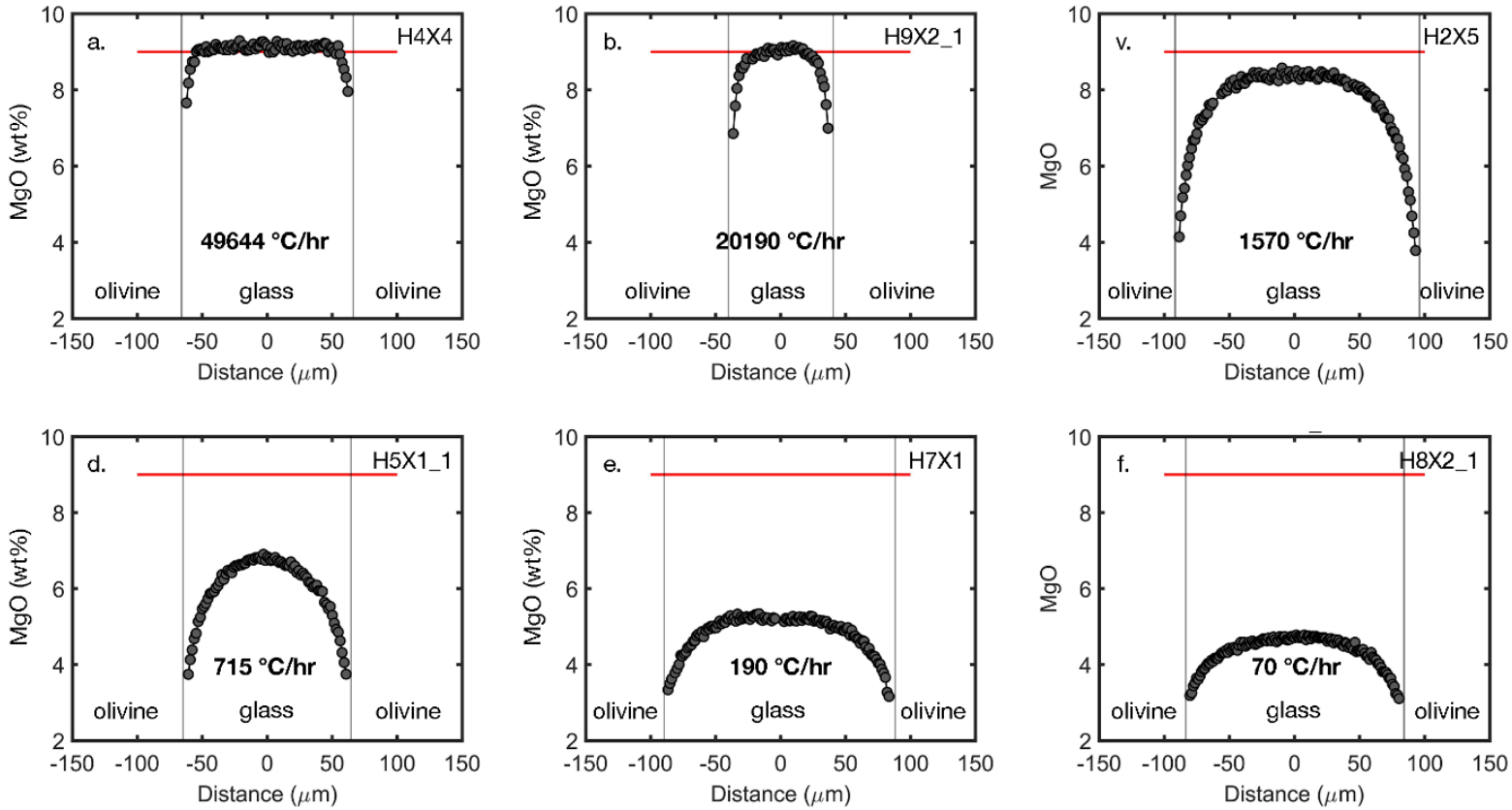


**Figure 7.** MgO profiles across olivine-hosted glass inclusions from different experiments, all of which were held at 1225 °C for 24 hours but cooled at different rates varying from ~50,000 °C/hr (panel a) to 70 °C/hr (panel f). The cooling rate for each panel is shown in bold text. All of the experiments were quenched at a temperature of 1000 °C along their respective cooling paths (Figure 2). The horizontal red lines correspond to the mean MgO contents (9 wt%) of glasses homogenized at 1225 °C (Table 2), and indicates the approximate MgO profile prior to the initiation of cooling. Vertical grey bars indicate the boundary between glass and olivine.

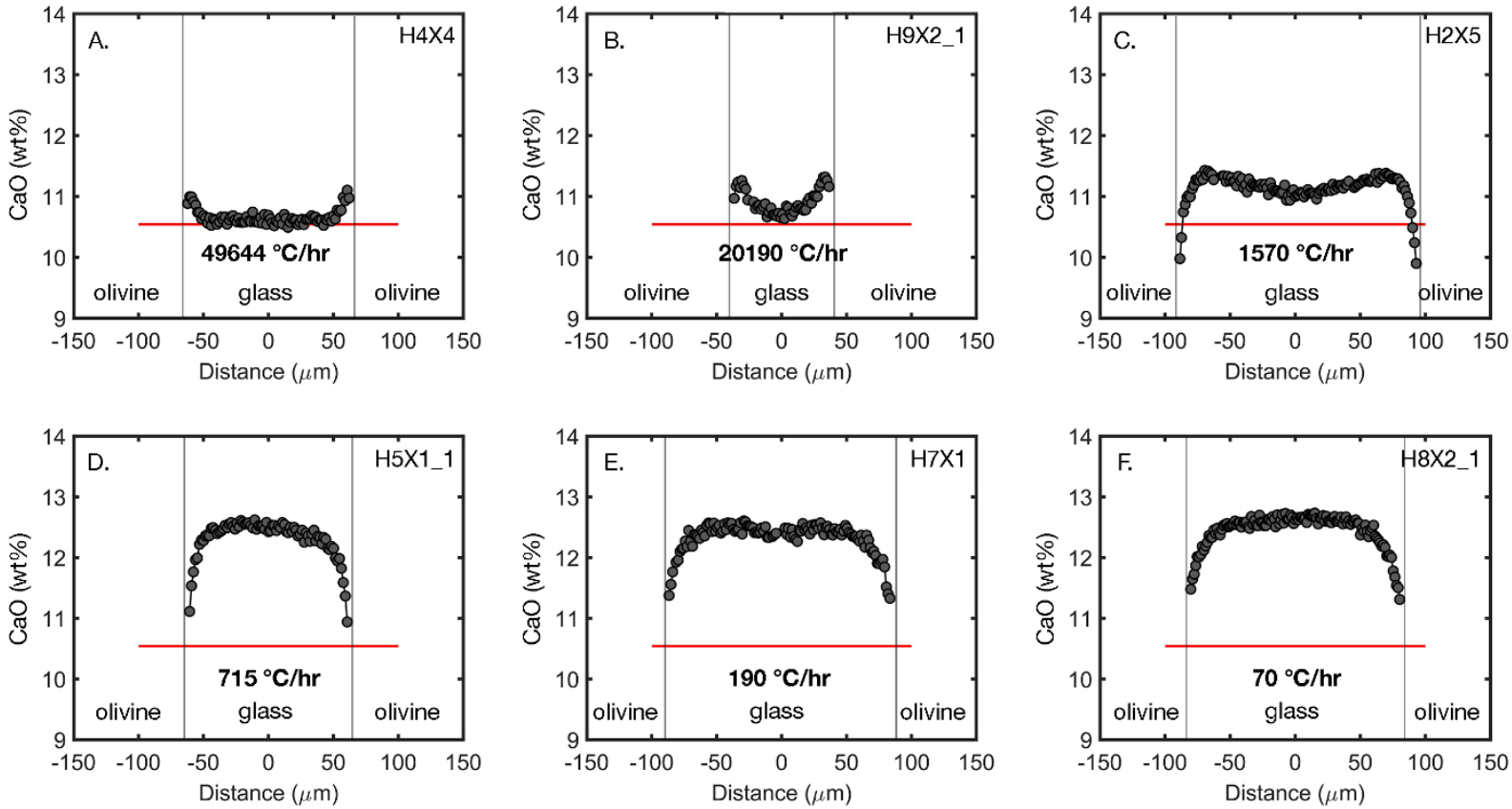


**Figure 8.** CaO profiles across experimentally cooled olivine-hosted melt inclusion glasses. Each panel corresponds to a sample from a different experiment. The cooling rate for each panel is shown in bold text. All experiments were held isothermally for 24 hours at 1225 °C prior to the initiation of cooling and then quenched into water at 1000 °C. The red line is the average CaO contents (10.5 wt%) of inclusions homogenized at 1225 °C, which is assumed to be the starting CaO for inclusions whose centers have been modified by diffusion.

inclusions reflects the competition between the changing composition of the melt at the inclusion wall as olivine crystallizes and diffusive exchange between this interface melt and the interior of the inclusion. The diffusion profile widths and shapes depend for each oxide on inclusion size, cooling rate, and on its diffusivity (including its composition and temperature dependence). For example, although all of the inclusions in experiment H5X were homogenized at 1225 °C, cooled at 715 °C/hr, and quenched at 1000 °C, the compositions at the inclusion centers are systematically related to the inclusion size (Supplementary Figure S4): central MgO contents from these inclusions are lower in smaller inclusions than in larger ones subjected to the same cooling history, whereas the central $Al_2O_3$ contents are enriched in smaller inclusions. This is consistent with the shorter distances necessary in small inclusions for diffusion to exchange between their walls and centers. Note, however, that even though $Al_2O_3$ is building up adjacent to olivine crystallizing on the inclusion walls during cooling, the effect of inclusion size is less dramatic on $Al_2O_3$ than for MgO because there has been less exchange between the inclusion wall and center for the relatively slowly diffusing $Al_2O_3$. This size-dependent behavior is important to consider when comparing inclusions across experiments, and it has implications for the interpretation of analyses of the centers of inclusions within a population of natural samples since central compositions are more likely to be diffusively modified for smaller inclusions and for samples subjected to lower cooling rates (Newcombe et al., 2014).

Concentration profiles from experimental inclusions of similar size (~50–80 μm radius) that were cooled at different rates (70 to ~50,000 °C/hr) over the same 1225–1000 °C temperature interval illustrate the cooling rate dependent aspects of the development of compositional zoning in melt inclusions (Figure 7). In the most rapidly cooled experiments, the diffusion profile terminates at an MgO content that is unchanged from

that established during the homogenization step (Figure 7ab). The width of the diffusively modified boundary layer grows with decreasing cooling rate until it reaches the center of the inclusion, after which the composition of the inclusion center no longer represents the homogeneous melt that initially occupied the whole inclusion (Figure 7c-f). This progressive behavior is qualitatively similar to that of the temperature-dependent evolution of profiles cooled at a single cooling rate but quenched at progressively lower temperatures (Figure 6). If low cooling rate samples were quenched at high enough temperature, they too would preserve the homogenized compositional plateau near the inclusion center because there would have been insufficient time for the boundary layer to have diffusively reached the inclusion centers, and cooling to an intermediate temperature followed by an extended isothermal period would result in erasure of the zonation across the inclusion; i.e., preservation of zonation only occurs when the system cools sufficiently rapidly to low temperatures.

Several of the experimentally generated concentration gradients have features that suggest the importance of uphill diffusion, analogous to those described in natural melt inclusions by Newcombe et al. (2014). Uphill diffusion refers to when a solution component appears to diffuse against its own concentration gradient due to interactions with other melt components, and can be manifested by non-monotonic and asymmetric diffusion profiles (Liang 2010). Diffusion profiles with local maxima and minima are evident in some experimental profiles of every oxide, including MgO (Figure 6de), but are most prominent in profiles of CaO (Figure 8), FeO, $SiO_2$, $Al_2O_3$, $TiO_2$, and $K_2O$ (Supplement Section 3). The local extrema in concentration profiles are transient features (Liang, 2010) and are thus generally less pronounced in the lowest cooling rate experiments. CaO, which arguably exhibits the most extreme uphill diffusion behavior, exemplifies this transience clearly; for the experiments cooled at >1000 °C/hr (Figure 8,

top row), the profiles show clear local extrema whereas at lower cooling rates the profiles have a nearly monotonic concave down shapes (Figure 8, bottom row). As noted earlier, the shape of CaO profiles from slowly cooled samples is anomalous considering its incompatibility in olivine, and, as we describe in Section 5, we ascribe it to a particularly extreme manifestation of multicomponent effects. For MgO, Newcombe et al. (2014) demonstrated that a simple model assuming a composition-independent effective binary diffusion coefficient (Chen & Zhang, 2008) could reproduce most of the variability measured in MgO profiles across natural inclusions. In the controlled cooling experiments there is subtle evidence that MgO may also be affected by uphill diffusion, including nearly horizontal compositional plateaus at MgO contents below the initial homogenized value (Figure 6e) and subtle but resolvable local maxima symmetric about the inclusion center (Figure 6d). The key point is that factors that produce uphill diffusion, such as diffusive coupling and solution non-ideality (e.g., Liang et al., 1997), play a role in olivine-hosted basaltic liquids and would need to be addressed when attempting to construct a complete model of diffusion in the liquid. In Section 4, following Newcombe et al. (2014), we choose to focus on MgO in our modeling, but we also extend their approach to include the dependence of the diffusivity of MgO on the evolving major element composition of the melt.

### 4.5 Zoning in olivine

Olivine growth drives chemical zonation in the inclusion liquid, so zoning in olivine adjacent to the glass that crystallized during cooling provides complementary information that can be used to close the mass balance and test conclusions based on observations of the glass. In natural samples, the olivine adjacent to melt inclusions is typically characterized by Fe enrichments and Mg depletions toward the inclusion interface, attributed to post-entrapment olivine growth on the inclusion wall and diffusive

exchange with olivine in the far-field (Gaetani & Watson, 2000; Danyushevsky et al., 2002a). The Fe/Mg zonation of olivine around natural inclusions from Papakōlea is characterized by two to three zones (Figure 9a): in some olivine, there is a steeply zoned, narrow band of low Fo content olivine typically extending a few micrometers (up to ~7 μm in the Papakōlea samples) into the olivine from the inclusion wall; this is adjacent to a broader zone with gradients of ~1–2 Fo% that extend an additional ca. 30–115 μm into the host olivine; beyond this, the far-field region is a compositional plateau or reflects grain-scale zoning formed during growth of the olivine phenocryst from the magma. In some samples there is an apparent break in slope between the broad zone and the steep narrow zone, consistent with the latter having formed by crystallization of olivine on the inclusion wall due to a perturbation of the olivine's environment (e.g., abrupt cooling on eruption). The broad zones are interpreted as relaxed gradients from a prior episode of crystallization on the inclusion wall and/or from open-system diffusive exchange with an evolving melt external to the olivine (e.g., Danyushevsky et al., 2000; Gaetani & Watson, 2000). In half of the Papakōlea samples, the break in slope between the broadly and steeply zoned olivine is not obvious, which results in two clearly recognizable zones (the broad zone and the far-field olivine), and either reflects the lack of any steep zone adjacent to the inclusion wall or that this zone is too narrow to be clearly identified by the electron microprobe.

The olivine zones defined for the natural inclusions in the previous paragraph are also observed in the experimentally heated and cooled inclusion-bearing olivines. Figure 9b illustrates these zones in the slowly cooled experimental sample H8X2_1 (70 °C/hr), which shows a steep narrow zone (~4.5 μm wide with an increase from $Fo_{84.4}$ to $Fo_{88.3}$ with increasing distance from the inclusion) adjacent to the inclusion wall interpreted to be due to growth during experimental cooling; this narrow zone is surrounded by a broad

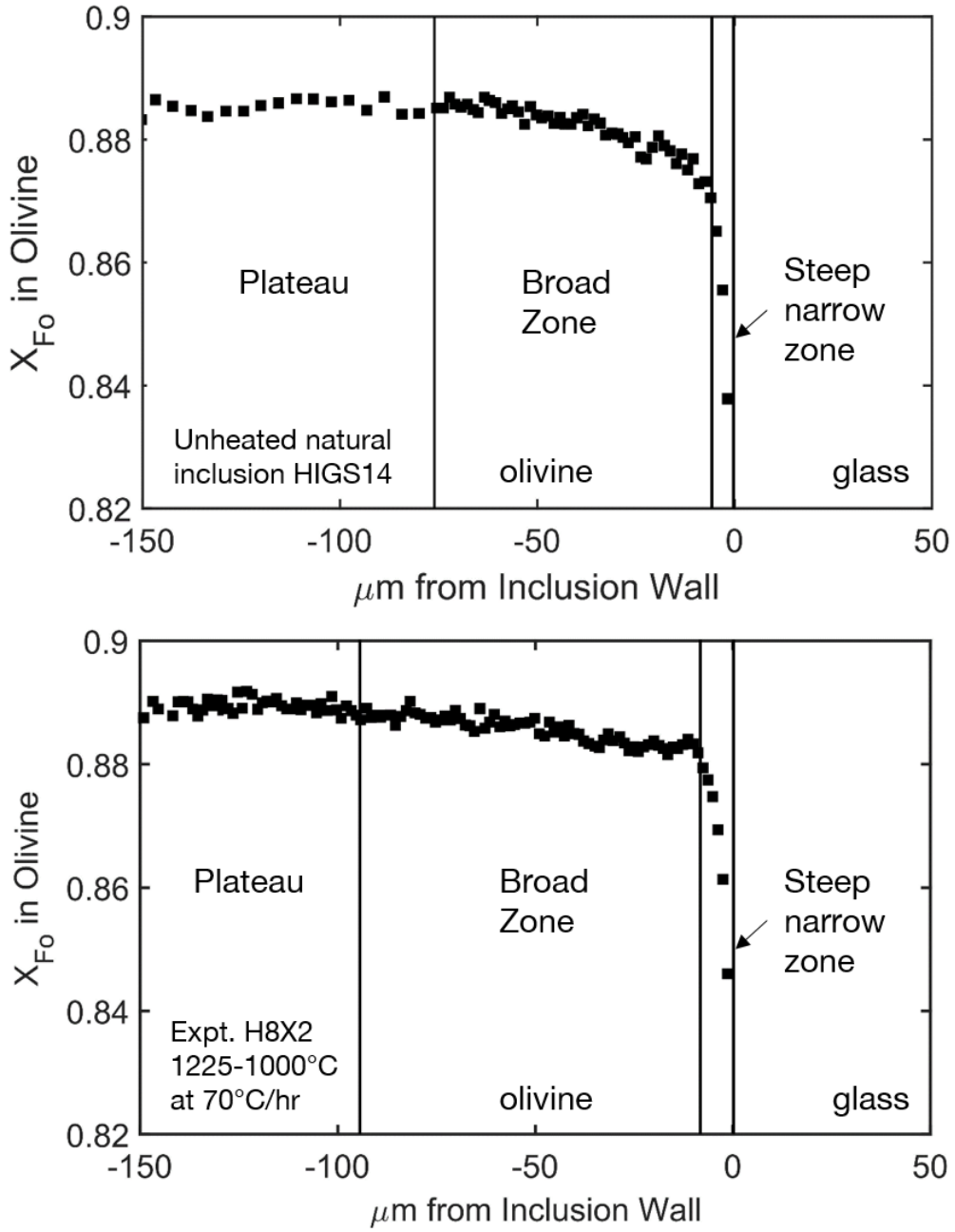


**Figure 9.** Zoning of forsterite contents Fo% = 100 x (MgO / (MgO + FeO)) in olivine adjacent to melt inclusions. Distance on the x-axis is measured relative to the olivine-glass boundary (rightmost gray vertical line). (a) Example of an unheated natural olivine from Papakolea, Hawaii (HIGS14). (b) Example from experiment H8X (olivine adjacent to inclusion H8X2_1), homogenized at 1225 °C for 24 hours, and then cooled at 70 °C/hr and quenched at 1000 °C. Vertical lines and corresponding labels are included to distinguish between three different zones observed in the olivine enclosing a melt inclusion; a steep, narrow zone adjacent to the olivine-glass boundary, a broad zone extending further from this boundary into the host olivine, and a plateau in forsterite contents in the far-field. Far-field olivine reported in the text corresponds to microprobe analyses taken >150 μm from the inclusion wall.

zone (~110 μm wide with an increase from $Fo_{88.4}$ to $Fo_{89.0}$); the broad zone terminates at a compositional plateau at ~$Fo_{89}$ that extends into the crystal interior. The experiments were homogenized at 1225 °C, at which temperature some Fe-rich olivine initially on the inclusion wall likely dissolved back into the inclusion, and Fe and Mg exchanged between the liquid and near-surface olivine until they were in local equilibrium. Once cooling was initiated, it led to re-growth of a steep narrow zone olivine zone: i.e., olivine more Fe-rich than that at the inclusion wall in equilibrium with the homogenized melt at 1225 °C grew during controlled cooling, forming a shell of increasingly Fe-rich olivine on the inclusion wall that is observed as the steep narrow zone in Figure 9b. This narrow band of Fe-enriched olivine immediately adjacent to the inclusion wall is absent in the experimentally homogenized samples (not shown in figures), and if, as we expect, such a zone was originally present in the natural sample formed during the natural cooling of the sample, we infer that it was reincorporated into the liquid during homogenization. We resolved no relaxation or homogenization of the broad zones in our experiments over the duration of the experiments, consistent with known Fe-Mg interdiffusion coefficients (e.g., Dohmen et al., 2007), which suggest a maximum diffusive length scale in the olivine of ~5 micrometers during the 24-hr homogenization at 1225 or 1260 °C. The presence of broad zones in some of the experimentally heated and cooled olivines is thus inferred to have been inherited from the natural cooling history and not generated or significantly altered during the experiments.

## *5* Modeling

### 5.1 Model description

In order to model the evolution of concentration profiles across olivine-hosted melt inclusions during cooling, the diffusion model of Newcombe et al. (2014) was adopted and modified. Described in detail in the original study, the numerical code

calculates a 1-dimensional forward model for diffusion of MgO across a spherical melt inclusion subjected to a cooling path, which we assume to be linear (i.e., a constant cooling rate). The model assumes local equilibrium between olivine and the liquid at the inclusion wall (referred to hereafter as the "interface liquid") and imposes a temperature-dependent relationship between MgO in the interface liquid and $Fo_{90.6}$ olivine; for this relationship, Newcombe et al. (2014) used the results of the olivine dissolution experiments of Chen and Zhang (2008). At each temperature decrement along the linear cooling path, MgO is specified in the interface liquid as a boundary condition and the corresponding gradient in MgO is allowed to relax diffusively.

Given a microprobe profile of MgO concentration across a glassy spherical melt inclusion and assuming an initially homogeneous liquid at an initial temperature, the cooling rate parameter can be varied so as to minimize the difference between the measured profile and the forward model. Newcombe et al. (2014) used this approach to quantify the cooling rates of olivine-hosted melt inclusions from the Siqueros Facture Zone and the Galapagos Islands, but could not assess the accuracy to which the best-fit thermal histories match those experienced by the samples in nature, since the rates were not known independently. In our experimentally cooled inclusions, the cooling rate, homogenization and quench temperatures, and initial melt composition are all known. The inverse model can then be run on the experimental inclusion MgO profiles to determine the cooling rate that results in the best fit between the model and data, which when compared to the measured experimental rates can be used to evaluate quantitatively the accuracy of the model.

The experiments can also be used to test, and if necessary modify, assumptions in the diffusion modeling because the temperature-time history of the samples as well as the initial composition of the melt in the inclusion after homogenization but prior to

cooling are known (Figure 2, Table 2). For example, the average composition of the melt inclusions homogenized at 1225 °C has MgO = 9.01±0.26 (2σ) wt %; however for these MgO contents the olivine-liquid thermometer of Chen and Zhang (2008) predicts a much lower temperature of 1157±8 °C. As a result, in the modeling presented here we use the 1 bar alphaMELTS model (hereafter referred to as MELTS, Ghiorso & Sack, 1995; Smith & Asimow, 2005) to define the MgO vs. temperature boundary condition rather than the Chen and Zhang (2008) olivine-liquid thermometer used by Newcombe et al. (2014). Specifying the average composition of inclusions homogenized at 1225 °C (Table 2) and approximating the experimental $fO_2$ as ΔFMQ ≈ -1, MELTS predicts the olivine-saturated liquidus to be 1229±2(2σ) °C with a liquidus olivine composition of $Fo_{87.3\pm0.9(2\sigma)}$, within error of the average composition of olivine analyzed at the olivine-glass interface in experimentally homogenized samples ($Fo_{88.2\pm1.8(2\sigma)}$). Starting with this initial condition, which closely approximates the experimental conditions after homogenization and prior to cooling, MELTS was programmed to batch crystallize only olivine, and the MgO content of the output liquid composition as a function of temperature at a constant pressure of 1 bar was used as the temperature-dependent boundary condition at the olivine-melt interface (using fractional rather than batch crystallization would make negligible difference; see the next paragraph and Figure 10a). We note that pressures of Mauna Loa melt inclusions are estimated to be ~0.5–1 kbar (Wallace et al., 2005), but because the pressures are not known for the experimental melt inclusions and the effect on olivine-liquid equilibria is relatively small (e.g., pMELTS predicts the 1 kbar liquidus to be 6 °C higher than at 1 bar), we adopt the 1 bar calculation.

For two set of experiments H2X (1570 °C/hr) and H11X (466 °C/hr), which were quenched at several temperatures, the correspondence between model batch and fractional crystallization calculations and analyses of glasses near the inclusion wall are

**Figure 10.**

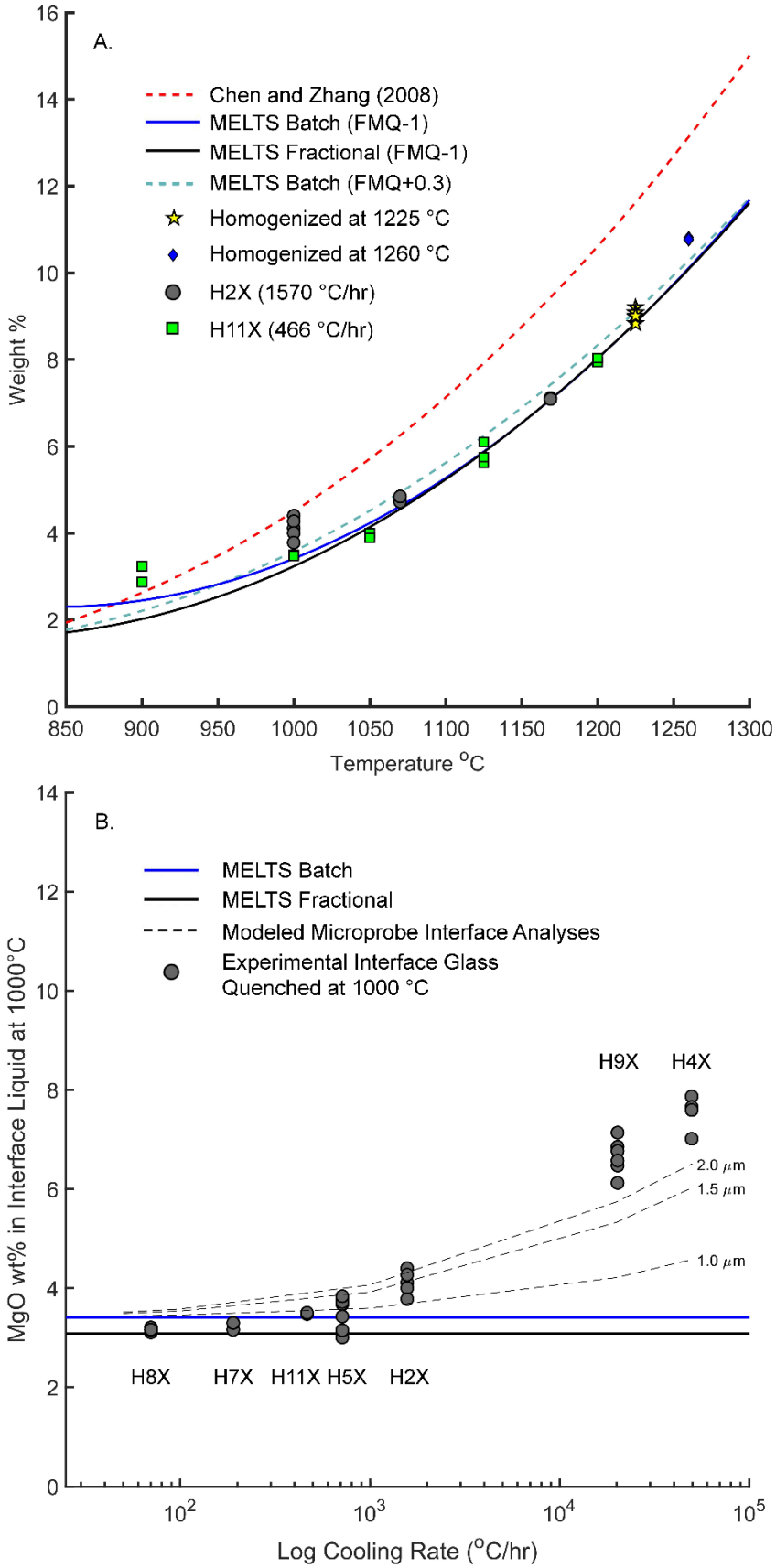


Figure caption is on the next page.

**Figure 10.** (**a**) MgO (wt %) in experimental glass inclusions measured as close as possible to the interface with olivine (~1.5–2 μm). The red dashed line shows the MgO vs. temperature parameterization from Chen and Zhang (2008). The blue and black solid lines correspond to the MELTS batch and fractional olivine crystallization models, respectively, showing the predicted MgO contents of the liquid homogenized at 1225 °C (Table 2) with progressive extraction of olivine. Yellow stars are MgO contents of interface glasses from inclusions homogenized at 1225 °C for 24 hours and drop-quenched into water, excluding analyses that were clearly affected by quench crystallization (e.g., Figure 5). Blue diamonds are MgO contents of inclusions homogenized at 1260 °C for 24 hours and drop-quenched into water. Grey circles are analyses of interface glasses from experiment H2X, which was homogenized at 1225 °C for 24 hours, then cooled at 1570 °C/hr and quenched at 1170 °C, 1060 °C, and 1000 °C. Green squares are analyses of interface glasses from experiment H11X, homogenized at 1225 °C, cooled at 466 °C/hr, and quenched at 1200 °C, 1125 °C, 1050 °C, 1000 °C, and 900 °C. (**b**) MgO in the interface glass of olivine-hosted melt inclusions cooled at different rates and all quenched at 1000 °C. The solid black and blue lines correspond to the predicted MgO contents of liquid coexisting with olivine at 1000 °C at ΔFMQ ≈ -1, according to MELTS batch and fractional olivine crystallization models, respectively. Grey circles are measurements of MgO in the interface glasses of experimental inclusions as a function of cooling rate for all experiments quenched at 1000 °C. Labels indicate which experiment the analyses were taken from. Dashed lines show the results of forward modeling an MgO profile for a particular cooling rate, and then sampling this synthetic profile at distances of 1.0, 1.5, and 2.0 μm from the true interface. The steepening of the MgO profile near the interface leads to synthetic microprobe analyses that tend to overestimate the MgO content of the interface melt value at the quench temperature of 1000 °C (panel **b**), which is consistent with local equilibrium between olivine and liquid but the low MgO is confined to a region too narrow to be analyzed at the spatial resolution of the microprobe (see Section 4.1, Supplement Section 2).

both good (Figure 10a), particularly at quench temperatures greater than 1000 °C where both sets of experiments agree with either model by less than 0.4 wt% MgO (see Supplementary Figure S5 for oxides other than MgO). For experiments cooled at rates ≤1000 °C/hr and quenched at 1000 °C, the average measured MgO content of the interface glass is 3.47±0.7(2σ) wt%, which is only slightly higher than that predicted by the MELTS fractional (3.24 wt%) or batch (3.41 wt%) calculations at 1000 °C (Figure 10b). For experiments cooled at higher rates (H2X, H9X, H4X), the MgO in the interface melt of inclusions quenched at 1000 °C based on analysis of glass as close as possible to the interface (~1.5 μm from olivine) is systematically higher than the MELTS predictions for both fractional and batch crystallization, and increasingly divergent at higher cooling rates (Figure 10b). This discrepancy can be mostly accounted for by extremely steep gradients near the interface in rapidly cooled experiments resulting in an inability of the microprobe to resolve this narrow zone (Figure 10b), although a failure to achieve local equilibrium is also possible.

In a crystallizing melt inclusion, the interface liquid will never actually follow a batch nor fractional crystallization path since it is continually influenced by diffusive exchange with the inclusion interior. However, the MELTS calculations provide an improved approximation of olivine-melt equilibria at the interface relative to the constant $Fo_{90.6}$ assumption of Chen and Zhang (2008) (e.g., compare the data and MELTS models with the red dashed curve in Figure 10a). For the purpose of modeling the experimental melt inclusions, the boundary condition of the temperature-dependence of the MgO content of the interface liquid was approximated by a 2$^{nd}$ order polynomial fit to the MgO contents of liquids on a MELTS-calculated batch crystallization liquid line of descent (at an $fO_2$ fixed at ΔFMQ ≈ -1) starting with the average composition of our 1225 °C homogenization experiments (Table 2). The batch crystallization calculation was

preferred over the fractional crystallization calculation due to better correspondence to the experimental data at lower temperatures (Figure 10a). The fit was for the 1229–850 °C temperature range (the upper temperature limit is the MELTS-calculated liquidus of the liquid composition):

$$C_{MgO}^{liq} = 4.471x10^{-5} \times T^2 - 0.09971 \times T + 57.89 \quad (1)$$

where $C_{MgO}^{liq}$ is the concentration in weight percent of MgO in liquid coexisting with olivine and T is temperature in Kelvin. This fit to the boundary condition is shown as the blue curve in Figure 10a.

The other modification made to the Newcombe et al. (2014) model was to the parameterization of $D_{MgO}$, the diffusivity of MgO in the liquid. Chen and Zhang (2008) parameterized $D_{MgO}$ as an effective binary diffusion coefficient (EBDC), which approximates diffusion in a multicomponent system as pseudobinary exchange between the component of interest and a second fictive component that is a combination of all of the other components in the solution (e.g., Cooper, 1968; Watson & Baker, 1991; Chakraborty, 1997; Liang, 2010). While the effective binary approach is useful in that it foregoes the need for a full diffusion matrix (e.g., Guo & Zhang, 2016, 2018), the EBDC is in general a function of composition (Cooper, 1968; Zhang, 1993) and can vary based on the geometry of the diffusion couple (Liang, 2010). Accordingly, the EBDC generally will vary across a diffusion profile, will be time-dependent unless the system has achieved steady state, and will in steady state depend on the geometry of the system (Cooper, 1968; Liang, 2010). Our experiments stress these limitations of the EBDC in that they are dynamic cooling rate experiments, substantial compositional gradients continually evolve in the melt boundary layer, and the inclusion radii are finite and for the smaller inclusions on the same order as the characteristic length scale for diffusion. This combination of factors likely contributes to variations in $D_{MgO}$ with time and

position within the inclusion during cooling, which may thus not be fully accounted for by a single temperature-dependent EBDC.

The grey dots in Figure 11a shows the measured MgO concentration profile of a representative experiment (inclusion H2X5) and the green curve is the result of a forward model with no free parameters (cooling at 1570 °C/hr from 1225–1000 °C/hr) that uses equation (1) as the boundary condition for the interface MgO contents and the temperature-dependent (but compositionally invariant) EBDC for $D_{MgO}$ from Chen and Zhang (2008) adopted by Newcombe et al. (2014). The modeled profile is systematically offset to lower MgO values, indicating that at a given temperature the $D_{MgO}$ is too high, leading us to consider using a $D_{MgO}$ that is a function of melt composition as well as temperature, following the approach of Zhang (2010). Accordingly, the following modified Arrhenius expressions for the dependence of $D_{MgO}$ on composition in dry melts was adopted (Zhang, 2010, pp. 334, equation 23), collectively referred to as equation (2),

$$\ln D_{MgO}\ [m^2/s] = D_o - E_A/(RT); \tag{2a}$$

$$D_o\ [m^2/s] = -5.17 - 11.37\ X_{Si} - 2.16\ X_{FM}; \tag{2b}$$

$$E_A/R = 10993 + 17839\ X_{SA;} \tag{2c}$$

where R is the gas constant; T is temperature in Kelvin; $X_{Si}$ is the cation mole fraction of Si; $X_{FM}$ is the sum of the cation mole fraction of Mg, Fe, and Mn; and $X_{SA}$ is the sum of the cation mole fractions of Si and Al. Zhang (2010) used available experimental data on MgO diffusion in melts ranging from basaltic to rhyolitic compositions (including self-, tracer-, and effective-binary-diffusion coefficients) to solve for the coefficients in equation (2) that best fit MgO diffusivities across temperature and composition space. Equation (2) reproduces these various diffusivities from available experiments of basaltic to rhyolitic compositions with a maximum deviation of 0.4 $\log_{10}$ units between calculated and measured values of

**Figure 11**

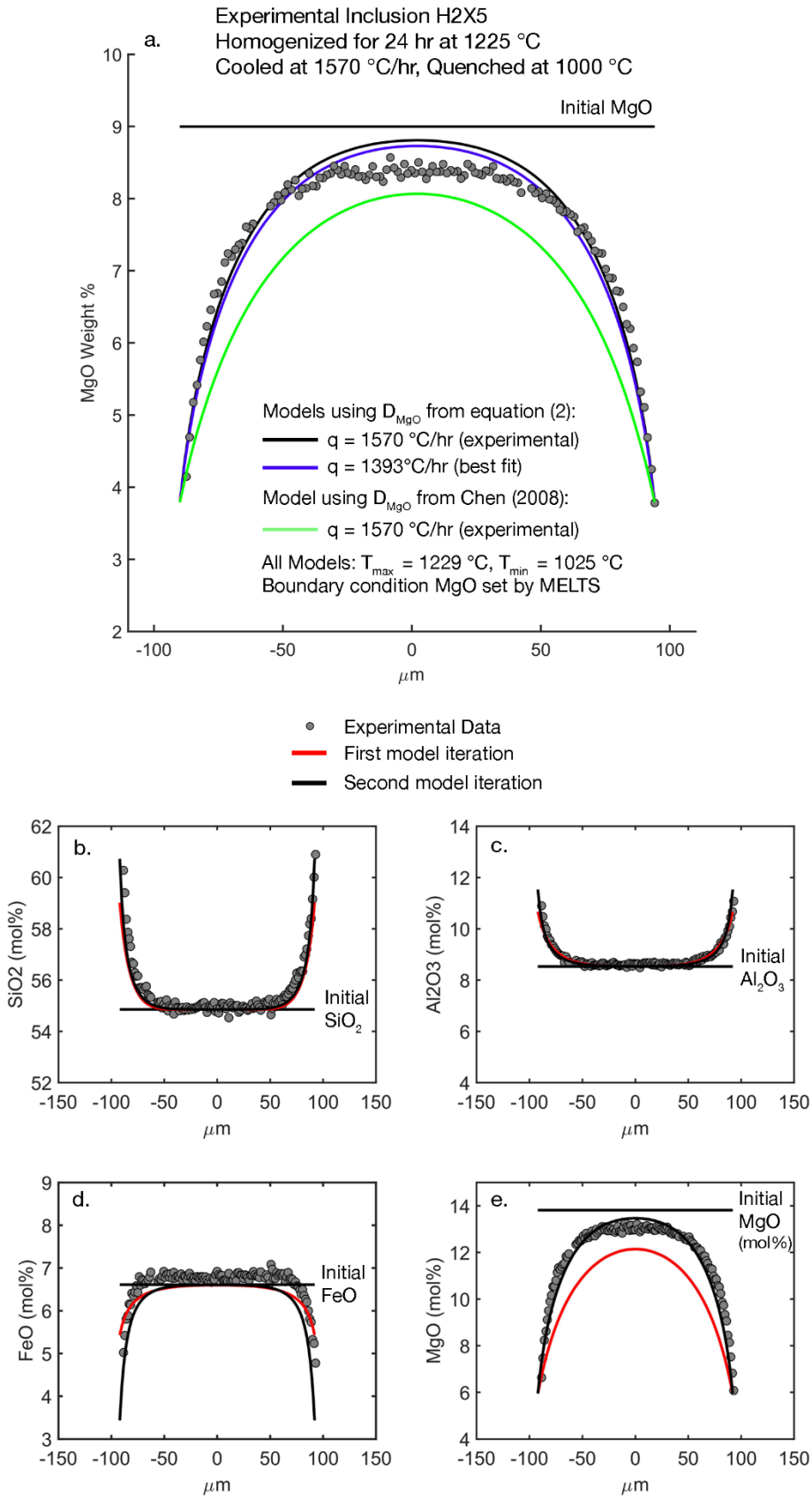


Figure caption is on the next page.

**Figure 11.** (**a**) Shaded circles are MgO data (wt%) from experimental melt inclusion H2X5 (cooled at 1570 °C/hr). Solid lines are different MgO diffusion models described in Section 4.1. Horizontal black line indicates the initial modeled MgO content in the liquid at 1229 °C prior to cooling (~9 wt%). The green curve is a forward model (no free parameters) using equation (1) as the boundary condition for the interface liquid MgO and the $D_{MgO}$ from Chen and Zhang (2008). The black curve is a forward model (no free parameters) using equation (1) as the boundary condition for the interface liquid MgO and the composition-dependent $D_{MgO}$ in equation (2). The blue curve is an inverse model that varied one parameter (linear cooling rate) to minimize the residuals between the model and data (best fit cooling rate is 1393 °C/hr). All models were run from $T_{max}$ = 1229 °C to $T_{min}$ = 1025 °C/hr. (**b**-**e**) Shaded circles are experimental microprobe data from inclusion H2X5. Solid lines are forward models (no free parameters) for (**b**) $SiO_2$, (**c**) $Al_2O_3$, (**d**) FeO, and (**e**) MgO (in mol %), corresponding to the best-fit cooling rate (1393 °C/hr). Horizontal black line indicates the initial mol% of the modeled oxide at 1229 °C. The red curves show models corresponding to the first iteration of the model calculation (using MELTS as the temperature-dependent boundary condition, $C_{MgO}^{liq}$), whereas the black lines show the second iteration which was used as the input to equation (2) (using mass balance with MgO to set $C_{MgO}^{liq}$; see Section 4.2, Supplement Section 2). For MgO in (**e**), the red line was calculated with $D_{MgO}$ from Chen and Zhang (2009) (cpx dissolution into basalt), whereas the black line was calculated using $D_{MgO}$ in equation (2).

$D_{MgO}$ (Zhang 2010). While the functional form for the effects of chemical composition on $D_{MgO}$ used by Zhang (2010) in equation (2) is arbitrary, it provides a quantitative basis for taking into account the compositional dependence of MgO diffusion in a multicomponent melt that is strongly zoned.

In equation (2), silica content has the dominant effect on $D_{MgO}$ due to its high cation mole fraction in basaltic liquids and the relatively large coefficient in the pre-exponential term in the Arrhenius equation. For example, in sample H2X5, cooled at 1570 °C/hr and quenched at 1000 °C, the concentration of $SiO_2$ increases from 52.4 wt% in the inclusion interior to 56.6 wt% near the olivine-melt interface, and based on equation (2) the diffusion coefficient of MgO is expected to decrease by 0.65 $\log_{10}$ units (at 1000 °C near the inclusion edge) solely due to this increase in silica. Accounting for additional changes due to the combined gradients in MgO, FeO, and $Al_2O_3$ between the inclusion center and edge only reduces $D_{MgO}$ by an additional 0.06 $\log_{10}$ units for H2X5. For more details related to the implementation of the composition-dependent $D_{MgO}$, see Supplement Section 2.1.

### 5.2 Application of the modified model

Using the MELTS boundary condition for $C_{MgO}^{liq}$ (equation 1) and the composition-dependent $D_{MgO}$ parameterization (equation 2) described in the previous section, forward models of the MgO profile vs. time for any cooling path can be calculated. For the case of the linear cooling paths of our experiments, the model was implemented given an initial temperature ($T_{max}$), final temperature ($T_{min}$), and cooling rate (q). At time t = 0, the liquid is homogeneous and $T = T_{max}$, which is set by substituting the initial MgO concentration in the liquid into equation (1). For each subsequent time step, T is decreased based on the specified cooling rate and the boundary condition $C_{MgO}^{liq}$ at the olivine-melt interface is set by substituting the new T into equation (1). At every

time step, the resulting MgO profile is allowed to diffusively relax, using as an initial guess the temperature-dependent $D_{MgO}$ from Chen and Zhang (2008). For a given $T_{max}$ and cooling rate, this procedure is repeated until reaching the minimum temperature $T_{min}$, which is defined by substituting the minimum value of MgO in the glass at the melt-olivine interface into equation (1) (as in Newcombe et al., 2014).

In order to implement the composition-dependent $D_{MgO}$ in equation (2), the $SiO_2$, $Al_2O_3$, and FeO profiles must also be forward modeled in tandem with MgO. The approach used to model $SiO_2$, $Al_2O_3$, and FeO is described in detail in Supplement Section 2 and example calculations for inclusion H2X5 are shown in Figure 11b-d. To summarize, diffusion of these oxides is calculated using temperature-dependent and composition-independent diffusivities, and the fluxes at the boundary between the olivine and interface liquid are calculated by satisfying mass balance with the MgO lost to the growth of olivine, the composition of which is defined at each time step by MELTS. These calculations produce concentration profiles of $SiO_2$, $Al_2O_3$, FeO, (and an initial guess of the MgO profile) at each time step. Using these profiles and applying equation (2), the concentration dependence of $D_{MgO}$ was calculated at each position and time for a given cooling path and inclusion size. The MgO profile, initially calculated with a composition-independent $D_{MgO}$, is then recalculated at each time step from $T_{max}$ to $T_{min}$, by numerically solving the diffusion equation where $D_{MgO}$ (equation 2) varies with position and time.

Given $T_{max}$ and the $T_{min}$ calculated for a particular inclusion, the cooling rate was allowed to vary such that the difference between the model MgO profile at $T_{min}$ and the experimental MgO data was minimized. Figure 12 shows examples of the model fits to MgO profiles from experimentally homogenized and cooled melt inclusions. The inverted model MgO concentration profiles fit the data with an average sum of square

residuals (SSR) between the model and data equal to 0.055 (Table 3). For H4X and H9X, the most rapidly cooled experiments, the residuals are artificially low because most of the data points in the profile correspond to the MgO plateau and so the difference between the data and the model, with the initial MgO set by the central plateau, is small (e.g., Figure 12ab). Qualitatively, the subtle misfits between the model and experimental profiles are systematic; MgO is sometimes overestimated by the model in the inclusion centers (typically by 0.1-0.2 wt% MgO) and the best-fit model profiles are often slightly too steep close to the inclusion walls (e.g., the difference between the blue lines and data in Figure 12c and e). Newcombe et al. (2014) observed the same discrepancies in their fitting of natural profiles and attributed it to a two-stage cooling history, but this cannot explain our experimental data since these samples experienced only a single stage of linear cooling. Where the systematic offset between model and data near the inclusion center is most obvious, the experimental MgO profiles are flattened near the center relative to the shape of the model profile (Figure 11a, Figure 12ce), in a similar region where MgO profiles have subtle local extrema indicative of uphill diffusion (e.g., Figure 6de, Figure 12e). These flattened MgO profiles (e.g., H2X5, Figure 12c) can look similar to the profiles produced in rapidly cooled samples (e.g., H4X4, Figure 12a) that also have MgO plateaus near inclusion centers. In the latter case the plateau is a relic of the original homogeneous MgO content, whereas in cases such as H2X5, the plateau is at an MgO content that has clearly been lowered by diffusion during the experiment relative to the original homogenized concentration of ~9 wt%. This may lead to confusion in inferring the initial MgO (and the related parameter, $T_{max}$) in some natural samples (as pointed out in Newcombe et al., 2014). These diffusion-influenced plateaus could be due to multicomponent effects on $D_{MgO}$ that are not captured in the parameterization of equation (2), e.g., as the humps in MgO (Figures 6d and 12e) migrate toward the inclusion center

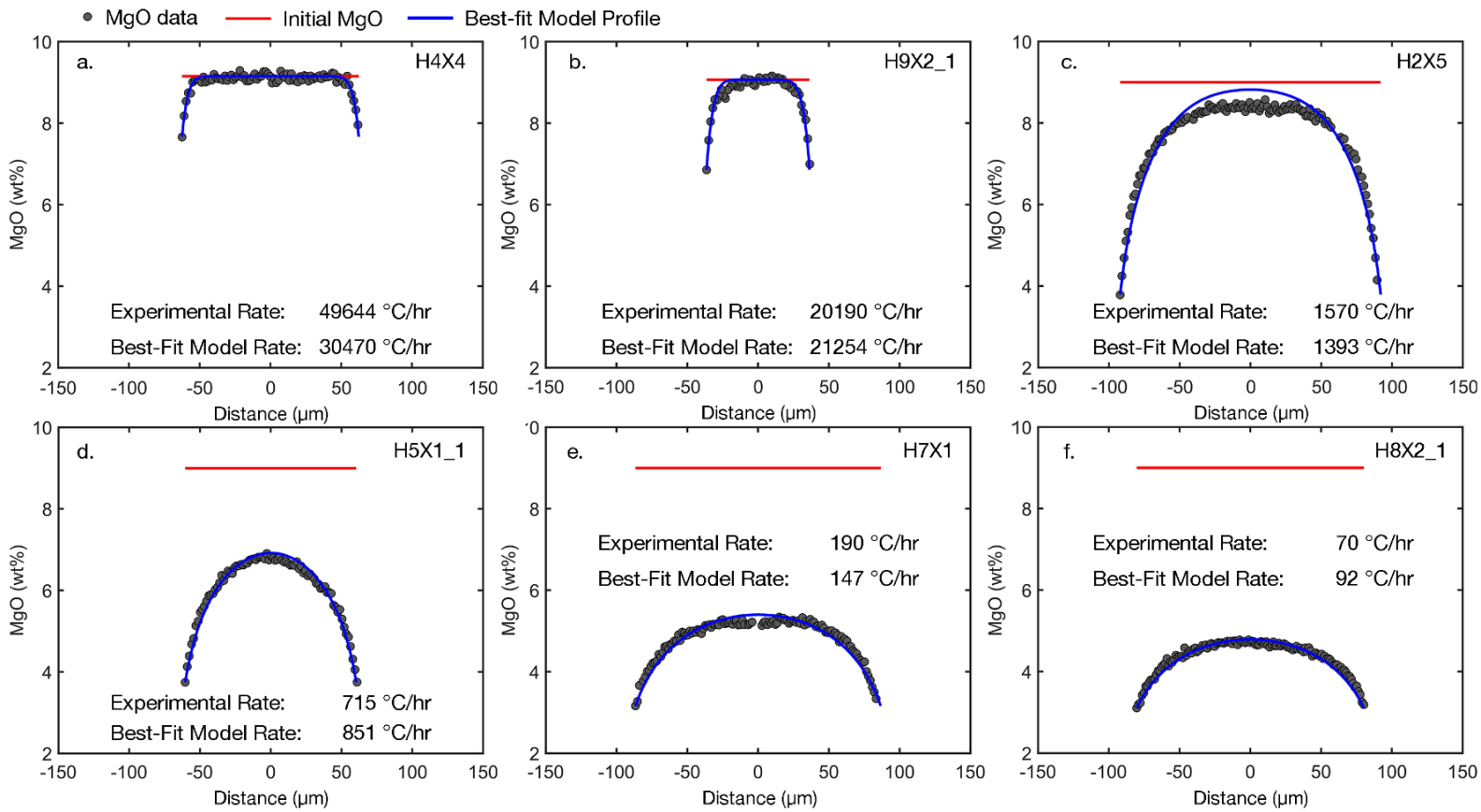


**Figure 12.** Application of the inverse model for MgO diffusion described in Section 4 to experimentally cooled olivine-hosted melt inclusions. The gray circles correspond to microprobe MgO data from inclusions quenched at 1000 °C. Each panel shows the MgO profile across experimental glass inclusions cooled at a different rate. The red horizontal line corresponds to the initial MgO of the model calculation, corresponding to $T = T_{max}$ via equation (1) (Section 4.2). The blue curves correspond to the best-fit result of the inverse model, where cooling rate was the only adjustable parameter, and the corresponding cooling rates are listed below each profile along with the linear best fits to the experimental thermocouple data in Figure 2.

**Table 3 -Summary[†] of Model Results (Section 4) Applied to Experimental Melt Inclusions**

| Name | Experimental cooling rate (°C/hr) | # of inclusions | Avg. calc. cooling rate ($\bar{q}$, °C/hr) | % Deviation from known rate[a] | Std dev. calculated cooling rate (1σ)[b] | Fractional Error (1σ/$\bar{q}$) | SSR[c] |
|---|---|---|---|---|---|---|---|
| H8X | 70 | n = 5 | 104 | +48.46% | 28 | 0.27 | 0.008 |
| H10X[d] | 93 | n = 3 | 97 | +4.50% | 30 | 0.31 | 0.011 |
| H7X | 190 | n = 3 | 239 | +25.70% | 100 | 0.42 | 0.017 |
| H11X | 466 | n = 11 | 428 | -8.23% | 105 | 0.24 | 0.054 |
| H5X | 715 | n = 7 | 731 | +2.17% | 161 | 0.22 | 0.098 |
| H2X | 1570 | n = 9 | 1488 | -5.19% | 355 | 0.24 | 0.086 |
| H9X | 20190 | n = 6 | 21536 | +6.67% | 3762 | 0.17 | 0.021 |
| H4X | 49644 | n = 5 | 31792 | -35.96% | 9024 | 0.28 | 0.012 |

[†] See Supplementary Table 2 for complete results.

[a] 100 x (Average Calculated Rate - Experimental Rate) / Experimental Rate

[b] Standard deviation of the mean calculated cooling rate for each inclusion, where the mean cooling rate was calculated by perturbing the MgO profile with gaussian noise 10x, refitting each profile, and taking the average cooling rate from the fits to these synthetic profiles

[c] Sum of the square of the residuals between the modeled MgO profile (calculated using the avg. best-fit cooling rate) and the best-fit MgO profile

[d] Stage 1 (1260 °C - 1134 °C) at 93 °C/hr of the 2-stage experiment

as a sample cools, they can merge to form a transient, approximate plateau, which evolves into a monotonic concave down profile that moves downward in MgO with further crystallization on the inclusion wall and diffusion of MgO from the inclusion center (e.g., Figures 12e and 12f). The composition-dependent $D_{MgO}$ in equation (2) provides a more realistic description of the diffusivity than one that is only temperature-dependent, but a more sophisticated treatment of multicomponent diffusion that allows for cross-terms and uphill diffusion in MgO would likely be necessary to improve the model fits to the data.

### 5.3 Assessing the accuracy of cooling rates extracted from zoning profiles of olivine-hosted melt inclusions

Modeling the development of zoning across olivine-hosted melt inclusions is a potentially useful quantitative tool for determining late-stage cooling histories of rapidly cooled igneous rocks (Newcombe et al., 2014). Because the experimental samples were subjected to known cooling histories, inverting their MgO profiles allows us to evaluate the accuracy of this approach to determine cooling rates. Figure 13a shows the ranges (gray squares are individual inclusions) and averages (blue circles) of cooling rates calculated for melt inclusions from each experiment compared to the measured cooling rate (i.e., linear fits to the thermocouple data in Figure 2). With the exception of two inclusions (H4X2 and H11X4C), the cooling rates calculated by inverting MgO profiles are within a factor of two of the experimental cooling rates (Table 3, Figure 13b, Supplementary Table 2), which span three orders of magnitude. The percent deviation of the average cooling rate calculated for inclusions from a given experiment from the experimental rate is between -36% in H4X (49644 °C/hr) and +48% in H8X (70 °C/hr), with four of seven experiments having mean percent deviations within ±10% relative to the known rate (Table 3). These data include experiments H2X (1570 °C/hr) and H11X (466 °C/hr), which have inclusions that were quenched at temperatures other than 1000

°C during cooling; for H11X there is no correlation between quench temperature and calculated cooling rate, however for H2X the four inclusions quenched at temperatures higher than 1000 °C had systematically higher calculated cooling rates (1600–2200 °C/hr) than the five quenched at 1000 °C (980–1400 °C/hr). The resolution of the model is calculated by dividing the standard deviation of the distribution of cooling rates calculated for a given experiment by the corresponding mean cooling rate, giving relative standard deviations which vary from 0.17 in H9X (20,190 °C/hr) to 0.42 in H7X (190 °C/hr) (Table 3). In the context of determining cooling rates of natural samples, which span many orders of magnitude (see Newcombe et al., 2014 and Section 6.1), the correspondence between the model and experimental rates demonstrates the usefulness of using diffusion across melt inclusions as a geospeedometer.

The 2-stage experiment (H10X) was modeled by varying three parameters (two cooling rates for each linear stage, and the temperature at which the second stage began), and while the model misfit is less than in the single stage experiments (due to the introduction of two additional fitting parameters), the accuracy is reduced; the calculated cooling rates are within a factor of 2.5 of the measured rates and the changeover temperature is underestimated by 24–50 °C (see Supplement Section 2.2 and Supplementary Figure S6).

The experimental profiles can also be fit with the unmodified model provided in Newcombe et al. (2014), and the single-stage cooling rates recovered from their model are as accurate as those calculated with the updated model (typically ±10% relative and within a factor of two). The accurate cooling rates calculated with the unmodified model is despite the fact that the modeled $T_{max}$ underestimates the homogenization temperature by ~70 °C (Section 4.1). When substituting the MELTS boundary condition (equation 1) in the forward model, we recover the correct $T_{max}$ for the experiments, however

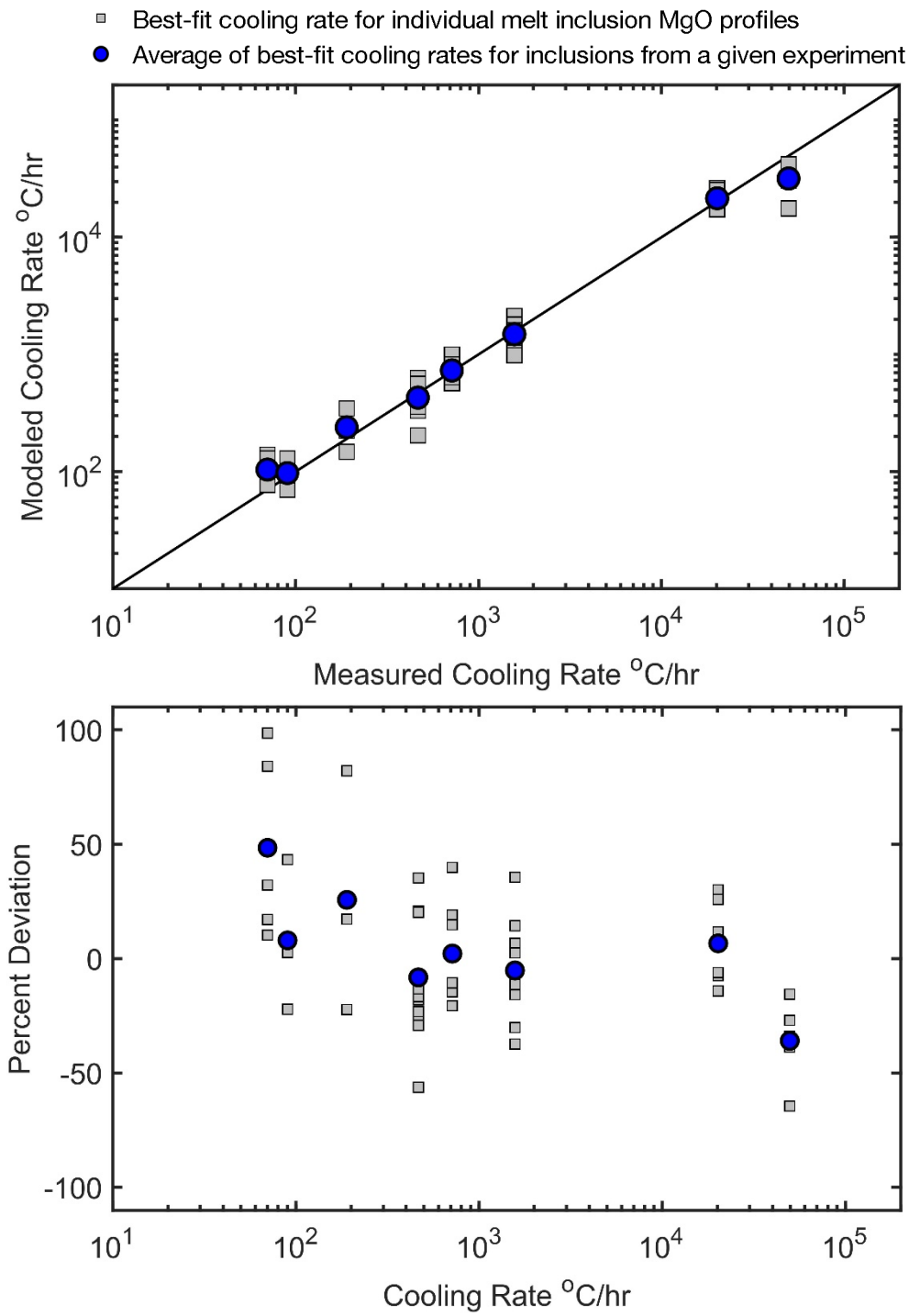


**Figure 13.** Accuracy of the inverse model for MgO diffusion described in Section 4 in recovering the cooling rates of experimentally cooled melt inclusions. (**a**) Comparison of modeled cooling rates to the linear fits to the thermocouple data (Figure 2) for experimentally cooled melt inclusions. Model cooling rate refers to the cooling rate that resulted in the best fit of the diffusion model (Section 4) to the microprobe MgO data from experimental samples. The gray squares show cooling rates for individual inclusions and the blue circles are the mean cooling rate for all inclusions modeled from a given experiment. The solid black line is 1:1. (**b**) Percent deviation (100*(Modeled-Measured)/Measured) between the best-fit model and the data for individual inclusions (gray squares) and the mean for all inclusions in a given experiment (blue circle). See Section 4.3 for discussion.

continuing to use the composition-independent $D_{MgO}$ in the model predicts MgO gradients across inclusions that are much shallower than those in the experimental profile indicating that the composition-independent $D_{MgO}$ is too high at a given temperature to describe the data (green curve in Figure 11a). This result suggests that by using the simultaneously determined $D_{MgO}$ and MgO in the liquid versus temperature functions from the single study of Chen and Zhang (2008), inaccuracies in each of these functions compensated for each other, such that the Newcombe et al. (2014) model provides an accurate overall description of diffusion in the system despite the temperature offset of the MgO in liquid thermometer.

The agreement between the known and best-fit cooling rates for the experimentally treated inclusions shows that for determining the cooling rate experienced during the last stages of the cooling history of an olivine-hosted melt inclusion, either the model presented here or that used by Newcombe et al. (2014) is accurate to within a few tens of percent. However, recovery of $T_{max}$, the temperature interval over which cooling occurred, and the cooling rate of our experiments requires a modified treatment of the problem that incorporates both the changing melt and olivine compositions at the inclusion wall during cooling and a composition-dependent $D_{MgO}$ that can take into account the fact that the inclusions become strongly zoned during cooling, particularly in $SiO_2$. The updated model presented here achieves this and is capable of accurately retrieving the experimentally imposed cooling paths that span three orders of magnitude in cooling rate. We also note that for experiments where the narrow zone of olivine grown during cooling could be measured (Section 3.5, Supplement Section 2.3), the model predicts olivine growth shell thicknesses that are within error of those measured by high-resolution EDS linescans. Although the function for interface liquid MgO vs. temperature is calculated for a particular composition and the $D_{MgO}$ represents a fit for dry basaltic to

rhyolitic liquids, the approach we have taken can be applied more broadly provided these functions are updated for the compositions of the melt (including and perhaps especially the water content of the melt, which increases the diffusivities of MgO and other oxides (Watson, 1981; Zhang, 2010) and lowers the olivine liquidus temperature).

# 6 CaO and Multicomponent Diffusion

## 6.1 Observations of CaO in the experiments

During olivine crystallization, concentration profiles of incompatible elements are expected to be highest at the inclusion wall and to have a concave up shape due to being excluded from the growing olivine and progressively enriched in the adjacent liquid relative to the inclusion center. This is observed for $Al_2O_3$, $SiO_2$, $Na_2O$, and $K_2O$ (Figure 4b,d and Supplement Section 3). For rapidly quenched melt inclusions, CaO is enriched as expected in the liquid boundary layer (Figure 8ab). However, despite its relatively low partition coefficient ($D_{CaO}^{ol/liq}$ = 0.02–0.1; Jurewicz and Watson 1988, Libourel 1999), in some natural inclusions studied by us and by Newcombe et al. (2014) and in our experiments at cooling rates ≤1570 °C/hr, CaO concentrations are lower at the olivine-melt boundary than in the inclusion center (Figure 9c-f). This leads to CaO profiles in the melt that are qualitatively more similar to the zonation in olivine-compatible oxides such as MgO and FeO than to $Al_2O_3$ or $Na_2O$.

Although the CaO concentration adjacent to the olivine crystallization front is low relative to the inclusion center, the *average* CaO contents in the experimental inclusions progressively increase with decreasing cooling rate, as is required to satisfy mass balance for an incompatible oxide. Based on analyses of olivine and melt as close as possible to the inclusion wall, we cannot distinguish ($p<0.005$) the measured $D_{CaO}^{ol/liq}$ (where the ol/liq superscript indicates that this is a partition coefficient as opposed to a diffusion coefficient) for our homogenization experiments at 1225 °C ($D_{CaO}^{ol/liq}$ = 0.013–

0.080, with a mean of 0.026±0.034(2σ), n = 10 olivine/glass pairs) from those in the cooling rate experiments (range $D_{CaO}^{ol/liq}$ = 0.009–0.037, with a mean of 0.018±0.008(2σ), n = 94 pairs). Note that the olivine CaO (mean = 0.30±0.09 wt % CaO at interface) for this calculation was uniformly lowered by 600 ppm to account for secondary fluorescence effects (Supplementary Figure S7) based on the average distance of a clean olivine analysis from the glass boundary (3 μm). While it is possible that a narrow <3 μm band of Ca-rich olivine exists that could satisfy the elevated $D_{CaO}^{ol/liq}$ necessary to account for low CaO in the liquid boundary layer, this high partition coefficient would be inconsistent with the observed accumulation of CaO in the integrated inclusion with progressive cooling and crystallization, and previous experimental data on phenocryst–matrix pairs (Jurewicz & Watson, 1988; Libourel, 1999). Furthermore, in high resolution EDS scans of olivines within 10 micrometers of the boundary with glass, no anomalously high Ca counts were observed. It is unlikely that changing olivine chemistry is driving the change in CaO profile shape in the liquid, and on the basis of the measured $D_{CaO}^{ol/liq}$, we proceed with assuming that local equilibrium between olivine and liquid was maintained at the crystallization front during the experiments.

As described in Section 3.2, evidence for multicomponent diffusion is widespread in natural (Newcombe et al., 2014, and this work) and experimentally cooled olivine-hosted melt inclusions (this work), with the development of the unexpected “reversed” CaO profiles being a particularly extreme manifestation of uphill diffusion. For example, at intermediate cooling rates (Figure 8bc) there are local maxima in CaO near the opposing walls of the inclusion. These local maxima appear to relax by propagating inwards at increasingly longer cooling durations (Figure 8b-d), until the CaO profile is inverted from the expected concave up shape, and all evidence of the profile showing the

expected enrichment in CaO at the olivine-melt interface appears to have been erased (Figure 8ef). In general, this evolution of transient asymmetric diffusion profiles is an indicator of uphill diffusion (Liang, 2010), and the particularly strong manifestation in CaO profiles across melt inclusions is consistent with experimental studies that demonstrate strong diffusive coupling between Ca-bearing melt species and other components, particularly $SiO_2$ (Liang et al., 1996b), FeO, $Al_2O_3$ and $Na_2O$ (Guo & Zhang, 2018), resulting in large magnitude cross-terms in calculated diffusion matrices. Further examination of the extreme CaO behavior in olivine-hosted melt inclusions — first described in Newcombe et al. (2014) — is now possible, however, due to its reproducibility and the systematic development of the CaO profile shape observed in our cooling experiments.

In natural samples from a variety of settings — including the Siqueros Fracture Zone and the Galapagos (Newcombe et al., 2014); Mauna Loa (see Section 6.1); and martian meteorites (see Section 6.2) — CaO profiles in olivine-hosted melt inclusions have shapes ranging from concave up with a maximum at the inclusion wall to concave down with a minimum at the wall. In addition, profiles with low CaO contents in melts near the olivine interface relative to the inclusion center display varying amounts of relaxation and inward movement of the local maxima at intermediate distances from the inclusion edge. Qualitatively, the CaO profile shape can be used to deduce a relative order in the cooling rates of melt inclusions of similar size: profiles with the highest CaO concentration near the inclusion edge indicate rapid cooling; profiles with the highest CaO contents at the inclusion center imply slow prolonged cooling; and profiles with maxima at intermediate distances from the inclusion wall indicate transients only preserved at intermediate cooling rates. Note, however, that when subjected to the same cooling history, inclusions of smaller size will invert to fully concave down more quickly

than larger inclusions, and this must be accounted for when comparing or modeling profiles.

An important point here is that the CaO profile shape can aid in interpreting cooling histories observed in other oxides: For example, as mentioned in Section 3.4.2, some MgO profiles from experiments at lower cooling rates have nearly flat concentration profiles near the inclusion center (Figure 6e, Figure 7c,e) but at MgO values significantly lower than the initially homogenized concentration prior to cooling and olivine growth on the wall, and they clearly do not indicate directly the MgO content of the initially homogeneous molten inclusion. Although we know in our experiments that the profile was initially homogeneous at a higher concentration than that defined by the flat central MgO content, in natural inclusions for which the initial, homogeneous MgO content of the inclusion prior to cooling is not known independently, this could be mistaken for a compositional plateau unaffected by diffusion due to rapid cooling. If so, the inferred cooling history would erroneously start at a lower temperature and therefore with an initially constant but low MgO content across the entire inclusion, as described by Newcombe et al. (2014). Examination of the CaO profile from the same inclusion can be used to indicate roughly whether cooling was so rapid that plateaus in MgO reflect the value at $T_{max}$, or alternatively that the MgO profile evolved during cooling to produce a central plateau at MgO contents lower than those prevailing at $T_{max}$ (e.g., by multicomponent diffusion), in which case the actual value of $T_{max}$ and the initial MgO must be reconstructed (Section 6).

### 6.2 A simplified model of CaO diffusion in olivine-hosted melt inclusions

In this section, we develop a simplified treatment that can explain semi-quantitatively the anomalous behavior of CaO in our experiments and in natural inclusions. The diffusion matrix [D], whose elements $D_{i\text{-}j}$ indicate the flux of component

*i* driven by the gradeient in the concentration of component *j*, can be decomposed into two other square matrices, one that describes activity-composition relationships ([G]), and a "kinetic matrix" ([L]) whose elements are phenomenological coefficients that satisfy Onsager's reciprocal relations (Onsager, 1945; de Groot & Mazur, 1962; verified in the $CaO$-$Al_2O_3$-$SiO_2$ (CAS) system by Spera & Trial, 1994, Liang, 1997). There are more constraints on activity-composition relationships (elements of [G]) in basalts than measurements of [L] and so we have developed a simplified model to provide insight into the observed behavior of CaO in natural and experimentally cooled melt inclusions that assumes [L] to be diagonal for oxide components; i.e., gradients in chemical potential or activity for each oxide can be described by one term (e.g., $L_{CaO\text{-}CaO}$), and thus diffusion profiles of chemical potential or activity (but not necessarily of concentration) are monotonic with respect to the distance variable. The consequence is that any off-diagonal terms in [D] are assumed to be due to off-diagonal terms in [G]; i.e., to non-ideality in the thermodynamic mixing relationships. The assumption of a diagonal [L] is probably not generally valid for silicate melts, as has been shown for CAS liquids (Spera & Trial, 1994; Liang, 1997). This can be tested on the experimental inclusion profiles by converting the oxide profiles into chemical potential profiles using MELTS (see Supplementary Figure S8 for details); the resulting profiles which have local extrema in concentration are also not monotonic in chemical potential, indicating that for these inclusions, in terms of the MELTS component space and thermodynamic model, [L] is not diagonal. While acknowledging the limitations of our approximation of a diagonal [L], we demonstrate in this section that such a model is capable of qualitatively describing and therefore providing insights into the cooling-rate dependent behavior of CaO concentration profiles in cooled, olivine-hosted melt inclusions.

Imagine a single increment of olivine crystallization followed by isothermal relaxation of the elevated CaO content in the olivine-depleted melt at the interface. If the melt were an ideal solution, diffusion of CaO would occur from the high-CaO melt at the interface to the interior of the inclusion, and the qualitatively simple, expected concave upward profile of $X_{CaO}$ would develop (as it does for $Al_2O_3$ and $SiO_2$ in Figures 11b and 11c). However, gradients in other oxides from the interface toward the center of the inclusion are also produced by crystallization of olivine at the interface, and these (especially the alkalis; e.g. in MELTS; Libourel, 1999) contribute to an increase in the CaO activity coefficient ($\gamma_{CaO} = a_{CaO}/X_{CaO}$) in the melt at the interface relative to the inclusion interior. If the diffusion of CaO is much faster than those of the components contributing to this increase in $\gamma_{CaO}$, diffusion of CaO from the interface toward the inclusion center would tend to equalize the chemical potential of CaO (and its activity, $a_{CaO}$) while the concentrations of other, slower diffusing components would remain largely unchanged. Given the increase in $\gamma_{CaO}$ toward the interface due to the effects of other melt components, equalizing $a_{CaO}$ across the inclusion in this extreme example (i.e., where the other components are essentially immobile except to provide a counterflow) must lead to a decrease in $X_{CaO}$ from the center of the inclusion toward its edge and, in order to satisfy mass balance, to an increase in $X_{CaO}$ in the center of the inclusion relative to its initial concentration (as observed in Figure 8). The situations in our experiments and in nature are more complex since olivine crystallization is continuous during cooling and the temperature is not constant, but provided that the effect of composition on $\gamma_{CaO}$ is large enough, the same behavior for CaO can be anticipated as we have described here for a single increment of olivine growth and isothermal relaxation of the CaO concentration profile.

To model CaO, we adopt an activity-based approach for diffusion where the flux of the CaO component in the liquid is proportional to its activity gradient (Zhang, 1993). In the context of this model, the batch olivine crystallization calculation based on MELTS used in Section 4 predicts that the activity of CaO in the residual liquid monotonically increases with decreasing temperature and progressive olivine crystallization, and that crystallization of olivine at the inclusion wall would thus produce a concave-up activity profile decreasing from the edge to the center of the inclusion at all cooling rates (Figure 14c). Analogous to the boundary condition defined for MgO in equation (1), a polynomial fit to the MELTS calculation was used to define $a_{CaO}^{liq}$, the CaO activity in the interface liquid in equilibrium with olivine as a function of temperature (Figure 14b). An intrinsic diffusion coefficient (Zhang, 1993) was adopted from $^{44}Ca$ self-diffusion in a haplobasaltic melt (LaTourrette, 1996), and along with the $a_{CaO}^{liq}$ boundary condition, was used to forward model the $a_{CaO}$ profile evolution, analogous to the procedure described in Section 4. The approximation of using the self-diffusion coefficient to model activity gradients is valid given that we chose to model an effectively binary system, in which the intrinsic diffusivity and self-diffusivity are equivalent (see Zhang, 1993, for details). This model produces concave up, monotonic profiles of $a_{CaO}$ across the melt inclusion at each cooling rate (Figure 14c), and reflects the expected shape of the activity (or chemical potential) profile as a function of cooling rate if the [L] matrix were diagonal.

For simplicity, the compositional dependence of $\gamma_{CaO}$ was modeled assuming that $X_{Na2O}$-is a monitor (if not the driver) of changes in the activity coefficient across the zoned inclusion. This assertion is supported by peridotite melting experiments, where $\gamma_{CaO}$ has been shown to be elevated in alkali-rich low-degree melts from fertile compositions compared to alkali-poor depleted compositions at the same melt fraction (Wasylenki et

al., 2003). Additionally, the $D_{CaO\text{-}Na2O}$ cross-terms in the diffusion matrices of Guo and Zhang (2016, 2018) are the largest magnitude coupling term between CaO and another oxide, indicating strongly coupled diffusion. $Na_2O$ is itself strongly coupled to the slowly diffusing $SiO_2$ (Watson, 1982; Liang, 2010) and $Al_2O_3$ (Guo & Zhang, 2018), the result being that steep gradients in $X_{Na2O}$ persist (i.e., do not diffuse away rapidly, Supplement Section 3) in the diffusive boundary layer. A function relating $\gamma_{CaO}$ to $X_{Na2O}$ in the liquid (Figure 14b) was defined by taking the liquid composition from melt inclusions experimentally homogenized at 1225°C (Table 2), diluting or enriching it with $Na_2O$, and monitoring the corresponding changes in $\gamma_{CaO}$ at constant temperature using MELTS, ignoring changes in other melt components, which were proportionally changed at each dilution so the sum of mole fractions equaled one. The development of $X_{Na2O}$ profiles across a melt inclusion was modeled (Figure 14a) assuming that $Na_2O$ is incompatible in olivine (analogous to modeling $Al_2O_3$, see Supplementary Material Section 2) and has a diffusion coefficient $D_{Na} = D_{Si}$ ($D_{Si}$ adopted from Chen & Zhang, 2008). Using the relationship between $X_{Na2O}$ and $\gamma_{CaO}$ shown in Figure 14b, $\gamma_{CaO}$ can be calculated at each position and time.

The $X_{CaO}$ profile is then obtained at each time step by dividing the modeled $a_{CaO}$ profile by the corresponding $\gamma_{CaO}$ profile, calculated from the $Na_2O$ model. Results of this forward model are shown in Figure 14d for linear cooling from 1225 to 1000 °C for a range of cooling rates comparable to those achieved experimentally. Despite the oversimplification of using a single cross-term to describe the activity-composition relations, this forward model captures the distinctive features of the CaO profile evolution as a function of cooling rate: an elevated $X_{CaO}$ close to the interface relative to the center at the highest cooling rate; the inward movement and broadening of local maxima near the inclusion walls at intermediate rates; the ultimate complete inversion of the model

**Figure 14**

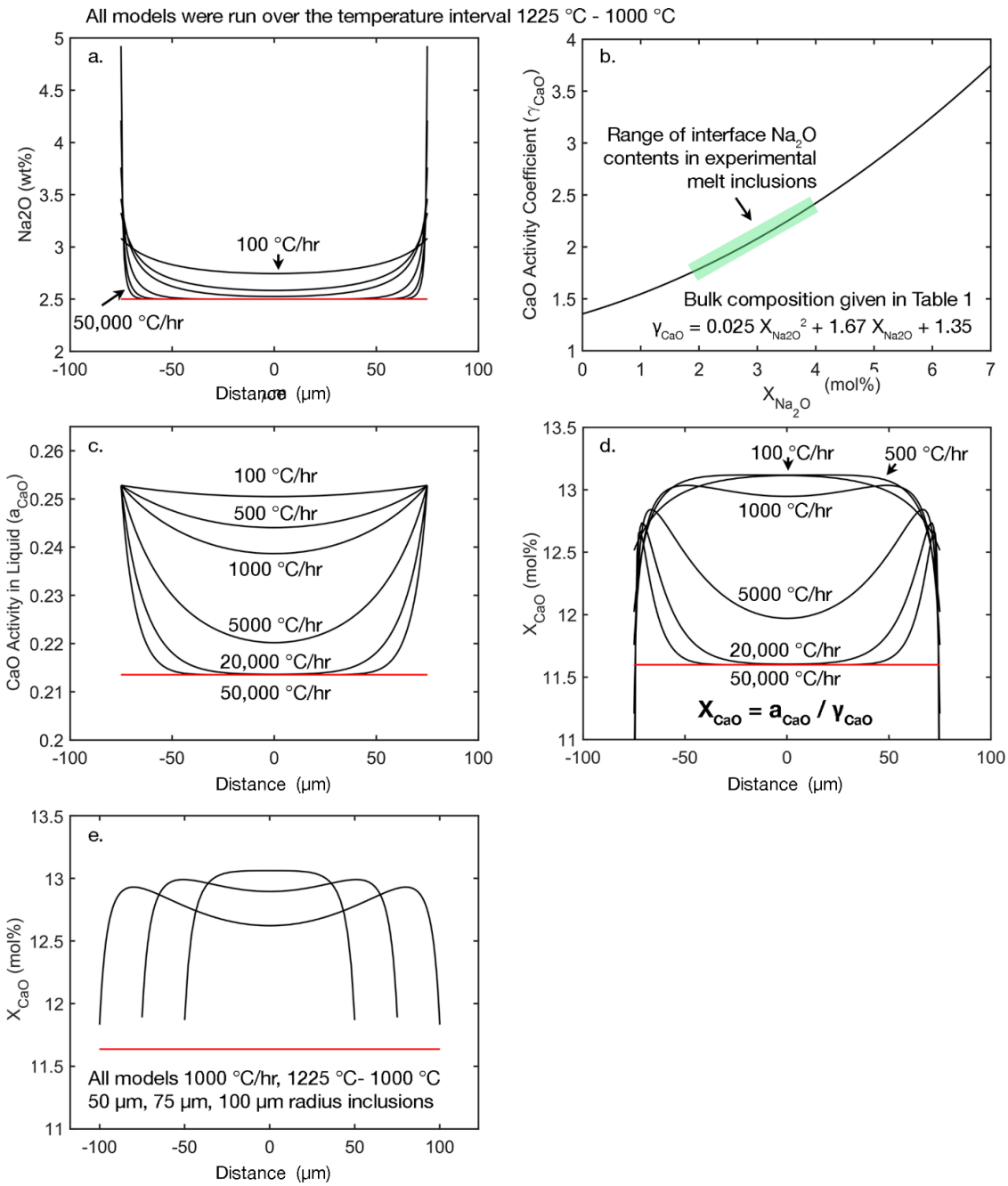


Figure caption on the following page.

**Figure 14.** All of the forward models shown on panels a and c-e were run over the temperature interval 1225 °C–1000 °C. (**a**) Forward models of $Na_2O$ profiles (black curves) across a 75 μm radius melt inclusion cooled from 1225 °C–1000 °C at rates of 50,000 °C/hr, 20,000 °C/hr, 5000 °C/hr, 1000 °C/hr, 500 °C/hr, and 100 °C/hr. Red horizontal line is the initial $Na_2O$ of the liquid. The interface $Na_2O$ was calculated by mass balance with olivine growth calculated with the MgO diffusion model (Section 4) and is built up in the liquid near the inclusion wall because the $Na_2O$ gradients are slow to relax. (**b**) Mole fraction $Na_2O$ ($X_{Na2O}$) vs. the CaO activity coefficient ($\gamma_{CaO}$) in the liquid according to MELTS. Described in Section 5.1, the melt composition given in Table 2 was diluted by varying the mole fraction of $Na_2O$ and then monitoring the corresponding changes in the activity coefficient of CaO in the liquid. The black curve is a 2$^{nd}$ order polynomial fit to the output of this exercise. (**c**) Forward models of the CaO activity in the liquid ($a_{CaO}$), calculated as described in Section 5.1. Horizontal red line corresponds to the MELTS calculated activity of $a_{CaO}$ at 1225 °C in a liquid whose composition is given in Table 2. The boundary condition of $a_{CaO}$ in the interface liquid is given by the MELTS calculation of batch olivine crystallization with the starting composition given in Table 2. (**d**) Forward models of the CaO mole percent in the liquid ($X_{CaO}$), calculated by dividing the $a_{CaO}$ profile at each temperature step by the corresponding $\gamma_{CaO}$, which was calculated by substituting the $Na_2O$ profiles into the equation shown in panel **b**. Horizontal red line is the initial $X_{CaO}$ in the models. (**e**) Forward models for three inclusions of different sizes (50 μm, 75 μm, and 100 μm) all cooled at 1000 °C/hr from 1225 °C–1000 °C, which show how the transient maxima in the CaO profiles relax more quickly for smaller inclusions than for larger inclusions subjected to the same cooling path.

profiles to concave down shapes at lower cooling rates where CaO is low at the olivine-liquid boundary relative to the inclusion interior; and the progressive increase in the average CaO in modeled melt inclusion as required by its incompatibility in the olivine crystallizing on the wall. The low $X_{CaO}$ near the inclusion wall for all profiles results from the buildup of $Na_2O$ in the interface region during progressive olivine crystallization. The model also reproduces the expected effect of inclusion size on the shape of the CaO profile for a given cooling path (1225–1000 °C), where the transient humps relax more quickly in smaller inclusions for which diffusive exchange between the inclusion edge and center is more rapid (Figure 14e). We note, however, that in this model, due to the assumption that changes in $\gamma_{CaO}$ are solely due to $X_{Na2O}$, CaO does not strictly obey mass balance, however the magnitude of the deviation from mass balance is small. For example, at rates of 500–50,000 °C the integrated modeled CaO contents for a 75 μm radius inclusion (Figure 14d) deviate by less than 0.15 wt% from the expected bulk CaO assuming mass balance and $D_{CaO}^{ol/melt} = 0.02$, and at 100 °C/hr the modeled inclusion is 0.42 wt% deficient in CaO, corresponding to a 4% relative deficit from mass balance. While a more sophisticated approach may be necessary to accurately model CaO diffusion, the simplified model presented here reproduces the overall effect observed in melt inclusions.

Figure 15 compares microprobe data from four experiments to the corresponding forward model calculations for CaO, MgO, and $Na_2O$, run with no free parameters by specifying $T_{max}$ = 1225 °C, $T_{min}$ = 1000 °C, and cooling rate. The shapes of the CaO profiles — as well as those of $Na_2O$ and MgO — reproduce well those measured in the experimental inclusions, with elevated CaO near the interface is the more rapidly cooled experiments (Figure 15ab) and low CaO at the interface relative to the inclusion center in the slowly cooled experiments (Figure 15cd). The model is offset in absolute

concentration from the measured experimental profiles, almost certainly reflecting the oversimplification that all changes in $\gamma_{CaO}$ are due to $Na_2O$ and inherent variability in the initial $Na_2O$ concentration of experimental inclusions (Table 2, Figure 5b). Nevertheless, this simple model demonstrates that under certain plausible assumptions it is possible to describe the main features of the CaO profile evolution as a manifestation of increased $\gamma_{CaO}$ in the boundary layer melt, which is enriched in those oxides that are slow to diffuse and which have a substantial influence on the solution properties of Ca-bearing liquid components. The model also shows that except for the most rapidly quenched samples and for the largest melt inclusions, the CaO contents measured at the center of the inclusion will be high relative to the initial concentration prior to crystallization during cooling, and thus in order to obtain the correct concentration of CaO in a glassy melt inclusion either the inclusion needs to be homogenized at the correct temperature or the CaO profile can be integrated across the inclusion (i.e., a single analysis from the inclusion center is likely to be an unreliable measure in all but the most rapidly cooled inclusions).

## 7 Natural samples: Hawai‘i and shergottite Y980459

### 7.1 Hawai‘i

Cooling rates were determined for glassy melt inclusions from Papakōlea Beach olivine by fitting their measured MgO concentration profiles using the model described in Section 4. For modeling natural inclusions, it is necessary to calculate either the composition or temperature ($T_{max}$) of the homogeneous inclusion liquid prior to cooling, which serves to define the model initial condition. There are several possible approaches to estimating this composition (see Supplement Section S2 in Newcombe et al., 2014), and as described in Section 5, the shape of the CaO profile can help distinguish whether plateaus in MgO are due to rapid cooling or to multicomponent effects. Half of the natural

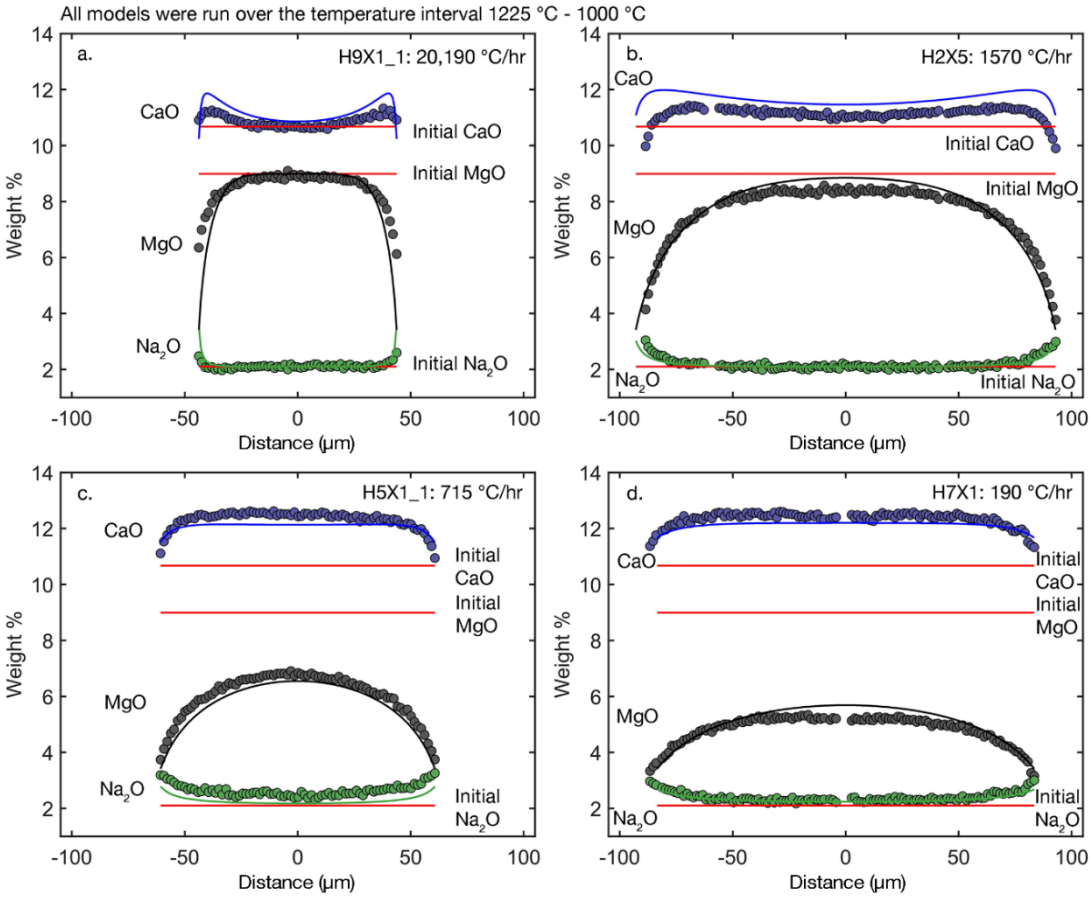


**Figure 15**. Horizontal red lines indicate the initial CaO, MgO, and $Na_2O$ contents of the liquid in weight %. Colored circles are microprobe data from selected experimental melt inclusions, blue: CaO, gray: MgO, green: $Na_2O$. The corresponding colored lines are forward models calculated with the CaO model described in Section 5 over a temperature interval of 1225 °C–900 °C and specifying the measured experimental cooling rate. (**a**) H9X1_1: 20,190 °C/hr; (**b**) H2X5: 1570 °C/hr; (**c**) H5X1_1: 715 °C/hr; (**d**) H7X1: 190 °C/hr.

inclusions we have studied show evidence for protracted cooling, either with CaO profiles that are highest in the inclusion center and lowest at the olivine-glass interface or with CaO maxima at positions between the inclusion center and the olivine interface; for such inclusions, the central MgO contents have likely been modified by diffusive exchange with the evolving interface melt (e.g., compare the MgO and CaO profiles in Figures 7 and 8 panels c-f, and HIGS2 and HIGS14 in Figure 16cd). In these cases, the initial temperature or MgO contents must be estimated using an alternative to taking the measured central MgO content as representative of the initial MgO content.

Five of the ten natural Papakōlea inclusions studied have CaO profiles that indicate they experienced rapid cooling and have compositional plateaus in MgO that can be used to directly set the model initial conditions (e.g., HIGS9 and HIGS4, Figure 16ab). Because the unheated Papakōlea samples are considerably more oxidized than in the experiments (see XANES results in Section 2.2), a new boundary condition was calculated using a fit to the MELTS-calculated liquid line of descent for olivine crystallization at FMQ+0.3,

$$C_{MgO}^{liq}(FMQ+0.3) = 3.352x10^{-5} \times T^2 - 0.06828 \times T + 36.18 \quad (3)$$

Where T is in K and $C_{MgO}^{liq}$ is weight percent MgO in the liquid. Equation (3) has the same form as equation (1) but takes into account that forsteritic olivine is stabilized at higher $fO_2$ (Nitsan 1974) and is shown for comparison as the dashed light blue line in Figure 10a. Applying equation (3) using the corresponding central plateau MgO contents in the rapidly cooled samples (which ranges from 6.2 to 7.2 wt% in the different inclusions) gives temperatures of 1123–1160 °C (compared to using equation (1), giving 1137–1174 °C). For each inclusion with an MgO plateau interpreted as representing the initial MgO content of a homogeneous inclusion prior to cooling and crystallization, this calculation was used to set the initial temperature,

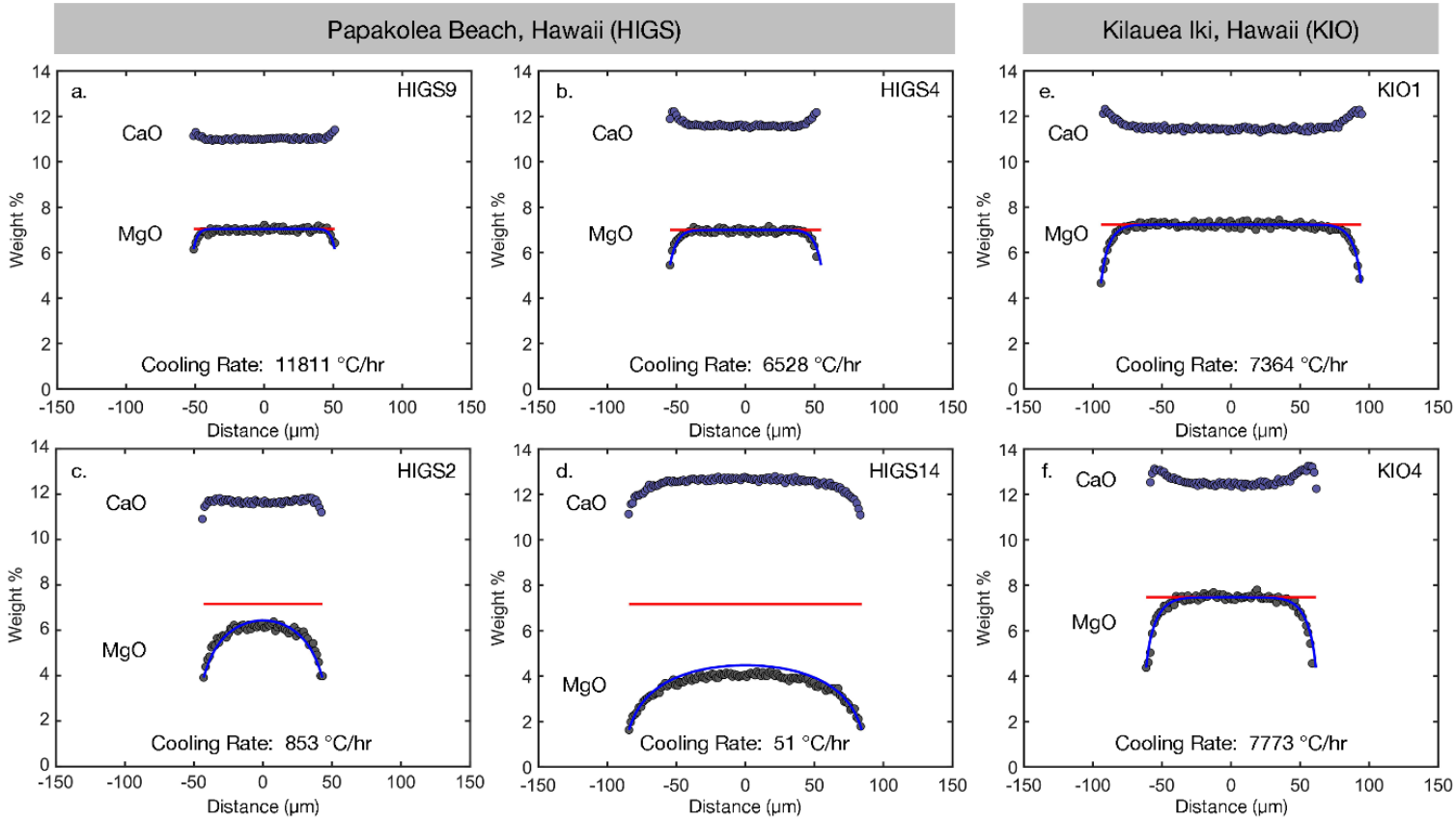


**Figure 16.** Application of the inverse model for MgO diffusion described in Section 4 and Section 6 to natural Hawaiian olivine-hosted melt inclusions. Panels (**a-d**): Papakolea, Hawaii. Panels (**e** and **f**): Kilauea Iki, Hawaii. The blue curves show the best-fit model to the data, and the corresponding cooling rate (°C/hr) is listed in each panel. The red horizontal line is the calculated initial MgO in the liquid prior to cooling at $T_{max}$. In addition to the MgO profile shown in dark gray filled circles, the corresponding CaO profiles are shown in blue circles to demonstrate the cooling-rate dependent shapes described in Section 5 and used to evaluate relative cooling rates as discussed in Section 6.

$T_{max}$, after which the inversion model was run as described in Section 4 for the experiments but with equation (3) substituting as the boundary condition for the temperature dependence of $C_{MgO}^{liq}$. Cooling rates that correspond to the best fit profiles for the five rapidly cooled inclusions (subset shown in Figure 16ab, all results in Supplementary Table 2) have a range of 7500–11800 °C/hr. In addition to the errors inherent to the inverse model, there are additional uncertainties related to the precision of the MgO microprobe data. These errors are particularly important for rapidly cooled inclusions with narrow boundary layers because the model fit is sensitive to the few data points near the inclusion wall that have MgO contents less than the central plateau (Supplement Section 2). Following the bootstrap approach employed by Newcombe et al. (2014), the errors were calculated by perturbing the MgO profiles with Gaussian noise sampling the uncertainty of the MgO microprobe data ($1\sigma$ = 0.075 wt%), and then refitting each synthetic profile and calculating the distribution of best-fit cooling rates. For the rapidly cooled inclusions, the errors in the calculated cooling rate correspond to 6–14% relative, and for the slowly cooled inclusions with no central plateau described below these errors are typically <1%. The inversions were also run assuming equation (1) as the boundary condition, which resulted in best-fit cooling rates that differed by -20% (HIGS11) to +36% (HIGS4) from the rates calculated using equations (2) and (3).

In order to determine $T_{max}$ for those inclusions with center compositions that have been modified by diffusion during cooling, Newcombe et al. (2014) adopted the approach of taking the highest MgO value recorded for a given inclusion population and applying the MgO vs. T thermometer of Chen and Zhang (2008). For the Papakōlea samples, the highest MgO (7.2 wt%) comes from the compositional plateau of HIGS11, and applying equation (3) corresponds to a $T_{max}$ of 1160 °C. An alternative to this assumption would

be to reconstruct the initial composition of the liquid by adding liquidus olivine in increments to the integrated bulk composition of the inclusion until reaching a target liquidus olivine composition, as is commonly done to determine the composition and conditions of melt inclusion entrapment. Due to ambiguity in accurately knowing what olivine composition along its zoning profile was in equilibrium with the inclusion liquid at $T_{max}$ (see Supplement Section 2 for details), for the Papakōlea inclusions the centers of which were modified by diffusion we adopt the approach of Newcombe et al. (2014) by setting $T_{max}$ via the maximum plateau MgO contents from a population of related olivines. For inclusions HIGS2, HIGS15, HIGS8_1, and HIGS6, the best-fit cooling rates calculated using $T_{max}$ = 1160 °C are 854 °C/hr, 615 °C/hr, 279 °C/hr, and 226 °C/hr, respectively, while HIGS14 has a substantially lower rate at 51 °C/hr. We note that when using $T_{max}$ set by reconstructing the inclusion to be in equilibrium with the olivine analysis measured closest to the inclusion wall (giving $T_{max}$ = 1223–1276 °C, Supplement Section 2), the calculated cooling rates are 25–45 % higher relative to those using $T_{max}$ = 1160 °C.

In addition to the Papakōlea samples, melt inclusions in four olivines collected in the Kīlauea Iki crater were measured. The scoracious olivine gravels are interpreted to be from a fire fountaining stage of the 1959 eruptions (Richter et al., 1970). All four inclusions have elevated CaO contents at the inclusion edge and compositional plateaus in the inclusion centers for MgO (Figure 16ef) and all other oxides, indicating rapid cooling and permitting a straightforward calculation of $T_{max}$. The $Fe^{3+}/Fe_{Total}$ from measured in Kīlauea Iki melt inclusions by Helz et al. (2016) (ranging from 0.16–0.18, mean = 0.17, n = 5 inclusions) overlap with the Papakōlea inclusions ($Fe^{3+}/Fe_{Total}$ = 0.16–0.20, mean = 0.18, n = 4 inclusions). Expressed relative to FMQ at 1225 °C and 1 bar (Kress & Carmichael,1991), equation 7), the data sets are statistically indistinguishable

in terms of the oxygen fugacity recorded in their glasses (ΔFMQ = + 0.29±0.19 and + 0.45±0.18 (1σ), respectively). Accordingly, equation (3) (calculated at ΔFMQ = + 0.3) was used to evaluate the T-dependent boundary condition of MgO in the evolving interface liquid for the model calculation, as for the Papakōlea inclusions. The MgO contents at the plateaus of these inclusions range from 7.2 to 7.7 wt%, giving modeled $T_{max}$ of 1161–1181°C via equation (3). The best-fit cooling rates for these four Kīlauea samples range from 5100 °C/hr to 8800 °C/hr (Figure 17, Supplementary Table 2). Errors associated with the uncertainty in the MgO microprobe analyses correspond to a 4–7% relative difference in the calculated cooling rate (1σ).

The Papakōlea samples form two distinct groups, those with low cooling rates (51–854 °C/hr) and rapidly cooled samples (6520–11,810 °C/hr); the Kīlauea Iki samples (5100–8800 °C/hr) correspond well to the more rapidly cooled Papakōlea samples. Taken together, these Hawaiian inclusions span a similar range of cooling rates as those obtained by Newcombe et al. (2014) for subaqueous and subaerial basalts (Figure 17a). Assuming a simple model of one-dimensional heat diffusion (Carslaw & Jaeger, 1959) into an infinite basaltic melt (thermal diffusivity $\kappa = 0.35$ mm$^2$/second, Patrick et al., 2004), and that the inclusions cooled over the interval from $T_{max}$ to $T_{min}$, these cooling rates are consistent with olivine phenocrysts located 0.3–0.5 cm from a 0 °C boundary for the rapidly cooled group and ~2–8 cm for the more slowly cooled group. The difference between the more rapidly and more slowly cooled Papakōlea inclusions — which do not differ significantly in their major element compositions — could be related to cooling at different depths in either subaerial or submarine basalt flows, but the implication that all formed within ~10 cm of a flow surface seems highly restrictive, unless glassy inclusions can only form under these conditions. On the other hand, the correspondence of the cooling rate ranges of the more rapidly cooled Papakōlea samples, subaerial spatter from

the Santiago volcano in the Galapagos (Newcombe et al. 2014), and the Kīlauea Iki samples (which are known to have formed during fire fountaining events) may reflect that they all experienced similar histories as ballistic molten basaltic fragments. This would be consistent with the conclusion of Walker (1992) that most of the Papakōlea olivine beach sands were derived from erosion of overlying pyroclastic ash beds. In this case, the group of Papakōlea inclusions that yield significantly lower cooling rates could represent a different emplacement mechanism, perhaps derived from the massive basalt flows that overlie the ash beds (Walker, 1992), or formed in larger droplets of molten basalt that cooled more slowly during fallout and/or continued cooling in the pyroclastic pile after deposition (e.g., Thomas & Sparks, 1992; Capaccioni & Cuccoli, 2013).

Another possibility is that water in the inclusion liquids affects MgO diffusion and that the apparent variability in cooling rate is due to different $H_2O$ contents. Using a $D_{MgO}$ determined from dry diffusion data to calculate a cooling rate from an MgO profile formed in a wet liquid would lead to erroneously low cooling rates, implying that the group of inclusions with low cooling rates should have significantly higher $H_2O$ contents. However, although the natural inclusion from Papakōlea with the lowest calculated cooling rate (HIGS14, 51 °C/hr, Figure 16d) has $H_2O$ = 0.20±0.02 wt% (2σ), which is higher than the $H_2O$ contents measured in a rapidly cooled inclusion (HIGS11, 7900 °C/hr with $H_2O$ = 0.10±0.04 wt% (2σ)), the low water contents in both and the relatively small difference between the two $H_2O$ contents are unlikely to account for the three order of magnitude difference in calculated cooling rate. Kīlauea Iki melt inclusions have $H_2O$ contents from 0.25 to 0.95 wt% (Anderson & Brown, 1993; Sides et al., 2014; Tuohy et al., 2016), and yet the inclusions have uniformly high cooling rates. More samples would need to be analyzed to understand whether the bimodality in cooling rates determined for

the Papakōlea melt inclusions is robust or an undersampling a continuum, however it is unlikely that the variability in cooling rates is due to different $H_2O$ contents.

Most of the literature on quantifying cooling rates of natural volcanic glasses comes from enthalpy relaxation geospeedometry, where glasses are subjected to heating and cooling cycles through the glass transition in a differential scanning calorimeter that monitors heat capacity (Wilding et al., 1995). This technique has been applied to natural glasses, including several studies of Hawaiian glasses that report a wide range in cooling rates measured at the glass transition (Figure 17). These include degassed hyaloclastites and undegassed pillow rims from the Hawai‘i Science Drilling Project (HSDP) Core 2, giving rates of 360–260,000 °C/hr and 720–167,000 °C/hr, respectively (Nichols et al., 2009); glassy crusts of pahoehoe flows from Pu’u ‘O’o with cooling rates of 480–8400 °C/hr (Gottsmann et al., 2004); and cooling rates recorded in sieved glass shards (300,000–600,000 °C/hr for the 0.8 - 1.2 mm fraction, and $10^8$ °C/hr for 30–80 μm fraction) from explosive submarine eruptions at Loihi Seamount (Potuzak, 2008). The upper half of the distribution of cooling rates calculated based on of zoning in melt inclusions overlap with the cooling rates based on the enthalpy relaxation approach applied to glassy pahoehoe crusts (Gottsman et al., 2014) (compare Figure 17a and 17b) and the lower half of the distribution of HSDP glasses (for which the pillow rims are likely most comparable to the submarine MORB and OIB samples investigated by Newcombe et al., 2014). However, the melt inclusion results do not approach the highest rates (up to ~$10^5$-$10^6$ °C/hr) inferred by enthalpy relaxation on the HSDP hyaloclastites and pillow rims or to the ~$10^6$–$10^8$ °C/hr measured by enthalpy relaxation on the Loihi glass shards. However, applying our model to inclusions that were

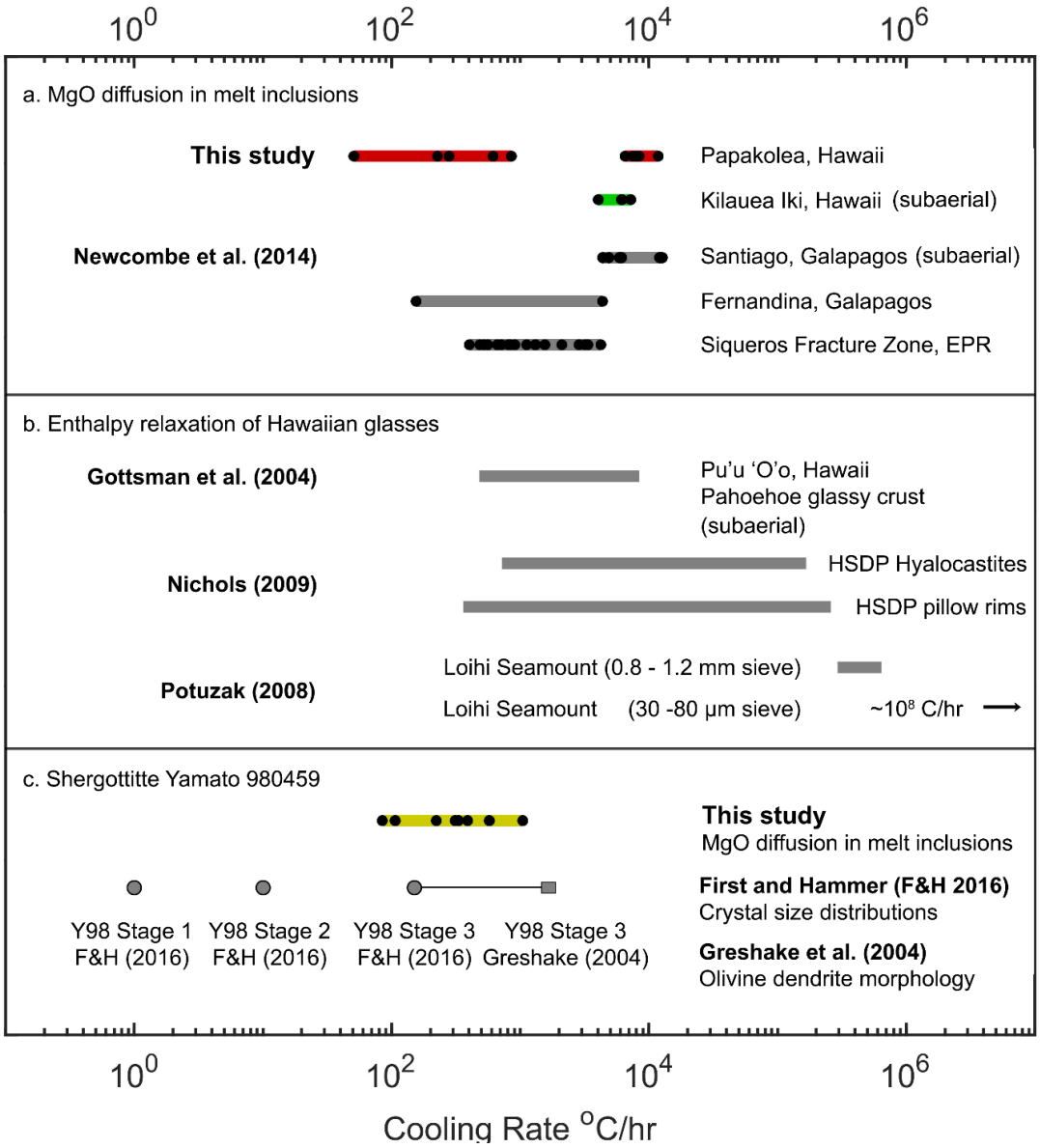


**Figure 17.** Histograms of cooling rates calculated for volcanic samples. (**a**) Cooling rates determined by MgO diffusion in olivine-hosted melt inclusions. The colored bars show the range of cooling rates calculated from MgO diffusion speedometry in natural melt inclusions from this study: Papakolea (red bars), Kilauea Iki (green bar). The three gray bars below show cooling rates calculated by MgO diffusion speedometry in melt inclusions from the Galapagos and Siqueros Fracture Zone (Newcombe et al., 2014). The filled circles correspond to cooling rates from individual inclusions. (**b**) Cooling rates of Hawaiian glasses determined by enthalpy relaxation. The gray bars show ranges of cooling rates from Pu'u O'o (Gottsman et al., 2004), HSDP hyaloclastites and pillow rims (Nichols et al., 2009), and from Loihi Seamount (Potuzak, 2008). Note that the cooling rates calculated for the fine grain sieve from Loihi Seamount plot off of the chart ($10^8$ °C/hr), and are indicated by an arrow. (**c**) Cooling rates calculated using a variety of techniques for shergottite Yamato 980459. Yellow bar and filled circles show cooling rates calculated from this study using MgO diffusion in glassy melt inclusions. The gray circles on the row below the yellow bar show estimated cooling rates for Stages 1-3 of martian meteorite Yamato 980459 from the dynamic cooling experiments of First and Hammer (2016), and the gray rectangle shows the range of estimates for Stage 3 from Greshake et al. (2004) based on the morphology of olivine dendrites.

experimentally drop-quenched directly from the 1260 °C hotspot in experiment H10X into room temperature water (i.e., inverting the narrow MgO diffusion profiles caused by quench growth of olivine in the homogenized samples, black rectangles labeled "generated by quench growth" in Figure 5) yield cooling rates ranging from 44,000–120,000 °C/hr, suggesting that our approach may be capable of resolving rates at least this high in natural inclusions (although for such drop-quenched inclusions, there are sparse MgO analyses in the narrow boundary layer in the interface liquid and so the inversion for cooling rate is more sensitive to the uncertainty in MgO analyses ($1\sigma$ = 0.075), giving associated errors of 16,000–100,000 °C/hr). In any case, the uncertainties on our derived cooling rates are far too small to explain the absence of natural samples extending to the extraordinarily high cooling rates determined for some submarine glasses based on enthalpy relaxation. Perhaps the difference reflects the higher temperature range probed by our approach relative to the enthalpy relaxation measurements, which measures cooling rates at the glass transition. And although asymptotic cooling would be expected to lead to lower cooling rates for the lower temperatures probed by the enthalpy relaxation technique, it is also possible that more complex thermal histories are involved in the low temperature thermal histories, especially for the Loihi glass shards produced by explosive submarine eruptions. Application of the techniques developed here and in Newcombe et al. (2014) to melt inclusions in olivines with adhered matrix glass to which the enthalpy relaxation technique could be applied would provide useful information on whether the two techniques are comparable when applied to samples that experienced identical cooling histories, and if not, what this might signify.

## 7.2 Mars

Melt inclusions occur in the olivines of martian meteorites (i.e., olivine-bearing shergottites, nakhlites, and chassignites), but they are rarely entirely glassy (as opposed to partially crystalline) and even more rarely do they have $SiO_2$ contents <60 wt% comparable to the basaltic glassy inclusions from Hawai‘i that we have studied (Ikeda, 2005). Moreover, the glassy inclusions in martian meteorites are typically <10 μm in radius, and they are often in the same host grains as larger, partially crystallized inclusions. Because the number of microprobe points across such small glassy inclusions is limited, they typically preclude applying the inversion model described in Section 4. The lack of large glassy inclusions in martian minerals, and the prevalence of multiphase crystalline magmatic inclusions, has been interpreted to reflect prolonged episodes of slow cooling in most of the inclusion-bearing samples (Ikeda, 2005).

An exception is the olivine-phyric shergottite Yamato 980459 (Y980459), which has been extensively studied due to its vitrophyric groundmass texture indicative of rapid cooling, and a whole-rock composition that has been interpreted as a relatively primitive melt of the martian mantle (Greshake et al., 2004; Musselwhite et al., 2006; Usui et al., 2008; First & Hammer, 2016). Thin sections of Y980459 have relatively large (up to ~100 μm longest dimension) glassy magmatic inclusions contained in olivine (Ikeda, 2004; Greshake et al., 2004; Ikeda, 2005). A multi-stage magmatic thermal history of Y980459 has been proposed to explain: (1) large olivine phenocrysts formed during slow cooling from a liquidus temperature of 1440 °C at rates <1 °C/hr (First & Hammer, 2016); (2) the crystal size distributions (CSD) of pyroxene phenocrysts, interpreted as requiring cooling rates <10 °C/hr (Lentz and McScween 2005, First & Hammer, 2016); and (3) the vitrophyric groundmass texture, interpreted as evidence of a late stage of rapid cooling with rate estimates ranging from ~150 °C/hr (First & Hammer, 2016) up to 1450–1890

°C/hr (Greshake et al., 2004) (Figure 17). Although the melt inclusions were likely trapped during the growth of phenocrysts early in the cooling history of the magma, the proposed cooling rates from stages 1 and 2 are too low to preserve measurable diffusion profiles in melt inclusion based on our results. For example, a forward model of an inclusion cooling from 1150 °C to 1050 °C predicts that the MgO gradient will be less than the 2σ uncertainty in the microprobe measurements (<0.15 wt%) for inclusions <50 μm in radius. The initial slow cooling stages were likely at temperatures of 1440 °C down to ~1115 °C (First & Hammer, 2016) where diffusion would have been even more efficient at homogenization of inclusions than in the example given in the previous sentence. Accordingly, the inverse model developed in Section 4 is only applicable to cooling stage 3, the final cooling interval, which produced the vitrophyric matrix. We applied our model to determine cooling rates on glassy, olivine-hosted melt inclusions in Y980459, assuming that these inclusions were initially homogeneous at a reconstructed $T_{max}$ that postdates the growth of the olivine and pyroxene phenocrysts formed during cooling stages 1 and 2.

The sample analyzed was a polished thin section of Y980459. As opposed to the Hawaiian samples, which were individually selected and then polished to expose melt inclusions at their maximum dimension, the meteorite thin section was analyzed as received and so the original dimensions of exposed inclusions are unknown, as well as the orientation of the thin section cut through their initial shapes. When applying the inverse model to progressively off-center cuts through a model spherical melt inclusion, which sample more of the boundary layer (Newcombe et al., 2014), best-fit cooling rates calculated by running the inversion model on the synthetic off-center MgO profiles always skew to lower rates the further off-center is the cut (Supplementary Figure S9). For an inclusion exposed along an unknown cut, the individual cooling rate is thus

considered a minimum estimate (while still subject to the other uncertainties inherent to the model).

Eight glassy inclusions were analyzed with the electron microprobe using the same conditions as described in Section 2.3 (Figure 18). The inclusions chosen for analysis were roughly circular, with longest dimensions of 12–40 μm (median = 18 μm); their small sizes limited the number of microprobe points that could be acquired in a traverse, but enough high-quality points (9 to 19) were collected in some inclusions to produce an interpretable profile. As in the terrestrial samples, some inclusions contained an Fe-rich spinel phase that was avoided in the analyses. Relative to most other martian melt inclusions (e.g., Ikeda, 2005), these are relatively low $SiO_2$ glasses with a minimum of 56.3 wt% (center of inclusion Y98MI6), and six of ten inclusions with minimum $SiO_2$ contents <60 wt% (the minimum $SiO_2$ ranged from 56.3–64.3 wt%). Compared to other martian samples (e.g., Ikeda, 2005), the inclusions also have relatively high MgO contents (up to ~3 wt% along zoned profiles), permitting the application of the MgO profile geospeedometer as described in Section 4. The $D_{MgO}$ in equation (2) was fit over a range of $SiO_2$ values from 43–70 wt% (Zhang, 2010), so it can be applied to model a composition-dependent $D_{MgO}$ in liquids spanning the range of the studied inclusion compositions. All of the martian inclusions are zoned, and the shapes of oxide concentration profiles are qualitatively similar to those in terrestrial and experimental samples: MgO, CaO, and FeO are concave down whereas $SiO_2$, $Al_2O_3$, and $Na_2O$ are concave up (Figure 18 for MgO, Supplement Section 3 for all oxides). However, the glass compositions differ systematically from the Hawaiian inclusions we have studied: MgO contents are lower in the martian glasses (1.9–2.8 wt%) compared to the Hawaiian glasses (3.6–7.2 wt%), and $SiO_2$ (56.3–66.0 wt %) and $P_2O_5$ (0.7–1.5 wt%) contents are generally higher than in the Hawaiian samples (52.7–58.5 wt% $SiO_2$ and up to 0.7 wt%

$P_2O_5$). Total Fe expressed as FeO* overlap, ranging from 5.7–9.5 wt% in Y980459 and 6.2–9.8 wt% in the Papakōlea glasses. The far-field host olivines in Y980459 range from $Fo_{72.0}$ to $Fo_{76.7}$ (compared to the average Hawaiian olivine at ~$Fo_{87}$) and are progressively enriched in FeO closer to the inclusion wall, with a minimum of $Fo_{62.8}$ to $Fo_{70}$ at the inclusion boundaries. Within 1–4 μm of the inclusion wall there is a narrow zone of steep Fe enrichment in the olivine, which is adjacent to a broader zone of more magnesian olivine enclosing melt inclusions that extends ~5–15 μm from the inclusion wall grading into the far-field olivine compositions, similar to the zoning observed in the terrestrial olivine (Figure 9, Supplement Section 3.3 for zoning profiles around the Y980459 melt inclusions). The broad zone is consistent with a period of prolonged cooling, crystallization, and Fe-Mg interdiffusion in the olivine, likely related to cooling stages 1 and 2.

The inclusions are small relative to the Hawaiian olivines, and on the basis of their concave down CaO profiles (Supplement Section 3.3, see Online Version), the diffusive boundary layer has reached the centers of all of the martian inclusions; i.e., the glass compositions in the inclusion centers have been modified by exchange with the interface melt, and so the initial compositions and $T_{max}$ of the inclusions need to be reconstructed. An average composition for each inclusion was calculated by spherically integrating the zoned compositional profile, and then iteratively adding olivine back to the inclusion until it was in equilibrium with the olivine at the boundary between the narrow fayalitic zone (1.5–4 μm thick) adjacent to the inclusion wall and the onset of the broad zone. Corresponding target forsterite contents ranged from $Fo_{73.2}$ to $Fo_{75.8}$. The $fO_2$ for the olivine addition calculation was set to the iron-wüstite buffer, consistent with

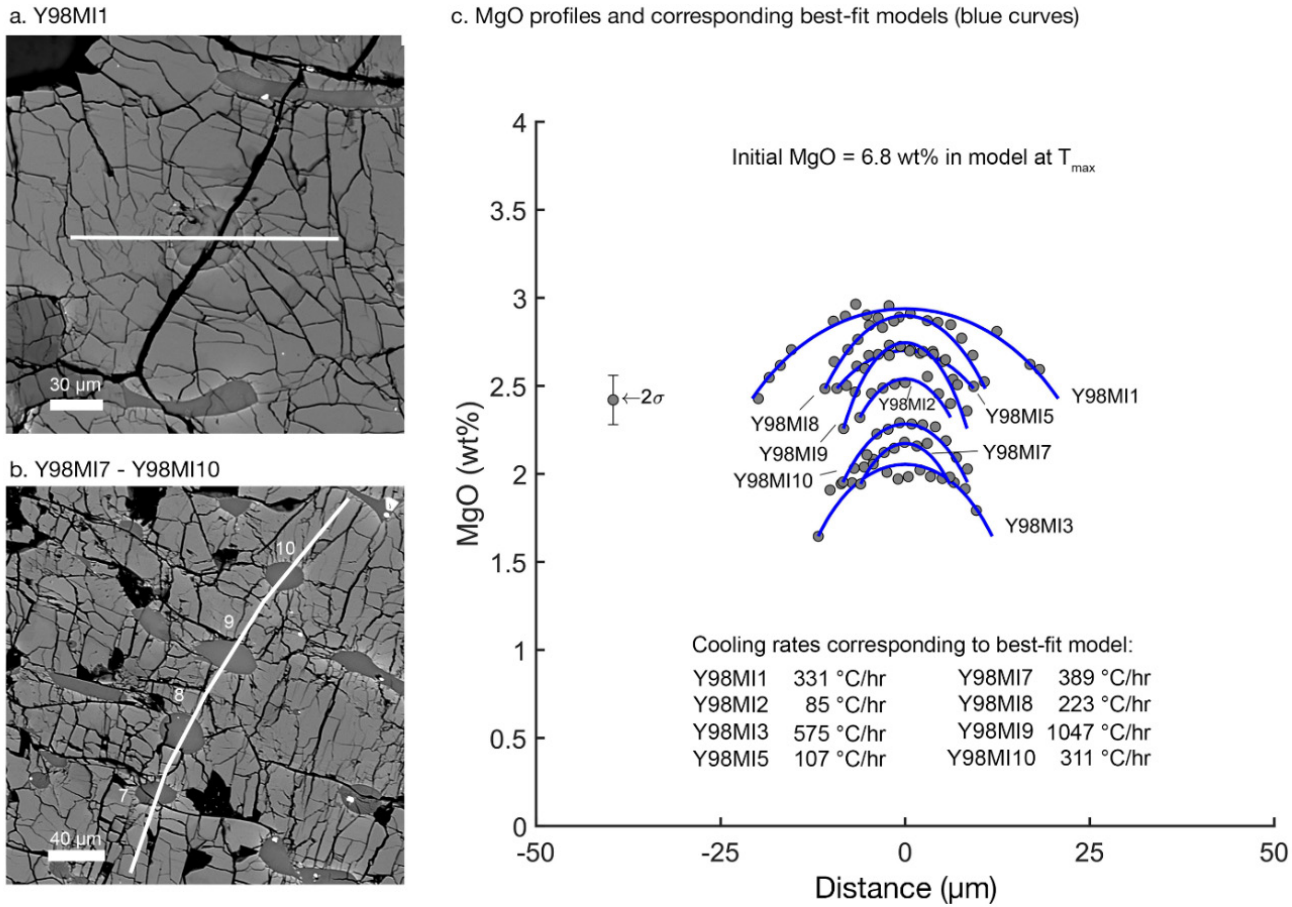


**Figure 18.** Glassy inclusions in martian meteorite Yamato 980459. (**a**, **b**): BSE images showing the locations of a subset of the glassy inclusions analyzed; note that Y98MI7-10 were enclosed in the same olivine host. White lines indicate the locations of microprobe traverses. (**c**) Gray circles show microprobe MgO data measured across the glass inclusions from Y980459. Blue curves are the best-fit model calculated based on the cooling rates listed in the lower right corner.

vanadium partitioning oxybarometry between glass and olivine in Y980459 (Shearer et al., 2006). This calculation yielded a range of $T_{max}$ from 1148 to 1244 °C with a mean of 1179 °C, which was chosen as the preferred $T_{max}$ for the cooling rate calculation. Following this procedure for eight inclusions gave reconstructed initial inclusion compositions of MgO of 5.1–8.5 wt%, $SiO_2$ = 51.5–61.8 wt%, $Al_2O_3$ = 8.4–11.6 wt%, and FeO = 8.2–16.2 wt%. These reconstructed melt compositions correspond to addition of 30–45% olivine by volume back into the inclusions to achieve equilibrium with the enclosing olivine, consistent with the 30–40% by volume addition estimated for reconstructions of Y984059 melt inclusion compositions from Peters (2015) using Petrolog3 (Danyushevsky & Plechov, 2011). Reconstruction of small glassy melt inclusions in Tissint by Sonzogni & Treiman (2015) similarly required 25–51% olivine addition by mass to the glasses in order to achieve equilibrium with the host olivine ($Fo_{58}$–$Fo_{72}$). This calculated amount of olivine extraction necessary to reconstruct compositions of shergottite melt inclusions is also consistent with the measured thickness of the narrow Fe-rich olivine zone adjacent to the inclusion walls (i.e., 4 μm of inward olivine growth on the wall of a spherical 20 μm radius inclusion represents a 49% change in volume).

For inclusions with centers that have been modified by diffusion during cooling, the cooling rates calculated using the model from Section 4 are relatively insensitive to the choice of $T_{max}$ (Supplement Section 2), and no choice of $T_{max}$ leads to a statistically significant improvement in the fitting of the microprobe data: For example, varying $T_{max}$ from 1102–1251°C (2σ of range of reconstructed $T_{max}$) results in relative changes in the calculated cooling rate of 5% for inclusion Y98MI1 and <1% for all other inclusions. Accordingly, $T_{max}$ = 1179 °C was chosen as the initial condition for all the inclusions, corresponding to an average initial MgO of 6.82 wt% in the reconstructed liquids. The initial $SiO_2$, $Al_2O_3$, and FeO were adjusted for each inclusion based on olivine addition.

For the temperature-dependent boundary condition of MgO in the interface liquid, a MELTS batch olivine crystallization was used, starting from the average reconstructed liquid composition of the Y980459 inclusions. Forward modeling of these $SiO_2$, $Al_2O_3$, and FeO was done with the approach described in Section 4.

Substituting the MELTS parameterization of the $C_{MgO}^{liq}$ calculated at an $fO_2$ at the iron-wüstite buffer, the model as described in Section 4 was run for the inclusions from Y980459. Because the MgO contents of the zoned inclusions are low and the gradients are relatively shallow (~1.5–3 wt% MgO with gradients of 0.5–1 wt% from the center to the edge of the inclusion; Figure 18c), the error associated with uncertainty in the MgO microprobe analysis has a more substantial effect on the calculated cooling rates (~10% relative, 1σ) compared to the Hawaiian examples (<1% relative for low cooling rates). The errors reported for these inclusions correspond to perturbing the profiles with 1σ MgO noise (0.075 wt%) and inverting 10 iterations of these synthetic datasets, and exclude errors associated with the choice of $T_{max}$ or associated with an off-center cut. Cooling rates for individual inclusions vary from 85±11 °C/hr (Y98MI2) to 1047±109 °C/hr (Y98MI9), and the largest inclusion measured, Y98MI1 (42 μm longest dimension), has a calculated cooling rate of 331±21 °C/hr. The distribution of the average cooling rates (10 iterations perturbed with 1σ noise) calculated for each inclusion is 383±43 °C/hr (n = 8). The different cooling rates are not correlated with size nor location in the thin section; i.e., Y98MI9 has the highest cooling rate of the samples measured, but is enclosed in the same olivine grain as Y98MI7, Y98MI8, and Y98MI10, which have rates from 223–389 °C/hr (Figure 18b). Boundary motion is not accounted for in the model and by excluding its effect we tend to overestimate the cooling rate by incorrectly using a smaller initial inclusion radius than was originally present at $T_{max}$, an effect which becomes increasingly important for smaller inclusions. For example,

rescaling the MgO profile from a 20 μm radius inclusion (Y98MI1) to 16 μm radius and fitting each profile separately gives cooling rates of 555±40(1σ) °C/hr and 328±20(1σ) °C/hr, respectively.

Cooling rates calculated from MgO diffusion in melt inclusions correspond to stage 3 of the proposed cooling history of Y980459, which produced the vitrophyric texture in the rock. The distribution of rates recovered from the eight inclusions (ranging from 85–1047 °C/hr) overlaps with the 150 °C/hr estimate based on CSDs from the cooling experiments of First and Hammer (2016) and is within a factor of two of the estimates of 1450 to 1890 °C/hr from Greshake et al. (2004). (Figure 17c). The very low $H_2O$ contents measured in two melt inclusions from Y980459 (146-251 ppm and 458-841 ppm, Usui et al., 2012) indicate that the range in cooling rates is likely not due to the effect of variable $H_2O$ on diffusion in the inclusion liquids. The cooling rates calculated with the MgO diffusion model are subject to uncertainties in reconstructing $T_{max}$, in the MELTS approximation of the olivine liquidus surface at martian conditions (Balta & McSween, 2013), and that the small inclusions (<40 μm in longest dimension) permit only short profiles which may be influenced by boundary motion. Despite these uncertainties, which are reflected in the range of cooling rates calculated from the eight inclusions, the inverse model produces profiles that fit the MgO profiles in glassy inclusions from Y980459 as well as in the terrestrial examples described in Section 6.1. The quenched diffusion profiles in melt inclusions provide an independent quantitative estimate that further supports the hypothesis that Y980459 experienced rapid cooling through the glass transition, likely at or near the martian surface (Greshake et al., 2004; Balta & McSween, 2013; First & Hammer, 2016).

# 8 Conclusions

(1) A series of 1-atm experiments on olivine-hosted melt inclusions were homogenized for 24 hours at 1225 and cooled at controlled rates of 70–50,000 °C/hr. Additionally, one set of experiments was homogenized at 1260 °C with a cooling history of two linear segments. These experiments document the cooling rate and temperature-dependent evolution of compositional zoning across glassy melt inclusions that develops during cooling due to progressive crystallization of olivine on the inclusion wall. All of the experimentally cooled inclusions are compositionally zoned, characterized by lower MgO and FeO, and higher $SiO_2$, $Al_2O_3$, $Na_2O$ (and other incompatible oxides) near the inclusion wall relative to the inclusion center. The observed zoning evolves with time due to competition between continuous formation of a boundary layer in the melt adjacent to the inclusion wall and diffusive exchange between this boundary layer and the interior of the inclusion. The inclusion centers eventually become modified by diffusive exchange with the boundary layer liquid, resulting in central compositions that differ from that established during the homogenization step. Modification of central compositions by diffusion is more effective at lower cooling rates and for smaller inclusions. The experiments are consistent with and allow quantification of the hypothesis that the ubiquitous zoning in natural melt inclusions forms during syneruptive cooling of basaltic lavas (Newcombe et al., 2014).

(2) A model for MgO diffusion (Newcombe et al., 2014) was modified to accommodate a boundary condition that uses MELTS to calculate the interface liquid composition at each temperature during the cooling history, and a composition- and temperature-dependent diffusivity of MgO (Zhang, 2010) that

takes into account that the diffusivity of MgO decreases with the increases in $SiO_2$ and $Al_2O_3$ concentrations in the boundary layer that develops with progressive crystallization of olivine on the inclusion wall. By varying the cooling rate, the model was fit to MgO profiles measured along transects of experimental glass inclusions. When comparing the cooling rates that resulted in the best-fit between model and data, the model accurately recovers the experimental rates: for intermediate cooling rate experiments (at 93 °C/hr, 466 °C/hr, 715 °C/hr, 1570 °C/hr, and 20,190 °C/hr) the best-fit model cooling rates for inclusions from a given experiment deviate by less than ±10% from the known rate; for the lowest (70 °C/hr) and highest (49,644 °C/hr) experimental rates the best-fit model cooling rates deviate from the known cooling rate by up to a factor of two. These results indicate that such a model can be used to quantify eruptive cooling rates, which span several orders of magnitude in nature based on application of this model to natural inclusions from Hawai‘i.

(3) The effects of multicomponent diffusion were observed in every liquid component measured in the experimental melt inclusions, including uphill diffusion producing local extrema along diffusion profiles (for instance in CaO) and flattening of the central portions of MgO profiles. CaO exhibits the most extreme manifestation of multicomponent diffusion effects: In particular, CaO is incompatible in olivine and is expected to be continually enriched in the liquid at the olivine crystallization front, and though this is observed in rapidly cooled samples, in more slowly cooled samples CaO is low at the inclusion interface relative to the center. This leads to CaO profiles that qualitatively appear more similar to the profiles of compatible components such as MgO and FeO rather than to other incompatible components such as $Al_2O_3$. The CaO behavior was

semi-quantitatively modeled by assuming that the CaO component in the liquid diffuses down its own activity gradient but that increases in the CaO activity coefficient are driven by increases in $Na_2O$ in the boundary layer near the inclusion wall. This model reproduces the cooling rate dependent evolution of the CaO profile shape and is consistent with the extreme CaO diffusion behavior being due to the progressive buildup of steep gradients in elements such as Na, Al, and Si in the liquid adjacent to the olivine crystallization front that lead to strongly non-ideal behavior of the CaO component. The CaO profile shape can be used as a qualitative indicator of cooling rate: a profile with elevated CaO at the inclusion wall relative to the center is indicative of rapid cooling whereas low CaO at the inclusion wall and a concave down profile is characteristic of prolonged cooling.

(4) The MgO diffusion model was applied to natural glassy olivine-hosted melt inclusions from Papakōlea, Hawai‘i (the olivine beach sands that were used as the starting materials for the experiments); from Kīlauea Iki, Hawai‘i; and from the martian meteorite Yamato 980459. The natural Papakōlea inclusions yielded two inclusion populations, rapidly cooled (7500–11,800 °C/hr, n = 5) and slowly cooled (51–854 °C/hr, n =5), which is consistent with the beach sands being derived from both olivine-bearing ash beds and basalt flows (Walker, 1992). The cooling rates calculated using olivine-hosted melt inclusions from the fire-fountaining stage of Kīlauea Iki uniformly gave rapid cooling rates of 5100–8800 °C/hr, which are consistent with rapid quenching of tephra in air. Cooling rates from zoned melt inclusions in Yamato 980459 range from 85–1047 °C/hr with a mean and 1σ of the average cooling rate calculated for each inclusion of 383±43 °C/hr (n = 8 inclusions). These rates overlap with estimates for cooling

associated with stage 3 of the inferred thermal history of Y980450 (Greshake et al., 2004; First & Hammer, 2016), and support the hypothesis that the sample erupted at or near the Martian surface and was rapidly cooled through the glass transition.

## 9 Acknowledgments

Additional information and figures can be found in the Supplementary Materials. Data tables containing melt inclusion and olivine microprobe analyses can be accessed at the EarthChem Portal (www.earthchem.org/portal, doi: https://doi.org/10.1594/IEDA/111467). We would like to thank Dr. Megan Newcombe for providing guidance on the Matlab code from Newcombe et al. (2014), and for details on useful protocols for sample preparation. We would also like to thank Dr. Michael B. Baker for providing thoughtful discussion and guidance on the experimental procedures, without which the project would have not had been successful. Lastly, we would like to thank Dr. Mary Peterson and Dr. Maryjo Brounce for assistance with XANES analysis. This work was funded by the Leon T. Silver Graduate Fellowship and a NSF Graduate Research Fellowship (GRFP) awarded to Lee Saper.

## 10 References

Albarede, F., & Bottinga, Y. (1972). Kinetic disequilibrium in trace element partitioning between phenocrysts and host lava. *Geochimica et Cosmichimica Acta*, 36(2), p.141-156, https://doi.org/10.1016/0016-7037(72)90003-8

Anderson, J.T. (1974). Evidence for a picritic, volatile-rich magma beneath Mt. Shasta, California. *Journal of Petrology*, 15(2), p.243-267, https://doi.org/10.1093/petrology/15.2.243

Anderson, Jr., A.T., & Brown, G.G. (1993). CO2 contents and formation pressures of some Kīlauean melt inclusions. *American Mineralogist*, 78, p.794-803

Armstrong, J.T. (1988). Quantitative analysis of silicate and oxide minerals: comparison of Monte Carlo, ZAF, and Φ(ρz) procedures. In: Newbury DE (editor) Microbeam analysis – 1988. San Francisco Press, San Francisco, p.239-246

Balta, J.B., & McSween, Jr., H.Y. (2013). Application of the MELTS algorithm to Martian compositions and implications for magma crystallization. *Journal of Geophysical Research*: *Planets*, 118, p.2502-2519, https://doi.org/10.1002/2013JE004461

Beckett, J.R., & Mendybaev, R.A. (1997). The measurement of oxygen fugacities in flowing gas mixtures at temperatures below 1200°C. *Geochimica et Cosmochimica Acta*, 41(20), p.4331-4336, https://doi.org/10.1016/S0016-7037(97)00186-5

Behrens, H., Zhang, Y., & Xu, Z. (2004). H2O diffusion in dacitic and andesitic melts. *Geochimica et Cosmochimica Acta*, 68, p.5139-5150, https://doi.org/10.1016/j.gca.2004.07.008

Brounce, M., Stolper, E., & Eiler, J. (2017). Redox variations in Mauna Kea lavas, the oxygen fugacity of the Hawaiian plume, and the role of volcanic gases in Earth's oxygenation. *Proceedings of the National Academy of Sciences*, 114 (34) p.8997-9002, https://doi.org/10.1073/pnas.1619527114

Bucholz, C.E., Gaetani, G.A., Behn, M.D., & Shimizu, N. (2013). Post-entrapment modification of volatiles and oxygen fugacity in olivine-hosted melt inclusions. *Earth and Planetary Science Letters*, 374, p.145-155, https://doi.org/10.1016/j.epsl.2013.05.033

Capaccioni, B., & Cuccoli, F. (2005). Spatter and welded air fall deposits generated by fire-fountaining eruptions: Cooling of pyroclasts during transport and deposition. *Journal of Volcanology and Geothermal Research*, 145. p.263-280, https://doi.org/10.1016/j.jvolgeores.2005.02.001

Carslaw, H.S., & Jaeger, J.C. (1959). Conduction of heat in solids. Oxford University Press p.1-510

Chakraborty, S. (1995). Diffusion in silicate melts. *Reviews in Mineralogy and Geochemistry*, 32, p.411-503

Chen, Y., & Zhang, Y. (2008). Olivine dissolution in basaltic melt. *Geochimica et Cosmochimica Acta*, 72, p.4756-4777, https://doi.org/10.1016/j.gca.2008.07.014

Chen, Y., & Zhang, Y. (2009). Clinopyroxene dissolution in basaltic melt. *Geochimica et Cosmochimica Acta*, 73, p.5730-5747, https://doi.org/10.1016/j.gca.2009.06.016

Colin, A., Faure, F., & Burnard, P. (2012). Timescales of convection in magma chambers below the Mid-Atlantic ridge from melt inclusions investigations. *Contributions to Mineralogy and Petrology*, 164, p.677-691, https://doi.org/10.1007/s00410-012-0764-2

Cooper, A.R. (1968). The use and limitations of the concept of an effective binary diffusion coefficient for multi-component diffusion. In: Mass Transport in Oxides. NBS Special Publication 296. Wachtman JB, Franklin AD (Editors) p.79-84

Danyushevsky, L.V., Della-Pasqua, F.N., & Sokolov, S. (2000). Reequilibration of melt inclusions trapped by magnesian olivine phenocrysts from subduction-related magmas: petrological implications. *Contributions to Mineralogy and Petrology*, 138, p.68-83, https://doi.org/10.1007/PL00007664

Danyushevsky, L.V., McNeill, A.W., & Sobolev, A.V. (2002a). Experimental and petrological studies of melt inclusions in phenocrysts from mantle-derived magmas: an overview of techniques, advantages and complications. *Chemical Geology*, 183, p.5-24, https://doi.org/10.1016/S0009-2541(01)00369-2

Danyushevsky, L.V., Sokolov, S., & Falloon, T.J. (2002b). Melt inclusions in olivine phenocrysts: using diffusive re-equilibration to determine the cooling history of a crystal, with implications for the origin of olivine-phyric volcanic rocks. *Journal of Petrology*, 43(9), p.1651-167, https://doi.org/10.1093/petrology/43.9.1651

Dohmen, R., Becker, H-.W., Chakraborty, S. (2007). Fe-Mg diffusion in olivine I: experimental determination between 700 and 1,200°C as a function of composition, crystal orientation and oxygen fugacity. *Physics and Chemistry of Minerals*, 34, p. 389-407, https://doi.org/10.1007/s00269-007-0157-7

Drignon, M.J., Nielsen, R.L., Tepley, III., F.J., & Bodnar, R.J. (2019). Reequilibration processes occurring in plagioclase-hosted melt inclusions from plagioclase ultraphyric basalts. *Geochemistry, Geophysics, Geosystems*, 20, p.109-119, https://doi.org/10.1029/2018GC007795

Efron, B., & Tibshirani, R. (1985). The bootstrap method for assessing statistical accuracy. DTIC document

Fincham, C.J.B., & Richardson, F.D. (1954). The behavior of Sulphur in silicate and aluminate melts. *Proceedings of the Royal Society A, Mathematical, Physical and Engineering Sciences*, 223, p.40-62, https://doi.org/10.1098/rspa.1954.0099

First, E., Hammer, J. (2016). Igneous cooling history of olivine-phyric shergottite Yamato 980459 constrained by dynamic crystallization experiments. *Meteoritics & Planetary Science,* 51(7) p.1233-1255, https://doi.org/10.1111/maps.12659

Frost, B.R. (1991). Introduction to oxygen fugacity and its petrologic importance. *Reviews in Mineralogy and Geochemistry*, 25., p.1-9

Gaetani, G.A., & Watson, E.B. (2000). Open system behavior of olivine-hosted melt inclusions. *Earth and Planetary Science Letters*, 183, p.27-41, https://doi.org/10.1016/S0012-821X(00)00260-0

Gaetani, G.A., O'Leary, J.A., Shimizu, N., Bucholz, C.E., & Newville, M. (2012). Rapid reequilibration of H2O and oxygen fugacity in olivine-hosted melt inclusions. *Geology*, 40(10), p.915-918, https://doi.org/10.1130/G32992.1

Ghiorso, M.S., & Sack, R.O. (1995). Chemical mass transfer in magmatic processes IV. A revised and internally consistent thermodynamic model for the interpolation and extrapolation of liquid-solid equilibria in magmatic systems at elevated temperatures and pressures. *Contributions to Mineralogy and Petrology*, 119., p.197-212, https://doi.org/10.1007/BF00307281

Goodrich, C.A., Fioretti, A.M., Tribaudino, M., & Molin, G. (2001). Primary trapped melt inclusions in olivine in the olivine-augite-orthopyroxene ureilite Hughes 009. *Geochimica et Cosmichimica Acta*, 65(4), p.621-652, https://doi.org/10.1016/S0016-7037(00)00521-4

Gottsmann, J., Harris, J.L., & Dingwell, D.B. (2004). Thermal history of Hawaiian pahoehoe lava crusts at the glass transition: implications for flow rheology and emplacement. *Earth and Planetary Science Letters*, 228, p.343-353, https://doi.org/10.1016/j.epsl.2004.09.038

Greshake, A., Fritz, J., & Stoffler, D. (2004). Petrology and shock metamorphism of the olivine-phyric shergottite Yamato 980459: Evidence for a two-stage cooling and single-stage ejection history. *Geochimica et Cosmochimica Acta*, 68(10), p.2359-2377, https://doi.org/10.1016/j.gca.2003.11.022

Guo, C., & Zhang, Y. (2016). Multicomponent diffusion in silicate melts; SiO2-TiO2-Al2O3-MgO-CaO-Na2O-K2O system. *Geochimica et Cosmochimica Acta*, 195, p.126-141, https://doi.org/10.1016/j.gca.2016.09.003

Guo, C., & Zhang, Y. (2018). Multicomponent diffusion in basaltic melts at 1350 °C. *Geochimica et Cosmochimica Acta*, 228, p.190-204, https://doi.org/10.1016/j.gca.2018.02.043

Hauri, E. (2002). SIMS analysis of volatiles in silicate glasses, 2: isotopes and abundances in Hawaiian melt inclusions. *Chemical Geology*, 183, p.115-141, https://doi.org/10.1016/S0009-2541(01)00374-6

Helz, R.T., Cottrell, E., Brounce, M.J., & Kelley, K.A. (2016). Olivine-melt relationships and syneruptive redox variations in the 1959 eruption of Kīlauea Volcano as revealed by XANES. *Journal of Volcanology and Geothermal Research*, 333:334, p.1-14, https://doi.org/10.1016/j.jvolgeores.2016.12.006

Ikeda, Y. (2004). Petrology of the Yamato 980459 shergottite. *Anatarctic Meteorite Research*, 17, p.35-54

Ikeda, Y. (2005). Magmatic inclusions in martian meteorites. *Antarctic Meteorite Research*, 18, p.170-187,

Jochum, K.P., Stoll, B., Herwig, K., Wilbold, M., Hofmann, A.W., Amini, M., et al. (2006). MPI-DING reference glasses for in situ microanalysis: New reference values for element concentrations and isotope ratios. *Geochemistry Geophysics Geosystems*, 7(2), p.1-44, https://doi.org/10.1029/2005GC001060

Koyaguchi, T. (1989). Chemical gradient at diffusive interfaces in magma chambers. *Contributions to Mineralogy and Petrology*, 103, p.143-152, https://doi.org/10.1007/BF00378500

Kress, V.C., & Carmichael, I.S.E. (1991). The compressibility of silicate liquids containing Fe2O3 and the effect of composition, temperature, oxygen fugacity and pressure on their redox states. *Contributions to Mineralogy and Petrology*, 108., p.82-92, https://doi.org/10.1007/BF00307328

Lasaga, A.C. (1982) Toward a master equation in crystal growth. *American Journal of Science*, 282, p.1264-1288, http://doi.org/10.2475/ajs.282.8.1264

Lentz, R.C.F., & McSween, Jr., H.Y. (2005). A textural examination of the Yamato 980459 and Los Angeles shergottites using crystal size distribution analysis. *Antarctic Meteorite Research*, 18, p.66-82,

Lesher, C.E., & Walker, D. (1986). Solution properties of silicate liquids from thermal diffusion experiments. *Geochimica et Cosmochimica Acta*, 50, p.1397-1411, https://doi.org/10.1016/0016-7037(86)90313-3

Liang, Y., Richter, F.M., & Chamberlin, L. (1997). Diffusion in silicate melts: III. Empirical models for multicomponent diffusion. *Geochimica et Cosmochimica Acta*, 61(24), p.5295-5312, https://doi.org/10.1016/S0016-7037(97)00301-3

Liang, Y. (2010). Multicomponent diffusion in molten silicates: Theory, experiments, and geological applications. *Reviews in Mineralogy and Geochemistry*, 72, p.409-446

Lowry, R.K., Henderson, P., & Nolan, J. (1982). Tracer diffusion of some alkali, alkaline-earth and transition element ions in a basaltic and an andesitic melt, and the implications concerning melt structure. *Contributions to Mineralogy and Petrology*, 80, p.254-261, https://doi.org/10.1007/BF00371355

Manzini, M., Bouvier, A.-S., Buampgartner, L.P., Muntener, O., Rose-Koga, E.F., Schiano, P., Escrig, S., Meibom, A., & Shimizu, N. (2017). Weekly to monthly time scale of melt inclusion entrapment prior to eruption recorded by phosphorus

distribution in olivine from mid-ocean ridges. *Geology*, 45(12), p.1059-1062, https://doi.org/10.1130/G39463.1

Matzen, A.K., Baker, M.B., Beckett, J.R., & Stolper, E.M. (2011). Fe-Mg partitioning between olivine and high-magnesian melts and the nature of Hawaiian parental liquids. *Journal of Petrology*, 52(7:8), p.1243-1263, https://doi.org/10.1093/petrology/egq089

Mercier, M. (2009). Abondance et signification de l'eau dans les magmas mafiques. Dévelopment de la spectrscopie vibrationnelle (Raman et FTIR). Thesis, Université Paris Sud-Paris XI

Musselwhite, D.S., Dalton, H.A., Kiefer, W.S., & Treiman, A.H. (2006). Experimental petrology of the basaltic shergottite Yamato 980459: Implications for the thermal structure of the martian mantle. *Meteoritics & Planetary Science*, 41(9), p.1271-1290, https://doi.org/10.1111/j.1945-5100.2006.tb00521.x

Nash, W.M., Smythe, D.J., & Wood, B.J. (2019). Compositional and temperature effects on sulfur speciation and solubility in silicate melts. *Earth and Planetary Science Letters*, 507, p.187-198, https://doi.org/10.1016/j.epsl.2018.12.006

Newcombe, M.E., Fabbrizio, A., Zhang, Y., Ma, C., Le Voyer, M., Guan, Y., Eiler, J.M., Saal, A.E., & Stolper, E.M. (2014). Chemical zonation in olivine-hosted melt inclusions. *Contributions to Mineralogy and Petrology*, 168(1030), p.1-26,

Newcombe ME, Brett A, Beckett JR, Baker MB, Newman S, Guan Y, Eiler JM, Stolper EM (2017) Solubility of water in lunar basalt at low pH2O. Geochimica et Cosmochimica Acta 200 p.330-352, https://doi.org/10.1007/s00410-014-1030-6

Ni, H., Behrens, H., & Zhang, Y. (2009). Water diffusion in dacitic melt. *Geochimica et Cosmochimica Acta*, 73, p.3642-3655, https://doi.org/10.1016/j.gca.2009.03.029

Nichols, A.R.L., Potuzak, M., & Dingwell, D.B. (2009). Cooling rates of basaltic hyaloclastites and pillow lava glasses from the HSDP2 drill core. *Geochimica et Cosmochimica Acta*, 74(4) 1052-1066, https://doi.org/10.1016/j.gca.2008.11.023

Nitsan, U. (1974). Stability field of olivine with respect to oxidation and reduction. *Journal of Geophysical Research*, 79(5), p.706-711, https://doi.org/10.1029/JB079i005p00706

O'Neill, H.S.C., & Mavrogenes, J.A. (2002). The sulfide capacity and the sulfur content at sulfide saturation of silicate melts at 1400 °C and 1 bar. *Journal of Petrology*, 43, p.1049-1087, https://doi.org/10.1093/petrology/43.6.1049

Patrick, M.R., Dehn, J., & Dean, K. (2004). Numerical modeling of lava flow cooling applied to the 1997 Okmok eruption: Approach and analysis. *Journal of Geophysical Research*, 109, p.1-17, https://doi.org/10.1029/2003JB002537

Rhodes, J.M., & Vollinger, M.J. (2005). Ferric/ferrous ratios in 1984 Mauna Loa lavas: a contribution to understanding the oxidation state of Hawaiian magmas. *Contributions to Mineralogy and Petrology*, 49, p.666-675, https://doi.org/10.1007/s00410-005-0662-y

Richter, D.H., Eaton, J.P., Murata, K.J., Ault, W.U., & Krivoy, H.L. (1970). Chronological narrative of the 1959-60 eruption of Kīlauea volcano, Hawai'i. *Geological Survey Professional Papers*, 537-E, p.1-73

Rubin, M., Gargulinksi, L.K., & McGeehin, J.P. (1987). Hawaiian radiocarbon dates. In: Decker RW, Wright TL, Stauffer PG (Editors), Volcanism in Hawai'i. *U.S. Geological Survey Professional Papers*,1350, p.213-242

Sides, I.R., Edmonds, M., Maclennan, J., Swanson, D.A., & Houghton, B.F. (2014). Eruption style at Kīlauea Volcano in Hawai'I linked to primary melt composition. *Nature Geoscience*, 7, p.464-469, https://doi.org/10.1038/ngeo2140

Smith, P.M., & Asimow, P.D. (2005). Adiabat 1ph: A new public front-end to the MELTS, pMELTS, and pHMELTS models. Geochemistry Geosphysics Geosystems 6, art. no. Q02004m, doi:10.1029/2004GC000816

Sobolev, A.V., Hogmann, A.W., & Nikogosian, I.K. (2000). Recycled oceanic crust observed in 'ghost plagioclase' within the source of Mauna Loa lavas. *Nature*, 404(6781), p.986-990, https://doi.org/10.1038/35010098

Sonzogni, Y., & Treiman, A. (2015). Small melt inclusions can record bulk magma compositions: A planetary example from the Martian basalt (shergottite) Tissint. *Meteoritics & Planetary Science*, 50(11), p.1880-1895, https://doi.org/10.1111/maps.12516

Stearns, H.T., & Macdonald, G.A. (1947). Geology and ground-water resources of the island of Hawai'i, *Hawai'i Division of Hydrography*, 9(363)

Thomas, R.M.E., & Sparks, R.S.J. (1992). Cooling of tephra during fallout from eruption columns. *Bulletin of Volcanology*, 54(7), p.542-553, https://doi.org/10.1007/BF00569939

Tuohy, R.M., Wallace, P.J., Loewen, M.W., Swanson, D.A., & Kent, A.J.R. (2016). Magma transport and olivine crystallization depths in Kīlauea's east rift zone inferred from experimentally homogenized melt inclusions. *Geochimica et Cosmochimica Acta*, 185, p. 232-350, https://doi.org/10.1016/j.gca.2016.04.020

Usui, T., McSween, Jr., H.Y., & Floss, C. (2008). Petrogenesis of olivine-phyric shergottite Yamato 980459, revisited. *Geochimica et Cosmochimica Acta*, 72, p.1711-1730, https://doi.org/10.1016/j.gca.2008.01.011

Usui, T., Alexander, C.M.O'D., Wang, J., Simon, J.I., & Jones, J.H. (2012) Origin of water and mantle-crust interactions on Mars inferred from hydrogen isotopes and volatile element abundances of olivine-hosted melt inclusions of primitive

shergottites. *Earth and Planetary Science Letters*, 357-358, p.119-129, https://doi.org/10.1016/j.epsl.2012.09.008

Walker, G.P.L. (1992). Puu Mahana near South Point in Hawai‘i is a primary surtseyan ash ring, not a sandhills-type littoral cone. *Pacific Science*, 46(1)

Wallace, P.J., Kamenetsky, V.S., & Cervantes, P. (2015). Melt inclusion CO2 contents, pressures of olivine crystallization, and the problem of shrinkage bubbles. *American Mineralogist*, 100, p.787-794, https://doi.org/10.2138/am-2015-5029

Watson, E.B. (1981). Diffusion in magmas at depth in the Earth: the effects of pressure and dissolved $H_2O$. *Earth and Planetary Science Letters*, 52, p.291-301, https://doi.org/10.1016/0012-821X(81)90184-9

Watson, E.B. (1982). Basalt contamination by continental crust: some experiments and models. *Contributions to Mineralogy and Petrology*, 80(1), p.70-87, https://doi.org/10.1007/BF00376736

Watson, E.B., & Baker, D.R. (1991). Chemical diffusion in magmas: An overview of experimental results and geochemical applications. In: Physical Chemistry of Magmas. Perchuk LL, Kushiro I (Editors) Springer-Verlag, New York, p.120-151

Wilding, M.C., Webb, S.L., & Dingwell, D.B. (1995). Evaluation of a relaxation geospeedometer for volcanic glasses. *Chemical Geology*, 123, p.137-148, https://doi.org/10.1016/0009-2541(95)00067-V

Wilding, M., Dingwell, D., Batiza, R., & Wilson, L. (2000). Cooling rates of hyaloclastites: applications of relaxation geospeedometry to undersea volcanic deposits. *Bulletin of Volcanology*, 61(8), p.527-536, https://doi.org/10.1007/s004450050003

Xu, Z., & Zhang, Y. (2002). Quench rates in air, water, and liquid nitrogen, and interference of temperature in volcanic eruption column. *Earth and Planetary Science Letters*, 200(3), p.315-330, https://doi.org/10.1016/S0012-821X(02)00656-8

Zhang, Y. (1989). Diffusive crystal dissolution. *Contributions to Mineralogy and Petrology*, 102(4), p.492-513, https://doi.org/10.1007/BF00371090

Zhang, Y. (2010). Diffusion data in silicate melts. *Reviews in Mineralogy and Geochemistry*, 72, p.311-408

# 11 Supplementary Materials

## Supplementary Figures

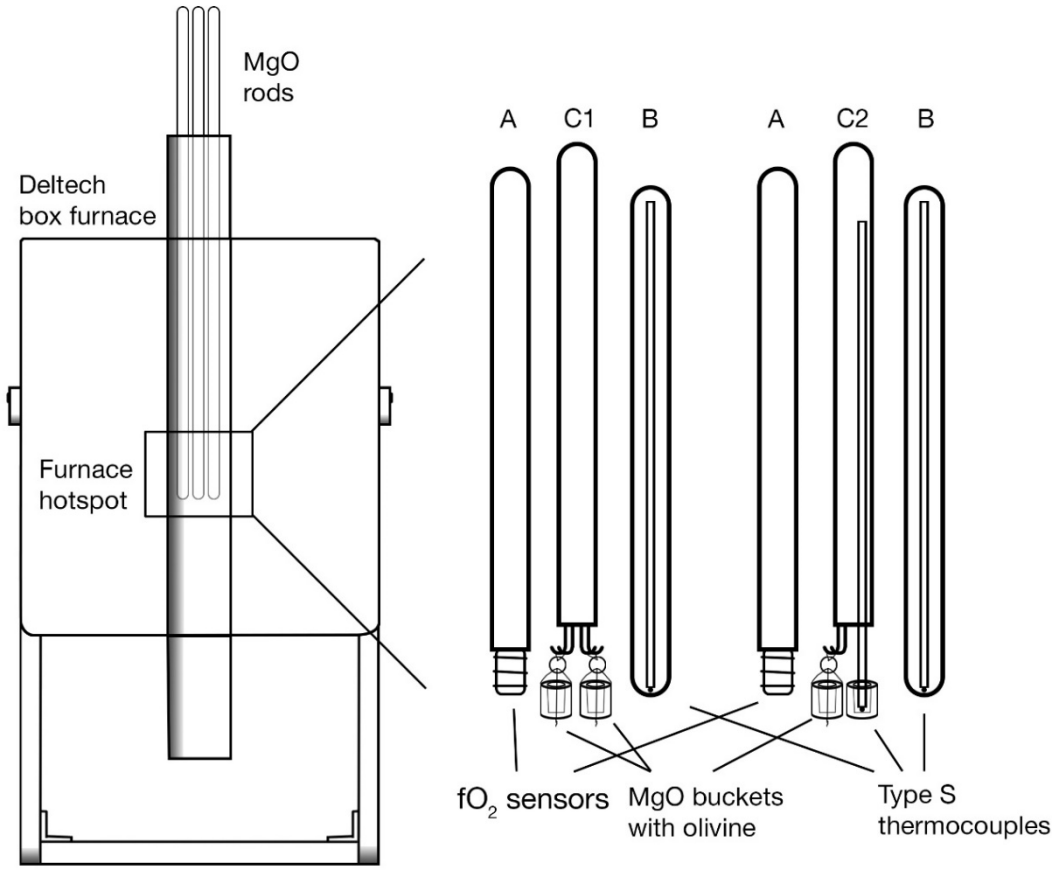


**Supplementary Figure S1.** Schematic diagram of experimental setup. Left hand side shows a simplified Deltech 1 atm vertical gas-mixing furnace, showing the location of the three MgO rods used in the experimental apparatus. The three different MgO rods used in the experiments are shown on the right side of the figure. Rod A is an Y-stabilized Zr oxygen sensor, which measures the difference in oxygen potential between the furnace atmosphere and a pure $O_2$ reference gas that is introduced into the interior of the sensor and the MgO tube in which it resides. Rod B is an MgO tube with a Type-S thermocouple which continuously monitored temperature at the furnace hotspot. Rod C had two configurations based on the experiment type. For experiments that were cooled by programming the control Type B thermocouple, the setup used Rod C1, which had 2 to 3 MgO buckets containing the inclusion-bearing olivine grains suspended from platinum quench hooks at the base of the MgO rod. Each of these buckets could be independently quenched by passing a current through the Pt hooks and fusing the 0.127 mm hanging wire that attached the MgO buckets to the rod. For experiments that were cooled by displacing the samples out of the hotspot, the setup used Rod C2, which held one bucket containing olivine (left side of C2) alongside another Type-S thermocouple (right side of C2) that was contained within an MgO bucket in order to faithfully record the thermal history experienced by the olivine in the adjacent bucket. In these experiments, Rod C2 was displaced downwards by up to 9 cm (H4X) as a digital temperature logger attached to the thermocouple on Rod C2 recorded the temperature during cooling at 1 second intervals. To quench, the Pt hanging wire was fused, releasing the olivine bucket, which dropped through the bottom of the furnace into a Pyrex dish filled with room temperature distilled water.

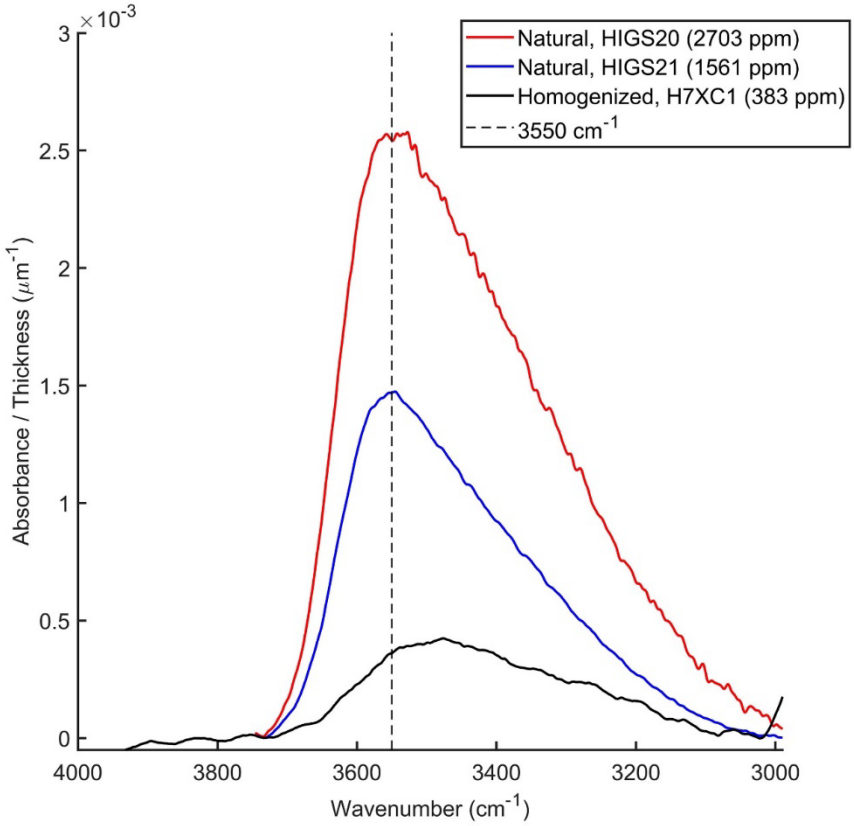


**Supplementary Figure S2.** Background removed FTIR of olivine-hosted melt inclusions. The analytical conditions and parameters for calculated the concentration of water are listed in Section 2.3. The red and blue curves are FTIR absorbance spectra from two natural olivine-hosted melt inclusions from Papakolea (HIGS20 and HIGS21), the black curve is the spectrum of experimental inclusion H7XC1, which was homogenized for 24 hours in H2-CO2 gas at an fO2 of ΔlogFMQ-1.15 (Frost, 1991) and then drop quenched directly into water. Water contents were calculated using the absorbance at 3550 $cm^{-1}$ (dashed black line in figure).

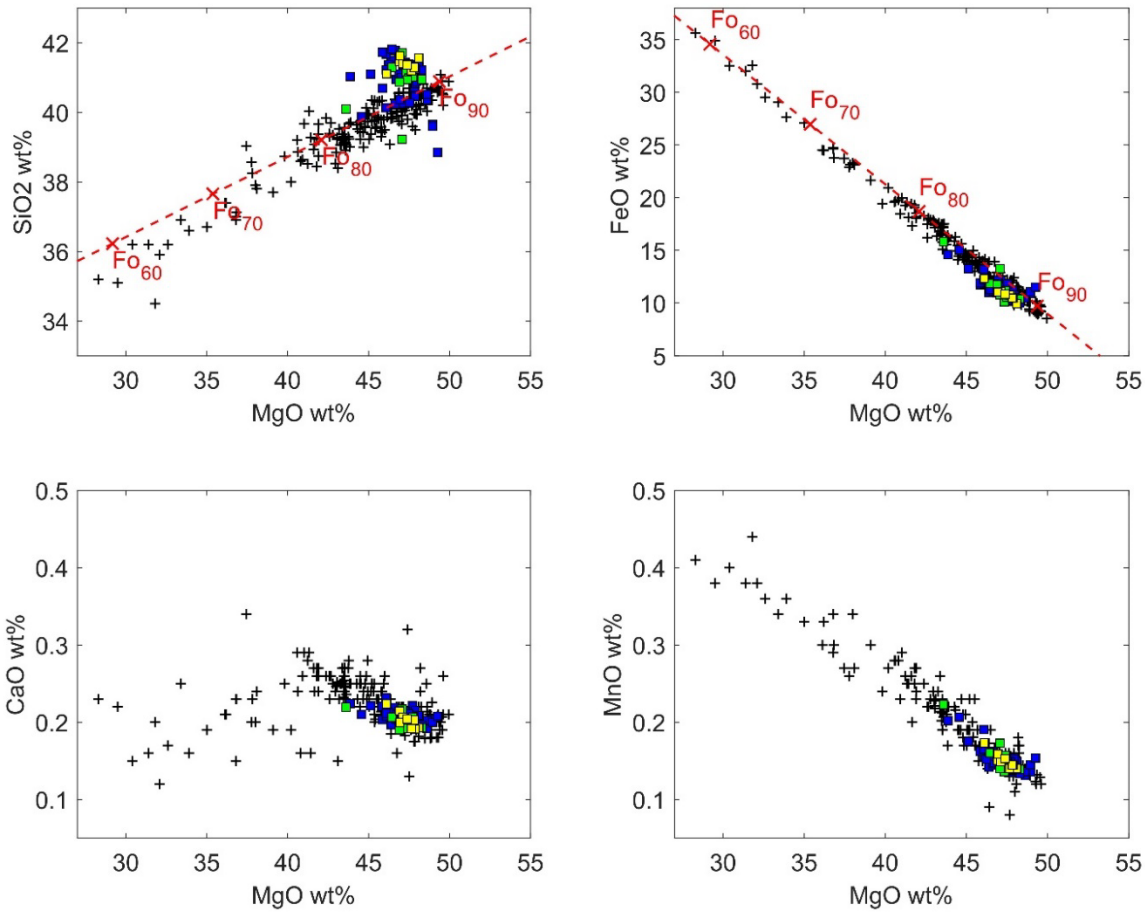


**Supplementary Figure S3.** Compositions of the Papakolea olivines used in the study compared to analyses of Mauna Loa olivine from the Georoc database (http://georoc.mpch-mainz.gwdg.de/georoc/). Black "+" symbols are individual spot EPMA analyses of olivine from the Georoc data. Square symbols are Papakolea olivine analyses taken >100 µm from melt inclusions and > 50 µm from the edge of the crystal. Green squares are averages of ten microprobe points in each of the ten unheated Papakolea olivines grains at a plateau in olivine composition ("far field olivine", see Section 3.1). Blue squares are averages of ten far-field analyses of 48 experimental olivine that were homogenized at 1225 °C for 24 hr; yellow squares are averages of far-field analyses from 9 experimental olivines homogenized at 1260 °C for 24 hr. Dashed red line in panels A and B show the compositions of stoichiometric Fo-Fa olivine, labeled at increments of 10 Fo units, where Fo = 100*(MgO/(MgO+FeO)). Data sources for the Georoc literature data are: Sobolev (1994) Petrology 2 p. 111-144, Rhodes (1995) Mauna Loa Revealed p. 241-262, Garcia (1995) Mauna Loa Revealed p. 219-239, Garcia (1996) JGR B101 p. 11701-11713, Baker (1996) JGR B101 p. 11715-11727, Nichols (1997) Can. Mineral. 35 p. 909-922, Gaffney (2002) J. Petrology 43 p. 963-980, Althaus (2003) GGG 4, McCarter (2006) Lithos 90 p. 187-213, Ireland (2009) Chem. Geo. 260 p. 112-128, Gaetani (2012) Geology 12 p. 915-918, Sakyi (2012) GCA 95.

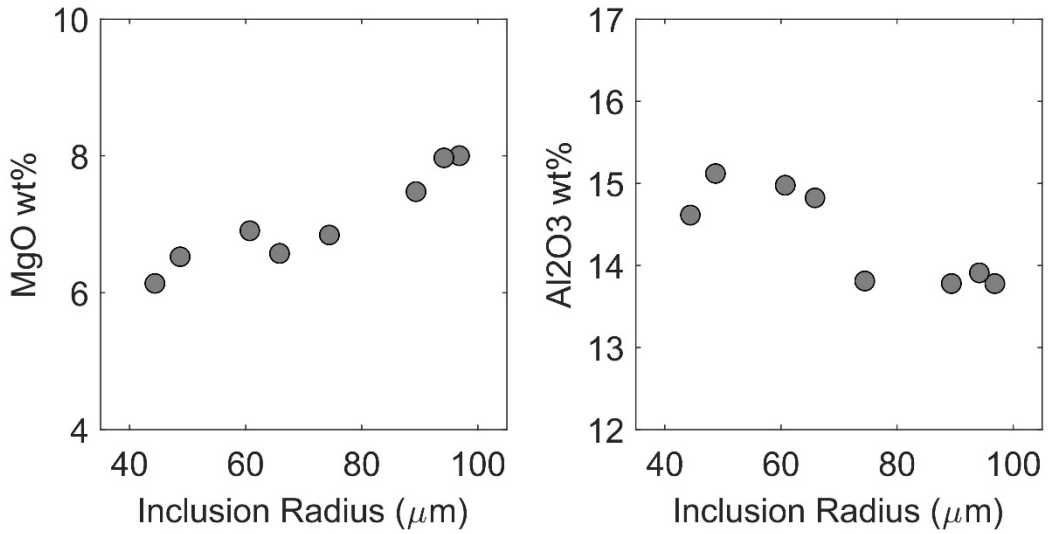


Central MgO and $Al_2O_3$ contents of glass inclusions of different sizes from experiment H5X (1225°C for 24 hr; cooled to 1000°C at 715 °C/hr)

**Supplementary Figure S4.** Central MgO (a) and $Al_2O_3$ (b) contents of glasses from melt inclusions of different sizes in experiment H5X (1225 °C for 24 hr, then cooled at 715 °C to 1000 °C). X-axis are the measured radii (longest dimension) of glass inclusions. Because some of the diffusion profiles were asymmetric with respect to the measured center of the inclusion, for MgO the central value was taken as the maximum across the profile (concave down), whereas for $Al_2O_3$ (concave up) the central value was taken as the minimum. Even though excess $Al_2O_3$ is continually building up adjacent to olivine crystallizing on the inclusion walls during cooling, the effect of inclusion size is less dramatic on $Al_2O_3$ than for MgO because there has been less exchange between the inclusion wall and center for the relatively slowly diffusing $Al_2O_3$.

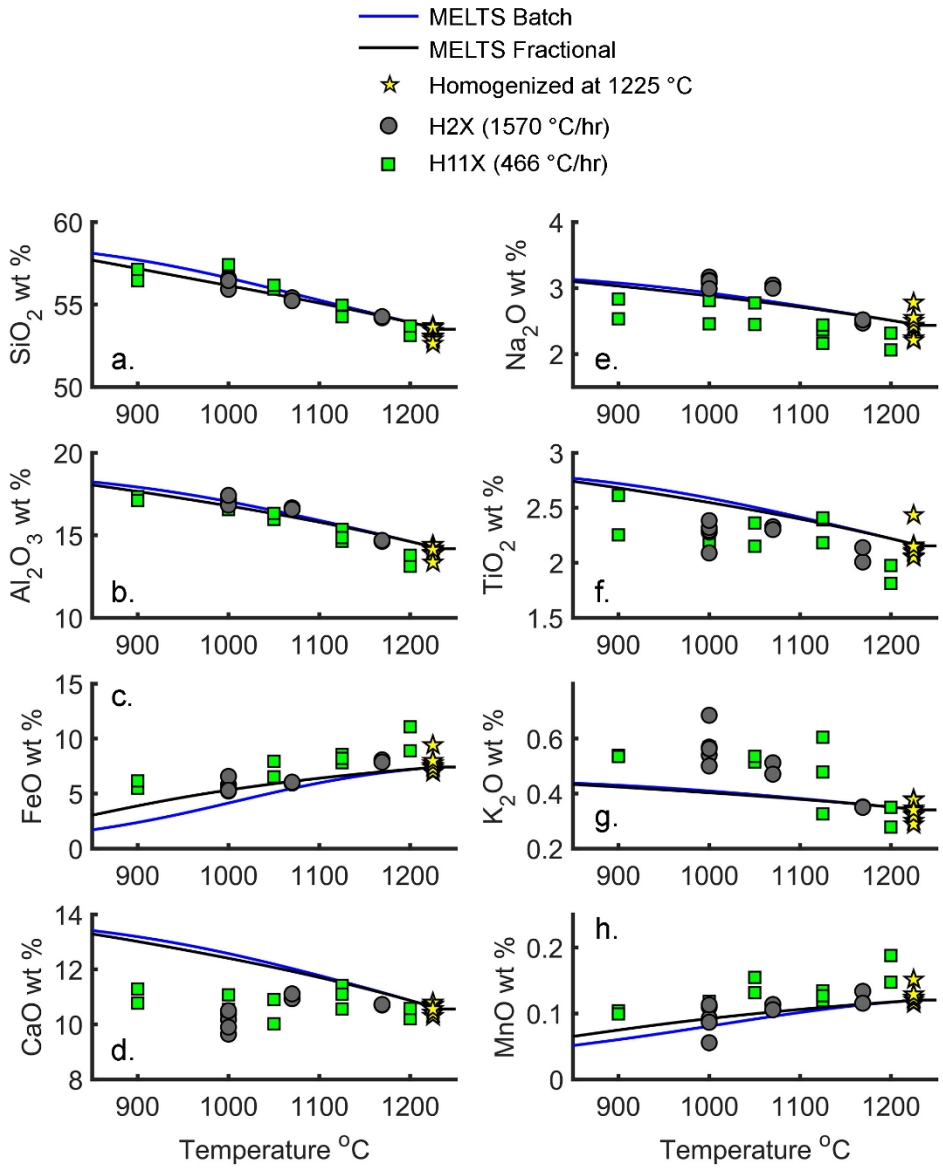


**Supplementary Figure S5.** Measured compositions of interface glasses in experimental inclusions; yellow stars are inclusions homogenized at 1225 °C for 24 hrs and drop quenched into water, gray circles are from the set of experiments H2X (1225 °C for 24 hrs, then cooled at 1570 °C/hr), green squares are from the set of experiments H11X (1225 °C for 24 hrs, then cooled at 466 °C/hr). In each set of experiments, MgO buckets with olivine were quenched at various temperatures to monitor the time-dependent changes in the interface liquids during cooling. Note that for the inclusions drop quenched directly from the 1225 °C hotspot (yellow stars) the interface liquid is influenced by quench growth of olivine (see Section 3.4.1) and for these inclusions the value plotted corresponds to the average composition of the central plateau of the inclusion excluding the data influenced by quench. The solid curves are MELTS calculations of the liquid composition during batch (blue) and fractional (black) crystallization of olivine starting with the liquid composition listed in Table 2.

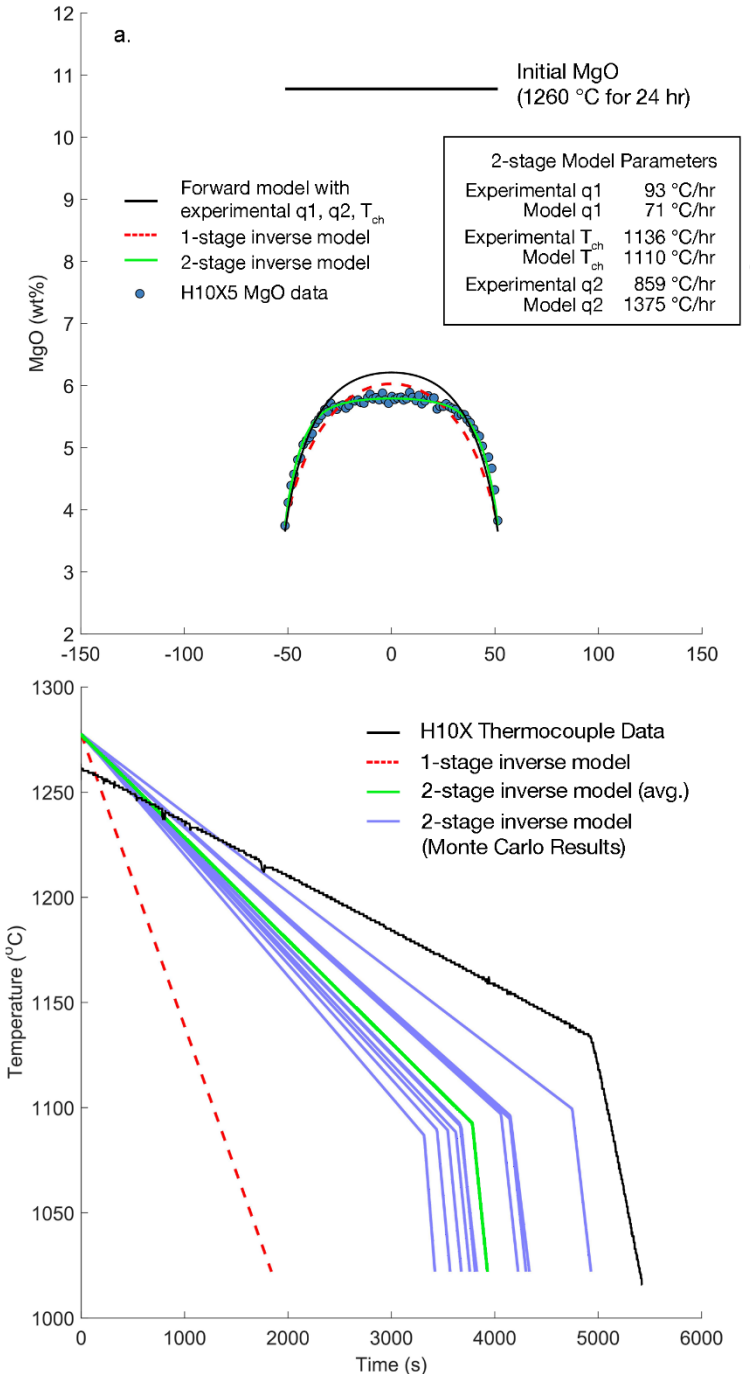


**Supplementary Figure S6.** Example model results for an inclusion from the two stage cooling experiment, H10X. (a) Blue circles are MgO microprobe data from experimental glass inclusion H10X5, which was homogenized at 1260 °C and then subjected to two stages of cooling and quenched at 1016 °C. Black horizontal line shows the initial MgO used in the model. The black solid curve near the microprobe data is a forward model calculated with no free parameters, and a cooling path specified by the measured thermocouple data (i.e., the black line in panel b). Red dashed line shows an inverse model allowing only a single stage of cooling, with the corresponding thermal history shown as the red dashed line in panel b. Green solid line show the best-fit cooling history calculated using a two-stage inverse model (see Section 4.4), again with the corresponding thermal history shown in panel b. The cooling rates (q1 for stage 1, q2 for stage 2) and crossover temperature (Tch) calculated using the best-fit 2-stage model are shown alongside the experimentally measured values in panel a. (b) Black line, measured thermocouple data during cooling. Red dashed line, 1-stage inverse model cooling history. Blue solid lines, individual model results of the 2-stage inverse model Monte Carlo simulation where the MgO data was perturbed with Gaussian noise and then refit multiple times. Green solid line, average 2-stage inverse model cooling history (mean of the three parameters q1, q2, and Tch from the distribution of Monte Carlo results).

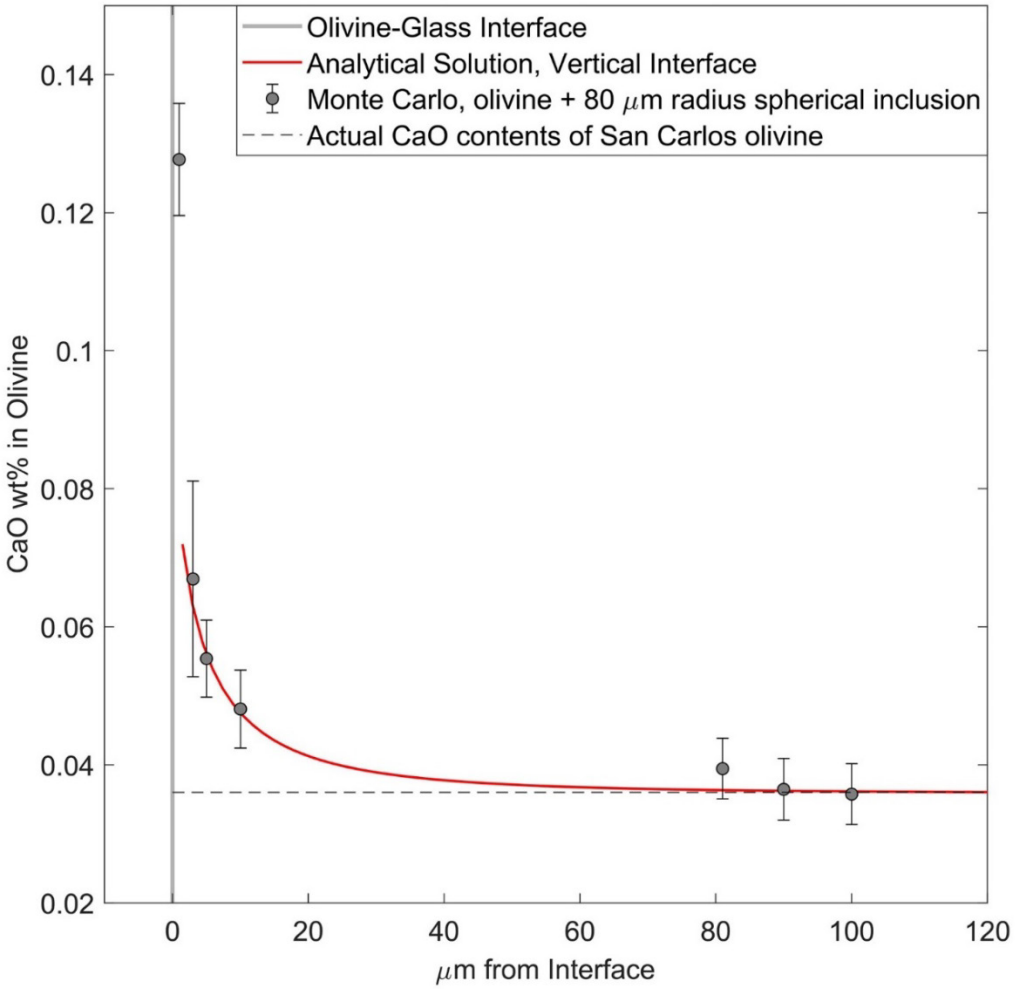


**Supplementary Figure S7**. PENEMPA (Penelope Monte-Carlo simulation software for EPMA, Probe for EPMA software, John Donovan) simulations of secondary fluorescence of CaO in olivine adjacent to basaltic glass. Dashed black line is the initial CaO contents of the modeled olivine. Red line is the analytical solution for the expected CaO profile in olivine approaching a vertical interface with basaltic glass. Grey circles are results of individual 15 hour Monte Carlo simulations of a 160 μm spherical inclusion embedded in olivine, and demonstrate the contribution of secondary fluorescence on measurements of the CaO contents of olivine at various distances from the spherical interface.

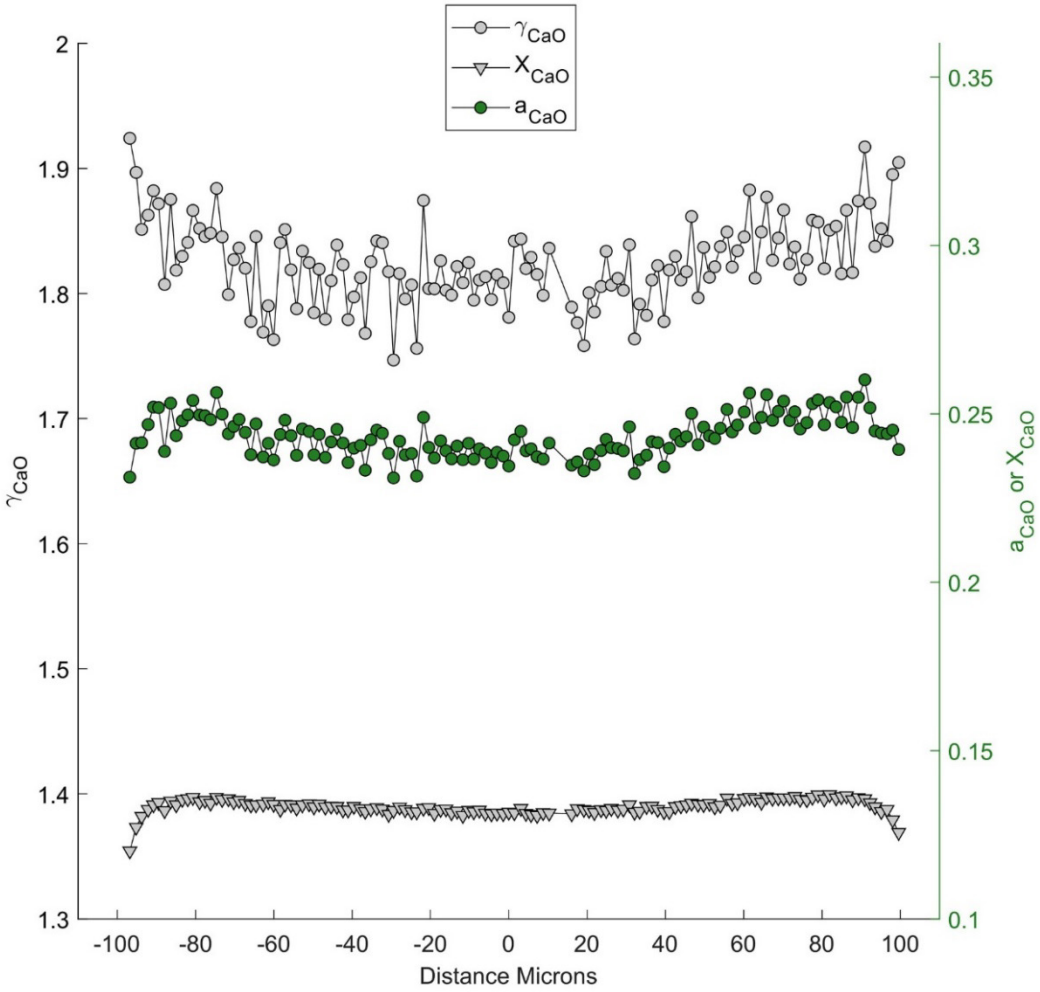


**Supplementary Figure S8.** MELTS calculated properties of the CaO component in experimental melt inclusion H2X5 (cooled at 1570 °C/hr from 1225–1000 °C. The gray triangles are mole fraction of CaO (XCaO) in the glass (scale on right y-axis), the green circles are the activity of the CaO component (aCaO) (scale on right y-axis), and the gray circles are the activity coefficient of CaO (γCaO). For the calculation, a vector of composition at each microprobe data point was input to MELTS and the thermodynamic properties were received assuming the quench temperature of 1000 °C. The chemical potential of the CaO component was taken by subtracting μCaSiO3 - μSiO2 and the standard state chemical potential for pure CaO component in the liquid was taken from Berman and Brown (1988). Note how both the activity and mole fraction profiles are not monotonic.

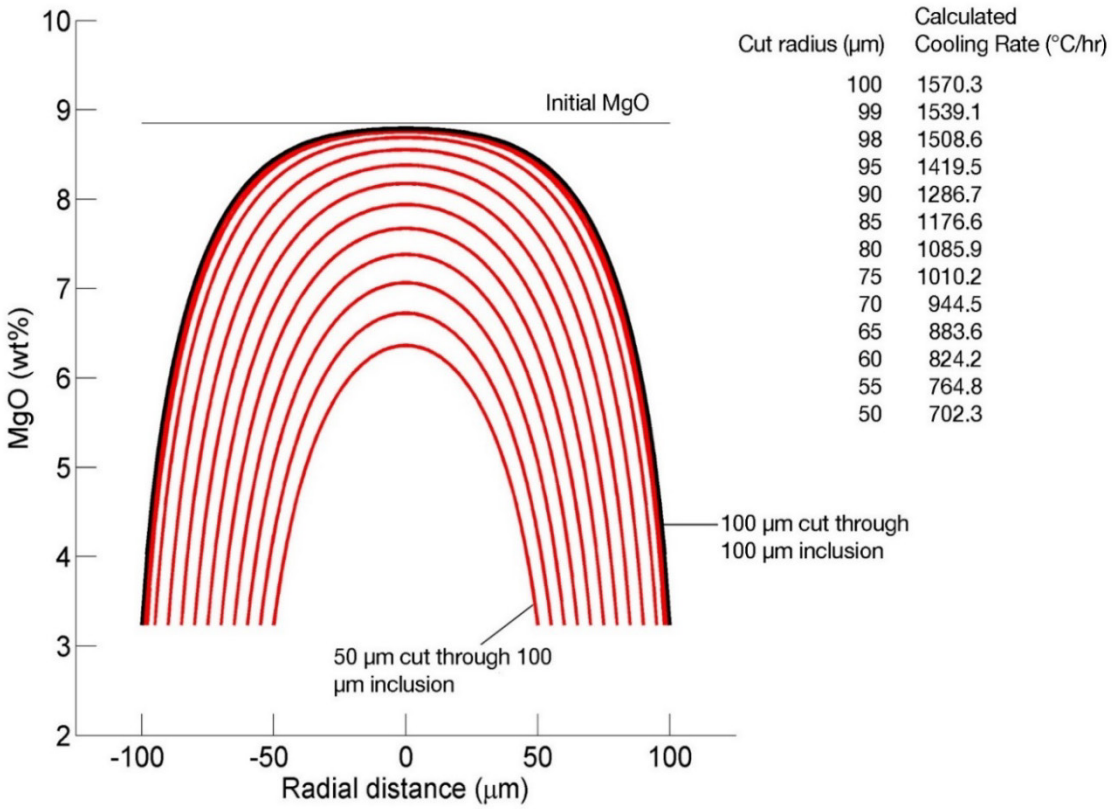


**Supplementary Figure S9.** Effect of taking off-center cuts through a synthetic melt inclusion on the cooling rate calculated by inverting the MgO profile with the model described in Section 4. The model was calculated for a 100 μm radius inclusion with initial MgO contents designated by the horizontal black line. The thick black curve shows the corresponding MgO profile for the melt inclusion exposed at its maximum dimension (200 μm diameter). The red curves show synthetic cuts through the melt inclusion at different distances from the maximum dimension. These synthetic MgO profiles from off-center cuts were then used as input to the inverse model, which given the same initial MgO, varied cooling rate until the residuals between the model and the synthetic off-center profiles were minimized. The cooling rates listed in the figure are the cooling rates associated with the best-fit model for each off-center cut, showing the effect of decreasing calculated cooling rate the further off-center a particular cut.

## Supplementary Tables

**Supplementary Table 1 - FTIR and XANES Results.**

| Inclusion name | Experimental $log_{10}fO2$ (bars) | FTIR $H_2O$ (weight %) | XANES Fe3+/ΣFe | XANES session | $SiO_2$ | $TiO_2$ | $Al_2O_3$ | FeO* | MgO | CaO | $Na_2O$ | $K_2O$ | MnO | $P_2O_5$ | Total |
|---|---|---|---|---|---|---|---|---|---|---|---|---|---|---|---|
| HIGS20 | Natural | 0.27 | 0.18<br>0.19 | 1 | 54.34 | 2.17 | 14.48 | 8.14 | 5.95 | 11.44 | 2.21 | 0.35 | 0.13 | 0.17 | 99.38 |
| HIGS21 | Natural | 0.16 | 0.16<br>0.17 | 1 | 54.30 | 2.15 | 13.99 | 8.28 | 6.16 | 11.38 | 2.23 | 0.33 | 0.13 | 0.23 | 99.19 |
| HIGS11 | Natural | 0.10 | 0.18<br>0.19 | 2 | 53.73 | 2.17 | 13.63 | 8.96 | 7.28 | 11.05 | 2.11 | 0.33 | 0.14 | 0.05 | 99.46 |
| HIGS14 | Natural | 0.2 | 0.20<br>0.20 | 2 | 55.55 | 2.41 | 15.17 | 6.80 | 4.04 | 12.69 | 2.18 | 0.34 | 0.12 | 0.05 | 99.34 |
| H7XC1 | -9.15 | 0.04 | 0.06<br>0.07 | 1 | 53.05 | 2.03 | 14.22 | 6.90 | 8.87 | 10.18 | 2.75 | 0.37 | 0.11 | 0.29 | 98.79 |
| H11XC1 | -9.18 | | 0.08<br>0.08 | 2 | 52.72 | 2.08 | 13.26 | 9.21 | 9.32 | 10.26 | 2.24 | 0.43 | 0.15 | 0.28 | 99.94 |

**Supplementary Table 2 – Results of MgO Diffusion Model Described in Section 4**

*Experimental Melt Inclusions*

| Inclusion name | Experimental quench temperature (°C) | Experimental cooling rate (°C/hr) | Model calculated cooling rate (°C/hr) | Std dev. calculated cooling rate (1σ) | Sum of squared residuals (SSR) |
|---|---|---|---|---|---|
| H8X1_1 | 1000 | 70 | 82 | 4 | 0.007 |
| H8X1_2 | 1000 | 70 | 139 | 5 | 0.005 |
| H8X2_1 | 1000 | 70 | 93 | 1 | 0.013 |
| H8X2_2 | 1000 | 70 | 129 | 2 | 0.008 |
| H8X4 | 1000 | 70 | 77 | 1 | 0.009 |
| H10X1 | 1134 | 90 | 70 | 1 | 0.016 |
| H10X2 | 1134 | 90 | 129 | 6 | 0.008 |
| H10X3 | 1134 | 90 | 92 | 2 | 0.009 |
| H7X1 | 1000 | 190 | 148 | 1 | 0.020 |
| H7X3 | 1000 | 190 | 223 | 1 | 0.021 |
| H7X4 | 1000 | 190 | 346 | 6 | 0.008 |
| H11X2B | 1200 | 466 | 382 | 22 | 0.013 |
| H11X3A | 900 | 466 | 357 | 2 | 0.033 |
| H11X4C | 1125 | 466 | 204 | 2 | 0.008 |
| H11X5C | 1000 | 466 | 388 | 5 | 0.044 |
| H11X6A | 1050 | 466 | 340 | 3 | 0.121 |
| H11X2A | 1200 | 466 | 630 | 15 | 0.013 |
| H11X3B | 900 | 466 | 563 | 2 | 0.026 |
| H11X4A_1 | 1125 | 466 | 330 | 2 | 0.062 |
| H11X4A_2 | 1125 | 466 | 404 | 3 | 0.009 |
| H11X5A | 1000 | 466 | 560 | 2 | 0.046 |
| H11X6B | 900 | 466 | 358 | 1 | 0.052 |
| H5X1_1 | 1000 | 715 | 852 | 5 | 0.017 |
| H5X1_2 | 1000 | 715 | 1000 | 0 | 0.031 |
| H5X2 | 1000 | 715 | 821 | 3 | 0.081 |
| H5X4a | 1000 | 715 | 624 | 1 | 0.162 |
| H5X4b | 1000 | 715 | 610 | 4 | 0.182 |
| H5X5 | 1000 | 715 | 568 | 2 | 0.149 |
| H5X6 | 1000 | 715 | 639 | 4 | 0.063 |
| H2X1 | 1000 | 1570 | 1095 | 13 | 0.085 |
| H2X2_1 | 1000 | 1570 | 1394 | 7 | 0.059 |
| H2X2_2 | 1000 | 1570 | 1322 | 8 | 0.163 |
| H2X3 | 1000 | 1570 | 984 | 7 | 0.203 |
| H2X5 | 1000 | 1570 | 1393 | 13 | 0.076 |
| H2X6 | 1160 | 1570 | 2129 | 54 | 0.019 |
| H2X7 | 1160 | 1570 | 1675 | 47 | 0.017 |
| H2X8 | 1070 | 1570 | 1796 | 12 | 0.050 |
| H2X9 | 1070 | 1570 | 1609 | 13 | 0.100 |
| H9X1 | 1000 | 20190 | 18694 | 890 | 0.016 |
| H9X2_1 | 1000 | 20190 | 26262 | 2485 | 0.019 |
| H9X2_2 | 1000 | 20190 | 18953 | 1188 | 0.029 |
| H9X3_1 | 1000 | 20190 | 17340 | 1035 | 0.018 |

| | | | | | |
|---|---|---|---|---|---|
| H9X3_2 | 1000 | 20190 | 22555 | 1384 | 0.015 |
| H9X4 | 1000 | 20190 | 25412 | 1361 | 0.030 |
| H4X1 | 1000 | 49644 | 36236 | 5302 | 0.015 |
| H4X2 | 1000 | 49644 | 17612 | 1935 | 0.011 |
| H4X3 | 1000 | 49644 | 41904 | 4655 | 0.014 |
| H4X4 | 1000 | 49644 | 30470 | 4818 | 0.010 |
| H4X5 | 1000 | 49644 | 32740 | 3547 | 0.011 |

*Natural (unheated) Melt Inclusions*

| Inclusion name | $T_{max}$ (°C) | $T_{min}$ (°C) | Model calculated cooling rate (°C/hr) | Std dev. calculated cooling rate (1σ) | Sum of squared residuals (SSR) |
|---|---|---|---|---|---|
| *Papakōlea, Hawai'i* | | | | | |
| HIGS9 | 1153 | 1122 | 11811 | 2753 | 0.009 |
| HIGS4 | 1149 | 1094 | 6528 | 738 | 0.011 |
| HIGS7 | 1141 | 1083 | 8392 | 1836 | 0.012 |
| HIGS19 | 1121 | 1079 | 7497 | 2040 | 0.015 |
| HIGS11 | 1160 | 1097 | 7964 | 798 | 0.021 |
| HIGS15 | 1160 | 985 | 615 | 9 | 0.107 |
| HIGS8_1 | 1160 | 1045 | 279 | 11 | 0.097 |
| HIGS2 | 1160 | 1015 | 854 | 21 | 0.052 |
| HIGS6 | 1160 | 895 | 226 | 5 | 0.031 |
| HIGS14 | 1160 | 844 | 51 | 1 | 0.018 |
| *Kīlauea Iki, Hawai'i* | | | | | |
| KIO1 | 1174 | 1068 | 6180 | 448 | 0.010 |
| KIO1 | 1183 | 1030 | 4039 | 184 | 0.023 |
| KIO3 | 1193 | 1092 | 7217 | 630 | 0.016 |
| KIO4 | 1184 | 1057 | 6112 | 293 | 0.021 |
| *Yamato Y980459* | | | | | |
| Y98MI1 | 1179 | 1010 | 331 | 19 | 0.005 |
| Y98MI2 | 1179 | 1003 | 85 | 11 | 0.004 |
| Y98MI3 | 1179 | 956 | 575 | 35 | 0.018 |
| Y98MI5 | 1179 | 1013 | 107 | 10 | 0.013 |
| Y98MI7 | 1179 | 978 | 389 | 115 | 0.015 |
| Y98MI8 | 1179 | 1013 | 223 | 14 | 0.019 |
| Y98MI9 | 1179 | 999 | 1047 | 109 | 0.017 |
| Y98MI10 | 1179 | 969 | 311 | 23 | 0.013 |

## Supplementary Text

*Contents*

***Supplement Section 2***



### 2.1 – Modeling Details

Diffusion modeling was based on the model of Newcombe et al. (2014), which calculates diffusion in one dimension for a spherical melt inclusion in equilibrium with olivine, subjected to a temperature-time path. The Supplementary Materials Sections S1, S2, and S3 in Newcombe et al. (2014) provide a detailed description of the model (S1), discussion of model assumptions (S2), as well as sensitivity tests (S3). This information is not repeated here and the reader is encouraged to read and refer to this material for a complete understanding of how the underlying model was constructed.

In this study, two modifications to the original model were made: (1) replacing the parameterization of the temperature dependence of the interface liquid composition, which serves as the changing boundary condition that drives diffusion during cooling, and (2) incorporating a composition-dependent diffusivity for MgO ($D_{MgO}$) that accounts for the steep compositional gradients that can develop across the inclusion during cooling. For (1), Newcombe et al. (2014) used a temperature-dependent relationship between MgO in the liquid and $Fo_{90.6}$ olivine based on olivine dissolution experiments of Chen and Zhang (2008). In this study, the interface liquid composition was specified using a MELTS calculation of batch olivine crystallization, which takes into account the composition of the host olivine (in

this study, ~$Fo_{88}$) and the changing olivine composition in equilibrium with liquid as a function of temperature (the olivine becomes increasingly fayalitic with decreasing temperature). Taking the average composition of melt inclusions experimentally homogenized at 1225 °C for 24 hrs at ΔFMQ = -1.15 (Table 1) as the bulk composition, MELTS accurately predicts the liquidus temperature (1229 °C±2(2σ)) and the olivine composition in equilibrium with the liquid; MELTS predicts $Fo_{87.3\pm0.9(2\sigma)}$ olivine, within error of the average composition of olivine analyzed at the olivine-glass interface in experimentally homogenized samples ($Fo_{88.2\pm1.8(2\sigma)}$). For the particular composition of the experiments, this was an improvement when compared to the prediction of Chen and Zhang (2008), which predicts the liquidus to be 1157±8 °C at a fixed olivine composition of $Fo_{90.6}$. The correspondence of the MELTS calculation of MgO vs. temperature and the measured MgO contents of interface glasses from melt inclusions that were experimentally homogenized, cooled, and quenched at different temperatures (Main Text Figure 10), led us to prefer using this MELTS-determined boundary condition. During relatively rapid cooling, the interface liquid will never truly follow an equilibrium crystallization path due being continually influenced by diffusive exchange with the inclusion interior, however as shown in Figure 10 at natural rates the model and data agree quite well especially at temperatures greater than 1000 °C where both experiments agree with either model by less than 0.4 wt % MgO.

Confident that the MELTS calculation provided a good approximation to the measured interface glass contents, we ran forward models with no free parameters specifying the initial temperature ($T_{max}$), final temperature ($T_{min}$), cooling rate (q), and inclusion composition (Table 1). As shown in Main Text Figure 11A for the particular example cooling

rate of 1570 °C/hr (cooling rate experiment H2X), when coupling the MELTS boundary condition at each temperature to a temperature-dependent but composition-independent $D_{MgO}$ (also from Chen and Zhang (2008) and used by Newcombe et al. (2014)), the resulting forward model produces an MgO profile that is too shallow when compared to the profile measured on an experimental inclusion. This indicated that at a given temperature, the $D_{MgO}$ from Chen and Zhang (2008) is too high and led us to consider using a $D_{MgO}$ that is a function of melt composition as well as temperature, following the approach of Zhang (2010). When using the $D_{MgO}$ from Zhang (2010), pp. 334, equation 23, which depends on the cation mole fraction of Si, Al, Mg, Fe, and Mn (in our application Mn is assumed to be a constant of 0.001), it is necessary to model $SiO_2$, $Al_2O_3$, and FeO in tandem with MgO, because each of these cations must be defined at every position and time step in the model in order to define $D_{MgO}$. A description of the iterative procedure used to achieve this can be found in Main Text Section 4.2. Here we list additional details on the parameters used to model $SiO_2$, $Al_2O_3$, and FeO

To model the diffusion of $SiO_2$, $Al_2O_3$, and FeO, temperature-dependent but composition-independent diffusivities were used. This is despite evidence (Supplement Section S3) that all three oxides display effects of multicomponent diffusion, and well-established evidence that $D_{SiO2}$ is inversely correlated with $X_{SiO2}$ (i.e. $SiO_2$ diffusion depends on the $SiO_2$ content of the liquid, Lesher and Walker 1986, Macris et al. 2018 and references therein). In order to take into account the compositional dependence of the diffusivities a full diffusion matrix would have to be used, which is computationally intensive and would require the temperature dependence of each term in the matrix, which are poorly constrained. The composition-independent Arrhenius relationships used for $D_{SiO2}$, $D_{Al2O3}$, and $D_{FeO}$,

provide reasonably good fits to the experimental diffusion profiles (see Main Text Figure 11) and to the extent that these calculations are used to calculate changes in $D_{MgO}$ across the inclusion, we deemed this approach satisfactory although acknowledge that a treatment that uses the full diffusion matrix may lead to better fits of the model to the data.

For $Al_2O_3$, we adopt an effective binary diffusion coefficient from experiments on olivine and clinopyroxene dissolution in basalt (Chen & Zhang, 2008; Chen & Zhang, 2009; Zhang, 2010). For FeO, tracer diffusion of $Fe^{3+}$ in andesite melt from Lowry et al. (1982) was found to give a better fit to the data than diffusion of $Fe^{3+}$ into basalt from the same study and from other determinations of Fe diffusion nominally as $Fe^{2+}$. This may be due to the fact that Fe diffusion is composition-dependent (correlated and slowed by high $SiO_2$ liquids), and so the lower diffusivity of $Fe^{3+}$ was found to better describe the experimental inclusion data. Because the composition-dependent $D_{MgO}$ needs to be calculated iteratively, for the initial guess of modeling MgO diffusion, the concentration-independent effective binary diffusion coefficient from experiments on clinopyroxene dissolution into basalt was used (Chen & Zhang, 2009). Again, these experiments were found to give a better fit to the MgO data than the experiments measuring $D_{MgO}$ using olivine dissolution into basalt (Chen & Zhang, 2009) because of the higher $SiO_2$ contents of the liquid coexisting with clinopyroxene in the former.

In the Zhang (2010) functional form for $D_{MgO}$, the Si cation fraction is the dominant control on the diffusivity. In building the model, we explored the compilation of literature Arrhenius expressions determined for $D_{SiO2}$ given in Zhang (2010) by running forward models specifying $T_{max}$, $T_{min}$, and cooling rate for a particular sample and comparing the resulting model profiles to those measured. The only expression that was able to adequately account for $SiO_2$ diffusion profiles across the range of cooling rates covered by the

experiments was the global fit of Zhang (2010) to all available dry basalt data on Si self and EBDC data from 1270 – 1600 °C and 0.5 – 2.0 GPa (Zhang, 2010, Diffusion Data, Table 2, Entry #180). To test if this fit could be improved, we used our experimental data to invert for $D_o$ and $E_A$ in the Arrhenius expression. Two inclusions were selected from each experiment and the $SiO_2$ profiles were jointly fit by varying $D_0$ and $E_A/R$, specifying the experimental cooing rate, and minimizing the residuals between the model profile and measured data.

The following expression best describes the experimental data for $SiO_2$ diffusion, from 1000 – 1225 °C, at 1 atm, with the initial melt composition based on the average of the inclusions homogenized at 1225 °C, as listed in Table 1:

$$\ln D_{SiO2}\ (m^2/s) = -9.3993(\pm 1.2) - 26919(\pm 1200) / T\ (K) \quad (3)$$

The values in parentheses denote 1σ uncertainties based on jointly fitting different sets of two inclusions from the experiments. These inverted parameters are within the error of that calculated by Zhang (2010) ($D_0 = -9.33\pm3.056$, $E_a/R = 25356\pm5126$). Specifying the experimental cooling rates and temperatures in the forward model, equation (3) reproduces 70% of the measured $SiO_2$ profiles within a mean sum of the squared residuals (SSR) of 0.3. The misfit in model $SiO_2$ profiles is mostly due to low predicted initial $SiO_2$, which is set by MELTS at $T_{max}$, resulting in an offset between the modeled and measured profiles of up to 1 wt% at a given location along a profile. In addition, the measured $SiO_2$ profiles exhibit local extrema that indicate uphill diffusion, consistent with previous observations that Si diffusivity is likely dependent on composition, including on its own concentration (Lesher & Walker, 1986; Koyaguchi, 1989; Behrens et al., 2004; Ni et al., 2009), but equation (3) has no compositional terms so cannot reproduce this feature of our data; our treatment can only produce monotonic, concave-up $SiO_2$ profiles from the inclusion center, and this

contributes to the misfit between our model and data with non-monotonic profiles. For the purposes of the data treatment in this paper, we adopt the original Zhang (2010) parameterization because the inverted parameters fall within its uncertainty.

**Application of the model**

In order to implement the composition-dependent $D_{MgO}$ in equation (2), the $SiO_2$, $Al_2O_3$, and FeO profiles must also be forward modeled in tandem with MgO. As an initial guess, the interface values for $SiO_2$, $Al_2O_3$, and FeO were, as for MgO, set at each temperature by a fit to the MELTS batch crystallization calculation (Supplementary Figure S6). Following the algorithm used for MgO, the diffusion equation is then solved numerically separately for the FeO, $SiO_2$, and $Al_2O_3$ fluxes assuming temperature-dependent (but concentration-independent) diffusivities (see Supplement Section 2 for details on the model parameters). Once the concentrations of MgO, FeO, $SiO_2$, and $Al_2O_3$ as a function of position and time are calculated, the concentration dependence of $D_{MgO}$ is calculated at each position and time by applying equation (2). The MgO profile, initially calculated with a composition-independent $D_{MgO}$, is then recalculated at each time step from $T_{max}$ to $T_{min}$, by numerically solving the diffusion equation where $D_{MgO}$ (equation 2) varies with position and time.

The calculation is repeated in a second approach where instead of using the MELTS boundary condition to specify the interface values for $SiO_2$, $Al_2O_3$, and FeO as functions of temperature, they were calculated to satisfy mass balance with the MgO removed as olivine crystallizing on the inclusion wall during each model time step. This approach takes into account that the interface liquid is continually affected by diffusion (Lasaga, 1982), for example producing a buildup of $SiO_2$ at the olivine boundary relative to that calculated using equilibrium growth. To achieve this, at each time step the amount of MgO extracted from

the melt is converted into a volume of olivine, the composition of which is specified by MELTS, and this volume of olivine is divided by the surface area of the melt inclusion to calculate an instantaneous thickness of olivine grown in each model calculation (see Newcombe et al., 2014 S1.2). Once the composition and volume of olivine extracted in each time step is known, the corresponding interface values for $SiO_2$, FeO, and $Al_2O_3$ can be specified based on a zone of an assumed thickness in the liquid into which the oxides are partitioned, following the procedure described in Newcombe et al. (2014) S2.1. The diffusion profile for each oxide is calculated with each decrement in temperature until $T_{min}$, and the resulting time-dependent profiles of $SiO_2$, $Al_2O_3$, FeO, and MgO are plugged into equation (2) to update $D_{MgO}$ as a function of time and position based on the results of this second mass balanced iteration. The MgO profile is recalculated based on this composition-dependent $D_{MgO}$ (calculated for a system which satisfies mass balance) and this calculation is taken to be the final result (the model converges after one iteration). Finally, in order to obtain a best-fit to a measured MgO profile, the cooling rate parameter was allowed to vary and the Matlab fitting procedure *fminsearch* was used to find the linear cooling rate from $T_{max}$ to $T_{min}$ that minimized the sum of the squared residuals (SSR) between the forward model described above and MgO concentration profiles from experimental or natural olivine-hosted melt inclusions.

$T_{max}$ was prescribed via equation (1) using the average MgO of homogenized inclusions (9.0 wt %) corresponding to a temperature of 1229 °C. The 2σ variability in homogenized MgO values (0.26 wt%, Table 2) translates to a range of $T_{max}$ of 1222–1237 °C through equation (1), and the sensitivity of the model to this initial temperature was calculated. At lower cooling rates (≤715 °C/hr, experiments H5X, H7X, H8X, H9X, H11X)

the uncertainty in $T_{max}$ results in <2% relative difference in the cooling rate that minimized the residuals between model and data and 10–15 % relative for experiment H2X (1570 °C/hr). In the most rapidly cooled experiments (H4X and H9X), the inclusion concentration profiles have unambiguous plateaus corresponding to the initial homogenized liquid composition (Figure 4c, Figure7ab). Accordingly, the initial MgO (and $T_{max}$) for these inclusions were set using the constraint of the average plateau MgO contents (resulting in $T_{max}$ ranging from 1225–1240 °C). Due to the relative insensitivity of the model to the initial temperature, for experiments cooled ≤1570 °C/hr (all except H4X and H9X), the profiles shown in Figure 13 and data presented in Figure 14 correspond to data inversions that assume $T_{max}$ = 1229 °C.

The minimum temperature ($T_{min}$) used in the inversions was calculated for each sample based on equation (1) using the lowest MgO value along a profile, measured as close as possible to the wall olivine (same approach used for natural samples with unknown thermal histories in Newcombe et al., 2014). For the 22 inclusions cooled at rates ≤1570 °C/hr and quenched at 1000 °C, the mean calculated $T_{min}$ using equation (1) is 1008 °C, with a 2σ standard deviation of 56 °C. As discussed in Section 3.2 (Figure 11b), the interface MgO is elevated in the rapidly cooled experiments H4X and H9X, corresponding to high calculated mean $T_{min}$ of 1183 °C and 1154 °C, respectively. Inclusions H11X3A and H11X3B (cooled at 466 °C/hr and quenched at 900 °C) were the only samples quenched below 1000 °C, and the calculated $T_{min}$ (via equation 1) given the minimum MgO in the glass (2.87 and 3.24 wt%) is 955 and 987 °C (Figure 11a). The closure temperature of the diffusion model is calculated to be ~850 °C, and was defined as the T at which changes in the interface-adjacent grid cell during additional cooling reduce to within the 1σ uncertainty of MgO microprobe

measurements (0.075 wt%), i.e., when diffusion slows down such that no further measurable changes would occur if extrapolating the linear cooling path to lower temperatures. The actual closure temperature may be at a higher T, given the relatively high glass transition temperatures (>900 °C, Nichols 2009) inferred for the low $H_2O$ experimental glasses, corresponding to cessation of olivine growth at higher T than the closure temperature calculated for our model.

Given $T_{max}$ and $T_{min}$ calculated for a particular inclusion, the cooling rate was allowed to vary such that the difference between the model MgO profile at $T_{min}$ and the experimental MgO data was minimized. Figure 12b-e shows an example of the forward models for $SiO_2$, $Al_2O_3$, FeO, and MgO along with the microprobe data for experimentally cooled inclusion H2X5 at $T_{min}$, which is the final profile in the sequence of forward models that are used to calculate $D_{MgO}$ via equation (2) at each time step. The modeled profiles fit the experimental data well, particularly for $SiO_2$ (Main Text Figure 11b), which is the main driver of the changes in $D_{MgO}$ via equation (2). The resulting MgO profile, calculated with equations (1) and (2) is shown in Figure 12a for the measured cooling rate (1570 °C/hr, black line) and the cooling rate resulting in the best-fit model (1393 °C/hr, blue line). A forward model at 1570 °C/hr using equation (1) with the compositionally invariant $D_{MgO}$ from Chen and Zhang (2008) is shown for comparison (green line). All of the forward models shown in Figure 12a were run with $T_{max}$ = 1229 °C and $T_{min}$ = 1025 °C, and equation (1) was used to set $C_{MgO}^{liq}$ at each time step. Given these parameters and the cooling rate from experiment H2X (1570 °C/hr), Main Text Figure 11a illustrates the improvement in the fit to the data that results from including the dependence of $D_{MgO}$ on melt composition (especially $SiO_2$). It is also important to emphasize that no available composition-independent parameterization of $D_{MgO}$

is available that can describe the inclusion data across cooling rate space when coupled to the MELTS MgO thermometer. In lieu of a full diffusion matrix treatment, the composition-dependent $D_{MgO}$ of equation (2) provides a realistic description of MgO diffusion across a zoned inclusion, where $D_{MgO}$ can vary by an order of magnitude from the edge to the center of a given inclusion. When used in conjunction with equation (1), which provides a good approximation of the temperature-dependent $C_{MgO}^{liq}$ (Figure 11a), the resulting model can be used to fit the experimental data at known laboratory temperature and cooling rate conditions.

**Reconstruction of $T_{max}$ for natural inclusions whose centers were modified by diffusion**

In order to determine $T_{max}$ for those inclusions with center compositions that have been modified by diffusion during cooling, Newcombe et al. (2014) adopted the approach of taking the highest MgO value recorded for a given inclusion population and applying the MgO vs. T thermometer of Chen and Zhang (2008). For the Papakōlea samples, the highest MgO (7.2 wt %) comes from the compositional plateau of HIGS11, and applying equation (3) corresponds to a $T_{max}$ of 1160 °C. An alternative to this assumption would be to reconstruct the initial composition of the liquid by adding liquidus olivine in increments to the integrated bulk composition of the inclusion until reaching a target liquidus olivine composition, as is commonly done to determine the composition and conditions of melt inclusion entrapment. Due to ambiguity in accurately knowing what olivine composition along its zoning profile was in equilibrium with the inclusion liquid at $T_{max}$, for the Papakōlea inclusions whose centers were modified by diffusion we adopt the approach of Newcombe et al. (2014) by setting $T_{max}$ via the maximum plateau MgO contents from a population of related olivines. For inclusions HIGS2, HIGS15, HIGS8_1, and HIGS6, the best-fit cooling rates calculated using $T_{max}$ = 1160 °C are 854 °C/hr, 615 °C/hr, 279 °C/hr, and 226 °C/hr,

respectively, while HIGS14 has a substantially lower rate at 51 °C/hr. We note that when using $T_{max}$ set by reconstructing the inclusion to be in equilibrium with the olivine analysis measured closest to the inclusion wall (giving $T_{max}$ = 1223–1276 °C), the calculated cooling rates are 25 – 45 % higher relative to those using $T_{max}$ = 1160 °C.

The target olivine composition for this modeling exercise should be the outer edge of the steep zone of fayalitic olivine (Figure 9), however HIGS14 (Figure 9a) is the only natural sample that unambiguously displays the three distinct Fe/Mg zones (it also has the lowest modeled cooling rate of the natural samples). Broad Fe/Mg zoning in olivine enclosing the other natural inclusions extends 15–35 μm from the inclusion wall and likely represents growth on the inclusion wall *and* diffusive exchange with the olivine interior prior to cooling during eruption (Danyushevsky, 2000). To minimize bias, the target olivine for the reconstruction calculation was chosen to be the measurement closest to the inclusion wall, implying that any olivine growth during cooling was confined to a narrow region inaccessible by the microprobe. The calculation was done using MELTS at one bar and an initial oxygen fugacity of +0.3 log units above FMQ. Target interface Fo% (100 x MgO/(MgO+FeO) in olivine) ranged from 83.4–86.4 Fo%, corresponding to reconstructed $T_{max}$ of 1227–1248 °C, with the exception of sample HIGS6 which had a more forsteritic host olivine (88.0 Fo%) and a reconstructed $T_{max}$ of 1286 °C. Because of the narrow widths of olivine expected to grow during cooling, this approach is susceptible to overestimating T because the chosen target olivine composition is likely more magnesian than that at equilibrium with the liquid at the true $T_{max}$ prior to eruption. The inverse model was run for these 5 inclusions under two assumptions, using either $T_{max}$ = 1160 °C (set by the HIGS11 plateau) or the reconstructed $T_{max}$, as a means to quantify the uncertainty associated with the choice of $T_{max}$ on the resulting

calculated cooling rates. For inclusions HIGS2, HIGS15, HIGS8_1, and HIGS6, the best-fit cooling rates calculated using $T_{max}$ = 1160 °C are 854 °C/hr, 615 °C/hr, 279 °C/hr, and 226 °C/hr, while HIGS14 has a substantially lower rate at 51 °C/hr. The rates calculated using the reconstructed bulk inclusion composition to determine $T_{max}$ are 25 – 40% higher than the calculated rates using $T_{max}$ = 1160 °C for the samples whose reconstructed liquidi are 67 – 88 °C higher than $T_{max}$ (HIGS15, HIGS8_1, HIGS6, and HIGS14) and 66% higher for HIGS2, which has a calculated liquidus that is 127 °C higher than $T_{max}$. Note that the particular choice of $T_{max}$ does not produce a statistically better fit to the MgO profile. In general, for samples with an unknown initial condition, determining which of the two approaches is most appropriate depends on the suite of samples and other *a priori* information about their thermal histories. The Papakōlea olivine represent the amassed remains of wave-eroded ash beds (Walker 1992) and any petrographic information or relationships between individual olivine is lost. Therefore, following the discussion by Newcombe et al. (2014), for the purposes of reporting cooling rates we adopt the calculations which use $T_{max}$ = 1160 °C acknowledging that while there is uncertainty in backing out this initial condition, it only modestly affects the calculated cooling rate. It is clear from the CaO profile shape and the lack of plateau in the MgO profiles that the centers of these five inclusions have been modified by diffusion during cooling, consistent with calculated cooling rates 1-2 orders of magnitude lower than in the population with concave up CaO profiles.

**2.2 – Two-stage experiment modeling results**

One two-stage cooling experiment (H10X) was conducted to see how accurately it could be modeled and whether a 2-stage best-fit model is statistically better than if a 1-stage cooling history had been assumed. In this experiment, three MgO crucibles each containing

three melt inclusion-bearing olivine crystals were held at $T_{max}$ = 1260°C for 24 hr, at which point one crucible was drop quenched into water. The homogenized inclusions quenched at this point contain 10.78±0.07 wt% MgO (Main Text Figure 5cd); and as discussed in Section 4.1, this corresponds to $T_{max}$ = 1277 °C based on equation (1), and this was used as $T_{max}$ for inverse modeling. One of the two remaining crucibles was cooled from 1260 to 1134 °C at 93 °C/hr, and drop quenched into water at $T_{ch}$ = 1134 °C, where $T_{ch}$ is the changeover temperature between the first and second cooling stage. Three inclusions from three olivine grains quenched at this point were modeled as 1-stage experiments and are included in the preceding section (inclusions H10X1-3, Supplementary Figure S7, Table 3). The remaining bucket with three olivine grains (inclusions H10X4-6) was then cooled for a second stage at 859 °C/hr starting at $T_{ch}$ = 1134 °C and quenched at 1016 °C (i.e., after having experienced two linear segments of cooling; the thermocouple data are shown in Supplementary Figure S7).

For inclusions subjected to the 2-stage cooling history (i.e., those samples quenched at 1016 °C), the model was run by varying three parameters: a stage 1 cooling rate (q1), a stage 2 cooling rate (q2), and the changeover temperature between the two linear cooling stages ($T_{ch}$), following Newcombe et al. (2014), who used this approach to obtain improved fits relative to a 1-stage cooling history for some natural melt inclusions. Specifying the known experimental conditions ($T_{max}$ = 1260 °C, q1 = 93 °C/hr, $T_{ch}$ = 1134 °C, q2 = 859 °C/hr, $T_{min}$ = 1016 °C) such that all parameters in the forward model are fixed, produces an MgO profile that has higher concentrations (by ~0.4 wt. % MgO) in the center than in the measured glass data (Supplementary Figure SX, black line). Allowing q1, q2, and $T_{ch}$ to vary until the SSR is minimized between the two-stage model and the data produces profiles that

nearly perfectly fit the experimental data (Supplementary Figure S7, green line, mean SSR = ~0.005 for the three inclusions, compared to mean SSR = 0.026 for the three 1-stage inclusions quenched at 1134°C discussed in the preceding section, and a SSR = 0.08 when the experimental conditions are prescribed explicitly), as would be expected by the introduction of two additional independently adjustable parameters in the fitting procedure. The best-fit modeled parameters calculated for the three inclusions subjected to the same 2-stage cooling history vary from 71–236 °C/hr for q1, from 1084–1110 °C for $T_{ch}$, and from 955–1925 °C/hr for q2 (Main Text Table 3). These parameters combine to give fits to the experimental profiles that are improved relative to those calculated for the 1-stage cooling experiments, but with three free model parameters that deviate more from the known experimental conditions than the single model parameter (cooling rate) in the 1-stage cooling experiments. For example, relative to the experimental rates the best-fit 2-stage model parameter q1 differs by -60 to +150 % and q2 by -30 % to +120 %, with the $T_{ch}$ underestimated by 24–50 °C. Despite the factor of two difference between the experimental rates and the calculated values for the adjustable parameters in the inverse model, the 2-stage fit and solution are demonstrably better than simply assuming a 1-stage fit to the inclusions that experienced a 2-stage history (Figure 15, red dashed line, 500 °C/hr, SSR = 0.05). Note that the misfit between the single-stage model and the two-stage inclusion data in Supplementary Figure S7 is similar to that observed for some of the inclusions described in Section 4.4 that experienced single-stage cooling histories, and so other *a priori* information must be considered before assuming that the misfit is due to a more complex cooling history. Future work should investigate whether the development of systematic zoning patterns of Fe/Mg in the host olivine surrounding the melt inclusion can provide extra constraint on prior

periods of slow cooling (Gaetani et al., 2000; Danyushevsky et al., 2002), but we note that the 2-stage experiments, while limited in the number (n = 3), show no systematic or measurable differences in the olivine profiles generating during cooling compared to the single-stage cases.

**2.3 – Olivine Growth**

The thickness of olivine in the steep narrow zone adjacent to the olivine-melt interface that grew during experimental cooling approached the spatial resolution limit of quantitative WDS measurements made on the electron microprobe (in which analyses were spaced 1.5 μm apart; e.g., Figure 9b), so a Field Emission Zeiss 1550 SEM (FE-SEM) was used to measure energy dispersive (EDS) traverses across the olivine-glass boundary at submicrometer resolution (Supplementary Figure S5). Each EDS traverse was measured three times at a working distance of 8 mm, an accelerating voltage of 15 kV, and acquired using AZtec Software by Oxford Instruments. For the purpose of measuring the olivine overgrowth associated with experimental cooling, we used the Fe kα data from each traverse. Fe always increases in the experimental olivine as the inclusion wall is approached; it is lower in the adjacent glass relative to the olivine; and it increases in the glass with increasing distance from the interface (e.g., Figure 4). Leveraging this contrast in the shape of the Fe profile approaching the olivine-glass interface, a criterion was developed to estimate the thickness of the rim of olivine grown during the cooling and the location of the olivine-liquid boundary. We assume that maximum Fe kα in the olivine corresponds to the point along the traverse closest to the inclusion wall that is least contaminated by low Fe glass, providing an estimate for the location of the olivine-glass interface. Inspection of electron images corresponding to the traverses show that the actual location of the interface is up to 0.4 μm closer to the inclusion from the maximum in Fe kα, and so our reported thicknesses of the

narrow overgrowth zones are probably minimum estimates. To calculate the location of the break in slope between the broad and steep Fe zones marking the outer edge of the zone of olivine grown during the cooling experiments, lines were fit to each segment, and their intersection was taken as the position of this boundary (i.e., the intersection of the two red, best-fit lines in each panel of Supplementary Figure S5). The thickness of experimentally grown olivine was then determined by the distance from the maximum in Fe to the slope break between the two zones in the olivine. This exercise was done for inclusions cooled between 70 and 1570 °C/hr, resulting in thicknesses of the olivine grown on the inclusion wall during cooling of 3.4 to 1.5 μm (Supplementary Figure S5a-e), that vary inversely with cooling rate (Supplementary Figure S5f). Errors were estimated by randomly adding or subtracting Gaussian noise to the traverse ($2\sigma \approx 40$ counts per second) and then refitting the data, resulting in a representative error in measured thickness of approximately 0.3 μm. Multiple profiles for a single inclusion in different locations gave the same thickness within the reported errors, and comparison of thicknesses determined by visual inspection of the microprobe data and by the FE-SEM for inclusions with the thickest growth zones yielded estimates that are within error of each other. For the two highest cooling rate experiments (H4X and H9X), no clear Fe maximum was observed above the noise, and so we infer that the olivine growth distance during cooling was below the resolution of this method (estimated to be ~0.5 μm). The thicknesses of olivine overgrowths were also measured in the samples sequentially quenched in experiment H11X (homogenized at 1225°C, cooled at 466 °C/hr; Supplementary Figure S5). Although the thickness of 0.3 μm for the sample quenched at 1200 °C (H11X2B) is likely below our ability to resolve, the profiles for samples quenched at lower temperature show a progressive thickening of the measured olivine growth zone

with decreasing temperature, interpreted to be the result of continuous growth of olivine on the interior of the inclusion walls during cooling.

**2.4 – Determination of errors in calculated cooling rates**

The parametric bootstrap method (e.g. Efron & Tibshirani, 1985) was used to estimate the error on the cooling rate due to the microprobe precision, following the approach employed by Newcombe et al. (2014). Each MgO analysis was assumed to be normally distributed with a mean corresponding to the measured value and a standard deviation of 0.075 wt%, which is estimated by calculating the standard deviation of replicate analyses of secondary glass standards from each analytical session (15 sessions in total) and then taking the average of these standard deviations, giving uncertainties for BHVO-2g ($1\sigma$ = 0.06 wt%) and BIR-1g ($1\sigma$ = 0.09). A set of at least 10 synthetic profiles were generated by drawing from this distribution for each data point and then running the inverse model on each synthetic profile by vary cooling rate until the residuals between the model and data are minimized. The standard deviation of the cooling rates calculated by inverting the synthetic profile served as a measure of the uncertainty in microprobe precision on the resulting cooling rate. Because $T_{max}$ is set by the plateau MgO contents for the rapidly cooled inclusions, for these inclusions this was recalculated for each synthetic profile; adjusting the MgO by ±0.075 wt% results in an uncertainty in $T_{max}$ of ±2.65 °C via equation (1) in the Main Text.

*Chapter 3*

# The temperature-dependence and kinetics of electron transfer between S and Fe in silicate melts: perspectives from olivine-hosted melt inclusions

Lee M. Saper

## 1. Abstract

The relationship between Fe and S valence as a function of oxygen fugacity ($fO_2$), temperature, and cooling rate was explored using natural olivine-hosted melt inclusions as experimental vessels. XANES measurements of both $Fe^{3+}/Fe^{2+}$ and $S^{6+}/S^{2-}$ represent the first co-determinations of Fe and S valence in experimental basaltic glasses equilibrated at high-T with the $fO_2$ of a 1 atm gas-mixing furnace. Experimental melt inclusions were equilibrated for 24 hr at 1225 °C and at values of $fO_2$ imposed by the external $H_2$-$CO_2$ furnace gases of FMQ-1, FMQ+0.35, FMQ+2.8, and FMQ+4.7. They were then either drop-quenched directly from the hotspot or subjected to different cooling paths. All the experimental melt inclusions lost water during the homogenization step (inclusions initially had ~2000 ppm, recovered experimental glasses had 63-785 ppm $H_2O$), however the $H_2O$ contents do not conform to the expected relationship among $fO_2$, $fH_2O$, and $H_2O$ solubility in basalt. Thus it is unclear whether the melt inclusions attained H-O equilibrium with the furnace atmosphere. Even so, they can be used as a case study to make several important points about redox equilibria in Fe and S bearing liquids.

The $Fe^{3+}/Fe^{Total}$ measured in unheated melt inclusions from Papakōlea, Mauna Loa, Hawai‘i ranged from 0.165-0.199; the experimental melt inclusions have $Fe^{3+}/Fe^{Total}$ ranging from 0.065 (FMQ-1) to 0.688 (FMQ+4.7). For experiments homogenized at FMQ-1 and FMQ+0.35 the $S^{6+}/S^{Total} = 0$; one experiment that was cooled at 2900 °C/hr from 1225°C to 1150°C at FMQ+0.35 had $S^{6+}/S^{Total} = 0.04$-$0.09$. S valence was not measured in the experiments run at FMQ+2.8 or FMQ+4.7, however all S is expected to be present as $S^{6+}$ at those conditions. Based on the nominal $fO_2$ imposed by furnace gases in the experiments run at or below FMQ+2.8, the $Fe^{3+}/Fe^{Total}$ predicted by various Fe

oxybarometers is systematically higher than that measured by XANES, with the one exception being the model of O'Neill (2018). At FMQ+4.7, all the oxybarometers underestimate the $Fe^{3+}/Fe^{Total}$ of the experimental inclusion glasses by 10-25% relative. While it is unclear whether the inclusions attained equilibrium with the $fO_2$ of the furnace atmosphere, the discrepancies between the models and measurements of $Fe^{3+}/Fe^{Total}$ are systematic and are interpreted to be due to (i) the presence of sulfide nanolites in the analytical volume of the Fe XANES measurement, and/or (ii) the compositional dependencies coded in the oxybarometers, which were all calibrated on S-free melts, not being accurate for S-bearing melt inclusions.

The degree to which uncertainty in the Fe oxybarometers propagates into determining the $fO_2$ of the sulfide to sulfate transition is explored. Models that seek to describe Fe-S redox equilibria but which ignore compositional effects, including the bulk Fe/S ratio, can only be valid for narrow ranges in composition and may not be applicable to natural scenarios in which Fe/S becomes fractionated by degassing or crystal growth. For example, melts with initially the same $fO_2$, T, $Fe^{3+}/Fe^{2+}$, and $S^{6+}/S^{2-}$, but different bulk Fe/S, when cooled to different T can reach the same $fO_2$ (and $Fe^{3+}/Fe^{2+}$) but have different $S^{6+}/S^{2-}$.

Two unheated olivine-hosted inclusions from Papakōlea were used as a case study to demonstrate that at least for these inclusions, the T-dependence of Fe-S electron exchange is either weak or proceeds in a direction that consumes $S^{2-}$ and decreases $Fe^{3+}/Fe^{2+}$. Based on MgO diffusion speedometry, one inclusion was rapidly cooled during eruption whereas the other inclusion was slowly cooled at ~55°C/hr while progressively crystallizing olivine on the inclusion walls down to T<900°C. The slowly cooled inclusion

has 154 ppm S and $S^{6+}/S^{Total} = 1$, which is incompatible with models that suggest a strong down-T tendency for $S^{6+}$ convert to $S^{2-}$ in the presence of Fe. Additional experiments are required to assess the temperature- and cooling-rate dependence of Fe-S electron exchange and whether room T measurements of the oxidation states of multivalence elements in silicate glasses are representative of that at high T in silicate liquids. These include time-series experiments exploring $H_2/H_2O$ and $fO_2$ equilibration across olivine-hosted melt inclusions, additional cooling rate experiments run at conditions where $S^{6+}/S^{Total}$ is unambiguously between 0 and 1, and experiments where S-bearing melt inclusions are hung simultaneously alongside S-free melts exposed directly to the furnace atmosphere.

## 2. Introduction

One of the most important intensive variables that petrologists, geochemists, and geophysicists are interested in quantifying is the oxygen fugacity ($fO_2$) in different environments and how it has changed over time. This topic has generated tremendous interest due to the role that $fO_2$ and redox chemistry play in the chemical evolution of planetary bodies and atmospheres, which has implications for determining the conditions required for life to thrive at (or near) the planetary surface. A widely used indicator of $fO_2$ in magmas is based on the $Fe^{3+}/Fe^{2+}$ ratio of quenched glasses; the Fe oxybarometer. This approach is calibrated using experiments where beads of silicate melts of various compositions are exposed to mixed-gas atmospheres at 1 atm in a tube furnace, allowing the $fO_2$ to be precisely controlled and varied, and then measuring the resulting $Fe^{3+}/Fe^{2+}$ of the recovered experimental glasses. Such experiments provide a calibration whereby one can parameterize the dependence of $Fe^{3+}/Fe^{2+}$ on $fO_2$, which can then be used to determine the $fO_2$ experienced by natural glasses (quenched silicate melts) based on measurements

of their major and minor element compositions and $Fe^{3+}/Fe^{2+}$ ratios. Most natural glasses contain sulfur, which is multivalent (-2 to +6 oxidation state) and is an important participant in redox chemistry, and can therefore influence the $Fe^{3+}/Fe^{2+}$ as well as its dependence on T and $fO_2$. However, all of existing models that relate the $Fe^{3+}/Fe^{2+}$ and composition of melts to T and $fO_2$ were calibrated on sulfur-free liquid (e.g., Sack et al. 1980; Kilinc et al. 1983; Borisov & Shapkin 1990; Kress & Carmichael 1991; Jayasuriya et al. 2004; Nikolaev et al. 1996; Borisov et al. 2018, O'Neill et al. 2018).

Although 1 atm gas-mixing experiments using S-bearing gases can be done, they typically only access a narrow range of sulfur fugacity ($fS_2$) such that the S contents of the coexisting silicate melts are lower than those observed in many natural samples at comparable $fO_2$ (e.g., Nash et al. 2019). Traditional high-pressure experiments result in higher solubilites of sulfur in silicate melt, but are limited by relatively coarse controls of $fO_2$ and $fS_2$. The failure to utilize experiments on melts with S contents comparable to those of undegassed silicate melts results in two major flaws in efforts to relate measured $Fe^{3+}/Fe^{2+}$ ratios in natural glasses to $fO_2$: (1) the presence of S itself may have effects on $fO_2$ that have yet to be characterized; and (2) therefore, while measurements of $Fe^{3+}/Fe^{2+}$ may be accurate, the conversion to $fO_2$ may be inaccurate for natural S-bearing melts because the calibrations are based on sulfur-free experiments.

Experimental studies on olivine-hosted melt inclusions have demonstrated that olivine acts a semi-permeable membrane with respect to volatile elements (e.g., Roedder 1979; Sobolev and Danyushevsky 1994; Hauri 2002; Gaetani et al. 2012; Bucholz et al. 2013; Mironov et al. 2015; Portnyagin et al. 2019; Saper & Stolper 2020), which means that during experimental treatment melt inclusions are closed to sulfur escape but are

capable of equilibrating with the external $fO_2$ imposed by the furnace atmosphere. Because gas-mixing furnaces have exquisite $fO_2$ control, this offers a highly promising technique to explore the properties of the S-bearing melts inside melt inclusions at variable $fO_2$. Data from an initial set of experiments (Saper & Stolper 2020) show that the $Fe^{3+}/Fe^{2+}$ ratios measured by XANES in experimentally equilibrated olivine-hosted inclusion glasses equilibrated at FMQ-1 are systematically lower than the those predicted by the S-free models that relate $fO_2$ to the $Fe^{3+}/Fe^{2+}$ of basaltic liquids. A similar magnitude and direction of the effect of S on $Fe^{3+}/Fe^{2+}$ was also documented in high-pressure experiments described in an AGU abstract (Graz et al. 2006), which were never published. These preliminary data raise the very real possibility that previous calculations of the $fO_2$ of natural sulfur-bearing melts may need to be reevaluated and recalculated by taking into account the effect of sulfur.

The same experimental approach can be used to explore the possibility that $Fe^{3+}/Fe^{2+}$ ratios in natural glasses may change during cooling, and are only "frozen in" at the glass transition temperature. If this is the case, it greatly complicates the use of room T measurements of the $Fe^{3+}/Fe^{2+}$ ratios in glasses to extract information, such as $fO_2$, about high-T magmatic liquids. The same uncertainty arises for the ratios of redox species of other multivalent elements in silicate melts, including $Cr^{3+}/Cr^{2+}$ (Berry et al. 2003), $S^{6+}/S^{2-}$ (e.g., Metrich et al. 2009), and $V^{5+}/V^{4+}/V^{3+}/V^{2+}$ (e.g., Mallman & O'Neill 2009). In its simplest form the relationship between the oxidation states of iron and sulfur in silicate melts can be modeled by the redox reaction:

$$S^{2-} + 8Fe^{3+} \rightleftharpoons 8Fe^{2+} + S^{6+} \quad (1)$$

A consequence of the eight electrons exchanged in this reaction is that, although sulfur concentrations are generally much lower than iron in natural melts, sulfur can play a disproportionately important role in redox chemistry. The sulfur-iron electron exchange reaction has been suggested to be strongly temperature-dependent (e.g., Metrich et al. 2009; Nash et al. 2019), which would mean that both the $Fe^{3+}/Fe^{2+}$ and $S^{6+}/S^{2-}$ measured at room temperature in S-bearing glasses are dependent on cooling rate and so may differ from the ratios present in the melt at high temperature. Curiously, although both Metrich et al. 2009 and Nash et al. 2019 agree that the effect of temperature on equation (1) is strong, they disagree on which direction the reaction will proceed with decreasing T. Very little is known about the kinetics of reaction (1), in part due to the experimental challenges described above. If reaction (1) proceeds sufficiently rapidly, which is expected at least at T above the solidus based on in-situ measurements of Fe-Cr electron exchange in melts (Berry et al. 2003), then the additional constraint of cooling rate is required in order to evaluate the fidelity of room T measurements of $Fe^{3+}/Fe^{2+}$ and $S^{6+}/S^{2-}$ as proxies for the same ratios at high T in both experimental and natural melts.

This chapter describes preliminary experiments using olivine-hosted melt inclusions as S-bearing experimental vessels where $fO_2$ is precisely controlled by $H_2$-$CO_2$ gases in a 1 atm tube furnace atmosphere. In addition to isothermal experiments that are quenched directly from the hotspot, which achieves the highest cooling rates permissible for the experimental setup (Xu & Zhang 2002), a protocol is described for running a series of cooling experiments which can be used to evaluate the cooling rate at which the high-temperature $Fe^{3+}/Fe^{2+}$ and $S^{6+}/S^{2-}$ ratios begin to be modified by electron exchange with sulfur (or whether the high T ratio can be quenched at all), while keeping melt composition

roughly constant. This information can be used to provide guidance on which natural glasses may have had their $Fe^{3+}/Fe^{2+}$ and $S^{6+}/S^{2-}$ modified during cooling, and to assess the magnitude and direction of this effect.

The results reported in this chapter represent only the second set of experimentally treated basaltic glasses to have had both $Fe^{3+}/Fe^{2+}$ and $S^{6+}/S^{2-}$ measured by synchrotron micro X-ray absorption near edge spectroscopy (XANES). Head et al. (2018) rehomogenized basanitic olivine-hosted melt inclusions from Nyamuragira, East African Rift for 10 minutes in a 1 atm furnace at 1130-1140°C and an $fO_2$ on the fayalite-quartz-magnetite buffer (FMQ buffer), and then used XANES to measure the valences of sulfur and iron (and vanadium) in the quenched inclusion glasses (n=5). The Head et al. (2018) experiments were designed to be short duration specifically to mitigate exchange with the furnace atmosphere. Therefore, the melt inclusion experiments described hereafter represent the first co-determined measurements of S and Fe valences in experimental basaltic glasses that were left to equilibrate at high-T for >10 minutes in a 1 atm furnace with precisely known $fO_2$ and thus to have constraints on nearly all of the relevant variables: $fO_2$, T, cooling rate, melt composition, $Fe^{3+}/Fe^{2+}$, and $S^{6+}/S^{2-}$. Note that Beerman et al. (2011) is the only other experimental study (IHPV) with co-determined Fe and S valences in quenched glasses, $Fe^{3+}/Fe^{2+}$ was determined by Mössbauer spectroscopy and S by electron microprobe Kα shifts (Wallace & Carmichael 1994; Carroll & Rutherford 1998). The accuracy of the latter technique has been questioned (Jugo et al. 2010). In addition to these experiments, Fe and S XANES results from two natural melt inclusions from Papakōlea, Mauna Loa, Hawai‘i with drastically different cooling rates provide a case study to explore the cooling-rate and temperature dependences of equation (1).

Because most natural igneous melts contain some sulfur, the results of this project can inform more accurate interpretations of the redox and thermal histories of volcanic, plutonic, and mantle rocks on the Earth and other terrestrial planets. For example, constraints on the temperature-dependence of equation (1) and accurate placement of the transitions of $S^{2-}$ to $S^{6+}$ and $Fe^{2+}$ to $Fe^{3+}$ as a function of $fO_2$ are critical for evaluating the role of S in modulating the $fO_2$ in the mantle wedge proximal to subducting and devolatilizing slabs of oceanic crust (e.g., Klimm et al. 2012), the effect of S degassing on the $fO_2$ of magmas (e.g., Gaillard and Scaillet 2009, Gaillard et el. 2011, Moussallam et al. 2016, Edmonds & Woods 2018), and the genesis of porphyry ore deposits (e.g., Tang et al. 2020).

## 3. Methods

### 3.1 Experimental Approach

Starting materials and the basic experimental approach were the same as that described in Saper & Stolper (2020), and more details can be found therein. The starting materials were olivines from Papakōlea Beach, Hawai‘i that contained spherical melt inclusions. Because Fe XANES requires doubly polished samples, only large melt inclusions (>80 μm in shortest dimension), found by inspection under an optical microscope, were selected for the new set of experiments. Note that the results reported below include melt inclusions from the experiments described in Chapter 1 (denoted H#X or HTOX#), only some of which contained very large melt inclusions, and as a result these inclusions were difficult to doubly polish, resulting in the destruction of several samples. Those that survived were prepared for quantitative analysis. The new set of experiments described below are labeled “SF#”.

Homogenization and cooling experiments were run in a 1-atm Deltech vertical gas-mixing furnace, using $H_2$-$CO_2$ gas mixes to control $fO_2$, which was calibrated and monitored using a $Y_2O_3$-stabilized $ZrO_2$ oxygen sensor. The $fO_2$ sensor was calibrated to the Fe-FeO reaction and was accurate to within 0.1 log units of the accepted value (Huebner 1971). Based on monitoring the sensor output over the experimental duration the precision was ±0.03 log units of $fO_2$. Four different values of $fO_2$ were used in the experiments, expressed relative to the fayalite-magnetite-quartz buffer (FMQ; referenced to the data of O'Neill 1987): $fO_2$ = FMQ-1 ("HX", n=15), FMQ+0.35 ("SF", n=27), FMQ+2.8 ("HTOX", n=2), and FMQ+4.7 ("H3X", n=4) where n refers to the number of inclusions that were recovered and polished. The $fO_2$ chosen for the SF experiments, FMQ+0.35, was based on the average $Fe^{3+}/Fe^{2+}$ measured by XANES in two natural Papakōlea melt inclusions, which ranged from $Fe^{3+}/Fe^{2+}$ = 0.20 (HIGS21) to 0.25 (HIGS14), from which $fO_2$ was calculated using the expression of Kress & Carmichael (1991). Based on T = 1225 °C, the $Fe^{3+}/Fe^{2+}$ measured in the natural inclusions and the model of Nash et al. (2019), the liquids in the SF experiments were expected to have a fraction of total S present as $S^{6+}$ ($S^{6+}/S^T$) = 0.55-0.88, or, based on the nominal experimental $fO_2$ (FMQ+0.35) and the model of Jugo et al. 2010, $S^{6+}/S^T$ = 0.04. Note that the high $fO_2$ experiment (H3X) was run in pure $CO_2$ gas, which at 1225 °C results in a CO-$CO_2$ gas mix whose $fO_2$ is outside the stability region for the $Fo_{89.8(\pm1.9)\ olivines}$ in the starting materials (Nitsan 1974). Two olivines recovered from this experiment were used as a "reversal" experiment and rehomogenized for 24 hr at 1225 °C at FMQ-1 in $H_2$-$CO_2$ gases (experiments H3XR).

Temperature (T) was recorded using a Type-S thermocouple, which was calibrated at the melting point of gold, and which was hung in the furnace hotspot alongside MgO

buckets that held the inclusion-bearing olivines. In each experiment, the MgO buckets were gradually lowered into the furnace hotspot and held isothermally at 1225 °C for 24 hr at the target $fO_2$. The isothermal dwell period was designed to homogenize the melt inclusions and to equilibrate these inclusions with the $fO_2$ imposed by the furnace gases at the exterior of the host olivines (Gaetani et al. 2012; Bucholz et al. 2013). During the cooling stages of the experiments, temperature was recorded digitally at a resolution of one measurement per second by attaching the in-situ Type-S thermocouple to a temperature logger.

In order to evaluate the temperature and cooling-rate dependence of the Fe-S electron transfer in experimental melt inclusions, three cooling schemes were designed for the SF experiments (homogenized at FMQ+0.35). All the HX experiments described in this chapter and several (20) of the SF experimental inclusions were homogenized for 24 hr and then drop quenched directly from the hotspot at 1225 °C into water – these are referred to as homogenization experiments in that they experienced the highest quench rates attainable using this experimental setup (Xu and Zhang 2002), except perhaps by using colder water. Two different types of cooling experiments were run: Type-B thermocouple-controlled cooling rate and displacement cooling. The controlled cooling rate experiments (SF3 and SF4) were run by programming the Type B control thermocouple placed near the furnace elements to cool as quickly as possible (setting the cooling rate to 5000 °C/hr); however, because of limitations on how fast the furnace is capable of conducting heat out of the hotspot, the maximum cooling rate achieved was a factor of two lower. For experiment SF3, which was cooled from 1225-1150°C a linear fit to the thermocouple time vs. temperature data gives a cooling rate of 2900 °C/hr; for

experiment SF4, which was cooled from 1225-1000°C the linear cooling rate is ~1900 °C/hr. Although the program was set to linear cooling, the cooling path is curved (Figure 1B), indicating that cooling was dominated by conduction of heat out of the furnace hotspot and not by the reduced power delivered to the furnace elements. The remaining experiments were run using the displacement method where the ceramic quench rod from which the olivine-bearing buckets were suspended was manually displaced out of the furnace hotspot at 1225 °C into a cooler part of the furnace in less than two seconds. The vertical thermal profile of the furnace tube was measured by equilibrating the Type-S thermocouple at different heights above and below the hotspot (Figure 1A). Once displaced into a cooler region of the furnace, the olivines cooled via conduction in the thermal gradient of the furnace, and the MgO buckets were drop quenched into water at different times along these cooling paths. Experiment SF10 was displaced to ~1150 °C and quenched at the same time after initiation of cooling as the controlled cooling rate experiment SF3 (also quenched at 1150°C), in order to compare two different cooling paths quenched at nearly the same temperature. Experiments SF4 (controlled cooling and quench at 1000 °C) and SF6, SF7, and SF9 (displacement) were designed in a similar manner, and the latter set of three displacement experiments were displaced to and quenched from ambient furnace temperatures of 950-981°C. For the very short duration experiment SF13, the thermocouple rod was displaced far from the hotspot to a region with ambient T = 600 °C and the experiment was quenched at 900 °C; this served as an intermediate between the rapidly cooled experiments that were quenched at 1000 °C and the homogenization experiments that were drop quenched directly into water from 1225 °C. A summary of the experimental conditions for the

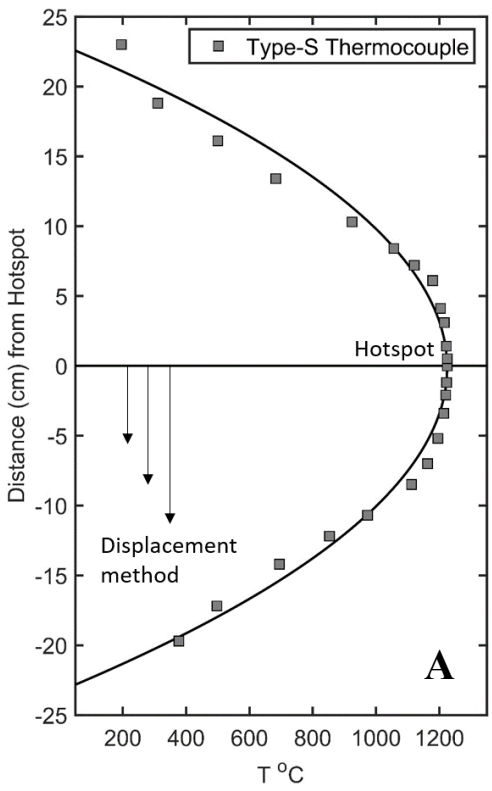


**Figure 1. (A)** Thermal profile of the Deltech 1-atm furnace. Gray squares are Type-S thermocouple measurements taken at different heights above and below the hotspot. Black curve is a polynomial fit to the thermocouple data. The arrows indicate the direction that experimental samples traveled using the displacement method. **(B)** Digitally logged thermocouple measurements during experimental cooling. Red diamonds indicate homogenization experiments that were drop quenched directly from the furnace hotspot. Green circles are experiments that were cooled using the Type-B control thermocouple. Blue squares are displacement method experiments. The red X on SF6 indicates that the inclusions in this experiment partially or nearly completely crystalline. The ambient T in the furnace at the final position of the quench rod in experiment SF13 was 600 °C.

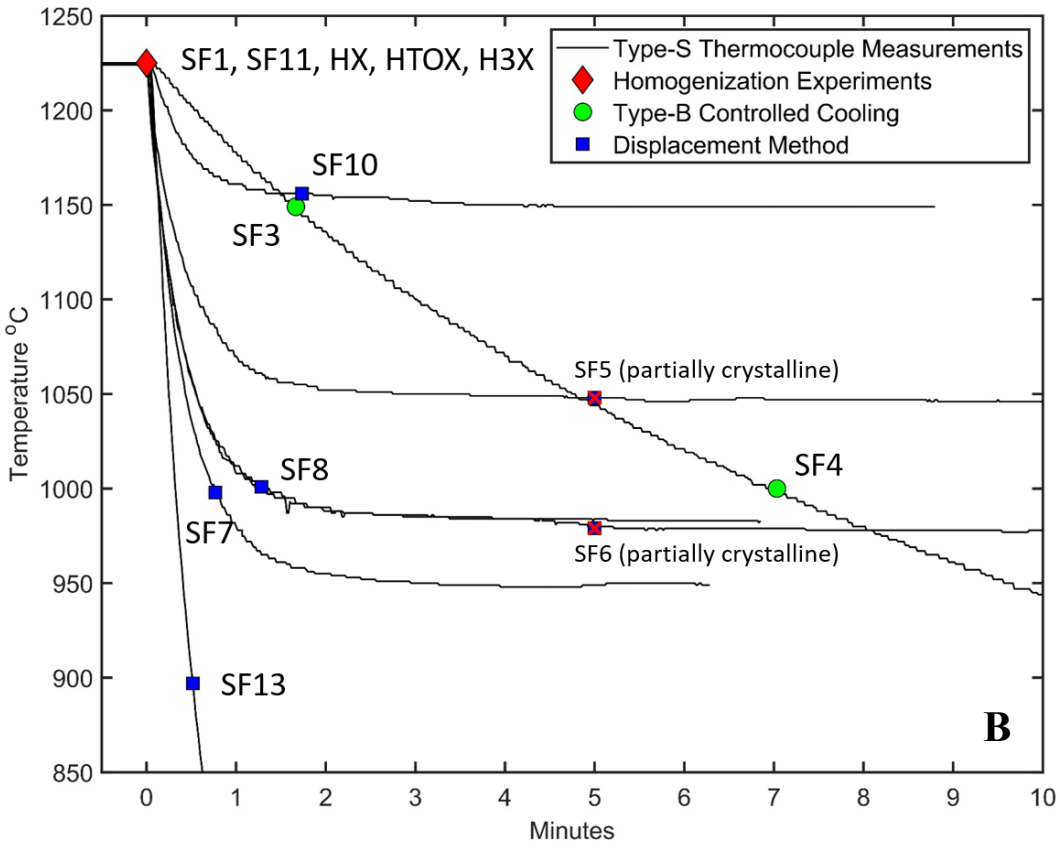

experimental inclusions that were analyzed for XANES are reported in Table 1; additional information on the HX experiments can be found in Chapter 1 (Saper & Stolper 2020).

Note that the diffusion model described in Chapter 1, given the cooling rates and large sizes of the melt inclusions, predicts that chemical gradients due to olivine crystallization on the inclusion walls were not expected to reach near the inclusion centers in these experiments, except possibly for experiment SF4. This is important because it allows for different cooling rates while holding the melt compositions roughly constant at the inclusion centers, where the XANES analyses were planned to be taken, in attempt to reduce systematic sources of error due to variable melt composition. Thus this experimental setup yields a means to vary $fO_2$, cooling rate, and quench temperature in S-bearing olivine-hosted melt inclusions, while keeping the melt compositions at their centers constant; in theory this type of approach can be used to explore both the T-dependence and kinetics of the Fe-S electron exchange reaction. However, I note here that the quenched experimental inclusions had little if any sulfur present as $S^{6+}$ (consistent with Jugo et al. 2010, but also possibly due to the low $Fe^{3+}/Fe^{2+}$ measured in the glasses compared to the nominal $fO_2$ of the experiments, see section 4.4) and so any effects of $S^{6+}$ reduction and $Fe^{2+}$ oxidation (the inferred down-T direction of equation (1) by Nash et al. 2019) during cooling were likely to be small, if at all measurable. Cooling rate experiments at higher $fO_2$ were planned, however in 2020 the CoVID-19 pandemic meant that the availability of the XANES beamline in the near future became unlikely (especially considering I had been piggybacking on other researcher's sessions), and so in the interest of finishing my Ph.D. those experiments were abandoned for the meantime. In retrospect, to test the results of Nash et al. (2019), the SF experiments should have been conducted at slightly higher $fO_2$,

guided by Jugo et al. (2010), to ensure that $S^{6+}$ was present – this is explored more fully in section 5.

### 3.2 Sample Analysis

Routine electron probe analysis of the melt inclusions was the same as that described in Chapter 1. The olivines that were recovered from the experiments were mounted in epoxy and first ground down to expose the largest melt inclusion near its center and then polished with increasingly fine grit lapping papers and diamond powders. The polished olivines and melt inclusions were carbon coated. Concentration profiles of major and minor oxides were measured using wavelength-dispersive spectroscopy (WDS) analyses at beam conditions of 10 nA, 15 kV, and a 1 μm beam along transects across the glasses and host olivines to document chemical gradients that formed during quenching or cooling. These analyses were corrected using a modified ZAF procedure (Armstrong, 1988) and the mean atomic number (MAN) method for background esimation.

Microprobe measurements of S used a custom analytical technique based on the fact that across the range of experimental $fO_2$, sulfur in the experimental glasses was expected to have variable average oxidation states between sulfide, $S^{2-}$ and sulfate, $S^{6+}$ (e.g. Wallace & Carmichael 1994). A consequence of these different electronic environments for S is that the position of the $K_\alpha$ peak is not a fixed value, and thus the spectrometer position where maximum counts are achieved might be expected to vary in the experimental unknowns. High-resolution wavescans in the region of S $K_\alpha$ were conducted on two primary standards (anhydrite and FeS), one secondary standard (VG-2 glass) and on each of the experimentally produced inclusion glasses in order to map out which spectrometer position corresponded to the maximum number of counts for S. Because the Caltech JEOL JXA-8200 microprobe has three spectrometers with PET crystals (all with

30 cm Rowland circles) suitable for S analysis, the probe was set up as a “multicollector”, with simultaneous collection of S counts at three different spectrometer positions. For each experimental unknown S was measured at the peak position for anhydrite (L = 171.884 mm, using a PETJ crystal), FeS (171.948 mm, using a PETJ crystal), and VG-2 glass (172.042 mm, using a PETL crystal). For each experimental glass, regardless of their underlying experimental $fO_2$, and their $S^{6+}/S^{2-}$, the actual peak positions for S straddled that of VG-2 glass, ranging from 172.005 mm (H3XC2, FMQ+4.7) to 172.210 mm (H9X2, FMQ-1). Interestingly, this result is opposite to what is observed in the primary standards, where the reduced species FeS (the $S^{2-}$-bearing phase) has a lower peak position than anhydrite ($S^{6+}$-bearing). This peak-position behavior and its impact on the accuracy of S microprobe measurements in glasses of variable oxidation state and composition needs to be explored further. Although the best practice may be to measure each unknown at the spectrometer position corresponding to the maximum number of counts for S, for consistency and ease of automating analyses (peak positions cannot be automatically changed between samples using the probe software) a static three spectrometer setup was used for all unknowns and the results reported herein correspond to S measured at the VG-2 peak position using the PETL crystal (which yielded maximum S counts of the three spectrometers on the experimental glasses). Using anhydrite or FeS as the primary standard for calculating S concentrations makes no measurable difference in the calculated concentrations; anhydrite was used because the O contents of the FeS standard was measured, whereas the anhydrite is stoichiometric.

The beam current for S analyses was 20 nA using a 10 μm defocused beam to avoid diffusion of elements away from the beam center; counting times were 40 seconds on and

off peak. Literature measurements of S in VG-2 glasses based on microprobe measurements range from 1270 ppm (Dixon and Clague 2001) up to 1610 ppm (Jego and Dasgupta 2013) with an average of 1437 ppm and a standard deviation of the means of 88 ppm for the 27 studies listed in the GeoREM database (Jochum et al. 2006); two SIMS determinations give 1430 ppm (Evans et al. 2008) and 1406 ppm (Florentin et al. 2017). Repeat analysis of the VG-2 standard using the analytical conditions described above gave S = 1428±54 (1σ), which is consistent with previous determinations of S. The detection limit based on these conditions was approximately 100 ppm. Analyses using beam sizes of 1 μm and 10 μm on the standard VG-2 glass produced distributions in S concentrations that are indistinguishable ($p<0.05$).

After characterizing the glasses with the microprobe, the inclusions were prepared for Fe XANES analysis. The opportunity to do S XANES on these glasses arose later; unlike Fe XANES, the S XANES does not require doubly polished glasses. In retrospect, the proper order of characterization should be (1) microprobe, (2) S XANES, and (3) Fe XANES, where between (2) and (3) the sample surfaces are slightly ground and re-polished, and then doubly polished. This serves to (1) remove glass surfaces that may have been damaged during the S XANES session prior to the Fe XANES session, and more importantly (2) because melt inclusions are very difficult to doubly polish, decreases the likelihood of sample destruction prior to the S XANES analysis. In any case, most experimental inclusions were first characterized by microprobe, then Fe XANES, and finally S XANES. Because of the timing of XANES sessions, not all inclusions were measured in the same order and for some inclusions there is incomplete data (e.g. due to destruction from handling the delicate samples in between analytical sessions).

Each individual olivine recovered from an experiment was initially mounted in epoxy in a 0.5 cm brass cylinder, which was used to polish the first side of the sample and for microprobe analysis. After microprobe characterization, the brass cylinders were sliced with a diamond saw (0.006” thick blade) to produce a wafer; one side was the high-polish side with the melt inclusion exposed near its center and the other side was roughly cut by the saw. This wafer was then carefully mounted using acetone-soluble CrystalBond to a circular glass microprobe slide, with the rough saw-cut side facing up, and then very carefully ground to expose the melt inclusion so that glass was at the surface on both sides of the wafer. This process, and the subsequent attempt to achieve a high polish on this side, was extremely delicate and had a relatively low success rate, especially at first. The experimental olivines are replete with cracks from thermal contraction during quenching, and when the thicknesses of the polished samples were $\lesssim$100 μm some of these cracks extended between the two free surfaces of the wafer causing pieces of the surrounding olivine to spall off, sometimes taking with it portions (or the entirety) of the melt inclusions. Attempts to impregnate these cracks with epoxy after the wafer was cut did not lead to improved outcomes. This was another reason for choosing the largest diameter melt inclusions possible; they permitted thicker doubly polished samples that had inclusion glass exposed on both surfaces. Another way to improve success rates would be to only partially expose the melt inclusions on the first polish rather than to seek a polished surface through the inclusion centers. Because it is important to characterize chemical gradients across the centers of the spherical melt inclusions (Saper & Stolper 2020) and to limit compositional gradients within the Fe XANES analytical volume, however, the inclusion centers were exposed to their centers on one side. This preparation resulted in 13 doubly-

polished experimental melt inclusions, which were mounted on Fe-free $SiO_2$ glass slides for Fe XANES analyses. After Fe XANES analysis, the samples were too delicate for re-polishing, and so they were simply recycled for the S XANES. To the extent possible the areas that were measured for Fe XANES were avoided in the S XANES session.

Fe XANES analyses were generously performed by Dr. M. Peterson in two different sessions in 2018 and 2019 at the Advanced Photon Source (APS), Argonne National Laboratory. The reduced results of the earlier session were described in Chapter 1. The spot size at the glass surfaces was ~10 μm. Details of data acquisition and reduction can be found in the supplement of Brounce et al. (2017) and in Cottrell and Kelley (2009). In summary, the $Fe^{3+}/Fe^{2+}$ of glasses was quantified by fitting the two pre-edge features of the Fe spectra with Gaussian curves, and comparing the ratio of the integrated areas under each Gaussian to that measured for a suite of standard glasses with known $Fe^{3+}/Fe^{2+}$. Figure 2A shows the calibration curves used in the two sessions; the curves are empirical second order polynomial fits to the standard glass data. Note that the lowest $Fe^{3+}/Fe^{2+}$ in the standard glass set is 8%; extrapolating the calibration curve to zero $Fe^{3+}$ implies that the ratio of the two integrated peak areas is ~0.15, even though ostensibly no $Fe^{3+}$ is present. It is unclear whether this functional form is correct or applicable to $Fe^{3+}/Fe^{Total}$ lower than 8%, however it fits the data well at higher $Fe^{3+}/Fe^{2+}$, and based on its broad usage in the literature it was adopted here.

S XANES analyses were generously performed by Dr. M.-J. Brounce in 2019 at APS. Again, details can be found in the supplement of Brounce et al. 2017. The spot size

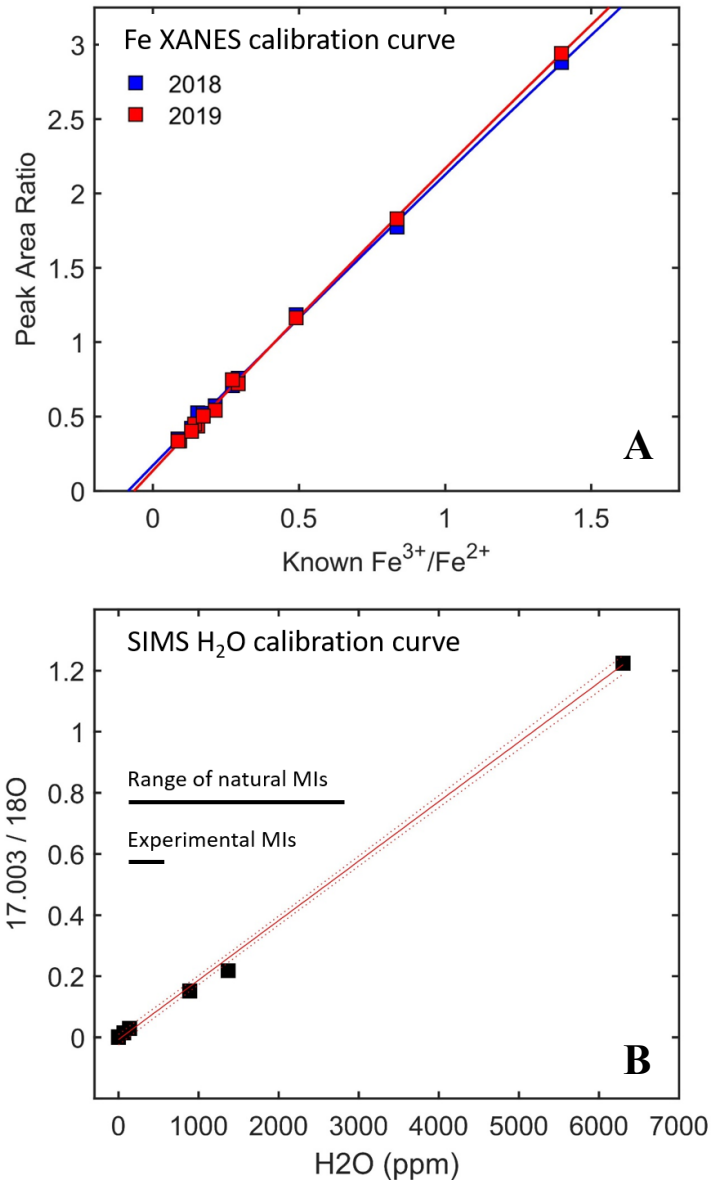


**Figure 2. (A)** Fe XANES calibration curve based on independently known $Fe^{3+}/Fe^{2+}$ in set of standard glasses and the measured peak area ratio of the $Fe^{2+}$ and $Fe^{3+}$ pre-edge features. 2018 (blue squares) and 2019 (red squares) show the calibration curves measured for two sessions a year apart, demonstrating long-term reproducibility. **(B)** SIMS $H_2O$ calibration curve based on independently known $H_2O$ contents of standard glasses and the measured $^{16}O^{1}H/^{18}O$. The range of measured $H_2O$ in experimental and natural melt inclusions from Papakolea are shown as black bars. The calibration curve is dominated by one glass standard with higher $H_2O$ (6200 wt% WOK16-2, Newman et al. 2000); excluding this sample and refitting the data with only the standards 2000 ppm results in lower calculated $H_2O$, however it is less than the 1σ error of the measurement. The data reported herein use the full calibration curve.

was 25 μm. Similar to the data reduction routine for Fe XANES, Gaussian curves were fit to three peaks corresponding to $S^{2-}$, $S^{4+}$, and $S^{6+}$. The sulfite ($S^{4+}$) peak is widely assumed to be an analytical artifact in oxidized hydrous glasses due to photo-reduction of $S^{6+}$ (Wilke et al. 2008, Metrich et al. 2009, Jugo et al. 2010, Klimm et al. 2012a). Quantifying $S^{6+}/S^{Total}$ is less straightforward than in the case of Fe XANES because of a lack of suitable standard glasses with independently determined S oxidation states. One possibility is to simply use the unscaled ratio of the integrated areas under the $S^{2-}$ and $S^{6+}$ Gaussian curves. However, the probability of the s→p electronic transition increases with oxidation state (Waldo et al. 1991), and so the absorption cross-section is not constant across the different energies measured in the XANES spectra. To account for this, Nash et al. (2019) used "generic scaling factors" from Manceau and Nagy (2012), which are based on natural organosulfur standards. It is unclear whether these empirically-derived values (1.864 for $S^{2-}$, 2.965 for $S^{4+}$, 4.446 for $S^{6+}$) are suitable for silicate glasses. Assuming that all the sulfite was derived from sulfate initially present in the glasses, Nash et al. (2019) also added the corrected area from the $S^{4+}$ peak back to the $S^{6+}$ peak to quantify $S^{6+}/S^{Total}$. A third approach from Konecke et al. (2019), based on S in apatites, uses the integrated peak area ratios for four peak absorptions, i.e., $S^{6+}$, $S^{4+}$, and two $S^{2-}$ peaks (broad and narrow). This method potentially underestimates $S^{6+}$ by including separate contributions from both sulfide peaks, which are redundant peaks that probe the same sulfide atoms in the glasses (pers. comm. M.-J. Brounce). The unscaled method and the Konecke et al. (2019) method gives comparable results; for the one natural sample (HIGS11) with intermediate $S^{6+}/S^{Total}$ (i.e., less than 100% but greater than 40%), the method using generic scaling factor results in a 40-50% higher estimate of $S^{6+}/S^{Total}$ than the other two approaches. Sorting out which quantification

scheme is best is beyond the scope of the present data, and the values reported in the text refer to both the unscaled and scaled method using the generic constants from Nash et al. (2019); because the glasses measured are comparable in composition, this is suitable for discussing relative differences in S oxidation states, but the accuracy of the sulfate to sulfide ratio in mixed-species glasses remains an unresolved and critical issue.

SIMS (secondary ion mass spectrometry) analyses of H and C in experimental and natural melt inclusions were measured using the Cameca 7f-GEO at Caltech. The inclusions were mounted in indium metal and baked in a vacuum oven at 110°C overnight, after which the mount was coated with gold and placed under vacuum in the SIMS sample storage chamber for three days. The glasses were analyzed using a Cs+ primary beam with 120s of presputtering over a ~15x15 $\mu m^2$ area and then rastered over a 5x5 $\mu m^2$ area during analysis. The measured species were $^{12}C$, $^{16}OH$, $^{18}O$, and $^{30}Si$. A suite of glass standards with known $H_2O$ and $CO_2$ contents were used to construct a calibration curve (shown for $H_2O$ in Figure 2B). Olivine standard GRR1017 and Papakōlea olivine HIGS14 were measured as blanks, and the measured $^{16}O^1H/^{18}O$ were ~0.0014 and 0.0024, respectively. The value for GRR1017 agrees with independent measurements by Mosenfelder et al. (2011), indicating that the sample surfaces were stripped of much of the adsorbed water during the pre-analysis heating and vacuum steps. No blank correction was applied to the unknown glasses.

## 4. Results

The petrography of the recovered olivines and melt inclusions were similar to that described in Chapter 1. All inclusions contained a shrinkage bubble, some inclusions contained spherical sulfide blebs, and some contained chromian spinels. Backscattered

electron (BSE) images of a representative set of experimentally treated inclusions are shown in Figure 3. Experiments SF5 and SF6 had thermal histories that resulted in the growth of crystals other than olivine on the inclusion walls, leading to partially crystallized melt inclusions (Figure 4C). These experiments (denoted with a red X in Figure 1B) are not included in the remaining discussion. Experimental inclusion SF4-3 contained sparse μm-sized quench crystals of olivine, but there was sufficient space between them for microprobe traverses as well as for careful positioning of Fe XANES analyses. Otherwise the inclusions were glassy and embedded in a cracked host olivine. For the experiments run in pure $CO_2$ gas at FMQ+4.7, the recovered olivines were opaque and appeared black. Dislocations in the olivine were pervasively decorated by Fe oxides (Figure 5A), and the olivine itself broke down in places to symplectites of magnetite and pyroxene, which emanate from crack traces and also appear as isolated ~10-40 μm sized domains (Figure 5B). EDS and Raman analyses of these phases indicate that they are Mg-rich pyroxene and Fe-Mg oxide in intimate contact (Figure 5C). The reversal experiments H3XR were run on black olivines that had been first homogenized in pure $CO_2$ for 24 hr at 1225 °C, and then re-homogenized for 24 hr at FMQ-1 and 1225°C. The olivines recovered from the reversal experiments were green and translucent and nearly free of symplectites (Figure 5D); 2-3 relict domains were identified across the entire ~2x1 mm exposed olivine chip. These experiments indicate that it is possible to both generate and re-dissolve symplectites over relatively short periods using natural olivine starting materials.

### 4.1 Petrography of Sulfides in Experimental Melt Inclusions

For the experiments run at $fO_2 \leq$ FMQ+0.35, the quenched melt inclusions contain variable amounts of a sulfide phase, which is easily recognized in transmitted light as

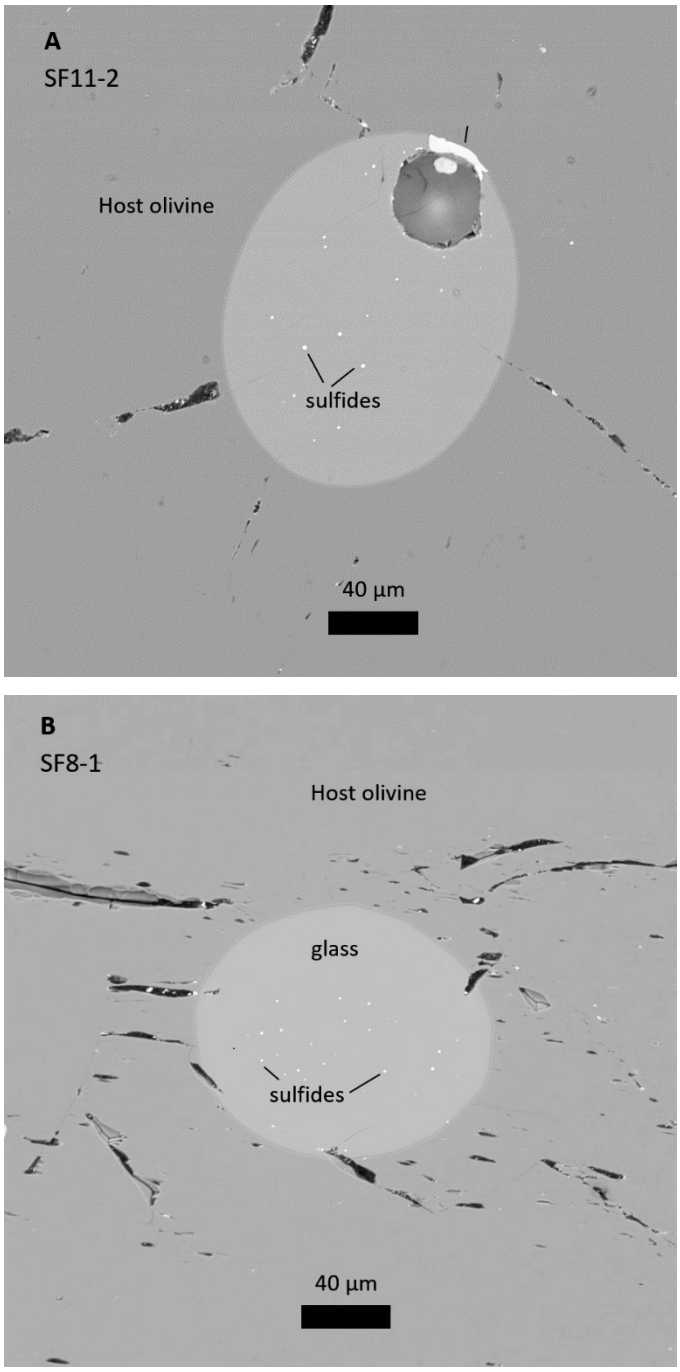


**Figure 3.** Backscattered electron (BSE) images of experimental melt inclusions. **(A)** SF11-2, homogenization experiment at 1225 °C and FMQ+0.35, **(B)** SF8-1, displacement method experiment cooled from 1225-1000 °C at FMQ+0.35. The vapor cavity in SF8-1 is not exposed at the sample surface. Sulfide blebs are seen as small bright spots within the inclusion glasses.

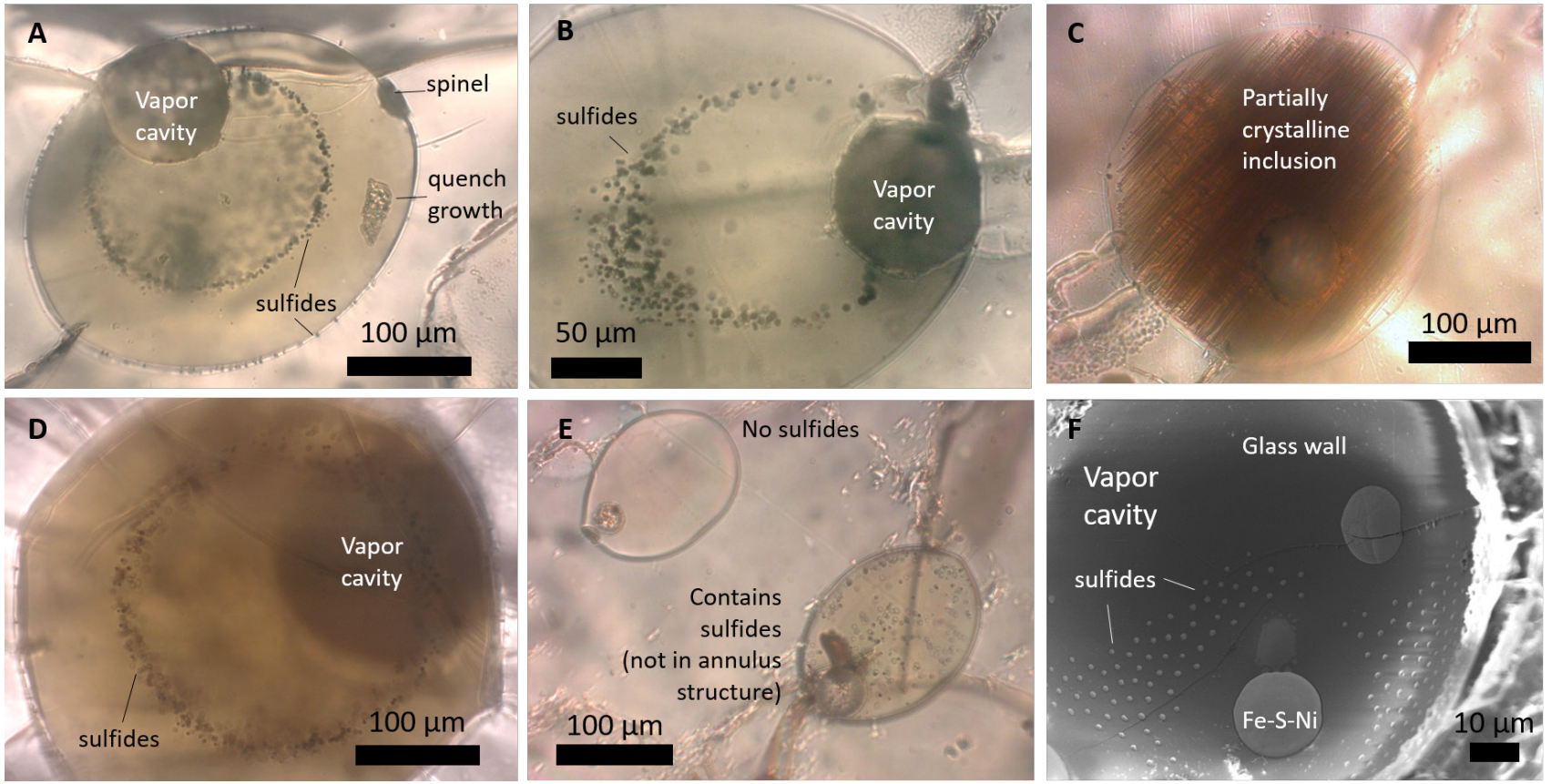


**Figure 4.** Optical microphotographs of experimentally homogenized and cooled melt inclusions homogenized at FMQ-1 and 1225 °C **(A-E)**. **(A)** Melt inclusion with an annulus of sulfide, as well as sulfides attached to the inclusion walls. Sulfide rings or annuli are also shown in **(B)**, and **(D)**. Panel **(E)** shows an experimental inclusion containing two melt inclusions ~100 µm apart, one has no sulfides whereas the other is sulfide saturated. **(C)** shows a displacement method experiment that generated substantial crystal growth in the melt inclusion. **(F)** is a secondary electron image of the interior of a large vapor cavity in an experimental melt inclusion. There are 10-15 µm wide Fe-S-Ni blebs, as well as micrometer-sized sulfides organized in a mat on the glass wall.

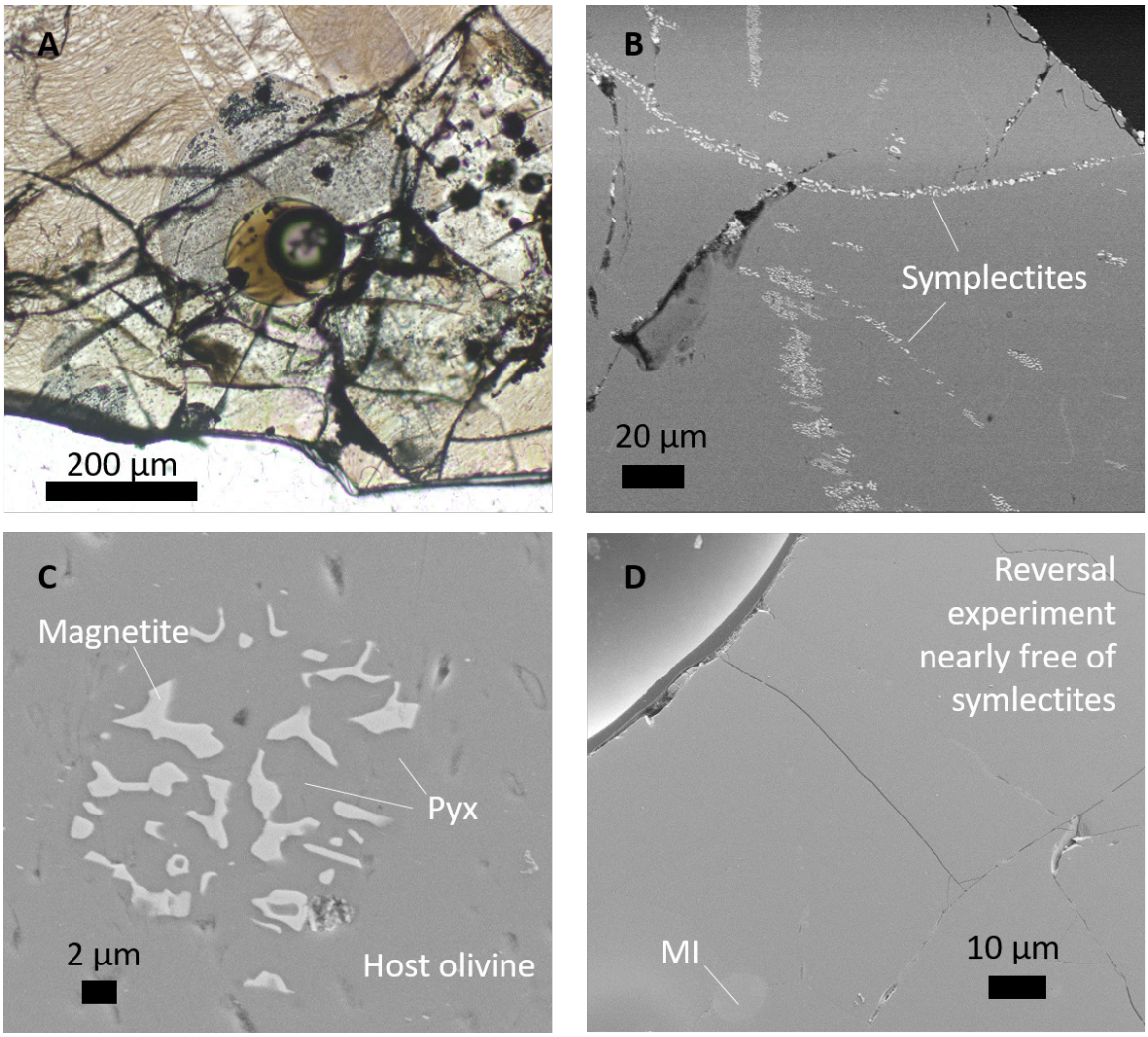


**Figure 5. (A)** Optical microphotograph of experiment H3XC1, which was held in pure $CO_2$ gas at 1225 °C (FMQ+4.7) for 24 hr. At the center of the image is a melt inclusion with a large vapor cavity. The surrounding olivine is pervaded by decorated dislocations (thin rust-colored lineaments). **(B)** Backscattered electron images reveal the growth of magnetite-pyroxene symplectites within the volume of the experimental olivine. The symplectites concentrate around and emanate from hairline cracks and traces of fractures in the olivine interior. **(C)** Secondary electron image of a symplectite domain in an experimentally oxidized olivine. The bright phase is magnetite, there is pyroxene in the interstices but it is almost indistinguishable from the olivine in secondary electron images. EDS spectra shows that the pyroxene has Mg:Si = 1 and for the olivine, 2. **(B)** Backscattered electron image of H3XR2, a reversal experiment, which was run on olivines such as that shown in **(A-C)** that were previously oxidized in pure $CO_2$ and then re-homogenized at FMQ-1 for 24 hr at 1225 °C. Except for a few relict areas, the remaining symplectites dissolved back into the olivine during the reversal experiment.

opaque spherical blebs (Figure 4), and which appear as bright (high-Z) in backscattered electron (BSE) imagery (Figure 3). Within a single olivine grain, there can be melt inclusions that contain no sulfides as well as inclusions that contain sulfides (Figure 4E). Sulfide blebs are often found to be attached to the inclusion walls (Figure 4A) or to vapor bubbles and spinels within the melt inclusions. In cooled experiments, some sulfides at the inclusion walls appeared to be embedded within the olivine that mantled the inclusion wall, indicating that they became trapped during olivine growth. In several, but not all, melt inclusions equilibrated at $fO_2 \leq$ FMQ+0.35 the sulfides that were not attached to other phase surfaces and which were suspended within the melt were organized in a striking and reproducible pattern, shown in Figure 4 panels A, B, and D, in which the sulfides were arranged in an annulus or ring that overlapped with the position of the vapor bubble. The sulfide annuli were observed more frequently in the more reducing experiments and qualitatively formed a more coherent structure in experiments with lower cooling rates (in particular H11X; Saper & Stolper 2020), although the annuli were also observed in experiments that were homogenized and then quenched directly from the hotspot and thus had chemically homogeneous melt inclusions. The mechanism for forming these rings is unclear, but it is apparent that the vapor bubble exerts some control on their presence and geometry. As far as I am aware, such structures are not observed in natural melt inclusions and certainly not in the Papakōlea Beach melt inclusions that served as starting materials for these experiments. In the Papakōlea natural melt inclusions, sulfides were observed in approximately 25% of the olivine-hosted melt inclusions; there are usually fewer individual spherules in a given inclusion when compared to the experimental inclusions and they are typically larger in diameter.

The importance of the vapor bubble is further demonstrated by inspection of the interior of the vapor cavity using secondary electron (SE) imaging – in a handful of cases the vapor bubbles expanded during the experiments to a diameter that was large enough to peer into and image using the SEM, revealing phases embedded at the vapor-melt interface (Figure 4F). Energy-dispersive measurements of these phases show that they are FeS±Ni and there are at least two distinct morphologies: larger ~10 μm blebs and a mat of subequally spaced ~1 μm domains. Solid phases inside or on the walls of vapor bubbles have been observed within natural olivine-hosted melt inclusions (Kamenetsky et al. 2002, Esposito et al. 2016, Moore et al. 2018), including from Mauna Loa, Hawai‘i, as well as on vesicles in quenched submarine glasses (Mathez and Yeats 1976, Yeats and Mathez 1976, Alt et al. 1993), and so it is unclear whether these formed experimentally and/or were inherited from the natural samples. Their occurrence indicates that the fluids themselves became saturated with respect to the sulfides, and/or they formed via diffusive exchange between the silicate melt and the vapor at the interface between the two phases. It is possible that the initial presence of these sulfides on the vapor cavity wall are related to the annulus structure observed in the experimental melt inclusions, however further study is warranted to determine their precise formation mechanism.

**Table 1.** Experimental run conditions and Fe and S XANES and SIMS results.

**Experimental olivine-hosted melt inclusions.**

| Name | ΔFMQ[a] | Homogenization T °C (24 hr) | Quench T °C | Cooling type[b] | $Fe^{3+}/Fe^{T}$ [c] | $S^{6+}/S^{T}$ [d] | S (ppm) | $H_2O$ (ppm) | $CO_2$ (ppm) |
|---|---|---|---|---|---|---|---|---|---|
| H3XC1 | +4.7 | 1225 | 1225 | Homogenization | 0.688 | | 1025 | | |
| HTOX2 | +2.8 | 1225 | 1225 | Homogenization | 0.299 | | 851 | | |
| SF11-5 | +0.35 | 1225 | 1225 | Homogenization | 0.103 | 0.03-0.06 | 800 | 526 | 48 |
| SF1-2 | +0.35 | 1225 | 1225 | Homogenization | 0.117 | | 823 | | |
| SF13-1 | +0.35 | 1225 | 900 | Displacement | 0.118 | | | 769 | 53 |
| SF8-3 | +0.35 | 1225 | 1000 | Displacement | 0.108 | 0 | | | |
| SF3-2 | +0.35 | 1225 | 1150 | T.C. Controlled | 0.137 | 0.04-0.10 | | | |
| SF4-3 | +0.35 | 1225 | 1000 | T.C. Controlled | 0.129 | 0 | 1041 | | |
| H11X1B | -1.0 | 1225 | 1225 | Homogenization | 0.076 | 0 | 842 | 526 | 48 |
| H7XC1 | -1.0 | 1225 | 1225 | Homogenization | 0.065 | | 788 | 188 | 15 |
| H3XR2[e] | +4.7 and -1 | 1225 | 1225 | Homogenization | | | 783 | 376 | 54 |

**Natural unheated olivine-hosted melt inclusions from Papakōlea, Mauna Loa, Hawai'i (starting materials for experiments)**

| Name | Calculated ΔFMQ[f] | Reconstructed T °C prior to eruption[g] | T °C (MgO in liquid at inclusion wall)[g] | Cooling Rate[h] | $Fe^{3+}/Fe^{T}$ [c] | $S^{6+}/S^{T}$ [d] | S (ppm) | $H_2O$ (ppm) | $CO_2$ (ppm) |
|---|---|---|---|---|---|---|---|---|---|
| HIGS11 | +0.10 to +1.22 | 1176 | 1115 | 8117±800°C/hr | 0.184 | 0.45-0.66 | | 1900[i] | |
| HIGS14 | +0.10 to +1.23 | 1154 | 881 | 55±5°C/hr | 0.199 | 1.0 | 154.0 | 1874 (2000[i]) | 19 |
| HIGS20 | +0.10 to +1.33 | (1175) | | | 0.185 | | 1035 | 2700[i] | |
| HIGS21 | -0.02 to +1.12 | (1175) | 974 | | 0.165 | | 129 | 1600[i] | |

**Caption to Table 1.**

**a** - Nominal $fO_2$ of the experiments, based on $H_2$-$CO_2$ gas mix in the furnace atmosphere. ΔFMQ is the difference in log units between the experimental $fO_2$ and the FMQ data of O'Neill (1987).

**b** - Method by which the experiments were cooled. See section 3.1 in text for details.

**c** - Based on the average of 2-3 XANES measurements of each glass. Repeat of the same glass differed by 0.01-0.02 and the estimated 1σ uncertainty is 0.015 (Brounce et al. 2017).

**d** - The lower value refers to using the unscaled integrated peak area ratios, whereas the higher value used the generic scaling factors of Nash et al. 2019.

**e** - H3XR2 was a reversal experiment, first run for 24 hr at 1225°C and FMQ+4.7, quenched, and then re-run for 24 hr at 1225 °C and FMQ-1.

**f** - The range of $fO_2$ - expressed relative to FMQ (O'Neill 1987) - calculated based on the $Fe^{3+}/Fe_T$ measured by XANES, the reconstructed melt T, and the inclusion compositions, using the six Fe oxybarometers described in the text.

**g** - See Saper & Stolper 2020 for details. Reconstructed T based on integrating the zoned melt inclusion compositions and adding equilibrium olivine back to the melt until it was in equilibrium with olivine adjacent to the melt inclusion walls. The inclusions HIGS20 and HIGS21 were not completely exposed at their centers, and so this calculation was not performed and instead a T = 1175°C was assumed, based on the T implied from MgO in the central plateaus of other melt inclusions from the same locality.

**h** - Cooling rate determined by MgO diffusion speedometry in the melt inclusions (Saper & Stolper 2020).

**i** – $H_2O$ determined by FTIR (Saper & Stolper 2020), otherwise it was determined by SIMS.

**Table 2. Major and minor element compositions of the centers of experimental and natural olivine-hosted melt inclusions.**

| Name | ΔFMQ[a] | Visible Sulfides | $SiO_2$ (wt%) | $TiO_2$ | $Al_2O_3$ | $Cr_2O_3$ | FeO* | MnO | MgO | CaO | $Na_2O$ | $K_2O$ | $P_2O_5$ | Totals | S (ppm) | $X_{Fo}$ Olivine[b] |
|---|---|---|---|---|---|---|---|---|---|---|---|---|---|---|---|---|
| H3XC1 | +4.7 | N | 52.66 | 1.58 | 10.76 | | 13.97 | 0.15 | 10.06 | 8.58 | 1.80 | 0.24 | 0.15 | 99.93 | 1025 | 89.2 |
| HTOX2 | +2.8 | N | 52.36 | 1.65 | 12.86 | | 10.92 | 0.16 | 9.64 | 10.10 | 1.90 | 0.26 | 0.38 | 100.23 | 851 | 87.1 |
| SF11-5 | +0.35 | Y | 52.56 | 2.01 | 14.17 | | 7.78 | 0.13 | 8.93 | 10.90 | 2.24 | 0.33 | 0.25 | 99.30 | 800 | 88.6 |
| SF1-2 | +0.35 | Y | 51.71 | 1.94 | 13.66 | | 8.36 | 0.13 | 9.10 | 10.81 | 2.16 | 0.30 | 0.16 | 98.35 | 823 | 88.4 |
| SF13-1 | +0.35 | Y | 51.55 | 1.88 | 13.29 | | 9.33 | 0.15 | 8.94 | 10.48 | 2.09 | 0.31 | 0.27 | 98.27 | | 86.5 |
| SF8-3 | +0.35 | Y | 50.71 | 2.11 | 14.15 | | 7.87 | 0.13 | 8.81 | 11.51 | 2.02 | 0.33 | 0.28 | 97.91 | | 87.9 |
| SF3-2 | +0.35 | N | 51.57 | 2.06 | 13.25 | | 9.73 | | 8.72 | 10.83 | 2.11 | 0.29 | 0.21 | 98.94 | | 88.5 |
| SF4-3 | +0.35 | Y | 52.31 | 2.12 | 13.41 | 0.10 | 9.25 | 0.13 | 7.62 | 11.70 | 2.09 | 0.32 | 0.19 | 99.23 | 1041 | 88.4 |
| H11X1B | -1 | Y | 52.72 | 2.08 | 13.26 | | 9.21 | 0.15 | 9.32 | 10.26 | 2.24 | 0.43 | 0.22 | 99.89 | 842 | 87.4 |
| H7XC1 | -1 | Y | 53.23 | 2.15 | 14.05 | | 7.66 | 0.13 | 9.01 | 10.53 | 2.42 | 0.33 | 0.28 | 99.79 | 788 | |
| H3XR2[e] | +4.7 & -1 | Y | | | | | | | | | | | | | 783 | |
| H11X1B_2 | -1 | Y | 51.47 | 2.31 | 13.15 | | 9.13 | 0.14 | 9.40 | 10.50 | 2.30 | 0.40 | 0.24 | 99.04 | 908 | 87.3 |
| H3XC4 | 4.7 | N | 52.72 | 1.60 | 10.83 | | 13.05 | 0.13 | 10.15 | 8.61 | 1.68 | 0.26 | 0.18 | 99.22 | 1121 | 90 |
| H9X2_1 | -1 | Y | 53.72 | 1.94 | 13.68 | 0.13 | 7.36 | 0.10 | 8.75 | 10.82 | 2.08 | 0.38 | 0.22 | 99.19 | 776 | 86.2 |
| H9X2_2 | -1 | N | 53.72 | 1.87 | 13.80 | 0.13 | 7.37 | 0.08 | 8.68 | 10.69 | 2.08 | 0.38 | 0.21 | 99.01 | 590 | 86.2 |
| H2XC3 | -1 | N | 52.59 | 2.02 | 13.59 | 0.13 | 7.45 | 0.08 | 9.07 | 10.59 | 2.36 | 0.43 | 0.22 | 98.54 | 488 | 88.2 |
| H3XC3_1 | 4.7 | N | 51.34 | 1.53 | 10.49 | | 13.60 | 0.15 | 9.80 | 8.36 | 1.76 | 0.23 | 0.21 | 97.48 | 1029 | 87.2 |
| H2XC2 | -1 | N | 53.40 | 2.10 | 14.19 | | 6.94 | 0.12 | 9.02 | 10.77 | 2.24 | 0.30 | 0.26 | 99.34 | 602 | 87.2 |
| H10XC1 | -1 | N | 50.69 | 1.82 | 13.01 | 0.18 | 8.27 | 0.11 | 10.62 | 10.12 | 2.28 | 0.40 | 0.24 | 97.75 | 518 | 88.3 |
| H10XC3 | -1 | N | 51.97 | 1.83 | 13.00 | 0.19 | 7.29 | 0.12 | 10.78 | 9.97 | 2.35 | 0.44 | 0.24 | 98.17 | 148 | 89.7 |
| H8XC2 | -1 | Y | 52.94 | 2.04 | 13.87 | 0.09 | 7.77 | 0.08 | 8.88 | 10.37 | 2.44 | 0.39 | 0.22 | 99.10 | 664 | 88.3 |
| H5XC2_1 | -1 | Y | 53.57 | 2.07 | 13.61 | | 8.05 | 0.14 | 8.72 | 10.45 | 2.27 | 0.35 | 0.21 | 99.44 | 777 | 87.5 |
| H5XC1 | -1 | N | 53.81 | 2.17 | 13.79 | | 7.72 | 0.13 | 8.46 | 10.17 | 2.58 | 0.31 | 0.34 | 99.48 | 440 | 87.8 |
| SF11_2 | 0.35 | Y | 52.36 | 1.86 | 13.56 | 0.09 | 7.92 | 0.10 | 8.93 | 10.61 | 2.34 | 0.41 | 0.26 | 98.44 | 1079 | 87.9 |
| HTOX1 | 2.8 | N | 51.81 | 1.75 | 11.95 | | 11.41 | 0.15 | 9.42 | 9.42 | 2.13 | 0.27 | 0.18 | 98.49 | 1353 | 89.8 |
| SF1-1 | 0.35 | Y | 52.33 | 1.69 | 12.16 | 0.12 | 10.18 | 0.15 | 8.84 | 11.25 | 2.10 | 0.42 | 0.24 | 99.48 | 1125 | 85.6 |
| H3XC3 | 4.7 | N | 51.36 | 1.54 | 10.49 | | 13.61 | 0.15 | 9.80 | 8.37 | 1.76 | 0.23 | 0.21 | 97.52 | 1027 | 87.3 |

**Experiments (con't)**

| Name | ΔFMQ[a] | Visible Sulfides | $SiO_2$ | $TiO_2$ | $Al_2O_3$ | $Cr_2O_3$ | FeO* | MnO | MgO | CaO | $Na_2O$ | $K_2O$ | $P_2O_5$ | Totals | S (ppm) | $X_{Fo}$ Olivine[b] |
|---|---|---|---|---|---|---|---|---|---|---|---|---|---|---|---|---|
| SF7-2 | 0.35 | Y | 52.37 | 1.98 | 13.23 | 0.11 | 8.61 | 0.11 | 8.59 | 11.31 | 2.20 | 0.34 | 0.19 | 99.03 | 1065 | 88.4 |
| SF8-1 | 0.35 | Y | 52.02 | 2.13 | 13.25 | 0.09 | 8.39 | 0.11 | 9.08 | 10.72 | 2.31 | 0.39 | 0.23 | 98.72 | 930 | 87.6 |
| H2XC2_1 | -1 | Y | 52.77 | 2.04 | 13.76 | 0.13 | 6.95 | 0.10 | 9.10 | 10.92 | 2.41 | 0.36 | 0.19 | 98.73 | 803 | 89.2 |
| H2XC2_2 | -1 | N | 52.70 | 2.08 | 13.96 | 0.13 | 6.86 | 0.08 | 9.22 | 10.73 | 2.25 | 0.36 | 0.30 | 98.65 | 633 | 89.2 |
| SF11-3_1 | 0.35 | Y | 53.21 | 2.15 | 13.61 | 0.08 | 7.92 | 0.11 | 9.11 | 10.74 | 2.30 | 0.43 | 0.24 | 99.91 | 754 | 88 |
| SF11-3_5 | 0.35 | Y | 53.29 | 2.11 | 13.66 | 0.08 | 7.95 | 0.11 | 9.12 | 10.84 | 2.30 | 0.43 | 0.25 | 100.14 | 775 | 88 |
| SF11-3_6 | 0.35 | Y | 53.04 | 2.18 | 13.75 | 0.08 | 7.90 | 0.12 | 9.18 | 10.80 | 2.27 | 0.42 | 0.31 | 100.05 | 710 | 88 |
| SF11-3_15 | 0.35 | Y | 53.66 | 2.09 | 13.72 | 0.09 | 7.88 | 0.12 | 9.12 | 10.71 | 2.28 | 0.43 | 0.24 | 100.33 | 718 | 88 |
| SF11-3_16 | 0.35 | N | 53.23 | 2.09 | 13.71 | 0.10 | 7.71 | 0.11 | 9.15 | 10.61 | 2.31 | 0.47 | 0.35 | 99.84 | 254 | 88 |
| SF11-3_2 | 0.35 | N | 53.29 | 2.16 | 13.72 | 0.10 | 7.54 | 0.12 | 9.06 | 10.65 | 2.30 | 0.46 | 0.31 | 99.71 | 126 | 88 |
| SF11-3_3 | 0.35 | N | 53.40 | 2.12 | 13.71 | 0.09 | 7.71 | 0.12 | 9.09 | 10.65 | 2.37 | 0.42 | 0.29 | 99.96 | 514 | 88 |
| SF11-3_4 | 0.35 | N | 54.00 | 2.04 | 13.87 | 0.08 | 7.56 | 0.11 | 9.05 | 10.60 | 2.29 | 0.47 | 0.31 | 100.38 | 53 | 88 |
| SF11-3_7 | 0.35 | N | 53.61 | 2.11 | 13.88 | 0.08 | 7.60 | 0.11 | 9.14 | 10.70 | 2.27 | 0.47 | 0.39 | 100.35 | 181 | 88 |
| SF11-3_8 | 0.35 | N | 53.52 | 2.12 | 13.90 | 0.09 | 7.74 | 0.12 | 9.10 | 10.67 | 2.29 | 0.50 | 0.34 | 100.40 | 196 | 88 |
| SF11-3_9 | 0.35 | N | 53.58 | 2.14 | 13.82 | 0.07 | 7.70 | 0.11 | 9.10 | 10.58 | 2.31 | 0.48 | 0.32 | 100.20 | 120 | 88 |
| SF11-3_10 | 0.35 | N | 53.57 | 1.97 | 13.94 | 0.10 | 7.70 | 0.12 | 9.20 | 10.50 | 2.25 | 0.39 | 0.45 | 100.19 | 124 | 88 |
| SF11-3_11 | 0.35 | N | 53.36 | 2.16 | 13.71 | 0.08 | 7.96 | 0.12 | 9.15 | 10.67 | 2.31 | 0.48 | 0.34 | 100.34 | 521 | 88 |
| SF11-3_12 | 0.35 | N | 53.69 | 2.08 | 13.72 | 0.08 | 7.67 | 0.11 | 9.09 | 10.65 | 2.27 | 0.46 | 0.32 | 100.15 | 46 | 88 |
| SF11-3_13 | 0.35 | N | 53.83 | 2.05 | 13.65 | 0.07 | 7.72 | 0.10 | 9.17 | 10.69 | 2.27 | 0.46 | 0.35 | 100.37 | 142 | 88 |
| SF11-3_14 | 0.35 | N | 53.50 | 2.08 | 13.63 | 0.08 | 7.78 | 0.10 | 9.02 | 10.61 | 2.31 | 0.46 | 0.35 | 99.92 | 73 | 88 |
| **Unheated melt inclusions from Papakōlea, Mauna Loa, Hawai'i** | | | | | | | | | | | | | | | | |
| HIGS11 | | N | 53.73 | 2.17 | 13.63 | | 8.96 | 0.14 | 7.28 | 11.05 | 2.11 | 0.33 | 0.05 | 99.46 | | 88.8 |
| HIGS14 | | N | 55.55 | 2.41 | 15.17 | | 6.80 | 0.12 | 4.04 | 12.69 | 2.18 | 0.34 | 0.05 | 99.34 | 154 | 88.5 |
| HIGS20 | | Y | 54.34 | 2.17 | 14.48 | | 8.14 | 0.13 | 5.95 | 11.44 | 2.21 | 0.35 | 0.17 | 99.38 | 1035 | |
| HIGS21 | | N | 53.73 | 2.17 | 13.63 | | 8.96 | 0.14 | 7.28 | 11.05 | 2.11 | 0.33 | 0.05 | 99.46 | 129 | 88.6 |

## 4.2 Chemical Compositions of Experimental Melt Inclusions

### 4.2.1 Major and Minor Element Compositions of Melt Inclusions

Major and minor element compositions of experimental melt inclusions are calculated by averaging analyses (~15 spots) taken within a ~15-20 μm radius region at the centers of the exposed melt inclusions (Table 2). As demonstrated in the following paragraphs, this constitutes a compositional plateau in all but one of the experiments (SF4-3, which was subjected to controlled cooling at 1900 °C/hr and quenched at 1000 °C), and is thus representative of the homogenized compositions of the inclusions after 24 hr at 1225 °C. For all experimental melt inclusions, FeO* ranges from 6.9-14.0 wt%, MgO from 7.6-10.8 wt%, $SiO_2$ from 50.7-54.0 wt%, $TiO_2$ from 1.5-2.3 wt%, $Al_2O_3$ from 10.5-14.2 wt%, CaO from 8.4-11.7 wt%, $Na_2O$ from 1.7-2.6 wt%, $K_2O$ from 0.23-0.50 wt%, and $P_2O_5$ from 0.15-0.45 wt%. Note that two inclusions in experiment H10X equilibrated at FMQ-1 were run at 1260 °C (square symbols with an x in Figure 6A); these glasses have high MgO contents (and low FeO) compared to the remaining experiments run at FMQ-1, which were homogenized at 1225 °C. For experiments run at the same T and $fO_2$, the range in MgO and FeO is governed by the composition of the host olivine; for example, the highest FeO* wt% glass in the FMQ+0.35 experiments (SF1-1) is embedded in an $Fo_{85.6}$ olivine (Fo = 100·[Mg/(Mg+Fe] molar), whereas the other inclusions with lower FeO* are in host olivines that are more Mg-rich with Fo contents between 87.3-88.6 (one intermediate experiment, SF11-5 has a $Fo_{86.5}$ host olivine). Note that the 1σ precision in Fo is around 0.01 absolute. Despite some inherent variability in both the Fe/Mg and the minor element compositions of the trapped melts (Saper & Stolper 2020), the experiments at different $fO_2$ define clear trends: high $fO_2$ experiments are associated with higher FeO* and MgO, and lower abundances of the incompatible oxides $TiO_2$, $Al_2O_3$, CaO, and $Na_2O$. This can be explained by oxidation of the fayalite component in olivine:

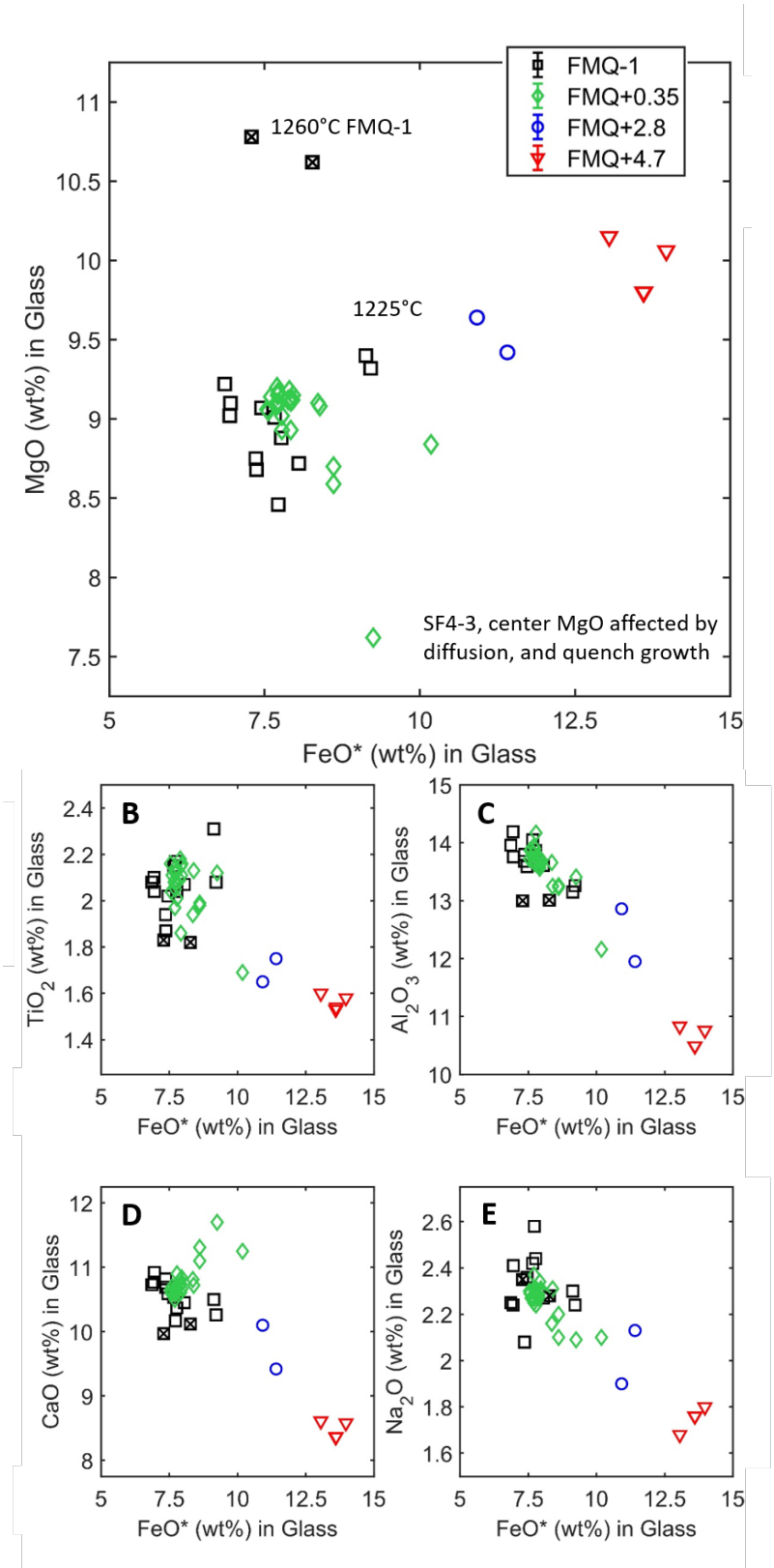


**Figure 6.** Microprobe analyses from the centers of experimental melt inclusions. Black squares – FMQ-1; Green diamonds – FMQ+0.35; Blue circles – FMQ+2.8; Red triangles – FMQ+4.7. The black squares with X's inscribed were homogenized at 1260°C (Saper & Stolper 2020), the remaining experiments were homogenized at 1225°C. FeO* wt% plotted vs. **(A)** MgO wt%, **(B)** $TiO_2$ wt%, **(C)** $Al_2O_3$ wt%, **(D)** CaO wt%, **(E)** $Na_2O$ wt%.

$$Fe_2SiO_4^{ol} + ½\ O_2 \rightleftharpoons Fe_2O_3^{liq} + SiO_2^{liq} \quad (2)$$

which occurs because of the lower solubility of fayalite in olivine at higher $fO_2$ (Nitsan 1974). In the case of melt inclusions exposed to an $H_2$-$CO_2$ atmosphere the external $fO_2$ is transmitted into the olivine interiors via H-bearing defects in olivine that act to equilibrate the $H_2/H_2O$ ratio of the furnace gases and the inclusion liquids across the host olivine (Bucholz et al. 2013). The higher MgO contents of the more oxidized liquids are due to back-reaction of the olivines in order to maintain satisfy the olivine/liquid $Fe^{2+}$/Mg exchange coefficient, $K_{D,Fe2+-Mg}^{ol/liq} = (Fe/Mg)^{ol}/(Fe/Mg)^{liq}$. It is challenging to extract $K_D$ values from the inclusion-olivine pairs because the olivine surrounding the inclusions are initially zoned and the narrow region of olivine that is in equilibrium with the inclusion liquids is difficult to analyze with the CIT probe (Saper & Stolper 2020). The dilution of incompatible oxides (Figure 6B-E) is also consistent with dissolution of olivine at higher $fO_2$; some of the variability observed in the incompatible elements is likely due to intrinsic heterogeneity in the compositions of the trapped melts.

### 4.2.2 Compositional Zoning in Cooled Melt Inclusions and Host Olivines

After the 24 hr homogenization step, three cooling regimes were employed: (1) quenching directly from the hotspot at the T of homogenization, (2) displacement method cooling, and (3) controlled cooling via the control thermocouple and diffusion of heat out of the furnace hotspot. As shown in Chapter 1 and in Saper & Stolper (2020), crystallization of olivine on the melt inclusion walls during cooling induces chemical gradients which relax by diffusion. Given sufficiently low cooling rates or high temperatures, these gradients can modify the centers of melt inclusions – the degree to which they are modified depends on the relative diffusivities of the melt components with MgO being one of the most rapid diffusers (Guo & Zhang, 2018 note: $Na_2O$ has a

very high self-diffusivity but is a slave to $SiO_2$ in basaltic melts, e.g., Watson 1982). To mitigate compositional variability beyond that which is present in the initially trapped melts in the starting materials, the experiments were designed to leave inclusion centers compositionally unchanged during cooling by picking large inclusions and employing high cooling rates. Experiments using cooling regime (1) have very narrow chemical boundary layers adjacent to the inclusion walls which were formed during quenching (Figure 7AB); for example, in inclusion SF1-1, MgO is 8.84±0.07 (1σ of distribution of 15 points) across the central compositional plateau, which extends from the inclusion center up to ~4 μm from the inclusion wall, where the MgO contents are slightly lower at ~8.65 wt%; CaO contents are high in this narrow boundary layer (11.64 wt% at wall) compared to the inclusion center (11.25 wt%), which is indicative of rapidly cooled melt inclusions (Saper & Stolper 2020). For regime (2) displacement method experiments, the boundary layer is wider than in regime (1): for example, in experiment SF7-2 (cooled for 46 seconds from 1225°C to 998 °C), the MgO boundary layer is ~20 μm wide (Figure 7C) and in experiment SF8-1 (cooled for 77 seconds from 1225 °C to 1000 °C) the boundary layer is ~35 μm wide (Figure 7D). Because these inclusions are well over 100 μm across each retains a wide compositional plateau that has not been modified by diffusion. Some of the largest melt inclusions found in the starting materials were reserved for the controlled cooling rate experiments, SF3 and SF4, which based on forward modeling were the most susceptible to having their central compositions modified by diffusion. SF3-2 (cooled at 2900 °C/hr from 1225°C to 1150°C has a broad ~100 μm wide central plateau (Figure 7E); SF4-3 (cooled at ~1900°C/hr from 1225°C to 1000 °C has central MgO contents that have been lowered relative to their initial value of ~9 wt% based on the central plateaus of regime (1) experiments conducted at the same T and $fO_2$ and with similar host olivine

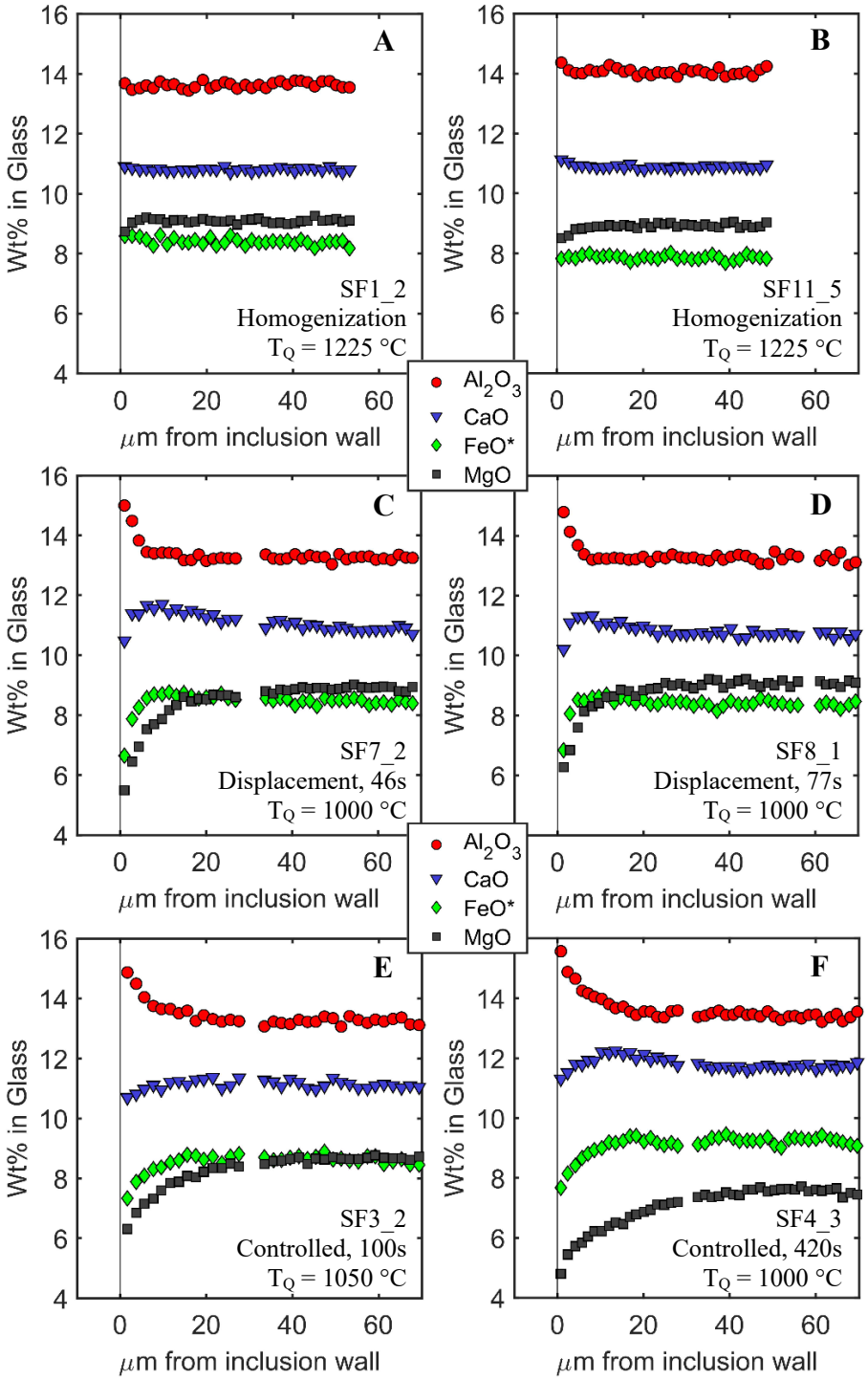


**Figure 7.** Chemical zoning across experimental olivine-hosted melt inclusions homogenized for 24 hr at 1225°C and FMQ+0.35 and subjected to different cooling rates. Vertical gray line indicates the olivine-glass boundary (inclusion wall). $Al_2O_3$ – red circles; CaO – blue triangles; FeO* – green diamonds; MgO – dark gray squares. $T_Q$ indicates the T of the sample at the time of quenching. **(A)** SF1_1, homogenized and drop quenched from $T_Q$ = 1225°C, **(B)** SF11_5, homogenized and drop quenched from $T_Q$ = 1225°C, **(C)** SF7_2, displacement method cooling for 46s, $T_Q$ = 1000°C, **(D)** SF8_1, displacement method cooling for 77s, $T_Q$ = 1000°C, **(E)** SF3_2, controlled cooling for 100s, $T_Q$ = 1050°C, **(F)** SF4_3, controlled cooling for 420s, $T_Q$ = 1000°C.

compositions (Figure 7F). This experiment can be clearly seen at low MgO for a given FeO* in Figure 6A, however the boundary layers of the other more slowly diffusing oxides (e.g., $Al_2O_3$) had not progressed into the inclusion interior by the T of quenching and maintain broad plateaus. Note that in this experiment the CaO profile has a local maximum in concentration at x = 13.5 μm from the inclusion wall, and a diffusion profile shape that is indicative of intermediate cooling rates (Saper & Stolper 2020). The two experiments shown in Figure 7 panels C and D also have local maxima in CaO at ~6-7 μm from the inclusion walls. With the exception of MgO in SF4-3, the compositions of the centers of the experimental melt inclusions represent that of the homogenized melt, and aside from the compositional variation imparted by heterogeneity of the initially trapped melts (which are minor, as shown by limited variability in the y-direction at a given FeO* and $fO_2$, Figure 6B-E), differences in the $Fe^{3+}/Fe^{2+}$ and $S^{6+}/S^{2-}$ for a set of experiments at a given $fO_2$ are unlikely to be due to these minor perturbations of melt composition.

As discussed in Chapter 1, the Fe/Mg zoning in olivines around natural melt inclusions is typically characterized by two to three zones: a steeply zoned narrow band of Fe-rich olivine a few micrometers wide directly adjacent to the inclusion, which is formed during syneruptive cooling; a broad zone that is sometimes present and can extend tens of micrometers from the narrow band into the olivine interior; and a zone in the 'far-field' that is either a compositional plateau or is continuous with large-scale growth zoning in the host olivine. Experimental homogenization of melt inclusions at any T and $fO_2$ condition that differs from that in which the natural melt inclusion was trapped and equilibrated will lead to disruption of the narrow zone, by dissolution and/or precipitation of new olivine on the inclusion walls and/or by diffusive exchange with the far-field olivine because of the different Fe/Mg imposed by local equilibrium at the

olivine-liquid interface (Gaetani 2000; Gaetani 2002; Danyushevsky 2002; Saper & Stolper 2020). Figure 8 shows $FeO^*$ wt% in four experimental melt inclusions and surrounding olivines that were homogenized at 1225 °C for 24 hr, but at different $fO_2$. Despite some uncertainty as to how much of the Fe/Mg zoning in the surrounding olivines was inherited from the natural samples, the trends observed over >5 orders of magnitude range of experimental $fO_2$ are strong enough to warrant comment.

The average FeO* of the inclusion glasses increases with increasing $fO_2$ (Figure 6A). Between FMQ+2.8 and FMQ+4.7 the FeO* contents of the liquids become greater than that in the coexisting olivine; the crossover is bracketed to be close to the upper $fO_2$ stability limit of $Fo_{88}$ olivine at 1225 °C, which is approximately ~FMQ+4.2 (Nitsan 1974). Recall that the initial FeO contents of the olivine starting materials were likely somewhere between 11-12 wt%, or $Fo_{87.5}$ to $Fo_{88.5}$, although in rare cases a more Fe-poor host olivine phenocryst was used, e.g., in experiment HTOX4 shown in Fig. 8C (~10 wt% FeO). The low FeO contents of the olivines in contact with, and presumably in local equilibrium with, the melt inclusions in the more oxidizing experiments ($Fo_{89.6}$ at FMQ+2.8 and $Fo_{90.1}$ at FMQ+4.7) reflect the lower solubility of fayalite in olivine at these $fO_2$, and the corresponding high FeO* contents of the coexisting liquids are a consequence of dumping Fe from the olivine into the melt inclusion. In this case, Fe is transported to the melt inclusions by diffusion through the olivine volume (e.g. Wu & Kohlstedt 1988). Note that in the most oxidizing experiments magnetite-pyroxene symplectites formed within the olivine (Figure 5), via the reaction: $6Fe_{1/2}SiO_2 + ½\ O_2 \rightleftharpoons Fe_3O_4 + 3FeSiO_3$, which leads to locally magnesian olivines in the FMQ+4.7 experiments. It cannot be ruled out whether the symplectite-forming reaction occurred first, and that the Fe that was added to the melt inclusions was scavenged from the products of this reaction.

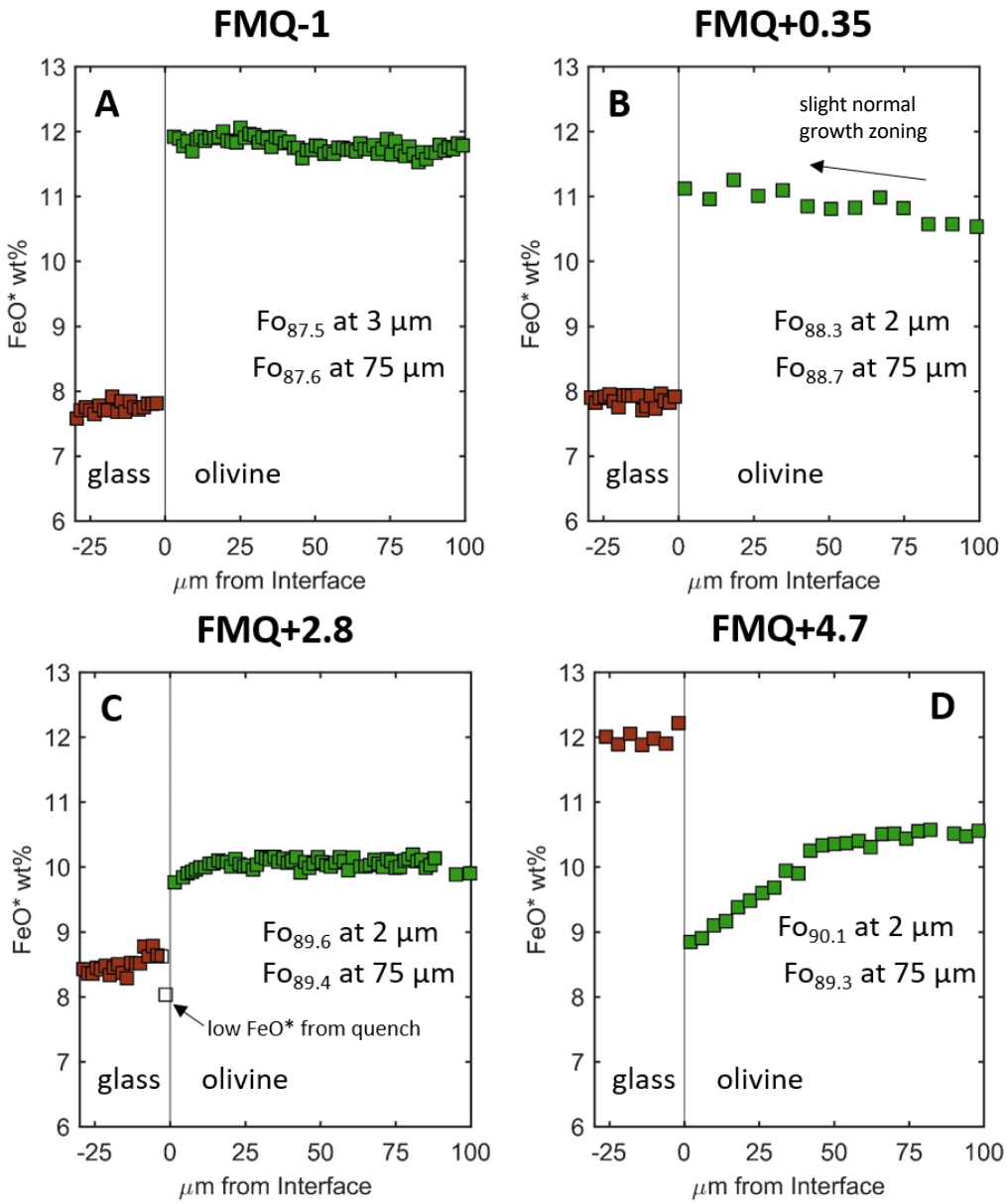


**Figure 8.** FeO* wt% traverses across experimental melt inclusions (red squares) and the surrounding host olivine (green squares). The vertical line corresponds to the interface between the glass and olivine. Olivine and inclusions from experiments conducted at **(A)** FMQ-1, **(B)** FMQ+0.35, **(C)**, FMQ+2.8, **(D)** FMQ+4.8. Listed in each panel is the Fo contents of the olivines adjacent to the inclusions and in the far-field 75 µm from the glass-olivine interface. All of the experiments shown were run for 24 hr at 1225°C and then drop-quenched directly from the hotspot.

It is worth pointing out that the length-scale of the Fe depleted zone of olivine adjacent to the melt inclusion in the FMQ+4.7 experiment is ~40 μm which is about 2x longer than that the diffusion distance (i.e., $x = (D \cdot t)^{1/2}$) estimated for Fe-Mg interdiffusion at the experimental condition ($x \approx 16$ μm, extrapolated to high $fO_2$ from Dohmen & Chakraborty 2007). It is possible that an $Fe^{3+}$-defect-rich olivine increases bulk diffusivities, especially of charged defect species, making it easier to transmit $fO_2$ information across the crystal volume at high $fO_2$; the fact that dislocations in olivine are rapidly decorated at oxidizing conditions (e.g., Wu and Kohlstedt 1988), and symplectites are found to follow traces of cracks in the experimental olivines (Figure 5A), indicates that fast paths for diffusion of oxygen or oxidant-bearing defects were likely present (e.g., Spandler and O'Neill 2010, Burgess and Cooper 2013).

### 4.3 S, H, and C Contents of Melt Inclusions

The S contents of experimental melt inclusions ranges from at or below the detection limit of ~100 ppm up to 1353 ppm in an experiment run at FMQ+2.8 (Figure 9, Table 2). Although the number of inclusions is small, the glasses equilibrated at or above FMQ+2.8 have S contents greater than 850 ppm. At 1225 °C above FMQ+2.0 essentially all of the S is expected to be present as $S^{6+}$ (Jugo et al. 2005, Nash et al. 2019), and the elevated S contents in these experiments are consistent with the higher solubility of sulfate compared to sulfide in silicate melts (e.g., Carroll & Rutherford 1987, Li & Ripley 2009). The S contents measured in unheated Papakōlea inclusions span a similar range (129 – 1235 ppm) to those that were experimentally treated, indicating that the initial S contents are likely preserved and are only modified by growth or dissolution of sulfide (and possibly sulfate) phases, olivine growth or dissolution, and possibly via exchange with the vapor bubble.

As described in section 4.1 on the petrography of sulfides, they are easy to identify as opaques in transmitted light under an optical microscope. Each inclusion

from experiments run at or below FMQ+0.35 was designated as either sulfide-saturated if sulfides were observed or sulfide-undersaturated if they were not observed. Note that this designation was usually made after half of the inclusion was ground away during polishing; if there were sulfides in the half that was destroyed and none in the remaining half then there may be some false-negative cases where inclusions were wrongly identified as sulfide-undersaturated. Despite this uncertainty, the petrographic designation is clearly consistent with the S contents of the inclusions: sulfide-saturated inclusions have uniformly high S (all >660 ppm) and all but two sulfide-undersaturated inclusions have S <520 ppm (Figure 9). The two sulfide-undersaturated inclusions with S between 602-633 ppm may be wrongly identified, or only slightly undersaturated with respect to sulfide. It has become increasingly evident that the sulfur concentration at sulfide saturation (SCSS) is sensitive to not only melt composition (e.g., O'Neill & Mavrogenes 2002), but also the composition of the coexisting sulfide (Smythe et al. 2017), the concentrations of siderophile elements in the melt (e.g., Ni and Cu, O'Neill 2020), and to $H_2O$ (Smythe et al. 2017, Liu et al. 2021). The effect of $H_2O$ is negligible for the low water contents of the natural (<0.30 wt%) and experimental (<0.08 wt%) inclusion; the inferred effect is to increase SCSS by about 100 ppm per 1 wt% dissolved $H_2O$. Ni and Cu were not measured in the experimental glasses. Only three experiments at FMQ-1 had sulfides large enough for quantitative WDS analyses (see Chapter 1), and the Ni+Cu was variable (from ~0.1 wt% to ~0.3 wt%) (Supplementary Figure 1).

In some olivine grains there are both sulfide-saturated and sulfide-undersaturated melt inclusions present and in a few cases both types of inclusions were exposed at the polished surface and could be analyzed. For two olivines equilibrated at FMQ-1 (H9X2 and H2XC2), sulfide-saturated inclusions have S = 776 and 803 ppm,

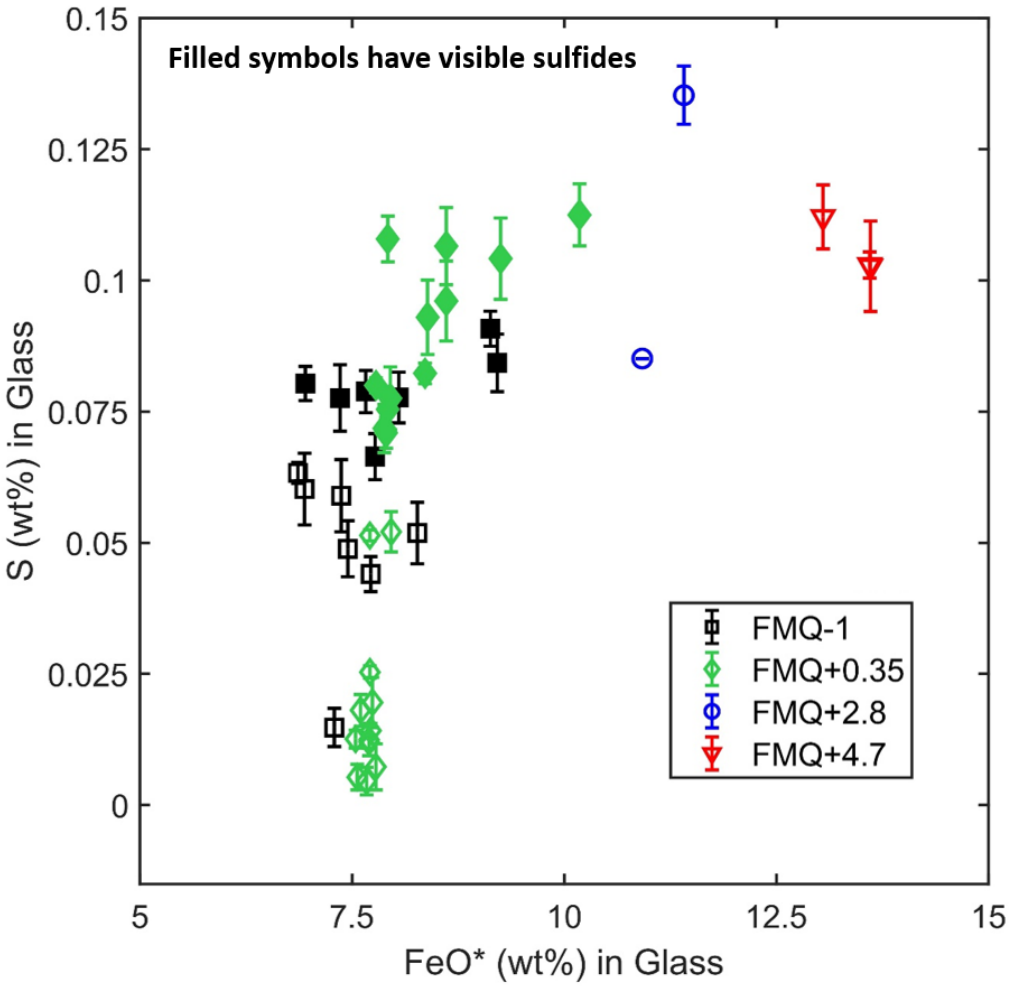


**Figure 9.** FeO* wt% vs. S wt% in experimental melt inclusions. Black squares – FMQ-1; Green diamonds – FMQ+0.35; Blue circles – FMQ+2.8; Red triangles – FMQ+4.7. Filled symbols had sulfides visibly identified either in backscattered electron images or optically with transmitted light. Open symbols had no sulfides visible.

respectively, whereas the nearby sulfide-undersaturated glasses have S = 590 and 633 ppm. A special olivine grain SF11-3, contained a high density of trapped melt inclusions, which allowed for simultaneous exposure of many melt inclusions (Figure 10). In this single grain, which was homogenized for 24 hr at 1225 °C and FMQ+0.35, 16 melt inclusions were analyzed for their S contents. Four of the sixteen exposed inclusions had visible sulfides; coincidentally this is the same fraction of melt inclusions (25%) that were observed to have sulfides by inspection of the whole population of unheated natural olivines from Papakōlea. The sulfide-saturated inclusions have S between 710-780 ppm, two of the sulfide-undersaturated inclusions have intermediate S = 514 and 520 ppm, and the remaining ten inclusions all have S < 254 ppm (cloud of green diamonds at FeO* = 7.7 wt% in Figure 9). Although the number of inclusions in each group are small, the major and minor element compositions are the indistinguishable except for their $P_2O_5$ contents, which fail a t-test for equal means and variances ($p>0.05$), and which are lower in the sulfide-saturated liquids. Comparing the sulfide-saturated and -undersaturated groups, the FeO* contents are 7.91±0.03 wt% (n=4 inclusions) and 7.7±0.11 wt% (n=12), respectively, and the $P_2O_5$ contents are 0.26±0.04 (n=4) and 0.34±0.04 (n=12), where the number after the plus-minus symbol is 1σ of the distribution of the average inclusion compositions based on three analyses of each inclusion. Because all the inclusions were hosted in the same olivine ($Fo_{88.4}$), these differences likely reflect heterogeneities in the compositions of the initially trapped melt inclusions. Note that $P_2O_5$ has been shown to have a very large effect on stabilizing $Fe^{3+}$ over $Fe^{2+}$ in silicate melts (~10x larger per mole compared to the effect of $Na_2O$, for example, Jayasuriya et al. 2004), which could possibly explain the lower P contents measured in sulfide-saturated inclusions versus sulfide-undersaturated inclusions of otherwise indistinguishable liquid compositions.

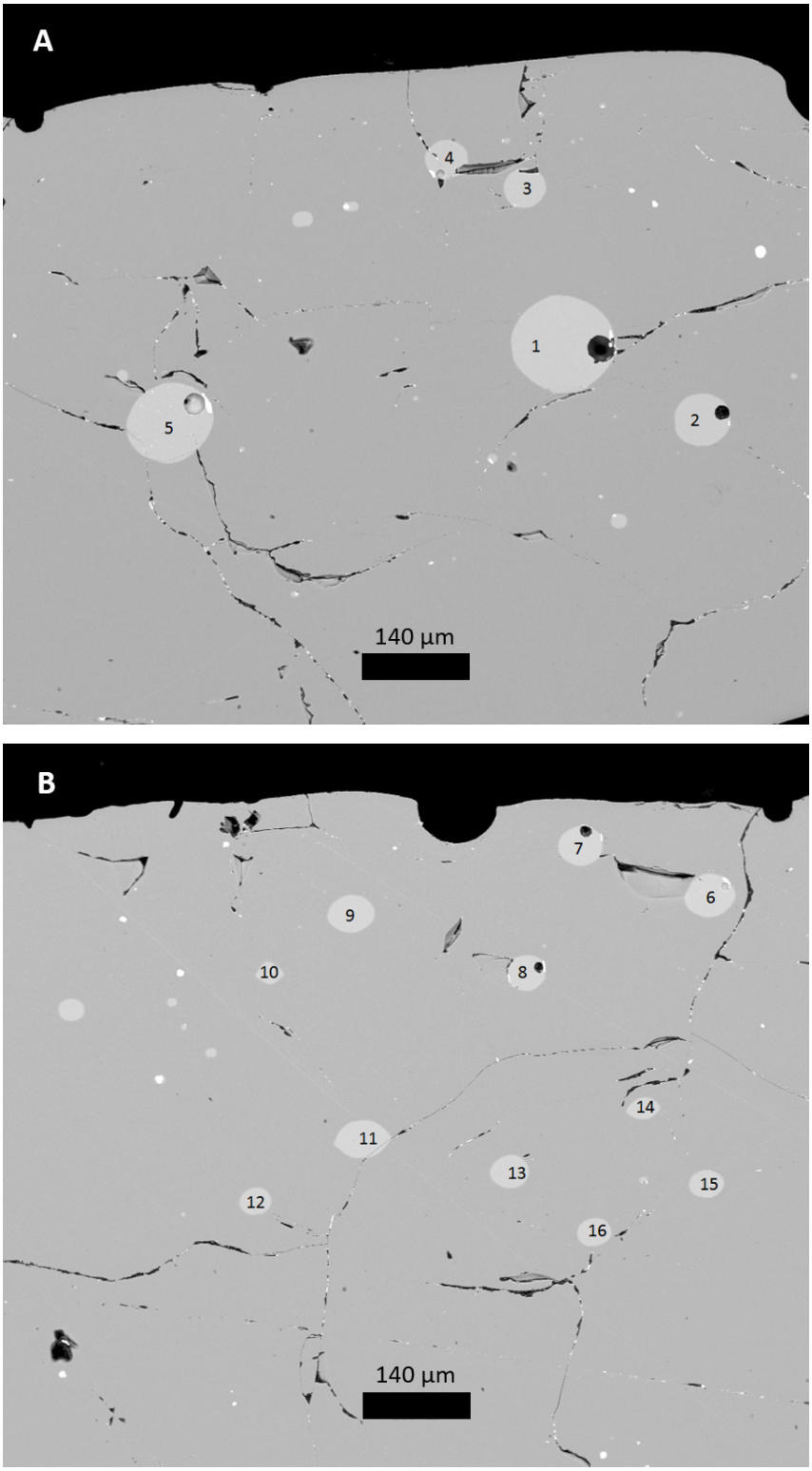


**Figure 10.** Backscattered electron images of experimental olivine SF11-3, which contained many melt inclusions that were simultaneously exposed on the polished sample surface. The melt inclusions are circular to ovoid shapes with numbers, and are brighter than the surrounding olivines. Sulfides are bright white and are visible in some of the melt inclusions. Scale bars are 140 µm.

**Figure 11**

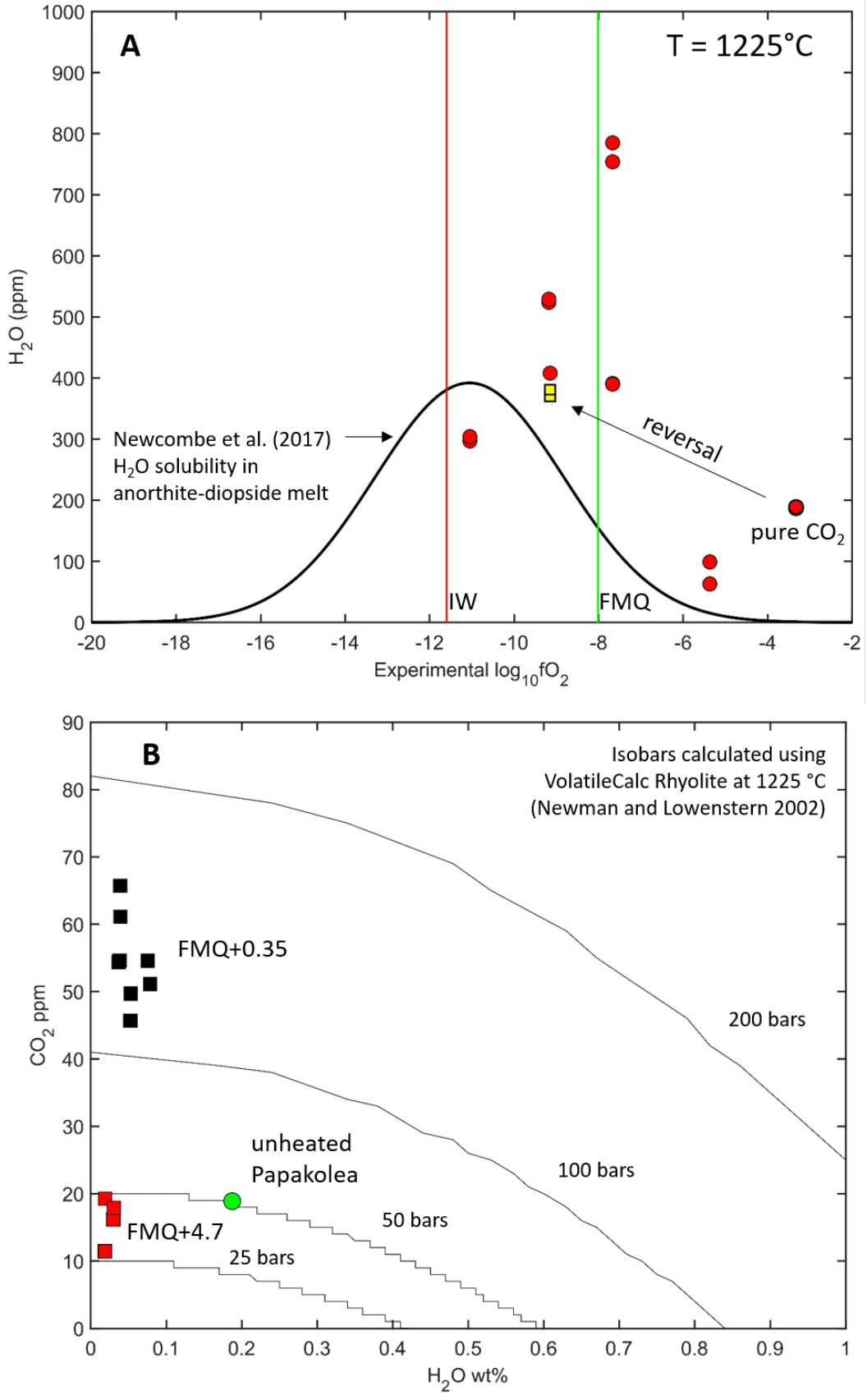


Figure caption is on the next page.

**Figure 11.** $H_2O$ and $CO_2$ contents of experimental melt inclusions measured by SIMS. **(A)** Experimental $\log_{10} fO_2$ versus $H_2O$ (ppm) measured in experimental inclusions. All of the experiments plotted as red circles were homogenized for 24 hr at 1225 °C. The yellow squares are the reversal experiments, which were first homogenized for 24 hr at 1225 °C and FMQ+4.7 and then re-homogenized for 24 hr at 1225 °C and FMQ-1. The black curve shows the calculated solubility of $H_2O$ in anorthite-diopside melt as a function of $fO_2$ from Newcombe et al. 2017. **(B)** $H_2O$ wt% vs. $CO_2$ wt% in experimental melt inclusions. The black squares are experiments run at $fO_2 \leq$ FMQ+0.35; red squares are inclusions equilibrated at FMQ+4.7; and the green circle is one unheated inclusion from Papakōlea (HIGS14). Black curves show isobars calculated using the rhyolite model of VolatileCalc at 1225 °C (Newman and Lowenstern 2002).

The $H_2O$ contents of four natural melt inclusions from Papakōlea were measured by FTIR in Saper & Stolper (2020), giving a range of 0.16-0.27 wt%. The low $H_2O$ contents of the experimental melt inclusions warranted quantification by SIMS – the one natural inclusion that was measured by FTIR (0.2 wt%) had a SIMS-determined $H_2O$ content of 0.187 wt% (using the calibration curve in Figure 2B). If this range of $H_2O$ contents is representative of the starting materials, then all the experimentally treated melt inclusions have lost water, which is consistent with the low solubility of $H_2O$ in melts equilibrated with $H_2$-$CO_2$ gases (Newcombe et al. 2017). Figure 11A shows the SIMS-determined water contents of experimental melt inclusions homogenized at 1225 °C and at different $fO_2$, which range from 188 to 769 ppm (0.0188-0.0769 wt%). Although these are lower than the initial $H_2O$ contents, they do not correspond to the bell-curve shape expected for plots of $fO_2$ vs. $H_2O$ based on the square-root dependence of $[H_2O]$ in the liquid versus $pH_2O$ in the vapor set by the

stoichiometry of the reaction $H_2 + ½ O_2 \rightleftharpoons H_2O$ (Newcombe et al. 2017 and black curve in Fig. 11A). This suggests, based on the temperature and duration of these experiments (1225 °C and 24 hr) as well as the distance of an individual melt inclusion from the edge of the host olivine, that the experiments were not run for sufficiently long durations to fully equilibrate the $pH_2O$ of the furnace with that of the included melts. Alternatively, aspects of the melt inclusion system, including the higher internal pressure and the presence of a vapor bubble, may conspire to complicate the simple model based on equilibrating melts hung on wire loops exposed directly to $H_2$-$CO_2$ furnace atmospheres. Note that the $H_2O$ content of a melt inclusion homogenized at FMQ+4.7 in pure $CO_2$ gas is low (188 ppm); the one inclusion with $H_2O$ measured from a 'reversal' experiment (24 hr in pure $CO_2$ followed by 24 hr in $H_2$-$CO_2$ at FMQ-1) has higher $H_2O$ (376 ppm). This apparent increase in $H_2O$ in the more reducing reversal experiment is consistent with the direction as a function of $fO_2$ anticipated based on $H_2O$ solubility (Newcombe et al. 2017) and is comparable to the $H_2O$ contents of the other inclusions that were homogenized for 24 hr at FMQ-1 (Figure 11A). Additional time-series experiments are required to see whether experimental melt inclusion $H_2O$ contents reach the equilibrium relationship between $\log_{10} fO_2$ and $[H_2O]$ given sufficient equilibration time (e.g., Gaetani et al. 2011, Chen et al. 2013, Lloyd et al. 2013).

The $CO_2$ contents were also measured by SIMS in one unheated melt inclusion (19 ppm) as well as in five experimental melt inclusions, which have $CO_2$ ranging from (48 to 63 ppm) (Figure 11B). For the inclusions homogenized at FMQ+4.7, the $CO_2$ contents are low (10-20 ppm), whereas the inclusions homogenized at or below FMQ+0.35 have $CO_2$ = 48-53 ppm. The reversal experiment has $CO_2$ = 54-55 ppm, which overlaps with the other experiments run at $fO_2 \leq$ FMQ+0.35. Given the $H_2O$ and $CO_2$ contents, minimum internal pressures ($P_{int}$) of the melt inclusions were estimated

using VolatileCalc (Newman & Lowenstern 2002); this implies that the unheated inclusion has $P_{int} \geq 50$ bars and the experiments at or below FMQ+0.35 have $P_{int}$ ~100-200 bars. These represent minimum pressures because of the presence of other volatile species such as S, and because a significant fraction, and perhaps the dominant reservoir, of C within the inclusion is hosted by the vapor bubble (Schiavi et al. 2016, Wallace et al. 2015, Maclennan 2017, Hanyu 2020, Rose-Koga et al. 2021 and refs therein).

### 4.4 Fe and S XANES Results

Figure 12 shows magnified views of both the EXAFS (top row) and pre-edge XANES (bottom row) regions of the Fe K-edge X-ray absorption spectra for experimentally treated (left column) and unheated Papakōlea (right column) olivine-hosted melt inclusions. Only the pre-edge region was used to calculate $Fe^{3+}/Fe^{Total}$, and the values reported in the text represent the average of 2-3 analyses per inclusion. For the Fe XANES analyses a 1σ uncertainty of $Fe^{3+}/Fe^{Total} = 0.015$ (absolute) is assigned (Brounce et al. 2017), which is comparable to the range of repeat measurements of $Fe^{3+}/Fe^{Total}$ in the same glasses (e.g. connected dots in Figure 13). For the experimental inclusions that were held at 1225 °C for 24 hr, the two inclusions measured with XANES that were homogenized at FMQ-1 have $Fe^{3+}/Fe^{Total} = 0.065$ and 0.076; at FMQ+0.35 two inclusions have $Fe^{3+}/Fe^{Total} = 0.103$ and 0.118; at FMQ+2.8 one inclusion has $Fe^{3+}/Fe^{Total} = 0.299$; and at FMQ+4.7 one inclusion has $Fe^{3+}/Fe^{Total} = 0.688$. These values correspond to the average of two to three XANES analyses of each inclusion, and the XANES results for all the inclusions can be found in Table 1.

In addition to the experimental inclusions that were homogenized and drop-quenched directly from the hotspot into water, four inclusions that were homogenized at FMQ+0.35 but subjected to different cooling paths also had their $Fe^{3+}/Fe^{Total}$ determined by XANES (not shown in Fig. 12). SF13-1 was cooled rapidly by displacement to a region of the furnace with an ambient T of ~600 °C, and quenched

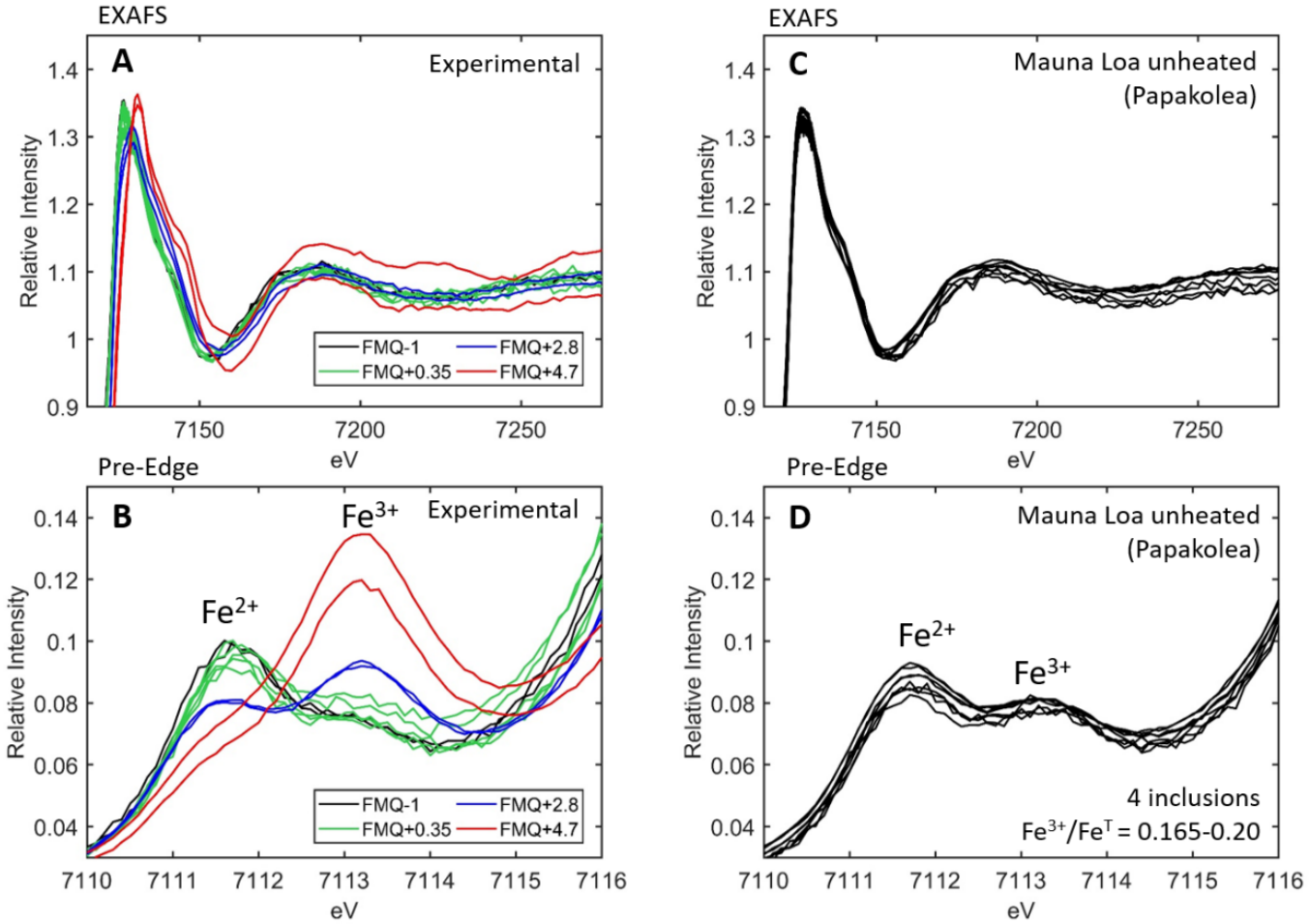


**Figure 12.** Zoomed in portions of EXAFS **(A)** and **(C)** and pre-edge **(B)** and **(D)** portions of Fe XANES spectra on experimental **(A)** and **(B)** and unheated inclusions **(C)** and **(D)** from Papakolea, Mauna Loa, Hawaii. In **(A)** and **(B)**, black curves are experiments conducted at FMQ-1; green curves – FMQ+0.35; blue curves – FMQ+2.8 red curves – FMQ+4.7. Black curves in panels **(C)** and **(D)** correspond to natural, unheated olivine-hosted melt inclusions from Papakolea. The $Fe^{2+}$ and $Fe^{3+}$ labels indicate the approximate peak positions in the XANES spectra.

into water at 900 °C after 31s of cooling, with an approximate cooling rate of 635 °C/min (or 38,000 °C/hr), the highest rate behind those experiments that were directly drop-quenched from the homogenization T (Figure 1B; note that the cooling rates of the drop-quenched experiments are estimate to be ~2000 °C/min (Saper & Stolper 2020). SF13-1 has an $Fe^{3+}/Fe^{Total}$ = 0.118. SF8-3 was also cooled by the displacement method to an ambient T = 983 °C and was quenched at 1000°C after 77s of cooling; it has $Fe^{3+}/Fe^{Total}$ = 0.108. The two remaining inclusions were subjected to cooling controlled by the Type B thermocouple, and had the lowest cooling rates; SF3-2 was quenched at 1150 °C after 100s of cooling and SF4-3 was quenched at 1000 °C after 420s of cooling. SF3-2 has $Fe^{3+}/Fe^{Total}$ measured at its center of 0.137. As described earlier, SF4-3 experienced the lowest cooling rate and was the only inclusion to have its central MgO contents modified by diffusion during cooling. Two measurements each were made at both the inclusion center and at its edge to see whether differences in $Fe^{3+}/Fe^{Total}$ could be detected across the zoned inclusion (FeO* ranges from 7.3 wt% near the inclusion wall to 9.3 wt% in its center). This inclusion has central $Fe^{3+}/Fe^{Total}$ = 0.119-0.139 (two analyses) and adjacent to the inclusion wall the $Fe^{3+}/Fe^{Total}$ = 0.109-0.124; the two values overlap within analytical uncertainty. In addition to the experimental melt inclusions, the $Fe^{3+}/Fe^{Total}$ of four unheated melt inclusions from Papakōlea were measured; HIGS21 (0.165), HIGS11 (0.184), HIGS20 (0.185), HIGS14 (0.199); these values are uniformly higher than any of the experimental melt inclusions run at $fO_2$ below FMQ+0.35.

Figure 13 compares experimental inclusions homogenized at 1225°C and cooled at different rates. The x-axis is an estimate of the integrated diffusion distance of electrons in the liquid over the duration of experimental cooling, $X = \sqrt{\int_{t0}^{tf} D\big(T(t)\big)dt}$, where *D(T)* refers to the temperature-dependent diffusion coefficient, *T(t)* emphasizes that temperature is varying with time *t*, $t_0$ is t = 0 at the initiation of cooling and $t_f$ = the

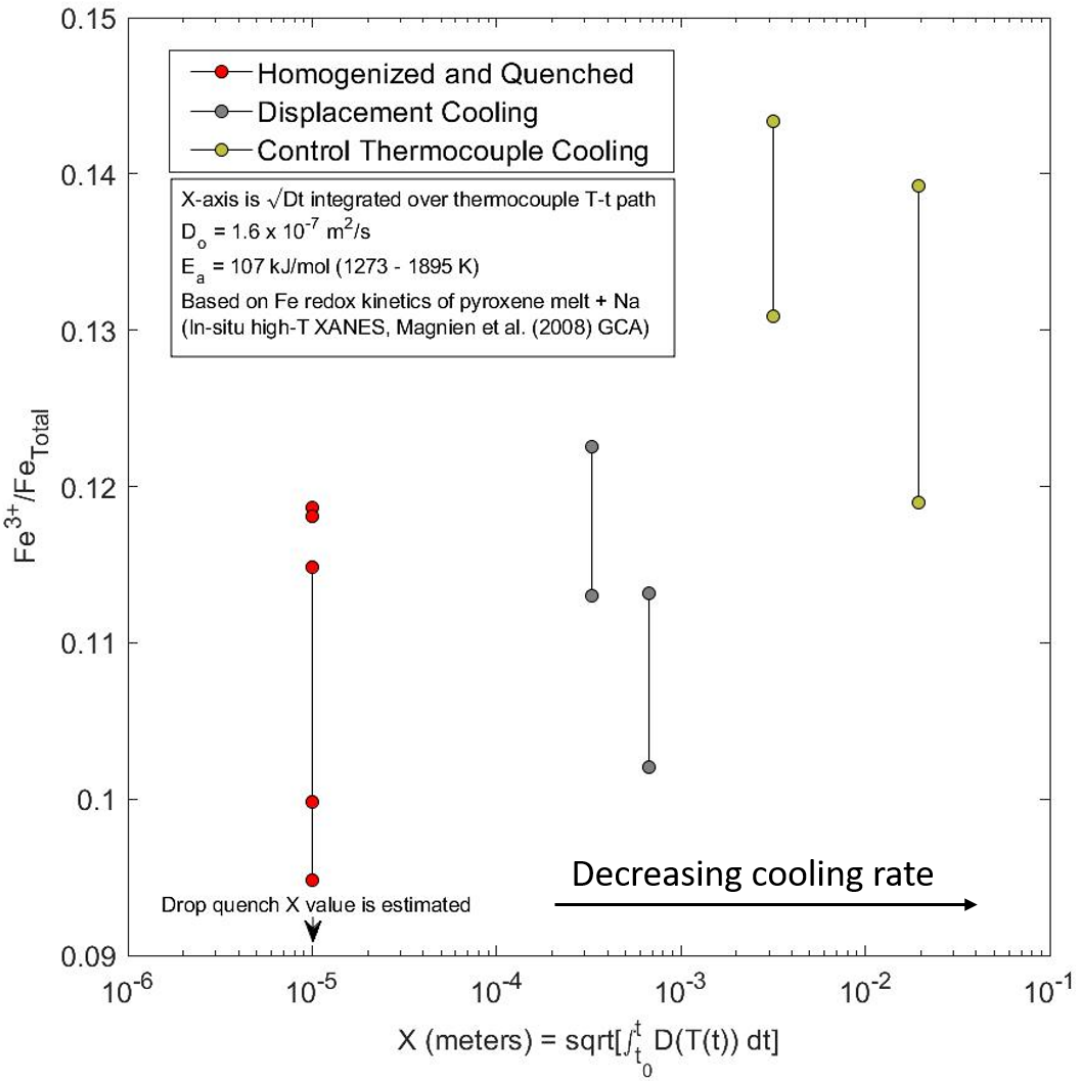


**Figure 13.** Integrated diffusion distance vs. $Fe^{3+}/Fe^{Total}$ in experimental melt inclusions that were homogenized at 1225°C at FMQ+0.35 for 24 hr and then cooled at different rates: red circles – homogenization and drop quench directly from hotspot; gray circles – displacement method; beige circles – controlled cooling. Lines connecting data markers indicate repeat Fe XANES measurements of the same melt inclusion. The x-axis is calculated by integrating the thermocouple measurements of temperature vs. time for each experiment (Figure 1B) and using a temperature-dependent "redox diffusivity" from Magnien et al. 2008 to calculate a length scale for diffusion (i.e., a time- and temperature-dependent form of the relationship $X \propto [Dt]^{1/2}$.

elapsed time at quench. Given the measured thermocouple temperature-time curves (Figure 1B) and an estimate for a T-dependent "redox diffusivity" coefficient for Fe electron transfer (based on in-situ high-T XANES measurements from Magnien et al. 2008; $D_o$ = 1.6x10$^{-7}$ m$^2$/s, $E_A$ = 107 kJ/mol) this length-scale can be calculated and allows for experiments with different cooling histories to be plotted together and ordered. This value for the homogenization experiments, for which there are no thermocouple measurements during cooling, was estimated to be close to zero. Lines connecting data markers in Figure 13 indicate repeat Fe XANES analyses of the same experimental inclusion. The $Fe^{3+}/Fe^{Total}$ of the homogenization and displacement method experiments overlap; the controlled cooling experiments, which experienced more olivine growth on the inclusion walls driving both $Fe^{2+}$ down and $Fe^{3+}$ up, have $Fe^{3+}/Fe^{Total}$ that only just overlap with the upper range of estimates from the more rapidly cooled experiments.

S XANES spectra for homogenized melt inclusions and unheated melt inclusions are shown in Figure 14 along with labels indicating the energy regions of the $S^{2-}$, $S^{4+}$, and $S^{6+}$ absorption bands. Inclusion H11X1B, which was homogenized at 1225 °C and FMQ-1 and drop quenched, has $S^{6+}/S^{Total}$ indistinguishable from zero. Inclusion SF11-5, homogenized at 1225 °C and FMQ+0.35 also has low $S^{6+}$ contents; four analyses gave $S^{6+}/S^{Total}$ = 0 and a fifth analysis gave $S^{6+}/S^{Total}$ = 0.06 (unscaled) or 0.129 (using generic scaling factors; Nash et al. 2019). The anomalous high $S^{6+}/S^{Total}$ measured in one of the five analyses is due to beam overlap with a crack which runs through the inclusion (pers. comm. M.-J. Brounce), which might contain residual CrystalBond. The other inclusion homogenized at 1225°C and FMQ+0.35, SF1-2, suffered from contamination by CrystalBond – there was a sulfur signal in the middle of otherwise clean olivine and the analyses of the inclusion glasses were deemed to be compromised by the analyst. Two

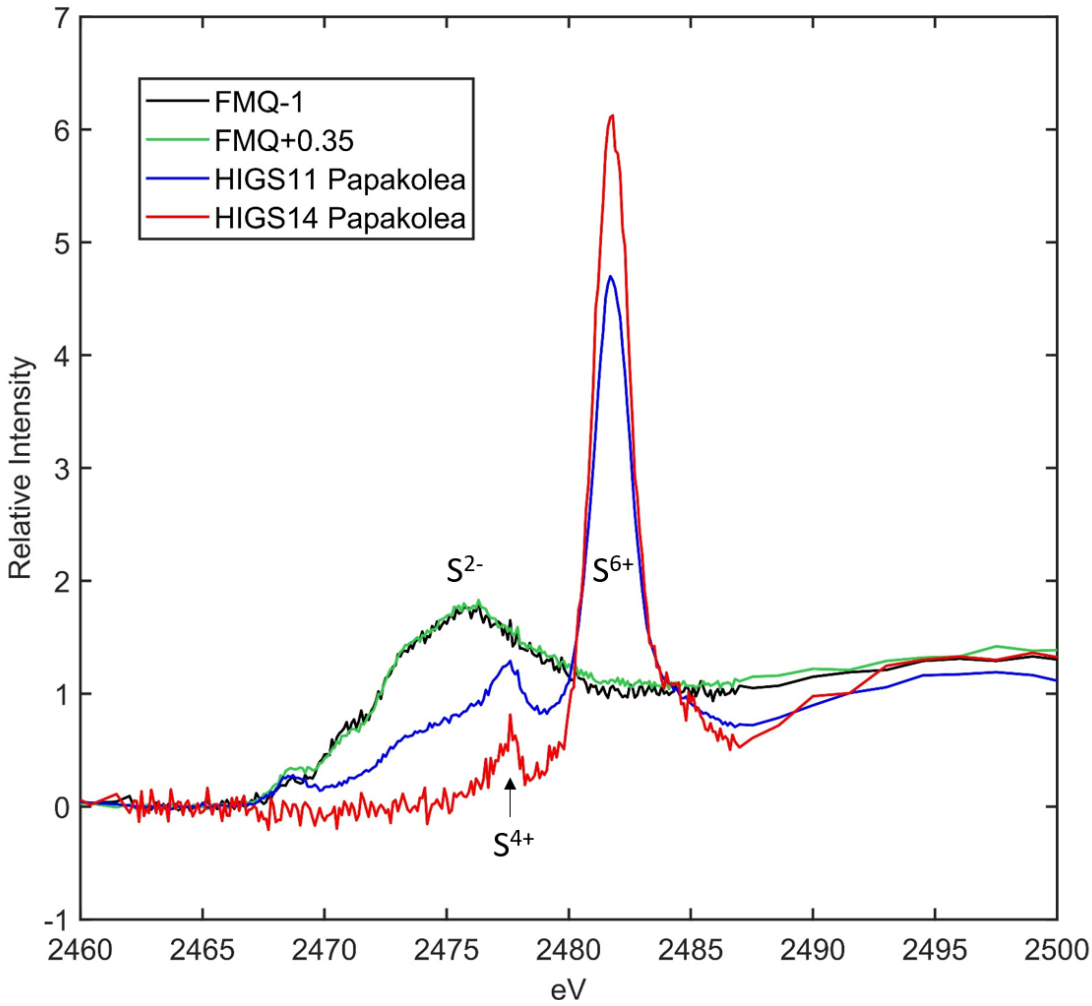


**Figure 14.** S XANES spectra of experimentally homogenized and unheated olivine-hosted melt inclusions from Papakolea, Mauna Loa, Hawaii. Black curve – experiment H11X1B at FMQ-1; green curve – experiment SF11_5 at FMQ+0.35; blue curve – natural inclusion HIGS11; red curve – natural inclusion HIGS14.

of the remaining three experimental inclusions that were homogenized at 1225 °C and FMQ+0.35 and cooled to lower T before quenching have $S^{6+}/S^{Total} = 0$ (SF8-3, SF4-3). Inclusion SF3-2 has a minor $S^{6+}$ peak; three repeat measurements give $S^{6+}/S^{Total} = 0.026$-0.069 (unscaled) or 0.06-0.15 (generic scaling factors). It is difficult to distinguish between these low $S^{6+}/S^{Total}$ values and essentially no $S^{6+}$, but it is clear that all of the experimentally treated melt inclusions equilibrated at $fO_2 \leq$ FMQ+0.35 have little, if any, $S^{6+}$. None of the experimental melt inclusions have a distinguishable $S^{4+}$ peak.

Two natural unheated melt inclusions from Papakōlea were also measured for S XANES. These two inclusions represent both rapidly cooled (HIGS11, ~8000 °C/hr) and very slowly cooled (HIGS14, ~50 °C/hr) endmembers among the natural melt inclusions measured from this locality (Saper & Stolper 2020). Both glasses are dominated by $S^{6+}$, and both show evidence for $S^{4+}$ (arrow in Figure 14). The sulfite peak is often assumed to be an analytical artifact due to photo-reduction of some of the high concentration of $S^{6+}$ present in the glasses (Wilke et al. 2008), however it is unclear whether it is due to beam damage or is present in the glass. HIGS11 has a shoulder in the $S^{2-}$ region and the ratio of the integrated peak areas (excluding $S^{4+}$) gives $S^{6+}/S^{Total} =$ 0.41-0.52 (5 analyses, unscaled) or 0.62-0.72 (with generic scaling factors). If the integrated area under the $S^{4+}$ is added to the $S^{6+}$ area (Nash et al. 2019) the $S^{6+}/S^{Total}$ is only slightly higher, 0.64-0.73, than the value calculated excluding contributions from $S^{4+}$. HIGS14 contains no $S^{2-}$, with all S present as $S^{6+}$ (and possibly a small amount of $S^{4+}$). Thus, the $S^{6+}/S^{Total}$ contents of the natural Papakōlea melt inclusions, which served as starting materials for the experiments, were much higher than the experimentally treated inclusions at $fO_2 \leq$ FMQ+0.35 and 1225 °C. Based on comparison of the measured $Fe^{3+}/Fe^{Total}$ of the natural inclusions with those equilibrated at FMQ+2.8 and FMQ+4.7, inclusions from these oxidizing experiments are expected to have all S

present as $S^{6+}$, although S XANES measurements of these experimental glasses were not acquired.

## 5. Discussion

### 5.1 $Fe^{3+}/Fe^{Total}$ Contents of Natural and Experimentally-Homogenized Melt Inclusions

In order to assess and interpret the measured $Fe^{3+}/Fe^{Total}$ and the implied $fO_2$ recorded in the melt inclusions, six of the available Fe oxybarometry expressions that relate melt composition, T, and $Fe^{3+}/Fe^{Total}$ to $fO_2$ were employed (Sack et al. 1980; Kilinc et al. 1983; Kress & Carmichael 1991; Jayasuriya et al. 2004; Borisov et al. 2018; O'Neill 2018). Critical assessments of several of these models have been provided recently (Matzen et al. 2011; Putirka 2016; Borisov et al. 2018), and there is still no consensus on which, if any, is the most accurate. It is important to note that all of these models were calibrated using experimental liquids that contained no sulfur. For the unheated Papakōlea melt inclusions, using their measured $Fe^{3+}/Fe^{Total}$, central glass compositions, and an inferred T = 1175°C representing the approximate temperature prior to syneruptive cooling (Saper & Stolper 2020), the calculated $fO_2$ varies widely for a given inclusion based on the model chosen, with differences between the minimum and maximum estimates of spanning 1.2-1.3 orders of magnitude for a single inclusion. The lowest estimate of $fO_2$ for the Papakōlea inclusions is calculated from Jayasuriya et al. (2004) – FMQ+0.20 to +0.30 – whereas the highest estimate of $fO_2$ is from O'Neill (2018) – FMQ+1.52 to +1.53. The median $fO_2$ calculated using all six models ranges from FMQ+0.63 to FMQ+0.86 for the four natural Papakōlea inclusions with Fe XANES measurements. Therefore, unless the low $fO_2$ estimate provided by the Jayasuriya et al. (2004) model is accurate, the homogenization and cooling experiments at FMQ+0.35 (and certainly FMQ-1) were run in an atmosphere more reducing than the

initial $fO_2$ levels in the unheated melt inclusions in the starting materials, while experiments at FMQ+2.7 (and FMQ+4.7) were run at more oxidizing conditions.

The Fe oxybarometers were applied to the experimental melt inclusions using in both the forward and inverse senses: (1) $Fe^{3+}/Fe^{Total}$ was calculated from the nominal $fO_2$ imposed by $H_2$-$CO_2$ gases in the furnace, the experimental T, and the inclusion glass compositions (Figure 15A), and (2) $fO_2$ was calculated from the XANES measurements of $Fe^{3+}/Fe^{Total}$ in the glasses, the experimental T, and the glass compositions (Figure 15B). With the exception of the O'Neill (2018) model, which predicts the lowest $Fe^{3+}/Fe^{Total}$ for a given $fO_2$, T, and melt composition, all the other models predict higher $Fe^{3+}/Fe^{Total}$ than that which was measured in the experimental melt inclusions homogenized at $fO_2 \leq$ FMQ+2.7; whereas for the oxidizing experiment at FMQ+4.7 all of the models underestimate the measured $Fe^{3+}/Fe^{Total}$ (Figure 15A). For one of the two inclusions at FMQ-1 (H11X1B, $Fe^{3+}/Fe^{T}$ measured = 0.076), three models come within 3% (relative) of the expected $Fe^{3+}/Fe^{Total}$ (Sack et al. 1980, Kilinc et al. 1983, and Borisov et al. 2018), however for the other inclusion at FMQ-1 (H7XC1, $Fe^{3+}/Fe^{T}$ measured = 0.065), these three models overestimate the $Fe^{3+}/Fe^{T}$ by +13-19% relative. The only major compositional difference between these two inclusions is the FeO*; which is 9.32 wt% in H11X1B and 7.66 wt% in H7XC1.

When translated into $fO_2$, the discrepancies between the nominal $fO_2$ of the $H_2$-$CO_2$ gas mixes in the furnace and the $fO_2$ calculated from the measured $Fe^{3+}/Fe^{T}$ of the experimental melt inclusions correspond to an underestimation of the nominal experimental $fO_2$ by up to -1.4 log units (Figure 15B). For the experiments at FMQ-1, which were unambiguously run under much more reducing conditions than the $fO_2$ inferred from the starting materials, the low estimates can be explained by one of the following reasons (or perhaps a combination): (1) the internal $fO_2$ recorded by the

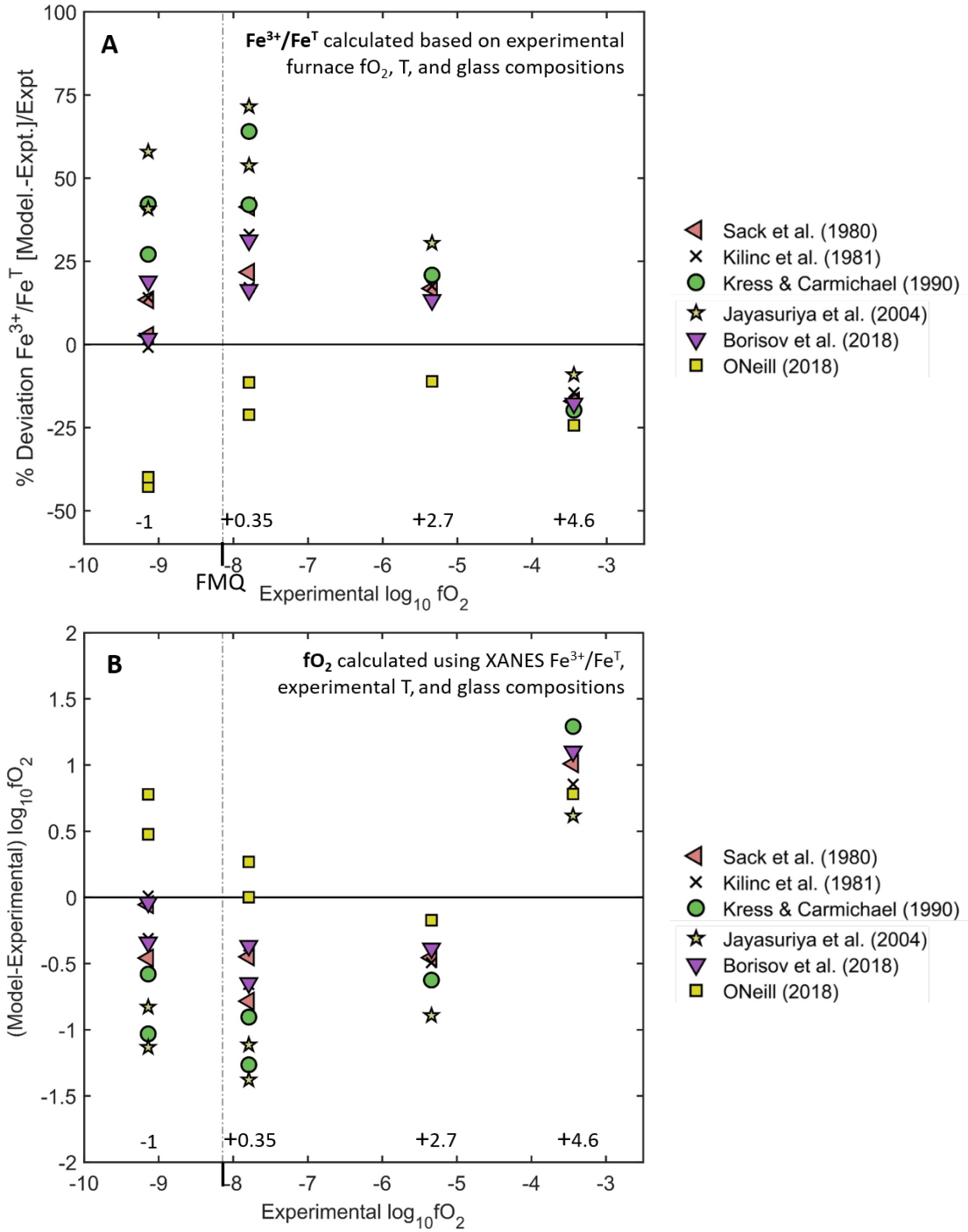


**Figure 15.** All experiments were run at 1225 °C for 24 hr. **(A)** Nominal experimental $fO_2$ (based on $H_2$-$CO_2$ gas mix) versus the % deviation of model estimates of $Fe^{3+}/Fe^T$ from the value measured by Fe XANES in the experimental glasses (% Deviation = $100 \bullet [(Fe^{3+}/Fe^T)_{Model} - (Fe^{3+}/Fe^T)_{Experimental}] / (Fe^{3+}/Fe^T)_{Experimental}$). Model $Fe^{3+}/Fe^T$ are calculated from the experimental T, $fO_2$, and glass compositions. **(B)** Model estimates of $fO_2$ calculated from the experimental T, glass composition, and XANES measurements of $Fe^{3+}/Fe^T$. The y-axis is the absolute difference ($\log_{10} fO_2$) between these estimates and the nominal $fO_2$ of the experiments. Fe oxybarometer models shown: pink leftward facing triangle – Sack et al. (1980); black X – Kilinc et al. 1981; green circle – Kress & Carmichael 1991; yellow star – Jayasuriya et al. 2004; purple downward facing triangle – Borisov et al. 2018; orange square – O'Neill et al. 2018.

$Fe^{3+}/Fe^{T}$ of the melt inclusions is drastically different than that imposed by the external furnace gases, (2) compositional dependencies coded in the various expressions for $Fe^{3+}/Fe^{2+}$ do not accurately account for the compositions of the experimental inclusions, possibly including the fact that they are S-bearing liquids, or (3) there is an analytical artifact. Reason (1) is difficult to explain by incomplete equilibration of the melt inclusions with the furnace atmosphere over the 24 hr experimental duration, because the internal $fO_2$ implied by the models (e.g., ~FMQ-2) is lower than that set by the furnace gases (e.g., FMQ-1). Incomplete equilibration would most likely yield an $fO_2$ between the initial $fO_2$ of the melt inclusions (e.g., ≥FMQ+0.35) and that imposed by the furnace gas mixture (low, but not as low as the $fO_2$ calculated based on the measured $Fe^{3+}/Fe^{T}$). It is, however, plausible that the low $fO_2$ recorded by the experimental melt inclusions reflects a transient overshoot process that temporarily leads to a lower $Fe^{3+}/Fe^{T}$ (and $fO_2$) in the melt inclusion interiors than what is expected when at equilibrium with the $fO_2$ of the furnace gases; a possible explanation along these lines is offered in a following paragraph. Alternatively, it could be that the models do not fully account for the effects of melt composition and/or they are much less accurate than is typically assumed in the literature. The intramodel variations span almost two orders of magnitude in $fO_2$, exceeding considerably the states uncertainty of each model, for example the Borisov et al. (2018) model has an uncertainty of ±0.38 log units in $fO_2$.

One possibility is that the presence of S in the liquids leads to this discrepancy; all the experimental inclusions with measurements of $Fe^{3+}/Fe^{Total}$ have S between 788 and 851 ppm, and all of the inclusions equilibrated at $fO_2 \leq$ FMQ+0.35 with Fe XANES measurements are sulfide saturated. Such an effect was suggested by an AGU abstract (Graz et al. 2006; never published), that reported 1 atm gas-mixing experiments on a model MORB composition at 1300 °C where $fS_2$ was varied along with CO-$CO_2$ gases

in order to vary the experimental $fO_2$ from FMQ-0.04 to FMQ-1.9. The recovered glasses "had $Fe^{2+}$ determined volumetrically", which is assumed to mean by wet chemistry. The effect they describe is in the same direction and of similar magnitude to that which is observed in the melt inclusion experiments: the $Fe^{3+}/Fe^{T}$ of S-bearing melts is lower than S-free melts equilibrated at the same T and $fO_2$; in the case of their FMQ-0.04 experiments the difference in $Fe^{3+}/Fe^{T}$ is about a factor of two. They report that for their S-free experiments, the Kress & Carmichael (1991) model agrees with their wet chemical results to within analytical error. This implies that even relatively small amounts of S may act to stabilize $Fe^{2+}$ over $Fe^{3+}$ in the melt at and below FMQ. Sulfur speciation will be discussed later in this section, but equation (1) implies that S present as $S^{6+}$ would serve to counteract this proposed effect by oxidizing some of the $Fe^{2+}$ to $Fe^{3+}$. However, the amount of $S^{6+}$ is predicted to be negligible below FMQ at 1300 °C (Jugo et al. 2010), and the S XANES results from the melt inclusions indicate that (nearly) all S was present as $S^{2-}$. This could potentially explain the smaller differences between the models and the higher $fO_2$ experiments, where $S^{6+}$ is stabilized (Figure 15). Because the stoichiometry of the Fe-S electron exchange equilibrium requires 8 moles of Fe for every mole of S, and because at $fO_2$ ~ FMQ or below the concentration of $[Fe^{3+}]$ in the liquid can be on the same order as $8\times[S^{2-}]$ (e.g., FeO* = 10 wt% and $Fe^{3+}/Fe^{T}$ = 0.125 implies $[Fe^{3+}]$ = 9,700 ppm, and at sulfide saturation [S] ~1000 ppm), S can potentially have disproportionate leverage on Fe redox equilibria for its relatively low bulk concentration. However, at least at T = 1370-1400°C, $S^{2-}$ has been shown to have a negligible effect on the olivine-liquid Fe/Mg exchange coefficient ($K_D^{ol/liq}$,$Fe^{2+}$-Mg), which indicates that the effect of $S^{2-}$ on the activity of $Fe^{2+}$ in the liquid is minor, (and/or is comparable to its effect on the activity of Mg in the liquid). Thus, further experiments exploring the effect of S on the relationship between melt composition and

$fO_2$ would be helpful, including suspending high-S olivine-hosted melt inclusions alongside exposed S-free melts of similar or the same composition hung from wire loops in the same furnace, where $fO_2$ can be precisely controlled and accurately measured.

A thought experiment is proposed that rules out the possibility that the low $Fe^{3+}/Fe^{T}$ measured in the experimental melt inclusions relative to model predictions are due to a transient experimental effect. For a fixed T and ratio of $H_2/CO_2$ gas in the furnace tube, the $fO_2$ is fixed and so is the ratio $H_2/H_2O$ by the reaction $H_2 + ½\ O_2 = H_2O$. It is widely thought that H-bearing defects in olivine are responsible for 'transmitting' the externally imposed $fO_2$ into the interior of olivine grains and ultimately to melt inclusions (Kohlstedt and Mackwell 1998) and in the case of an H-bearing external gas, equilibrium is achieved when the $H_2/H_2O$ of the furnace atmosphere (or, strictly, the chemical potentials of these components) is equal to that in the melt inclusion. The proton-polaron mechanism for $H^+$ incorporation in has been used to explain $H_2O$-loss haloes around water-rich melt inclusions from arc-derived olivines (Le Voyer et al. 2014). Additional mechanisms invoking coupled diffusion of protons and vacancies in olivine (proton-vacancy mechanism) have been proposed to explain the apparent decoupling of the experimental equilibration of $fO_2$ across olivines and the dehydration of melt inclusions (Gaetani et al. 2012, Bucholz et al. 2013), although in order to maintain a constant $H_2/H_2O$ ratio, loss of molecular water must be compensated by driving the following $Fe^{3+}$-reduction reaction in the melt to the right: $H_2 + Fe_2O_3 \rightleftharpoons 2FeO + H_2O$. The XANES results from the unheated inclusions indicate that the $fO_2$ of the melt inclusions was initially high relative to that in the furnace atmosphere for the FMQ≤0.35 experiments; and so initially the $H_2/H_2O$ ratio was lower in the melt inclusion. Based on the SIMS data, the melt inclusions dehydrated during the experiments, from ~0.2 wt% $H_2O$ to <0.06 wt% $H_2O$. One possible explanation for the

discrepancy between the experimental and modeled $Fe^{3+}/Fe^{2+}$ is that initial dehydration of $H_2O$ from the melt inclusion outpaced the incorporation of $H^+$ from the relatively high $pH_2$ of the furnace atmosphere, which transiently led to a higher $H_2/H_2O$ ratio in the melt inclusion than that which was imposed externally. However, this can be ruled out based on determinations of H diffusivities in olivines for the two diffusion mechanisms, where the proton-polaron mechanism has estimated diffusivities that are several orders of magnitude higher than the proton-vacancy mechanism (see Ferriss et al. 2018 for review). I acknowledge that considerable uncertainty in the activation energies of these diffusion mechanisms mean that it cannot be ruled out that at sufficiently high T the relative diffusivities cross over, however this seems unlikely. Therefore, the remaining explanation due to an experimental transient would be pumping of $H^+$ from the furnace into the melt inclusion without, or with incomplete, back-reaction of $H_2O$ out of the olivine, leading to higher than expected $H_2/H_2O$ in the melt inclusion and thus lower $Fe^{3+}/Fe^{2+}$. Additional time series experiments would be required to test this further, however, based on available estimates of both diffusion mechanisms in olivine (Bucholz et al. 2013, Ferriss et al. 2018, Barth et al. 2019) and the observation that much of the $H_2O$ was lost from the experimental inclusions, this explanation seems unlikely. Using the model of Bucholz et al. (2013) for a 75 μm radius melt inclusion located 500 μm from the crystal edge (comparable to conservative examples from the experiments), assuming an equilibrium $H_2O$ content in the melt of 175 ppm at FMQ (Newcombe et al. 2017), T = 1225 °C, and an initial melt $H_2O$ contents of 0.20 wt% (2000 ppm), the inclusion is expected to dehydrate to <400 ppm $H_2O$ within ~14 hr and ~200 ppm after 24 hr. Smaller inclusions and those closer to the edge of olivine grains will equilibrate more quickly than larger inclusions and those which are embedded more deeply in their

host olivines. Based on these considerations, an experimental transient is deemed unlikely as a culprit for the discrepancy between the XANES measurements and models.

Another consideration that might explain the low $Fe^{3+}/Fe^{T}$ measured by XANES is the presence of sulfide blebs (i.e., immiscible FeS) in the analytical volume. Given the contrast in densities of FeS (~4.84 g/cc) and the silicate glass at 25 °C and 100 bar (~2.89 g/cc, Iacovino and Till 2019), a relatively small volume of FeS (or $FeSO_4$) in the beam path could feasibly lead to an apparent increase in the $Fe^{2+}$. Consider experiment H7XC1, with two XANES measurements of $Fe^{3+}/Fe^{T}$ = 0.059 and 0.071; if the glass actually had an $Fe^{3+}/Fe^{T}$ = 0.10 (value predicted at FMQ-1 using the model of Jayasuriya et al. 2004), and if the Fe K-edge spectra of FeS and silicate glass mix linearly, a volume fraction of 0.02-0.03 FeS would be required to account for the difference between 0.10 and the XANES measurements (Figure 16A). For a 10 μm XANES beam, this translates to a single spherical bleb of radius 1.4-1.9 μm (Figure 16B), which would be easily identified by visual inspection in an optical microscope (Figure 4; Figure 17B). When whittled down to doubly polished thicknesses, sulfides are easy to identify in transmitted light, and target volumes which were free of visible sulfides were provided to the analyst to explicitly avoid this issue.

To explicitly test this, the analyst was instructed to acquire XANES data in a single experimentally homogenized melt inclusion, SF11-5, both in an area that was visibly free of sulfides (three analyses) and in an area that had a cluster of micrometer-sized FeS blebs (one analysis) (Figure 17B). The only obvious differences in the XANES spectrum of the analysis taken in the FeS bleb region (red curve, Figure 17CD) is that the K-edge peak intensity is slightly lower than in the sulfide-free spectra and the pre-edge features are slightly offset to higher intensities; it would be difficult to distinguish between the

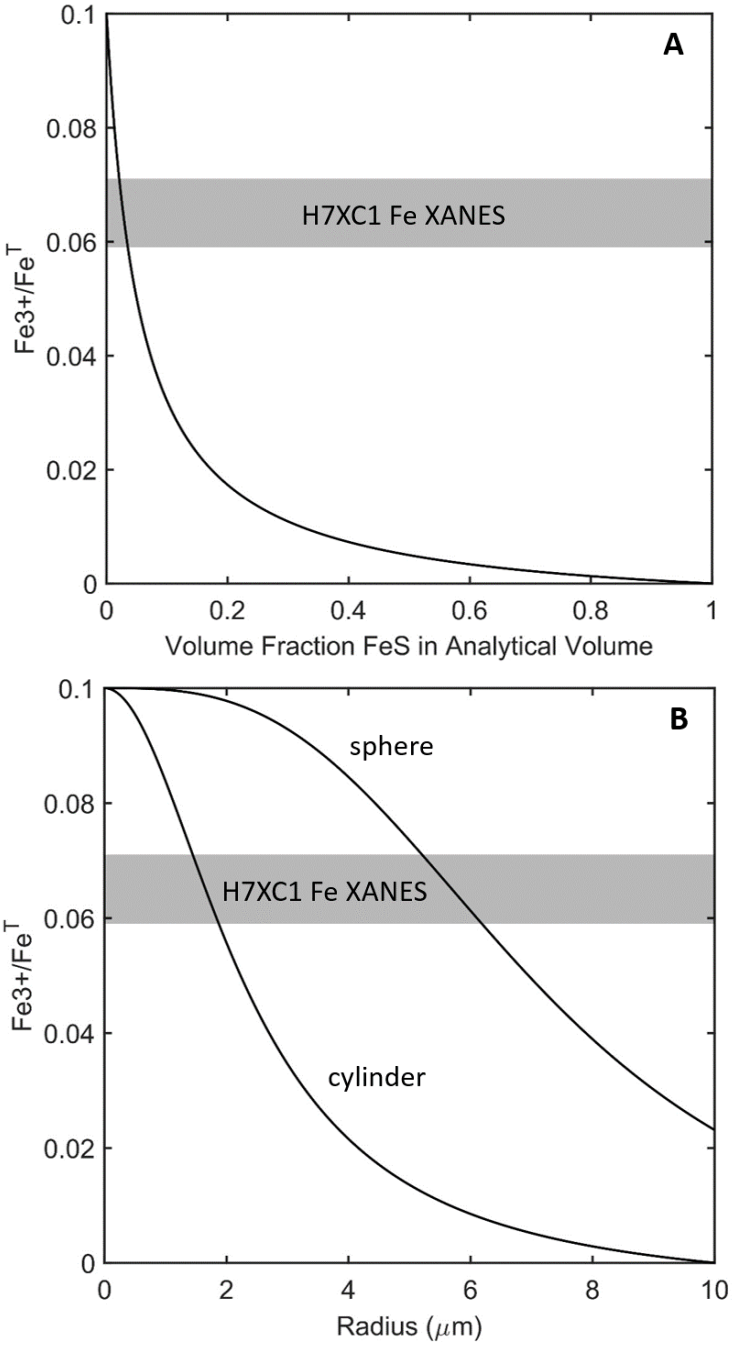


**Figure 16.** Calculations demonstrating the effect of mixtures of silicate glass and FeS on Fe XANES measurements. **(A)** $Fe^{3+}/Fe^{T}$ in a cylinder of glass with composition from experimental inclusion H7XC1 (FMQ-1, 1225°C, 24hr) as a function of the volume fraction of FeS in a cylindrical analytical volume. **(B)** same calculation as **(A)** but with volume fraction expressed as a single sphere or cylinder of FeS in a cylindrical analytical volume.

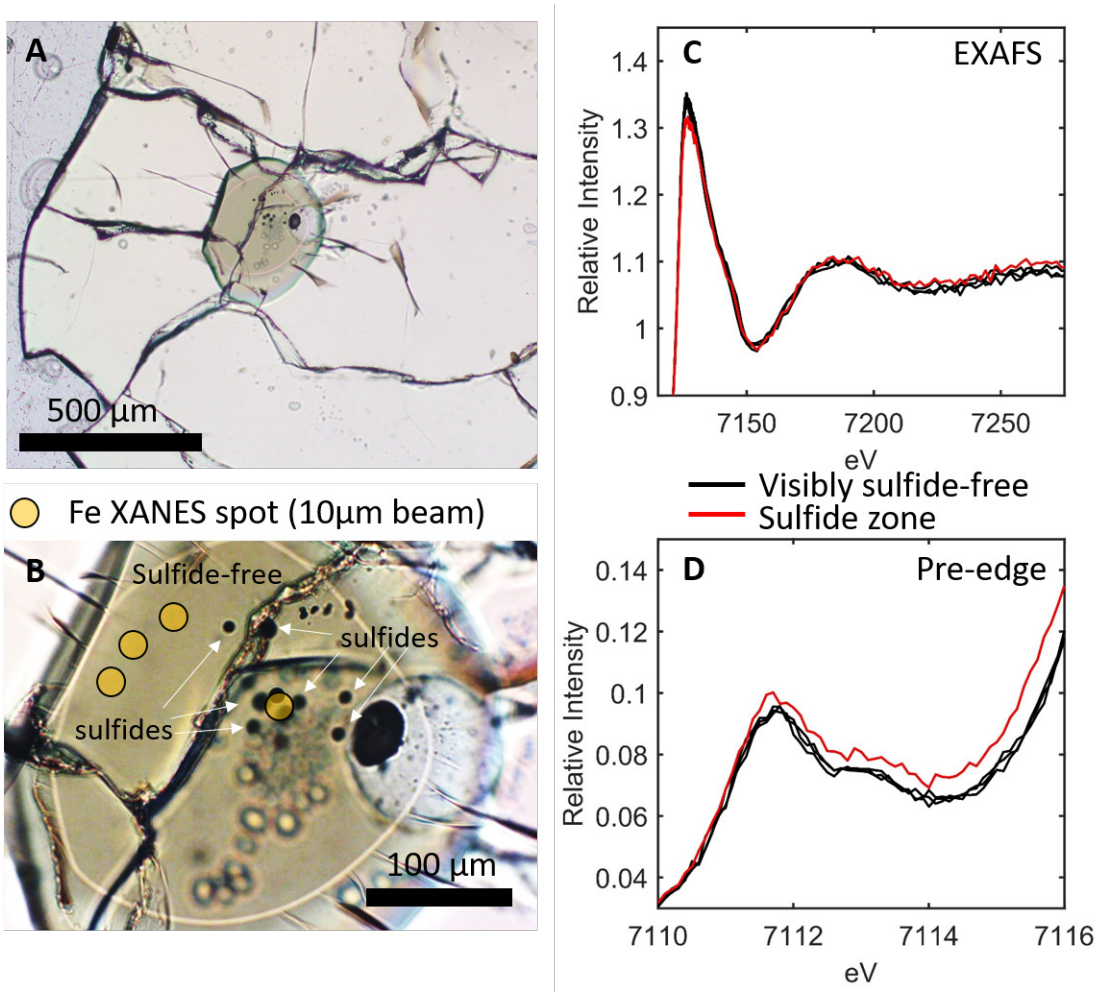


**Figure 17. (A)** and **(B)** are transmitted light optical microphotographs of experimental inclusion SF11-5 (FMQ+0.35, 1225°C, 24 hr). **(B)** Yellow circles indicate the locations of Fe XANES measurements of this inclusion – three analyses are in an area of glass that are visibly free of sulfides; one analysis is in an area with many sulfides, some of which are pointed out by white arrows, and can be identified as opaque circles. The out of focus bright spots are small amounts of CrystalBond that were not dissolved prior to mounting the sample on Fe-free glass slides (analyses taken in these regions are unaffected by the presence of the Fe-free organic CrystalBond. The bright thin quasi-circular outline shows the boundary of exposed glass on this side of the doubly polished inclusion. Notice how cracked the host olivine (and inclusion) are; this was why several of the experimental samples were destroyed during sample preparation. Zoomed in portions of the XANES spectra: **(C)** EXAFS and **(D)** pre-edge. Black curves correspond to the three analyses taken in the sulfide-free zone; the red curve is the single analysis from the zone densely populated by sulfides.

two without *a priori* knowledge of the presence of the blebs. The three analyses in the sulfide-free zone have calculated $Fe^{3+}/Fe^{T}$ = 0.100, 0.115, and 0.095, whereas the single analysis in the area with sulfides is significantly lower – 0.075. For the other melt inclusions, care was taken to avoid areas with visible sulfides, however the presence of submicroscopic nanolites (e.g., DiGenova et al. 2018) which compromised the XANES spectra cannot be ruled out. In-situ synchrotron observations of molten Mt. Etna basalt (DiGenova et al. 2021) demonstrated that magnetite nanolite growth is promoted by rapid cooling, and that 10-20 nm sized particles or agglomerates can occupy at least 4-5 vol% in quenched glasses, sufficient to account for the discrepancy in $Fe^{3+}/Fe^{T}$ in the experiments versus Fe oxybarometers. Sulfide nanolites have been inferred to be present in sulfide-saturated melt inclusions in tephra from Nyamuragira, Africa on the basis of S XANES spectra (Head et al. 2018), and their potential to obscure Fe XANES data is beginning to be recognized (Rose-Koga et al. 2021, Lerner et al. in press). If the effect of nanolites is significant, then they are likely a problem endemic to many, if not all, XANES determinations of sulfide-saturated liquids that were rapidly quenched, as well as liquids saturated with magnetite (DiGenova et al. 2018) or other Fe-bearing phases that nucleate nanolites.

Lastly, for completeness, the effect of pressure is explored as an explanation for the discrepancy between model calculations and measurements of experimental $Fe^{3+}/Fe^{T}$. The only model of $Fe^{3+}/Fe^{2+}$ in silicate glasses that includes a pressure term is Kress & Carmichael (1991), which indicates a modest decrease in $Fe^{3+}/Fe^{2+}$ with increasing pressure at constant T and $fO_2$. If pressure alone accounted for the differences between the calculated $Fe^{3+}/Fe^{2+}$ at one bar (which was used in the previous comparisons) and that measured in the melt inclusions, it would require an internal pressure of ~1.0 GPa. The internal pressures of the experimental melt inclusions based

on the $H_2O$ and $CO_2$ contents of the glasses are all less than 0.02 GPa. However, a significant fraction of the $CO_2$ contained in melt inclusions may be contained in the coexisting vapor bubble (e.g., Anderson & Brown 1993; Mironov et al. 2015; Wallace et al. 2015), and reconstructions of melt inclusion $CO_2$ by integrating contributions from both the melt and vapor have led to some extremely high estimates of $CO_2$ in Mauna Loa melt inclusions, up to 13,354 ppm when corrected for post-entrapment crystallization and an equation of state for $CO_2$ fluids (Tucker et al. 2019), although the median and mean $CO_2$ contents of the 137 inclusions reported in that study are 411 and 835 ppm, respectively, and only 7 inclusions had reconstructed $CO_2$ > 2000 ppm. Although the maximum pressures calculated based on these extremely high $CO_2$ contents are close to 0.5 GPa, the median $CO_2$ concentrations from the survey of unheated Mauna Loa melt inclusions imply trapping pressures closer to, or less than, 0.1 GPa. Additionally, reheating of melt inclusions will result in internal pressures that are lower than the original trapping pressure due to loss of $H_2O$ and thermoelastic deformation of the host olivine (Schiavi et al. 2016). Assuming a high estimate of 0.1 GPa internal P, the absolute difference between the $Fe^{3+}/Fe^{T}$ calculated at P and at 1 bar is ~0.01 at high $fO_2$ (FMQ+3 to FMQ+5) and <0.01 at or below FMQ, both of which are within the analytical uncertainties and not nearly enough to account for the discrepancies between the modeled and measured $Fe^{3+}/Fe^{T}$.

In summary, the available Fe oxybarometers that relate $fO_2$ and melt composition to $Fe^{3+}/Fe^{T}$ in silicate liquids do not agree with the $Fe^{3+}/Fe^{T}$ measured in experimental melt inclusions using XANES, based on the nominal $fO_2$ imposed by the furnace atmosphere. With the exception of O'Neill (2018), for the experiments at or below FMQ+2.7 the models predict higher $Fe^{3+}/Fe^{T}$ than that which was measured. It is unlikely that this discrepancy is due to a transient process during the experimental

equilibration of $fO_2$ across the host olivine. The higher internal pressure inside the melt inclusions accounts for some of the difference, however based on the one model that is calibrated for P ≥ 1 bar (Kress & Carmichael 1991) and the internal pressure of the heated melt inclusions, the effect of P imparts only a small (≤0.01 absolute) correction on the $Fe^{3+}/Fe^{T}$. Two possible explanations are preferred: (1) there is an effect of S on the $Fe^{3+}/Fe^{T}$, and (2) sulfide nanolites in the XANES analytical volume result in an apparently higher fraction of $Fe^{2+}$ than is actually present in the glasses. Explanation (1) is consistent with the fact that all the models were calibrated on S-free liquids, and the magnitude and direction of the effect observed is consistent with the unpublished data of Graz et al. (2007). The presence of a few volume percent nanolites cannot be ruled out; their presence or absence can be potentially verified using high resolution SEM imaging, Mössbauer spectroscopy (Rose-Koga et al. 2021), Raman spectroscopy (DiGenova et al. 2018), or transmission electron microscopy (DiGenova et al. 2020). The fact that the discrepancy between the models and XANES measurements is smaller for the more oxidizing experiments (Figure 15), which contain ~800 ppm S but which are sulfide-undersaturated, may indicate that explanation (2) is more viable. However, the fact that for only one experiment at FMQ-1, three of the models happen to conspire to give the right answer warrants further investigation, including time-series experiments and experiments run simultaneously with olivine-hosted melt inclusions and exposed S-free melts of the same or similar composition. Because many naturally quenched melts are undegassed, and/or saturated in sulfide or sulfate (sulfate nanolites would have the same effect on the apparent $Fe^{3+}/Fe^{T}$ as sulfide nanolites), it is important to evaluate whether the issues described herein are experimental, if they also pertain to Fe XANES analyses of natural glasses, and/or if they are due to not including the effects of S as a compositional parameter in Fe oxybarometers.

## 5.2 $S^{6+}/S^{Total}$ Contents of Natural and Experimental Fe-bearing Melt Inclusions

### 5.2.1 Effect of Fe oxybarometry models on the inferred $fO_2$ of the sulfide to sulfate transition

The speciation of S in silicate melts has been previously investigated as a function of oxygen fugacity, melt composition, and temperature in Fe-bearing melts (e.g., Carroll & Rutherford 1988; Jugo et al. 2010; Botcharnikov et al. 2011; Klimm et al. 2012; Nash et al. 2019), and it is widely accepted that the dominant forms of sulfur in basaltic melts are sulfide ($S^{2-}$) and sulfate ($S^{6+}$) species. The corresponding stoichiometry of sulfur redox equilibria (e.g., $S^{2-}_{liq} + \mathbf{2}O_2 \rightleftharpoons SO_4^{2-}$) means that it is more sensitive to changes in $fO_2$ than iron (e.g., $Fe^{2+} + ¼\ O_2 \rightleftharpoons Fe^{3+}O_{1.5}$), and so the transition between the reduced and oxidized forms of S occurs over a narrower $fO_2$ interval (Figure 18A). Note that although the thermodynamic variables of interest are the ratios $Fe^{3+}/Fe^{2+}$ and $S^{6+}/S^{2-}$, it is usually more convenient to express these as $Fe^{3+}/Fe^{Total}$ or $S^{6+}/S^{Total}$; using the simple ratios leads to infinite values in the oxidizing limit and using the logarithmic ratios leads to undefined values in the reducing limit, whereas fractions of the total are bounded between 0 and 1. The $S^{6+}/S^{Total}$ measured in experimental melt inclusions are plotted in Figure 18 at their nominal $fO_2$ (black squares) and are consistent with Jugo et al. (2010), however more experiments spanning the transitional $fO_2$ with intermediate $S^{6+}/S^{Total}$ are necessary. Due to the steepness of the Jugo et al. (2010) S valence sigmoid, which varies from all $S^{2-}$ to all $S^{6+}$ over a ~two order of magnitude $fO_2$ range, fitting experimental data to the curves in this transitional $fO_2$ region is not trivial and requires precise knowledge of the $fO_2$ (likely only realized in gas-mixing experiments) and the $S^{6+}/S^{T}$, or both the $Fe^{3+}/Fe^{T}$ and $S^{6+}/S^{T}$ of experimental glasses equilibrated at a known $fO_2$ (for which very limited data exist). If instead of a precisely determined $fO_2$ the $Fe^{3+}/Fe^{T}$ of the glasses are known, which is usually the case for natural glasses, the uncertainties associated with the choice of melt

**Figure 18**

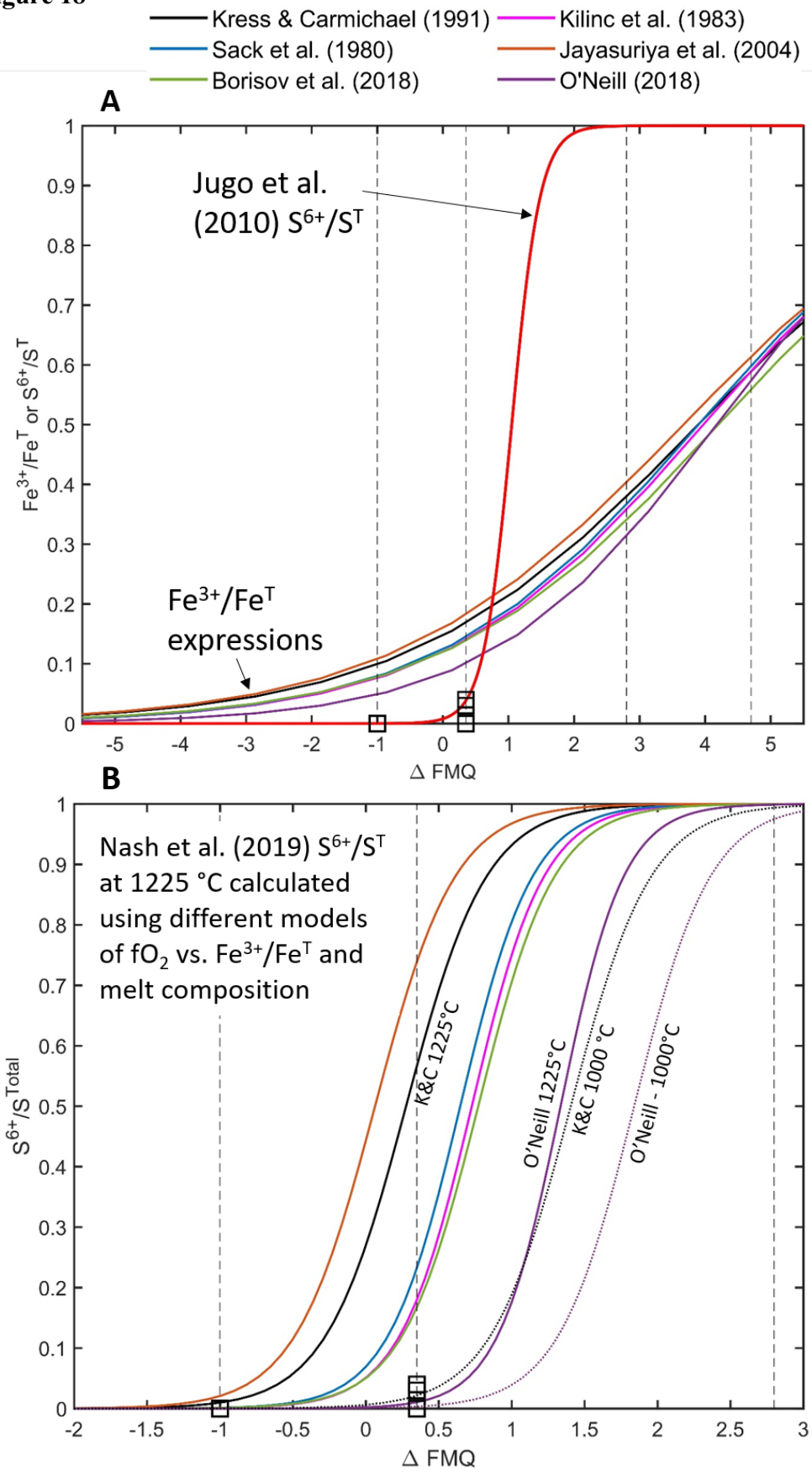


Figure caption is on the next page.

**Figure 18. (A)** $fO_2$ expressed as ΔFMQ versus models of either $Fe^{3+}/Fe^{T}$ or $S^{6+}/S^{T}$. The $Fe^{3+}/Fe^{T}$ expressions are based on six Fe oxybarometers: blue – Sack et al. 1980; pink – Kilinc et al. 1983; black – Kress & Carmichael 1991; orange – Jayasuriya et al. 2004; green – Borisov et al. 2018; purple – O'Neill et al. 2018. The red curve shows $S^{6+}/S^{T}$ from Jugo et al. 2010. The curves are calculated based on the melt composition of experimental inclusion SF1-2 at 1225 °C and 1 atm. Black open squares indicate S XANES measurements of $S^{6+}/S^{T}$ in experimental melt inclusions and are plotted at the nominal $fO_2$ of the experiments (dashed vertical lines). **(B)** Nash et al. (2019) relates $Fe^{3+}/Fe^{2+}$ to $S^{6+}/S^{2-}$ at a given T. The curves shown are calculated by converting $Fe^{3+}/Fe^{2+}$ to $fO_2$ using the six Fe oxybarometers, and then plotting the position of the 1225°C $S^{6+}/S^{T}$ curve using Nash et al. (2019) equation (11) as a function of $fO_2$, expressed as ΔFMQ. Note that the x-axis is zoomed in compared to panel **(A)**. The dotted black and purple curves show the 1000°C isotherms calculated using the Kress & Carmichael 1991 and O'Neill 2018 models, respectively.

Fe oxybarometer propagate into major uncertainties in the calculated $S^{6+}/S^{Total}$ (Figure 18A and 18B).

Nash et al. (2019) ran a series of 1 atm experiments at known $fO_2$ and $fS_2$, using both S XANES and the sulfide capacity method to determine S speciation in their experimental glasses, ultimately arriving at an equilibrium constant for equation (1) at 1300°C. The sulfide capacity method calculates the fraction of $S^{6+}$ as the difference between the logarithm of total S, $[S]_{Tot}$, measured in the glass and a line of constant sulfide capacity ($C_{S2-}$, O'Neill & Mavrogenes 2002), which is a composition-dependent term that satisfies: $\log [S^{2-}] = C_{S2-} + ½ \log (fS_2/fO_2)$, and $\log [S^{6+}] = \log[S]_{Tot} - \log[S^{2-}]$. In constructing their model, Nash et al. used the $S^{6+}/S^{2-}$ determined

by XANES for experiments run at $fO_2$ greater than FMQ+0.62, and the sulfide capacity method for experiments run at $fO_2$ less than FMQ+0.13, joining the two methods into one continuous dataset. They then used thermodynamic data from solid analogues to the melt species ($FeS + 8FeO_{1.5} \rightleftharpoons FeSO_4 + 8FeO$) in order to calculate the temperature-dependence of equation (1) (their equation 11) and found that, without fitting coefficients to the lower-T data, the expression accurately predicted the $Fe^{3+}/Fe^{2+}$ and $S^{6+}/S^{2-}$ measured in 1050 °C experiments from Jugo et al (2010) and Botcharnikov et al. (2011). Critically, the $Fe^{3+}/Fe^{2+}$ was not measured in any of these experiments; instead the Kress & Carmichael (1991) model was used to convert between the experimental $fO_2$ and $Fe^{3+}/Fe^{2+}$, which (along with T) is required to evaluate $S^{6+}/S^{2+}$ through equation (1) and Nash et al. (2019) equation (11). Although their approach is internally consistent (issues with the T-dependence are discussed next), using Nash et al. (2019) to calculate $S^{6+}/S^{T}$ means that the accuracy of the location of the S speciation sigmoid as a function of $fO_2$ is highly sensitive to the choice of Fe oxybarometer (O'Neill 2021). The magnitude of this uncertainty is illustrated in Figure 18B which shows that when using equation (11) from Nash et al. (2019), the $fO_2$ of the sulfide to sulfate transition (defined here as $S^{6+}/S^{T} = 0.50$) varies by about 1.4 orders of magnitude depending on the choice of Fe oxybarometer (recall that the transition itself occurs over ~2 orders of magnitude in $fO_2$). To make matters worse, the differences between the oxybarometers also depend on melt composition.

A consequence of this was likely expressed in my experiments. The choice of $fO_2$ = FMQ+0.35 was based in part on four XANES measurements of the $Fe^{3+}/Fe^{2+}$ of Papakōlea melt inclusions (0.17-0.20, Saper & Stolper 2020). Given their melt compositions and pre-eruptive temperatures the Kress & Carmichael (1991) model calculates an $fO_2$ of FMQ+0.18 to FMQ+0.48 with a mean of FMQ+0.33. Given T =

1225 °C and the $Fe^{3+}/Fe^{T}$ measured in the unheated Papakōlea inclusions, Nash et al. (2019) predicts $S^{6+}/S^{Total}$ of ~50%, which is much higher than the nearly sulfate-free inclusions that were equilibrated at FMQ+0.35 (Figure 14). Note that if the Kress & Carmichael (1991) model is applied to the XANES-determined $Fe^{3+}/Fe^{T}$ of the experimental inclusions equilibrated at FMQ+0.35, the calculated $fO_2$ is FMQ-0.55 to -0.14 (Figure 15B), corresponding to a calculated $S^{6+}/S^{T}$ on the Kress & Carmichael (1991) 1225°C isotherm in Figure 18B of ~0.05-0.17, which overlaps with the S XANES measurements of the FMQ+0.35 inclusions ($S^{6+}/S^{T}$ = 0-7% unscaled, or 0-15% scaled). For the $H_2O$ contents of the experimental (<0.053 wt%) and the natural (<0.27 wt%) melt inclusions, the effect of water on $S^{6+}/S^{2-}$ is likely to be negligible (unlike in the $H_2O$-rich, ~4 wt%, experimental glasses of Jugo et al. 2010 and Botcharnikov et al. 2011 used to validate the T-dependence of Nash et al. 2019 equation 11). Addition of $H_2O$ is expected to stabilize $S^{2-}$ species in the melt (O'Neill 2021). In designing the SF experiments, I had anticipated higher $S^{6+}$ contents, which are required to shift equation (1) towards the down-T direction predicted by Nash et al. (2011).

Therefore, extra care must be taken when applying models that relate $fO_2$ to $S^{6+}/S^{T}$; while Jugo et al. 2010 is independent of T and fits the limited experimental inclusion data well, it is only parameterized in terms of ΔFMQ and thus either requires precise knowledge of $fO_2$ or an Fe oxybarometer to convert between a measured $Fe^{3+}/Fe^{T}$ and $fO_2$. The Nash et al. (2019) model is internally consistent and has the benefit of not explicitly requiring conversion between $Fe^{3+}/Fe^{T}$ and $fO_2$, however because $Fe^{3+}/Fe^{T}$ was not measured in any of the glasses that went into calibrating their model, the location of the S sigmoid at 1300°C hinges on the conversion to $fO_2$ being accurate (O'Neill 2021), and neglects the fact that it will change with sufficient perturbations on melt composition (Kress & Carmichael 1991). This in turn affects the

coefficients used to fit the temperature-dependence as well as the equilibrium constants for Fe-S equilibria. This uncertainty was not quantified in Nash et al. (2019), who only pointed out that the two oxybarometers which are in closest agreement with Kress & Carmichael (1991) – Jayasuriya et al. 2004 and Sack et al. 1980 – "yield the same trend with similar coefficients of determination". Figure 18B shows that the $fO_2$ where $S^{6+}/S^T = 0.50$ predicted by Nash et al. (2019) spans a 0.6 order of magnitude range amongst these three models; including Kilinc et al. 1983, and the recent models of Borisov et al. (2018) and O'Neill (2018) increase the uncertainty of this transitional $fO_2$ to 1.3 orders of magnitude (Figure 18B).

This exercise emphasizes the need for more experimental data with accurate measurements of both T and $fO_2$ and where both Fe and S valences are measured using high-precision techniques such as XANES; as of this writing the only example of this are the melt inclusions reported in this chapter (the $fO_2$ of the Head et al. 2018 melt inclusions are not known directly). There is more abundant data with coupled Fe and S XANES measurements for natural glasses (de Moor et al. 2013; Brounce et al. 2017, Head et al. 2018; Lerner et al. 2020; Muth & Wallace 2021), however all of these require an Fe oxybarometer to calculate $fO_2$, and importantly, while magmatic T can be estimated from these samples, the cooling rates are not quantified or well-documented and as shown in the following section, this is another critical parameter for assessing whether high-T valence information for S and Fe in magmatic liquids is quenchable. At least for the 1 atm tube furnace experiments that are drop quenched into water, they experienced similar and rapid cooling rates and so can be compared directly to one another. All remaining data other than experiments similar to those described above require a transfer function to convert between $Fe^{3+}/Fe^T$ and $fO_2$, and until there is a clear consensus as to which of the Fe oxybarometers is the most accurate, any attempt to use

data with unknown $fO_2$ to accurately place the sulfide to sulfate transition sigmoid will be polluted by the uncertainties associated with those models.

### 5.2.2 The Temperature-Dependence of Fe-S electron transfer

For S- and Fe-bearing melts, the question of whether room T measurements of the ratios of both redox species are representative of that present at high T has been debated (Metrich et al. 2009), including the direction and magnitude of the T-dependence of reaction (1) and the kinetics of electron transfer (Nash et al. 2019). For example, using the strong T-dependence implied by Nash et al. (2019), in which $S^{6+}$ is reduced and $Fe^{2+}$ is oxidized with decreasing T, the experimental melt inclusion data at their nominal $fO_2$ can be brought into agreement with the Kress & Carmichael (1991) model by calculating $S^{6+}/S^T$ at ~1000 °C instead of 1225 °C (black dotted line in Figure 18B). A similar argument was used to explain the coupled Fe and S redox ratios measured in Kīlauean lavas (Brounce et al. 2017), which given Nash et al. (2019) indicates equilibration of Fe and S down to T ~ 993 °C, much lower than the pre-eruptive T of ~1200 °C.

The cooling rate experiments on melt inclusions were designed to address both the T-dependence and kinetics of Fe-S electron exchange at roughly constant bulk composition. For the inclusions homogenized at FMQ-1 and 1225 °C, all S was initially present as $S^{2-}$. The FMQ+0.35 experiments were at an $fO_2$ sufficiently close to the onset of measurable $S^{6+}$ in the melt that based on the small amount of data (one homogenized inclusion, SF11-5) it remains unclear whether there was initially some $S^{6+}$ present after 24 hr of homogenization for these experiments and prior to quenching. For the homogenized inclusion SF11-5, four out of five spectra show $S^{6+}/S^T$ indistinguishable from zero, whereas one spectrum has a minor sulfate peak indicating $S^{6+}/S^T$ = 0.06-0.12% (unscaled vs. scaled), which is likely due to contamination by organic S. Thus for the experiments with the maximum cooling rate, either there was little to no $S^{6+}$

present prior to quench, or, the small amount that was present was entirely converted to $S^{2-}$ during quenching via equation (1) and the proposed down-T direction of Nash et al. (2019). If the T-dependence of equation (1) is strong and the kinetics of electron transfer are sufficiently rapid that even for the drop-quenched experiments (~2000 °C/min) some $S^{6+}$ is converted to $Fe^{3+}$, this would pose a massive challenge for applying room T measurements of S and Fe oxidation states to higher T processes. In the following section an example using natural melt inclusions is presented where the cooling rates are known, and kinetics can be likely be ignored, to demonstrate that the T-dependence cannot be as strong as that implied by Nash et al. (2019), and may in fact proceed in the opposite direction (Metrich et al. 2009), which would be consistent with the temperature-dependence of Cr-Fe electron exchange (Berry et al. 2003).

Three additional S XANES measurements of inclusions from the SF cooling-rate experiments (homogenized at 1225 °C for 24 hr at FMQ+0.35) give similarly inconclusive results to the drop-quenched experiments; SF8-3 was rapidly cooled to 1000 °C and has $S^{6+}/S^{T}$ indistinguishable from zero, SF3-2 was slowly cooled and quenched at 1150 °C with $S^{6+}/S^{T}$ = 0.04-0.09, and SF4-3 had the most prolonged cooling history and was quenched at 1000 °C with $S^{6+}/S^{T}$ = 0. Note that Nash et al. (2019) and Kress & Carmichael (1991) predict $S^{6+}/S^{T}$ = 0.24 at 1150 °C at the nominal experimental $fO_2$ of FMQ+0.35. Given the measured $Fe^{3+}/Fe^{T}$ of experiment SF3-2 (0.137) Nash et al. predict $S^{6+}/S^{T}$ = 0.06 at 1150 °C, which is consistent with the measured value. These experiments cannot rule out the Nash et al. (2019) T-dependence because it cannot be conclusively determined whether any $S^{6+}$ was present prior to cooling; if so it is likely to have been <10%. Although 10% sulfate may seem inconsequential, if it was quantitatively reduced to sulfide during quenching or cooling it would lead to measurable changes in the $Fe^{3+}/Fe^{T}$. For example, for a melt with 9 wt% FeO* (≈ 7 wt%

elemental Fe), 1000 ppm S, of which with 10% is $S^{6+}$, and an initial $Fe^{3+}/Fe^{T}$ = 0.11, conversion of all the $S^{6+}$ to generate $Fe^{3+}$ would result in a final $Fe^{3+}/Fe^{T}$ = 0.13). The two slowly cooled inclusions have higher $Fe^{3+}/Fe^{T}$ (0.129 SF4-3, 0.137 SF3-2) than the drop quenched (0.103 SF11-5, 0.118 SF1-2) and rapidly cooled (0.108) inclusions (Figure 13), however the data are too sparse and at too low $S^{6+}/S^{T}$ to draw any definitive conclusions. If cooling proceeds faster than the $fO_2$ can equilibrate across the host olivine during cooling, as would be expected for these experiments (Bucholz et al. 2013), then crystallization of olivine on the inclusion wall will independently lead to an increase in the $Fe^{3+}/Fe^{T}$ in the inclusion liquid. For experiment SF4-3, olivine crystallization from 1225°C to 1000°C would lead to ~7% volume decrease of the ~150 μm diameter inclusion (Saper & Stolper 2020), resulting in an absolute increase in $Fe^{3+}/Fe^{T}$ of 0.007 (for a melt with initially 11% $Fe^{3+}$); the effect of olivine subtraction is comparable to the analytical uncertainty in the Fe XANES measurements. Additional experiments at slightly higher $fO_2$ conditions, with homogenized melts containing unambiguous amounts of $S^{6+}$, are required to further test the results of Nash et al. (2019).

### 5.2.3 The Effect of bulk Fe/S on cooling paths in redox couple space

An important consequence of Nash et al. (2019) equation (11) is that the path in $Fe^{3+}/Fe^{2+}$ vs. $S^{6+}/S^{2-}$ space during cooling must be dependent on the Fe/S ratio of the melt. It has been argued that the position of the S sigmoid vs. $fO_2$ and the inferred T-dependence may be relatively insensitive to differences in bulk composition (Jugo et al. 2010, Nash et al. 2019), however Fe-S redox equilibria (Klimm et al. 2012), and the oxidizing potential of $S^{6+}$ to convert $Fe^{2+}$ into $Fe^{3+}$, must depend on the bulk S contents; if there is only 100 ppm S to begin with, the oxidant pool will be exhausted much more quickly per decrement of cooling than if there is initially 1000 ppm S, and likewise, as the Fe/S ratio decreases the oxidation potential of sulfate per mole per degree °C becomes stronger.

The effect of bulk Fe/S on the redox equilibria is illustrated using a simple toy model that is based solely on the constraints of mass and charge balance and the T-dependence of Nash et al. (2019) equation (11) (Figure 19). The black diagonal lines in Figure 19 are isotherms calculated using Nash et al. (2019) equation (11), which are parallel with a positive slope of 8 in $Fe^{3+}/Fe^{2+}$ vs. $S^{6+}/S^{2-}$ logratio space. Consider a melt with 10 wt% FeO* and an initial $Fe^{3+}/Fe^{T} = 0.185$ held initially at 1200 °C; using the SF1-2 inclusion composition and Kress & Carmichael (1991) this corresponds to an $fO_2$ of FMQ+0.58. Each red curve shows the reaction progress of equation (1) during cooling as a function of the molar Fe/S ratio in the melt; note that for sulfide-saturated Papakōlea melt inclusions (e.g. SF1-2) Fe/S ~ 45 and for degassed melt inclusions Fe/S 195-290 (e.g., HIGS14 and HIGS21). At various places along the red curves that show the reaction progress during cooling, a black X symbol denotes the $fO_2$ (ΔFMQ, Kress & Carmichael (1991)) for a given $Fe^{3+}/Fe^{2+}$ in the melt. Thus, two melts with initially the same $fO_2$, $Fe^{3+}/Fe^{2+}$, and $S^{6+}/S^{2-}$ can end up with different $S^{6+}/S^{2-}$ at the same $fO_2$ when cooled to different T, solely due to having different bulk Fe/S. This composition-dependent effect challenges the conclusions of Nash et al. (2019), whose equation (11) predicts a unique value for $S^{6+}/S^{2-}$ for a given T and $Fe^{3+}/Fe^{2+}$. For closed systems the effect of the bulk Fe/S is relatively easy to model, however in open systems that experience S degassing, crystallization of Fe-oxides, and any other process that fractionates Fe/S during cooling, resolving this issue becomes complicated (Klimm et al. 2012). This potentially includes the separation (and dissolution) of sulfide and sulfate phases from the melt, and in the case of melt inclusions, exchange with the trapped vapor bubble. In the following section, I show (based on a set of natural melt inclusions cooled at different rates) that this issue may be rendered moot if the T-dependence is much smaller than that found by Nash et al. (2019).

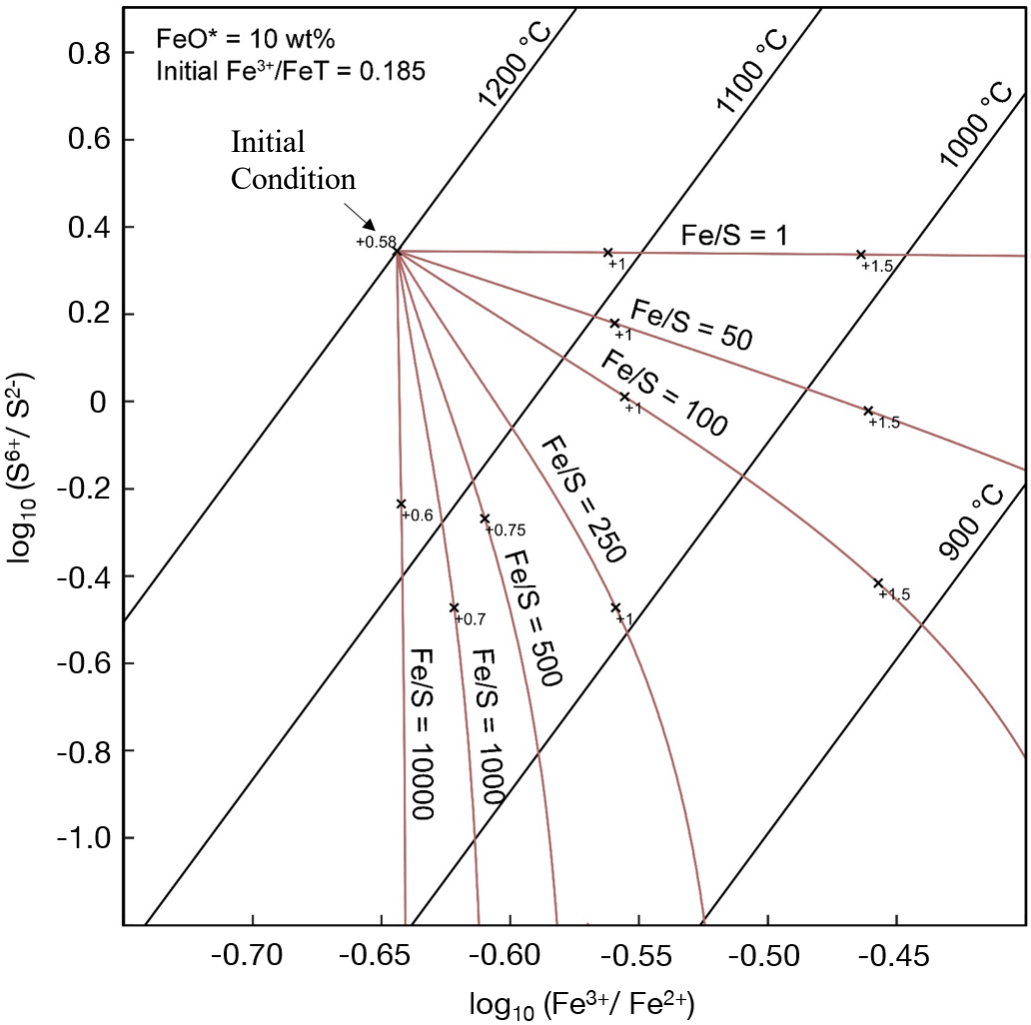


**Figure 19.** Calculation of the reaction progress of the S-Fe electron transfer equilibrium given by Nash et al. 2019 as a function of the bulk Fe/S ratio. The diagonal black lines are isotherms calculated using Nash et al. 2019 eq. 11, and are parallel with a slope of 8. The initial condition for the calculation is a melt at 1200 °C, with 10 wt% FeO* and an initial $Fe^{3+}/Fe^{T} = 0.185$, which according to Kress & Carmichael 1991 corresponds to an $fO_2$ of FMQ+0.58, given the glass composition of inclusion SF1-2. Each red curve shows the progress of the reaction $S^{6+} + 8Fe^{2+} \rightleftharpoons S^{2-} + 8Fe^{3+}$, constrained by mass balance and by Nash et al. (2019), corresponding to a melt with molar $Fe^{T}/S$ ranging from 1 to 10,000. The X marks along each red curve indicate the $fO_2$ (ΔFMQ) at a given $Fe^{3+}/Fe^{2+}$ according to Kress & Carmichael 1991. The figure shows that two melts with initially the same $fO_2$, $Fe^{3+}/Fe^{2+}$, and $S^{6+}/S^{2-}$, but different Fe/S, will end up with different $S^{6+}/S^{2-}$ at the same $fO_2$ if cooled to different T.

## 5.3 Using a "Natural Experiment" to Assess the T-dependence and Kinetics of Fe-S Electron Transfer

Two unheated melt inclusions from Papakōlea, Hawai'i provide a natural case study that can be used to test the predictions of Nash et al (2019) on the T-dependence of the Fe-S electron transfer reaction. Chemical zonation across melt inclusions can be used to accurately quantify syneruptive cooling rates (Newcombe et al. 2014; Saper & Stolper 2020) and the experiments described in Chapter 1 were calibrated using Papakōlea melt inclusions as starting materials and so the cooling rates calculated for these samples are likely to be quite accurate (<10% relative). Figure 20 shows microprobe measurements of MgO and CaO wt% profiles across unheated inclusions HIGS11 and HIGS14, for which both S and Fe XANES data were collected. HIGS11 has a broad central plateau in MgO at ~7.1 wt% and a CaO profile that is concave up, indicative of rapid cooling (Saper & Stolper 2020); applying the diffusion model of Saper & Stolper (2020) gives a cooling rate of ~8000 °C/hr (best-fit model is the light blue curve in Figure 20A). In contrast, HIGS14 is the melt inclusion with the lowest cooling rate calculated from Papakōlea, ~55 °C/hr, has low central MgO contents of 3.6 wt% and the liquid immediately adjacent to the olivine on the inclusion wall has MgO ~1.6-1.7 wt% (Figure 20B). The concave down CaO profile is another indication of very slowly cooled melt inclusions (Saper & Stolper 2020). The liquid immediately interior to the inclusion wall is inferred to be in local equilibrium with the olivine crystallizing on the inclusion walls. If true, the low MgO contents in the liquid in contact with olivine in HIGS14 imply that this inclusion was cooling slowly from ~1160 °C down to T as low as ~850 °C while crystallizing or maintaining Fe/Mg equilibrium with olivine mantling the inclusion walls. Both inclusions have ~0.20 wt% $H_2O$ (Table 1).

**Figure 20**

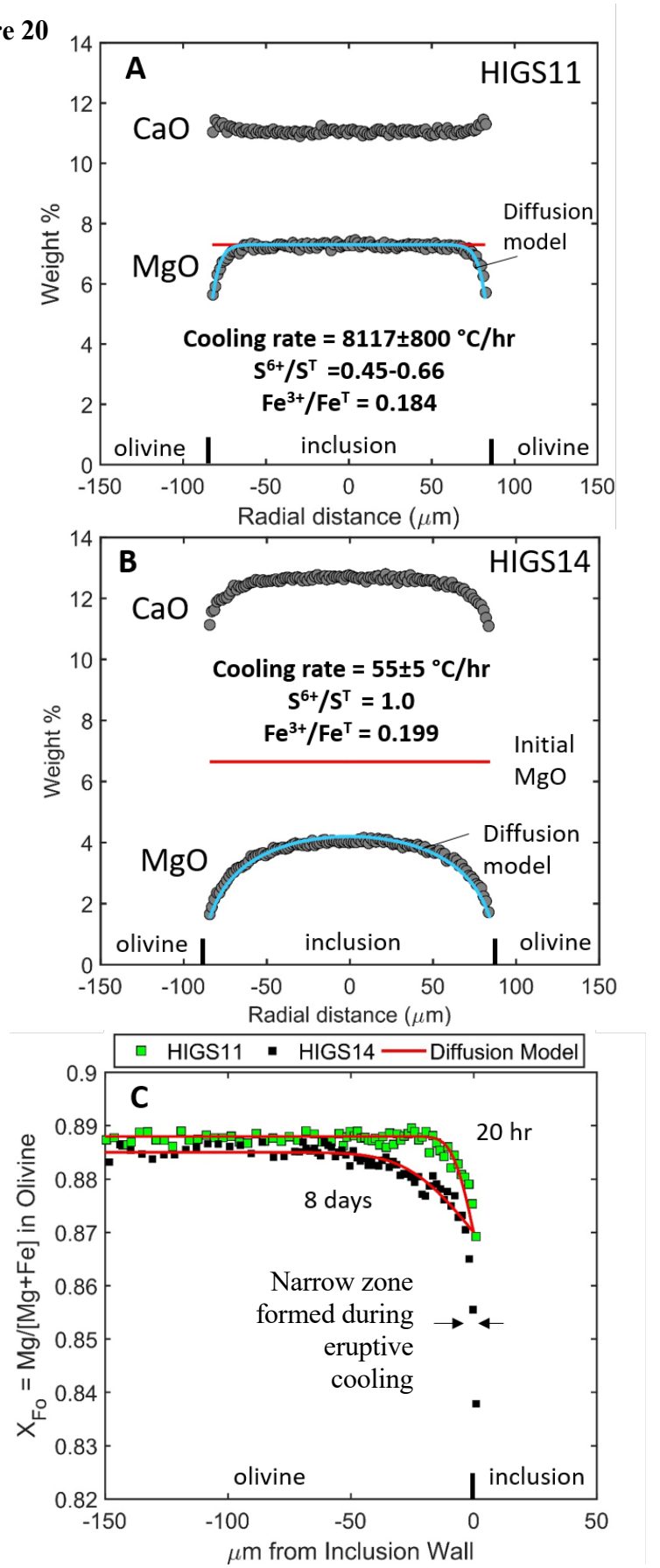


Figure caption is on the next page.

**Figure 20. (A)** and **(B)**: Microprobe traverses of CaO and MgO wt% across two unheated melt inclusions, HIGS11 and HIGS14, from Papakōlea, Mauna Loa, Hawai‘i. The x-axes are radial distance in μm from the inclusion centers. The horizontal red lines show the initial MgO used in diffusion modelling (Saper & Stolper 2020), and the blue curves are the resulting best-fit MgO profiles where cooling rate was the only adjustable parameter. The cooling rate for HIGS11 is estimated at 8117±800°C/hr, and for HIGS14 55±5°C/hr. Short vertical lines indicate the boundaries between olivines and inclusions. **(C)** Zoning in $X_{Fo}$ = Mg/[Mg+Fe] in olivines immediately surrounding the melt inclusions depicted in **(A)** and **(B)**. Green squares – HIGS11; black square – HIGS14. The red curves are simple diffusion models based on initially homogeneous olivines with $X_{Fo}$ = 88.8 (HIGS11) and 88.5 (HIGS14) that were instantaneously cooled to 1225 °C and held isothermally with a new boundary condition of $X_{Fo}$ = 88.7 at the inclusion wall. Fe-Mg interdiffusion was estimated at 1225 °C, $fO_2$ = FMQ, and $X_{Fo}$ = 0.13 to be ~1e-16 $m^2$/sec (Dohmen & Chakraborty 2007). The red curves show best-fit diffusion profiles for HIGS11 (20 hr at 1225 °C) and HIGS14 (8 days at 1225 °C).

The far-field host olivine compositions of the two inclusions are similar, Fo = 88.77 (HIGS11) and 88.47 (HIGS14), and profiles of $X_{Fo}$ = Mg/[Mg+Fe] in the olivines immediately adjacent to the melt inclusions show evidence for cooling and diffusive equilibration with changing melt compositions during a stage of cooling between entrapment and preceding eruption (Figure 20C, e.g., Gaetani 2000; Saper & Stolper 2020). The width of this Fe/Mg zone in olivine around the inclusions is larger in HIGS14, extending ~60 μm from the inclusion wall versus ~20 μm in HIGS11. HIGS14 also has a narrow zone of more Fe-rich olivine, which is interpreted to have formed during the syneruptive cooling stage that produced the MgO profile in the coexisting

melt inclusion. A simple isothermal diffusion model was fit to the $X_{Fo}$ profiles to get a rough minimum estimate of the residence times of the olivines at T less than or equal to their trapping T but prior to eruption and relatively rapid cooling through the glass transition. The far-field olivine contents ($X_{Fo}$ = 0.885 and 0.888) imply trapping temperatures of 1250-1260 °C (calculated using MELTS, Ghiorso & Sack 1995); for diffusion modeling it was assumed that T instantaneously decreased to 1225 °C where a new equilibrium olivine composition of $X_{Fo}$ = 0.87 was established as a boundary condition (diffusion in the liquid is ignored and both phases are considered semi-infinite with a planar interface). Given an Fe-Mg interdiffusion coefficient calculated at 1225°C, $X_{Fo}$ = 0.87, and $fO_2$ = FMQ (Dohmen & Chakraborty 2007), the HIGS11 $X_{Fo}$ profile is fit after ~20 hr at 1225 °C whereas the HIGS14 profile is fit after ~8 days at 1225 °C. The residence time of the olivines at the trapping T of the melt inclusions is unconstrained and is possibly >500 yr (e.g., Cooper et al. 2001), but the zoning around the melt inclusions implies a relatively short interval between a thermal perturbation that generated the 20-60 μm wide zones in the olivines and an increase in cooling rate associated with eruption, generating the narrow zone of Fe-rich olivine in HIGS14 and the diffusion profiles observed across both melt inclusions. It is likely that the olivines experienced more complex thermal histories as these model results are only consistent with the data but not unique, however the simple model illustrates that the two $X_{Fo}$ can be well-described by an isothermal model and at least two cooling stages between entrapment and eruption. Because the T implied by the MgO plateau across HIGS11 is 1175 °C, there was likely at least one additional stage of cooling between 1225 °C and 1175 °C that was of short enough duration to not perturb the pre-existing zone in the olivine but sufficiently long (or cooled at a low enough rate) such that the inclusion

remained homogeneous (on the order of 1-2 hours for the slowest diffusing species in the melt, e.g., $Al_2O_3$; Guo & Zhang 2018).

Despite the slightly different thermal histories just prior to eruption, these two melt inclusions from the same locality likely had very similar chemical and $fO_2$ histories and so differ mainly in their cooling rates during eruption. Note that due to sample handling issues, S analyses were not performed on HIGS11, although optical microscope images revealed that it, as well as HIGS14 (S = 154 ppm), contained no sulfide blebs. In addition, it is worth noting that this natural experiment of slow and rapid cooling melts would be challenging to replicate in matrix glasses (or in wire-loop experiments) cooled at low rates, as they would be expected to crystallize other phases with progressive cooling, whereas olivine-hosted melt inclusions can cool metastably down to low T while heterogeneously precipitating only olivine on the inclusion walls (e.g., Roedder 1984; Saper & Stolper 2020). Therefore, these two melt inclusions represent a key test of the T-dependence of Nash et al. (2019); if the T-dependence is strong and the kinetics are fast then differences in the coupled $Fe^{3+}/Fe^{2+}$ and $S^{6+}/S^{2-}$ ratios measured in the melt inclusions should reflect their different cooling rates and closure temperatures for Fe-S electron transfer. In other words, Nash et al. (2019) predicts that the oxidation state of the rapidly quenched HIGS11 may be representative of the ratios present at high-T, whereas HIGS14 cooled slowly enough to unambiguously maintain electronic equilibrium between Fe and S and would be expected to have all of its $S^{6+}$ reduced to $S^{2-}$ during cooling. Alternatively, if the kinetics of Fe-S electron equilibria are sufficiently fast that even at cooling rates of 8000°C/hr the low-T ratios are "locked in" near (or potentially below) the glass transition T, then both inclusions, having similar compositions and likely similar initial $fO_2$ should have essentially the same $S^{6+}/S^{2-}$ quenched in their glasses.

The two inclusions have $Fe^{3+}/Fe^{T}$ that overlap within 1σ analytical uncertainty – HIGS11 = 0.184 and HIGS14 = 0.199 – if the difference between the two values is real then it can be accounted for by the 8-9% olivine crystallization that accompanied the slow cooling of HIGS14. Critically, both inclusions have an unambiguously high fraction of $S^{6+}$ present; for HIGS11 $S^{6+}/S^{T}$ = 0.45-0.66 and HIGS14 contains no measurable sulfide, $S^{6+}/S^{T}$ indistinguishable from unity (Figure 14). The slightly lower $Fe^{3+}/Fe^{T}$ in HIGS11 indicates that these two inclusions populate a portion of the upper limb of the $fO_2$ vs. S sigmoid and that the $fO_2$ recorded by HIGS14 is close to that in which sulfide is wholly unstable in these melts. The T-dependence of Nash et al. (2019) predicts that during cooling $S^{6+}$ will be consumed in order to maintain equilibrium with $Fe^{2+}$ and $Fe^{3+}$ in the liquid; for a closed system initially at 1225 °C and $Fe^{3+}/Fe^{T}$ = 0.20, the model predicts that at 1100 °C $S^{6+}/S^{T}$ = 0.46, by 1000 °C the $S^{6+}/S^{T}$ = 0.11, and by 900 °C the $S^{6+}/S^{T}$ < 0.02 (Figure 18B). This is in stark disagreement with the $S^{6+}/S^{T}$ = 1.0 measured in inclusion HIGS14 which was slowly cooling down to low T (<900 °C). Note that, based on the composition at the inclusion center, HIGS14 has an Fe/S ratio of ~195, and if S was conserved in the melt inclusion during cooling (154 ppm) this ratio was likely to be even higher at its pre-eruptive T due to higher FeO* in the liquid. Therefore, if the T-dependence of Nash et al. (2019) were valid then any $S^{6+}$ present initially in the melt inclusion would have been fully reduced to $S^{2-}$ by 900 °C (Figure 19) and yet this is clearly not the case.

Although limited data exist for the kinetics of Fe-S electron exchange, it is likely to be extremely rapid in melts; in-situ XANES spectroscopy of Cr valence in Fe-bearing melts showed that $Cr^{2+}$ cannot be quenched, and oxidizes to $Cr^{3+}$ rapidly (Berry et al. 2003). In fact, this concern of rapid equilibration during cooling is the main basis for considering whether the high-T oxidation states of S and Fe can be preserved at all. Thus

it is highly unlikely that the sulfate-dominated melt in inclusion HIGS14 represents an inability for the kinetics of electron exchange to keep up with the thermodynamic relationship of equation (1) (or Nash et al. (2019) eq. 11) during cooling. If the kinetics were that sluggish, then quench effects could be ignored entirely. Instead, if the calculated low cooling rate and low T of olivine-melt equilibration recorded in HIGS14 are both accurate, the 154 ppm of S present as $S^{6+}$ is incompatible with Nash et al. (2019) equation (11).

One possibility is that that the T-dependence of the equation (1) is much weaker than that implied in Nash et al. (2019) eq. 11. This was the conclusion of O'Neill (2021) who showed that an expression based on equilibrium constants for $FeO + ¼ O_2 = FeO_{1.5}$ and Ca, Fe, Mg, and Na sulfide-sulfate equilibria (e.g., $CaS + 2O_2 \rightleftharpoons CaSO_4$, etc.) results in a T-dependence that is a factor of five smaller than Nash et al. (2019). The other explanation is that the down-T direction of equation (1) proceeds opposite to that shown by Nash et al. (2019) (i.e., the isotherms in Figure 19 have slopes of -8) by converting $S^{2-}$ to $S^{6+}$ and decreasing $Fe^{3+}/Fe^{2+}$ with cooling. Either of these two explanations are consistent with the S XANES measurements of HIGS14. In the case of little to no T-dependence, the inclusion simply represents a melt inclusion that retained its high-T sulfate and was slightly oxidized by olivine crystallization during cooling. If, instead, the T-dependence leads to Fe reduction and the inclusion initially had mixed $S^{6+}/S^{2-}$, then all of the sulfide initially present in the inclusion was oxidized to sulfate during cooling.

More experimental data on the kinetics and temperature-dependence of this reaction are necessary, including those described previously on melt inclusions at slightly higher $fO_2$, in order to verify that there is no significant effect of quench rate on the measured ratios $S^{6+}/S^{2-}$ and $Fe^{3+}/Fe^{2+}$. However, the case study of two natural melt

inclusions from Papakōlea demonstrates that the Fe-S electron transfer is either not strongly temperature-dependent or proceeds in the same direction as Cr-Fe electron exchange during cooling (Berry et al. 2003), where $S^{2-}$ is oxidized to $S^{6+}$. With a weak T-dependence, even if the kinetics of exchange are rapid, the ratios measured at room temperature are likely to be indicative of that above the glass transition temperature. In addition to experiments on the kinetics of rapid quenching from a liquid state, experiments run at slightly lower T than the glass transition are also desirable to see assess the role of subsolidus re-equilibration.

### 5.4 Comparison to Matrix Glasses and Melt Inclusions from Hawai‘i

In this final section, the systematics of S, FeO, and $Fe^{3+}/Fe^{T}$ are briefly compared for available literature data on Hawaiian whole rocks, glasses, and melt inclusions (Figure 21). In addition to the Papakōlea melt inclusions (Mauna Loa MI, large dark gray stars) described above, new previously unpublished data on glasses from Ko`olau are presented (red circles). These glasses were analyzed for H, C, and S using SIMS and for $Fe^{3+}/Fe^{T}$ using XANES by Dr. M. Peterson; the three measurements at high S (>300 ppm) contents from this dataset were found to be overestimated due an issue with the calibration curve used and so they were reanalyzed for S using the multicollector microprobe technique described in section 3.2, as well as for their major and minor element concentrations. Mauna Loa melt inclusions that were reheated to 1250°C (Hauri 2002) are excluded from this figure – they have systematically low FeO* (average 6.9 wt%) which is likely due to overheating relative to the temperature at which the melt inclusions were trapped, leading to olivine dissolution (Gaetani et al. 2000, Danyushevsky et al. 2002). Figure 21A shows the FeO* versus S contents of Hawaiian glasses and whole rocks; the dashed black curve is a fit to sulfide-saturated MORB data from Mathez (1976) and the red curve is the SCSS using the model and synthetic Tholeiite PAL composition described in O’Neill & Mavrogenes (2002), calculated as a

**Figure 21A**

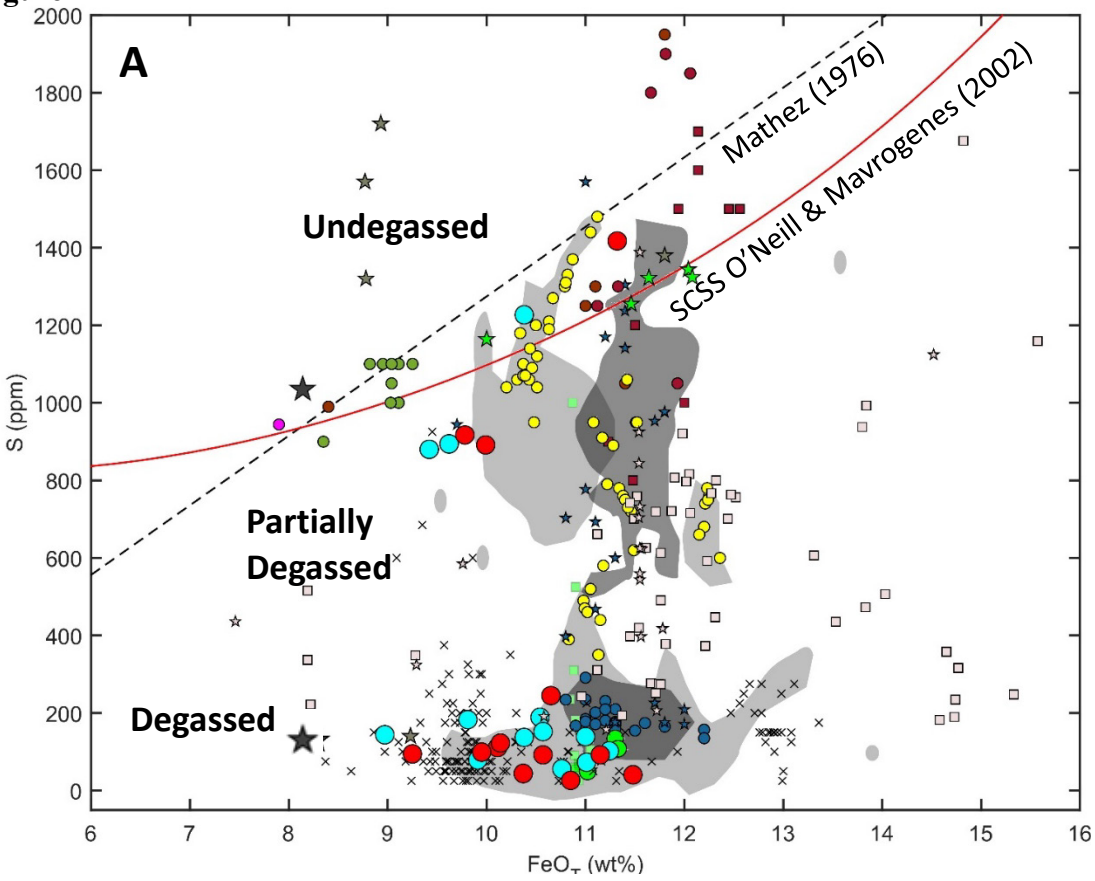


Mauna Loa MI (Saper & Stolper 2020)
Mauna Loa MI (Gaetani et al. 2012)
Mauna Loa WR (Rhodes & Vollinger 2005)
Koolau Glass (new data)
Koolau Glasses (Norman & Garcia 2004)
Mauna Kea (Brounce et al. 2017)
Kilauea (Moussallam et al. 2016)
Kilauea MI (Moussallam et al. 2016)
Kilauea (Lerner et al. 2002)
Kilauea MI (Lerner et al. 2002)
Kilauea Iki MI (Helz et al. 2016)
Kilauea Iki Matrix Glass (Helz et al. 2016)
Loihi Pillow Glass (Byers et al. 1985)
Loihi Seamount (Wallace & Carmichael 1992)
Lamont Seamount (Wallace & Carmichael 1992)
Hyaloclastites Oahu (Shinozaki et al. 2002)
Pillow Glass Oahu (Shinozaki et al. 2002)
High $SiO_2$ Low $SiO_2$ HSDP2 (Seaman et al. 2004)

Figure caption is on the next page.

**Figure 21B**

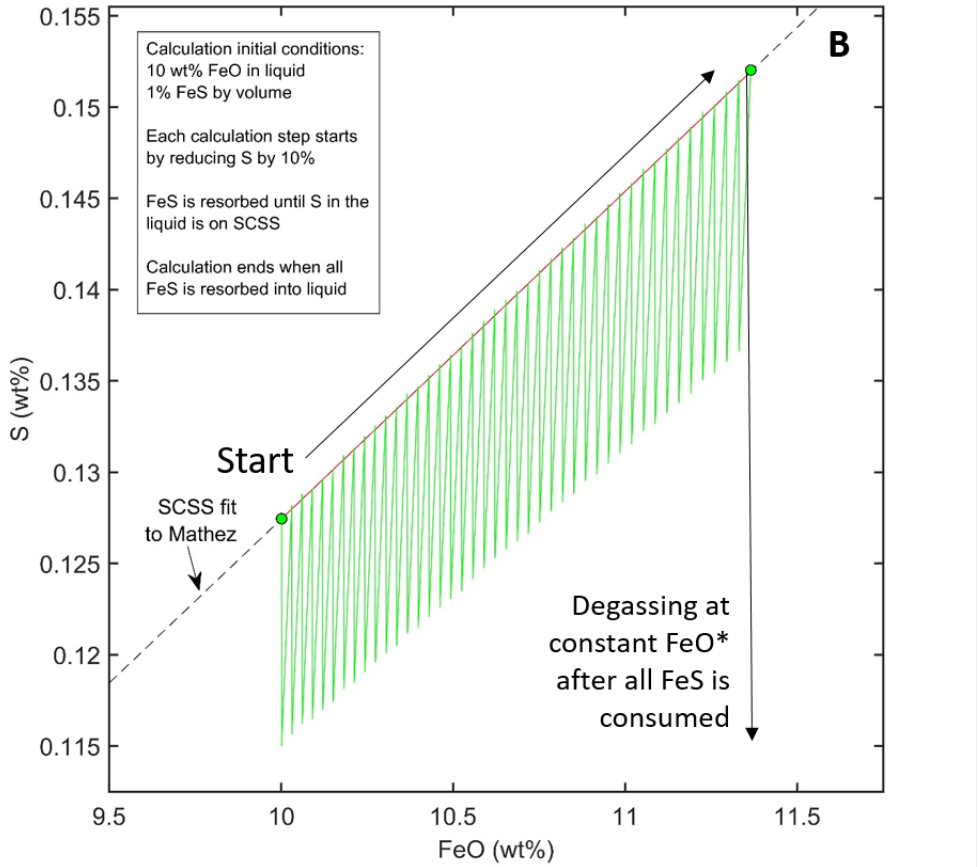


**Figure 21. (A)** Compilation of FeO* vs. S (ppm) for Hawaiian whole rocks, glasses, and melt inclusions (star symbols). The dashed black line shows a fit to sulfide-saturated MORB data from Mathez (1976); the red curve is the calculated sulfur contents and sulfide saturation (SCSS) from O'Neill & Mavrogenes (2002), assuming their synthetic PAL tholeiitic composition. The reader is referred to the figure legend for the symbology – it is also listed at the end of this figure caption. **(B)** Simple model calculation for the effect of sulfide resorption in actively degassing melts. The calculation starts at 10 wt% FeO in the liquid and 1 vol% FeS ("Start"), and is fixed at sulfide-saturation on the line representing the fit to the Mathez (1976) sulfide-saturated MORB data. Sulfur is then decreased in the melt, and FeS is resorbed until sulfide-saturation is reached, and this process continues until all of the sulfide has been exhausted, after which the melt degasses at constant FeO*****. ***Symbology and references for (A)*** *MI = melt inclusions:* Large black stars – Mauna Loa MI, Saper & Stolper 2020; gray stars – Mauna Loa MI, Gaetani et al. 2012); green squares – Mauna Loa whole rock, Rhodes & Vollinger 2005; red circles – Ko'olau glass, new data; cyan circles – Ko'olau glasses, Norman & Garcia 2004; yellow circles – Brounce et al. 2017; dark blue circles – Kilauea glasses, Moussallam et al. 2016; dark blue stars – Kilauea MI, Moussallam et al. 2016; pale pink squares – Kilauea, Lerner et al. 2021; pale pink stars – Kilauea, Lerner et al. 2021; green circles – Kilauea Iki, Helz et al. 2016; green stars – Kilauea Iki, Helz et al. 2016; maroon squares – Loihi pillow glasses, Byers et al. 1985; maroon circles – Loihi seamount glasses, Wallace & Carmichael 1992; dark green circles – Lamont seamount glasses, Wallace & Carmichael 1992; X symbols – hyaloclastites in submarine dredges off Oahu, Shinozaki et al. 2002; magenta circles – submarine pillow glasses off of Oahu, Shinozaki et al. (2002); light gray field – high $SiO_2$ HSDP-2 glasses (Hawaii Science Drilling Project) Seaman et al. 2004; dark gray field – low $SiO_2$ HSDP-2 glasses, Seaman et al. 2004.

function of FeO*, and assuming the activity of FeS in the sulfide phase equals unity. More complex parameterizations of SCSS exist (e.g., Smythe et al. 2017) that take into account melt $H_2O$, as well as the lower activity of FeS in the sulfide phase due to dissolved Cu, Ni, Zn, and oxygen; however, the Hawaiian melts have relatively low $H_2O$ contents (up to 1 wt%, Figure 22), and the transition-metal contents of most of these glasses have not been determined and they vary by factors of 2-4x in Hawaiian melts (Supplementary Figure 1). The data can be roughly grouped into three categories: degassed, partially degassed, and undegassed. The degassed melts have low S (≤ ~400 ppm), whereas the undegassed melts have S ≥ ~700 ppm, with partially degassed melts having intermediate S contents. The presence or absence of a sulfide phase is typically not reported in these studies, however many of the high-S undegassed liquids are likely sulfide-saturated, which is consistent with the detailed petrographic study of Mauna Loa melt inclusions described earlier, as well as Kīlauea Iki melt inclusions (Helz et al. 2016) where sulfides were identified within melt inclusions and included in olivines. The observation that olivines from Mauna Loa contain melt inclusions that are both sulfide-saturated and sulfide-undersaturated (Figure 4F) indicates that at Papakōlea olivine crystallization was coeval with sulfur degassing from the melt. Post-entrapment processes have been invoked to explain the presence of sulfides in Hawaiian melt inclusions (e.g. Lerner et al. 2021), and while that may be the case, it cannot explain the presence of both sulfur-saturated and -undersaturated melt inclusions of identical major and minor element composition contained within the same olivine (e.g., the two melt inclusions 100 μm from each other in Figure 4E).

Note that when comparing between undegassed and degassed melts from the same locality, there is a weak correlation suggesting that the degassed melts have higher FeO* than those that are undegassed. This can be seen most clearly in the Brounce et al.

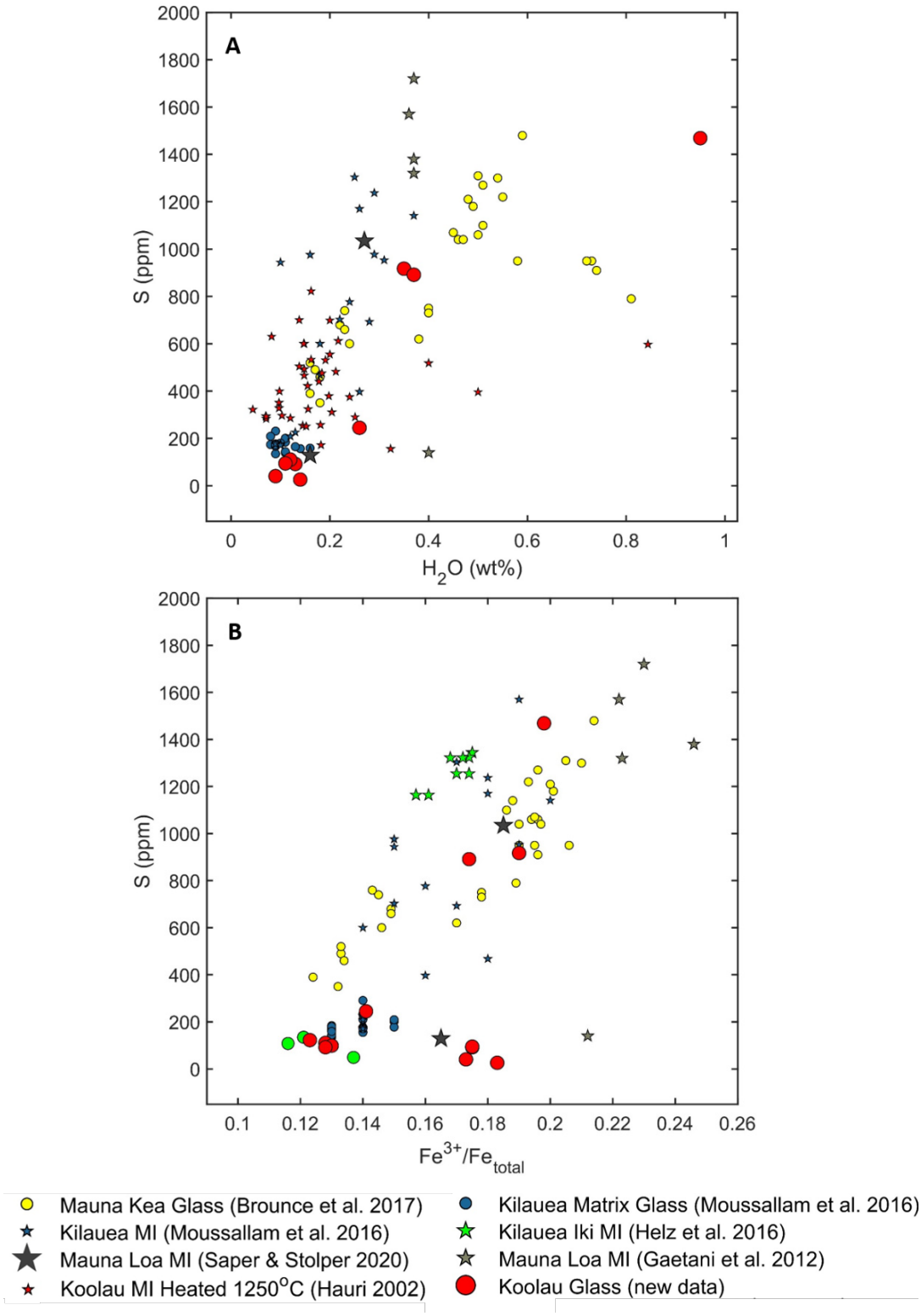


**Figure 22. (A)** $H_2O$ (wt%) vs. S (ppm) in Hawaiian glasses. **(B)** $Fe^{3+}/Fe^{T}$ determined using XANES vs. S (ppm). Symbology same as in Figure 21.

(2017) data from Mauna Kea (yellow circles), in the Ko`olau data (blue and red circles), and in the Kīlauea data from Lerner et al. (2021) (pale squares and stars). Although this warrants further detailed investigation – including verifying the presence or absence of sulfides in the undegassed melts – it is consistent with dissolution of FeS during degassing of S. Due to the slope of the SCSS in this space, S degassing leads to the somewhat counterintuitive result that during initial degassing when there is still FeS present in the liquids, both the FeO* and S contents of the liquids will increase until all of the FeS consumed, after which the S contents of the now sulfide-undersaturated melt decreases at constant FeO*. A two-step quantitative toy model was developed to illustrate this process (Figure 21B), in which an initially sulfide-saturated melt with 10 wt% FeO* and 1 vol% FeS is first 'degassed' by instantaneously lowering S by -10%, FeS is then resorbed into the melt until the S contents equals the SCSS (in this case, using the fit to Mathez 1976). When this condition is met, S is degassed again by -10%, and this process continues until all of the FeS is consumed, at which point the melt is no longer sulfide-saturated and further degassing lowers S at a constant FeO*. Note that this simple model does not account for changes in $fO_2$ imparted by heterogeneous reaction of S-bearing species in the melt and vapor phases (e.g., Gaillard and Scaillet 2009, Gaillard et el. 2011, Moussallam et al. 2016), and so is analogous to degassing of $H_2S$ in the melt to $H_2S$ in the vapor. For a melt with 10 wt% FeO* initially at FMQ (and an initial $Fe^{3+}/Fe^{T} \approx 0.16$), the effect of sulfide resorption dumps $Fe^{2+}$ into the liquid and contributes to melt reduction; for 1 vol% sulfide and ~1270 ppm initial S this corresponds to a change of -0.35 log units $fO_2$ (Kress & Carmichael 1991) during the initial stages of sulfide-saturated degassing. It is worth noting that estimates of the volume fraction of sulfides in Hawaiian whole rocks are lacking; estimates from MORB are on order 0.01-0.1 vol% (Mathez 1976, Czamanske 1977, Savelyev 2018) and a

similar estimate was documented in latites from Tintic, Utah (Larocque et al. 2000). In the model system shown in Figure 21B, resorption of 0.1 vol% FeS would lead to only a 0.2 wt% increase in FeO*. Either there is hidden sulfide (e.g., some of it was already resorbed, it was left behind via density separation, or it is undercounted due to sampling issues and nugget effects), or the observation of higher FeO* in undegassed basalts is an artifact, or it is due to some other process. Melt inclusions from Laki, Iceland (Hartley et al. 2017) clearly show higher FeO* in the sulfide-undersaturated and degassed glasses, however those from Hverfjall, Iceland show a continuum in S at nearly constant FeO* (Liu et al. 2018), which could mean that the initial undegassed melts were not sulfide-saturated or contained very little FeS. While FeS resorption leads to higher FeO*, lower $Fe^{3+}/Fe^{2+}$, and initially higher S in actively degassing sulfide-saturated liquids, further investigation is warranted to see whether this effect imparts a measurable signal in the compositions of natural lavas, as well as the role of vapor-melt interactions in modulating the $fO_2$.

A subset of the Hawaiian data have both $H_2O$ and S measurements, and an even smaller subset with $Fe^{3+}/Fe^{Total}$ determined by XANES or wet chemistry. For completeness these data are presented in Figure 22; the addition of the new Mauna Loa melt inclusion and Ko`olau data further support the conclusions of Moussallam et al. (2016) and Brounce et al. (2017), which is that S and $H_2O$ were degassing simultaneously and that degassing led to reduction of the melts, expressed as a decrease in $Fe^{3+}/Fe^{T}$ with decreasing S (Figure 22B) and $H_2O$. One Ko`olau data point has the highest $H_2O$ measured (0.95 wt%) in the compilation of Hawaiian glasses. The most oxidized samples are the four Mauna Loa melt inclusions from Gaetani et al. (2012) with $Fe^{3+}/Fe^{T}$ = 0.22-0.25; these are consistent with the elevated $[S]_{Total}$ measured in these inclusions for their FeO* relative to the predicted SCSS (Figure 21A), which

implies that some or all of the S is $S^{6+}$. Based on these considerations, the Loihi seamount samples from Wallace & Carmichael (1992) with S > 1700 ppm are likely from relatively oxidized magmas.

## 6. Conclusions

1. I report the first co-determined measurements of $Fe^{3+}/Fe^{2+}$ and $S^{6+}/S^{2-}$ in experimental basaltic glasses that were equilibrated at high-T in a 1 atm gas-mixing furnace with an atmosphere of variable and precisely known $fO_2$. The experiments, which were run on olivine-hosted melt inclusions from Papakōlea, Mauna Loa, Hawai‘i, were used to explore the thermodynamics and kinetics of electron transfer between sulfur and iron as a function of $fO_2$ and temperature at roughly constant major and minor element composition.

2. Over the 24 hr duration of experimental homogenization at $fO_2$ = FMQ-1, FMQ+0.35, FMQ+2.8, and FMQ+4.7, the melt inclusions lost most of their initial $H_2O$ (from ~2000 ppm down to 63-785 ppm $H_2O$), however they do not conform to the expected solubility curve of $fO_2$ vs. [$H_2O$] (Newcombe et al. 2017) and so it is unclear whether the inclusions reached equilibrium with the external $fO_2$ imposed by the furnace gases. The $Fe^{3+}/Fe^{Total}$ measured in unheated melt inclusions from Papakōlea, Mauna Loa, Hawai‘i ranged from 0.165-0.199; the experimental melt inclusions have $Fe^{3+}/Fe^{Total}$ ranging from 0.065 (FMQ-1) to 0.688 (FMQ+4.7). For experiments homogenized at FMQ-1 and FMQ+0.35 the $S^{6+}/S^{Total}$ is indistinguishable from zero; one experiment that was cooled at 2900 °C/hr from 1225°C to 1150°C at FMQ+0.35 had $S^{6+}/S^{Total}$ = 0.04-0.09. S valence was not measured in the experiments run at FMQ+2.8 or FMQ+4.7, however all of the S is $S^{6+}$ under these conditions (Jugo et al. 2010).

3. Some of the melt inclusions in experiments at FMQ≤0.35 were sulfide saturated with high S (>660 ppm) and had visible FeS blebs suspended in their glasses, other melt inclusions had low S (<129 to 520 ppm) and contained no visible sulfide blebs. Occasionally the two types of melt inclusions were present together within the same host olivine grain. In some of the experimental inclusions, the sulfides were organized in an annulus or ring structure. For the experiments at $fO_2$ higher than FMQ+2.8, the S contents of the melt inclusions were uniformly high (850 to 1353 ppm) and contained no visible sulfides, consistent with the prediction that all of the S is $S^{6+}$ at those conditions (Jugo et al. 2020).

4. Based on the nominal $fO_2$ imposed by furnace gases in the experiments run at or below FMQ+2.8, the $Fe^{3+}/Fe^{Total}$ predicted by various Fe oxybarometers is systematically higher than that measured by XANES, with the one exception being the model of O'Neill (2018). At FMQ+4.7, all the oxybarometers underestimate the $Fe^{3+}/Fe^{Total}$ of the experimental inclusion glasses by 10-25% relative. While it is unclear whether the inclusions attained equilibrium with the $fO_2$ of the furnace atmosphere, the discrepancies between the models and measurements of $Fe^{3+}/Fe^{Total}$ are systematic and are interpreted to be due to (i) the presence of sulfide nanolites in the analytical volume of the Fe XANES measurement, and/or (ii) the compositional dependencies coded in the oxybarometers, which were all calibrated on S-free melts, and may not be accurate for S-bearing melt inclusions.

5. Because the stoichiometry of oxidation of $S^{2-}$ to $S^{6+}$ requires 8 electrons, versus only one for $Fe^{2+}$ to $Fe^{3+}$, the sulfide-to-sulfate transition is much more sensitive to $fO_2$ and occurs over a narrow ~2 order of magnitude

range in the vicinity of FMQ. Limited experimental data exist where all of the quantities T (and cooling rate), $fO_2$, $Fe^{3+}/Fe^{2+}$, and $S^{6+}/S^{2-}$ are known and so the remaining data require the use of one of the Fe oxybarometers to convert between $fO_2$ and $Fe^{3+}/Fe^{2+}$. As a result, attempts to accurately place the $fO_2$ of the sulfide to sulfate transition are polluted by uncertainties in the Fe oxybarometers; depending on the choice of model the predicted $fO_2$ at which $S^{6+}/S^{T} = 0.50$ spans a range of 1.4 orders of magnitude, not including intramodel errors which are at least ±0.4 orders of magnitude. Thus, detailed experimental studies that do not hinge on the accuracy of any one of the Fe oxybarometers are required to accurately model the sulfide to sulfate transition. These experiments require precise control of $fO_2$ due to the narrow transition interval. Additional experiments similar to those described here at slightly higher $fO_2$ could be used to constrain the location of the sulfide to sulfate transition for the bulk composition of melt inclusions from Papakōlea, Mauna Loa, Hawai‘i.

6. The temperature-dependence of reaction (1) ($S^{2-} + 8Fe^{3+} \rightleftharpoons 8Fe^{2+} + S^{6+}$) in basaltic was explored. It was shown that equation (11) by Nash et al. (2019) cannot be applied to melts with different bulk Fe/S, because it follows from their equation and mass balance that melts with initially the same $fO_2$, T, $Fe^{3+}/Fe^{2+}$, and $S^{6+}/S^{2-}$, but different bulk Fe/S, when cooled to different T can end up at the same $fO_2$ (and $Fe^{3+}/Fe^{2+}$) but have different $S^{6+}/S^{2-}$. Two unheated melt inclusions from Papakōlea were measured for Fe and S XANES and had their cooling rates determined by diffusion speedometry (Saper & Stolper 2020) indicating that each experienced drastically different syneruptive cooling rates: one inclusion was rapidly cooled (~8000°C/hr from 1175°C) whereas the other inclusion was very slowly cooled (55°C/hr from >1160°C). The rapidly cooled

inclusion has $S^{6+}/S^{T}$ = 0.45-0.66 whereas the slowly cooled inclusion has $S^{6+}/S^{T}$ indistinguishable from unity. The slowly cooled inclusion was crystallizing olivine on its wall down to a closure temperature of <900°C, based on MgO olivine-liquid equilibrium at the inclusion wall. According to Nash et al. (2019), equation (1) proceeds strongly to the left with decreasing T ($S^{6+}$ is consumed and $Fe^{3+}/Fe^{2+}$ increases) which is incompatible with the slowly cooled melt inclusion that is sulfate dominated, has 154 ppm total S, and likely maintained Fe-S electron exchange equilibrium down to low T. The natural melt inclusions are consistent either with a weak T-dependence of Fe-S redox equilibria, or, a T-dependence of unknown magnitude that proceeds in the opposite direction to that deduced by Nash et al. (2019), i.e. $S^{2-}$ is consumed and $Fe^{3+}/Fe^{2+}$ decreases.

## 7. References

Alt, J.C., Shanks III, W.C., & Jackson, M.C. (1993). Cycling of sulfur in subduction zones: the geochemistry of sulfur in the Mariana Island Arc and back-arc trough

Anderson, Jr., A.T., & Brown, G.G. (1993). CO2 contents and formation pressures of some Kīlauean melt inclusions. *American Mineralogist*, 78, p.794-803

Armstrong, J.T. (1988). Quantitative analysis of silicate and oxide minerals: comparison of Monte Carlo, ZAF, and Φ(ρz) procedures. In: Newbury DE (editor) Microbeam analysis – 1988. San Francisco Press, San Francisco, p.239-246

Barth, A., Newcombe, M., Plank, T., Gonnerman, H., Hajimirza, S., Soto, G.J., Saballos, A., & Hauri, E. (2019). Magma decompression rate correlates with explosivity at basaltic volcanoes – constraints from water diffusion in olivine. *Journal of Volcanology and Geothermal Research*, 387, 106664

Berry, A.J, Shelley, J.M.G., Foran, G.J., O'Neill, H.S.C., Scott, D.R. (2003). A furnace design for XANES spectroscopy of silicate melts under controlled oxygen fugacities and temperatures to 1773K. *Journal of Synchotron Radiation*, 10, p.332-335

Borisov, A.A., Behrens, H., & Holtz, F. (2018). Ferric/ferrous ratio in silicate melts: a new model for 1 atm data with special emphasis on the effects of melt composition. *Contributions to Mineralogy and Petrology*, 173:98

Brounce, M., Stolper, E., & Eiler, J. (2017). Redox variations in Mauna Kea lavas, the oxygen fugacity of the Hawaiian plume, and the role of volcanic gases in Earth's oxygenation. *Proceedings of the National Academy of Sciences*, 114 (34) p.8997-9002

Botcharnikov, R.E., Koepke, J., Holtz, F., McCammon, C., & Wilke, M. (2005). High gold concnetrations in sulphide-bearing magma under oxidizing conditions.*Nature Geoscience*, 4(2), p.112-115

Bucholz, C.E., Gaetani, G.A., Behn, M.D., & Shimizu, N. (2013). Post-entrapment modification of volatiles and oxygen fugacity in olivine-hosted melt inclusions. *Earth and Planetary Science Letters*, 374, p.145-155, https://doi.org/10.1016/j.epsl.2013.05.033

Burgess, K.D., & Cooper, R.F. (2013). Extended planar defects and the rapid incorporation of $Ti^{4+}$ into olivine. *Contributions to Mineralogy and Petrology*, 166, p.1223-1233

Carroll, M.R., & Rutherford, M.J. (1987). The stability of igneous anhydrite: experimental results and implications for sulfur behavior in the 1982 El Chichon trachyandesite and other evolved magmas. *Journal of Petrology,* 28(5), p781-801

Cooper, K.M., Reid, M.R., Murrell, M.T., Clague, D.A. (2001). Crystal and magma residence at Kīlauea Volcano, Hawai‘i: $^{230}$Th-$^{226}$Ra dating of the 1955 east rift eruption. *Earth and Planetary Science Letters*, 184, p.703-718

Cottrell, E., Kelley, K.A., Lanzirotti, A., & Fischer, R.A. (2009). High-precision determination of iron oxidation state in silicate glasses using XANES. *Chemical Geology*, 268(3-4), p.167-179

Czamanaske, G.K., & Moore, J.G. (1977). Composition and phase chemistry of sulfide globules in basalt from the mid-Atlantic Ridge rift valley near 37°N lat. *Geological Society of America Bulletin,* 88, p.587-599

Danyushevsky, L.V., Sokolov, S., & Falloon, T.J. (2002). Melt inclusions in olivine phenocrysts: using diffusive re-equilibration to determine the cooling history of a crystal, with implications for the origin of olivine-phyric volcanic rocks. *Journal of Petrology*, 43(9), p.1651-167

DiGenova, D., Caracciolo, A., & Kolzenburg, S. (2018). Measuring the degree of “nanotilization” of volcanic glasses: understanding syn-eruptive processes recorded in melt inclusions. *Lithos*, 318-319, p.209-218

Dixon, J.E., & Clague, D.A. (2001). Volatiles in basaltic glasses from Loihi seamount, Hawai‘i: evidence for a relatively dry plume component. *Journal of Petrology*, 42(3), p.627-654

Dohmen, R., & Chakraborty, S. (2007). Fe-Mg diffusion in olivine II: point defect chemistry, change of diffusion mechanisms and a model for calculation of diffusion coefficients in natural olivine. *Physics and Chemistry of Minerals*, 34, p.409-430

Edmonds, M., & Woods, A.W. (2018). Exsolved volatiles in magma reservoirs. *Journal of Volcanology and Geothermal Research*, 368, p.13-30

Esposito, R., Lamadrid, H.M., Redi, D., Steele-MacInnis, M., Bodnar, R.J., Manning, C.E., de Vivo, B., Cannatelli, C., & Lima, A. (2016). Detection of liquid $H_2O$ in vapor bubble in reheated melt inclusions: implications for magmatic fluid composition and volatile budgets of magmas? *American Mineralogist*, 101, p.1691-1695

Evans, K.A., O'Neill, H.S.C., & Mavrogenes, J.A. Sulphur solubility and sulphide immiscibility in silicate melts as a function of the concentration of mangangese, nickel, tungsten and copper at 1 atm and 1400 °C, *Chemical Geology*, 255, p.236-249

Ferriss, E., Plank, T., Newcombe, M., Walker, D., & Hauri, E. (2018). Rates of dehydration of olivines from San Carlos and Kīlauea Iki. *Geochimica et Cosmochimica Acta*, 242, p.165-190

Florentin, L., Faure, F., Deloule, E., Tissandier, L., Gurenko, A., & Lequin, D. (2017). Origin of Na in glass inclusions hosted in olivine from Allende CV3 and Jbilet Winselwan CM2: implications for chondrule formation. *Earth and Planetary Science Letters*, 474, p.160-171

Gaetani, G.A., & Watson, E.B. (2000). Open system behavior of olivine-hosted melt inclusions. *Earth and Planetary Science Letters*, 183, p.27-41, https://doi.org/10.1016/S0012-821X(00)00260-0

Gaetani, G.A., & Watson, E.B. (2002). Modeling the major-element evolution of olivine-hosted melt inclusions. *Chemical Geology*, 183, p.25-41

Gaetani, G.A., O'Leary, J.A., Shimizu, N., Bucholz, C.E., & Newville, M. (2012). Rapid reequilibration of H2O and oxygen fugacity in olivine-hosted melt inclusions. *Geology*, 40(10), p.915-918

Gaillard, F., & Scaillet, S. (2009). The sulfur content of volcanic gases on Mars. *Earth and Planetary Science Letters*, 279, p.34-43

Gaillard, F., Scaillet, B., & Arndt, N.T. (2011). Atmospheric oxygenation caused by a change in volcanic degassing pressure. *Nature*, 478, p.229-232

Ghiorso, M.S., & Sack, R.O. (1995). Chemical mass transfer in magmatic processes IV. A revised and internally consistent thermodynamic model for the interpolation and extrapolation of liquid-solid equilibria in magmatic systems at elevated temperatures and pressures. *Contributions to Mineralogy and Petrology*, 119., p.197-212

Graz, Y., Scaillet, B., Pichavant, M., & Gaillard, F. (2006). The effect of sulfur on the Fe2+/Fe3+ ratio of MORB and its implications for the redox state of the mantle. *American Geophysical Union Fall Meeting 2007*, abstract id. V43B-01

Guo, C., & Zhang, Y. (2018). Multicomponent diffusion in basaltic melts at 1350 °C. *Geochimica et Cosmochimica Acta*, 228, p.190-204

Hauri, E. (2002). SIMS analysis of volatiles in silicate glasses, 2: isotopes and abundances in Hawaiian melt inclusions. *Chemical Geology*, 183, p.115-141

Hanyu, T., Yamamoto, J., Kimoto, K., Shimizu, K., & Ushikubo, T. (2020). Determination of total $CO_2$ in melt inclusions with shrinkage bubbles. *Chemical Geology*, 557, 119855

Hartley, M.E., Shorttle, O., Maclennan, J., Moussallam, Y., & Edmonds, M. (2017). Olivine-hosted melt inclusions as an archive of redox heterogeneity in magmatic systems. *Earth and Planetary Science Letters*, 479, p.192-205

Head, E., Lanzirotti, A., Newville, M., & Sutton, S. (2018). Vanadium, sulfur, and iron valances in melt inclusions as a window into magmatic processes: a case

study at Nyamuragira volcano, Africa. *Geochimica et Cosmochimica Acta*, 226, p.149-173

Helz, R.T., Cottrell, E., Brounce, M.J., & Kelley, K.A. (2016). Olivine-melt relationships and syneruptive redox variations in the 1959 eruption of Kīlauea Volcano as revealed by XANES. *Journal of Volcanology and Geothermal Research*, 333:334, p.1-14

Huebner, J.S. (1971). Buffering techniques for hydrostatic systems at elevated pressures. *Research Techniques for High Pressure and High Temperature*, Ed: Ulmer, G.C., Springer, Berlin, Heidelberg, p. 123-177

Iacovino, K., & Till, C.B. (2019). DensityX: A program for calculating the densities of magmatic liquids up to 1,627°C and 30 kbar. *Volcanica*. 2(1)

Jayasuriya, K.D., O'Neill, H.S.C., Berry A.J., & Campbell, S.J. (2004). A Mössbauer study of the oxidation state of Fe in silicate melts. *American Mineralogist*, 89(11-12), p.1597-1609

Jégo, S., & Dasgupta, R. (2013). Fluid-present melting of sulfide-bearing ocean-crust: experimental constraints on the transport of sulfur from subducting slab to mantle wedge. *Geochimica et Cosmochimica Acta*, 110, p.106-134

Jochum, K.P., Stoll, B., Herwig, K., Wilbold, M., Hofmann, A.W., & Amini, M., et al. (2006). MPI-DING reference glasses for in situ microanalysis: New reference values for element concentrations and isotope ratios. *Geochemistry Geophysics Geosystems*, 7(2), p.1-44

Jugo, P.J., Luth, R.W. & Richards, J.P. (2005). Experimental data on the speciation of sulfur as a function of oxygen fugacity in basaltic melts. *Geochimica et Cosmochimica Acta*, 69(2), p.497-503.

Jugo, P.J., Wilke, M., & Botcharnikov, R.E. (2010). Sulfur K-edge XANES analysis of natural and synthetic glasses: implications for S speciation and S content as function of oxygen fugacity. *Geochimica et Cosmochimica Acta*, 74(20), p.5926-5938

Kamenetsky, V.S., Davidson, P., Mernagh, T.P., Crawford, A.J., Gemmell, J.B., Portnyagin, M.V., & Shinjo, R. (2002). Fluid buble in melt inclusions and pillow-rim glasses: high-temperature precursors to hydrothermal fluids, *Chemical Geology*, 183, p.349-364

Kilinc, A., Carmichael, I.S.E., Rivers, M.L., & Sack, R.O. (1983). The ferric-ferrous ratio of natural silicate liquids equilibrated in air. *Contributions to Mineralogy and Petrology*, 84, p.136-140

Klimm, K., Kohn, S.C., & Botcharnikov, R.E. (2012). The dissolution mechanism of Sulphur in hydrous silicate melts. II: Solubility and speciation of Sulphur in hydrous silicate melts as a function of $fO_2$. *Chemical Geology*, 322-323, p.250-267

Kohlstedt, D.L., & Mackwell, S.J. (1998). Diffusion of hydrogen and intrinsic point defects in olivine. *Zeritschrift für Psysikalische Chemie,* Bd. 207, p.147-162

Konecke, B.A., Fiege, A., Simon, A.C., Linsler, S., & Holtz, F. (2019). *Geochimica et Cosmochimica Acta*, 265, .242-258

Kress, V.C., & Carmichael, I.S.E. (1991). The compressibility of silicate liquids containing Fe2O3 and the effect of composition, temperature, oxygen fugacity and pressure on their redox states. *Contributions to Mineralogy and Petrology*, 108

Larocque, A.C.L., Stimac, J.A., Keith, J.D., & Huminicki, M.A.E. (2000). Evidence for open-system behavior in immiscible Fe-S-O liquids in silicate magmas:

implications for contributions of metals and sulfur to ore-forming fluids. *The Canadian Mineralogist*, 38, p.1233-1249

Le Voyer, M., Asimow, P.D., Mosenfelder, J.L., Guan, Y., Wallace, P.J., Schiano, P., Stolper, E.M., & Eiler, J.M. (2014). Zonation of $H_2O$ and F concentrations around melt inclusions in olivines. *Journal of Petrology*, 55(4), p.685-707

Lerner, A.H., Wallace, P.J., Shea, T., Mourey, A.J., Kelley, P.J., Nadeau, P.A., Elias, T., Kern, C., Clor,. L.E., Gansecki, C., Lopaka Lee, R., Lowell, R.M., & Werner, C.A. (2021). The petrologic and degassing behavior of sulfur and other magmatic volatiles from the 2018 eruption of Kīlauea, Hawai‘i: melt concentrations, magma storage depths, and magma recycling. *Bulletin of Volcanlogy*, 83(6), p.1-32

Li, C., Ripley, E.M. (2009). Sulfur contents at sulfide-liquids or anhydrite saturation in silicate melts: empirical equations and example applications. *Economic Geology*, 104, p.405-412

Liu, K., Zhang, L., Guo, X., & Ni, H. (2021). Effects of sulfide composition and melt $H_2O$ on sulfur content at sulfide saturation in basaltic melts. *Chemical Geology*, 559, 119913

Maclennanm J. (2017). Bubble formation and decrepitation control the $CO_2$ content of olivine-hosted melt inclusions. *Geochemistry, Geophysics, Geosystems*, 18, p.597-616

Magnien, V., Neuville, D.R., Cormier, L., Roux, J., Hazemann, J.-L., de Ligny, D., Pascarelli, S., Vickridge, I., Pinet, O., & Richet, P. (2008). Kinetics and mechanisms of iron redox reactions in silicate melts: the effects of temperature and alkali cations. *Geochimica et Cosmochimica Acta*, 72, p.2157-2168

Manceau, A., & Nagy, K.L. (2012). Quantitative analysis of sulfur functional groups in natural organic matter by XANES spectroscopy. *Geochimica et Cosmochimica Acta*, 99, p.206-223

Mallmann, G., O'Neill, H.S.C. (2009) The crystal/melt partitioning of V during mantle melting as a function of oxygen fugacity compared with some other elements (Al, P, Ca, Sc, Ti, Cr, Fe, Ga, Y, Zr, and Nb). *Journal of Petrology*, 50, 9, p.1765-1794

Mathez, E.A. (1976). Sulfur solubility and magmatic sulfides in submarine basalt glass. *Journal of Geophysical Research*. 81(23), p. 4269-4276

Matzen, A.K., Baker, M.B., Beckett, J.R., & Stolper, E.M. (2011). Fe-Mg partitioning between olivine and high-magnesian melts and the nature of Hawaiian parental liquids. *Journal of Petrology*, 52(7:8), p.1243-1263, https://doi.org/10.1093/petrology/egq089

Metrich, N., Berry, A.J., O'Neill, H.S.C., & Susini, J. (2009) The oxidation state of sulfur in synthetic and natural glasses determined by X-ray absorption spectroscopy. *Geochimica et Cosmochimica Acta*, 73, p.2382-2399

Mironov, N., Portnyagin, M., Botcharnikov, R., Gurenko, A., Hoernle, K., & Holtz, F. (2015). Quantification of the $CO_2$ budget and $H_2O$-$CO_2$ systematics in subduction-zone magmas through experimental hydration of melt inclusions in olivine at high $H_2O$ pressure. *Earth and Planetary Science Letters*, 425, p.1-11

Moore, G. (2008). Interpreting $H_2O$ and $CO_2$ contents in melt inclusions: constraints from solubility experiments and modeling. *Reviews in Mineralogy & Geochemistry*, 69, p.333-361

Moussallam, Y., Edmonds, M., Scaillet, B., Peters, N., Gennaro, E., Sides, I., & Oppenheimer, C. (2016). The impact of degassing on the oxidation state of

basaltic magmas: a case study of Kīlauea volcano. *Earth and Planetary Science Letters*, 450, p.317-325

Nash, W.M., Smythe, D.J., & Wood, B.J. (2019). Compositional and temperature effects on sulfur speciation and solubility in silicate melts. *Earth and Planetary Science Letters*, 507, p.187-198, https://doi.org/10.1016/j.epsl.2018.12.006

Newcombe M.E., Brett A, Beckett J.R., Baker M.B., Newman S., Guan Y., Eiler J.M., & Stolper E.M. (2017) Solubility of water in lunar basalt at low pH2O. Geochimica et Cosmochimica Acta 200 p.330-352, https://doi.org/10.1007/s00410-014-1030-6

Newman, S., & Lowenstern, J.B. (2002). VolatileCalc: a silicate melt-$H_2O$-$CO_2$ solution model written in Visual Basic for excel. *Computers & Geoscience*, 28, p.597-604

Nitsan, U. (1974). Stability field of olivine with respect to oxidation and reduction. *Journal of Geophysical Research*, 79(5), p.706-711

O'Neill, H.S.C., & Mavrogenes, J.A. (2002).The sulfide capacity and the sulfur content at sulfide saturation of silicate melts at 1400 °C and 1 bar. *Journal of Petrology*, 43, p.1049-1087, https://doi.org/10.1093/petrology/43.6.1049

O'Neill, H.S.C., Berry, A.J., & Mallmann, G. (2018). The oxidation state of iron in Mid-Ocean Ridge Basaltic (MORB) glasses: implications for their petrogenesis and oxygen fugacties. *Earth and Planetary Science Letters*, 504, p.152-162

O'Neill, H.S.C. (2021). Comment on "Compositional and temperature effects on sulfur speciation and solubility in silicate melts" by Nash et al. [Earth Planet. Sci. Lett. 507 (2019) 187-198]. *Earth and Planetary Science Letters*, 560, 116843

Putirka, K. (2016). Rates and styles of planetary cooling on Earth, Moon, Mars, and Vesta, using new models for oxygen fugacity, ferric-ferrous ratios, olivine-liquid Fe-Mg exchange, and mantle pontential temperature. *American Mineralogist*., 101, p.819-840

Roedder, E. (1979). Origin and significant of magmatic inclusions. *Bulletin of Mineralogy*, 102, p.487-510

Roedder, E., (1992). Fluid inclusions. *Encyclopedia of Physical Science and Technology, Third Edition, Volume 6*, Academic Press

Rose-Koga, E.F., Bouvier, A.-S., Gaetani, G.A., Wallace, P.J., Allison, C.M., Andrys, J.A., Angeles de la Torre, C.A., Barth, A., Bodnar, R.J., Bracco Gartner, A.J.J., Butters, D., Castillejo, A., Chilson-Parks, B., Choudhary, B.R., Cluzel, N., Cole, M., Cottrell, E., Daly, A., Danyushevsky, L.V., DeVitre, C.L., Drignon, M.J., France, L., Gaborieau, M., Garcia, M.O., Gatti, E., Genske, F.S., Hartley M.E., Hughes, E.C., Iveson, A.A., Johnson, E.R., Jones, M., Kagoshima, T., Katzir, Y., Kawaguchi, M., Kawamoto, T., Kelley, K.A., Koornneef, M., Kurz, M.D., Laubier, M., Layne, G.D., Lerner, A., Lin, K.-Y., Liu, P.-P, Lorenzo-Merino, A., Luciani, N., Magalhaes, N., Marschall, H.R., Michael, P.J., Navon, B.O., Newcombe, M.E., Nichols, A.R.L., Nielsen, R.L., Pamukcu, A., Plank, T., Rasmussen, D.J., Roberge, J., Schiavi, F., Schwartz, D., Shimizu, K., Shimizu, K., Shimizu, N., Thomas, J.B., Thompson, G.T., Tucker, J.M., Ustunisik, G., Waelkens, C., Zhang, Y., & Zhou, T. (2021) Silicate melt inclusions in the new millennium: a review of recommended practices for preparation, analysis, and data presentation. *Chemical Geology*, 570, 120145

Savelyev, D.P., Kamenetsky, V.D., Danyushevsky, L.V., Botcharnikov, R.E., Kamenetsky, M.B., Park, J.-W., Portnyagin, M.V., Olin, P., Krasheninnikov,

S.P., Hauff, F., & Zelenski, M.E. (2018). Immiscible sulfide melts in primitive oceanic magmas: ecidence and implications from picrate lavas (Eastern Kamchatka, Russia). *American Mineralogist*, 103, p.886-898

Sack, R.O., Carmichael, I.S.E., Rivers, M., & Ghiorso, M.S. (1980). Ferric-ferrous equilibria in natural silicate liquids at 1 bar. *Contributions to Mineralogy and Petrology*, 75, p.369-376

Saper, L.M., & Stolper, E.M. (2020). Controlled cooling-rate experiments on olivine-hosted melt inclusions: chemical diffusion and quantification of eruptive cooling rates on Hawai‘i and Mars. *Geochemistry, Geophysics, Geosystems*, 21(2)

Schiavi, F., Provost, A., Schiano, P., & Cluzel, N. (2016). P-V-T-X evolution of olivine-hosted melt inclusions during high-temperature homogenization treatment. *Geochimica et Cosmochimica Acta,* 172, p.1-21

Smythe, D.J., Wood, B.J., & Kiseeva, E.S. (2017). The S content of silicate melts at sulfide saturation: new experiments and a model incorporating the effects of sulfide composition. *American Mineralogist*, 102, p.795-803

Sobolev, A.V., & Danyushevsky, L.V. (1994). Petrology and geochemistry of boninites from the north termination of the Tongo Trench: constraints on the generation conditions of primary high-Ca boninite magmas. *Journal of Petrology*, 35, p.1183-1211

Spandler, C., & O’Neill, H.S.C. (2010). Diffusion and partition coefficients of minor and trace elements in San Carlos olivine at 1,300°C with some geochemical implications. *Contributions to Mineralogy and Petrology*, 159, p.791-818

Tang, M., Lee, C.-T.A., Ji, W.-Q., Wang, R., & Costin. (2020). Crustal thickening and endogenic oxidation of magmatic sulfur. *Science Advances*, 6(31)

Tucker, J.M., Hauri, E.H., Pietruszka, A.J., Garcia, M.O., Marske, J.P., & Trusdell, F.A. (2019). A high carbon content of the Hawaiian mantle from olivine-hosted melt inclusions. *Geochimica et Cosmochimica Acta*, 254, p.156-172

Tuff, J., & O'Neill, H.S.C. (2010). The effect of sulfur on the partitioning of Ni and other first-row transition elements between olivine and silicate melts. *Geochimica et Cosmochimica Acta*, 74, p.6180-6205

Walso, G.S., Carlson, R.M.K., Moldowan, J.M., Peters, K.E., & Penner-Hahn, J.E. (1991). Sulfur speciation in heavy petrolums: information from X-ray absorption near-edge structure. *Geochimica et Cosmochimica Acta*, 55, p.801-814

Wallace, P.J., Kamenetsky, V.S., & Cervantes, P. (2015). Melt inclusion CO2 contents, pressures of olivine crystallization, and the problem of shrinkage bubbles. *American Mineralogist*, 100, p.787-794

Watson, E.B. (1982). Basalt contamination by continental crust: some experiments and models. *Contributions to Mineralogy and Petrology*, 80, p.73-87

Wilke, M., Jugo, P.J., Klimm, K., Susini, J., Botcharnikov, R., Kohn, S.C., & Janousch, M. (2008). The origin of $S^{4+}$detected in silicate glasses by XANES. *American Mineralogist*, 93(1), p.235-240

Wu, T., & Kohlstedt, D.L. (1988). Rutherford backscattering spectroscopy study of the kinetics of oxidation of $(Mg,Fe)_2SiO_4$. *J. Am Ceram. Soc.* 71(7), p.540-545

Xu, Z., & Zhang, Y. (2002). Quench rates in air, water, and liquid nitrogen, and interference of temperature in volcanic eruption column. *Earth and Planetary Science Letters*, 200(3), p.315-330, https://doi.org/10.1016/S0012-821X(02)00656-8

Yeats, R.S. & Mathez, E.A. (1976). Decorated vesicles in deep-sea basalt glass, Eastern Pacific. *Journal of Geophysical Research*, 81(23), p.4277-4284

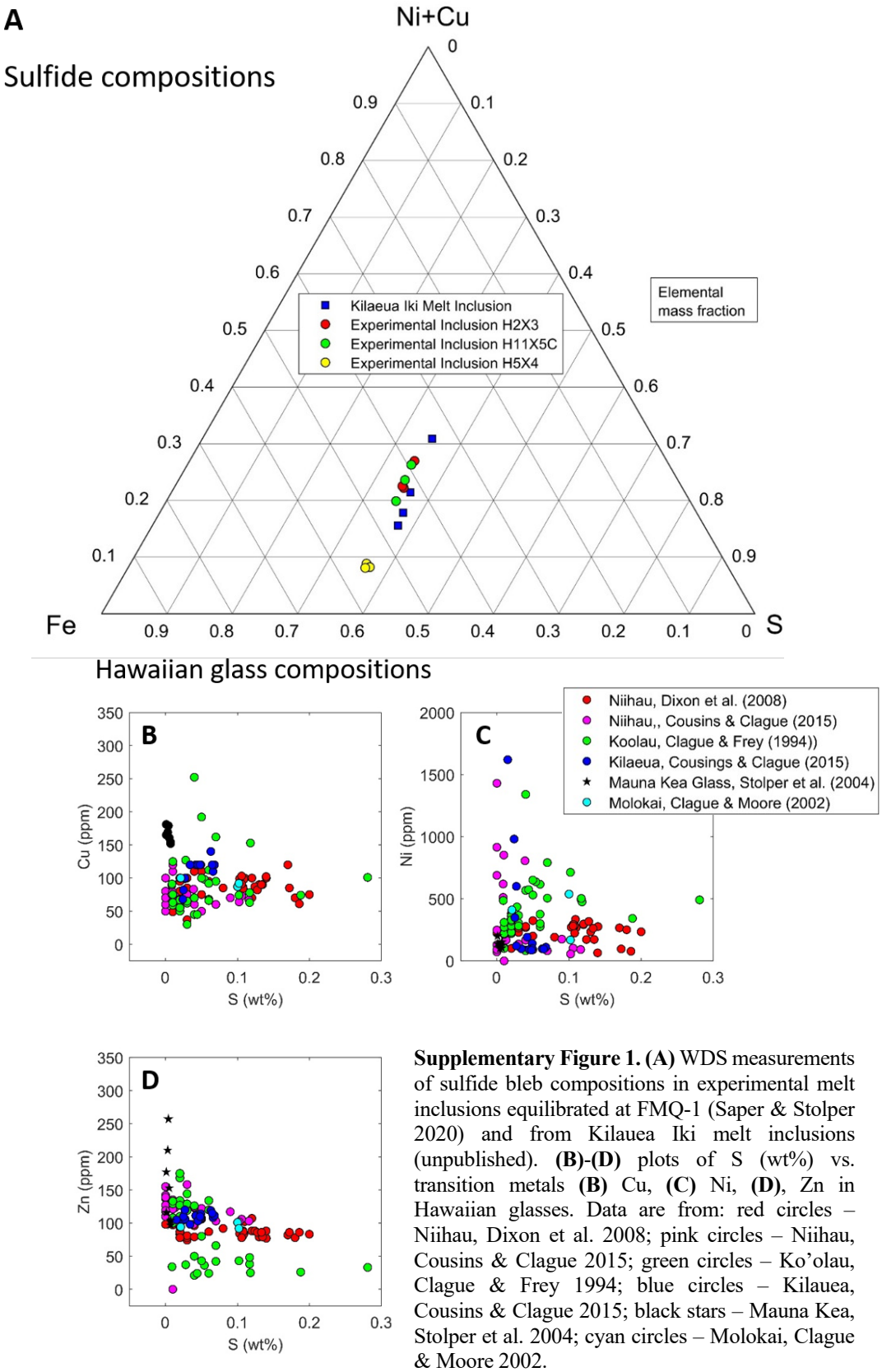


**Supplementary Figure 1. (A)** WDS measurements of sulfide bleb compositions in experimental melt inclusions equilibrated at FMQ-1 (Saper & Stolper 2020) and from Kilauea Iki melt inclusions (unpublished). **(B)-(D)** plots of S (wt%) vs. transition metals **(B)** Cu, **(C)** Ni, **(D)**, Zn in Hawaiian glasses. Data are from: red circles – Niihau, Dixon et al. 2008; pink circles – Niihau, Cousins & Clague 2015; green circles – Ko'olau, Clague & Frey 1994; blue circles – Kilauea, Cousins & Clague 2015; black stars – Mauna Kea, Stolper et al. 2004; cyan circles – Molokai, Clague & Moore 2002.

*Chapter 4*

# $Fe^{2+}$-Mg partitioning between olivine and liquid at low oxygen fugacity: an experimental and thermodynamic framework

Lee M. Saper

Michael B. Baker

Edward M. Stolper

## 1. Abstract

A set of 1 atm gas-mixing experiments ("RKD" experiments) using Re wire loops at $fO_2$ = IW±0.5 (n=34) and on Pt wire loops at $fO_2 \geq$ FMQ (n=3) at T = 1175 °C to 1400°C were run to explore the composition-dependence of the $Fe^{2+}$-Mg olivine-liquid exchange coefficient, $K_{D,Fe^{2+}-Mg}^{ol/liq}$, under conditions where corrections for $Fe^{3+}$ are small. Because the majority of previous experiments at low $fO_2$ containing olivine-liquid pairs were run on bulk compositions representative of the moon, Mars, chondrites, and basaltic asteroids, the bulk compositions used for the RKD experiments were designed to be representative of terrestrial magmas, including a picrite, a high-alumina basalt, and a suite of three MORB compositions with variable Fe/Mg. The $K_{D,Fe^{2+}-Mg}^{ol/liq}$ measured in the RKD experiments, after a minor correction for $Fe^{3+}$, was fit to a regular solution model that relates the $Fe^{2+}$-Mg exchange coefficient to temperature, melt, and olivine composition. The experiments were well-described by using three adjustable parameters: the $SiO_2$ and $Al_2O_3$ contents of the liquid and the coexisting olivine composition. A compilation of all existing experimental data on olivine-liquid pairs run at $fO_2 \leq$ IW+0.5 was compiled and each experiment tested for whether the bulk compositions and reported phase products passed mass balance, and other quality criteria including reporting stoichiometric olivine (n=178/305 passing experiments). These experiments, which spanned a larger region of composition space than the RKD experiments, required two additional liquid compositional terms to describe the $K_{D,Fe^{2+}-Mg}^{ol/liq}$:$TiO_2$, and an $SiO_2$-($Na_2O$+$K_2O$) cross-term. In order to accurately model the variability in $K_{D,Fe^{2+}-Mg}^{ol/liq}$ observed at low $fO_2$ liquid compositional terms must be used; any model that seeks to parameterize the composition dependence of $K_{D,Fe^{2+}-Mg}^{ol/liq}$ solely in terms of olivine composition can only be valid over limited ranges of liquid composition. Given sufficient information on individual divalent

cation partition coefficients between olivine and liquid (or sufficiently low concentrations of divalent cations in olivine other than Fe and Mg) the olivine composition can be expressed equivalently as the FeO or MgO contents of the coexisting liquid. Therefore, it is possible to model $K_{D,Fe^{2+}-Mg}^{ol/liq}$ only as a function of liquid composition. An implication is that the $K_{D,Fe^{2+}-Mg}^{ol/liq}$ decreases with increasing $fO_2$ due to the conversion of FeO to $Fe_2O_3$ in the liquid; this effect is larger in more Fe-rich bulk compositions.

## 2. Introduction

Experimental measurements of mineral-melt equilibria are integral to understanding crystallization and melting processes. For example, accurately modeling the chemical evolution of melts, their residues, and cumulate mushes relies on precise quantification of element partitioning between solid and liquid phases. Olivine is the predominant mineral phase in the upper mantle and is the primary liquidus phase during crystallization of most mafic melts. Consequently a large amount of effort has been dedicated to quantifying chemical exchange between olivine and liquid, and in particular the partitioning behavior of $Fe^{2+}$ and Mg. The goal of many of these studies, based on measurements of both experimental and natural olivine-liquid pairs, is to provide a basis for modeling the melting of olivine-bearing mantle assemblages and for reconstructing liquid lines of descent for basaltic liquids. Additionally, establishment of equilibrium in experimental studies and in nature is often loosely predicated on equilibrium between olivine and melt, and this is tested by measuring Fe and Mg in both phases and comparing them to an accepted value of the $Fe^{2+}$-Mg olivine-liquid exchange coefficient,

$$K_{D,Fe^{2+}-Mg}^{ol/liq} \equiv \left[\left(\frac{X_{MgO}}{X_{FeO}}\right)^{liq}\left(\frac{X_{FeSi1/2O2}}{X_{MgSi1/2O2}}\right)^{olv}\right] \quad (1a)$$

This quantity describes the Fe-Mg exchange equilibrium between olivine and silicate melt:

$$FeO^{liq} + MgSi_{1/2}O_2{}^{ol} \rightleftharpoons FeSi_{1/2}O_2{}^{ol} + MgO^{liq}, \quad (1b)$$

which has the equilibrium constant:

$$K_1 = \left(\frac{a_{MgO}}{a_{FeO}}\right)^{liq} \cdot \left(\frac{a_{FeSi1/2O2}}{a_{MgSi1/2O2}}\right)^{olv}, \quad (1c)$$

and therefore,

$$K_1 = K_{D,Fe^{2+}-Mg}^{ol/liq} \cdot \left[\left(\frac{\gamma_{MgO}}{\gamma_{FeO}}\right)^{liq} \left(\frac{\gamma_{FeSi1/2O2}}{\gamma_{MgSi1/2O2}}\right)^{olv}\right], \quad (1d)$$

where $FeO^{liq}$ and $MgO^{liq}$ refer to oxide components in the liquid; $MgSi_{1/2}O_2{}^{ol}$ and $FeSi_{1/2}O_2{}^{ol}$ are the forsterite and fayalite components in olivine expressed on a single divalent cation basis; $a_i^{\Phi}$ refers to the activity of component *i* in phase Φ; $X_i^{\Phi}$ is the mole fraction of component *i* in phase Φ, and $\gamma_i^{\Phi} = \frac{a_i^{\Phi}}{X_i^{\Phi}}$ is the activity coefficient of component *i* in phase Φ. In the special case that the activity coefficients all equal one, or if the γ ratio in both phases equals one, equation (1c) and (1d) can be reduced to:

$$K_{D,Fe^{2+}-Mg}^{ol/liq} = K_1 = \left(\frac{X_{MgO}}{X_{FeO}}\right)^{liq} \cdot \left(\frac{X_{FeO}}{X_{MgO}}\right)^{olv} = \frac{(\frac{X_{FeO}}{X_{MgO}})^{olv}}{(\frac{X_{FeO}}{X_{MgO}})^{liq}} \quad (1e)$$

Because only partitioning between olivine and liquid is considered hereafter, the "ol/liq" specifier is dropped from "$K_{D,Fe^{2+}-Mg}^{ol/liq}$" and the olivine/liquid $Fe^{2+}$-Mg exchange coefficient is referred to as $K_{D,Fe2+-Mg}$.

The use of $K_{D,Fe2+-Mg}$ for petrological problems is rooted in the seminal study of Roeder & Emslie (1970), who found that for Hawaiian basalts equilibrated near atmospheric pressure and for temperatures (T) ranging from 1150–1300 °C, the $K_{D,Fe2+-Mg}$ has roughly a constant value of 0.30±0.03. This value has been (and still is) widely used in the petrological literature. A recent re-evaluation of the original Roeder & Emslie (1970) data suggest that when the effects of capsule type and mass balance are considered their experimentally determined value is actually closer to 0.315 (Matzen et al. 2011).

Moreover, it has long been recognized that 0.30 is only a convenient reference point and, the exchange displays resolvable and systematic variations. In other words, the assumption of equal activity coefficients for FeO and MgO in both phases in equation (1d) is not a good approximation over the full range of natural basaltic compositions.

The publication of Roeder & Emslie (1970) coincided with the return of lunar samples, which stimulated experimental studies that included bulk compositions that are exotic relative to those most commonly found on Earth. These experiments were run under reducing conditions, often in Fe metal capsules, which constrains the $Fe^{3+}$ in the melt to low values, largely eliminating the need for correction of glass analyses for $Fe^{3+}$ to get at the true $K_{D,Fe2+-Mg}$ value. The experiments showed that for high-Ti lunar melts, the $K_{D,Fe2+-Mg}$ was systematically lower than 0.30, decreasing to 0.24 in Ti-enriched melts with up to 15 wt% $TiO_2$ (Longhi et al. 1978; Grove & Beaty 1980; Delano 1980). Roeder (1974) found that the FeO contents of Fe-metal and olivine-saturated liquids was lower in liquids with higher alkali and alumina contents, but concluded that the $K_{D,Fe2+-Mg}$ remained a roughly constant 0.30±0.03 in melts with up to 4.39 wt% $Na_2O$ and 1.38 wt% $K_2O$. Later work on alkali-rich compositions demonstrated that liquids with elevated Na and K displayed systematically low $K_{D,Fe2+-Mg}$ values, down to 0.23 in melts with 7.5 wt% $Na_2O$ (Sack et al. 1987; Shi 1993; Wasylenki et al. 2003; both studies run in Fe capsules). Variations in the concentrations of major elements in the liquid (e.g, $SiO_2$ – Longhi et al. 1978; Gee & Sack 1988; Toplis 2005; FeO+MgO – Kushiro & Walter 1998), as well as the composition of the olivine (Toplis 2005; Blundy et al. 2020) have also been recognized as important factors in the variability of $K_{D,Fe2+-Mg}$. Thus a variety of empirical and thermodynamic models have been developed to describe variations in $K_{D,Fe2+-Mg}$ as a function of melt and olivine composition, as well as other intensive variables such as T, P, and $fO_2$ (e.g., Longhi et al. 1978; Ford et al. 1983; Gee & Sack 1988; Snyder &

Carmichael 1992; Sobolev & Nikogosian 1994; Kushiro & Walter 1998; Kushiro & Mysen et al. 2002; Herzberg & O'Hara 2002; Toplis 2005 Filiberto et al. 2011; Blundy et al. 2020), and these provide more accurate descriptions of olivine-melt equilibria than is possible by simply adopting a constant value for $K_{D,Fe2+-Mg}$. For example, melting and crystallization calculations involving olivine are sensitive to the choice of value for the $K_{D,Fe2+-Mg}$; for high-MgO Hawaiian compositions, the MgO contents of parental melts reconstructed by olivine addition calculations decrease by ~1 wt% for every 0.015 absolute decrease in the $K_{D,Fe2+-Mg}$ (Matzen et al. 2011), which in turn affects estimates of mantle phase equilibria and potential temperatures. Therefore, for this and many other applications including reconstruction of primary melts (e.g., Herzberg & O'Hara 2002), reversing post-entrapment crystallization for olivine-hosted melt inclusions (e.g. Danyushevsky et al. 2002), and calculation of $Fe^{3+}/Fe^{2+}$ in olivine-saturated liquids (Blundy et al. 2020), accurate parameterization of the composition dependence of $K_{D,Fe2+-Mg}$ is important for accurately modeling mantle melting and crystallization processes.

$Fe^{3+}$ is incompatible in olivine and $Fe^{3+}/Fe^{2+}$ ratios in silicate melts vary significantly over the geologically relevant range of oxygen fugacity ($fO_2$). Therefore, an additional source of error in reported values for the $K_{D,Fe2+-Mg}$ arises from uncertainty in the fraction of ferric iron present in the melt ($Fe^{3+}/Fe^{Total}$), because routine microprobe measurements of glass (i.e., quenched melt) report all Fe as FeO (FeO*). Only a small fraction of experimental olivine-liquid pairs have direct measurements of $Fe^{3+}/Fe^{2+}$ in the quenched glasses, and for these the $K_{D,Fe2+-Mg}$ can be calculated directly (Mysen & Dubinsky 2004; Partzsch et al. 2004; Mysen & Shang 2005; Mysen 2006, 2007; Matzen et al. 2011; Blundy et al. 2020; Waters et al. 2020). However, for most experiments, the $Fe^{3+}/Fe^{2+}$ ratio of melt must be calculated using one of the many algorithms that relate the $fO_2$, T, P, and compositions of experimentally equilibrated glasses with their $Fe^{3+}/Fe^{2+}$

(e.g., Sack et al. 1980; Kilinc et al. 1983; Kress & Carmichael 1988; Borisov & Shapkin 1989; Kress & Carmichael 1991; Nikolaev et al. 1996; Jayasuriya et al. 2004; Ghiorso & Kress 2004; Putirka 2016; Borisov et al. 2018; O'Neill et al. 2018). There is considerable disagreement between the different parameterizations of $fO_2$ and $Fe^{3+}/Fe^{2+}$ in the liquid, the systematics of which have been recently reviewed (Matzen et al. 2011; Putirka 2016; Borisov et al. 2018). Consequently for experiments run at terrestrially relevant $fO_2$, where the fraction of Fe in the melt present as $Fe^{3+}$ can be up to ~70% (in air, e.g., Kress & Carmichael 1991), it is difficult to deconvolve the effect of melt and olivine composition on the $K_{D,Fe2+-Mg}$ from our incomplete understanding of how melt composition and $fO_2$ affect $Fe^{3+}/Fe^{2+}$ ratios in melt (Blundy et al. 2020).

One way to circumvent this confounding issue is to focus on experiments run under sufficiently reducing conditions that nearly all the Fe present in the liquid is $Fe^{2+}$. Although a considerable amount of experimental data is available for the reducing conditions necessary to apply this approach, most of these studies focus on lunar, martian, and asteroidal bulk compositions such that the experimentally produced liquids have compositions that are unrepresentative of those found on Earth. Many of these experimental liquids contain high Ti and Fe (see section 6.3), and a subset of the data have liquids with elevated alkali contents (Shi et al. 1993; Collinet & Grove 2020). Liquid compositional terms for Ti, Fe, Na, and K are amongst the most important parameters in models relating melt composition to $K_{D,Fe2+-Mg}$ (e.g., Longhi et al., 1978; Ford et al. 1983; Kushiro & Walter 1998; Toplis, 2005) and in models of the composition dependence of $Fe^{3+}/Fe^{2+}$ (most models contain both an alkali and FeO* term (a notable exception being O'Neill 2018), and $TiO_2$ appears in Borisov & Shapkin 1990, Nikolaev et al. 1996, and Borisov et al. 2018). Another important factor is that many of these studies are from the 1970s and 1980s, and in the intervening 40-50 years there have been substantial

improvements in electron microprobe technology and data reduction for WDS measurements, as well as improvements in imaging (e.g., back-scattered electron imaging), making it much easier to select rims of crystals that may be in equilibrium with the surrounding quenched melt.

The goal of the experiments described in this chapter (referred to as the **R**educed $\mathbf{K_D}$– or RKD experiments) was to generate a dataset of olivine-liquid pairs at $fO_2$s within ±0.5 log units of the iron-wüstite buffer (i.e., IW±0.5) using terrestrial basaltic compositions that are underrepresented among previous experiments run at similarly reducing conditions. At $fO_2$s ≤ IW+0.5, the concentration of $Fe^{3+}$ in the liquid is sufficiently low that any correction from $K_{D,Fe^*\text{-}Mg}$ (the measurable quantity that uses FeO* from electron probe analysis of glass) to $K_{D,Fe2+\text{-}Mg}$ (the themodynamically well-defined quantity that uses FeO in place of FeO*) is small and generally negligible, and absolute differences in $Fe^{3+}/Fe^{2+}$ ratios predicted by the various available models are also small. In addition, experimental and analytical protocols were designed to produce high-precision measurements of Fe and Mg (and Mn) in the coexisting phases in the experiments to more clearly isolate compositional effects on the $K_{D,Fe2+\text{-}Mg}$ described in equation (1) from those on $Fe^{3+}/Fe^{2+}$ in melts. Based on these new data and a subset of literature data that passed through various quality filters, we present a quantitative thermodynamically based parameterization of the compositional effects on $K_{D,Fe2+\text{-}Mg}$.

## 3. Methods

### 3.1 Starting Compositions

The bulk compositions used in this study are based on three basalt types [ocean island basalts (OIBs); high-Al basalts (HABs); and mid-ocean ridge basalts (MORBs)], and they were designed to have olivine as a liquidus phase and to exhibit a range of Mg#s (100·Mg/[Mg+Fe*], molar, where Fe* = total Fe as FeO). Bulk compositions are reported in Table 1. $SiO_2$ contents are 45-50.5 wt%; Mg# ranges from 40-80; $TiO_2$ contents are

0.55-1.42 wt%; and $CaO/Al_2O_3$ ratios are 0.65-0.89. SynHP1 is a synthetic, alkali-free picrite based on whole-rock compositions from Mauna Kea—i.e., the low-$SiO_2$ array collected by the Hawai‘i Scientific Drilling Project (see Matzen et al. 2011 for further details). To this oxide mix with ~25.7 wt% MgO, we added $Mn_2O_3$ and $Cr_2O_3$ to generate the synHP1+Cr+Mn mix listed in Table 1. All of the remaining bulk composition also have MnO contents (~0.5 wt%) that are higher than those typical of terrestrial basalts (0.1 – 0.2 wt%; e.g., Gale et al., 2013; Le Maitre, 1976) in order to facilitate more precise determinations of Mn partitioning between olivine and melt. The HAB+Ol+Mn composition is a natural high-alumina basalt from Medicine Lake Highland (82-72c; Baker et al. 1991), to which 15% synthetic $Mg_2SiO_4$ powder was added in order to expand the primary liquidus field of olivine to temperatures above 1300°C (based on calculations using MELTS; Ghiorso and Sack, 1995). The added forsterite resulted in a bulk composition with Mg# = 76, and the added $Mn_2O_3$ raised the MnO content from 0.16 to 0.49 wt%. In contrast to the synHP1±Cr+Mn compositions and the MORB compositions (discussed below) that are alkali-free, the $Na_2O + K_2O$ content of HAB+Ol+Mn is 1.96 wt%. Starting with an initial target MORB composition with 14 wt% MgO (Gale et al. 2014), three synthetic alkali-free bulk compositions were generated by varying the molar Fe/Mg ratio to generate bulk Mg# values of 80, 60, and 40. The initial target MORB composition (MgO = 14 wt%, listed in the notes to Table 1) is based on least-squares fits in oxide vs. MgO space to the $Fo_{90}$-corrected mid-ocean ridge segment average compositions from Gale et al. (2014). From this base composition (which has Mg# = 72), the bulk compositions synMORB80 (Mg# 80) and synMORB60 (Mg# 60) were generated by varying the ratio of MgO and FeO* at constant molar MgO+FeO*. MELTS calculations (Ghiorso and Sack 1995) at an $fO_2$ = IW+0.5 (referenced to Huebner 1971)

| | synHP1 Matzen[a] | synHP1+Cr+Mn[b] | HAB+Ol+Mn | synMORB80[c] | synMORB60 | synMORB40 |
|---|---|---|---|---|---|---|
| $SiO_2$ | 45.39 | 44.57 | 47.14 | 50.50 | 48.97 | 43.78 |
| $TiO_2$ | 1.41 | 1.38 | 0.55 | 1.07 | 1.04 | 0.92 |
| $Al_2O_3$ | 8.28 | 8.47 | 15.49 | 14.04 | 13.61 | 12.17 |
| $Cr_2O_3$ | 0.22 | 1.05 | 0.03 | 0.00 | 0.00 | 0.00 |
| FeO* | 12.03 | 11.82 | 8.56 | 7.09 | 13.75 | 24.16 |
| MnO | 0.18 | 0.81 | 0.49 | 0.50 | 0.50 | 0.50 |
| MgO | 25.48 | 25.02 | 15.53 | 15.92 | 11.58 | 9.04 |
| CaO | 6.72 | 6.60 | 10.13 | 10.88 | 10.55 | 9.43 |
| $Na_2O$ | 0.00 | 0.00 | 1.88 | 0.00 | 0.00 | 0.00 |
| $K_2O$ | 0.00 | 0.00 | 0.08 | 0.00 | 0.00 | 0.00 |
| NiO | 0.29 | 0.29 | 0.08 | 0.00 | 0.00 | 0.00 |
| $P_2O_5$ | 0.00 | 0.00 | 0.04 | 0.00 | 0.00 | 0.00 |
| Total | 100 | 100 | 100 | 100 | 100 | 100 |
| Mg# | 79.1 | 79.1 | 76.4 | 80.0 | 60.0 | 40.0 |

**Table 1.** Bulk compositions of starting compositions based on weighed masses of oxide and forsterite powders. FeO* = all Fe expressed as FeO. Mg# = 100·[Mg/(Mg+Fe)] molar. **(a)** From Matzen et al. (2011), Table 1 and Table 3 (the superliquidus experiments 43 and 34). The authors noted that the synHP1 mix had gained ~0.7 wt% $Al_2O_3$ during the grinding process, probably reflecting the fact that the grinding was done using an alumina mortar and pestle and that some fraction of the $Al_2O_3$ oxide powder had converted to corundum during repeated firings at 800–1000°C. This increase in $Al_2O_3$ is included in the synHP1 composition reported above. **(b)** Mass balance of the synHP1+Cr+Mn experiments showed a consistent increase in $Al_2O_3$ in the calculated bulk compositions relative to the nominal synHP1+Cr+Mn composition; the average increase was ~3.3% and is most likely due to the same issue discussed in (a) since synHP1+Cr+Mn was constructed using powder from the original batch of synHP1. The $Al_2O_3$ content of the nominal synHP1+Cr+Mn composition has been increased by 0.31 wt%, the remaining oxide concentrations were reduced proportionally. **(c)** Initial target MORB composition based on Gale et al. (2013) average subaqueous ridge segments, expressed in wt% on an alkali-free basis: $SiO_2$ = 50.2, $TiO_2$ = 1.07, $Al_2O_3$ = 13.95, FeO* = 9.54, MgO = 14.43, CaO = 10.81, Mg# = 74.

using a bulk composition with Mg# = 40 derived in the manner described above predicted pigeonite as the liquidus phase, followed by plagioclase, and then olivine at T ~ 1100°C. In order to expand the stability field for olivine, the total molar MgO+FeO was increased by 1.2x for this bulk composition (synMORB40) relative to the molar MgO+FeO in the two more magnesian synthetic MORBs. MELTS calculations on this modified mixture predicted olivine as the primary liquidus phase at T = 1215 °C. MnO contents in all three compositions were increased to 0.49-0.50 wt%.

High-purity oxides, $CaCO_3$, forsterite powder, and the preexisting synHP1 and HAB powders were dried to remove adsorbed water prior to weighing ($SiO_2$ and $TiO_2$ at 800 °C, $Al_2O_3$ at 1000 °C, $Fe_2O_3$ at 700 °C, $CaCO_3$ at 400 °C, and $Cr_2O_3$, $Mn_2O_3$, forsterite, and the synHP1 and HAB powders in a vacuum oven at 120 °C). The oxides were weighed then ground and mixed under ethanol in an alumina mortar for at least 1 hr. The homogenized powders were then pressed into ~1 cm diameter pellets under a vacuum, with acetone as a binding agent.

### 3.2 Experimental Design

All experiments were run at 1 atm in a vertical Deltech furnace using $H_2$-$CO_2$ gas mixtures to control the $fO_2$. Experimental run temperatures were determined with a type-S thermocouple calibrated at the melting point of gold. The $fO_2$ of the furnace atmosphere was measured using an yttria-stabilized zirconia oxygen sensor, which was calibrated by bracketing the $fO_2$ of the IW reaction ($Fe + ½ O_2 = FeO$) at 1350 °C. The $fO_2$ measured for the IW reaction was accurate to within 0.1 log units of the accepted value (Huebner 1971), and the typical precision in $fO_2$ for a given experiment was ±0.02 log units based on in-situ monitoring of the $fO_2$ sensor. Most experiments were conducted at either IW+0.5 or IW–0.5; however, three experiments using the synHP1+Cr+Mn composition were run under more oxidizing conditions ($fO_2$ = FMQ and FMQ+1, where FMQ corresponds to the β-quartz equation from Frost 1991). Samples on Re wire loops (IW±0.5

experiments) were lowered slowly into the hotspot after the furnace had been sealed and the furnace atmosphere had equilibrated (see below). In order to avoid the wire loop coming into contact with and sticking to the thermocouple or $fO_2$ sensor, these two sensors were not present in the furnace during these experiments. For experiments run at T ≥ 1225 °C, the $fO_2$ was set by inserting the $fO_2$ sensor and a thermocouple into the hotspot at 1000 °C, running the furnace up to the desired experimental T, adjusting the ratios of $H_2$ and $CO_2$ until the target emf reading was met, and running the back down to 1000 °C. For the experiments at 1175 °C, the $fO_2$ was set at 1250 °C to ensure that the $H_2$-$CO_2$ gas mixture was in equilibrium (Beckett and Mendybaev 1997); the furnace was then cooled to 1175 °C and the mix slightly adjusted to achieve the correct $fO_2$ for that temperature. The furnace tube was routinely checked for gas leaks, and after every two or three experiments, the thermocouple and $fO_2$ sensor were inserted into the hotspot to check for drift over time, which was not observed except in cases where a heating element or the furnace tube needed to be replaced, resulting in migration of the position of the hotspot. In these cases, the furnace hotspot was relocated and the T and $fO_2$ were reset before proceeding with experiments.

For each experiment, a chip weighing ~80-100 mg was broken off the pressed pellet of a given starting mixture/composition and attached to either a Re wire loop (for the IW±0.5 runs) or a Pt loop (for the FMQ and FMQ+1 runs) using polyvinyl alcohol as a binding agent. The Re (or Pt) loop and sample were suspended from a Pt quench wire (0.005″ diameter) attached to two 0.039″ diameter Pt wires encased in a ceramic rod. In order to prevent volatilization of Re in the oxidizing atmosphere of the furnace prior to initiating the flow of the $H_2$-$CO_2$ gas mixture (Borisov and Jones, 1999), the ceramic rod was positioned so that loop and sample were just below the underside of the brass sample-assembly plate and were thus at the top (and cool) part of the furnace tube when inserted

into the furnace. With the controller set at 1000 °C, the $H_2$-$CO_2$ gas mixture was then introduced into the sealed furnace tube, and allowed to equilibrate for ~30 minutes. The Re loop was then displaced in 2″ increments every five minutes until the silicate sample was suspended in the furnace hotspot. The Pt-loop experiments were placed directly into the furnace hotspot at ~1000 °C. For both types of loops, once the silicate chip was positioned in the hotspot, the furnace was ramped up to the target run temperature at a rate of ~10 °C/min. Most experiments were held isothermally at temperatures of 1175–1400 °C for 6–48 hr; however, two of the oxidizing experiments (SOCrAl-1c and SOCrAl-1d) involved temperature cycling (Mill & Glazner, 2013). Both of these experiments were run for 48 hr with temperatures varying between 1340 and 1360 °C (SOCrAl-1c had 4 cycles, 1.7 °C/hr; SOCrAl-1d had 36 cycles, 15 °C/hr). All experiments were terminated by electrically fusing the 0.005" Pt hanging wire and dropping the silicate and wire loop directly into deionized water. Temperature, run time, $fO_2$, and other notes on particular experiments, are reported in Table 2. After quenching, the silicate was physically separated from the wire loop by gently tapping with a hammer and a small-diameter drill blank, which was sufficient to remove nearly all the silicate material after each experiment. As described in the next paragraphs, loops were often reused, but were not shared for experiments using different bulk compositions to avoid cross-contamination and to avoid Fe transfer into or out of the loop for samples with different FeO contents.

In the experimentally usable region of T-$fO_2$ space, Re forms alloys with Fe to a lesser extent than Pt (e.g., Borisov and Jones 1999; Grove 1981; Kessel et al. 2001). Nevertheless, at $fO_2 \lesssim$ IW+1, Fe-loss to a Re sample container becomes non-trivial (Borisov and Jones, 1999) and for this reason the Re loops were preconditioned for each bulk composition and $fO_2$ (i.e., either IW+0.5 or IW–0.5) by running one or two "saturation" experiments for each loop (denoted "S" in Table 2). The preconditioned Re

loops were then reused for one or more subsequent experiments, and those experiments are referred to as "equilibration" experiments ("E" in Table 2). Because the affinity of Fe to alloy with Re is greater with decreasing $fO_2$ (Borisov & Jones 1999), two saturation experiments were run to precondition loops for equilibration experiments run at IW–0.5 before they were considered useable. The loop number for each experiment is also listed in Table 2, along with experimentally produced phases, and the % change in bulk FeO as determined by mass balance (see section 5.2.2).

### 3.3 Analytical Techniques

Chips of silicate material recovered from each experiment were mounted in epoxy, ground down with alumina papers, polished with increasingly fine diamond powder (2 to 0.25 μm), and ultrasonicated in ethanol. All experiments and secondary standards were carbon coated at the same time to ensure that the carbon-coat thicknesses were uniform. Quantitative wavelength-dispersive (WDS) analyses of glasses, silicates, and oxides were collected with a JEOL JXA-8200 electron microprobe at Caltech operating at an accelerating voltage of 15 keV. Backgrounds on both standards and unknowns were determined using the mean-atomic-number procedure of Donovan and Tingle (1996) and raw X-ray counts were reduced with a modified ZAF procedure (Armstrong 1988). Glasses were analyzed using a 10 nA beam current, and a 10 μm diameter beam. Secondary glass standards (BHVO-2g, BIR-1g, and GOR-128g) were analyzed before and after measuring the glasses in each experiment to monitor instrumental drift and to assess accuracy and precision. Glass analyses with oxide sums of 100 ± 1.5% were considered acceptable. Olivines were analyzed using a 40 nA beam current with a 1 μm diameter beam; secondary olivine standards from Caltech's collection (San Carlos olivine, CIT- SC, and Guadalupe Island olivine GRR-2159, GO)

**Table 2 – Experimental run conditions, phase products, and olivine-liquid Fe-Mg exchange coefficients**

| Name | Starting Mix | Run Type | Duration (hr) | T (°C) | $\log_{10}fO_2$ | ΔIW | Re[a] Loop # | Phases[b] | ΔFeO (%)[c] | $K_D^{ol/liq}$, Fe*-Mg[d] | 1σ[e] | $K_D^{ol/liq}$, $Fe^{2+}$-Mg[f] |
|---|---|---|---|---|---|---|---|---|---|---|---|---|
| RKD-1 | synHP1+CrMn | S | 6 | 1350 | -9.7 | +0.5 | 1 | ol, gl, sp, Re | -1.88 | 0.3124 | 0.0089 | 0.3247 |
| RKD-2 | synHP1+CrMn | S | 17 | 1350 | -9.7 | +0.5 | 2 | ol, gl, sp, Re | -10.80 | 0.3133 | 0.0102 | 0.3256 |
| RKD-3 | synHP1+CrMn | S | 17 | 1350 | -9.7 | +0.5 | 3 | ol, gl, sp | -13.17 | 0.3133 | 0.004 | 0.3253 |
| RKD-4 | synHP1+CrMn | S | 42 | 1350 | -9.7 | +0.5 | 4 | ol, gl, sp | -13.71 | 0.3108 | 0.0031 | 0.3224 |
| RKD-5 | synHP1+CrMn | **E** | 19 | 1350 | -9.7 | +0.5 | 4 | ol, gl, sp | -6.12 | 0.3154 | 0.0039 | 0.3273 |
| RKD-6 | synHP1+CrMn | **E** | 17 | 1300 | -10.2 | +0.5 | 4 | ol, gl, sp | -2.16 | 0.3152 | 0.0029 | 0.3264 |
| RKD-7 | synHP1+CrMn | **E** | 17 | 1400 | -9.2 | +0.5 | 4 | ol, gl, sp | -6.93 | 0.3158 | 0.0038 | 0.3286 |
| RKD-8 | HAB+Ol+Mn | S | 17 | 1300 | -10.2 | +0.5 | 5 | ol, gl | -1.23 | 0.3003 | 0.0034 | 0.3111 |
| RKD-9 | HAB+Ol+Mn | S | 48 | 1300 | -10.2 | +0.5 | 5 | ol, gl | -7.32 | 0.3031 | 0.0034 | 0.3135 |
| RKD-12 | HAB+Ol+Mn | **E** | 24 | 1300 | -10.2 | +0.5 | 5 | ol, gl | -4.04 | 0.3038 | 0.0047 | 0.3146 |
| RKD-13 | synMORB Mg80 | S | 20 | 1300 | -10.2 | +0.5 | 6 | ol, gl | -3.60 | 0.3174 | 0.003 | 0.3276 |
| RKD-14 | synMORB Mg80 | **E** | 24 | 1300 | -10.2 | +0.5 | 6 | ol, gl | -4.10 | 0.3149 | 0.0034 | 0.3250 |
| RKD-15 | synMORB Mg80 | **E** | 23 | 1225 | -11.1 | +0.5 | 6 | ol, gl, px, pl | -1.85 | 0.3155 | 0.0044 | 0.3247 |
| RKD-16 | synMORB Mg60 | S | 24 | 1225 | -11.1 | +0.5 | 7 | ol,gl | -3.61 | 0.3249 | 0.0036 | 0.3352 |

| Name | Starting Mix | Run Type | Duration (hr) | T (°C) | $log_{10}fO_2$ | ΔIW | Re[a] Loop # | Phases[b] | ΔFeO (%)[c] | $K_D^{ol/liq}$, Fe*-Mg[d] | 1σ[e] | $K_D^{ol/liq}$, $Fe^{2+}$-Mg[f] |
|---|---|---|---|---|---|---|---|---|---|---|---|---|
| RKD-17 | synMORB Mg60 | **E** | 24 | 1225 | -11.1 | +0.5 | 7 | ol, gl | -2.88 | 0.3247 | 0.0035 | 0.3350 |
| RKD-19 | HAB+Ol+Mn | S | 48 | 1225 | -11.1 | +0.5 | 5 | ol, gl, pl | -5.80 | 0.3042 | 0.0069 | 0.3140 |
| RKD-20 | HAB+Ol+Mn | **E** | 48 | 1225 | -11.1 | +0.5 | 5 | ol, gl, pl | -6.43 | 0.3073 | 0.0049 | 0.3171 |
| RKD-21 | synMORB Mg60 | **E** | 48 | 1175 | -11.7 | +0.5 | 7 | ol, gl, px, pl | -0.50 | 0.3284 | 0.0049 | 0.3395 |
| RKD-22 | synMORB Mg40 | S | 48 | 1175 | -11.7 | +0.5 | 6 | ol, gl, pl | 0.87 | 0.3489 | 0.0035 | 0.3618 |
| RKD-23 | synMORB Mg40 | S | 25 | 1175 | -11.7 | +0.5 | 9 | ol, gl, pl | -0.80 | 0.3354 | 0.0057 | 0.3478 |
| RKD-24 | synMORB Mg40 | **E** | 48 | 1175 | -11.7 | +0.5 | 9 | ol, gl, pl | -0.18 | 0.3387 | 0.0034 | 0.3512 |
| RKD-25 | synHP1 Matzen | **E** | 48 | 1350 | -9.7 | +0.5 | 4 | ol, gl | -8.75 | 0.3146 | 0.0036 | 0.3263 |
| RKD-26 | synHP1+CrMn | **E** | 48 | 1300 | -10.2 | +0.5 | 4 | ol, gl, sp | -5.71 | 0.3157 | 0.0026 | 0.3267 |
| RKD-27 | synHP1 Matzen | **E** | 48 | 1350 | -6.7 | +3.5 | Pt6 | ol, gl | -0.10 | 0.2851 | 0.0027 | 0.3301 |
| RKD-28 | synMORB Mg80 | S | 24 | 1300 | -11.2 | -0.5 | 10 | ol, gl | -5.25 | 0.3180 | 0.0035 | 0.3243 |
| RKD-29 | synMORB Mg80 | S | 22 | 1300 | -11.2 | -0.5 | 10 | ol, gl | -5.69 | 0.3136 | 0.0033 | 0.3198 |
| RKD-30 | synMORB Mg80 | **E** | 24 | 1300 | -11.2 | -0.5 | 10 | ol, gl | -5.18 | 0.3174 | 0.0032 | 0.3237 |
| RKD-31 | synMORB Mg40 | S | 24 | 1175 | -12.7 | -0.5 | 11 | ol, gl, pl | -0.84 | 0.3358 | 0.0069 | 0.3434 |
| *RKD-32* | *synMORB Mg40* | *S* | *24* | *1175* | *-12.7* | *-0.5* | *11* | ol, gl, pl | *-1.27* | *0.3344* | *0.0046* | *0.3420* |

| Name | Starting Mix | Run Type | Duration (hr) | T (°C) | $\log_{10}fO_2$ | ΔIW | Re[a] Loop # | Phases[b] | ΔFeO (%)[c] | $K_D^{ol/liq}$, Fe*-Mg[d] | 1σ[e] | $K_D^{ol/liq}$, $Fe^{2+}$-Mg[f] |
|---|---|---|---|---|---|---|---|---|---|---|---|---|
| RKD-33 | synMORB Mg40 | S | 48 | 1175 | -12.7 | -0.5 | 12 | ol, gl, pl | -1.58 | 0.3459 | 0.0034 | 0.3537 |
| RKD-34 | synMORB Mg40 | S | 24 | 1175 | -12.7 | -0.5 | 12 | ol, gl, pl | -0.84 | 0.3270 | 0.0041 | 0.3345 |
| RKD-35 | synMORB Mg40 | **E** | 48 | 1175 | -12.7 | -0.5 | 12 | ol, gl, pl | -1.22 | 0.3500 | 0.004 | 0.3579 |
| SOCrAl-1c | synHP1+CrMn | **E** | 48 | 1350[g] | -5.7 | +4.5 | Pt6 | ol, gl, sp | -1.99 | 0.2711 | 0.0024 | 0.3406 |
| SOCrAl-1d | synHP1+CrMn | **E** | 48 | 1350[g] | -5.7 | +4.5 | Pt6 | ol, gl, sp | -1.62 | 0.2676 | 0.0027 | 0.3369 |

**Table 2.** Experimental run conditions and products. Starting mixes are listed in Table 1 and colored rows correspond to the same bulk composition. Saturation type experiments (S) were those used to precondition wire loops; equilibration type experiments (E) were run using the pre-saturated loops; for the (E) experiments at IW-0.5, two (S) experiments were run prior. **(a)** Re loop number used in each experiment. Note that the three experiments at or above FMQ used a Pt instead of a Re loop; it is Pt loop #6 from Matzen et al. (2011). **(b)** Phase products; ol – olivine, gl – glass, sp – spinel, px – pyroxene, pl – plagioclase, Re – Re metal globules, which were only observed in RKD-1 and RKD-2 due to an experimental error (see text). As discussed in the text, trace amounts of Pt-Fe blebs were observed in about half of the experiments, but are likely present in all (just not observed in all of the chips prepared for analysis due to their rarity). **(c)** ΔFeO loss is the percent of FeO that was lost or gained during each experiment, calculated by the mass balance routine described in the main text. **(d)** $K_D^{ol/liq}$,$Fe^*$-Mg = $[FeO/MgO]^{olivine}$ / $[FeO^*/MgO]^{glass}$ and is calculated using the averages of olivine and glass analyses in each experiment (Table 3). **(e)** 1σ calculated by summing the errors in FeO and MgO in each phase in quadrature. **(f)** $K_D^{ol/liq}$,$Fe^{2+}$-Mg, where $Fe^{3+}/Fe^{2+}$ in the glass is calculated using the expression of Borisov et al. (2018). **(g)** Average T = 1350°C for two experiments run for 48 hr with continuous temperature cycling between 1340 and 1360 °C (SOCrAl-1c had 4 cycles, 1.7 °C/hr; SOCrAl-1d had 36 cycles, 15 °C/hr); the remaining experiments were isothermal.

were measured before and after analyzing the olivines in each experiment. Olivine analyses were accepted if they had analytical totals of 100 ± 1.5%, and the stoichiometric criteria of tetrahedral cation sum of 1.000 ± 0.015, and octahedral cation sum of 2.000±0.015, both calculated on a four oxygen basis (Supplementary Figure 1). Spinels were analyzed using a 10 nA beam current, and a focused beam (<1 μm) due to their small size, typically <10 μm across. The $Fe^{3+}/Fe^{2+}$ of spinels was calculated assuming ideal stoichiometry and analyses were accepted if the measured $SiO_2$ contents, which are nominally expected to be close to zero, were ≤0.6 wt% and if the $Fe^{3+}$ corrected oxide sum was 100 ± 2.5%. Measured $SiO_2$ contents in the spinels (0.2-0.6 wt%) are likely due to Si contamination from beam interaction with the surrounding glasses or olivines (e.g., Matzen et al. 2011; Davis and Cottrell, 2018 and references therein). A beam current of 10 nA and 1 μm beam diameter were used to analyze plagioclases and pyroxenes; analyses were accepted if the oxide sum was 100 ± 2%, and the cation sum for plagioclase was 5.00±0.02 per 8 oxygens and for pyroxene was 4.00±0.05 per 6 oxygens. See Table 3 for a summary of the average olivine and glass data from each experiment; complete data tables for all phases in each experiment and for secondary standards can be found in the Supplementary Data.

Olivine grains that were >20 μm in longest dimension and that displayed well-defined crystal edges were selected for analysis. Analyses were taken in the cores of some of these grains, and rim analyses were selected to be within 2–5 μm of the crystal edge. For the purpose of olivine-liquid partitioning calculations, olivine rim analyses were used as these are most likely to be in local equilibrium with the adjacent melt. In experiments quenched from T > 1225 °C, olivine crystals appear to have a <1 μm wide overgrowth of more Fe-rich olivine (Figure 1B), however attempts to quantify the composition of this narrow zone of quench growth were unsuccessful due to the spatial resolution of the

microprobe. For these experiments, olivine rim analyses were acquired within 2–5 μm of the inner edge of the overgrowth.

Due to stage drift and beam alignment issues, some of the rim analyses acquired close to the olivine edges were affected by beam interactions with the adjacent glasses, and these are indicated by diagnostically high $Al_2O_3$ contents. The olivine cores from each experiment were used to establish a baseline concentration of $Al_2O_3$ present in olivines that were unaffected by the nearby glasses. The olivine cores have $Al_2O_3$ contents ranging from ~100–1000 ppm, with the highest contents in the synHP1+Cr+Mn experiments with elevated Cr, possibly due to coupled substitution (Colson et al. 1989). In addition to the oxide sum and stoichiometric criteria, olivine rim analyses were passed through a final filter for glass contamination: rim analyses were accepted if their $Al_2O_3$ contents were either within 0.01 wt% or less than the highest measured $Al_2O_3$ contents in olivine cores from the same experiment.

## 4. Results

### 4.1 Phase Compositions

#### 4.1.1 Glass

The compositions of experimental glasses are listed in Table 3. The Mg# ranges from 31.5 to 78.1, and the glasses produced from the same bulk composition are more Mg-rich at higher T and $fO_2$ (Figure 2B). $SiO_2$ contents range from 45 to 52 wt% (Figure 2C); $Al_2O_3$ from 11 to 18 wt% (Figure 2F), MnO from 0.17 to 0.85 wt%; $TiO_2$ from 0.6 to 2.2 wt%; CaO from 8.5 to 13 wt%; and $Na_2O+K_2O$ from 0.2 to 1.70wt%. The fact that all experiments, including those on alkali-free synHP1 and synMORB bulk compositions, contained some Na and K will be addressed in the section on mass balance

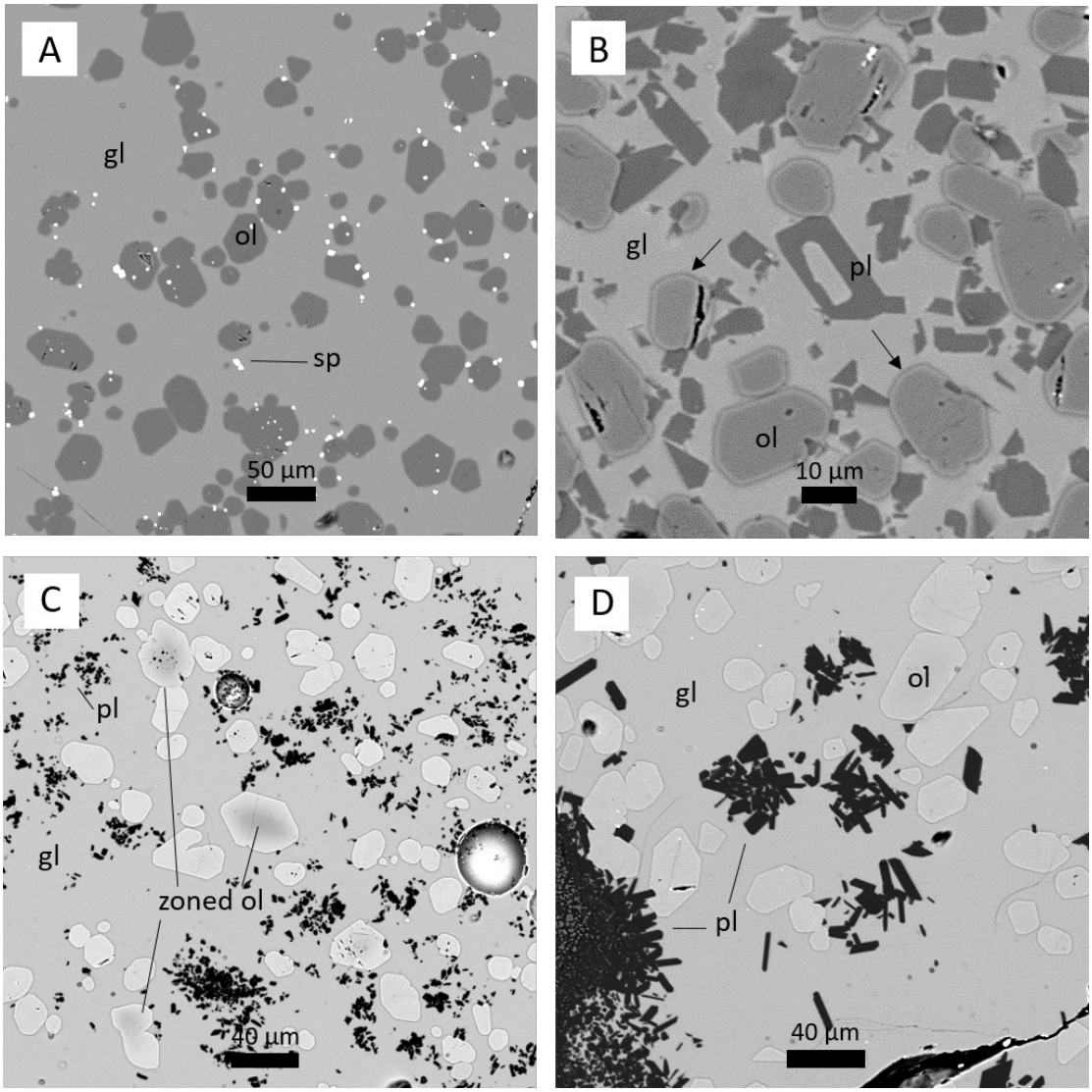


**Figure 1.** Backscattered electron (BSE) images of experimental run products. ol - olivine, gl – glass, sp – spinel, pl – plagioclase. (A) Olivine, glass, and spinel in experiment RKD-4 (synHP1+Cr+Mn). (B) Olivine, plagioclase, and glass in experimen RKD-19 (HAB+Ol+Mn), note the plagioclases contain small inclusions of melt. Arrows points to narrow quench overgrowth. (C) Olivine, plagioclase, and glass in experimen RKD-22 (synMORB40), with the contrast increased to enhance apparent zoning in some olivine phenocrysts (labeled zoned olivine). Note that most of the olivines in the field of view are unzoned. In the zoned olivines, the cores are $Fo_{\sim 67}$ and the rims are $Fo_{\sim 60}$ (D) Olivine, plagioclase, and glass in experiment RKD-35 (synMORB40 IW-0.5). None of the olivines in the field of view appear zoned. Note how feldspars tend to clump together forming clots with small pools of trapped melt.

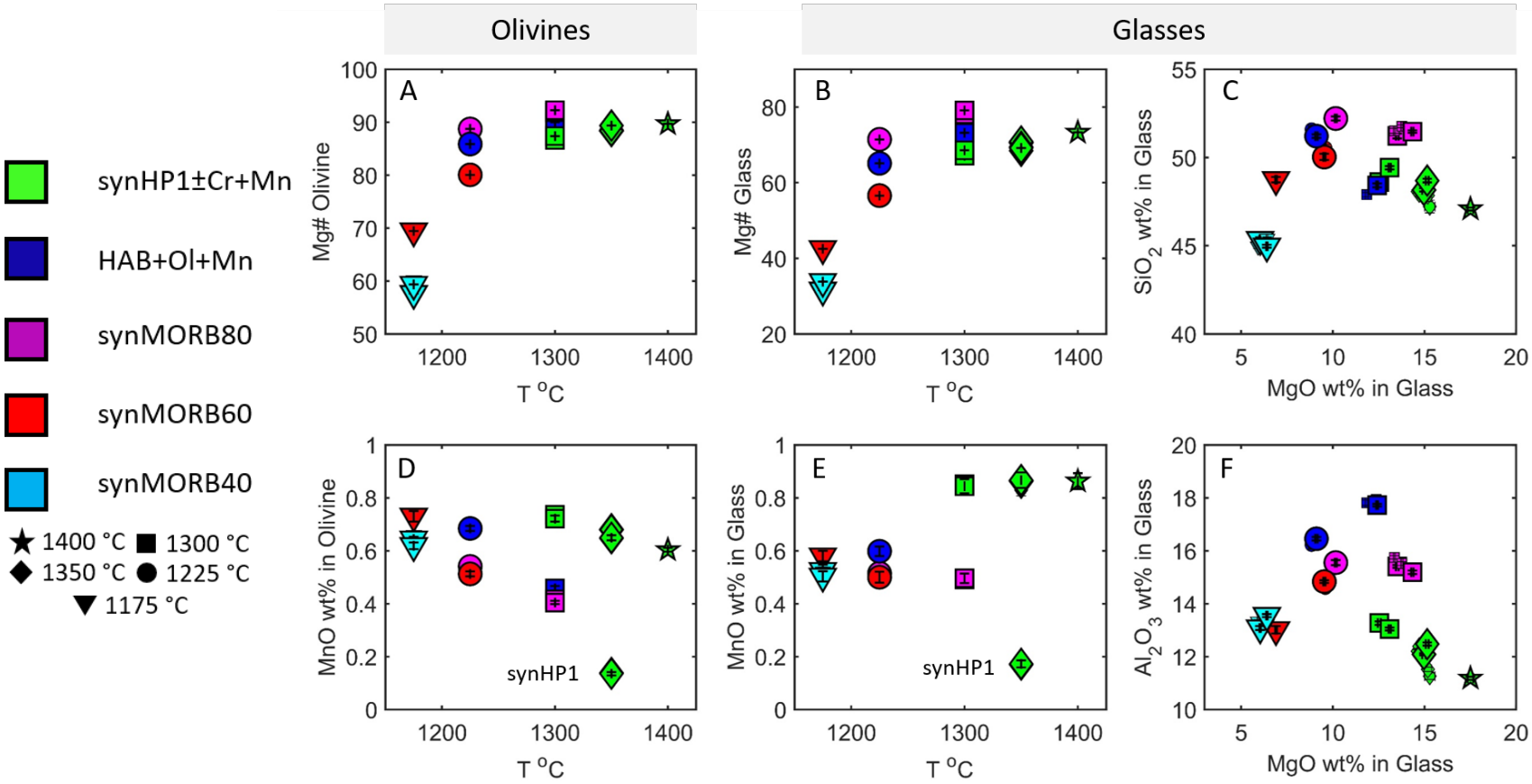


**Figure 2.** Compositional trends in experimentally formed olivines and glasses from equilibrium-type experiments (denoted E in Table 2). Green symbols are synHP1 and synHP1+Cr+Mn bulk composition experiments; dark blue symbols are HAB+Ol+Mn experiments; purple symbols are synMORB80 experiments; red symbols are synMORB60 experiments; light blue symbols are synMORB40 experiments. Triangles – 1175°C ; Circles – 1225°C; Squares – 1300°C ; Diamonds – 1350°C ; Star – 1400°C. This legend is listed here and the symbology for these RKD experiments is used throughout. Panels **(A)** and **(D)** show experimental T versus Mg# and MnO wt% in olivine rims, panels **(B)** and **(E)** show the same in experimental glasses. Panels **(C)** and **(D)** show MgO wt% in the glasses versus $SiO_2$ and $Al_2O_3$ wt%. 1σ errors are smaller than the symbol sizes.

(section 5.2.2). Except for high MnO contents, these glass compositions overlap with the range of natural basalt compositions (Gale et al. 2013), and they are all tholeiitic (Le Maitre 1976), with normative hypersthene (calculated using the CIPW norm). However, the alkali contents are low in the RKD experiments compared to most natural glasses, and the experimental glasses generated from the synMORB40 bulk composition extend to more Fe-rich compositions than are typically found in basalts on Earth.

Repeat analyses of secondary glass standards were used as a baseline for precision and accuracy that can be compared to the experimental glasses. The Fe/Mg ratios of the secondary glass standards agree within 1σ of the means of long-term reanalysis of the same glass chips over 17 different sessions spanning 2015 – 2021 (all analyses performed by L. Saper). The mean and 1σ standard deviations of Fe/Mg molar ratios measured in the three glass secondary standards (BIR-1g, BHVO-2g, and GOR-2g) are 0.612±0.005, 0.877±0.009, and 0.219±0.002, respectively, and these all overlap within 1σ of the preferred values listed in the GeoRem database (Jochum et al. 2005, 0.621±0.006 for BIR-2g, 0.889±0.008 for BHVO-2g, and 0.212±0.004 for GOR-128g). Note that there is some disagreement on the reported compositions of these standard glasses using different analytical techniques, e.g., microprobe and X-ray fluorescence (pers. comm. M. Baker), but the fact that analyses of all three secondary glasses correspond to their GeoRem database values was a sufficient criterion to conclude that the analyses of experimental glasses reported here are accurate and to forego any post-analysis corrections.

It is also instructive to compare the fractional errors (1σ of the distribution of analyses divided by the mean value) in oxide concentrations measured in the glasses as a gauge of how homogeneous the experimentally produced glasses are when compared to analyses of nominally homogeneous standard glass chips (Figure 3A,B). If the glasses in a given experiment were locally heterogeneous, we would expect its fractional errors to

be significantly higher than those of the presumed homogeneous secondary standards. The fractional errors for the three glass secondary standards (BIR-1g, BHVO-2g, and GOR-2g) range from 0.0059 to 0.0073 for FeO and from 0.0042 to 0.0068 for MgO, i.e., one standard deviation is less than a 1% deviation from the average value. Most of the experimental glasses have fractional errors that are within or close to the range defined by the secondary standards (Figure 3AB). With the exception of two saturation experiments (small blue circles at 1225 °C), which have fractional errors of 0.011 (FeO) and 0.019 (MgO), all of the experimental glasses have fractional errors <0.01. The correspondence in fractional errors between the experimentally produced glasses and the secondary standards demonstrates that, at the precision of the microprobe, the glasses represented homogeneous liquids at the time of quenching.

### 4.1.2 Olivine

Olivine Fo contents (Fo = 100·Mg/[Mg+Fe] molar) range from 57.7 to 92.3 (the minimum and maximum value is from experiment RKD-24, synMORB40 at IW+0.5 and 1175 °C; the maximum value is from RKD-30, synMORB80 at IW-0.5 and 1300 °C), Fo contents are higher in experiments run at higher T and at higher $fO_2$ using the same bulk composition (Figure 3A). MnO contents range from 0.14 to 0.74 wt% and olivines have $Cr_2O_3$ and NiO contents up to 0.50 wt% and 0.73 wt%, respectively (Table 3). All of the olivines in experiments conducted at T > 1175 °C have core and rim Fo contents that are indistinguishable within 1σ error (the analytical precision in Fo contents is on the order of 0.1 absolute, but varies somewhat based on olivine Fe/Mg). In the synMORB40 bulk composition experiments conducted at T = 1175 °C and at IW±0.5, high-contrast backscattered electron (BSE) imagery revealed two olivine populations: olivines that appear unzoned based on the BSE images and zoned olivines with cores that appear darker than their rims in BSE (Figure 1C). The zoned olivines make up less than 2% of the olivine grains exposed on the surface of a polished chip from a given experiment and

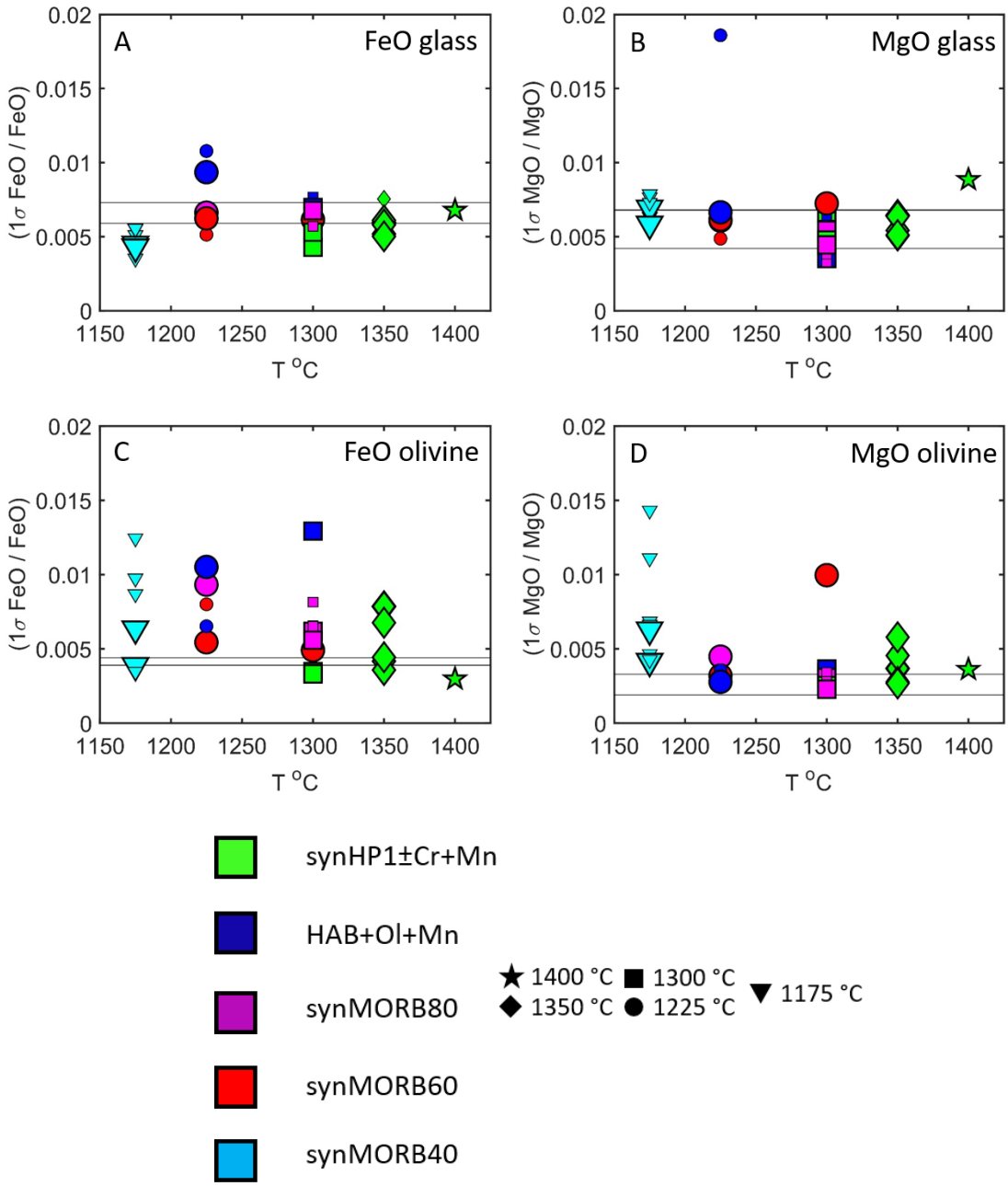


**Figure 3.** Fractional errors (1σ/mean) of analyses of FeO and MgO in experimental glasses (**A** and **B**) and of olivine rims (**C** and **D**) . The horizontal lines correspond to the range of fractional errors measured in repeat analyses of secondary standard olivines (SC-CIT and GO) and glasses (BHVO-2g, BIR-1g, and GOR-128g). Larger symbols represent equilibrium experiments, smaller symbols represent saturation experiments.

**Table 3.**

| Name | Bulk Mix | T °C | ΔIW | Phase | n | $SiO_2$ | $TiO_2$ | $Al_2O_3$ | $Cr_2O_3$ | FeO | MnO | MgO | CaO | $Na_2O$ | $K_2O$ | NiO | Totals |
|---|---|---|---|---|---|---|---|---|---|---|---|---|---|---|---|---|---|
| RKD-1 | synHP1+Cr+Mn | 1350 | +0.5 | Gl | 46 | 47.22 | 1.94 | 11.26 | 0.58 | 11.64 | 0.86 | 15.29 | 9.37 | 0.72 | 0.04 | | 98.92 |
| | | | | | | 0.36 | 0.11 | 0.12 | 0.15 | 0.23 | 0.03 | 0.28 | 0.10 | 0.04 | 0.01 | | 0.46 |
| | | | | Ol | 20 | 39.39 | 0.01 | 0.11 | 0.44 | 11.33 | 0.68 | 47.62 | 0.30 | 0.00 | 0.00 | | 99.88 |
| | | | | | | 0.36 | 0.02 | 0.02 | 0.02 | 0.09 | 0.01 | 0.22 | 0.02 | 0.00 | 0.00 | | 0.49 |
| RKD-2 | synHP1+Cr+Mn | 1350 | +0.5 | Gl | 48 | 47.85 | 1.94 | 11.52 | 0.52 | 10.48 | 0.84 | 15.18 | 9.52 | 1.13 | 0.07 | | 99.05 |
| | | | | | | 0.34 | 0.12 | 0.08 | 0.02 | 0.23 | 0.02 | 0.21 | 0.10 | 0.04 | 0.01 | | 0.38 |
| | | | | Ol | 25 | 39.21 | 0.01 | 0.11 | 0.46 | 10.55 | 0.68 | 48.79 | 0.30 | 0.00 | 0.00 | | 100.11 |
| | | | | | | 0.57 | 0.01 | 0.02 | 0.02 | 0.18 | 0.01 | 0.52 | 0.01 | 0.00 | 0.00 | | 0.52 |
| RKD-3 | synHP1+Cr+Mn | 1350 | +0.5 | Gl | 20 | 48.07 | 1.95 | 12.20 | 0.50 | 10.14 | 0.83 | 14.63 | 9.55 | 1.04 | 0.07 | 0.02 | 98.99 |
| | | | | | | 0.09 | 0.03 | 0.06 | 0.02 | 0.08 | 0.02 | 0.08 | 0.03 | 0.05 | 0.01 | 0.02 | 0.22 |
| | | | | Ol | 15 | 40.09 | 0.05 | 0.09 | 0.44 | 10.20 | 0.67 | 46.96 | 0.30 | 0.02 | 0.00 | 0.17 | 99.00 |
| | | | | | | 0.25 | 0.01 | 0.01 | 0.01 | 0.08 | 0.01 | 0.18 | 0.01 | 0.01 | 0.00 | 0.02 | 0.30 |
| RKD-4 | synHP1+Cr+Mn | 1350 | +0.5 | Gl | 20 | 47.95 | 1.96 | 12.39 | 0.55 | 10.11 | 0.85 | 14.71 | 9.54 | 0.69 | 0.06 | 0.01 | 98.82 |
| | | | | | | 0.15 | 0.03 | 0.08 | 0.04 | 0.06 | 0.03 | 0.09 | 0.03 | 0.04 | 0.00 | 0.01 | 0.22 |
| | | | | Ol | 10 | 40.31 | 0.05 | 0.08 | 0.44 | 10.07 | 0.66 | 47.14 | 0.28 | 0.01 | 0.00 | 0.14 | 99.19 |
| | | | | | | 0.12 | 0.01 | 0.00 | 0.02 | 0.04 | 0.01 | 0.11 | 0.01 | 0.01 | 0.00 | 0.01 | 0.21 |
| RKD-5 | synHP1+Cr+Mn | 1350 | +0.5 | Gl | 20 | 48.16 | 1.95 | 12.09 | 0.56 | 11.13 | 0.87 | 14.97 | 9.48 | 0.48 | 0.04 | 0.06 | 99.78 |
| | | | | | | 0.10 | 0.02 | 0.04 | 0.02 | 0.07 | 0.02 | 0.10 | 0.02 | 0.04 | 0.01 | 0.02 | 0.17 |
| | | | | Ol | 15 | 39.97 | 0.05 | 0.08 | 0.44 | 10.97 | 0.68 | 46.79 | 0.27 | 0.01 | 0.00 | 0.33 | 99.59 |
| | | | | | | 0.31 | 0.01 | 0.01 | 0.02 | 0.09 | 0.01 | 0.17 | 0.01 | 0.01 | 0.00 | 0.02 | 0.44 |
| RKD-6 | synHP1+Cr+Mn | 1300 | +0.5 | Gl | 18 | 48.61 | 2.14 | 13.27 | 0.40 | 10.93 | 0.85 | 12.53 | 10.39 | 0.35 | 0.03 | 0.08 | 99.58 |
| | | | | | | 0.12 | 0.03 | 0.07 | 0.02 | 0.05 | 0.02 | 0.08 | 0.04 | 0.03 | 0.01 | 0.02 | 0.20 |
| | | | | Ol | 12 | 39.63 | 0.04 | 0.07 | 0.34 | 12.42 | 0.74 | 45.18 | 0.28 | 0.01 | 0.00 | 0.53 | 99.24 |
| | | | | | | 0.09 | 0.01 | 0.00 | 0.01 | 0.04 | 0.01 | 0.15 | 0.01 | 0.01 | 0.00 | 0.02 | 0.23 |

| Name | Bulk Mix | T °C | ΔIW | Phase | n | $SiO_2$ | $TiO_2$ | $Al_2O_3$ | $Cr_2O_3$ | FeO | MnO | MgO | CaO | $Na_2O$ | $K_2O$ | NiO | Totals |
|---|---|---|---|---|---|---|---|---|---|---|---|---|---|---|---|---|---|
| RKD-7 | synHP1+Cr+Mn | 1400 | +0.5 | Gl | 19 | 47.08 | 1.78 | 11.18 | 0.74 | 11.37 | 0.86 | 17.51 | 8.65 | 0.29 | 0.04 | 0.04 | 99.55 |
| | | | | | | 0.08 | 0.03 | 0.06 | 0.02 | 0.08 | 0.03 | 0.15 | 0.04 | 0.04 | 0.01 | 0.02 | 0.19 |
| | | | | Ol | 12 | 39.95 | 0.04 | 0.09 | 0.50 | 9.74 | 0.60 | 47.48 | 0.27 | 0.01 | 0.00 | 0.22 | 98.91 |
| | | | | | | 0.18 | 0.01 | 0.00 | 0.02 | 0.03 | 0.01 | 0.17 | 0.01 | 0.01 | 0.00 | 0.01 | 0.32 |
| RKD-8 | HAB+Ol+Mn | 1300 | +0.5 | Gl | 20 | 47.89 | 0.60 | 17.81 | 0.03 | 8.26 | 0.49 | 11.84 | 11.29 | 1.56 | 0.08 | 0.03 | 99.90 |
| | | | | | | 0.12 | 0.02 | 0.10 | 0.01 | 0.05 | 0.02 | 0.08 | 0.03 | 0.06 | 0.01 | 0.01 | 0.24 |
| | | | | Ol | 7 | 39.98 | 0.01 | 0.08 | 0.03 | 9.95 | 0.47 | 47.54 | 0.36 | 0.01 | 0.00 | 0.28 | 98.71 |
| | | | | | | 0.16 | 0.01 | 0.01 | 0.00 | 0.07 | 0.01 | 0.12 | 0.01 | 0.01 | 0.00 | 0.01 | 0.24 |
| RKD-9 | HAB+Ol+Mn | 1300 | +0.5 | Gl | 20 | 48.33 | 0.60 | 17.94 | 0.03 | 7.78 | 0.48 | 12.36 | 11.28 | 1.00 | 0.07 | 0.02 | 99.90 |
| | | | | | | 0.13 | 0.02 | 0.08 | 0.01 | 0.06 | 0.02 | 0.07 | 0.03 | 0.04 | 0.01 | 0.01 | 0.18 |
| | | | | Ol | 11 | 40.30 | 0.01 | 0.07 | 0.02 | 9.21 | 0.45 | 48.30 | 0.32 | 0.01 | 0.00 | 0.16 | 98.85 |
| | | | | | | 0.16 | 0.01 | 0.02 | 0.00 | 0.05 | 0.01 | 0.14 | 0.01 | 0.01 | 0.00 | 0.02 | 0.27 |
| RKD-12 | HAB+Ol+Mn | 1300 | +0.5 | Gl | 15 | 48.42 | 0.60 | 17.72 | 0.03 | 8.11 | 0.49 | 12.41 | 11.33 | 1.34 | 0.08 | 0.02 | 100.58 |
| | | | | | | 0.11 | 0.02 | 0.05 | 0.01 | 0.06 | 0.02 | 0.04 | 0.02 | 0.05 | 0.01 | 0.02 | 0.13 |
| | | | | Ol | 15 | 40.45 | 0.01 | 0.07 | 0.03 | 9.58 | 0.46 | 48.25 | 0.34 | 0.01 | 0.00 | 0.20 | 99.38 |
| | | | | | | 0.13 | 0.01 | 0.02 | 0.01 | 0.12 | 0.01 | 0.18 | 0.01 | 0.01 | 0.00 | 0.02 | 0.21 |
| RKD-13 | synMORB80 | 1300 | +0.5 | Gl | 20 | 51.18 | 0.79 | 15.49 | 0.00 | 6.76 | 0.48 | 13.42 | 11.64 | 0.34 | 0.02 | 0.00 | 100.12 |
| | | | | | | 0.10 | 0.01 | 0.05 | 0.00 | 0.04 | 0.02 | 0.05 | 0.04 | 0.03 | 0.00 | 0.01 | 0.14 |
| | | | | Ol | 14 | 40.84 | 0.02 | 0.05 | 0.00 | 7.94 | 0.42 | 49.66 | 0.30 | 0.01 | 0.00 | 0.01 | 99.25 |
| | | | | | | 0.24 | 0.01 | 0.02 | 0.00 | 0.04 | 0.01 | 0.15 | 0.01 | 0.01 | 0.00 | 0.01 | 0.38 |
| RKD-14 | synMORB80 | 1300 | +0.5 | Gl | 20 | 51.22 | 0.80 | 15.41 | 0.00 | 6.75 | 0.49 | 13.51 | 11.77 | 0.27 | 0.02 | 0.01 | 100.24 |
| | | | | | | 0.13 | 0.02 | 0.05 | 0.00 | 0.04 | 0.02 | 0.07 | 0.03 | 0.03 | 0.01 | 0.01 | 0.15 |
| | | | | Ol | 10 | 41.19 | 0.02 | 0.04 | 0.00 | 7.88 | 0.42 | 50.09 | 0.30 | 0.01 | 0.00 | 0.00 | 99.94 |
| | | | | | | 0.14 | 0.01 | 0.01 | 0.00 | 0.05 | 0.01 | 0.15 | 0.01 | 0.01 | 0.00 | 0.00 | 0.28 |
| RKD-15 | synMORB80 | 1225 | +0.5 | Gl | 20 | 52.21 | 1.07 | 15.55 | 0.00 | 7.24 | 0.51 | 10.16 | 12.89 | 0.13 | 0.01 | 0.01 | 99.79 |
| | | | | | | 0.11 | 0.03 | 0.10 | 0.00 | 0.05 | 0.02 | 0.06 | 0.04 | 0.03 | 0.00 | 0.02 | 0.15 |
| | | | | Ol | 10 | 40.39 | 0.02 | 0.04 | 0.00 | 10.65 | 0.54 | 47.38 | 0.34 | 0.00 | 0.00 | 0.00 | 99.38 |

| Name | Bulk Mix | T °C | ΔIW | Phase | n | $SiO_2$ | $TiO_2$ | $Al_2O_3$ | $Cr_2O_3$ | FeO | MnO | MgO | CaO | $Na_2O$ | $K_2O$ | NiO | Totals |
|---|---|---|---|---|---|---|---|---|---|---|---|---|---|---|---|---|---|
| | | | | | | 0.26 | 0.01 | 0.02 | 0.00 | 0.10 | 0.01 | 0.21 | 0.01 | 0.01 | 0.00 | 0.01 | 0.40 |
| RKD-16 | synMORB60 | 1225 | +0.5 | Gl | 21 | 50.55 | 1.06 | 14.60 | 0.00 | 12.98 | 0.50 | 9.59 | 11.25 | 0.11 | 0.00 | 0.01 | 100.65 |
| | | | | | | 0.20 | 0.02 | 0.07 | 0.00 | 0.07 | 0.02 | 0.05 | 0.03 | 0.02 | 0.00 | 0.01 | 0.26 |
| | | | | Ol | 7 | 39.31 | 0.02 | 0.03 | 0.00 | 18.28 | 0.52 | 41.56 | 0.31 | 0.00 | 0.00 | 0.01 | 100.05 |
| | | | | | | 0.15 | 0.01 | 0.01 | 0.00 | 0.15 | 0.02 | 0.12 | 0.01 | 0.00 | 0.00 | 0.01 | 0.18 |
| RKD-17 | synMORB60 | 1225 | +0.5 | Gl | 20 | 50.03 | 1.08 | 14.83 | 0.00 | 13.04 | 0.50 | 9.53 | 11.31 | 0.09 | 0.01 | 0.01 | 100.43 |
| | | | | | | 0.18 | 0.02 | 0.05 | 0.00 | 0.08 | 0.02 | 0.06 | 0.03 | 0.02 | 0.00 | 0.01 | 0.22 |
| | | | | Ol | 14 | 39.02 | 0.02 | 0.04 | 0.00 | 18.33 | 0.51 | 41.28 | 0.32 | 0.01 | 0.00 | 0.01 | 99.53 |
| | | | | | | 0.15 | 0.01 | 0.01 | 0.00 | 0.10 | 0.01 | 0.13 | 0.02 | 0.01 | 0.00 | 0.01 | 0.31 |
| RKD-19 | HAB+Ol+Mn | 1225 | +0.5 | Gl | 19 | 51.60 | 1.03 | 16.22 | 0.03 | 8.87 | 0.60 | 8.84 | 12.07 | 1.42 | 0.12 | 0.01 | 100.82 |
| | | | | | | 0.25 | 0.02 | 0.18 | 0.01 | 0.10 | 0.02 | 0.16 | 0.09 | 0.04 | 0.01 | 0.01 | 0.36 |
| | | | | Ol | 8 | 40.32 | 0.03 | 0.04 | 0.04 | 13.77 | 0.70 | 45.09 | 0.39 | 0.01 | 0.00 | 0.21 | 100.59 |
| | | | | | | 0.08 | 0.01 | 0.01 | 0.01 | 0.09 | 0.01 | 0.16 | 0.01 | 0.01 | 0.00 | 0.01 | 0.20 |
| RKD-20 | HAB+Ol+Mn | 1225 | +0.5 | Gl | 14 | 51.21 | 0.99 | 16.45 | 0.04 | 8.69 | 0.60 | 9.11 | 12.14 | 1.35 | 0.11 | 0.01 | 100.69 |
| | | | | | | 0.10 | 0.02 | 0.06 | 0.01 | 0.08 | 0.02 | 0.06 | 0.04 | 0.03 | 0.01 | 0.01 | 0.22 |
| | | | | Ol | 12 | 40.27 | 0.03 | 0.05 | 0.04 | 13.33 | 0.68 | 45.44 | 0.38 | 0.01 | 0.00 | 0.19 | 100.42 |
| | | | | | | 0.21 | 0.01 | 0.01 | 0.00 | 0.14 | 0.01 | 0.13 | 0.01 | 0.01 | 0.00 | 0.01 | 0.30 |
| RKD-21 | synMORB60 | 1175 | +0.5 | Gl | 19 | 48.74 | 2.04 | 13.01 | 0.00 | 16.28 | 0.58 | 6.90 | 12.14 | 0.22 | 0.01 | 0.01 | 99.93 |
| | | | | | | 0.15 | 0.03 | 0.14 | 0.01 | 0.10 | 0.02 | 0.05 | 0.05 | 0.02 | 0.00 | 0.01 | 0.26 |
| | | | | Ol | 5 | 37.24 | 0.03 | 0.10 | 0.00 | 26.44 | 0.75 | 34.12 | 0.45 | 0.00 | 0.00 | 0.00 | 99.14 |
| | | | | | | 0.36 | 0.02 | 0.03 | 0.01 | 0.13 | 0.03 | 0.34 | 0.03 | 0.00 | 0.00 | 0.00 | 0.56 |
| RKD-22 | synMORB40 | 1175 | +0.5 | Gl | 20 | 44.96 | 1.10 | 13.33 | 0.00 | 23.44 | 0.51 | 5.92 | 10.66 | 0.08 | 0.01 | 0.01 | 100.02 |
| | | | | | | 0.13 | 0.02 | 0.07 | 0.00 | 0.12 | 0.03 | 0.04 | 0.02 | 0.02 | 0.00 | 0.01 | 0.26 |
| | | | | Ol | 15 | 35.08 | 0.04 | 0.05 | 0.00 | 36.31 | 0.66 | 26.28 | 0.47 | 0.01 | 0.00 | 0.01 | 98.92 |
| | | | | | | 0.13 | 0.01 | 0.01 | 0.00 | 0.14 | 0.01 | 0.12 | 0.03 | 0.01 | 0.00 | 0.01 | 0.22 |
| RKD-23 | synMORB40 | 1175 | +0.5 | Gl | 19 | 45.30 | 1.09 | 12.88 | 0.00 | 23.18 | 0.51 | 6.00 | 10.60 | 0.07 | 0.00 | 0.00 | 99.63 |
| | | | | | | 0.07 | 0.02 | 0.04 | 0.00 | 0.09 | 0.02 | 0.05 | 0.03 | 0.02 | 0.00 | 0.01 | 0.15 |

| Name | Bulk Mix | T °C | ΔIW | Phase | n | $SiO_2$ | $TiO_2$ | $Al_2O_3$ | $Cr_2O_3$ | FeO | MnO | MgO | CaO | $Na_2O$ | $K_2O$ | NiO | Totals |
|---|---|---|---|---|---|---|---|---|---|---|---|---|---|---|---|---|---|
| | | | | Ol | 13 | 35.77 | 0.03 | 0.03 | 0.01 | 35.51 | 0.64 | 27.43 | 0.43 | 0.01 | 0.00 | 0.01 | 99.86 |
| | | | | | | 0.19 | 0.01 | 0.01 | 0.00 | 0.35 | 0.01 | 0.30 | 0.03 | 0.00 | 0.00 | 0.01 | 0.20 |
| RKD-24 | synMORB40 | 1175 | +0.5 | Gl | 20 | 45.35 | 1.11 | 13.08 | 0.00 | 23.34 | 0.53 | 6.03 | 10.54 | 0.08 | 0.01 | 0.00 | 100.07 |
| | | | | | | 0.13 | 0.02 | 0.07 | 0.01 | 0.11 | 0.02 | 0.04 | 0.03 | 0.02 | 0.00 | 0.00 | 0.26 |
| | | | | Ol | 12 | 35.46 | 0.03 | 0.04 | 0.00 | 35.64 | 0.64 | 27.20 | 0.41 | 0.01 | 0.00 | 0.01 | 99.44 |
| | | | | | | 0.20 | 0.01 | 0.01 | 0.00 | 0.14 | 0.01 | 0.11 | 0.02 | 0.01 | 0.00 | 0.01 | 0.30 |
| RKD-25 | synHP1 | 1350 | +0.5 | Gl | 19 | 48.69 | 2.07 | 12.47 | 0.24 | 11.09 | 0.17 | 15.15 | 10.02 | 0.34 | 0.04 | 0.05 | 100.34 |
| | | | | | | 0.11 | 0.03 | 0.06 | 0.01 | 0.07 | 0.02 | 0.08 | 0.04 | 0.03 | 0.01 | 0.02 | 0.18 |
| | | | | Ol | 17 | 40.50 | 0.04 | 0.06 | 0.17 | 11.01 | 0.14 | 47.76 | 0.26 | 0.00 | 0.00 | 0.29 | 100.24 |
| | | | | | | 0.30 | 0.01 | 0.00 | 0.00 | 0.07 | 0.01 | 0.22 | 0.01 | 0.00 | 0.00 | 0.02 | 0.48 |
| RKD-26 | synHP1+Cr+Mn | 1300 | +0.5 | Gl | 20 | 49.42 | 2.10 | 13.04 | 0.43 | 10.71 | 0.84 | 13.10 | 10.32 | 0.25 | 0.03 | 0.05 | 100.29 |
| | | | | | | 0.10 | 0.03 | 0.05 | 0.02 | 0.06 | 0.03 | 0.06 | 0.02 | 0.02 | 0.01 | 0.02 | 0.14 |
| | | | | Ol | 13 | 40.45 | 0.04 | 0.06 | 0.35 | 11.91 | 0.72 | 46.16 | 0.26 | 0.00 | 0.00 | 0.42 | 100.38 |
| | | | | | | 0.08 | 0.01 | 0.00 | 0.01 | 0.04 | 0.01 | 0.12 | 0.01 | 0.01 | 0.00 | 0.01 | 0.19 |
| RKD-27 | synHP1 | 1350 | +3.5 | Gl | 20 | 47.68 | 2.02 | 12.32 | 0.19 | 12.47 | 0.17 | 15.18 | 9.80 | 0.13 | 0.01 | 0.09 | 100.07 |
| | | | | | | 0.10 | 0.03 | 0.05 | 0.01 | 0.06 | 0.01 | 0.10 | 0.04 | 0.02 | 0.01 | 0.02 | 0.16 |
| | | | | Ol | 20 | 40.47 | 0.03 | 0.07 | 0.12 | 11.10 | 0.14 | 47.39 | 0.26 | 0.01 | 0.00 | 0.64 | 100.24 |
| | | | | | | 0.15 | 0.01 | 0.01 | 0.01 | 0.05 | 0.01 | 0.13 | 0.01 | 0.01 | 0.00 | 0.02 | 0.29 |
| RKD-28 | synMORB80 | 1300 | -0.5 | Gl | 20 | 51.51 | 0.80 | 15.75 | 0.00 | 6.67 | 0.50 | 13.36 | 11.79 | 0.21 | 0.02 | 0.02 | 100.63 |
| | | | | | | 0.14 | 0.02 | 0.06 | 0.01 | 0.04 | 0.02 | 0.04 | 0.02 | 0.02 | 0.01 | 0.01 | 0.20 |
| | | | | Ol | 15 | 40.92 | 0.02 | 0.04 | 0.00 | 7.96 | 0.42 | 50.08 | 0.29 | 0.00 | 0.00 | 0.00 | 99.73 |
| | | | | | | 0.25 | 0.01 | 0.01 | 0.00 | 0.06 | 0.01 | 0.17 | 0.01 | 0.01 | 0.00 | 0.01 | 0.34 |
| RKD-29 | synMORB80 | 1300 | -0.5 | Gl | 20 | 51.77 | 0.78 | 15.52 | 0.00 | 6.70 | 0.49 | 13.76 | 11.74 | 0.28 | 0.02 | 0.02 | 101.07 |
| | | | | | | 0.08 | 0.02 | 0.07 | 0.01 | 0.05 | 0.02 | 0.05 | 0.04 | 0.02 | 0.01 | 0.02 | 0.16 |
| | | | | Ol | 19 | 41.29 | 0.02 | 0.04 | 0.00 | 7.72 | 0.41 | 50.58 | 0.30 | 0.01 | 0.00 | 0.01 | 100.37 |
| | | | | | | 0.16 | 0.01 | 0.01 | 0.00 | 0.05 | 0.01 | 0.14 | 0.01 | 0.01 | 0.00 | 0.01 | 0.25 |
| RKD-30 | synMORB80 | 1300 | -0.5 | Gl | 20 | 51.47 | 0.75 | 15.19 | 0.00 | 6.75 | 0.50 | 14.34 | 11.54 | 0.23 | 0.02 | 0.01 | 100.79 |

| Name | Bulk Mix | T °C | ΔIW | Phase | n | $SiO_2$ | $TiO_2$ | $Al_2O_3$ | $Cr_2O_3$ | FeO | MnO | MgO | CaO | $Na_2O$ | $K_2O$ | NiO | Totals |
|---|---|---|---|---|---|---|---|---|---|---|---|---|---|---|---|---|---|
| | | | | | | 0.07 | 0.02 | 0.07 | 0.00 | 0.05 | 0.02 | 0.06 | 0.04 | 0.02 | 0.00 | 0.01 | 0.11 |
| | | | | Ol | 18 | 41.07 | 0.02 | 0.04 | 0.00 | 7.57 | 0.40 | 50.67 | 0.30 | 0.00 | 0.00 | 0.01 | 100.09 |
| | | | | | | 0.17 | 0.01 | 0.01 | 0.00 | 0.04 | 0.01 | 0.12 | 0.02 | 0.01 | 0.00 | 0.01 | 0.22 |
| RKD-31 | synMORB40 | 1175 | -0.5 | Gl | 21 | 45.08 | 1.03 | 13.47 | 0.00 | 22.88 | 0.52 | 6.36 | 10.61 | 0.05 | 0.01 | 0.01 | 100.02 |
| | | | | | | 0.07 | 0.02 | 0.06 | 0.00 | 0.08 | 0.02 | 0.05 | 0.03 | 0.02 | 0.00 | 0.02 | 0.14 |
| | | | | Ol | 17 | 36.08 | 0.05 | 0.04 | 0.00 | 34.43 | 0.62 | 28.49 | 0.41 | 0.01 | 0.00 | 0.01 | 100.13 |
| | | | | | | 0.22 | 0.01 | 0.01 | 0.00 | 0.43 | 0.02 | 0.41 | 0.04 | 0.01 | 0.00 | 0.01 | 0.39 |
| RKD-32 | synMORB40 | 1175 | -0.5 | Gl | 21 | 45.12 | 1.02 | 13.47 | 0.00 | 22.54 | 0.51 | 6.37 | 10.56 | 0.04 | 0.00 | 0.01 | 99.63 |
| | | | | | | 0.11 | 0.02 | 0.06 | 0.00 | 0.12 | 0.02 | 0.04 | 0.02 | 0.02 | 0.00 | 0.01 | 0.24 |
| | | | | Ol | 6 | 35.97 | 0.04 | 0.04 | 0.00 | 33.89 | 0.60 | 28.65 | 0.42 | 0.01 | 0.00 | 0.00 | 99.62 |
| | | | | | | 0.18 | 0.01 | 0.02 | 0.00 | 0.29 | 0.01 | 0.20 | 0.01 | 0.01 | 0.00 | 0.00 | 0.32 |
| RKD-33 | synMORB40 | 1175 | -0.5 | Gl | 20 | 45.40 | 1.03 | 13.50 | 0.00 | 22.47 | 0.51 | 6.42 | 10.56 | 0.06 | 0.01 | 0.01 | 99.98 |
| | | | | | | 0.09 | 0.02 | 0.06 | 0.00 | 0.12 | 0.02 | 0.04 | 0.02 | 0.02 | 0.00 | 0.01 | 0.18 |
| | | | | Ol | 13 | 36.15 | 0.04 | 0.04 | 0.00 | 34.42 | 0.62 | 28.42 | 0.42 | 0.00 | 0.00 | 0.01 | 100.13 |
| | | | | | | 0.23 | 0.01 | 0.01 | 0.00 | 0.12 | 0.01 | 0.12 | 0.02 | 0.01 | 0.00 | 0.01 | 0.32 |
| RKD-34 | synMORB40 | 1175 | -0.5 | Gl | 20 | 44.89 | 1.07 | 13.42 | 0.00 | 22.87 | 0.52 | 6.25 | 10.65 | 0.05 | 0.01 | 0.01 | 99.74 |
| | | | | | | 0.10 | 0.03 | 0.06 | 0.00 | 0.09 | 0.02 | 0.05 | 0.02 | 0.02 | 0.01 | 0.01 | 0.18 |
| | | | | Ol | 17 | 36.10 | 0.04 | 0.04 | 0.00 | 34.18 | 0.61 | 28.56 | 0.42 | 0.01 | 0.00 | 0.00 | 99.96 |
| | | | | | | 0.30 | 0.01 | 0.02 | 0.00 | 0.21 | 0.01 | 0.19 | 0.03 | 0.01 | 0.00 | 0.01 | 0.41 |
| RKD-35 | synMORB40 | 1175 | -0.5 | Gl | 20 | 44.97 | 1.07 | 13.55 | 0.00 | 22.32 | 0.50 | 6.40 | 10.57 | 0.07 | 0.00 | 0.01 | 99.47 |
| | | | | | | 0.08 | 0.02 | 0.06 | 0.00 | 0.10 | 0.02 | 0.04 | 0.02 | 0.03 | 0.00 | 0.01 | 0.17 |
| | | | | Ol | 16 | 35.83 | 0.03 | 0.04 | 0.00 | 34.42 | 0.62 | 28.21 | 0.42 | 0.01 | 0.00 | 0.00 | 99.58 |
| | | | | | | 0.15 | 0.01 | 0.01 | 0.00 | 0.22 | 0.01 | 0.18 | 0.03 | 0.01 | 0.00 | 0.00 | 0.17 |
| SOCrAl1c2 | synHP1+Cr+Mn | 1350 | +4.5 | Gl | 20 | 48.13 | 1.91 | 11.76 | 0.18 | 12.04 | 0.86 | 15.38 | 9.29 | 0.38 | 0.03 | 0.11 | 100.07 |
| | | | | | | 0.10 | 0.03 | 0.05 | 0.01 | 0.07 | 0.03 | 0.08 | 0.03 | 0.03 | 0.01 | 0.03 | 0.14 |
| | | | | Ol | 18 | 40.31 | 0.03 | 0.08 | 0.18 | 10.09 | 0.65 | 47.54 | 0.25 | 0.01 | 0.00 | 0.73 | 99.88 |
| | | | | | | 0.20 | 0.01 | 0.01 | 0.01 | 0.04 | 0.01 | 0.13 | 0.01 | 0.01 | 0.00 | 0.01 | 0.27 |

| Name | Bulk Mix | T °C | ΔIW | Phase | n | $SiO_2$ | $TiO_2$ | $Al_2O_3$ | $Cr_2O_3$ | FeO | MnO | MgO | CaO | $Na_2O$ | $K_2O$ | NiO | Totals |
|---|---|---|---|---|---|---|---|---|---|---|---|---|---|---|---|---|---|
| SOCrAl1d2 | synHP1+Cr+Mn | 1350 | +4.5 | Gl | 20 | 47.83 | 1.90 | 11.78 | 0.18 | 12.07 | 0.87 | 15.19 | 9.35 | 0.48 | 0.04 | 0.10 | 99.79 |
| | | | | | | 0.09 | 0.04 | 0.03 | 0.01 | 0.06 | 0.03 | 0.08 | 0.02 | 0.04 | 0.01 | 0.02 | 0.15 |
| | | | | Ol | 15 | 40.24 | 0.03 | 0.09 | 0.18 | 10.09 | 0.65 | 47.47 | 0.27 | 0.01 | 0.00 | 0.68 | 99.71 |
| | | | | | | 0.21 | 0.01 | 0.01 | 0.02 | 0.04 | 0.01 | 0.27 | 0.02 | 0.01 | 0.00 | 0.02 | 0.47 |

**Table 3.** Compositions of experimentally produced glasses and olivines. The glass compositions are averages of *n* analyses from each experiment; the second row corresponds to one standard deviation. Each olivine composition is the average of the rim compositions taken from *n* different olivine grains from a given experiment; the second row is 1σ of this distribution. ΔIW refers to the $fO_2$ of the experiments expressed in log units relative to the iron-wüstite buffer reaction at the experimental T and P. gl – glass, ol – olivine. n = number of analyses that passed the various quality filters and which were used to calculate averages and standard deviations. Note that the olivines and glasses in RKD-1 and RKD-2 were measured using a different analytical protocol than the remaining experiments, and NiO was not analyzed in this session.

were easily identifiable. Quantitative traverses across the olivines displaying BSE contrast show Mg-rich interiors and that they are also zoned in MnO and CaO (Suppl. Fig. 2, and further discussion in section 5.2.1). However, an important finding is that the rim Fo contents of zoned olivines are indistinguishable from the rim compositions of unzoned olivines from the same experiment, consistent with local Fe/Mg equilibrium being approached at the boundary between all olivine crystal edges and the surrounding melt. Traverses across olivines identified as unzoned in BSE show no core to rim gradients, with the exception of CaO which is likely due to secondary fluorescence in analyses near the surrounding glass (Suppl. Fig. 3 and Salvat et al. 2006). In summary, the rim Fe/Mg, MnO, and CaO contents of all analyzed olivines from a given experiment overlap within analytical uncertainty, and so for the purposes of calculating olivine/liquid partitioning, the rim analyses were used and assumed to be in local equilibrium with the adjacent melt. We emphasize that the only equilibration type experiments where any Fe/Mg zoning in olivines was observed, either in BSE images or by comparison of the core and rim analyses from an experiment, were in the two synMORB40 experiments run at 1175 °C (RKD-24 and RKD-35)—the remaining experiments approached bulk Fe/Mg equilibrium and were populated entirely by unzoned olivines.

Multiple analyses of nominally homogeneous secondary olivine standards SC-CIT and GO were used to assess both the accuracy and precision of the analyses of the experimentally produced olivines. In addition to measuring these standards during the same session in which the experimental olivines were analyzed, the same olivine standards were measured over several previous sessions using different analytical protocols (e.g., counting times, spectrometer choices) and beam conditions. We found no drift at the 1σ level in the Fo contents of the secondary standards within individual sessions or between sessions. Both secondary standards define a narrow range in Fe/Mg

contents: SC-CIT Fo = 89.83-89.90 over three sessions and GO Fo = 89.94-89.99 over four sessions. Note that published analyses of San Carlos (Jarosewich et al. 1979; Houlier et al. 1990; Spandler & O'Neill 2010; Batanova et al. 2015; Tollan et al. 2018) range from Fo = 88.5 to 91.5, mean = 90.2; measurements of a single chip of SC-CIT olivine are slightly more Fe-rich than the mean literature value, but well within the reported range.

Fractional errors in FeO in the experimental olivines can be either higher or lower than that measured in the secondary standards (average fractional errors of 0.0039 for GO and 0.0044 for SC-CIT) (Figure 3C). The fractional errors in MgO are clustered more closely around the average secondary standard values (0.0019 and 0.0033) (Figure 3C). The more variable fractional errors in the experimental olivine FeO analyses could be due to heterogeneity and zoning in the olivines; e.g., the analytical spots may slightly overlap the Fe-rich quench overgrowth at the edges of some experimental olivines. It could also be from surface effects; e.g., from polishing multi-phase experimental charges versus single crystal olivines, or from slightly different take-off angles on experimental olivine rim analyses versus analyses taken in the centers of large grains. The fact that the fractional errors for experimental and standard glasses agree (Figure 3AB) implies that the variability seen in the olivines is not due to an underlying analytical issue affecting both phases, but rather is specific to the olivines. While there does seem to be greater heterogeneity of the olivine rims in the experiments compared to the olivine secondary standards, the variability is still small (fractional errors are all <1.5%). As we show below, the olivine and glass data that passed the various filters we applied (see previous section) are sufficiently precise to allow variations in Fe/Mg partitioning as functions of the experimentally controlled variables to be quantified and are sufficiently accurate to allow confident comparison with results reported previously in the literature.

### 4.1.3 Spinel

Chromian spinels were present in all runs using the synHP1+Cr+Mn mix and were absent in all of the other runs (i.e., in experiments on bulk compositions not doped with Cr). Individual spinel crystals are typically <10 μm in longest dimension. Most of the analyzed spinels were are surrounded by glass, although the spinels are often, but not always, observed to be attached to the exteriors of olivine crystals or to vesicles present in the experimental charges. The molar Cr/Al ratio of the spinels ranges from 1.50 at 1300 °C to 1.92 at 1400 °C, and the molar Fe/Mg ratio ranges from 0.50 at 1300 °C to 0.37 at 1400 °C. Five focused beam (<1 μm) microprobe analyses were positioned at the centers of the largest spinels (up to 10 μm) in each experiment to avoid contributions from nearby silicates, but even so, all analyses contained minor amounts of $SiO_2$ (0.22–0.57 wt%). Repeat analyses of a natural chromite crystal from the Tiebaghi massif (the primary standard used for Cr, treated as an unknown) gave $SiO_2$ concentrations of <0.015 wt%. The two experiments run at FMQ+1 have spinels with low $SiO_2$ and tight distributions, 0.22±0.020 and 0.22±0.017 wt% (± refers to 1σ of five crystals) for experiments SOCrAl-1c and SOCrAl-1d, respectively. The IW+0.5 experiments have spinels with higher average $SiO_2$ contents 0.28-0.50, and the distributions are less well-defined (1σ ranging from 0.04 to 0.12 wt%). It is unclear whether the elevated $SiO_2$ of the experimental spinels reflects truly high Si contents or an analytical artifact related to the individual grains being small and surrounded by Si-rich materials (note that the calculated electron penetration radius for a perpendicular 15 keV beam on pure chromite is 1.4 μm; Kanaya & Okayama 1972). The elevated $SiO_2$ may be due to analyzing small spinel grains that all suffer to some degree from beam interaction effects, with the distribution of $SiO_2$ for a given experiment reflecting slightly different-sized crystals. There is no correlation between $SiO_2$ in the spinels and $SiO_2$ in the surrounding glasses.

### 4.1.4 Plagioclase

Plagioclase crystals are present in the 1225 °C HAB experiments and in the 1175 °C synMORB40 and synMORB60 experiments. They are typically <10 μm in longest dimension and have shapes ranging from equant to elongated laths, which can be up to 55 μm long. In BSE images, many of the individual plagioclase crystals contain melt inclusions in their cores (e.g., Figure 1B), and in several of the experiments there are clots of plagioclase crystals with interstitial micrometer-sized pools of melt, and in some cases micrometer-sized spinels. In the alkali-free synMORB experiments, the plagioclase is nearly pure anorthite, with Ca/(Na+Ca) > 0.98 (molar) and 1–2 wt% FeO + MgO. The HAB experiments contain some alkalis and the resulting plagioclases are more sodic, with Ca/(Na+Ca) = 0.82–0.83 and < 1 wt% FeO + MgO. Although the FeO+MgO contents of the plagioclases overlap with the high end of measurements of experimentally-produced plagioclases (e.g., Longhi et al. 1976, Sugawara 2000), they could be in part due to secondary fluorescence due to the small crystal sizes and surrounding. The plagioclase compositions were not corrected for secondary fluorescence, and this choice makes no difference in the interpretations of the experiments nor in the mass balance calculations. The average compositions of plagioclases in each experiment are given in the Supplementary Tables.

### 4.1.5 Pyroxene

Pyroxene was only present in two synMORB experiments, RKD-15 (synMORB80, 1225 °C) and RKD-21 (synMORB60, 1175 °C). It forms equant euhedral grains up to 35 x 35 μm in size, as well as grains with rounded edges. In RKD-15, the synMORB80 experiment run at 1225 °C, the pyroxene composition is $Wo_2En_{87}Fs_{11}$. In the more Fe-rich RKD-21 experiment, the pyroxene composition is $Wo_8En_{66}Fs_{25}$. The $Al_2O_3$ contents of individual pyroxene crystals range from 0.43 to 1.25 wt% in RKD-21, but in RKD-15 the $Al_2O_3$ contents of analyzed pyroxenes (n=4) defines a much narrower

range of 1.59-1.63 wt%. See the Supplementary Tables for complete compositional information about the experimentally produced pyroxenes.

### 4.1.6 Pt-Fe metal blebs

In 15 out of 29 experiments run at IW±0.5 there are trace amounts of Pt-Fe metal alloy present as rare and isolated blebs (Suppl. Fig 4A,B). The proportion of blebs in the experiments is difficult to estimate given they exist as rare vestiges, but they likely make up <<0.1% of the experimental volume; for example, in a 2.1x1.4 mm chip of experiment RKD-15, there are 4 blebs exposed that make up a total surface area of ~100 $\mu m^2$ (the total area exposed is ~$3x10^6$ $\mu m^2$). The blebs are typically 1–10 μm in diameter, up to 30 μm in longest dimension, range in shape from roughly spherical to cylindrical, and high-resolution SEM imaging shows that some contained micrometer-sized melt inclusions. Although the blebs were only observed in about half of the experiments, it is likely that they are present in more of the experiments but are sufficiently rare that they are only exposed in a subset of the mounted and polished chips.

Using the microprobe, Pt, Fe, Re, Mn, Cr, Ni, and Al (to check for interference with the surrounding glass) were analyzed at 25 nA using pure metal standards. The elemental weight percent totals for these analyses are low (~94%), but they reveal that the metal is nearly binary Pt-Fe alloy, with $X_{Fe}$ ranging from 0.45 to 0.73. These blebs also contain Ni contents ranging from ~800-1800 ppm (detection limit ~500 ppm); this is the case even in those experiments that contained no Ni in their bulk compositions, suggesting that the metal was derived from an exogeneous source. Re contents were all below the detection limit of ~0.9 wt%. The ratios of $X_{Pt}$ to $X_{Fe}$ define clear trends (Suppl Fig. 4C-F): $X_{Fe}$ is higher in experiments run at lower $fO_2$ using the same bulk composition, in experiments run at the same $fO_2$ but on bulk compositions with more Fe, and in experiments run at lower T, using the same bulk composition and run at the same $fO_2$. $X_{Fe}$ is the same for 24 hr and 48 hr experiments run at the same T and $fO_2$. The

magnitude of the temperature effect on $X_{Fe}$ is small relative to the effects of bulk Fe and $fO_2$ and these trends are broadly consistent with previous determinations of activity-composition relations in Pt-Fe metal alloys (Kessel et al. 2001), suggesting that the blebs were partially equilibrated with the surrounding silicate material during the experiments. The analyzed compositions of the Pt-Fe alloys are listed in the Supplementary Tables.

Given that no Pt metal was in direct contact with the silicate portions of the experiments run using Re loops and given the high Ni contents measured in the blebs, we infer that the Pt was a contaminant. A possible explanation is that it was derived from the thick Pt wire legs that held the hanging experimental charges. These legs protrude from tubes of slightly larger diameter that run through the ceramic hanging rod, and when the rod is inserted into the furnace the space between the Pt legs and the tube walls is filled with air. One possibility is that Pt from the legs transiently oxidizes to $PtO_2$ (g) when the tube is inserted into the furnace and then reacts back to Pt when it encounters the more reducing atmosphere of the furnace. Most of this Pt metal likely condenses on the Pt legs or tube wall but some may condense onto the experimental charge. Whatever their origin, these blebs constitute a very small volume fraction of the experimental charges and are insignificant in mass balance considerations (see below).

### 4.2 Approach to Equilibrium

In this section we evaluate the internal consistency of the experiments and the extent to which they can be inferred to represent close approaches to equilibrium. Two criteria we applied are that (1) each phase is homogeneous within the spatial resolution of the probe and the precision of the analysis; and (2) the experiments can be mass balanced based on the starting compositions and measurements of each phase recovered from an experiment. Because this study is focused on Fe-Mg partitioning between olivine and liquid, the zonation of phases and variations associated with experiments run for

different duration are considered below. Note that the only unambiguous demonstration of equilibrium would be reversal experiments.

### 4.2.1 Homogeneity of Olivine and Liquid

As described in section 5.1.2, with the exception of the synMORB40 experiments run at 1175 °C, all of the olivines in experiments conducted at T > 1175 °C have olivine core and rim Fo contents that overlap within 1σ error and are considered homogeneous in their Fe/Mg ratios. In the two synMORB40 equilibrium-type experiments (i.e., those used for partitioning data, RKD-24 and RKD-35, as opposed to the "saturation" experiments) there are two populations of olivines distinguished by their BSE contrast (Figure 1C and described above). Microprobe traverses across the olivines that were identified as unzoned in BSE yield core and rim Fe/Mg contents that overlap within 1σ errors (Supplementary Figure 3). Importantly the rims of both zoned and unzoned olivines in the same experiment have indistinguishable Fe/Mg at the 1σ level, which is evidence that although some of the olivine crystals are zoned, their rims were in local equilibrium with the surrounding melt when the experiments were quenched. Some of the zoned grains have Fe/Mg gradients that extend over tens of micrometers; for example from ~$Fo_{67}$ in the cores to $Fo_{60}$ in the rims in olivines from experiment RKD-35 (Supplementary Figure 3). Using an Fe-Mg interdiffusion coefficient (Dohmen et al. 2007) calculated at the experimental condition (1175 °C, log $fO_2$ = IW-0.5, $X_{Fo}$ = 0.6), results in a calculated diffusion length scale of ~6 μm for a 48 hr experiment, and so the zoned grains likely represent partial relaxation of zoning formed during the initial growth of these olivines. We emphasize that for the purposes of calculating partitioning values, only the rims of olivine grains recognized as unzoned in BSE images were used.

Analyses of the glasses provide information complementary to the olivine analyses about the internal consistency of the experiments and whether they represent close approaches to equilibrium. In particular, due to relatively rapid diffusion in the

liquid, glass analyses of experiments run at different times and experimental conditions can capture the degree to which certain elements (e.g., Fe and Na) were lost or gained over the course of an experiment. In the next section, a quantitative treatment of mass balance is presented, but first we look at a series of experiments where time-dependent changes in the Fe and Na contents of the recovered glasses were monitored. Note that reconnaissance microprobe traverses with a 1 μm beam show no resolvable zonation in the glass adjacent to olivine grain edges, in experiments with and without apparent submicrometer thick olivine quench overgrowths (Figure 1B). The width of any zonation in the glass associated with quenching is thus estimated to be less than ~1.5–2 μm, which is the closest approach possible with the microprobe and is consistent with modeling of compositional melt gradients next to olivine as a function of cooling rate (Saper and Stolper 2020). Defocused 10 μm beam analyses of the glass were all chosen to cover areas more than 5 μm from any olivines exposed on the sample surface and the glass analyses are unlikely to be affected by any gradient formed during quenching. Comparisons of fractional errors of FeO and MgO in glasses from all equilibration experiments to secondary standards (Figure 3AB) demonstrate that the melts were homogeneous at the time of quenching and, along with the absence of observed zonation adjacent to olivines, is consistent with our assumption that the composition of the far-field melt is representative of the melt that was in direct contact with the olivine rim.

Loss of Fe to the Re wire loop is expected under the reducing experimental conditions studied here (Borisov and Jones 1999). We attempted to minimize this in order to avoid the experimental liquid composition changing with time thus leading to a continually varying condition at the boundaries of the equilibrating olivines, in which diffusion is much slower than in the surrounding melt. A time-series of experiments was conducted using the synHP1+Cr+Mn bulk mix at 1350 °C and log $fO_2$ = IW+0.5 to

monitor Fe-loss. Each of the four experiments RKD-1 through RKD-4 were conducted using a fresh Re loop, and experiments RKD-5 (first) and RKD-25 (second) were run on the Re loop initially pre-saturated during experiment RKD-4 (see Table 2). The FeO* contents of the glasses from these experiments are shown in Figure 4 along with a calculation of the expected FeO* (11.8 wt%) at the experimental condition based on the synHP1+Cr+Mn bulk composition and the calculated phase proportions in the equilibration experiments determined by mass balance (see next section). The data on experiments using a fresh loop show a rapid drawdown in FeO* within the first 15 hours of experimental equilibration, approximately leveling off at a value 15% loss of FeO* relative to the initial value calculated by mass balance (i.e., the FeO* contents of RKD-3 and RKD-4, run for 17 and 42 hr respectively, are within 1σ error of each other). Equilibration experiments RKD-5 and RKD-25, which were run in the order listed in Table 2 using the same Re loop (#4) that was pre-saturated in experiment RKD-4, had durations of 19 and 48 hr, respectively. Comparison of their FeO* with the saturation experiments run using initially pure Re wires shows that preconditioning and recycling the Re loops reduces the relative Fe loss by about half (i.e., to ~6% for RDK-5 and 9 % for RDK-25; Figure 4 and Table 2); these two experiments have FeO* in the liquid that overlap within 1σ error. Note that experiments RKD-1 and RKD-2 were not properly lowered into the furnace hotspot, leading to volatilization of Re and incorporation of Re globules throughout the silicate portion of the experiment. Because these were the only two experiments to suffer from this artifact they were excluded them from olivine/liquid partitioning analysis, however the fact that RKD-2 has indistinguishable FeO* from RKD-3, which was properly lowered into the hotspot and run for the same duration, suggests that Fe loss was not measurably more efficient with Re dispersed throughout the silicate portion of the experiment.

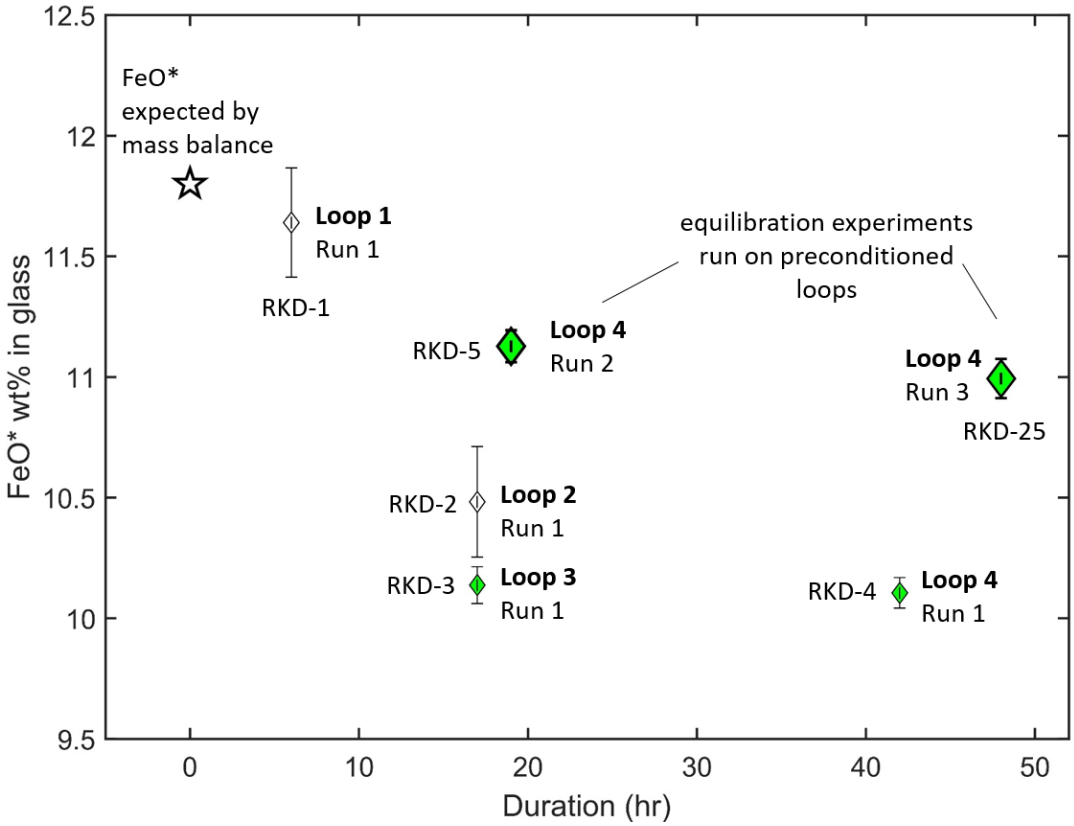


**Figure 4.** FeO* wt% in glasses from a time-series of experiments using the synHP1+CrMn bulk composition. All experiments were run at 1350 °C and an $fO_2$ of ΔIW+0.5, but with variable durations. The star shows the expected FeO* in the glass based on the phase proportions calculated by mass balance in experiment RKD-5 and the bulk composition listed in Table 1. The small sized symbols represent saturation runs using fresh Re loops. The two large diamonds were run on pre-saturated loops and have lost significantly less FeO than similar duration experiments run on fresh Re loops. The unfilled diamonds are experiments RKD-1 and RKD-2 where Re volatilized and is dispersed through the silicate. The similar FeO* of RKD-2 and RKD-3 (no Re incorporation) implies that the dispersed Re droplets did not increase the efficiency of Fe loss from the silicate. The larger errors on the open diamonds are due to lower counting times in the analytical protocol used to analyze these experiments. Error bars are 1σ.

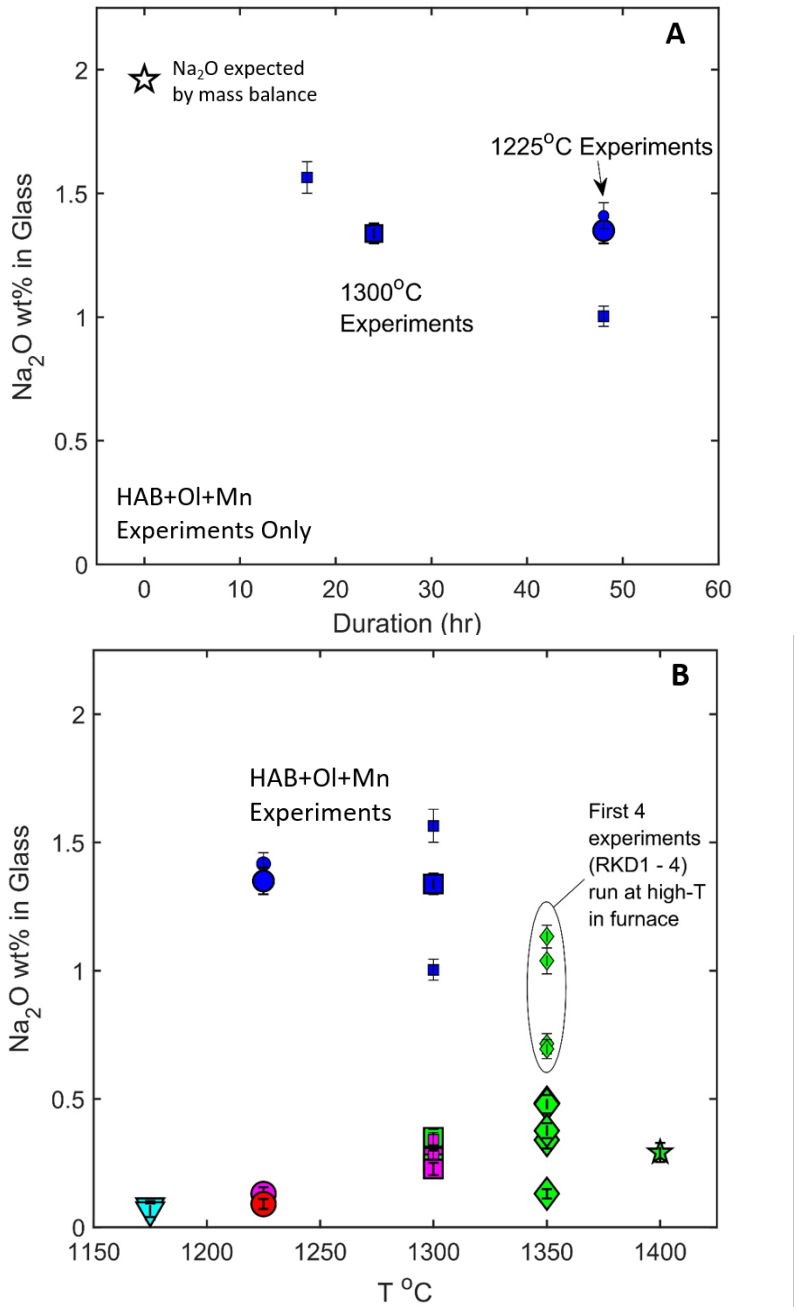


**Figure 5.** $Na_2O$ gain and loss in experimental glasses. (A) $Na_2O$ loss in the alkali-bearing HAB+Ol+Mn bulk mixture. The star shows the expected $Na_2O$ in the glass based on the phase proportions calculated by mass balance in experiment RKD-8 and the bulk composition listed in Table 1. The blue squares show experiments run at 1300 °C and fir different durations, and the two blue circles (which plot on top of one another) are experiments run at 1225 °C, which have lost less $Na_2O$ than the higher T experiments run for the same duration. (B) $Na_2O$ wt% in all experimental glasses. The ellipse refers to the first four experiments that were run for extended time at high-T in the furnace (furnace was briefly at high T for calibration prior to these experiments). Aside from these experiments, the remaining experiments on nominally alkali-free bulk compositions have $Na_2O < 0.5$ wt%.

HAB+Ol+Mn was the only bulk composition that used natural basalt powder as a starting material and the only initial bulk composition containing $Na_2O$ and $K_2O$. Figure 5A shows a time-series of HAB+Ol+Mn experiments run at 1300 °C along with two 48 hr experiments run at 1225 °C. The open star is the expected $Na_2O$ in the glass (1.96 wt%) based on the phase proportions calculated by mass balance in experiment RKD-8 (see next section) and the bulk composition listed in Table 1. The 1300 °C experiments show Na decreasing as a function of time, with nearly 50% of the original $Na_2O$ lost by 48 hrs (Figure 5A). The higher $Na_2O$ contents in 48 hr experiments run at 1225 °C reflects the slower rate of $Na_2O$ evaporation from the melt surface at lower temperatures and the higher $Na_2O$ concentration in the melt at lower T (mass balance shows that the phase proportion of liquid is ~93% at 1300°C versus 55% at 1225 °C). Both effects conspire to give the same $Na_2O$ liquid contents (1.34-1.35 wt%) in the two equilibration experiments on the HAB+Ol+Mn bulk composition, run at both 1225 °C and 1300 °C.

Note that all of the experiments run on nominally alkali-free bulk compositions have glasses with $Na_2O$ contents (0.04 -1.13 wt%, Table 3), well above the minimum modeled detection limit at our electron microprobe condition (~0.025 wt%, Scott & Love, 1983). As pointed out by Matzen et al. (2011), who ran experiments in the same furnaces, glasses from higher-T experiments generally have higher $Na_2O$ contents (Figure 5B). The first four experiments run at high T in the furnace, RKD-1 through RKD-4, have the highest $Na_2O$ contents of the nominally alkali free bulk compositions, and with the exception of the short duration experiment RKD-1, successive experiments at the same T have decreasing $Na_2O$ contents. This effect was also observed by Matzen et al. (2011), and the source of the Na was attributed to the gradual depletion of contaminant Na on the inner wall of the $Al_2O_3$ furnace tube. All the RKD equilibration experiments on nominally alkali-free bulk compositions that were run on pre-conditioned loops have <0.50 wt%

$Na_2O$ in the glass (Suppl. Fig. 2); in addition to mitigating Fe loss, the saturation experiments also served to flush out some of the alkali contaminant reservoir in the furnace tube. All the glasses recovered from experiments run on alkali-free bulk compositions had $K_2O$ contents of <0.07 wt%.

### 4.2.2 Mass Balance and Phase Proportions

The proportions of phases in each experiment and estimates of the extent to which FeO*, $Na_2O$, and $K_2O$ were gained or lost during a run were determined by mass-balance using a non-linear minimization routine based on Albarède & Provost (1977). The routine uses the uncertainties on all analyzed phases in addition to those estimated for the bulk composition. Including analytical uncertainties for the quenched glass and coexisting solid phases renders chi-squared ($\chi^2$, the quantity being minimized) non-linear. In addition to the phase proportions, bulk FeO*, $Na_2O$ and $K_2O$ can be defined as free variables, i.e., their concentrations are allowed to vary when minimizing $\chi^2$ in order to assess closure of the system with respect to these oxides. If one or more of these three oxides are defined as variables, the concentrations of the remaining oxides in the bulk composition are adjusted proportionately in order to maintain a constant oxide sum. The difference between the initial bulk concentration of an oxide selected as a variable and the final "best fit" bulk concentration provides an estimate of the percent loss or gain of that oxide from the charge (in the case of bulk compositions that were nominally alkali-free, increases in sodium and/or potassium bulk concentrations represent the gain in $Na_2O$ and/or $K_2O$ in wt%). Since most of the bulk compositions used in this study are synthetic mixes and have not been analyzed directly (i.e., they are based on the weighed masses of oxide and olivine powders), 1 sigma values for each bulk oxide were calculated using power law fits to fractional errors (1 sigma/mean) determined on a large number of primary and secondary standards in the Caltech probe lab that covered a wide range of oxide concentrations (e.g., olivines and basaltic to rhyolitic glasses, pers. comm. M.

Baker). The use of these power law fits also allowed the 1 sigma values to vary as individual bulk oxide concentrations varied in those cases where FeO*, MnO, $Na_2O$, or $K_2O$ were defined as variables. Experiments were deemed to satisfy mass balance if the $\chi^2$ value was statistically significant at or above the 95% confidence level. All the RKD experiments passed this test of mass balance. Results of the mass balance calculations, including the proportions of product phases and the loss or gain of FeO*, $Na_2O$, and $K_2O$ in each experiment, are given in Supplementary Table 2.

All the equilibration experiments, which were run on pre-saturated Re or Pt loops, lost less than 9% relative of their total FeO, with an average of -3.5%; only one experiment was found to gain FeO (RKD-22 $\Delta$FeO = +0.87% relative, Table 2). In the initial long-duration saturation runs on fresh loops designed to monitor Fe loss, a maximum loss of ~13-14% FeO was calculated for the saturation experiments RKD-3 and RKD-4. For the 14 experiments where PtFe blebs were observed, the $\Delta$FeO ranges from <1% (essentially no change) to -5.4% and the $\Delta$FeO is uncorrelated with $X_{Fe}$ in the blebs.

Experiments using the alkali-bearing mix HAB+Ol-Mn show a calculated loss of up to 50% of the original $Na_2O$ present in the bulk mixtures, and the two equilibration experiments using the alkali-bearing starting composition (RKD-12 and RKD-20) both lost approximately 35% of their initial $Na_2O$ (Figure 5). For these two experiments no gradients in Na were detected in the glasses near the external edges of the experimental charges, consistent with rapid diffusivity of Na in melts (e.g., Guo and Zhang 2018) and indicating that although Na was varying, instantaneously it was roughly constant across the charge. This is further supported by the fact that the fractional errors in $Na_2O$ measurements in the experimental glasses from an individual experiment ($1\sigma$/mean = 0.02-0.03) are as good as, if not better, than that measured in the alkali-bearing secondary

standard glasses (1σ/mean = 0.03 for BIR-1g and BHVO-2g and 0.06 for GOR-2g, which only has 0.60 wt% $Na_2O$). For these two experiments we conclude that the average $Na_2O$ concentrations reported in Table 2 are representative of that at the olivine edges, and that the liquids were homogeneous at the time of quenching.

In summary, analysis of the compositions of experimentally produced olivines and coexisting glasses demonstrate that both phases were homogeneous at the time of quenching in nearly all equilibration experiments. The three exceptions are the experiments run at 1175 °C that contained occsional zoned olivines; however only analyses of the rims of unzoned olivines from these experiments were used in olivine-liquid partitioning calculations and are reported in Table 2. All the experiments satisfy mass balance constraints within analytical uncertainties based on measurements of the experimentally produced phases and the starting mix compositions (see footnotes to Table 1 for adjustments to the bulk compositions synHP1 Matzen and synHP1+Cr+Mn based on $Al_2O_3$ gain during the grinding of powders).

### 4.3 Olivine-Liquid Partitioning

For each experiment, the olivine rim and glass analyses that passed the various quality filters were averaged to obtain a mean composition (typically ~10 individual olivine crystals and ~20 glass analyses, Table 2). Standard deviations refer to the distribution of multiple microprobe analyses of each phase in each experiment (i.e., not to the standard error of the mean). Olivine-liquid exchange coefficients were calculated based on these phase averages for each experiment. Uncertainties in the exchange coefficients were calculated by summing the fractional errors for each oxide in each phase in quadrature. Unless specified otherwise, references to standard deviations and the use of ± symbols in the text refer to 1σ errors.

#### 4.3.1 The Apparent Fe*/Mg Olivine-Liquid Exchange Coefficient, $K_D$*

We first define the apparent Fe*-Mg exchange coefficient, $K_D$* in olivine:

$$K_D^{ol/liq}{}_{Fe*-Mg} = \left(\frac{w_{MgO}}{w_{FeO*}}\right)^{liq} \cdot \left(\frac{w_{FeO}}{w_{MgO}}\right)^{ol} \equiv K_D* \quad (2)$$

where $w_i^{\Phi}$ is the weight % of oxide $i$ in phase Φ and $K_D$* is the shorthand used hereafter. This corresponds to the quantity that can be directly measured using the microprobe, where all Fe present in the glasses is expressed as FeO*. We demonstrate in section 6.1 that the amount of $Fe^{3+}$ in our experiments is expected to be so small that it has essentially no impact on our results, and this was the reason for doing the experiments at low $fO_2$. Nevertheless, at this point the data are presented in terms of the measured quantity, $K_D$*, in order to highlight relative differences between experiments without obscuring the raw data with a model-dependent correction factor for $Fe^{3+}/Fe^{2+}$. Because $FeO^{liq}$ is always less than $FeO*^{liq}$, $K_{D,Fe2+-Mg}$ will always be greater than $K_D$*, and the magnitude of the difference depends on the $Fe^{3+}/Fe^{2+}$ of the melt.

Figure 6 shows experimentally determined $K_D$* as a function of run temperature (6A); FeO* wt% in the glass (6B); Fo content of the olivine rims (6C); and $Al_2O_3$ wt% in the glass (6D). Note that some green symbols at T = 1300 °C and 1350 °C in Fig. 6A have been offset by ±5°C for clarity. The smaller-sized symbols represent saturation experiments run on pure Re loops, and the large bold outlined symbols are equilibration experiments run on pre-saturated metal loops. The three experiments run under more oxidizing conditions have $K_D$*< 0.29 (Table 2) and are not plotted; the higher $Fe^{3+}/Fe^{2+}$ in these experiments lead to a significant correction on the $K_{D,Fe2+-Mg}$ compared to the low $fO_2$ experiments, and this will be evaluated in section 6. All bulk compositions except for synMORB40 were run at two or more temperatures at IW+0.5 (synMORB80 was run at both 1225 °C and 1300 °C at IW±0.5). The $K_D$* for experiments with the same bulk composition run at different T and the same $fO_2$ (Figure 6A) all overlap within 1σ errors, indicating that any effects of temperature on the $K_D$* are smaller than the analytical uncertainty, including effects due to the changing olivine and glass compositions over

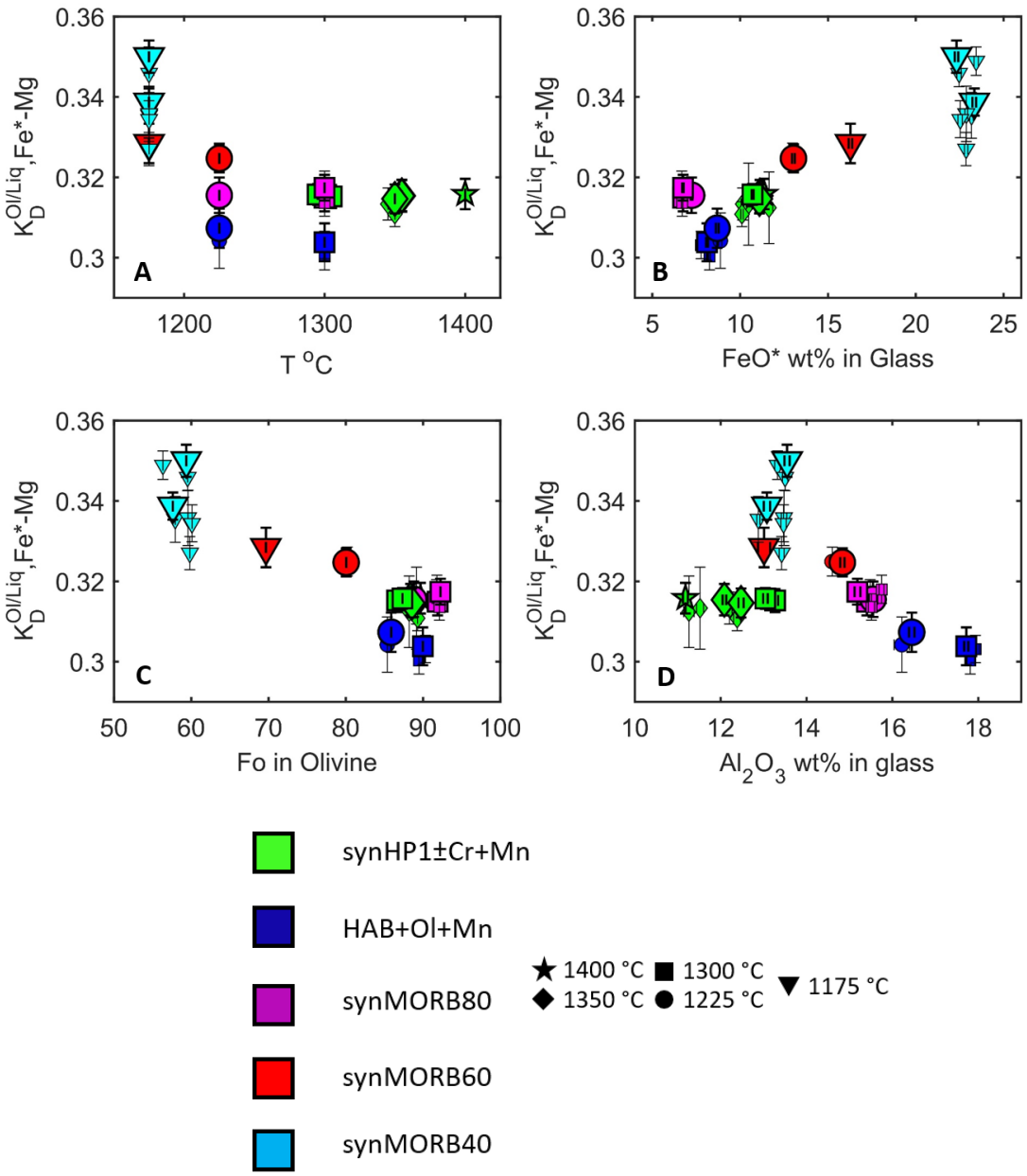


**Figure 6.** Experimentally determined $K_D^{ol/liq}$,Fe*-Mg for experiments run at $fO_2$ ≤ IW+0.5 plotted vs. (A) Temperature, (B) FeO* wt% in glass (C) Fo = 100·(Mg/[Mg+Fe]) in olivine, and (D) $Al_2O_3$ wt% in glass. Smaller symbols correspond to saturation type experiments; large symbols are equilibration experiments run on pre-saturated Re loops. Some green symbols in panel (A) at 1300 °C and 1350 °C were offset for clarity. Symbology is the same as in Figure 2. Error bars are 1σ.

the 75-100 °C temperature interval spanned by different experiments that used the same bulk composition (e.g., for the synHP1+Cr+Mn bulk composition, Fo = 86.6 at 1300 °C (RKD-6) and Fo = 89.7 at 1400 °C (RKD-7)).

There are, however, systematic differences in $K_D$* above the 1σ level, between experiments that have different bulk compositions. For example, the HAB+Ol+Mn experiments (dark blue symbols, Figure 6A) have uniformly lower $K_D$* than the MORB or picritic bulk compositions run at the same T and $fO_2$ – at 1225 °C the mean HAB+Ol+Mn $K_D$* is 1.7σ to 3.5σ below the $K_D$* of synMORB80 and synMORB60; at 1300 °C the HAB+Ol+Mn $K_D$* is 1.5σ to 1.7σ below the $K_D$* of synHP1+Cr+Mn and synMORB80. The MORB suite of bulk compositions was designed to vary the molar Fe/Mg ratio while keeping the relative proportions of the other oxides constant. Figure 6B shows that the $K_D$* for the MORB suite is correlated with the FeO* wt% measured in the glass; a weighted linear fit to the synMORB experiments run at IW+0.5 has an $r^2$ = 0.90 ($p<0.001$) and indicates an increase of ~0.01 in the $K_D$* for every 6 wt% absolute increase in FeO*.

The HAB+Ol+Mn and synHP1±Cr+Mn experiments run at IW+0.5 are displaced to lower $K_D$* from the trend defined by the MORB suite. The HAB glasses contain elevated $Na_2O$ and the synHP1 glasses contain high $TiO_2$ contents relative to the other bulk compositions. It is well known that increasing the concentrations of either of these two oxides results in a decrease in $K_{D,\ Fe2+-Mg}$ (Longhi et al. 1978, Gee and Sack 1988), and our $K_D$* results are consistent with expected trend. Although our bulk compositions have up to ~0.8 wt% MnO (compared to typical basaltic and tholeiitic values of ~0.1–0.2 wt%; e.g., Le Maitre 1976; Gale et al. 2013), our experimental results suggest that such elevated MnO contents have no apparent effect on $K_D$*; i.e., RKD-25 (synHP1; 0.18 wt% MnO) and RKD-5 (synHP1+Cr+Mn; 0.81 wt% MnO), run at the same T and $fO_2$, have

indistinguishable $K_D$* values: 0.315±0.004 and 0.315±0.006. A quantitative treatment of these compositional dependencies will be explored in the section 6.1 where the new experimental data are fit to a thermodynamic model and in section 6.3 where these data are fitted along with a literature compilation of other experiments run at comparably reduced conditions that contain both olivine and liquid.

### 4.3.2 $Mn^{2+}$/Mg Olivine-Liquid Exchange Coefficient, $K_D^{ol/liq}{}_{,Mn\text{-}Mg}$

The olivine-liquid exchange coefficient for Mn, $K_D^{ol/liq}{}_{,Mn\text{-}Mg} = (MnO/MgO)^{ol}/(MnO/MgO)^{liq}$ follows from equations analogous to (1a-d), but with FeO replaced by MnO. For the temperatures and $fO_2$ range of our experiments, all Mn in the melt is expected to be $Mn^{2+}$ (Huebner & Sato 1970; Watson 1977; Borisov 2013). Figure 7A shows the experimental T versus $K_{D,Mn\text{-}Mg}$, which for all of the equilibration RKD experiments (large symbols) ranges from 0.228±0.010 to 0.279±0.012, indicating that the range of $K_{D,Mn\text{-}Mg}$ measured is larger than the 2σ uncertainty in the measurements from an individual experiment. The $K_{D,Mn\text{-}Mg}$ in the synHP1±Cr+Mn experiments run at the same T = 1350 °C (green diamonds in Fig. 7A) and with $fO_2$ ranging from IW+0.5 to IW+4.5 all overlap within 1σ error, and the mean and 1σ of the average $K_{D,Mn\text{-}Mg}$ measured in each of these experiments (n=4) is 0.244±0.005 (1σ of the means). This narrow range in $K_{D,Mn\text{-}Mg}$ over four orders of magnitude in $fO_2$ is consistent with all Mn being present as $Mn^{2+}$ at the experimental conditions. The synHP1+Cr+Mn experiments run at IW+0.5 and at T = 1300 °C and 1400°C overlap within 1σ (RKD-6, $K_{D,Mn\text{-}Mg}$ = 0.243±0.009 and RKD-7, $K_{D,Mn\text{-}Mg}$ = 0.258±0.010), as do the other bulk compositions run at different T indicating that like for Fe-Mg, any T-dependence on the Mn-Mg exchange coefficient is less than the analytical uncertainties.

Experiments run using the undoped synHP1 composition can be used to test whether bulk Mn contents have any effect on the $K_{D,Mn\text{-}Mg}$. The lower Mn contents in these experiments lead to lower counts on the microprobe at the same beam conditions

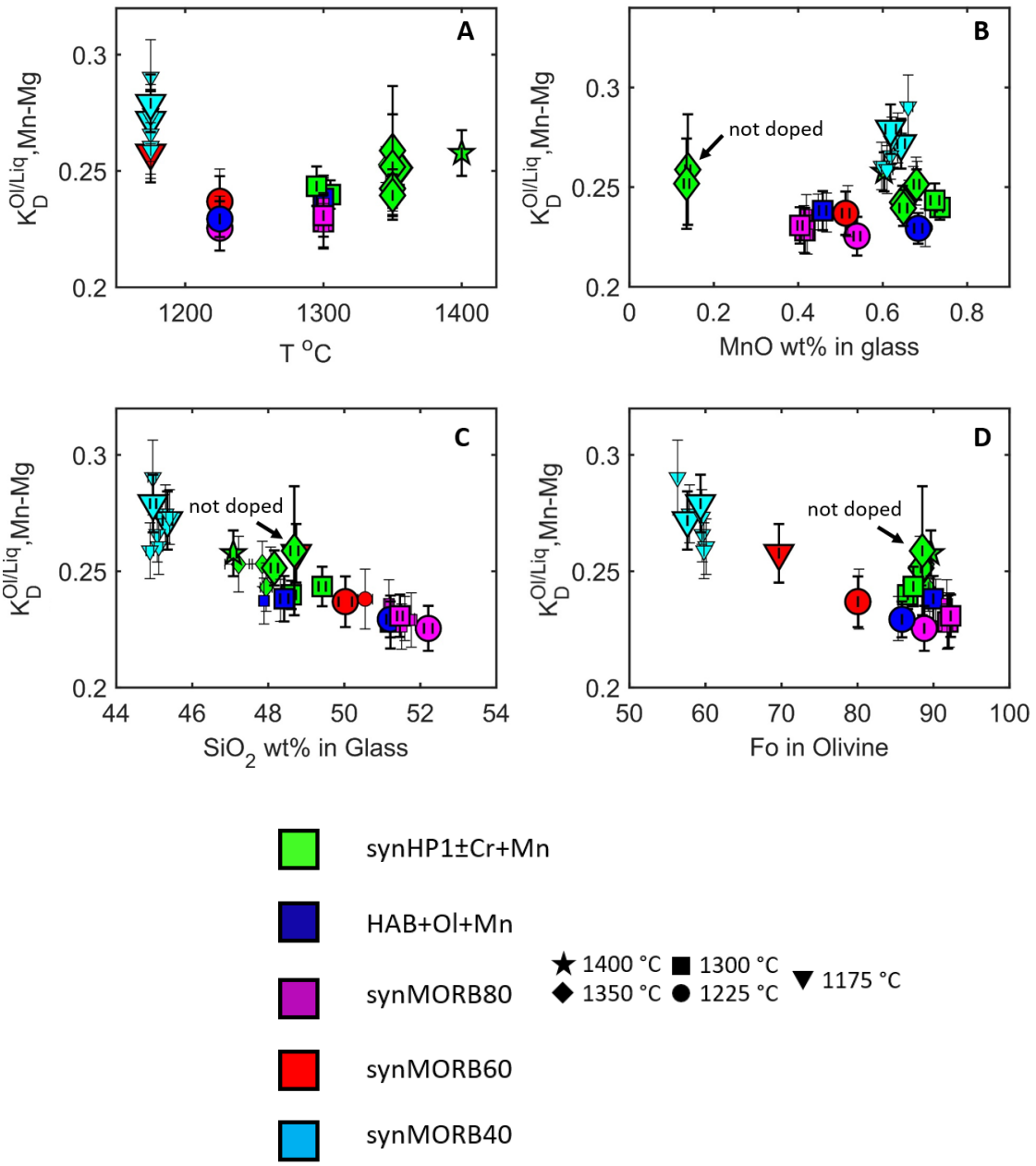


**Figure 7.** Experimentally determined $K_D^{Mn^*/Mg}$ for all experiments plotted vs. **(A)** Temperature, **(B)** MnO wt% in glass, **(C)** $SiO_2$ wt% in glass, and **(D)** Fo = 100(Mg/[Mg+Fe]) in olivine. Smaller symbols correspond to saturation type experiments, large symbols are equilibration experiments run on pre-saturated Re loops. Some green symbols in panel **(A)** at 1300 °C and 1350 °C were offset for clarity. The arrows point to experiments run on bulk compositions that were not doped with extra Mn or Cr (i.e., synHP1 in Table 1). Error bars are

and thus larger measurement errors (e.g., error bars on symbols pointed out by arrows in Figure 7B). $K_{D,Mn\text{-}Mg}$ overlaps within 1σ of the synHP1+Cr+Mn doped experiments and no correlation is observed between the Mn contents of the glasses or olivines and $K_{D,Mn\text{-}Mg}$. $K_{D,Mn\text{-}Mg}$ is correlated with both the glass and olivine in a manner that is similar to that observed for the $K_{D,Fe2+\text{-}Mg}$. Low Fo% in olivines (Figure 7D) and low $SiO_2$ in the glasses (Figure 7C), are associated with systematically higher $K_{D,Mn\text{-}Mg}$, given the uncertainties in Mn and Mg in both the olivines and the glasses.

## 5. Discussion

### 5.1 Parameterizing the compositional dependence of $K_D^{ol/liq}$,$Fe^{2+}$-Mg based on the RKD data only

Recall equation (1d):

$$K_1 = K_{D,Fe^{2+}-Mg}^{ol/liq} \cdot \left[ \left( \frac{\gamma_{MgO}}{\gamma_{FeO}} \right)^{liq} \left( \frac{\gamma_{FeSi1/2O2}}{\gamma_{MgSi1/2O2}} \right)^{olv} \right], \quad (1d)$$

where, $\gamma_i^{\Phi}$ refers to the mole fraction and activity coefficient of component *i* in phase Φ, respectively (note that this is $K_D$,$Fe^{2+}$-Mg and not $K_D$*). Because the mole fractions of the Fe- and Mg- bearing components in both the olivine and liquid can be measured very precisely, the parameters that remain unconstrained in equation (1d) are the activity coefficients in each phase and how they vary with composition, T, and P. It has long been recognized that using exchange coefficients to model mineral-melt equilibria is useful because the temperature dependence of the ratio of partition coefficients is significantly smaller than that of individual element partition coefficients (e.g., Roeder and Emslie 1970; Longhi et al. 1978). In the case of Fe-Mg olivine, this is a consequence mainly of the small differences in the enthalpies of fusion of fayalite and forsterite (Toplis 2005). Therefore, it is often assumed that any temperature effects can be ignored (Blundy et al. 2020) except through their indirect influence on activity-composition relations in the olivine and liquid phases. This assumption is supported by the RKD experimental data

(Figure 6A) and any direct temperature effect on the $K_{D,Fe2+-Mg}$ is ignored. The effect of pressure is also not considered here, but it generally leads to a small increase in the $K_{D,Fe2+-Mg}$, on order 0.01 absolute per 100 °C (Ulmer 1989; Herzberg & O'Hara 1998; Toplis 2005).

We adopt the approach taken by Toplis (2005) to parameterize the compositional dependence of $K_{D,Fe2+-Mg}$, first using our data set and then in section 6.3 using available published data for other experiments conducted at $fO_2 \leq$ IW+0.5. The functional form of Toplis (2005) equation (5) is used:

$$\ln K_D^{ol/liq}{}_{,Fe2+-Mg} = -\Delta G°/RT + \ln \left(\frac{\gamma FeO}{\gamma MgO}\right)^{liq} + \frac{W_{Fe-Mg}^{ol}}{RT}(1 - 2\, X_{Fo}^{ol}) \quad (3a)$$

where $W_{Fe-Mg}^{ol}$ is an interaction parameter describing Fe-Mg non-ideality in a symmetric binary olivine solid solution. Equation (3a) explicitly takes into account non-ideality in both the olivine and in the liquid. Toplis (2005) inferred that the ratio $\left(\frac{\gamma FeO}{\gamma MgO}\right)^{liq}$ is a function of the $SiO_2$ and alkali contents of the liquid and came up with an empirical function that relates these quantities. We adopt a functional form for the activity coefficients in the liquid based on a truncated symmetric, strictly regular solution model (e.g., Ghiorso 1983) excluding, for now, any cross-terms in the Margules parameters (i.e., all of the W interaction terms are symmetric and each pair of binary interaction terms is independent of the others and of temperature):

$$RT \ln \gamma_i = \Sigma_j W_{i-j} X_j^{liq} \; ; \; j \neq i \quad (3b)$$

where i = MgO or FeO, $W_{i-j}$ is a binary interaction parameter, and $X_j^{liq}$ is the single-cation mole fraction of component j in the liquid, and $j \neq i$ indicates that there are no terms for MgO-MgO or FeO-FeO in the summation. Because only the ratio $\left(\frac{\gamma FeO}{\gamma MgO}\right)^{liq}$ is considered, equation (3b) can be simplified by taking the difference of the expressions for FeO and MgO, and defining $B_j \equiv (W_{FeO-j} - W_{MgO-j})$, giving:

$$\text{RT ln } \left(\frac{\gamma FeO}{\gamma MgO}\right)^{liq} = \Sigma_j B_j X_j^{liq} \text{ ; } j \neq i \quad (3c)$$

This can be substituted into equation (3a) to give a thermodynamically consistent equation where the $B_j$ terms are adjustable parameters that describe the ratio of the compositional dependences of the MgO and FeO activity coefficients in the liquid, and where $W_{Fe\text{-}Mg}^{ol}$ is an adjustable parameter for non-ideality in the olivine:

$$\ln K_D^{ol/liq}{}_{,Fe2+/Mg} = -\Delta G°/RT + \Sigma_j B_j X_j^{liq} + \frac{W_{Fe-Mg}^{ol}}{RT}(1 - 2 X_{Fo}^{ol})/RT \quad (3d)$$

This is the functional form that was explored when fitting the RKD experimental data. The expression for ΔG° used in equation (3d) was adopted from Toplis (2005) (ΔG° = –6766 – 7.34 x T(K), kJ/mol), which Toplis (2005) calculated from thermochemical data for forsterite and fayalite.

At this point it is worth noting that $X_{Fo}^{ol}$ and $X_{FeO}^{liq}$ can be explicitly related to each other through the set of transformations described below in equations (4a-4g). This means that the choice of using $X_{Fo}^{ol}$ as opposed to $X_{FeO}^{liq}$ (or $X_{MgO}^{liq}$) as one of the independent variables in describing the compositional dependence of the $K_{D,Fe2+/Mg}$ is arbitrary, and an equally valid form of equation (3d) can be written only in terms of liquid components. The Toplis (2005) model used both the olivine and melt compositions, whereas Blundy et al. (2020) parameterized $K_{D,Fe2+/Mg}$ as a function of only the olivine composition. In either case, given a liquid composition and an expression for one of the single cation partition coefficients: $D_{Mg}^{ol/liq} = \frac{X_{Mg}^{ol}}{X_{Mg}^{liq}}$ or $D_{Fe}^{ol/liq} = \frac{X_{Fe}^{ol}}{X_{Fe2+}^{liq}}$, can be calculated via the following algebraic transformations:

$$(Fe,Mg)O^{liq} + \frac{1}{2}SiO_2^{liq} = (Fe,Mg)Si_{1/2}O_2^{ol} \quad (4a)$$

$$D_i^{ol/liq} = \frac{\gamma_i^{ol} X_i^{ol}}{\gamma_i^{liq} X_i^{liq}} = \frac{a_i^{ol}}{a_i^{liq}} \text{ ; } i = \text{Fe, Mg} \quad (4b)$$

$$ln\, D_i^{ol/liq} = \frac{\Delta S°}{R} - \frac{\Delta H°}{RT} = A_i + \frac{Bi}{T} \quad (4c)$$

$$\eta = X_{Fe}^{ol} + X_{Mg}^{ol} = [D_{Fe}^{ol/liq} \cdot X_{Fe}^{liq}] + [D_{Mg}^{\mathrm{ol/liq}} \cdot X_{Mg}^{liq}] \quad (4d)$$

$$X_{Fa}^{ol} = \frac{X_{Fe}^{ol}}{\eta} \; ; \; X_{Fo}^{ol} = \frac{X_{Mg}^{ol}}{\eta} \quad (4e)$$

$$X_{Fa}^{ol} + X_{Fo}^{ol} = 1 \quad (4f)$$

$$X_{Fo}^{ol} = 1 - \frac{D_{Fe}^{ol/liq} \cdot X_{Fe}^{liq}}{\eta} = \frac{D_{Mg}^{ol/liq} \cdot X_{Mg}^{liq}}{\eta} \quad (4g)$$

where equation (4a) is the formation reaction of fayalite and forsterite from the oxides, $X_i^{\Phi}$ is the cation mole fraction of component *i* in phase Φ (activity – $a_i^{\Phi}$ ; activity coefficient – $\gamma_i^{\Phi}$), ΔS° and ΔH° refer to the change in entropy and enthalpy of the fayalite (Fa) or forsterite (Fo) formation reactions in (4a), the coefficients $A_i$ and $B_i$ represent fitted parameters that describe activity-composition relations, and η is based on stoichiometry: for a binary Fe-Mg olivine $\eta = \frac{2}{3}$, and for olivines containing other divalent cations is $\frac{2}{3} - \Sigma X_{j2+}^{ol}$ where *j2+* ≠ Fe, Mg (but can be Mn, Cr, Ni, Co, etc.). Therefore if A and B are well-constrained (and as shown later, they can be cast as a function of liquid composition), for olivines where Fe+Mg >> $\Sigma X_{j2+}^{ol}$, equations (4a)-(4e) can be used to convert directly from $X_{FeO}^{liq}$ or $X_{MgO}^{liq}$ to $X_{Fo}^{ol}$. In the RKD experiments, $X_{Fo}^{ol}$ and $X_{FeO}^{liq}$ are simply correlated by a linear function (Supplementary Figure 5, $X_{Fo}^{ol}$ = 1.0688 – 2.4695 $X_{FeO}^{liq}$ , $r^2$ = 0.95), but this relationship only holds for the range of compositions represented by the RKD experiments. The individual partition coefficients $D_{Fe}^{ol/liq}$ and $D_{Mg}^{ol/liq}$ are explored in more detail in section 6.3, which introduces a compilation of literature experiments at low $fO_2$ that span a much broader compositional range.

Equation (4g) emphasizes the point that the $K_{D,Fe2+/Mg}$ can be expressed only in terms of melt composition, as opposed to both melt and olivine composition or olivine composition alone (Blundy et al. 2020). The flexibility afforded by such a transformation is useful because the $K_{D,Fe2+/Mg}$, and the equilibrium olivine composition, can be

calculated in cases where only the melt composition and T are specified, given sufficient information about the individual partition coefficients of divalent cations between olivine and liquid. It follows that for the RKD experiments, based on the linear correlation between $X_{Fo}^{ol}$ and $X_{FeO}^{liq}$ (Suppl. Fig. 5), equation (3d) can be rearranged to exclude any dependence on olivine composition:

$$\ln K_{D,Fe2+/Mg} = \frac{-\Delta G^{\circ}}{RT} + \Sigma_j B_j X_j^{liq} + \frac{W_{Fe-Mg}^{ol}}{RT}(2.1375\, X_{FeO}^{liq} - 1.1760) \quad (3e)$$

For the fitting exercise described below, equation (3d) was used (function of both melt and olivine compositions), in part because we have yet to develop a reliable and internally consistent parameterization for $D_i^{ol/liq}$ (although such parameterizations exist, e.g., Beattie 1993). A parameterization for $\ln D_{Fe2+}^{ol/liq}$ and $\ln D_{Mg}^{ol/liq}$ is presented in a later section.

Another consideration in fitting the compositional dependence of the $K_{D,Fe2+-Mg}$ is that microprobe measurements of Fe in the glasses are reported as FeO*, but the exchange coefficient is calculated using the $Fe^{2+}O$ contents of the liquids, which were not measured directly. The RKD experiments were designed to mitigate these uncertainties, however some $Fe^{3+}$ will always be present in the liquid, even if it is saturated with Fe metal (e.g., Bowen & Schraier 1935). Based on calculations using a eight of the available expressions for $Fe^{3+}/Fe^{2+}$ in silicate liquids (Sack et al. 1980; Kilinc et al. 1983; Borisov and Shapkin 1990; Kress and Carmichael 1991; Nikolaev et al. 1996; Jayasuriya et al. 2004; Borisov et al. 2018; O'Neill 2018), for the experiments run at IW+0.5 the maximum $Fe^{3+}/Fe^{Total}$ calculated in the liquid based on the measured glass compositions ranges from 0.02 (O'Neill 2018) to 0.06 (Nikolaev et al. 1991), and the median for all experiments at IW+0.5 and models is $Fe^{3+}/Fe^{Total}$ = 0.03. For those experiments run at IW-0.5 the maximum estimated $Fe^{3+}/Fe^{Total}$ ranges from 0.01 (O'Neill 2018) to 0.04 (Nikolaev et al. 1996). Note that for the IW+0.5 experiments, using the minimum estimate of 2% $Fe^{3+}$

results in a correction $\Delta(K_{D,Fe2+-Mg} - K_D^*)$ of ~0.006 absolute, which is comparable to the 2σ measurement error; a liquid with 4% $Fe^{3+}$ corresponds to a correction of ~0.013 absolute in $K_{D,Fe2+-Mg}$. However, an important insight is that for the compositional variability of glass compositions from different bulk compositions equilibrated at the same $fO_2$ and T, the absolute differences in $Fe^{3+}/Fe^{2+}$ predicted for any given model are small (<0.01 $\Delta Fe^{3+}/Fe^{2+}$ for a given model over the range of experimental glass compositions). This variation of <0.01 $\Delta Fe^{3+}/Fe^{2+}$ translates to a $\Delta(K_{D,Fe2+-Mg} - K_D^*)$ that is on order to or less than analytical uncertainties, and thus variations in the measured $K_D$ that are larger than the analytical uncertainties must reflect the effects of composition on the $K_{D,Fe2+-Mg}$ and are unlikely to be due to compositional effects on the small amount of $Fe^{3+}$ present in the experimental liquids equilibrated at IW±0.5.

Equation (3d) was fit to the 14 RKD equilibrium experiments listed in Table 2. Although at $fO_2 \leq$ IW+0.5, the low $Fe^{3+}/Fe^{2+}$ contents impart only a minor correction to calculate $K_D^{ol/liq}{}_{,Fe2+-Mg}$ from $K_D^*$, we nevertheless chose to make the minor correction of $X_{FeO^*}$ to $X_{FeO}$ for each sample at the T and $fO_2$ of the experiment. The Borisov et al. (2018) model was chosen to calculate the $Fe^{3+}/Fe^{2+}$ in the liquids based on giving the best agreement of all available models between the $K_{D,Fe2+/Mg}$ calculated from synHP1 experiments run at 1300°C and IW+0.5 and the value calculated from experiments run using the same bulk composition at 1300°C but under the more oxidizing conditions of FMQ to FMQ+1, with higher $Fe^{3+}$ contents in their liquids (see the following section for more details). The Borisov et al. (2018) model is also in the middle of the range of predictions of the various Fe oxybarometry models at low $fO_2$ (Suppl. Fig. 6). The cation mole fractions of oxide components in the liquid were then renormalized based on the adjusted FeO and $Fe_2O_3$ contents. The fitting routine used to calculate the unknown coefficients in equation (3d) was a linear least squares method weighted by the

uncertainties in the measured FeO and MgO in the olivines and FeO* and MgO in the glasses, where the differences between the sum of the squared residuals between the measured and calculated $K_{D,Fe2+-Mg}$ were minimized. Different permutations of compositional variables $X_j$ were tested in order to find the minimum number of $X_j$s required to explain the experimental $K_{D,Fe2+/Mg}$ with all coefficients satisfying a t-test at the $p<0.05$ confidence level. This exercise yielded only two choices of a minimum of two $X_j$ parameters in equations (3d): Si and Al, or Si and Mg. The components $X_{Si}^{liq}$ and $X_{Al}^{liq}$ were chosen as independent variables, in part because the two represent an analogue to other melt structural considerations such as NBO/T (e.g., Mysen et al. 1982) which have been used previously to parameterize the $K_{D,Fe2+-Mg}$ (e.g., Kushiro & Walter 1998), and because it avoids inconsistencies with the construction of the activity-composition relations in equation (3d) (i.e., including $X_{Mg}^{liq}$ implies an MgO-MgO term). Note that this fitting exercise does not preclude that the other interaction terms (and cross-terms) in the liquid are non-zero (which they surely must be), only that including them does not improve the quality of the fit to the RKD $K_{D,Fe2+-Mg}$ data (which has a small range of alkalis and $TiO_2$, which are known to influence $K_D^{ol/liq}{}_{,Fe2+-Mg}$, e.g., Longhi et al. 1978; Ford et al. 1983; Toplis et al. 2005).

The resulting fitted equation has three adjustable parameters: $B_{Si}$, $B_{Al}$, and $W_{Fe-Mg}$. Figure 8A compares the measured and calculated $K_{D,Fe2+-Mg}$ for the RKD experiments given the best-fit parameters: $B_{Si}$ = 1.035±0.02, $B_{Al}$ = -1.605±0.10, and $W_{Fe-Mg}$ = 3338±320, where the numbers after the ± symbols correspond to 1σ errors calculated using a Monte Carlo approach. This result, referred to as Model 1, corresponds to an

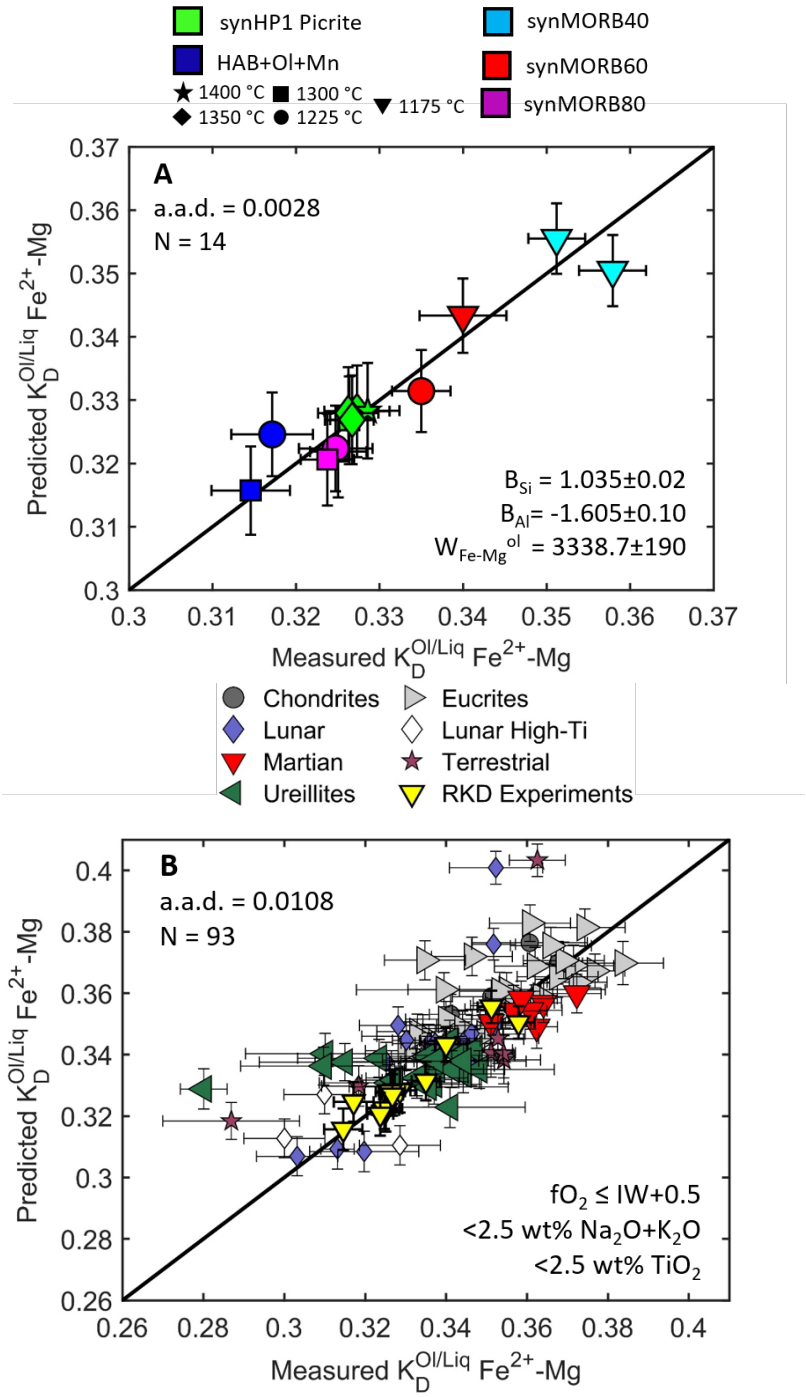


**Figure 8.** Results of fitting Model 1 ($K_{D,Fe2+-Mg}^{ol/liq}$ as a function of $X_{Si}^{liq}$ , $X_{Al}^{liq}$, $X_{Fo}^{ol}$) to the RKD data. $Fe^{3+}/Fe^{2+}$ in the glasses is calculated by Borisov et al. (2018). **(A)** Measured vs. predicted $K_{D,Fe2+-Mg}$ for RKD equilibration experiments; the coefficients used were based on the best-fit of equation (3d) to the RKD data (Model 1). The black diagonal lines indicate are 1:1 contours. a.a.d = absolute average deviation between the measured value of $K_d^{ol/liq}{}_{,Fe2+-Mg}$ and the model result. **(B)** Results of Model 1 applied to a compilation of literature experiments run at $fO_2 \leq$ IW+0.5 that have <2.5 wt% $Na_2O+K_2O$, <2.5 wt% $TiO_2$ and passed quality filters for mass balance and olivine stoichiometry. The yellow triangles correspond to the RKD experiments shown in panel **(A)**. Error bars are 1σ.

average absolute deviation (a.a.d.) between the measured and predicted $K_D^{ol/liq}{}_{,Fe2+-Mg}$ of 0.003, which is nearly equivalent to the analytical precision in $K_D$*. The best fit value for $W_{Fe-Mg}^{ol}$, 3338±320 J/mol, overlaps within error of previous literature estimates of this value (3700±800 J/mol, Wiser & Wood 1991; 2600±500 J/mol, O'Neill et al. 2003; 3000 J/mol used by Toplis 2005; and 3060±980 J/mol Tuff and O'Neill 2010).

It is worth emphasizing that given the relatively restricted range in $Na_2O+K_2O$ and $TiO_2$ in our experimental glasses (0.05-1.65 wt% and 0.60-2.14 wt%, respectively) these oxides need not be considered to describe the composition-dependence of $K_{D,Fe2+-Mg}$ in the RKD experiments. Including $B_i$ terms for the alkalis and/or Ti does lead to an improvement of the fit to the RKD data, as would be expected by the addition of two adjustable parameters, but the added variables fail a t-test for significance and thus the data are indistinguishable at the 95% confidence level from setting those $B_i$ values to zero. The two RKD experiments using the HAB+Ol+Mn bulk composition (blue symbols, RKD-12 and RKD-12) are the runs with elevated alkalis and the 1225 °C experiments has high predicted $K_{D,Fe2+-Mg}$ using Model 1 compared to the measured values (Figure 8A, blue circle, $\Delta K_{D,Fe2+-Mg} = 0.008$), which is consistent with the expected effect of alkalis on the $K_D$ (Toplis 2005). Including such compositional terms becomes important for the compositions of common igneous rocks found on the Earth, Moon, and other planetary bodies, and in order to calibrate the effect of alkalis and Ti on the $K_{D,Fe2+-Mg}$; in section 6.3 a low $fO_2$ literature dataset was compiled which spans a much wider range of bulk compositions.

### 5.2 Comparison to Matzen et al. (2011)

The focus of this study is to assess $Fe^{2+}$-Mg exchange between olivine and liquid under conditions where the activity of $Fe^{3+}$ in the liquid is low. This involved a tradeoff between running experiments at the low $fO_2$ levels required to keep the $Fe^{3+}/Fe^{Total}$ as low as possible while minimizing Fe-loss to the Re wire loop holding the experimental

charge (Borisov & Jones,1998), and accepting the larger amount of alkali loss that occurs under more reducing conditions (e.g. Tsuchiyama et al. 1981; Sossi & Gegley 2018). This approach allows for an accurate, nearly direct determination of the $K_D^{ol/liq}{}_{,Fe2+-Mg}$, because corrections for $Fe^{3+}$ are minor and are predicted to be comparable to the analytical uncertainty in $K_D$*. Even so, it is useful to compare our results to experiments run using the same or similar melt compositions at higher $fO_2$ where calculated $Fe^{3+}/Fe^{2+}$ of the experimental liquids were used to extract values of $K_D^{ol/liq}{}_{,Fe2+-Mg}$ from measurements of $K_D$*.

The synHP1 bulk composition was originally used in the experiments of Matzen et al. (2011), and an additional experiment (RKD-27) was run under oxidizing conditions to compare directly with the results of that study in order to rule out possible differences in thermocouple and $fO_2$ sensor calibration, and the fact that the analytical protocols had changed between 2010 and 2020 (in particular, as discussed above, the experimental charges from this study were analyzed using mean atomic number backgrounds versus off-peak backgrounds in Matzen et al. 2011). Experiment RKD-27 was run using the original synHP1 bulk composition (undoped with Mn and Cr as in synHP1+Mn+Cr) under nearly identical conditions (T = 1350 °C, $fO_2$ = FMQ) as Run 15 in Matzen et al. (2011); the only difference in experimental conditions was that RKD-27 was run under slightly more oxidizing conditions, as a result of using the Frost (1991) FMQ buffer (log $fO_2$ = -6.73), whereas Matzen et al. used the Huebner (1971) equation for FMQ (log $fO_2$ = -6.86 at 1350 °C). RKD-27 was also hung from a preconditioned Pt loop that was originally used in Matzen et al. (2011) Run 26. The measured $K_D$* values for the two experiments are 0.284±0.006 (1σ) for Run 15 and 0.285±0.003 (1σ) for RKD-27, which are indistinguishable at 1σ, signifying that we have been able to reproduce the Matzen et al. (2011) experimental result.

To calculate $K_D^{ol/liq}{}_{,Fe2+-Mg}$, Matzen et al. (2011) adopted the Jayasuriya et al. (2004) parameterization of $Fe^{3+}/Fe^{2+}$ in the liquid because, compared to the other $Fe^{3+}/Fe^{2+}$ parameterizations available at the time, it lead to the smallest difference between the median calculated $K_D^{ol/liq}{}_{,Fe2+-Mg}$ values for a compilation of olivine-liquid pairs run at $fO_2 \leq$ IW+0.5 and FMQ±0.5. The RKD experiments that used the synHP1 base composition can provide an alternative and direct comparison for which of the $Fe^{3+}/Fe^{2+}$ models (including two parameterizations that post-date Matzen et al. 2011), when applied to glasses of similar composition from both the oxidized and reduced experiments, results in the closest agreement in their calculated $K_D^{ol/liq}{}_{,Fe2+-Mg}$ values. For the experiments run at 1350 °C and FMQ, the eight models give estimates of $Fe^{3+}/Fe^{Total}$ ranging from 0.07 (O'Neill 2018) to 0.14 (Jayasuriya et al. 2004) and for the experiments run at the same T but at IW+0.5 the estimates of $Fe^{3+}/Fe^{Total}$ range from 0.02 (O'Neill 2018) to 0.04 (Nikolaev et al. 1996). The model that resulted in the smallest difference between calculated $K_D^{ol/liq}{}_{,Fe2+-Mg}$ values from the 1350 °C synHP1±Cr+Mn mix experiments run at FMQ (Run 15 [Matzen et al. 2011], and RKD-27) and from the experiments run at IW+0.5 (RKD-5 and RKD-25, redundant experiments), was Borisov et al. (2018), which gave $K_D^{ol/liq}{}_{,Fe2+-Mg}$ values that agreed to within 0.001 absolute. The $Fe^{3+}/Fe^{2+}$ calculated by the Borisov et al. (2018) model is also typically around the average value calculated using all 8 models for a single composition and $fO_2$. For comparison, using Jayasuriya et al. (2004) there is a difference of ~0.004 absolute between the $K_D^{ol/liq}{}_{,Fe2+-Mg}$ of the oxidized and reduced experiments, and the model predicts the highest $Fe^{3+}/Fe^{2+}$ of all the models at QFM resulting in the largest correction on the $K_D$*. The Borisov et al. (2018) model was adopted hereafter to correct for $Fe^{3+}/Fe^{2+}$, based on the internal consistency it produces in the synHP1 RKD experiments and because it predicts $Fe^{3+}/Fe^{2+}$ values that are intermediate to the other available

models. Note that this exercise is based on only a handful of experiments and so is not meant to be an endorsement of Borisov et al. (2018) over the other Fe oxybarometers, only that it leads to the most internally consistent calculation of $K_{D,Fe2+-Mg}$ between similar experiments run at different $fO_2$.

The RKD experiments run using the synHP1±Cr+Mn bulk composition at IW+0.5 and at T = 1300-1400 °C (n=5), corrected for $Fe^{3+}/Fe^{2+}$ using Borisov et al. (2018), define a narrow range in their calculated $K_D^{ol/liq}{}_{,Fe2+-Mg}$ of 0.3263 to 0.3286 ± 0.003, where the error corresponds to the typical 1σ analytical precision in $K_D$*. Note that experiments run at the same T and $fO_2$ using the doped composition synHP1+Cr+Mn have $K_{D,Fe2+-Mg}$ (0.3152±0.003, RKD-6) that is within 1σ error of the experiment using the undoped synHP1 composition (0.3157±0.003, RKD-25). For the nine oxidized experiments in Matzen et al. (2011) using synHP1, excluding Run #39 (see their paper for a discussion of this experiment run in air), the Borisov et al. (2018) corrected $K_{D,Fe2+-Mg}$ range from 0.326 to 0.355, with a typical error on $K_D$* of 0.006 (Matzen et al. 2011). The RKD experimental $K_{D,Fe2+/Mg}$ thus overlap with the lower end of the distribution of $K_{D,Fe2+-Mg}$ values calculated from the Matzen et al. (2011) data. The mean and standard error of the RKD synHP1 experiments at IW+0.5, FMQ, and FMQ+1 based on using the Borisov et al. correction for $Fe^{3+}$ is $K_{D,Fe2+-Mg}$ = 0.330±0.002, n=8, with the two highest $K_{D,Fe2+-Mg}$ (0.337±0.002 and 0.341±0.003) calculated from the FMQ+1 experiments. Although these distributions overlap with the Matzen data the average values in the higher precision RKD experiments are offset to slightly lower $K_D$.

The two datasets can be brought into closer agreement after considering that the Matzen et al. (2011) glass data were corrected using the BHVO-2g standard, whereas the RKD glass data were not. The same BHVO-2g glass chips were analyzed in Matzen et al. (2011) as those described in section 4.3 and 5.1.1, and as mentioned earlier we found

that the measured molar Fe*/Mg ratio (0.877±0.009) overlapped within 1σ of those reported in the GeoRem database (0.889±0.008). The original Matzen et al. (2011) microprobe measurements of BHVO-2g (using off-peak backgrounds) were recovered from the CIT probe computer and the Fe/Mg ratio over several sessions was 0.884±0.01, which overlaps with the values measured in the more recent probe sessions between 2015 and 2021 (which used mean atomic number backgrounds). Although the accepted BHVO-2g value that was used by Matzen et al. (2011) is not reported, based on pre-2010 analyses it likely had an Fe/Mg closer to 0.86. This correction factor would account for a ~3% increase in the Fe/Mg of the glasses reported in Matzen et al. (2011); undoing this correction then results in a mean and standard error $K_{D,Fe2+-Mg}$ = 0.331±0.003 (N=9), which is in agreement with the value for the RKD experiments (0.330±0.002).

### 5.3 Experimental Olivine-Liquid Literature Data Run at $fO_2 \leq$ IW+0.5

The experimental olivine-liquid literature at low $fO_2$ is dominated by studies focused on lunar, martian, and asteroidal bulk compositions because most igneous processes on those bodies occur under relatively reducing conditions compared to those encountered on Earth (e.g., Wadhwa 2008; Putirka 2016). Literature data were compiled for coexisting olivines and glasses in nominally anhydrous experiments run at or near atmospheric pressure (max pressure is 260 bars) and at $fO_2 \leq$ IW+0.5. This search returned 42 unique studies published between 1975 and 2021, corresponding to 305 individual experiments. The experiments were broadly categorized according to the planetary body or materials they focused on: chondrites (Ehlers et al. 1992; Usui et al. 2015; Collinet & Grove 2020); eucrites (Stolper 1977; Bartels & Grove 1991; Jurewicz et al. 1993; Jurewicz et al. 1995); ureilites (Walker & Grove 1993; Singletary & Grove 2003; Singletary & Grove 2006), lunar low-Ti basalts with bulk $TiO_2$ <6 wt% (Donaldson et al. 1975; Merrill & Williams 1975; Huebner et al. 1976; McKay & Weill 1977; Walker et al. 1976; Walker et al. 1977; Delano 1977; Grove & Vaniman 1978; Irving et al. 1978;

Longhi et al. 1978; Grove 1981; Nielsen et al. 1988; Elardo et al. 2015; Prissell et al. 2018; Dygert et al. 2020); high-Ti lunar basalts with bulk $TiO_2$ > 6 wt% (Akella et al. 1976; Longhi et al. 1978; Rhodes et al. 1979; Delano 1980; Grove & Beaty 1980; Longhi & Pan 1988); martian meteorites (Herd et al. 2002; Castle & Herd 2017); and terrestrial compositions (MORB – Kadik et al. 1982; Sato 1989; Jurewicz & Watson 1988; picrites or olivine tholeiites – Hanson & Jones 1998; Bell et al. 2021; komatiites – Bickle 1978; mafic intrusives – Murck & Campbell 1986; Snyder & Carmichael 1992; absakorites – Snyder et al. 1993; and basalts in the system SiAlMgFeCaNaO with bulk $Na_2O$ up to 5.8 wt% - Shi 1993). The composition space of the literature data set is much broader than that sampled by the RKD experiments, and includes bulk compositions with up to 12.7 wt% TiO2, 5.8 wt% $Na_2O$, 1.94 wt% $K_2O$, and experimental olivine compositions ranging from Fo 32.6 to 96.2. One of the motivations for the RKD experiments was to produce a complementary dataset of high precision $K_D^{ol/liq}{}_{,Fe2+-Mg}$ measurements run at low $fO_2$ but on bulk compositions that more closely resemble basalts found on Earth.

For each literature experiment, the reported compositions of all run products (and uncertainties where provided) were compiled into a database along with the experimental run conditions. The $fO_2$ of experiments run in pure Fe capsules was calculated using the activity model of Snyder & Carmichael (1992) and using a $\Delta G°$ for the reaction $Fe + ½ O_2 = FeO$ calculated from the thermodynamic data of Robie et al. (1979), assuming that the activity of Fe in the metal phase was unity. Otherwise, the $fO_2$ was reported as listed in the original studies, either from direct measurement in a gas-mixing furnace or from calculations based on the capsule type (e.g., C-CO equilibria for graphite capsules).

Each experiment that reported complete compositional information of the reported phase products was run through the same mass balance routine as described for

the RKD experiments. If Fe metal was present as a run product, it was either assumed to be 100% Fe, or if measurements of Ni contents were available then a binary Fe-Ni alloy. Otherwise FeO (and MnO ± $Na_2O$ ± $K_2O$ ± $P_2O_5$) were allowed to vary as free parameters using the same scheme as described above in the section on mass balance. Of the 276 experiments that had sufficient compositional information to run the mass balance calculation, 193 (70%) passed the mass balance criterion (Q>0.05, where Q is the p-value adjusted for the false discovery rate). Of those experiments that did not achieve this mass balance criterion, inspection of the individual $\chi^2$ values did not reveal any obvious systematics to explain why some experiments passed and others failed. There are a range of possible factors including incorrect data reporting (wherever possible, these errors were identified and if they could not be reconciled the data were omitted), severe loss of volatile elements such as alkalis, and/or loss of continuous loss of Fe to the sample container. Experiments that failed mass balance were flagged as potentially problematic and were not included in the fitting exercises. In addition, the stoichiometry of olivine analyses was checked and subjected to slightly more lenient constraints than those applied to the RKD experimental data, reflecting the fact that early studies used microprobes that lacked many of the features present in current instruments; olivine analyses were accepted with a tetrahedral sum of 1.00±0.02 and a cation sum of 3.00±0.03, per 4 oxygens (the criteria described in Papike et al. 2009). All glass analyses in the compilation had oxide sums between 98.44 and 102.20. Application of these quality filters resulted in a preferred dataset of 178 olivine-liquid experiments that passed mass balance based and reported olivine analyses that satisfied the stoichiometric criteria. Using all of the literature data or a subset of preferred experiments makes almost no difference in the final fitting results of the compositional dependence of $K_{D,Fe2+-Mg}$, suggesting that any systematic errors in the experiments related to poor mass balance,

olivine stoichiometry, and/or oxide sums are normally distributed throughout the compilation. However, only those experiments in the preferred subset of the literature data were used to calibrate model coefficients.

Figure 8B shows the $K_{D,Fe2+-Mg}$ predicted by applying Model 1 (which was only calibrated on the RKD experiments) to a subset of the preferred literature data with glasses containing <2.5 wt% $TiO_2$ and <2.5 wt% $Na_2O+K_2O$ (N = 93), where the upper limit is comparable to the highest concentrations of these oxides measured in the RKD experimental glasses. The average absolute deviation between the measured and modeled $K_{D,Fe2+-Mg}$ for these low-Ti and low-alkali literature experiments is 0.011, substantially higher than the 0.003 deviation from the RKD experiments, which are shown in Figure 8B as yellow triangles for reference. It is important to reemphasize that the analytical precision of the literature data is typically much worse than the new data presented for the RKD experiments; for example, the median 1σ uncertainty in $K_D$* is ~0.01 for the literature data for which uncertainties are reported (note, however, in many cases the errors are not reported) compared to 0.003 for the RKD experiments. Therefore, for both the high-precision RKD data and the noisier literature data, Model 1 recovers the $K_{D,Fe2+-Mg}$ to about the reported analytical precision for experiments with liquids that have $TiO_2$ and $Na_2O + K_2O$ < 2.5 wt%. Of the 66 preferred experiments with these alkali and Ti contents that report analytical errors, 39 (59%) of the average $K_{D,Fe2+-Mg}$ predicted with Model 1 fall within 1σ of the reported value; 54 (82%) overlap within 2σ of the reported value. If the standard deviations in the model are also taken into account, nearly all of the predictions of $K_{D,Fe2+-Mg}$ overlap within 2σ of the experimental measurements.

### 5.3.1 Systematics of the individual partition coefficients, $D_{Fe2+}$ and $D_{Mg}$

Using the high-precision RKD data as context along with the preferred literature data that have passed the filters we have applied, it is instructive at this point to compare systematics of the individual partition coefficients, $D_{Fe2+}^{ol/liq}$ and $D_{Mg}^{ol/liq}$ , because the

effects of T and composition are more clearly illustrated for these parameters than when comparing to the $K_{D,Fe2+-Mg}$, which is based on the ratio of $D_{Fe2+}^{ol/liq}$/ $D_{Mg}^{ol/liq}$. The Borisov et al. (2018) expression was used to calculate $Fe^{3+}/Fe^{Total}$, which based on the reported glass compositions and $fO_2$ ranges from 0.01 to 0.04 with a mean of 0.01 for the preferred literature data. Figure 9 shows plots of inverse temperature versus ln $D_{Fe2+}^{ol/liq}$ (Figure 9A) and ln $D_{Mg}^{ol/liq}$ (Figure 9B); the T range in the RKD experiments is 1175-1400 °C and for the literature experiments 1050-1503 °C. The red lines show a fit to the RKD experiments using equation (4a) ($\ln D_i = A_i + B_i/T$); this form with a constant $A_i$ only takes into account the change in the standard state entropies and enthalpies of formation of fayalite and forsterite and are independent of composition or the effects of mixing. Deviations from this line represent the effects of solution components on the activity coefficients in equation (4b). The RKD experiments presented here are well-described by this simple functional form for both $\ln D_{Fe2+}$ ($A_{Fe2+}$ = -4.41±0.05, $B_{Fe2+}$ = 6827±140, $r^2$ = 0.99) and for $\ln D_{Mg}$ ($A_{Mg}$ = -2.83±, $B_{Mg}$ = 6094±184, $r^2$ =0.95); note that the ratio of $B_{Fe2+}/B_{Mg}$ = 1.12±0.04 is close to unity, which is the basis for the relative insensitivity of the $K_{D,Fe2+-Mg}$ to changes in temperature (values after ± are all 1σ). For both D's, the high-alkali, high-$SiO_2$ experiments on chondrites (Collinet & Grove 2020) and on terrestrial Ti-free compositions (Shi 1993) are systematically high, as are experiments with the highest $SiO_2$ in the compilation ($SiO_2$ = 69.5 wt%, Usui et al. 2015). High-Ti lunar compositions are systematically low in $D_{Fe2+}$; interestingly, they collapse onto the main cloud of data for $D_{Mg}$; this implies that the effect of Ti on $\gamma_{FeO}^{liq}$ is important and much less so for $\gamma_{MgO}^{liq}$.

These considerations imply that unlike the RKD data for $K_{D,Fe2+-Mg}$, which could be well-modeled using only $X_{Si}^{liq}$, $X_{Al}^{liq}$, and $X_{Fo}^{ol}$, or for the $D_i^{ol/liq}$, which can be parameterized only as a function of 1/T, in order to fit the full range of compositions

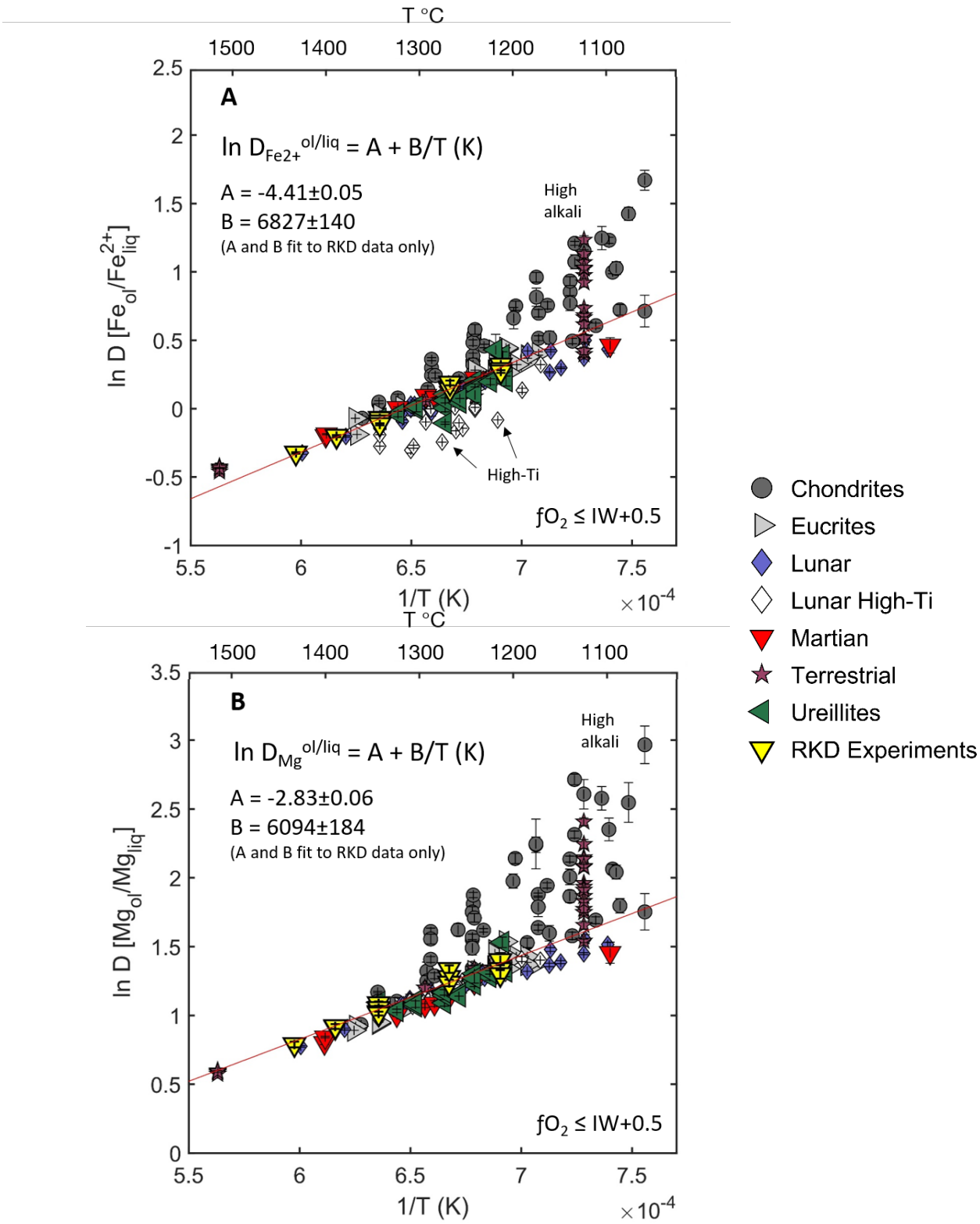


**Figure 9.** 1/T (K) vs. **(A)** ln $D_{,Fe2+}^{ol/liq}$ and **(B)** ln $D_{,Mg}^{ol/liq}$, for the preferred literature experiments run at $fO_2 \leq$ IW+0.5 and the RKD experiments (yellow triangles). T corresponds to the reported experimental temperature. The upper x-axis shows T in Celsius for clarity. The thin red lines are fits of the form ln $D_i = A_i + B_i/T$, where A and B are adjustable parameters, to the RKD experimental data only. Error bars are 1σ.

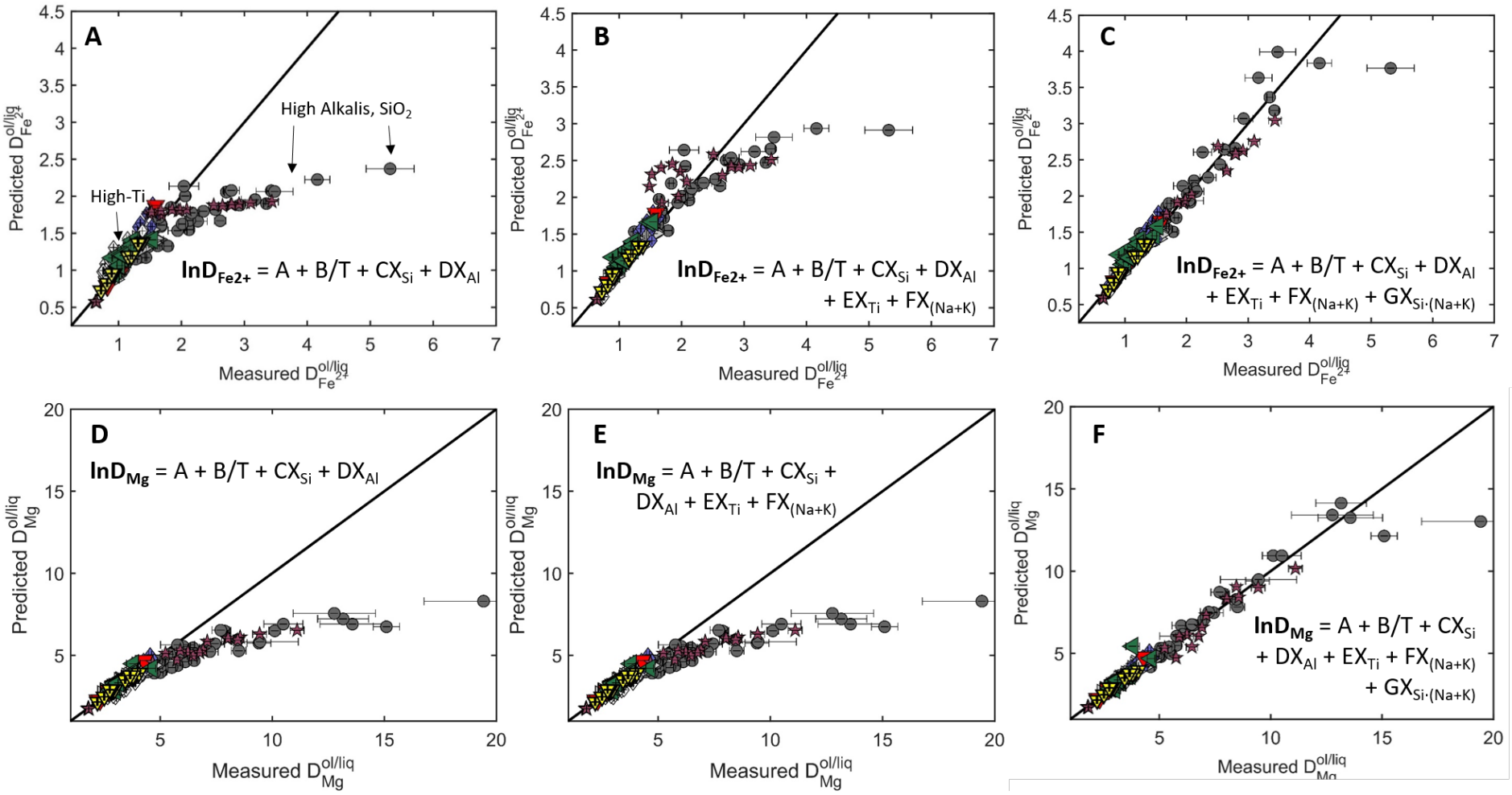


**Figure 10**. Results of fitting equations of the form $\ln D_i = A_i(X) + B_i/T$ to the RKD experiments (N=14, yellow triangles) and literature experiments (N=178) at $fO_2 \leq$ IW+0.5. $A_i(X)$ is a function of melt composition, with different choices of liquid compositional variables shown in different panels. The top row is ln $D_{Fe2+}^{ol/liq}$ and the bottom row is ln $D_{Mg}^{ol/liq}$. Thick black lines are 1:1 contours and error bars are 1σ. Panels **(A)** and **(D)** show best-fit models that are a function of $X_{Si}^{liq}$ and $X_{Al}^{liq}$; panels **(B)** and **(E)** show models that are a function of $X_{Si}^{liq}$, $X_{Al}^{liq}$, $X_{Ti}^{liq}$, $X_{Na+K}^{liq}$, and **(C)** and **(F)** include an additional term, $X_{Si\text{-}(Na+K)}^{liq}$, which is a cross-term corresponding to the product of $X_{Si}$ and $X_{(Na+K)}$ in the liquid.

represented by the low $fO_2$ literature data additional terms are required. Before jumping into the $K_{D,Fe2+-Mg}$, the individual $D_i^{ol/liq}$ were fit to an expanded form of equation (4a), where $A_i$ is treated as a linear combination of liquid components, analogous to the $B_jX_j$ terms used in equation (3d). The first column in Figure 10 (panels A and C) compares measured and predicted $D_i^{ol/liq}$ first using only $X_{Si}$ and $X_{Al}$ (and T) as independent variables whose coefficients were fit to the RKD experiments; the thick black lines are 1:1 contours. These panels highlight the low predicted $D_i$'s for the high-alkali and high-Si literature experiments, as well as the high predicted $D_{Fe2+}$ values for the high-Ti experiments. Terms for $X_{Ti}$ and $X_{Na+K}$ were added and the preferred literature data was used to calculate coefficients that minimized the difference between the measured and model $D_i$'s. Although including these terms lead to an improved the fit and close correspondence between the models and data for $D_{Fe2+}$ up to ~2.0 and $D_{Mg}$ up to ~8.0, the high-alkali high-$SiO_2$ data (Shi 1993, Usui et al. 2005, Collinet & Grove 2020) are still underestimated by the model, and define a cluster of points that appear to be systematically rotated away from the 1:1 line.

Note that $SiO_2$ appears explicitly in the formation reactions for fayalite and forsterite (equation 4a) and so the $D_i$'s are a function of the activity coefficients of $\gamma_{(Fe,Mg)O}^{liq}$ as well as $\gamma_{SiO2}^{liq}$. Alkalis have a significant effect on the activity of $SiO_2$ in melts (Kushiro 1975; Watson 1982; Ryerson 1985, Grove & Juster 1989; Hirschmann et al. 1998; Wasylenki et al. 2003), which leads to sympathetic increases in the $SiO_2$ and alkali contents of silicate liquids. The Toplis (2005) composition-dependent model of $K_{D,Fe2+-Mg}$ requires an empirical function that relates Si and Na+K, which is linear for glasses with $SiO_2 \leq 60$ mol% and non-linear for glasses with $SiO_2 > 60$ mol%. We expanded the Margules equation to include a cross-term, $B_j$ where $j = X_{Si} \cdot (X_{Na}+X_K)$ and found that it led to a significant improvement of the $D_i$ fits ($p<0.05$ based on the chi-

square test), and does a much better job at describing the high-Si high-alkali experiments (Figure 10B and 10D). The final expression for the $D_i$'s, shown in Figure 10 panels B and D, includes a constant plus terms for 1/T, $X_{Si}$, $X_{Al}$, $X_{Ti}$, $X_{(Na+K)}$, and $X_{Si-(Na+K)}$. This exercise helped inform which variables to use for calibrating the composition-dependent model for $K_{D,Fe2+-Mg}$ described below. Note that although $a_{SiO2}$ cancels out in the exchange reaction equation (1a), the ratio of $B_{Si-(Na+K)}$ fitted for the $D_{Fe2+}$ expression divided by that for the $D_{Mg}$ expression is not unity (~1.2) and so this term was retained in the expression for $K_{D,Fe2+-Mg}$. While these fits to the $D_{Fe2+}$ and $D_{Mg}$ vs. 1/T data are useful both in applications (e.g., for determining liquidus temperatures of olivine-saturated melts) and for the insights they provide into the effects on the D's of the compositional parameters used to fit the data, we will use them below to remove $X_{Fo}$ from the fit to $K_{D,Fe2+-Mg}$ (as described previously in equations 4a-4g), which can be useful for determining $K_D$ when only the melt composition is known.

### 5.3.2 Modeling compositional dependence of $K_{D,Fe2+-Mg}$ using low *f*O2 experimental data

The preferred low *f*O2 literature data (n = 178) was also used to calibrate the compositional effects of Ti, and Na+K on $K_{D,Fe2+-Mg}$ using the range of bulk compositions encompassed by this data set, excluding the RKD data. The fitting procedure was bootstrapped iteratively in the following way in order to weight the RKD experimental data based on the good fit produced using Model 1:

(1) As described above, best-fit coefficients $B_{Si}^{liq}$, $B_{Al}^{liq}$, $W_{Fe-Mg}^{ol}$ were first determined by fitting the high-precision RKD experimental data to equation (3d), e.g., Model 1.

(2) With these coefficients fixed, a second least-squares fit to equation (3d) was done on the literature data (RKD excluded) to constrain the values of $B_{Ti}$, $B_{Na+K}$, and $B_{Si-(Na+K)}$.

(3) Now fixing $B_{Ti}$, $B_{Na+K}$, and $B_{Si-(Na+K)}$ to the values fit as describe in (2), the RKD data were refit for $B_{Si}$, $B_{Al}$, and $W_{Fe-Mg}^{ol}$.

(4) Finally, the literature data were refit, fixing the new $B_i$ coefficients calculated in (3) and recalculating the $B_{Ti}$, $B_{Na+K}$, and $B_{Si-Na+K}$ that best fit the data.

The coefficients were found to converge after one iteration. In addition, it was found that the $B_{Na+K}$ term could be omitted while retaining $B_{Si-Na+K}$ without significantly reducing the quality of the fit to the $K_{D,Fe2+-Mg}$.

Although the correction to from $K_D$* to $K_{D,Fe2+-Mg}$ is small, for internal consistency (since such a correction was applied to the RKD data), such a correction based on Borisov et al. (2018) was applied to all experiments to correct the measured $K_D$* for $Fe^{3+}/Fe^{2+}$. The least squares method was weighted by the propagated measurement errors in FeO and MgO in the olivines and glasses; where this information was not available, the error assigned to the reported $K_D^{ol/liq}{}_{,Fe2+-Mg}$ was set to 0.01 absolute, which is the median value for all other studies that report measurement errors. The errors on the coefficients were calculated using a Monte Carlo approach, by creating 1000 synthetic datasets based on the mean and 1σ of the $K_{D,Fe2+-Mg}$ for each experiment and then refitting the data.

The best-fit coefficients $B_i$ where i = $X_{Si}^{liq}$, $X_{Al}^{liq}$, $X_{Ti}^{liq}$, $X_{Si-(Na+K)}^{liq}$, and $X_{Fo}^{ol}$ using the bootstrapped procedure jointly fit to the RKD and literature experiments are referred to as Model 2 and are listed along with their uncertainties in Table 4. The final expression for Model 2 is:

$$\ln K_D^{ol/liq}{}_{,Fe2+-Mg} = -\Delta G°/RT + \Sigma_j B_j X_j^{liq} + W_{Fe-Mg}^{ol}(1 - 2 X_{Fo}^{ol})/RT$$

$$= -\Delta G°/RT + 0.9637 X_{Si}^{liq} - 0.5462 X_{Al}^{liq} - 1.151 X_{Ti}^{liq}$$

$$- 11.02 X_{Si-(Na+K)}^{liq} + 3031 (1 - 2 X_{Fo}^{ol})/RT \qquad \text{(Model 2)}$$

where, $\Delta G° = -6766 - 7.34 \times T$ (kJ/mol), T is in Kelvin, $X_i^{liq}$ are single-cation mole fractions in the liquid, $X_{Fo}^{ol}$ is mole fraction of forsterite in olivine, and R is the gas constant. Note that freely varying all five parameters using only the literature data results in coefficients that are within error of those shown in Model 2, with the exception of $B_{Al}$ (also note that $W_{Fe\text{-}Mg}^{ol}$ calculated for the literature data is 3333±228 J/mol). Applying Model 2 to the RKD dataset results in an a.a.d. of 0.002 (Figure 11A); for the preferred literature data (N=178) the a.a.d. is 0.015 (Figure 11B); and for the entire literature dataset (N=305) the a.a.d. is also 0.015, which again demonstrates that despite various quality filters the errors are roughly the same in the preferred as in the comprehensive literature datasets. The $W_{Fe\text{-}Mg}^{ol}$ term fitted to both the RKD data and to the literature dataset are in close agreement with previously reported values, including the 3000 J/mol from Toplis (2005), whose $\Delta G°$ term was adopted for Models 1 and 2. We emphasize again that the alkali-silica cross-term is only required to fit those experimental data with $K_{D,Fe2+\text{-}Mg}$ lower than ~0.30 or with single cation mole fraction $X_{Si} \cdot (X_{Na}+X_K) \gtrsim 0.02$; coefficients for $X_{Ti}$ and $X_{Na+K}$ fitted without this cross-term are also listed in Table 4 and can be applied with confidence to compositions with lower $SiO_2$ and alkali contents.

**Table 4 –** Fitted parameters to equation (3d) for Model 1 (RKD only) and for two versions of Model 2 (with and without a Si-(Na+K) cross-term) that were fitted the preferred low $fO_2$ literature compilation. RMSE is the root mean square error between the modeled $K_{D,Fe2+\text{-}Mg}$ and the experimental values. The values in alternate rows correspond to 1σ erorrs determined by a Monte Carlo approach. Model 2 shows the fit with a $B_{Si\text{-}(Na+K)}$ cross-term; Model 2* shows the fit with a $B_{Na+K}$ term (no cross-term)

**Table 4**

$$\ln K_D^{ol/liq}{}_{,Fe2+\text{-}Mg} = -\Delta G°/RT + B_i X_j^{liq} + W_{Fe\text{-}Mg}^{ol}(1 - 2 X_{Fo}^{ol})/RT \quad \text{(equation 3d)}$$

| | Fitted Parameters | | | | | | RMSE, all data N = 319 |
|---|---|---|---|---|---|---|---|
| | $B_{Si}$ | $B_{Al}$ | $B_{Ti}$ | $B_{Na\text{-}K}$ | $B_{Si\text{-}(Na+K)}$ | $W_{Fe\text{-}Mg}^{Ol}$ | |
| Model 1 | 1.035 | -1.605 | - | - | - | 3338 | 0.0457 |
| (RKD only) | 0.02 | 0.1 | - | - | - | 251 | |
| Model 2 | 0.9637 | -0.5462 | -1.151 | - | -11.02 | 3031 | 0.0216 |
| (cross-term) | 0.02 | 0.04 | 0.17 | - | 0.92 | 190 | |
| Model 2* | 0.9637 | -0.5462 | -1.107 | -7.151 | - | 3031 | 0.0229 |
| (no cross-term) | 0.02 | 0.04 | 0.17 | 0.61 | - | 190 | |

As shown in equation (4), utilizing the parameterizations of $D_i^{ol/liq}$ it is possible to express Model 2 only as a function of melt composition. This is potentially useful for instances where only the melt composition is known; i.e., given T and $D_i^{ol/liq}$ the equilibrium olivine composition can then be calculated. First, the use of the $D_i^{ol/liq}$ as a means to calculate T from olivine-liquid pairs is evaluated by specifying the measured $D_{Fe2+}$ and $D_{Mg}$ and re-arranging the fitted expressions for $\ln D_i$ to calculate T (i.e., $T = B_i / [\ln D_i^{ol/liq} - A_i]$). For this exercise the full experimental database N=305 was used. Histograms of $\Delta T = T_{measured}-T_{predicted}$ are shown in Suppl. Fig. 7A and 7B; the median $\Delta T$ for the $D_{Fe2+}$ and $D_{Mg}$ models are +0.3° and -8.9° and the a.a.d. in T are 21° and 25°.

The thermometer of Beattie (1993), which is based on the functional form of Takahashi & Irvine (1981), is widely adopted in petrology and can be applied to the low $fO_2$ data without any correction because the glasses are nominally anhydrous (Putirka 2007). Although it outperforms the new expression for $D_{Fe2+}$ (median $\Delta T$ = +0.4 and a.a.d. = 14°), this approach does a poor job at predicting the observed variations in $K_{D,Fe2+-Mg}$ with composition (i.e., if $K_{D,Fe2+-Mg}$ is calculated by taking the ratio $D_{Fe2+}/D_{Mg}$). The $D_i^{ol/liq}$ expressions can also be used to calculated $X_{Fo}^{ol}$ using equation (4e) and measurements of $X_{Fe}^{liq}$ and $X_{Mg}^{liq}$; for this calculation, the stoichiometric number ($\eta = X_{Fe}^{ol}+X_{Mg}^{ol}$) was set to 2/3, although the true value is lower because the olivines contain other divalent cations (additional expressions for these $D_i$'s would be needed to calculate this from only the liquid composition, as in Beattie 1993). Despite this approximation, the expressions do a good job in recovering the measured $X_{Fo}^{ol}$ values (Supp. Fig 7B and 7D); if the $D_{Fe2+}$ is substituted in to remove $X_{Fo}$ from the equation (4e) the median $\Delta X_{Fo}$ is -0.002 and the absolute average deviations in $X_{Fo}$ is 0.015; the comparable numbers for $D_{Mg}$ are -0.01 and 0.046. Thus, either version of equation (4e) can be substituted for $X_{Fo}^{ol}$ into Models 1 and 2 in order to calculate $K_{D,Fe2+-Mg}$ from only the melt composition

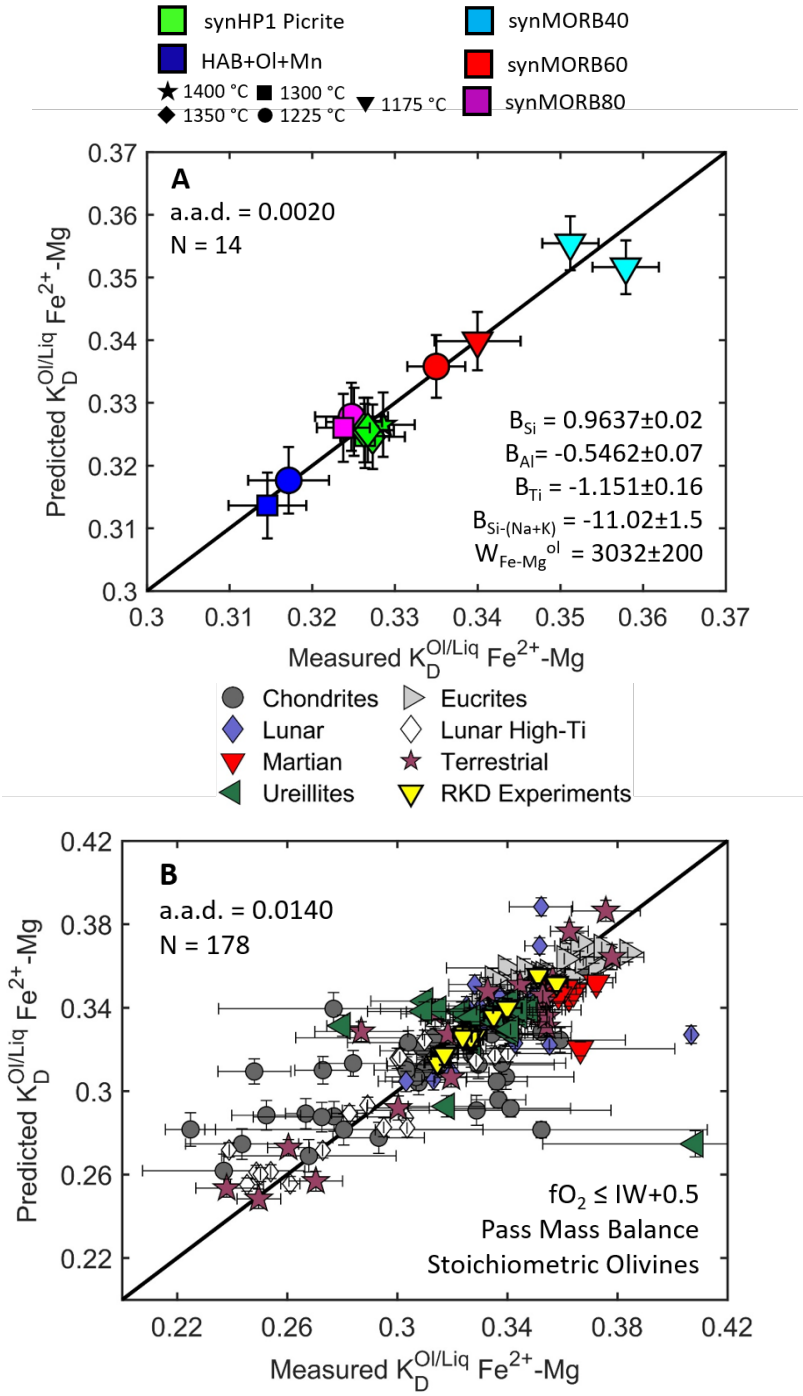


**Figure 11.** Results of iteratively fitting Model 2 (function of $X_{Si}^{liq}$, $X_{Al}^{liq}$, $X_{Ti}^{liq}$, $X_{Si-(Na+K)}$, $X_{Fo}^{ol}$) to the RKD data (N=14) and literature data (N=178). $Fe^{3+}/Fe^{2+}$ in the glasses was calculated by Borisov et al. (2018). Thick black lines are 1:1 contours. **(A)** Model results for the best fit to the RKD equilibrium experiments. The coefficients listed are based on a joint fit to the RKD and literature data, described in the text. **(B)** Results of Model 1 applied to a compilation of literature experiments run at $fO_2 \leq$ IW+0.5 that have <2.5 wt% $Na_2O+K_2O$, <2.5 wt% $TiO_2$ and passed quality filters for mass balance and olivine stoichiometry. The yellow triangles correspond to the RKD experiments shown in panel **(A)**. The black diagonal lines indicate are 1:1 contours. a.a.d = absolute average deviation between the measured value of $K_D^{ol/liq}$,Fe2+-Mg and the model result.

in a manner that is internally consistent, but the expression for $D_{Fe2+}$, which can be applied at low $fO_2$ (or when $Fe^{3+}/Fe^{2+}$ of the melt is known independently) is more accurate than the expression for $D_{Mg}^{ol/liq}$. Because the $B_j$ terms are linear and have the same origin (functional form) in the expressions for $K_D$ and $D_i$, they can be combined into a new expression, Model 2B, that only is a function of T and melt composition, substituting equation (4e) into (3d):

$$\ln K_D^{ol/liq}{}_{,Fe2+\text{-}Mg} = -\Delta G°/RT + \Sigma_j B_j X_j^{liq} - \frac{W_{Fe-Mg}^{ol}}{RT}(1 + 2 \cdot [\frac{D_{Fe}^{ol/liq} \cdot X_{FeO}^{liq}}{\eta}]) \qquad \text{(Model 2B)}$$

### 5.3.2 Comparison to previous parameterizations of $K_{D,Fe2+\text{-}Mg}$

In Figure 12, Model 2A is compared to other parameterizations of the composition-dependence of $K_{D,Fe2+\text{-}Mg}$ that are based on thermodynamic frameworks (Ford et al. 1983; Toplis 2005; Blundy et al. 2020). Each of these models was calibrated using available data from olivine-liquid experiments run at conditions ranging from very reducing (including many of the studies compiled here) to very oxidizing experiments run in air, and by incorporating a model for $Fe^{3+}/Fe^{2+}$ in the melt to calculate the $FeO^{liq}$ and $K_{D,Fe2+\text{-}Mg}$. The Ford et al. (1983) model contains terms for 1/T, and compositional terms for Mg, $Fe^{2+}$, Ca, Mn, Cr, Ni, Si, Al, $Fe^{3+}$, Na+K, Ti, and P in the liquid and utilized the Sack et al. (1980) model to calculate $Fe^{3+}/Fe^{2+}$. Note that an error was uncovered in Ford et al. (1983) Table 2 for the reported value of the coefficient on the phosphorus term, $C_{10} \cdot \ln(1\text{-}P)$: the value for $C_{10}$ should be -3.3034 instead of the reported value of -1.3034; previous calculations of $K_{D,Fe2+\text{-}Mg}$ using this model will be slightly off for bulk compositions that contain P. As mentioned earlier, the Toplis (2005) model is a function of $X_{Fo}^{olv}$, $X_{Si}^{liq}$, and $X_{Na+K}^{liq}$, with $Fe^{3+}/Fe^{2+}$ calculated using Kilinc et al. (1983), modified by the $P_2O_5$ term from Toplis et al. (1994). The Blundy et al. (2020) model (their equation 8) parameterizes the $K_{D,Fe2+\text{-}Mg}$ only in terms of olivine composition, and used the Borisov et al. (2018) model to calculate $Fe^{3+}/Fe^{2+}$. Model 2 also uses Borisov et al. (2018), but we

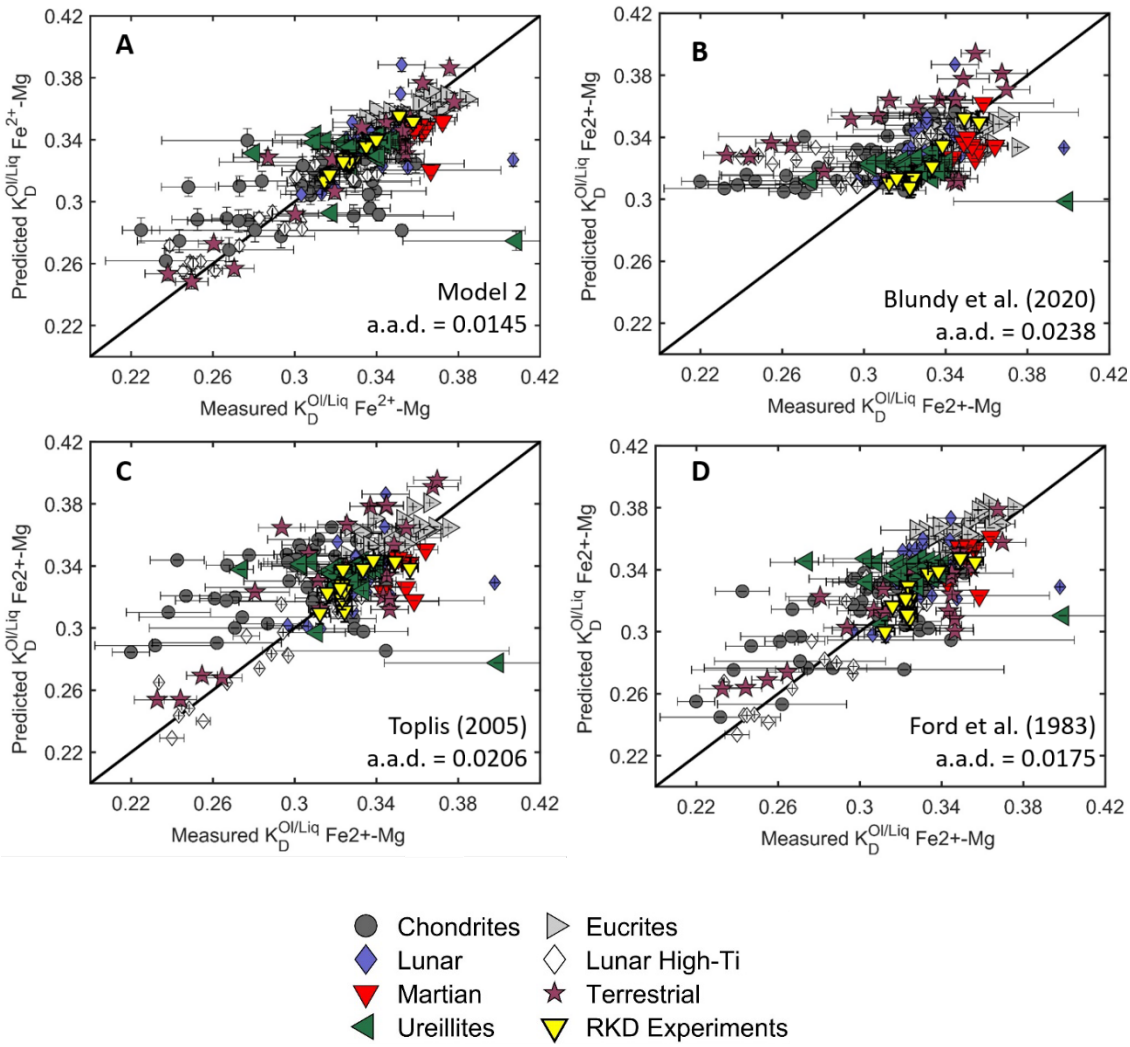


**Figure 12.** Comparison of different models describing the composition dependency of the $K_D^{ol/liq}{}_{,Fe2+-Mg}$ . Literature data at $fO_2 \leq IW+0.5$ that passed mass balance are shown (N = 178 experiments) as well as the 14 RKD experiments (yellow triangles). a.a.d. refers to the mean absolute deviation between the model and the measured value. The thick black lines are 1:1 contours. The expression used to calculate $Fe^{3+}/Fe^{2+}$ is based on **(A)** Borisov et al. 2018, **(B)** Borisov et al. 2018, **(C)** Kilinc et al. 1983, **(D)** Sack et al. 1980.

again emphasize that for the literature dataset at $fO_2 \leq$ IW+0.5, the corrections for $Fe^{3+}$ are minor as are the differences between the various parameterizations used in these models of $K_{D,Fe2+-Mg}$.

Figure 12 shows the result of applying each model to the preferred literature data and the RKD experiments; the $K_{D,Fe2+-Mg}$ are calculated from the measured $K_D$* using whichever $Fe^{3+}/Fe^{2+}$ expression was employed in each model (i.e., for Toplis (2005) the "measured" $K_{D,Fe2+-Mg}$ is $K_D$* modified by Kilinc et al. 1983). In terms of average absolute deviations, Model 2 and the Ford et al. (1983) model fare the best, followed by Toplis (2005) and then Blundy et al. (2020), which fails to capture any of the experiments with measured $K_{D,Fe2+-Mg}$ less than ~0.30 and over-estimates the $K_{D,Fe2+-Mg}$ for all melts with $TiO_2$ > 3.3 wt% and for all but two compositions with $Na_2O+K_2O$ > 4 wt%. Because liquid compositional terms are necessary, the ratio of FeO and MgO activity coefficients in the melt cannot be treated as a constant (Toplis 2005), except over limited ranges in liquid composition. The extra degrees of freedom afforded by including liquid compositional parameters is a requirement to explain the low $fO2$ olivine-liquid Fe-Mg partitioning data. It is still debatable which, if any, of the functional forms used to describe the liquid and olivine solution behaviors is preferable; this task is left as an exercise for the future, most likely when independently known or constrained activity-composition relationships for FeO and MgO can be utilized as guides to the proper functional forms to be used for the activity coefficients in equation (3d), which can then be fit more confidently to available $K_{D,Fe2+-Mg}$ data.

Despite the cross-terms included in Toplis (2005) and in Model 2, the Collinet & Grove (2020) chondrite melting experiments (gray circles that plot above the 1:1 line with measured $K_{D,Fe2+-Mg}$ <0.30) –which provide critical information on $K_{D,Fe2+-Mg}$ for

high-silica, high alkali liquids – are nevertheless not as well described as the other sets of experiments. This could be due to the omission of additional interaction parameters needed to model the liquid, or perhaps it is a consequence of the experiments themselves: based on mass balance, 24 of 57 experiments lost >10% (absolute) FeO (up to 45% FeO loss); the $K_D$ data at low MgO are noisy; and many of the low-MgO experiments were run at low T (10 were <1120°C) where zoning and equilibrium concerns could be an issue. In addition, there are two persistent outliers with very high measured $K_D$'s of ~0.40; the blue diamond is from the lunar experiments Donaldson et al. 1975 and there is no obvious reason why it has a high $K_D$ (uncertainties were not reported); the green triangle is a ureilite experiment Ptl9 from Singletary & Grove (2006) which has a mass-balance calculated FeO loss of ~22 wt%, much higher than other experiments from that study – it is also their lowest T experiment (1050 °C). If Fe is actively being lost from the experimental liquids at the time of quenching, and if diffusion in the olivine is sluggish such that the boundary cannot maintain equilibrium with the continually changing liquid composition, then the measured Fe/Mg in the olivine, which formed in equilibrium with a more Fe-rich liquid than its current surroundings, will be higher than expected for the coexisting Fe/Mg of the adjacent liquid, resulting in an artificially high $K_{D,Fe2+-Mg}$. Note that there is no correlation between FeO loss and model residuals; an experiment can initially lose Fe, achieve a constant value, and then re-equilibrate, and the effect described in the previous sentence would no longer be an issue; however in some instances it could be a symptom of disequilbrium. Inspection of histograms of the residuals (i.e., $\Delta K_D^{ol/liq}{}_{,Fe2+-Mg}$ (model – measured), Supplementary Figure 8) shows that the distribution of misfits in Model 2, Toplis (2005), and Ford et al. (1983) have relatively narrow peaks that are slightly skewed by around +0.005 from misfit = 0. All four distributions of

residuals fail a one-sample Kolmogorov-Smirnov test indicating that they are not normally distributed about $\Delta K_D^{ol/liq}{}_{,Fe2+-Mg} = 0$.

In summary, the Ford et al. (1983) model performs well in recovering the olivine-liquid Fe-Mg exchange coefficient in experiments at $fO_2 \leq$ IW+0.5, however Model 2 has the lowest residuals of the available models and compared to Ford et al. has the benefit of having far fewer parameters (6 instead of their 10, excluding pressure), as well as offering two analogous expressions for the $K_{D,Fe2+-Mg}$ that can be used if both the glass and olivine compositions (Model 1) are known or if only the glass (Model 2) compositions are available. The Toplis (2005) model tends to overestimate the measured $K_{D,Fe2+-Mg}$ (Suppl. Fig. 8C) and is less accurate than Model 2 or Ford et al. (1983). The model proposed in Blundy et al. (2020), which is based only on olivine composition, does not permit $K_{D,Fe2+-Mg}$ values less than ~0.30 which are required to explain the compilation of literature data at low $fO_2$ where the uncertainties related to $Fe^{3+}$ in the liquid are minimized. Thus, only models that take into account liquid composition can be universally applied to the range of bulk compositions found in nature.

### 5.4 Inferences from the relationship between $K_D$* and $K_{D,Fe2+-Mg}$

The relationship between $K_D$* and $K_{D,Fe2+-Mg}$ can be written as:

$$Fe^{3+}/Fe^{Total}(X, T, P, fO_2) = 1 - (K_D^*/ [K_{D,Fe2+-Mg}(X, T, P)]) \quad (5)$$

where (X,T,P) included to emphasize the fact that these quantities are dependent on composition *X*, as well as T and P, and for $Fe^{3+}/Fe^T$, explicitly on $fO_2$. If the $K_D^{ol/liq}{}_{,Fe2+-Mg}$ can be modeled accurately, it can be used in conjunction with a measurement of $K_D$* as a means to calculate the $Fe^{3+}$ contents of the glasses (Blundy et al. 2020). In the RKD experiments, the compositional dependence of the $K_{D,Fe2+-Mg}$ was parameterized by running experiments where $Fe^{2+} >> Fe^{3+}$ and measuring $K_D$*; in this limit, the value of $K_D$* approaches $K_{D,Fe2+-Mg}$ and only very minor corrections are required to calculate FeO in the liquid. Note that even under metal-saturated conditions there is still some $Fe^{3+}$

present in the liquid and so FeO* will always be greater than FeO (e.g., Bowen and Schraier 1935 showed that in olivine-saturated liquids coexisting with metal, 1.5 – 2.6% of the Fe is $Fe^{3+}$). All of the parameterizations of $Fe^{3+}/Fe^{2+}$ yield similar results, e.g. a few percent of Fe is $Fe^{3+}$ near IW. The RKD experiments thus represent a parameterization of the compositional dependence $K_D^{ol/liq}{}_{,Fe2+-Mg}$, which were designed to mitigate to the extent possible the effects of $Fe^{3+}$, thereby reducing the number of unknowns in equation (5).

### 5.4.1 Calculation of $Fe^{3+}/Fe^{Total}$ and $fO_2$ from $K_{D,Fe2+-Mg}$ and $K_D$*

An alternative approach for exploring the compositional dependence of the $K_{D,Fe2+-Mg}$ is to use experiments run over a range of $fO_2$ where the $Fe^{3+}/Fe^T$ contents of the glasses are known and FeO in the liquid can be calculated directly, and then monitor changes in the $K_{D,Fe2+-Mg}$ with changes in olivine and/or melt composition (including $Fe^{3+}$), T, and P. Using this method, Blundy et al. (2020) found that the $K_{D,Fe2+-Mg}$ could be parameterized as a function of olivine composition alone and that the liquid compositional terms (i.e., the $\left(\frac{\gamma_{FeO}}{\gamma_{MgO}}\right)^{liq}$ term in equation (1c)) could be approximated as a constant. The resulting functional form predicts that at constant T and $fO_2$, more forsteritic olivines result in lower values of $K_{D,Fe2+-Mg}$ and that the relationship between $Fe^{3+}/Fe^T$ and $K_D$* is linear, such that $K_D^* = K_{D,Fe2+-Mg}$ at $Fe^{3+} = 0$ and $K_D^* = 0$ at $Fe^{2+} = 0$ (i.e., equation 5). This model is described for basic liquids by equation (8) in Blundy et al. (2020). Given that their parameterization does not include the effects of variations in liquid composition and concomitant variations in $\left(\frac{\gamma_{FeO}}{\gamma_{MgO}}\right)^{liq}$ it cannot account for the well-documented effects of alkalis, $SiO_2$, and $TiO_2$ on the $K_{D,Fe2+-Mg}$. Similarly, although their model captures aspects of the variation in $K_{D,Fe2+-Mg}$ at values above ~0.30, because $X_{Fo}^{ol}$ and T are the only independent variables in their expression and the two values are

correlated (e.g., Fig. 2A), the Blundy et al. (2020) model does not permit values of $K_{D,Fe2+-Mg} \leq \sim 0.30$, which would be required to explain the variability in experiments run at low $fO_2$ (Fig. 12B). Blundy et al. (2020) attribute the misfit between their model and the large amount of data at low $fO_2$ that document $K_{D,Fe2+-Mg}$ (and $K_D$*) values <0.30 to poor calibration of available $Fe^{3+}/Fe^T$ models at low $Fe^{3+}$ contents (Borisov et al. 2018). However, as described above, at low $fO_2$ such corrections are small, and there are many experiments at low $fO_2$ with precisely determined $K_{D,Fe2+-Mg}$ that are <0.30 (as low as ~0.22, chondrite melting – Collinet & Grove 2020; and high-Ti lunar compositions – Dygert et al. 2020), which are unambiguously associated with high levels of alkalis, $SiO_2$, and $TiO_2$ in the liquid and cannot be dismissed. This was after all the motivation of the experiments presented here: experiments at low $fO_2$ compilation to provide an anchor for understanding the compositional dependence of $K_{D,Fe2+-Mg}$ that is uninfluenced by the effects of $Fe^{3+}$ or problems with its quantification. Any efforts aimed at understanding the behavior of $K_{D,Fe2+-Mg}$ under more oxidizing experiments must be able to account for and approach continuously the behavior at low $fO_2$.

Interactions between $Fe^{3+}$ and $Fe^{2+}$ in the liquid are not accounted for in Model 2: i.e., for simplicity, we assumed $B_{Fe3+}=0$ in our model and that there are no cross-terms involving $Fe^{3+}$. It has been variously argued that such interactions are important to describe $Fe^{3+}$-$Fe^{2+}$ equilibria in melts (e.g., Lange & Carmichael 1987; Kress & Carmichael 1988; Jayasuriya et al. 2004) or that they are unnecessary (Blundy et al. 2020) to describe olivine-liquid partitioning across the range of $fO_2$ that is experimentally accessible and petrologically important. Knowing which of the two scenarios is correct is crucial for any attempt to model Fe-Mg partitioning with olivine over a range of $fO_2$. If $Fe^{3+}$-$Fe^{2+}$ (and $Fe^{3+}$-$Mg^{2+}$) interactions are negligible, then Model 2 (or any alternative, as long as it assumes the equivalent of $B_{Fe3+}=0$) should be able to predict accurately the

$K_{D,Fe2+-Mg}$ for any given melt as a linear function of $Fe^{3+}/Fe^{Total}$. On the other hand, if there are non-zero interaction parameters involving $Fe^{3+}$, including with other cations in the melt which would appear as cross-terms in equation (3d), $K_{D,Fe2+-Mg}$ would change continuously with increasing $Fe^{3+}/Fe^{2+}$ (and $fO_2$).

Blundy et al. (2020) argue against $Fe^{3+}$-$Fe^{2+}$ interactions in the melt being important for olivine-liquid Fe-Mg exchange on the basis of (1) the "linearity" of 52 experiments with measurements of both $Fe^{3+}/Fe^{T}$ (0.04-0.80) and $K_D$* (0.055 - 0.322), where low $K_D$* values are due to high $Fe^{3+}$ in the experimental liquids, and (2) because the intercept of their best-fit line is in agreement with the "canonical 0.30±0.03 value of Roeder and Emslie (1970)", even though when looking in detail, the experiments run at low $fO_2$ with $Fe^{3+}/Fe^{T}$ < ~0.15 have $K_{D,Fe2+-Mg}$ that are systematically higher than the best-fit line, and when using their equation (8) the $K_{D,Fe2+-Mg}$ at the intercept $Fe^{3+}$=0 for the same experimental dataset is closer to 0.375 and not 0.30 (see their Figures 6a and 9a). The "linearity" of the relationship between $Fe^{3+}/Fe^{T}$ and $K_D$* would imply that, although $Fe^{3+}$-$Fe^{2+}$ interactions may exist in the melt, based on the available experimental data on olivine-liquid pairs it is not possible to discern deviations in the $K_{D,Fe2+-Mg}$ due to $Fe^{3+}$. A compelling argument for the presence of appreciable $Fe^{3+}$-$Fe^{2+}$ interactions comes from detailed studies on Fe redox equilibria based on experiments that did not contain olivine and for which $Fe^{3+}/Fe^{T}$ was measured either by wet chemistry (Lange & Carmichael 1987; Kress & Carmichael 1988) or by Mössbauser spectroscopy (Jayasuriya et al. 2004). A flaw in the various oxybarometers that relate $Fe^{3+}/Fe^{2+}$ in the liquid to $fO_2$ is that they do not have the expected relationship of $Fe^{3+}/Fe^{2+} \propto fO_2^{0.25}$ based on the stoichiometry the reaction:

$$FeO^{liq} + 0.25\ O_2 = FeO_{1.5}^{liq} \quad (6a)$$

When the proportionality constant is left as a free parameter and fit to experimental data it is always less than 0.25 (Sack et al. 1980; Kilinc et al. 1983; Borisov & Shapkin 1990; Kress & Carmichael 1991; Jayasuriya et al. 2004; Nikolaev et al. 1996; Borisov et al. 2018, note that O'Neill 2018 fixes the value to be 0.25). The thermodynamic relationship of $Fe^{3+}/Fe^{2+} \propto fO_2^{0.25}$ is in fact recovered when the experimental liquid compositions are expressed using a regular solution model analogous to that described in equation (3), requiring a strong $W_{Fe3+-Fe2+}$ interaction term (Jayasuriya et al. 2004) and/or possibly an additional Fe species with stoichiometry $FeO_{1.3}$ (Kress & Carmichael 1989, 1991). Because the empirical expressions (which do not obey the thermodynamic relationship) are found to fit the data as well as those that include an $Fe^{3+}$-$Fe^{2+}$ interaction term (Jayasuriya et al. 2004), they are typically used for petrological applications because they are computationally facile.

Although the low $fO_2$ experiments used to calibrate Model 2 cannot resolve the question of whether $Fe^{3+}$-$Fe^{2+}$ interactions in the melt play an important role in olivine-liquid equilibria, if they are not significant and we accept the parameterization of Model 2, then we should be able to accurately predict the $K_{D,Fe2+-Mg}$ for any composition at all $fO_2$ levels and in turn calculate the $Fe^{3+}/Fe^{Total}$ via equation 5. We followed this procedure using the relatively small number of experimental olivine-liquid pairs for which the $Fe^{3+}/Fe^{2+}$ was measured in the glasses, and where suitable compositional data was available to evaluate the $K_{D,Fe2+-Mg}$ (N=53; Ulmer 1989; Mysen and Dubinsky 2004; Kagi et al. 2005; Mysen 2006; Pichavant & Macdonald 2007; Matzen et al. 2011; Stamper et al. 2014; Melekhova et al. 2015; Melekhova et al. 2017; Blundy et al. 2020; Waters et al. 2020). These experiments were done using a variety of experimental techniques (i.e., gas-mixing furnaces, piston cylinder apparatuses (PC), and internally-heated pressure vessels (IHPV) – in Figure 13 experiments run in gas-mixing furnaces have circled symbols for

clarity), and the $Fe^{3+}/Fe^{2+}$ ratios were measured using a variety of analytical techniques, including wet chemistry, Mössbauser, and Fe micro x-ray near edge absorption spectroscopy. Experiments in PC and IHPV were run at pressures ranging from 2.4 to 13 kbar, but for this exercise neither the effects of pressure or $H_2O$ are considered, since both of which are expected to have only minor effects on the $K_{D,Fe2+-Mg}$ (Blundy et al. 2020). For each experiment, the $K_{D,Fe2+-Mg}$ was calculated using Model 2 based on the reported glass and olivine compositions and this value is compared in Figure 13A to value calculated from the measured $K_D$* for the experiment and the measured $Fe^{3+}/Fe^{Total}$ of the glass (equation 5). A related calculation using equation (5) gave a predicted value of $Fe^{3+}/Fe^{Total}$ for each experimental glass based on the value of $K_{D,Fe2+-Mg}$ generated by Model 2 – this is compared to the measured $Fe^{3+}/Fe^{Total}$ in Figure 13B. Note that errors in the $Fe^{3+}/Fe^{Total}$ measurements were not propagated into the calculation of $K_{D,Fe2+-Mg}$ on the x-axis of Figure 13A, however a typical error on $Fe^{3+}/Fe^{Total}$ of 0.01 absolute corresponds to an additional ±0.005 uncertainty on the measured $K_{D,Fe2+-Mg}$.

For the 1 atm gas-mixing furnace experiments only (N=35), the calculated $K_{D,Fe2+-Mg}$ has an average absolute deviation from the means of the measured values of 0.030 (Figure 13A) which is twice the a.a.d. when using Model to calculate $K_D$ for the low $fO_2$ literature experiments (0.015) (Figure 12A); including the higher pressure runs (n=18) produces an a.a.d. of 0.037. There are a few outlier points that have very low measured $K_{D,Fe2+-Mg}$; the outlier experiment from Mysen et al. 2004 (black triangle) has extremely high $K_2O$ (~11 wt% in the glass); the Waters et al. 2020 experiment MR13 (tan diamond) lost alkalis during the run (pers. comm. with L. Waters); the other two points were outliers flagged in Blundy et al. 2020 and do not have any obvious experimental or analytical problems. We note that a plot of the residuals $\Delta K_{D,Fe2+-Mg}$(measured – predicted) vs. $Fe^{3+}/Fe^{Total}$ are uncorrelated ($r^2 = 0.04$) which implies that

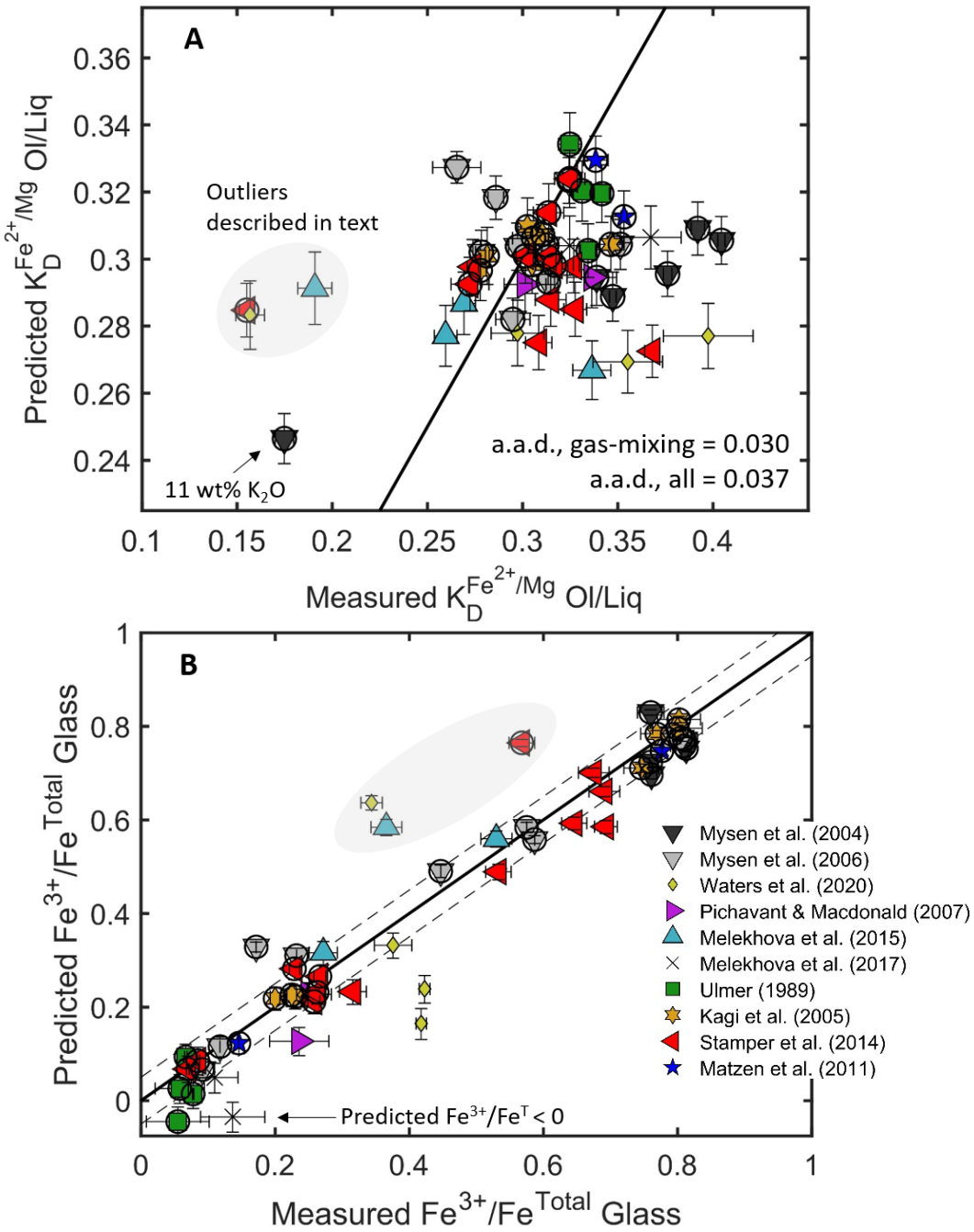


**Figure 13.** Measured vs. predicted values of **(A)** $K_D^{ol/liq},Fe^{2+}/Mg$ (Model 2) and **(B)** $Fe^{3+}/Fe^{Total}$ for the available experiments with coexisting olivine and liquid and measurements of the $Fe^{3+}/Fe^{2+}$ in the glasses. The predicted $Fe^{3+}/Fe^{Total}$ is calculated by 1 – ($K_D$*/ [$K_D$,$Fe^{2+}/Mg$]). Thick solid line is 1:1, dashed lines in **(B)** are offset from the 1:1 line by ±0.05 absolute. Circles indicate experiments run in gas-mixing furnaces at 1 bar.

based on these experimental data the effects of $Fe^{3+}$-$Fe^{2+}$ interactions on $K_{D,Fe2+-Mg}$ cannot be deduced and that introduction of a single $Fe^{3+}$ interaction term would not lead to an improvement of the fit of Model 2 to the oxidized data.

The accuracy of using equation (5) as a means to calculate $Fe^{3+}/Fe^{Total}$ solely from microprobe measurements of coexisting olivines and glasses can be evaluated in Figure 13B; the solid line is 1:1 and the dashed lines are offset ±0.05 absolute. For the gas-mixing furnace experiments, 27 of 35 have predicted $Fe^{3+}/Fe^{Total}$ that are within 0.05 of the measured values; the average absolute deviation for the 35 experiments is 0.04 and the average of positive and negative deviations is 0.002. Considering that typical XANES measurements have errors in $Fe^{3+}/Fe^{Total}$ on order 0.01-0.02 absolute, the fact that the Model 2 reproduces measured $Fe^{3+}/Fe^{Total}$ in glasses equilibrated at 1 atm to within 0.04-0.05 suggests that this could be a useful tool for reconnaissance measurements of $Fe^{3+}/Fe^{Total}$ in glasses, especially considering the relative ease in making the microprobe measurements. Note that there are two experiments that have negative predicted values for $Fe^{3+}/Fe^{Total}$, a consequence of the calculated $K_{D,Fe2+-Mg}$ being lower than the measured $K_D$*. Note that the same would happen when applying the Blundy et al. 2020 parameterization to those experiments with low measured $K_{D,Fe2+-Mg}$. This exercise shows that the $K_{D,Fe2+-Mg}$ predicted using Model 2 can successfully retrieve the fraction of Fe present as $Fe^{3+}$ in experimentally produced glasses to a precision of ~0.04-0.05 absolute, which is comparable to the precision cited based on the same approach in Blundy et al. (2020), however it should be applied with caution at low $fO_2$ levels where $Fe^{3+}/Fe^{Total} \lesssim$ 0.10. This is due to uncertainties in the measurement of $K_D$*, in the parameterization of Model 2, and in the Borisov et al. (2018) model, all of which can lead to large uncertainties at low $Fe^{3+}$ concentrations. This is shown quantitatively in Blundy et al. (2021) Figure 10 assuming 5% relative error in the $K_D$* (for the RKD experiments, the

relative error is closer to 1%) and an uncertainty of ±0.38 log units in $fO_2$ from applying the oxybarometer of Borisov et al. (2018).

The utility of using this approach as an oxybarometer can be further evaluated by using Borisov et al. (2018) to convert the calculated $Fe^{3+}/Fe^{Total}$ using Model 2 to $fO_2$ and then comparing that $fO_2$ to the imposed values in experiments. In theory application of the Fe oxybarometer should account for compositional effects on $Fe^{3+}/Fe^{Total}$ with Model 2 accounting for the independent compositional effects on the $K_{D,Fe2+-Mg}$. Figure 14A shows the results of this calculation on the 39 experiments shown in Figure 13 that report an experimental $fO_2$; these data include 1 atm gas-mixing experiments as well as IHPV experiments that report experimental $fO_2$ based on $H_2O$ dissociation (Pichavant & Macdonald 2007; Melekhova et al. 2017). The effect of pressure and of water was not considered for these experiments. Most of the experiments have calculated $fO_2$ that fall within ±1 log unit (dashed lines) of the reported experimental value; 22 of 39 calculated $fO_2$s are within ±0.5 log units which is comparable to the uncertainty in the Borisov et al. (2018) oxybarometer (0.38 log units in $fO_2$). Figure 14B shows a histogram of the deviation between the experimental and calculated $fO_2$ for a much larger set of 1 atm gas-mixing experiments with olivine-liquid pairs and precisely known $fO_2$; this compilation includes 112 unique studies and 1788 experiments, and an abbreviated bibliography is provided in Appendix A. The distribution is broad and skewed slightly towards underestimation of the $fO_2$, with a median $\Delta\log_{10}fO_2$[Experimental-Predicted] = -0.78 log units, and is considerably less accurate than for the subset of experiments shown in Figure 14. Despite the uncertainties in using this approach as an oxybarometer, considering that microprobe measurements of olivine and liquid are routine, this exercise shows that equation (5) can be potentially useful for reconnaissance estimations of $fO_2$ that otherwise require much more laborious and analytically challenging techniques

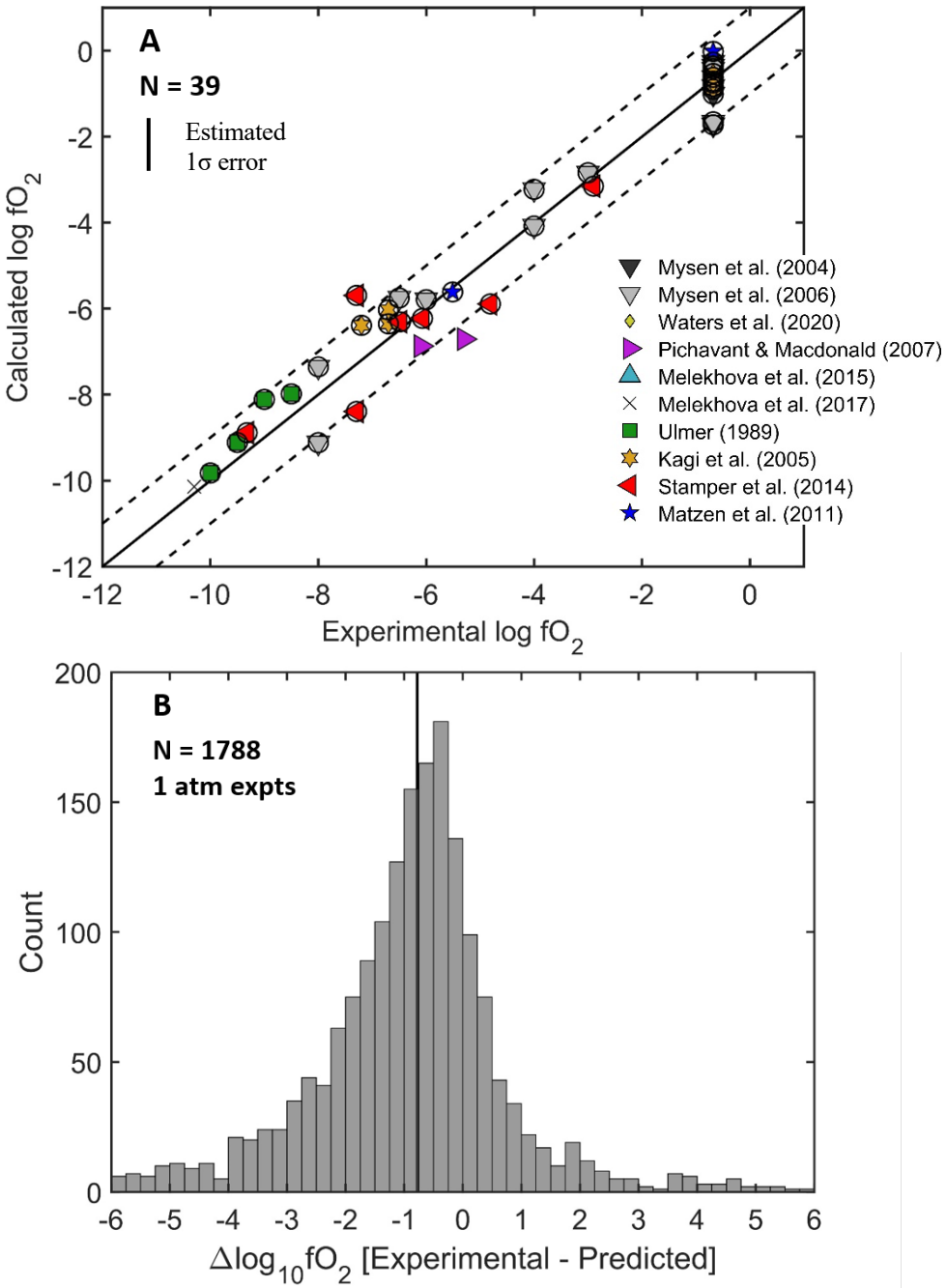


**Figure 14.** Estimation of $fO_2$ using the measured $K_D$* from literature experiments and the $K_{D,Fe2+-Mg}$ calculated using Model 2 to calculate $Fe^{3+}/Fe^{2+}$, and then using Borisov et al. (2018) to calculated $fO_2$ based on the calculated $Fe^{3+}/Fe^{2+}$ and the measured glass compositions from literature experiments. **(A)** Experimental vs. calculated $fO_2$ for the experiments shown in Figure 14 with known experimental $fO_2$. Solid line is 1:1 and dashed lines contour ±1 log unit. Black vertical line is the estimated 1σ error based on Borisov et al. (2018) and Model 2. Symbology is the same as in Figure 14. **(B)** Histogram showing the difference ($\Delta log_{10}fO_2$) between experimental and calculated values of $fO_2$ for a compilation of 1788 1-atm experiments with olivine-liquid pairs. The dark black line indicated the median of the distribution, -0.78. For a list of references in **(B)** see Appendix A.

(such as Fe micro X-ray absorption near edge spectroscopy techniques that require doubly-polished sections and access to a synchrotron beamline).

### 5.4.2 The Effects of $fO_2$ on the $K_{D,Fe2+-Mg}$

As shown by Model 2B, the expression for the composition-dependent $K_{D,Fe2+-Mg}$ can be expressed as a function of the liquid composition alone (i.e., without needing to specify $X_{Fo}$). This enables forward modeling of the indirect effect of $fO_2$ on $K_{D,Fe2+-Mg}$ through conversion of FeO to $Fe_2O_3$ in the liquid as oxygen is added to a system otherwise closed to mass transfer. Because the $K_{D,Fe2+-Mg}$ was parameterized with almost no $Fe^{3+}$ present, it can be used to illustrate differences between the expressions for $Fe^{3+}/Fe^{2+}$ in the melt when mapped onto the $K_D$ (Figure 15). The calculation was initialized using a value of $K_{D,Fe2+-Mg}$ based on representative measurements from the RKD experiments run at low $fO_2$ for each of the three synMORB bulk compositions, choosing a model of $Fe^{3+}/Fe^{2+}$ vs. $fO_2$ and melt composition, and then monitoring the changes in the $K_{D,Fe2+-Mg}$ based on Model 2B as $X_{FeO}^{liq}$ decreases (and $X_{Fe2O3}^{liq}$ increases) as $Fe^{2+}$ converts to $Fe^{3+}$ with increasing $fO_2$ at constant T, ignoring any interactions between $Fe^{3+}$-$Fe^{2+}$. This calculation is analogous to one that monitors changes in the stability of forsterite relative to fayalite with increasing $fO_2$ (e.g., Nitsan 1974), but there are many more parameterizations of the effect of $fO_2$ on Fe redox equilibria in the liquid, and these models have more compositional degrees of freedom. The calculation results are shown in Figure 15, where each colored curve corresponds to a different model of $Fe^{3+}/Fe^{2+}$ vs. $fO_2$ and melt composition. Recall that the three synMORB bulk compositions were designed to vary the FeO/MgO, while keeping the relative proportions of the other components constant, and so the different panels in Figure 16 reflect how changes in the bulk FeO/MgO are manifested in $K_{D.Fe2+-Mg}$ at constant T, as well as in the various parameterizations of the composition dependence of $Fe^{3+}/Fe^{2+}$. The $K_{D,Fe2+-Mg}$ values

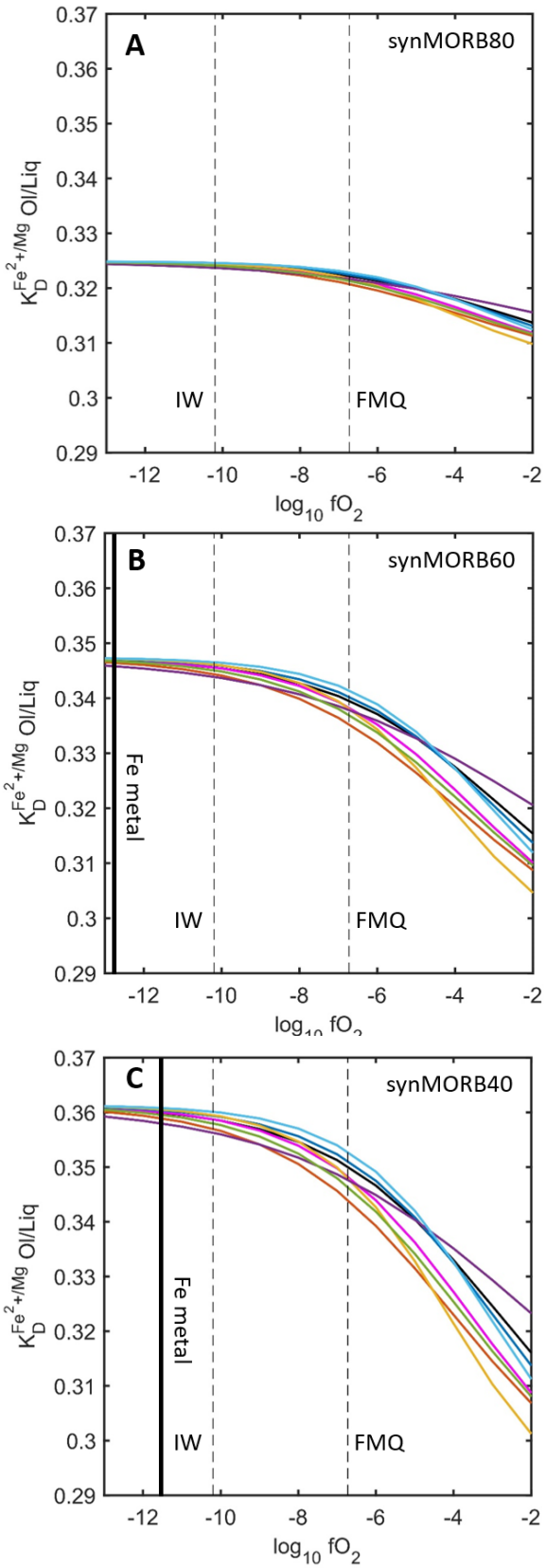


**Figure 15.** Calculation of $K_{D,Fe2+-Mg}$ as a function of $fO_2$ for three MORB compositions with different Mg#: (A) synMORB80, (B) synMORB60, (C) synMORB40. The calculation is initialized using a representative measurement of $K_{D,Fe2+-Mg}$ in low $fO_2$ experiments using each bulk composition. The $Fe^{3+}/Fe^{2+}$ was calculated for each glass composition as a function of $fO_2$ using eight available parameterizations (black – Kress & Carmichael 1991; pink – Kilinc et al. (1983); darker blue – Sack et al. 1980; dark orange – Jayasuriya et al. 2004; light orange – Borisov & Shapkin 1990; dark purple – Nikolaev et al. 1996; green – Borisov et al. 2018; light blue – O'Neill 2018). Equation (3e), which is Model 1 written only in terms of liquid composition, was used to calculate $K_{D,Fe2+-Mg}$ at a constant T = 1300 °C based on the calculated FeO, which is diluted by increasing $Fe_2O_3$ contents with increasing $fO_2$. The dashed vertical lines correspond to the $fO_2$ of the IW and FMQ reactions at 1300 °C; thick vertical lines in panels (B) and (C) indicate the calculated $fO_2$ of Fe metal saturation assuming pure Fe metal (for panel (A) this line plots just beyond the axis limits).

measured in the RKD experiments anchor the vertical position of each curve in the limit of low $fO_2$, with more FeO-rich bulk compositions having higher $K_{D,Fe2+-Mg}$.

Models of $Fe^{3+}/Fe^{2+}$ equilibria are based on the following expressions:

$$FeO^{liq} + 0.25\ O_2 = FeO_{1.5}^{liq} \quad (6a)$$

$$K_6 = \frac{a_{FeO_{1.5}}^{lia}}{a_{FeO}^{liq} \cdot fO_2^{1/4}} \quad (6b)$$

$$\ln\left(\frac{X_{FeO_{1.5}}^{lia}}{X_{FeO}^{liq}}\right) = \tfrac{1}{4} \ln fO_2 + K' \quad (6c)$$

where $a_i^{liq}$ and $X_i^{liq}$ refer to the activity and mole fraction, respectively, of component *i* in the liquid, $K_6$ is the equilibrium constant for equation 6a, and K' is a term that includes effects of temperature, pressure, and melt composition, which is attributed a functional form and then fitted to experimental data. Equation (6a) is written with the oxidized species on the right-hand side of the equation so that in equation (6c), in the limit of low $fO_2$ (metal saturation), $\ln\left(\frac{X_{FeO_{1.5}}^{lia}}{X_{FeO}^{liq}}\right)$ asymptotically approaches a minimum value that is close to zero, whereas in the limit of high $fO_2$ where $X_{FeO}^{liq} \rightarrow 0$, $\ln\left(\frac{X_{FeO_{1.5}}^{lia}}{X_{FeO}^{liq}}\right)$ is infinite (note that the $fO_2$ where $X_{FeO}^{liq}$ asymptotically approaches zero is much more oxidizing than most, if not all, natural magmatic conditions). A consequence of this construction is that the models converge in the limit of low $fO_2$, but because many of the fits to equation (6c) include the coefficient in front of $\ln fO_2$ as an adjustable parameter, and because the K' compositional terms are different, the models diverge from one another with increasing $fO_2$. This can be seen in Figure 15, which shows these expressions mapped onto the $K_{D,Fe2+-Mg}$; the model curves are tightly clustered at $fO_2$ < IW and define a wider band of uncertainty at higher $fO_2$. The effect of $fO_2$ on the $K_{D,Fe2+-Mg}$ is more pronounced in Fe-rich bulk compositions, e.g., $\Delta(Fe^{3+}/Fe^{2+}) / \Delta fO_2$ is larger for more Fe-rich bulk compositions and so the effect of FeO dilution by $Fe_2O_3$, which

drives the changes in the $K_{D,Fe2+-Mg}$ shown in Figure 15, is stronger. This leads to some interesting outcomes: the $K_{D,Fe2+-Mg}$ is relatively insensitive to changes in $fO_2$ between IW and FMQ for Mg-rich bulk compositions but can lead to changes of up to ~0.01 absolute (Jayasuriya et al. 2004) in Fe-rich compositions over this $fO_2$ range solely due to conversion of $Fe^{2+}$ to $Fe^{3+}$; at sufficiently high $fO_2$ some models predict that Fe-rich compositions will have a lower $K_{D,Fe2+-Mg}$ than in an Mg-rich composition at the same $fO_2$; and lastly, it emphasizes that despite the fact that most of the data that went into calibrating these expressions was based on experiments run at relatively oxidizing conditions, the models diverge at higher $fO_2$. This is also somewhat odd because wet chemical and XANES measurements of $Fe^{3+}/Fe^{2+}$ in glasses are more accurate when the concentrations of $Fe^{3+}$ are higher (Blundy et al. 2020), and yet despite better constraints on those oxidized data the models disagree more than at low $fO_2$. An attribute of using the equation (5) to calculate $Fe^{3+}/Fe^{2+}$ is that it bypasses any knowledge of the $Fe^{3+}/Fe^{2+}$ and allows for calculation of this value based on measurements of major elements in olivines and glasses; in the case of using Model 2, which requires knowledge of $X_{FeO}^{liq}$, the calculation for a glass with unknown $Fe^{3+}/Fe^{2+}$ would have to be done iteratively based on an initial guess of $X_{FeO}^{liq}$ and $X_{Fe2O3}^{liq}$. In summary, the $K_{D,Fe2+-Mg}$ is a function of $fO_2$ only indirectly through dilution of FeO by $Fe_2O_3$ in the liquid, and while this effect can be largely ignored for Mg-rich compositions between IW and FMQ, it is stronger for more Fe-rich bulk compositions and over a wide enough range, changes in $fO_2$ can have an indirect effect that is larger than the analytical uncertainty in $K_D$*.

## 6. Conclusions

1. A set of 1 atm Re wire loop experiments run at IW±0.5 and T = 1175-1400°C demonstrate that the $Fe^{2+}$-Mg olivine-liquid exchange coefficient, $K_{D,Fe^{2+}-Mg}^{ol/liq}$, systematically varies with bulk compositions which were designed

to span common terrestrial rock types – a picrite, a high-alumina basalt, and three MORBs with variable Fe/Mg ratio. The $K_{D,Fe2+-Mg}$ measured in the experiments ranges from 0.317±0.005 in a high-alumina basalt (with 1.35 wt% $Na_2O$ in the liquid) up to 0.358±0.004 in the most Fe-rich MORB bulk composition. The $K_{D,Fe2+-Mg}$ is higher in liquids with high $SiO_2$ and FeO.

2. Unpolluted by the effects of composition on the $Fe^{3+}/Fe^{Total}$, the new low $fO_2$ "RKD" experiments (N=14) were fit to a modified version of the regular solution model proposed by Toplis (2005) that relates $ln\ K_{D,Fe^{2+}-Mg}^{ol/liq}$ to T and olivine and melt composition by using three fitted parameters: two for the effect of $SiO_2$ and $Al_2O_3$ on the activity coefficients of FeO and MgO in the liquid ($B_{Si}$ and $B_{Al}$), and one for Fe-Mg mixing in the coexisting olivine ($W_{Fe\text{-}Mg}^{ol/liq}$). This model – Model 1 – produces an average absolute deviation in $K_{D,Fe^{2+}-Mg}^{ol/liq}$ for the RKD experiments of 0.0028, which is comparable to the analytical precision in $K_D$ based on propagated errors for measurements of MgO and FeO in both the olivine and the glasses.

3. A database of all existing experimental data on olivine-liquid pairs run at $fO_2 \leq$ IW+0.5 was compiled and each experiment tested for whether the bulk compositions and reported phase products passed mass balance, and other quality criteria including reporting stoichiometric olivines (N=178/305 passing experiments). These data, which spanned a much larger region compositional space than the RKD experiments, required two additional liquid compositional terms: $TiO_2$, and an $SiO_2$-($Na_2O$+$K_2O$) cross-term ($B_{Ti,}$ and $B_{Si\text{-}(Na+K)}$ – Model 2). This model produces an average absolute deviation of 0.014 in $K_{D,Fe^{2+}-Mg}^{ol/liq}$ between the modeled and measured values.

4. For both the RKD experiments (whose liquids had $SiO_2$ = 45-52 wt%, $TiO_2$ = 0.6-2.2 wt%, $Al_2O_3$ = 11-18 wt%, and $Na_2O+K_2O$ = 0.2-1.7 wt%) and the preferred low $fO_2$ literature experimental database ($SiO_2$ = 33.4-69.5 wt%, $TiO_2$ = 0-18.35 wt%, $Al_2O_3$ = 3.2-19.6 wt%, and $Na_2O+K_2O$ = 0-8.43 wt%), in order to accurately model the variability in $K_{D,Fe^{2+}-Mg}^{ol/liq}$ liquid compositional terms must be used. Models that seek to parameterize the composition dependence of $K_{D,Fe^{2+}-Mg}^{ol/liq}$ solely in terms of olivine composition are only valid over limited ranges in liquid composition. Given sufficient information on individual divalent cation partition coefficients between olivine and liquid (or sufficiently low concentrations of divalent cations in olivine other than Fe and Mg) that olivine composition can be expressed equivalently as the FeO* or MgO contents of the coexisting liquid. Therefore, it is possible to model the $K_{D,Fe^{2+}-Mg}^{ol/liq}$ only as a function of liquid composition, e.g., Model 2B.

5. An implication of Model 2B is that the $K_{D,Fe^{2+}-Mg}^{ol/liq}$ decreases with increasing is $fO_2$ due to the conversion of FeO to $Fe_2O_3$ in the liquid; this effect is larger in more Fe-rich bulk compositions.

## 7. References

Akella, J., Williams, R.J., & Mullins, O. (1976). Solubility of Cr, Ti, and Al, in co-existing olivine, spinel, and liquid at 1 atm. *Proc. Lunar Sci. Conf.*, 7, p.1179-1194

Albarède, F., & Provost, A. (1977). Petrological and geochemical mass-balance equations: an algorithm for least-square fitting and general error analysis. *Computers & Geosciences*, 3(2), p. 309-326

Armstrong, J.T. (1988). Quantitative analysis of silicate and oxide minerals: comparison of Monte Carlo, ZAF, and Φ(ρz) procedures. In: Newbury DE (editor) Microbeam analysis – 1988. San Francisco Press, San Francisco, p.239-246

Baker, M.B., Grove, T.L., & Kinzler, R.J. (1991). Origin of compositional zonation (high-alumina basalt to basaltic andesite) in the Giant Crater Lava Field, Medicine Lake Volcano, Northern California. *Journal of Geophysical Research*, 98(B13), p.21819-21842

Bartels, K.S., & Grove, T.L. (1991). High-pressure experiments on magnesian eucrite compositions: constraints on magmatic processes in the eucrite parent body. *Proc. Lunar Sci. Conf.*, 21, p.351-365

Batanova, V.G., Sobolev, A.V., & Kuzmin, D.V. (2015). Trace element analysis of olivine: high precision analytical method for JEOL JXA-8230 electron probe microanalyzer. *Chemical Geology*, 419, p.149-157

Beattie, P. (1993). Olivine-melt and orthopyroxene-melt equilibria. *Contributions to Mineralogy and Petrology*, 115, p.103-111

Beckett, J.R., & Mendybaev, R.A. (1997). The measurement of oxygen fugacities in flowing gas mixtures at temperatures below 1200°C. *Geochimica et Cosmochimica Acta*, 61(20), p.4331-4336

Bell, A.S., Váci, Z., & Lanzirotti, A. (2021) An experimental-XANES investigation of Cr valence systematics in basaltic liquids and applications to modeling $Cr^{2+}/\Sigma Cr$ evolution in crystallizing basaltic magma systems. *Geochimica et Cosmochimica Acta*, 292, p.130-151

Bickle, M.J. (1978). Melting experiments on peridotitic komatiites. *Progress in Experimental Petrology, NERC*, Editor: Mackenzie, W.S. In: Fourth progress report of research supported by N.E.R.C. 1975-1978, p.178-195

Blundy, J., Melekhova, E., Ziberna, L., Humphreys, M.C.S., Cerantola, V., Brooker, R.A., McCammon, C.A., Pichavant, M., & Ulmer, P. (2020). Effect of redox on Fe-Mg-Mn exchange between olivine and melt and an oxybarometer for basalts. *Contributions to Mineralogy and Petrology*. 175:103

Borisov, A.A., & Shapkin, A.I. (1989). New empiric equation equation of dependence of $Fe^{3+}/Fe^{2+}$ ratio in natural Melts on their composition, oxygen fugacity and temperature. *Geokhimiya*, 6, p.892-897

Borisov, A.A., & Jones, J.H. (1999). An evaluation of Re, as an alternative to Pt, for the 1 bar loop technique: an experimental study at 1400 °C. *American Mineralogist*, 84, p.1528-1534

Borisov, A.A. (2013). Mutual interaction of redox pairs in silicate melts: $V^{5+}/V^{4+}/V^{3+}/V^{2+}$ tetrad and other equilibria. *Petrology*, 21(4), p.305-315

Borisov, A.A., Behrens, H., & Holtz, F. (2018). Ferric/ferrous ratio in silicate melts: a new model for 1 atm data with special emphasis on the effects of melt composition. *Contributions to Mineralogy and Petrology*, 173:98

Bowen, N.L., & Schraier, J.F. (1935). The system MgO-FeO-$SiO_2$. *American Journal of Science*, s.5-29, 170, p.151-217

Castle, N., & Herd, C.D.K. (2017). Experimental petrology of the Tissint meteorite: redox estimates, crystallization curves, and evaluation of petrogenic models. *Meteoritics & Planetary Science*, 52(1), p.125-146

Collinet, M., & Grove, T.L. (2020). Widespread production of silica- and alkali-rich melts at the onset of planetisimal melting. *Geochimica et Cosmochimica Acta*, 277, p.334-357

Colson, R.O., McKay, G.A., & Taylor, L.A. (1989). Charge balancing of trivalent trace elements in olivine and low-Ca pyroxene: a test using experimental partitioning data. *Geochimica et Cosmochimica Acta,* 53(3), p.643-648

Davis, F.A., & Cottrell, E. (2018). Experimental investigation of basalt and peridotite oxybarometers: implications for spinel thermodynamic models and $Fe^{3+}$ compatibility during generation of upper mantle melts. *American Mineralogist*, 103(7), p.1056-1067

Danyushevsky, L.V., Sokolov, S., & Falloon, T.J. (2002b). Melt inclusions in olivine phenocrysts: using diffusive re-equilibration to determine the cooling history of a crystal, with implications for the origin of olivine-phyric volcanic rocks. *Journal of Petrology*, 43(9), p.1651-167

Delano, J.W. (1977). Experimental melting relations of 63545, 76015, 76055. *Proc. Lunar Sci Conf.*, 8, p.2097-2123

Delano, J.W. (1980). Chemistry and liquidus phase relations of Apollo 15 red glass: implications for the deep lunar interior. *Proc. Lunar Sci. Conf.*, 11, p.251-288

Dohmen, R., Becker, H-.W., & Chakraborty, S. (2007). Fe-Mg diffusion in olivine I: experimental determination between 700 and 1,200°C as a function of composition, crystal orientation and oxygen fugacity. *Physics and Chemistry of Minerals*, 34, p. 389-407

Donaldson, C.H., Usselman, T.M., Wililams, R.J., & Lofgren, G.E. (1975). Experimental modeling of the cooling history of Apollo 12 olivine basalts. *Proc. Lunar Sci Conf.,* 8, p.2097-2123

Donovan, J.J., & Tingle, T.N. (1996). An improved mean atomic number background correction for quantitative microanalysis. *Microscopy and Microanalysis*, 2(1), p.1-7

Dygert, N., Draper, D.S., Rapp, J.F., Lapen, T.J., Fagan, A.L., & Neal, C.R. (2020). Experimental determinations of trace element partitioning between plagioclase, pigeonite, olivine, and lunar basaltic melts and an $fO_2$ dependent model for plagioclase-melt Eu partitioning. *Geochimica et Cosmochimica Acta*, 729, p.258-280

Ehlers, K., Grove, T.L., Sisson, T.W., Recca, S.I., & Zervas, D.A. (1992). The effect of oxygen fugacity on the partitioning of nickel and cobalt between olivine, silicate melt, and metal. *Geochimica et Cosmochimica Acta*, 56(10), p.3733-3743

Elardo, S.M., Shearer, C.K., Vander Kaaden, K.E., McCubbin, F.M., & Bell, A.S. (2015). Petrogenesis of primitive and evolved basalts in a cooling Moon: experimental constraints from the youngest known lunar magmas. *Earth and Planetary Science Letters*, 422, p.126-137

Filiberto, J., & Dasgupta, R. (2011). $Fe^{2+}$-Mg partitioning between olivine and basaltic melts: applications to genesis of olivine-phyric shergottites and conditions of melting in the Martian interior. *Earth and Planetary Science Letters*, 304(3-4), p.527-537

Ford, C.E., Russell, D.G., Craven, J.A., & Fisk, M.R. (1983). Olivine-liquid equilibria: temperature, pressure, and composition dependence of the crystal/liquid cation partition coefficients for Mg, $Fe^{2+}$, Ca and Mn. *Journal of Petrology*, 24(3), p.256-266

Gale, A., Dalton, C.A., Langmuir, C.H., Su, Y., & Schilling, J.-G. (2013). The mean composition of ocean ridge basalts. *Geochemistry, Geophysics, Geosystems*, 14(3), p.489-518

Gale, A., Langmuir, C.H., & Dalton, C.A. (2014). The global systematics of ocean ridge basalts and their origin. *Journal of Petrology*, 55(6), p.1051-1082

Gee, L.L., & Sack, R.O. (1988). Experimental petrology of melilite nephelinites. *Journal of Petrology*, 29(6), p.1233-1255

Ghiorso, M.S., & Kress, V.C. (2004). An equation of state for silicate melts. II. Calibration of volumetric properties at $10^5$ Pa. *American Journal of Science*, 304(8-9), p.679-751

Ghiorso, M.S., Carmichael, I.S.E., Rivers, M.L., & Sack, R.O. (1983). The Gibbs free energy of mixing of natural silicate liquids; an expanded regular solution approximation for the calculation of magmatic intensive variables. *Contributions to Mineralogy and Petrology*, 84, p.107-145

Ghiorso, M.S., & Sack, R.O. (1995). Chemical mass transfer in magmatic processes IV. A revised and internally consistent thermodynamic model for the interpolation and extrapolation of liquid-solid equilibria in magmatic systems at elevated temperatures and pressures. *Contributions to Mineralogy and Petrology*, 119., p.197-212

Grove, T.L., & Beaty, D.W. (1980). Classification, experimental petrology and possible volcanic histories of the Apollo 11 high-K basalts. *Proc. Lunar. Sci. Conf.*, 11, p.149-177

Grove, T.L., & Juster, T.C. (1989) Experimental investigation of low-Ca pyroxene stability and olivine-pyroxene-liquid equilibria at 1-atm in natural basaltic and andesitic liquids. *Contributions to Mineralogy and Petrology*, 103, p.287-305

Grove, T.L., & Vaniman, D.T. (1978). Experimental petrology of very low Ti (VLT) basalts. *Mare Crisium: The View from Luna 24*, Ed: Merrill, R.B., Papike, J.J., others. Pergamon Press (New York), p.445-471

Grove, T.L. (1981). Use of FePt alloys to eliminate the iron loss problem in 1 atmosphere gas mixing experiments: theoretical and practical considerations. *Contributions to Mineralogy and Petrology*, 78, p.298-304

Guo, C., & Zhang, Y. (2018). Multicomponent diffusion in basaltic melts at 1350 °C. *Geochimica et Cosmochimica Acta*, 228, p.190-204

Hanson, B., & Jones, J.H. (1998). The systematics of $Cr^{3+}$ and $Cr^{2+}$ partitioning between olivine and liquid in the presence of spinel. *American Mineralogist*, 83, p.669-6846

Herd, C.D.K., Borg, L.E., Jones, J.H., & Papike, J.J. (2002). Oxygen fugacity and geochemical variations in the martian basalts: implications for martian basalt petrogenesis and the oxidation state of the upper mantle of Mars. *Geochimica et Cosmochimica Acts*, 66(11), p.2025-2035

Herzberg, C., & O'Hara, M.J. (2002). Plume-associated ultramafic magmas of Phanerozoic age. *Journal of Petrology*, 43(10), p.1857-1883

Houlier, B., Cheraghmakani, M., & Jaoul, O. (1990). Silicon diffusion in San Carlos olivine. *Physics of the Earth and Planetary Interiors*, 62(3-4), p.329-340

Hirschmann, M.M., Baker, M.B., & Stolper, E.M. (1998). The effect of alkalis on the silica content of mantle-derived melts. *Geochimica et Cosmochimica Acta*, 62(5), p.883-902

Huebner, J.M. & Sato, M. (1970). The oxygen fugacity-temperature relationships of manganese oxide and nickel oxide buffers. *American Mineralogist*, 55, p.934-952

Huebner, J.S. (1971). Buffering techniques for hydrostatic systems at elevated pressures. *Research Techniques for High Pressure and High Temperature*, Ed: Ulmer, G.C., Springer, Berlin, Heidelberg, p. 123-177

Huebner, J.S., Lipin, B.R., & Wiggins, L.B. (1976). Partitioning of chromium between silicate crystals and melts. *Proc. Lunar Sci. Conf.*, 7, p.1195-1220

Irving, A.J., Merrill, R.B., & Singleton, D.E. (1978). Experimental partitioning of rare earth elements and scandium among armalcolite, ilmenite, olivine, and mare basalt liquid. *Proc. Lunar Sci Conf.,* 9, p.601-612

Jarosewich, E., Nelen, J.A., & Norberg, J.A. (1979). Electron microprobe reference samples for mineral analyses. *Smithsonian Contributions to the Earth Sciences, Mineral Sciences Investigations 1976-1977*, 22, p.68-73

Jayasuriya, K.D., O'Neill, H.S.C., Berry A.J., & Campbell, S.J. (2004). A Mössbauer study of the oxidation state of Fe in silicate melts. *American Mineralogist*, 89(11-12), p.1597-1609

Jochum, K.P., Stoll, B., Herwig, K., Wilbold, M., Hofmann, A.W., & Amini, M., et al. (2006). MPI-DING reference glasses for in situ microanalysis: New reference values for element concentrations and isotope ratios. *Geochemistry Geophysics Geosystems*, 7(2), p.1-44

Johnston, W.D. (1964). Oxidation-reduction equilibria in iron-containing glasses. *Journal of the American Ceramic Society*, 47(4), p.198-201

Jurewicz, A.J.G., & Watson, E.B. (1988). Cations in olivine, Part 2: Diffusion in olivine xenocrysts, with applications to petrology and mineral physics. *Contributions to Mineralogy and Petrology*, 99, p.186-201

Jurewicz, A.J.G., Mittlefehldt, D.W., & Jones, J.H. (1993). Experimental partial melting of the Allende (CV) and Murchison (CM) chondrites and the origin of asteroidal basalts. *Geochimica et Cosmochimica Acta*, 57(9), p.2123-2139

Jurewicz, A.J.G., Mittlefehldt, D.W., & Jones, J.H. (1995). Experimental partial melting of the St. Severin (LL) and Lost City (H) chondrites. *Geochimica et Cosmochimica Acta*, 59(2), p.391-408

Kadik, A.A., Biggar, G.M., Lukanin, O.A., & Dmitriev, L.V. (1982). An experimental study of the crystallization of Atlantic tholeiites at a given oxygen fugacity. *Geokhimiya*, 10, p.1390-1414

Kanaya, K., & Okayama, S. (1972). Penetration and energy-loss theory of electrons in solid targets. *Journal of Physics D: Applied Phyiscs*, 5(1),

Kessel, R., Beckett, J.R., & Stolper, E.M. (2001). Thermodynamic properties of the Pt-Fe system. *American Mineralogist*, 86(9), p.1003-1014

Kilinc, A., Carmichael, I.S.E., Rivers, M.L., & Sack, R.O. (1983). The ferric-ferrous ratio of natural silicate liquids equilibrated in air. *Contributions to Mineralogy and Petrology*, 84, p.136-140

Kress, V.C., & Carmichael, I.S.E. (1988). Stoichiometry of the iron oxidation reaction in silicate melts. *American Mineralogist*, 73(11-12), p.1267-1274

Kress, V.C., & Carmichael, I.S.E. (1991). The compressibility of silicate liquids containing Fe2O3 and the effect of composition, temperature, oxygen fugacity and pressure on their redox states. *Contributions to Mineralogy and Petrology*, 108, p.82-92

Kushiro, I. (1975). On the nature of silicate melt and its significance in magma genesis: regularities in the shift of the liquidus boundaries involving olivine, pyroxene, and silica minerals. *American Journal of Science*, 275, p.411-431

Kushiro, I., & Walter, M.J. (1998). Mg-Fe partitioning between olivine and mafic-ultramafic melts. *Geophysical Research Letters*, 25(13), p.2337-2340

Kushiro, I., & Mysen, B.O. (2002). A possible effect of melt structure on the Mg-$Fe^{2+}$ partitioning between olivine and melt. *Geochimica et Cosmochimica Acta*, 66(12), p.2267-2272

Lange, R.A., & Carmichael, I.S.E. (1987). Densities of $Na_2O$-$K_2O$-CaO-MgO-FeO-$Fe_2O_3$-$Al_2O_3$-$TiO_2$-$SiO_2$ liquids: new measurements and derived partial molar properties. *Geochimica et Cosmochimica Acta*, 51, p.2931-2946

Le Maitre, R.W. (1976). The chemical variability of some common igneous rocks. *Journal of Petrology*, 17(4), p.589-598

Longhi, J., Walker, D., & Hays, J.F. (1976). Fe and Mg in plagioclase. *Proc. Lunar Sci. Conf.,* 7, p.1281-1300

Longhi, J., Walker, D., & Hays, J.F. (1978). The distribution of Fe and Mg between olivine and lunar basaltic liquids. *Geochimica et Cosmochimica Acta*, 42(10), p.1545-1558

Longhi, J., & Pan, V. (1988). A reconnaissance study of phase boundaries in low-alkali basaltic liquids. *Journal of Petrology*, 29(1), p.115-147

Matzen, A.K., Baker, M.B., Beckett, J.R., & Stolper, E.M. (2011). Fe-Mg partitioning between olivine and high-magnesian melts and the nature of Hawaiian parental liquids. *Journal of Petrology*, 52(7:8), p.1243-1263

McKay, G.A., & Weill, D.F (1977). KREEP petrogenesis revisited. *Proc. Lunar Sci Conf.,* 8, p.2339-2355

Melekhova, E., Blundy, J., Robertson, R., & Humphreys, M.C.S. (2015). Experimental evidence for polybaric differentiation of primitive arc basalt beneath St. Vincent, Lesser Antilles. *Journal of Petrology*, 56(1), p.161-192

Melekhova, E., Blundy, J., Martin, R., Arculus, R., & Pichavant, M. (2017). Petrological and experimental evidence for differentiation of water-rich magmas

beneath St. Kitts, Lesser Antilles. *Contributions to Mineralogy and Petrology*, 172:98

Merrill, R.B., & Williams, R.J. (1975). The system anorthite-forsterite-fayalite-silica to 2 kbar with lunar petrologic applications. *Proc. Lunae Sci Conf,* 6, p.959-971

Mill, R.D., & Glazner, A.F. (2013). Experimental study on the effects of temperature cycling on coarsening of plagioclase and olivine in an alkali basalt. *Contributions to Mineralogy and Petrology*, 166, p.97-111

Murck, B.W., & Campbell, I.H. (1986). The effects of temperature, oxygen fugacity and melt composition on the behavior of chromium in basic and ultrabasic melts. *Geochimica et Cosmochimica Acta*, 50(9), p.1871-1887

Mysen, B.O., Virgo, D., & Seifert, F.A. (1982). The structure of silicate melts: implications for chemical and physical properties of natural magma. *Review of Geophysics*, 20(3), p.353-383

Mysen, B.O., & Dubinsky, E.V. (2004). Melt structural control on olivine/melt element partitioning of Ca and Mn. *Geochimica et Cosmochimica Acta*, 68(7), p.1617-1633

Mysen, B.O., & Shang, J. (2005). Evidence from olivine/melt element partitioning that nonbridging oxygen in silicate melts are not equivalent. *Geochimica et Cosmochimica Acta*, 69(11), p.2861-2876

Mysen, B.O. (2006). Redox equilibria of iron and silicate melt structure: implications for olivine/melts element partitioning. *Geochimica et Cosmochimica Acta*, 70(12), p.3121-3138

Nielsen, R.L., Davidson, P.M., & Grove, T.L. (1988). Pyroxene-melt equilibria: an updated model. *Contributions to Mineralogy and Petrology*, 100, p.361-373

Nikolaev, G.S., Borisov, A.A., Ariskin A.A. (1996). Calculation of the ferric-ferrous ratio in magmatic melts: testing and additional calibration of empirical equations for various magmatic series. *Geochemistry International*, 34(8), p.641-649

Nitsan, U. (1974). Stability field of olivine with respect to oxidation and reduction. *Journal of Geophysical Research*, 79(5), p.706-711

O'Neill, H.S.C., Pownceby, M.I., & McCammon, C.A. (2003). The magnesiowüstite iron equilibrium and its implications for the activity-composition relations of $(Mg,Fe)_2SiO_4$ olivine solid solutions. *Contributions to Mineralogy and Petrology*, 146, p.308-325

O'Neill, H.S.C., Berry, A.J., & Mallmann, G. (2018). The oxidation state of iron in Mid-Ocean Ridge Basaltic (MORB) glasses: implications for their petrogenesis and oxygen fugacties. *Earth and Planetary Science Letters*, 504, p.152-162

Partzsch, G.M., Lattard, D., & McCammon, C. (2004). Mössbauer spectroscopic determination of $Fe^{3+}/Fe^{2+}$ in synthetic basaltic glass: a test of empirical $fO_2$ equations under superliquidus and subliquidus conditions. *Contributions to Mineralogy and Petrology*, 147, p.565-580

Pichavant, M., & MacDonald, R. (2007). Crytallization of primitive basaltic magmas at crustal pressures and genesis of the calc-alkaline igneous suite: experimental evidence from St. Vincent, Lesser Antilles arc. *Contributions to Mineralogy and Petrology*, 154, p.535-558

Prissell, K.B., Krawczynski, M.J., Nie, N.X., Dauphas, N., Couvy, H., Hu, M.Y., Alp, E.E., & Roskosz, M. (2018). Experimentally determined effects of olivine crystallization and melt titantium content on iron isotopic fractionation in planetary basalts. *Geochimica et Cosmochimica Acta*, 238, p. 580-598

Putirka, K. (2016). Rates and styles of planetary cooling on Earth, Moon, Mars, and Vesta, using new models for oxygen fugacity, ferric-ferrous ratios, olivine-liquid Fe-Mg exchange, and mantle potential temperature. *American Mineralogist*, 101, p.819-840

Rhodes, J.M., Dungan, M.A., Blanchard, D.P., & Long, P.E. (1979). Magma mixing at mid-ocean ridges: evidence from basalts drilled near 22°N on the mid-Atlantic ridge. *Tectonophysics*, 55(1-2), p.35-61

Robie, R.A., Hemingway, B.S., & Fisher, J.R. (1979). Thermodynamic properties of minerals and related substances at 298.15K and 1 bar ($10^5$ pascals) pressure and at higher temperatures. *U.S. Geological Survey Bulletin*, 1452

Roeder, P.L., & Emslie, R.F. (1970). Olivine-liquid equilibrium. *Contributions to Mineralogy and Petrology*, 29, p.275-289

Ryerson, F.J. (1985). Oxide solution mechanisms in silicate melts: systematic variations in the activity coefficient of $SiO_2$. *Geochimica et Cosmochimica Acta*, 49(3), p.637-649

Sack, R.O., Carmichael, I.S.E., Rivers, M., & Ghiorso, M.S. (1980). Ferric-ferrous equilibria in natural silicate liquids at 1 bar. *Contributions to Mineralogy and Petrology*, 75, p.369-376

Sack, R.O., Walker, D., Carmichael, I.S.E. (1987). Experimental petrology of alkali lavas: constraints on cotectics of multiple saturation in natural basaltic liquids. *Contribution to Mineralogy and Petrology*, 96, p.1-23

Salvat, F., Fernández-Varea, J.M., & Sempau, J. (2006). PENELOPE-2006: A code system for Monte Carlo simularion of electron and photon transport. *Nuclear Energy Agency Organization for Economic Co-operation and Development*

Saper, L.M., & Stolper, E.M. (2020). Controlled cooling-rate experiments on olivine-hosted melt inclusions: chemical diffusion and quantification of eruptive cooling rates on Hawai‘i and Mars. *Geochemistry, Geophysics, Geosystems*, 21(2)

Sato, H. (1989). Mg-Fe partitioning between plagioclase and liquid in basalts of hole 504B, ODP leg 111: a study of melting at 1 atm. *Proc. Ocean Drilling Program, Scientific Results*, 111, p.17-26

Scott, V.D., & Love., G. (1983). Quantitative electron-probe microanalysis. Wiley, New York.

Shi, P. (1993). Low-pressure phase relationships in the system $Na_2O$-CaO-FeO-MgO-$Al_2O_3$-$SiO_2$ at 1100°C, with implications for the differentiation of basaltic magmas. *Journal of Petrology*, 34(4), p.743-762

Singletary, S.J., & Grove, T.L. (2003). Early petrologic processes on the ureilite parent body. *Meteoritics & Planetary Science*, 38(1), p.95-108

Singletary, S.J., & Grove, T.L. (2006). Experimental constraints on ureilite petrogenesi. Geochimica et Cosmichimica Acta, 70(5), p.1291-1308

Snyder, D.A., & Carmichael, I.S.E. (1992). Olivine-liquid equilibria and the chemical activities of FeO, NiO, $Fe_2O_3$, and MgO in natural basic melts. *Geochimica et Cosmochimica Acta*, 56(1), p.303-318

Snyder, D.A., Carmichael, I.S.E., & Wiebe, R.A. (1993). Experimental study of liquid evolution in an Fe-rich layered mafic intrusion: constraints of Fe-Ti oxide precipitation on the T-$fO_2$ and T-ρ paths of tholeiitic magmas. *Contributions to Mineralogy and Petrology*, 113, p.73-86

Sossi, P.A., & Fegley, Jr., B. (2018). Thermodynamics of element volatility and its application to planetary processes. *Reviews in Mineralogy & Geochemistry*, 84, p.393-459

Spandler, C., & O'Neill, H.S.C. (2010). Diffusion and partition coefficients of minor and trace elements in San Carlos olivine at 1,300°C with some geochemical implications. *Contributions to Mineralogy and Petrology*, 159, p.791-818

Sobolev, A.V., & Nikogosian, I.K. (1994). Petrology of long-lived mantle plume magmatism: Hawai'i, Pacific, and Reunion Island, Indian Ocean. *Petrology*, 2(2), p.111-144

Stamper, C.C., Melekhova, E., Blundy, J.D., Arculus, R.J., Humphreys, M.C.S., & Brooker, R.A. (2014). Oxidised phase relations of a primitive basalt from Grenada, Lesser Antilles. *Contributions to Mineralogy and Petrology*, 167, p.953-954

Stolper, E.M. (1977). Experimental petrology of eucritic meteorites. *Geochimica et Cosmochimica Acta*, 41(5), p.587-611

Sugawara, T. (2000). Empirical relationships between temperature, pressure, and MgO content in olivine and pyroxene saturated liquid. *Journal of Geophysical Research: Solid Earth*, 105(B4), p.8457-8472

Takahashi, E., & Irvine, T.N. (1981). Stoichiometric control of crystal/liquid single-component partition coefficients. *Geochimica et Cosmochimica Acta*, 45(7), p.1181-1185

Tollan, P.M.E., O'Neill, H.S.C., & Hermann, J. (2018). The role of trace elements in controlling H incorporation in San Carlos olivine. *Contributions to Mineralogy and Petrology*, 173(89)

Toplis, M.J. (2005). The thermodynamics of iron and magnesium partitioning between olivine and liquid: criteria for assessing and predicting equilibrium in natural and experimental systems. *Contributions to Mineralogy and Petrology*, 149, p.22-39

Tsuchiyama, A., Nagahara, H., & Kushiro I. (1981). Volatilization of sodium from silicate melt spheres and its application to the formation of chondrules. *Geochimica et Cosmichimica Acta*, 45, p.1357-1367

Tuff, J., & O'Neill, H.S.C. (2010). The effect of sulfur on the partitioning of Ni and other first-row transition elements between olivine and silicate melt. *Geochimica et Cosmochimica Acta*, 74(21), p.6180-6205

Ulmer, P. (1989). The dependence of the $Fe^{2+}$-Mg cation-partitioning between olivine and basaltic liquid on pressure, temperature and composition. *Contributions to Mineralogy and Petrology*, 01, p.261-273

Usui, T., Jones, J.H., & Mittlefehldt, D.W. (2015). A partial melting study of an ordinary (H) chondrite composition with application to the unique achondrite Graves Nunataks 06128 and 06129. *Meteoritics & Planetary Science*, 50(4), p.759-781

Wadhwa, M. (2008). Redox conditions on small bodies, the moon and Mars. *Reviews in Mineralogy & Geochemistry*, 68, p.493-510

Walker, D., & Grove, T.L. (1993). Ureilite smelting. *Meteoritics*, 28(5), p.629-636

Walker, D., Kirkpatrick, R.J., Longhi, J., & Hays, J.F. (1976). Crystallization history of lunar picritic basalt sample 12002: phase-equilibria and cooling-rate studies. *Geological Society of America Bulletin*, 87, p.646-656

Walker, D., Longhi, J., Lasaga, A.C., Stolper, E.M., Grove, T.L., & Hays, J.F. (1977). Slowly cooled microgabbros 15555 and 15065. *Proc. Lunar Sci. Conf.*, 8, p.1521-1547

Wasylenki, L.E., Baker, M.B., Kent, A.J.R., & Stolper, E.M. (2003). Near-solidus melting of the shallow uppe rmantle: partial melting experiments on depleted peridotite. *Journal of Petrology*, 44(7), p.1163-1191

Waters, L.E., Cottrell, E., Coombs, M.L., & Kelley, K.A. (2020). Generation of calc-alkaline magmas during crystallization at high oxygen fugacity: an experimental and petrologic study of tephras from Buldir Volcano, Western Aleutian Arc, Alaska, USA. *Journal of Petrology*, 62(3)

Watson, E.B. (1977). Partitioning of manganese between forsterite and silicate liquid. *Geochimica et Cosmochimica Acta*, 41, p.1363-1374

Watson, E.B. (1982). Basalt contamination by continental crust: some experiments and models. *Contributions to Mineralogy and Petrology*, 80(1), p.70-87, https://doi.org/10.1007/BF00376736

Wiser, N.M., & Wood, B.J. (1991). Experimental determination of activities in Fe-Mg olivine at 1400 K. *Contributions to Mineralogy and Petrology*, 108, p.146-153

## 8. Appendix A: Abbreviated bibliography of references used in Figure 14B

1 Agee & Walker (1990) CMP 105, 243-254
2 Akella et al. (1976) PLSC 7th 1179-1194
3 Arndt, NT (1977) CIWYB 76, 553-557
4 Auwera & Longhi (1994) CMP 118, 60-78
5 Baker & Eggler (1987) Am Mineral 72, 12-28
6 Baker et al. (1994) CMP 118, 111-129
7 Baker, DR & Eggler, DH (1983) JVGR 18, 387-404
8 Bartels & Furman (2002) Am Mineral 87, 217-226
9 Bartels & Grove (1991) PLPSC 21, 351-365
10 Bartels et al. (1991) CMP 108, 253-270
11 Bickle (1978) Prog. in Exp. Petrol. 4th, 187-195
12 Biggar, GM et al. (1971) Proc 2nd LPSC 1, 617-643
13 Borisov, A et al. (2008) GCA 72, 5558-5573
14 Brenan et al. (2003) EPSL 212, 135-150
15 Brenan et al. (2005) EPSL 237, 855-872
16 Brophy (1995) PODP, Sci Results 142, 41-49
17 Campbell et al (1979) Canad. Mineral. 17, 495-505
18 Canil (1999) GCA 63, 557-572
19 Canil, D & Bellis, AJ (2008) Lithos105, 111-117
20 Canil, D & Fedortchouk, Y (2001) Can Min 39, 319-330
21 Castle & Herd (2017) M&PS 52, 125-146
22 Davis & Cottrell (2018) Am. Min., 103, 1056-1067
23 Di Stefano et al. (2018) Lithos 316-317, 104-121
24 Donaldson et al. (1975) PLSC 6th, 843-869
25 Draper & Johnston (1992) CMP 112, 501-519
26 Dunn & Sen (1994) GCA 58, 717-733

27 Dunn & Stringer (1990) CMP 105, 55-65
28 Ehlers et al (1992) GCA 56, 3733-3743
29 Elardo et al. (2015) EPSL 422, 126-137
30 Ford et al. (1983) J Pet 24, 256-265
31 Gaetani & Grove (1998) GCA 61, 1829-1846
32 Gaetani et al. (1994) Proc. ODPSR 135, 557-563
33 Gardner-Vandy, KG et al. (2013) GCA 122, 36-57
34 Gee & Sack (1988) J. Pet. 29, 1233-1255
35 Gerke et al. (2005) CMP 148, 735-745
36 Grove & Bryan (1983) CMP 84, 293-309
37 Grove (1981) CMP 78, 298-304
38 Grove et al. (1982) CMP 80, 160-182
39 Grove et al. (1990) Proc. ODP Sci. Results 106/109, 9-17
40 Grove et al. (2003) CMP 145, 515-533
41 Grove, TL & Juster, TC (1989) CMP 103, 287-305
42 Hanson, B and Jones, JH (1998) Am Mineral 83, 669-684
43 Henao HM et al (2010) Met Mat Trans 41B, 767-779
44 Herd et al. (2002) Meteoritics Planet Sci 37, 987-1000
45 Herd, CDK et al. (2009) Am Mineral 94, 244-255
46 Huebner et al. (1976) PLSC 7th, 1195-1220
47 Irving et al. (1978) PLPSC 9th, 601-612
48 Johnston & Draper (1992) JVGR 52, 27-41
49 Jurewicz & Watson (1988) CMP 99, 176-185
50 Jurewicz et al. (1993) GCA 57, 2123-2139
51 Jurewicz et al. (1995) GCA 59, 391-408
52 Juster et al. (1989) JGR 94, 9251-9274
53 Kadik et al. (1982) Geochem Int 19 no. 5, 104-127
54 Kennedy et al. (1990) CMP 104, 722-734
55 Kilinc et al. (1983) CMP 83, 136-140
56 Kinzler & Grove (1985) Am Min 70, 40-51
57 Kinzler et al. (1990) GCA 54, 1255-1265
58 Kohut & Nielsen (2003) GGG 4, 1057, doi:10.1029/2002GC000451
59 Leeman (1974) Thesis
60 Leitzke, F.P. et al. (2017) EPSL 474, 503-515
61 Longhi & Pan (1988) J Pet 29, 115-147
62 Longhi & Pan (1989) Proc. LPSC 19th, 451-464
63 Mallmann, G & O'Neill HStC (2009) JPet 50, 1765-1794
64 Mallmann, G & O'Neill, HStC (2013) JPet 54, 933-949
65 Matzen et al. (2011), JPet, 52, 1243-1263
66 McKay & Weill (1977) PLPSC 8th 2339-2355
67 Médard, E & Grove, TL (2008) CMP 155, 417-432
68 Meen (1987) CMP 97, 333-351
69 Meen (1990) CMP 104, 309-331
70 Merrill & Williams (1975) PLSC 6th, 959-971
71 Monders, AG et al. (2007) Meteoritics & Planet Sci 42, 131-148
72 Montierth et al. (1995) In AGU Monograph 92, 207-217
73 Murck & Campbell (1986) GCA 50, 1871-1887
74 Mysen & Dubinsky (2004) GCA 68, 1617-1633
75 Mysen & Shang (2005) GCA 69, 2861-2875
76 Mysen, BO (2006) GCA 70, 3121-3138

77 Mysen, BO (2007) Am Mineral 92, 844-862
78 Nabelek (1980) EPSL 48, 293-302
79 O'Hara, MJ (2000) J Pet 41, 1545-1651
80 Parman et al. (1997) EPSL 150, 303-323
81 Reynolds & Langmuir (1997) JGR 102, 14915-14946
82 Rhodes et al. (1979) PLPSC 10th, 407-422
83 Roeder (1974) EPSL 23, 397-410
84 Sack & Carmichael (1984) CMP 85, 103-115
85 Sack et al (1987) CMP 96, 1-23
86 Sano, T & Yamashita, S (2004) Geol Soc London Sp Pub 229, 185-218
87 Sato (1989) Proc Ocean Drilling Prog, Sci Results 111, 17-26
88 Shi & Libourel (1991) CMP 108, 129-145
89 Snyder & Carmichael (1992) GCA 56,303-318
90 Snyder et al. (1993) CMP 113, 73-86
91 Stolper (1977) GCA 41, 587-611
92 Takahashi, E (1978) GCA 42, 1829-1844
93 Thy (1991) Lithos 26, 223-243
94 Thy (1992) PODP, Sci Results 127/128, pt 2, 861-868
95 Thy (1995) J Petrol 36, 1529-1548
96 Thy (1995) Lithos 36, 103-114
97 Thy et al (1991) J. Pet. 32, 303-332
98 Thy et al (1998) Proc. Ocean Drilling Program, Sci Results 152, 359-372
99 Thy et al (1999) Proc. Ocean Drilling Program, Sci Results 163, 95-112
100 Thy et al. (2006) Lithos 92, 154-180
101 Toplis & Carroll (1995) J Petrol 36, 1137-1170
102 Toplis et al. (1994) GCA 58, 797-810
103 Tormey et al (1987) CMP 96, 121-139
104 Tuff, J & O'Neill, HStC (2010) GCA 74, 6180-6205
105 Ussler III & Glazner (1989) CMP 101, 232-244
106 Usui, T et al. (2015) M&PS 50, 759-781
107 Veksler et al. (2007) J Pet 48, 2187-2210
108 Walker et al. (1979) CMP 70, 111-125
109 Walker, D et al. (1988) CMP 99, 306-319
110 Wan, Z et al (2008) Am Mineral 93, 1142-1147
111 Wang, Z & Gaetani, GA (2008) CMP 156, 661-678
112 Weill & McKay (1975) PLSC 6th, 1143-1158
113 Yang et al (1996) CMP 124, 1-18

## 9. Supplementary Figures

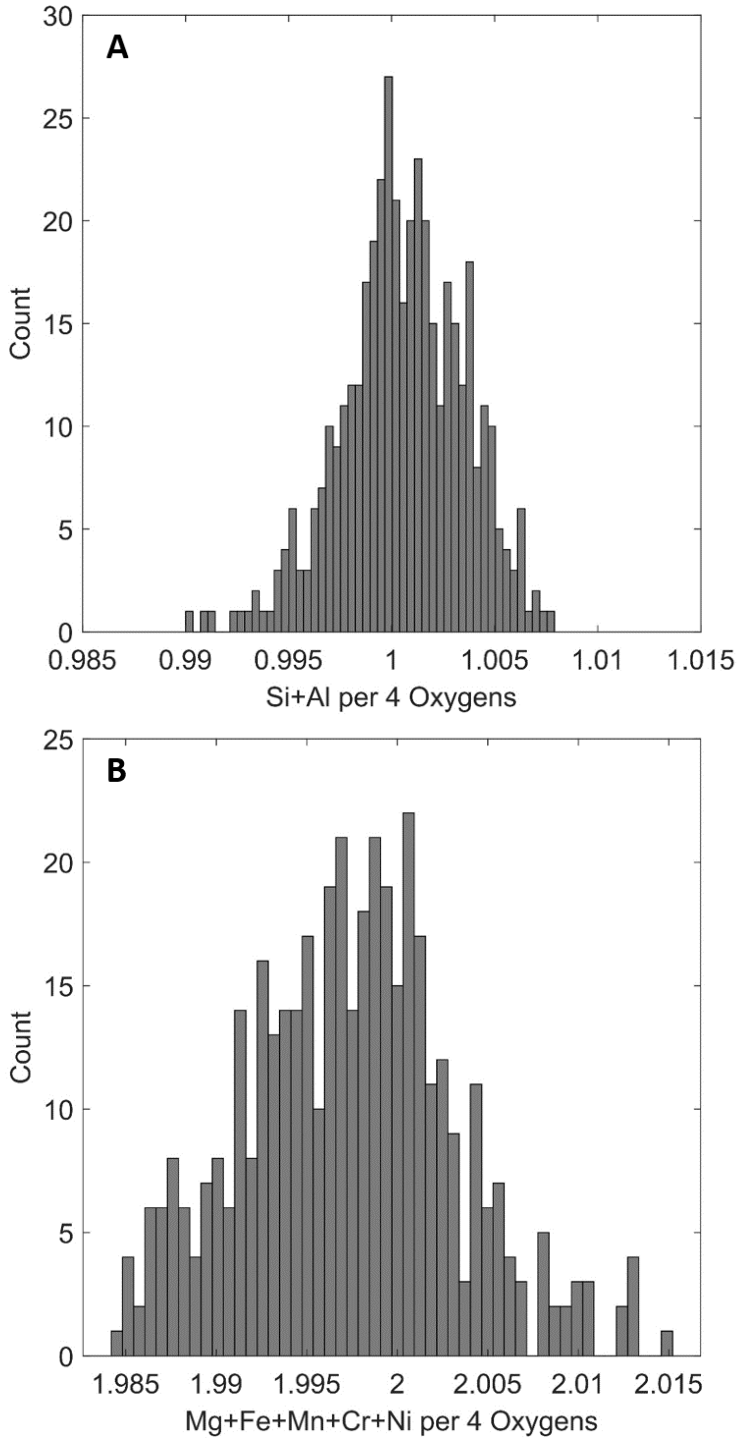


**Supplementary Figure 1.** Histograms of the stoichiometry of experimentally produced and analyzed olivines that passed through the quality filters explained in the Analytical Methods section. **(A)** Sum of tetrahedral cations per 4 oxygens, **(B)** Sum of octahedral cations per 4 oxygens.

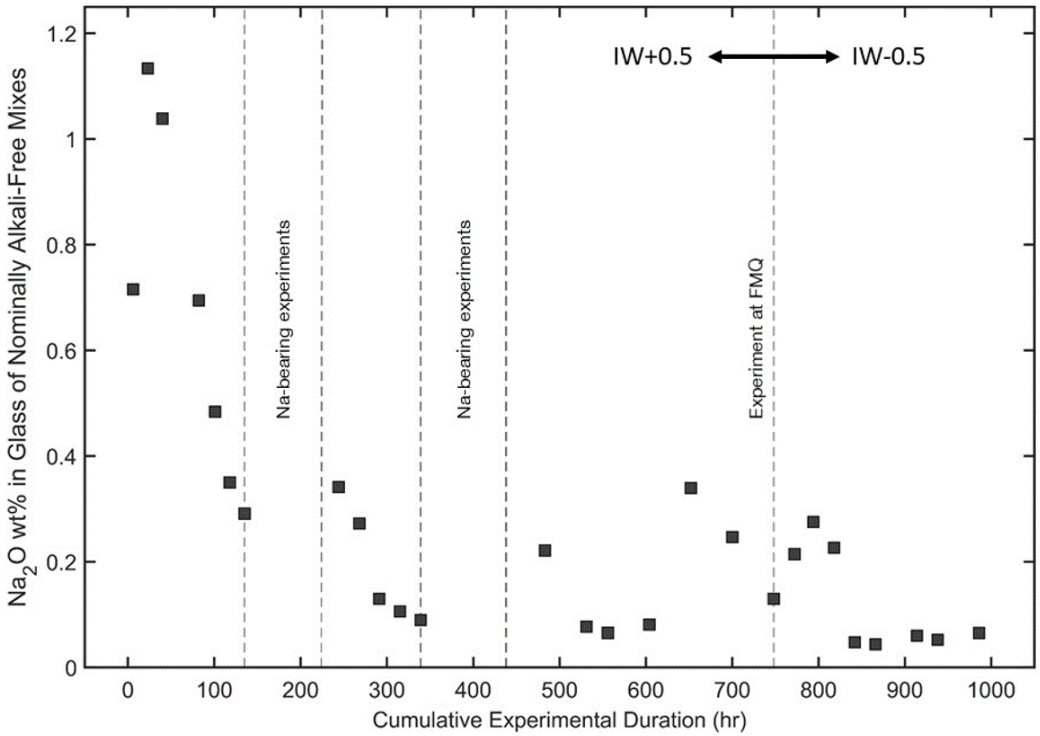


**Supplementary Figure 2.** $Na_2O$ wt% contents of experimental glasses from nominally alkali-free bulk mixes, plotted against the cumulative duration of experiments run in the same furnace over the course of the study. The first four squares show higher $Na_2O$ than the remaining experiments, indicating that alkalis were being flushed from the furnace tube at the start of the series of experiments. All of the nominally alkali-free experiments run after these first four experiments have $Na_2O$ <0.50 wt%. The pairs of dashed lines show when alkali-bearing experiments, using mix HAB+Ol+Mn were run, and the dashed line at T ~ 750 hr indicates one experiment that was run at FMQ.

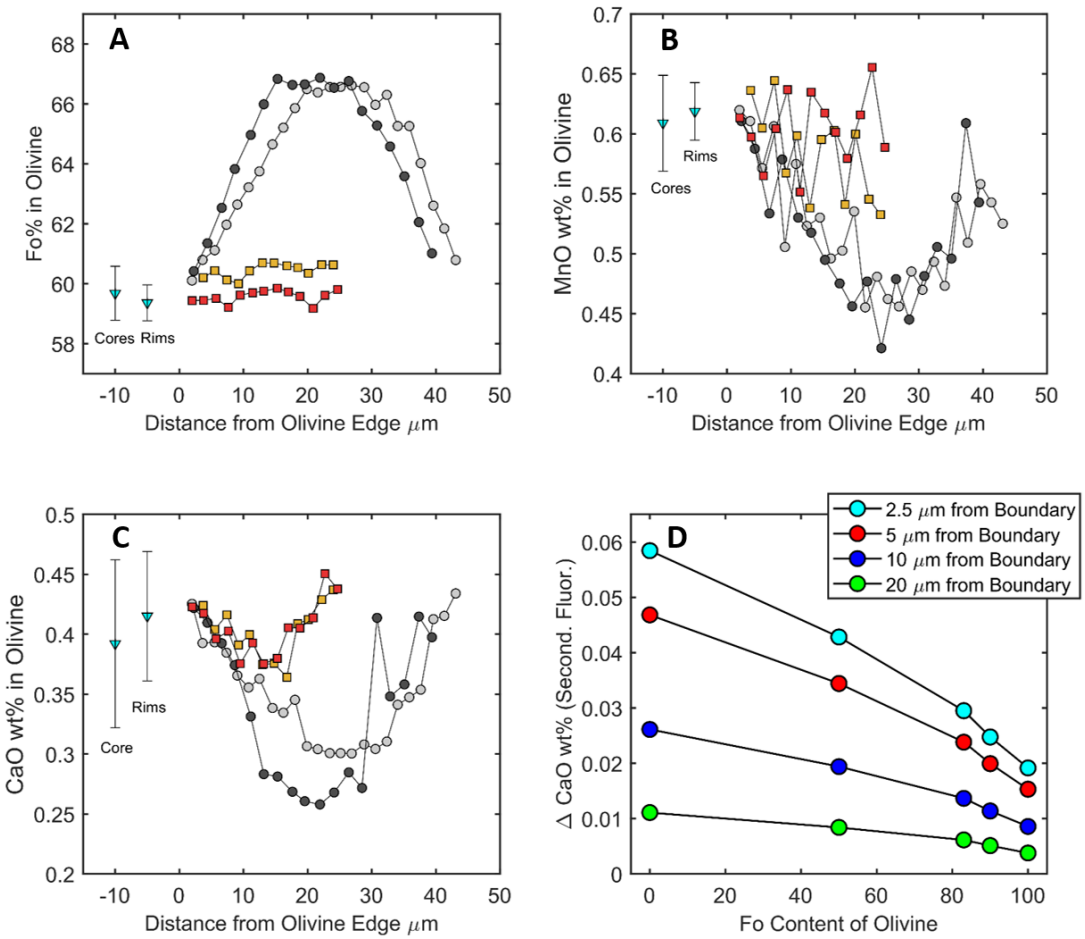


**Supplementary Figure 3.** Microprobe traverses across olivines grains from experiment RKD-35 . The gray circles are analyses of large phenocrysts that showed evidence of zoning in high-contrast BSE images; the colored squares are olivines that show no obvious BSE contrast between cores and rims. The blue triangles show the means and 2σ of the distribution of core and rim analyses from all of the olivine grains measured in RKD-35. **(A)** Fo% in olivine, **(B)** MnO wt% in olivine, **(C)** CaO wt% in olivine. **(D)** Forward model using the PENEPMA algorithm to calculate the expected contribution of secondary fluorescence to CaO measurements in olivine taken in close proximity to glass. The model materials used for the incident beam were pure Fayalite (Fo = 0), MgFeSiO4 (Fo =50), Springwater Olivine (Fo = 83), USMN111312 (Fo = 90), and pure forsterite (Fo = 100). The adjacent glass composition was based on the VG-2 glass standard. The model assumes a planar boundary between olivine and glass and the results plotted in (D) correspond to the analytical solution. Each curve corresponds to contours of constant distance from the olivine / glass interface, showing the effect of Fe in the olivine on the contribution from secondary fluorescence to measurements of CaO in olivine.

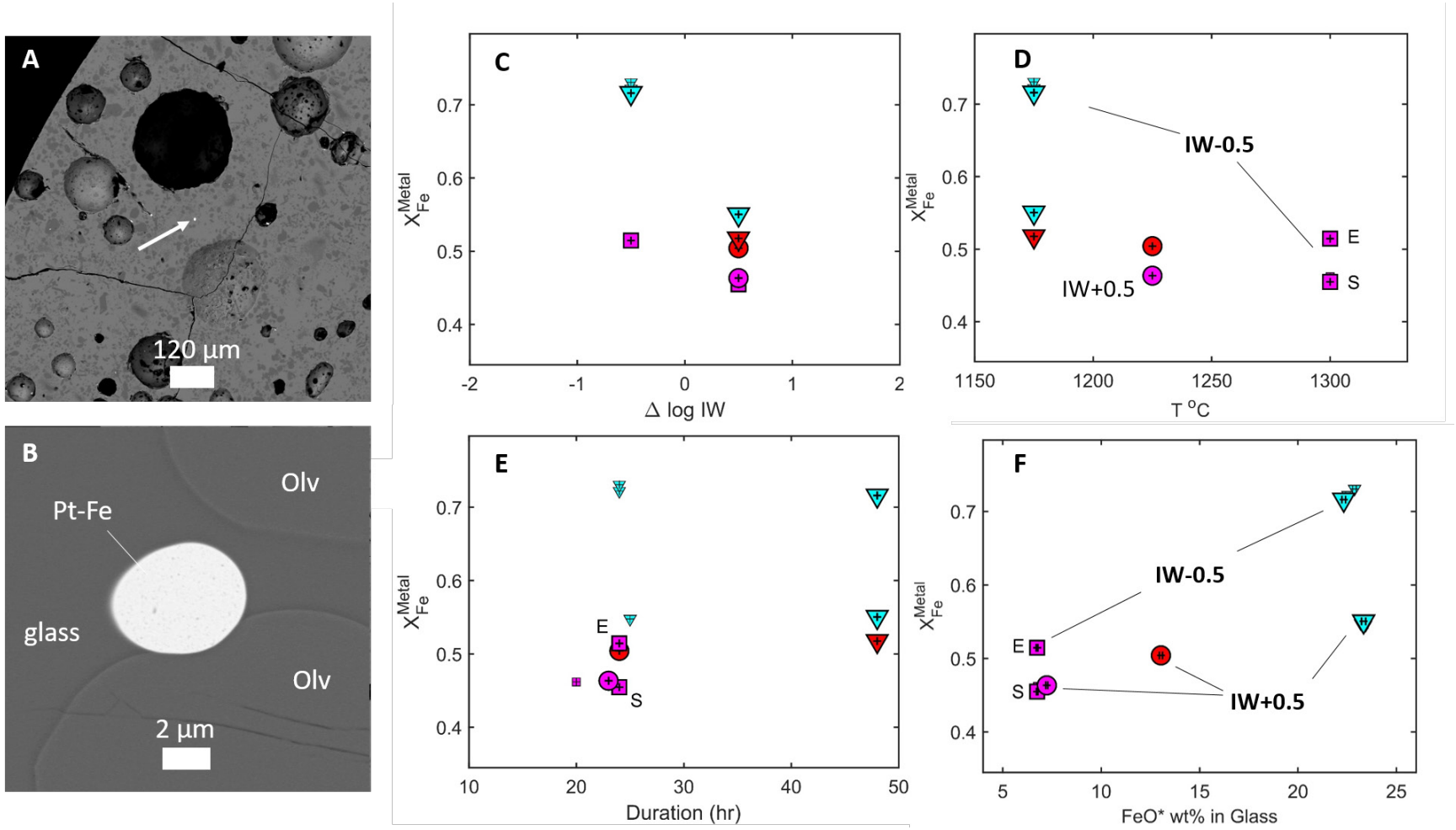


**Supplementary Figure 4. (A)** BSE image showing an isolated PtFe metal bleb (arrow) in petrographic context (RKD-15). **(B)** High-magnification BSE image of a PtFe bleb and surrounding olivines (olv) and glass. **(C)-(F)** Atomic $X_{Fe}$ measured in Pt-Fe metal blebs plotted vs. **(C)** Δlog IW, **(D)** T °C, **(E)** experimental duration in hours, **(F)** FeO* wt% in experimental glasses. S refers to saturation experiment RKD-28, which was the first of two pre-saturation experiments before RKD-30, which is denoted E. Both of these experiments were run at IW-0.5 and 1300 °C.

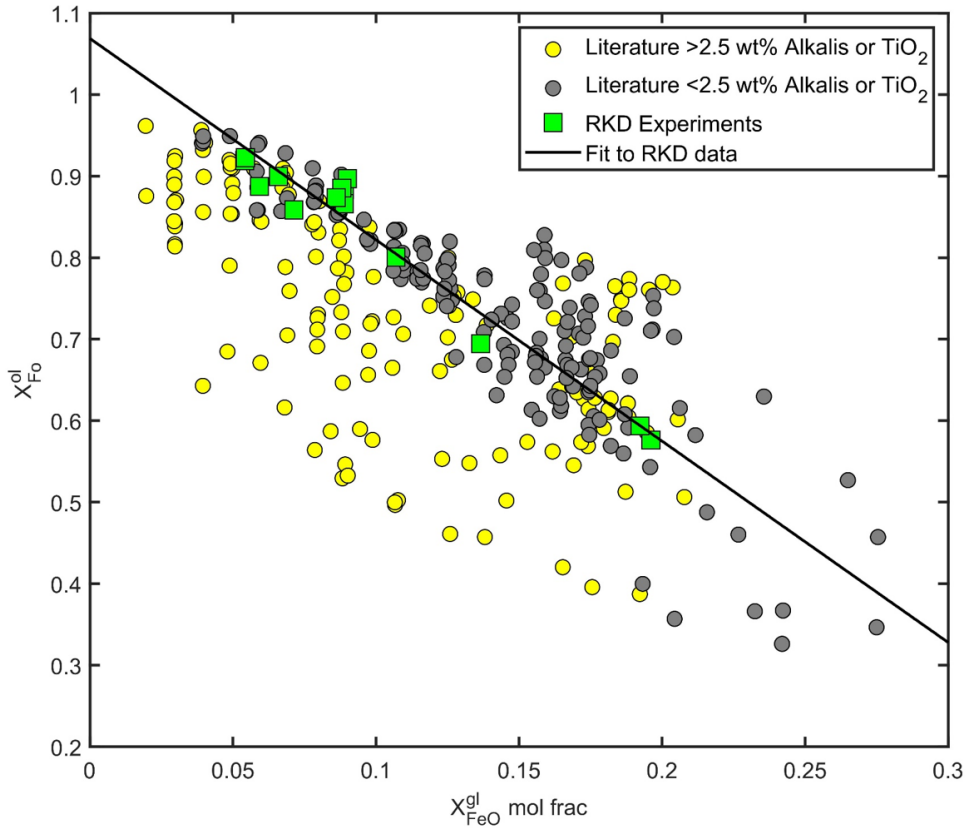


**Supplementary Figure 5.** Mole fraction of FeO* in experimental glasses versus the forsterite content of coexisting olivines. The green squares are the RKD experiments and the black line is a linear fit to these data ($X_{Fo}^{ol} = 1.0688 - 2.4695\ X_{FeO}^{liq}$ , $r^2 = 0.95$). The gray circles are literature experiments run at $fO_2 \leq IW+0.5$ with $Na_2O+K_2O$ or $TiO_2$ less than 2.5 wt%; the yellow circles have high alkalis and Ti contents.

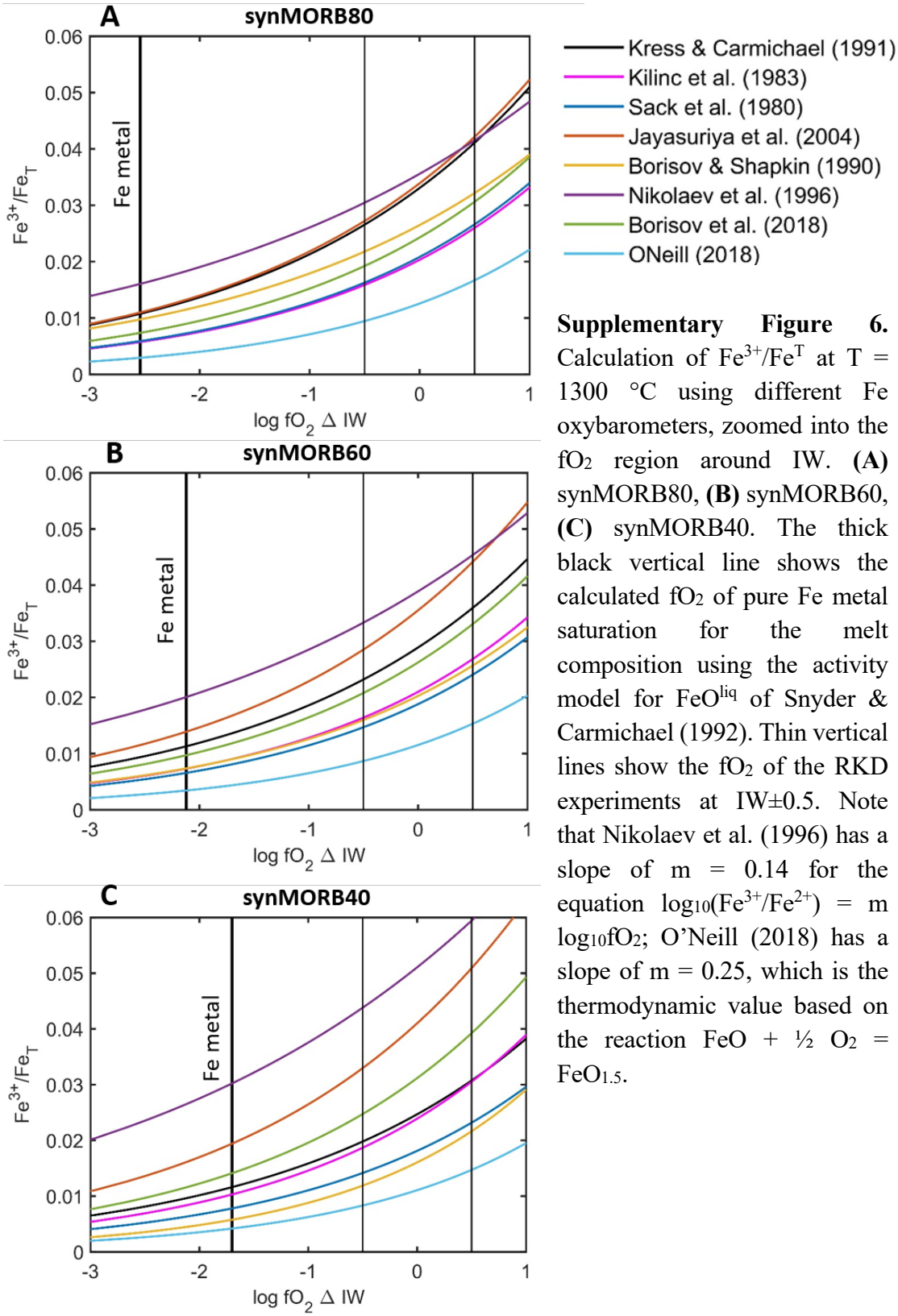


**Supplementary Figure 6.** Calculation of $Fe^{3+}/Fe^{T}$ at T = 1300 °C using different Fe oxybarometers, zoomed into the $fO_2$ region around IW. **(A)** synMORB80, **(B)** synMORB60, **(C)** synMORB40. The thick black vertical line shows the calculated $fO_2$ of pure Fe metal saturation for the melt composition using the activity model for $FeO^{liq}$ of Snyder & Carmichael (1992). Thin vertical lines show the $fO_2$ of the RKD experiments at IW±0.5. Note that Nikolaev et al. (1996) has a slope of m = 0.14 for the equation $\log_{10}(Fe^{3+}/Fe^{2+}) = m \log_{10} fO_2$; O'Neill (2018) has a slope of m = 0.25, which is the thermodynamic value based on the reaction $FeO + ½ O_2 = FeO_{1.5}$.

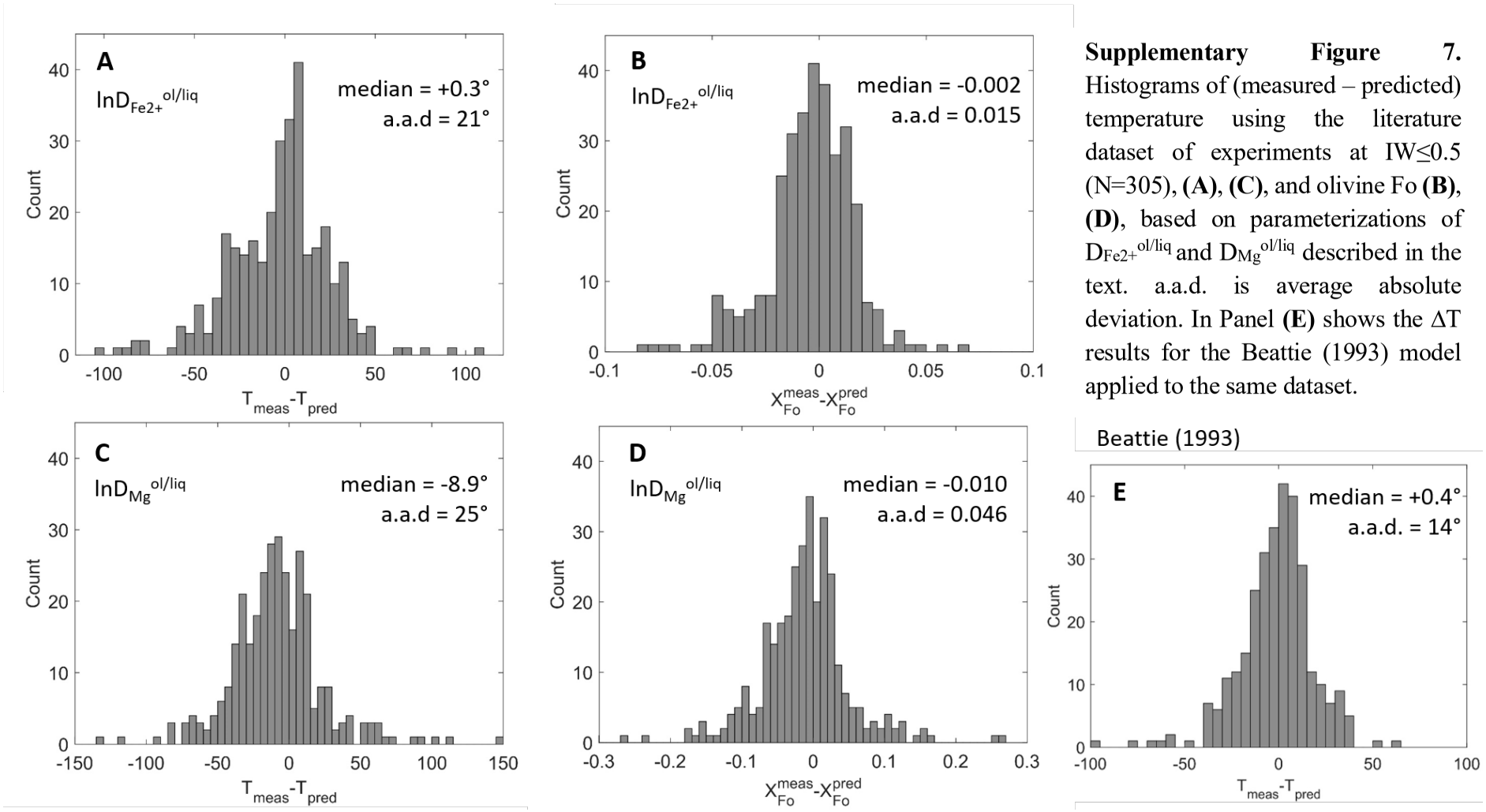


**Supplementary Figure 7.** Histograms of (measured – predicted) temperature using the literature dataset of experiments at IW≤0.5 (N=305), **(A)**, **(C)**, and olivine Fo **(B)**, **(D)**, based on parameterizations of $D_{Fe2+}^{ol/liq}$ and $D_{Mg}^{ol/liq}$ described in the text. a.a.d. is average absolute deviation. In Panel **(E)** shows the ΔT results for the Beattie (1993) model applied to the same dataset.

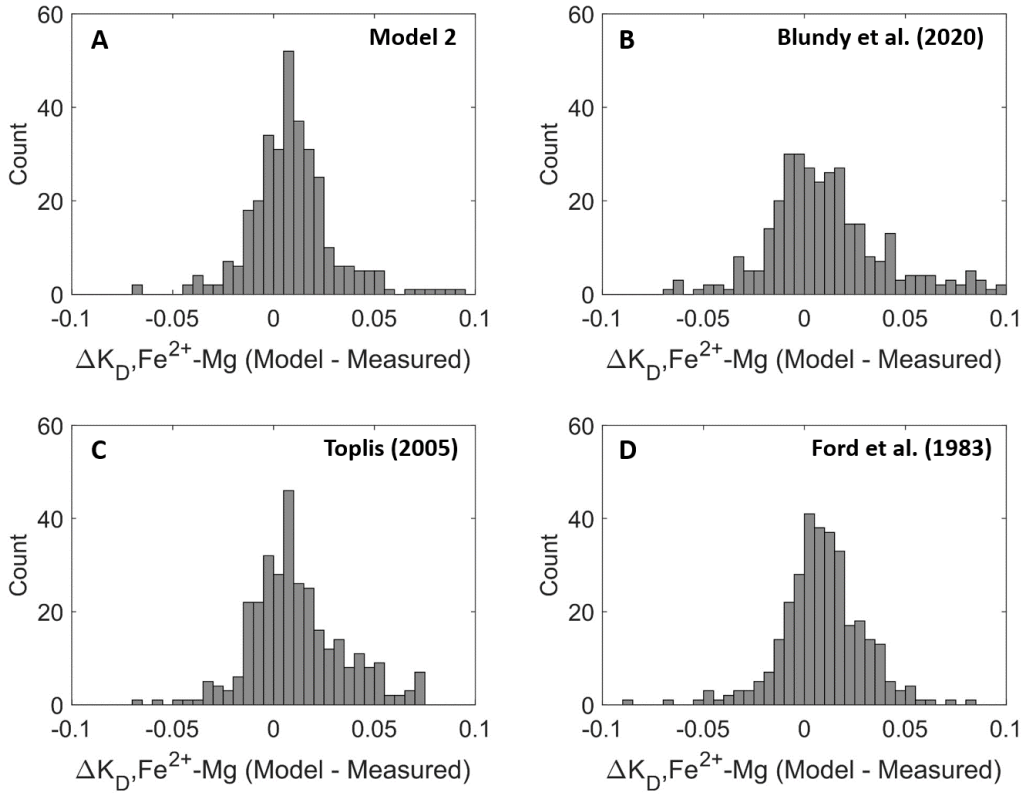


**Supplementary Figure 8.** Histograms showing the difference in the $K_d^{ol/liq}{}_{,Fe2+-Mg}$ calculated by different composition-dependent models from that measured experimentally. The bin width is 0.005. $Fe^{3+}/Fe^{2+}$ was calculated by the expression specified by each model **(A)** and **(B)** Borisov et al. 2018, **(C)** Kilinc et al. 1983, **(D)** Sack et al. 1980. All four distributions of residuals fail a one-sample Kolmogorov-Smirnov test that they are normally distributed about $\Delta K_D^{ol/liq}{}_{,Fe2+-Mg} = 0$.

## 10. Supplementary Tables

### Supplementary Table 1

**Microprobe measurements of other experimental phase products.**
**Plagioclases**

| Name | n | $SiO_2$ | $TiO_2$ | $Al_2O_3$ | FeO | MnO | MgO | CaO | $Na_2O$ | Totals |
|---|---|---|---|---|---|---|---|---|---|---|
| RKD-15 | 3 | 45.08 | 0.10 | 32.81 | 1.13 | 0.07 | 1.67 | 18.68 | 0.13 | 99.70 |
| | 1σ | 0.68 | 0.07 | 1.63 | 0.55 | 0.03 | 0.46 | 0.28 | 0.03 | 0.09 |
| RKD-19 | 8 | 48.52 | 0.05 | 31.13 | 0.55 | 0.03 | 0.41 | 16.53 | 1.98 | 99.23 |
| | 1σ | 1.41 | 0.02 | 1.03 | 0.10 | 0.02 | 0.12 | 0.77 | 0.42 | 0.75 |
| RKD-20 | 5 | 48.71 | 0.05 | 31.79 | 0.54 | 0.03 | 0.39 | 16.72 | 1.83 | 100.10 |
| | 1σ | 1.16 | 0.02 | 0.85 | 0.07 | 0.02 | 0.12 | 0.69 | 0.37 | 0.69 |
| RKD-21 | 7 | 44.56 | 0.06 | 34.39 | 1.08 | 0.04 | 0.50 | 19.21 | 0.22 | 100.08 |
| | 1σ | 0.80 | 0.04 | 0.73 | 0.16 | 0.02 | 0.14 | 0.26 | 0.03 | 0.70 |
| RKD-22 | 7 | 44.29 | 0.06 | 33.93 | 1.67 | 0.05 | 0.40 | 19.39 | 0.08 | 99.87 |
| | 1σ | 0.20 | 0.03 | 0.78 | 0.50 | 0.02 | 0.18 | 0.35 | 0.02 | 0.61 |
| RKD-23 | 9 | 43.97 | 0.05 | 33.77 | 1.37 | 0.03 | 0.31 | 19.55 | 0.07 | 99.14 |
| | 1σ | 0.52 | 0.02 | 0.46 | 0.16 | 0.02 | 0.05 | 0.17 | 0.02 | 0.48 |
| RKD-24 | 7 | 44.62 | 0.06 | 32.84 | 1.86 | 0.05 | 0.39 | 19.17 | 0.10 | 99.10 |
| | 1σ | 0.41 | 0.09 | 1.81 | 1.49 | 0.05 | 0.30 | 0.77 | 0.02 | 0.98 |
| RKD-31 | 10 | 44.32 | 0.04 | 34.34 | 1.22 | 0.01 | 0.30 | 19.84 | 0.06 | 100.15 |
| | 1σ | 0.71 | 0.02 | 0.74 | 0.21 | 0.01 | 0.09 | 0.17 | 0.02 | 0.72 |
| RKD-33 | 6 | 44.21 | 0.02 | 34.00 | 1.01 | 0.01 | 0.24 | 19.76 | 0.07 | 99.34 |
| | 1σ | 0.50 | 0.01 | 0.23 | 0.11 | 0.01 | 0.03 | 0.10 | 0.02 | 0.61 |
| RKD-34 | 9 | 44.33 | 0.04 | 33.69 | 1.26 | 0.03 | 0.32 | 19.73 | 0.06 | 99.48 |
| | 1σ | 0.47 | 0.03 | 0.78 | 0.31 | 0.03 | 0.11 | 0.26 | 0.03 | 0.65 |
| RKD-35 | 9 | 43.91 | 0.03 | 33.84 | 1.06 | 0.03 | 0.28 | 19.68 | 0.08 | 98.92 |
| | 1σ | 0.69 | 0.01 | 0.50 | 0.12 | 0.01 | 0.07 | 0.20 | 0.03 | 0.79 |

**Pyroxenes**

| Name | n | $SiO_2$ | $TiO_2$ | $Al_2O_3$ | $Cr_2O_3$ | FeO | MnO | MgO | CaO | Totals |
|---|---|---|---|---|---|---|---|---|---|---|
| RKD-15 | 4 | 57.02 | 0.18 | 1.61 | 0.00 | 6.68 | 0.50 | 31.44 | 1.95 | 99.41 |
| | | 1.10 | 0.03 | 0.01 | 0.01 | 0.12 | 0.03 | 0.47 | 0.04 | 0.85 |
| RKD-21 | 8 | 54.73 | 0.22 | 0.87 | 0.02 | 15.58 | 0.72 | 22.75 | 4.21 | 99.13 |
| | | 0.93 | 0.08 | 0.32 | 0.01 | 0.27 | 0.06 | 0.53 | 0.65 | 0.67 |

## Spinels

| Name | n | $SiO_2$ | $TiO_2$ | $Al_2O_3$ | $Cr_2O_3$ | $Fe_2O_3$ | FeO | MnO | MgO | CaO | NiO | Sum |
|---|---|---|---|---|---|---|---|---|---|---|---|---|
| RKD-1 | 5 | 0.31 | 1.17 | 19.99 | 46.64 | 2.25 | 10.99 | 0.72 | 15.63 | 0.22 | 0.13 | 98.09 |
| | 1σ | 0.09 | 0.05 | 1.25 | 1.24 | | 0.05 | 0.03 | 0.23 | 0.01 | 0.03 | |
| RKD-2 | 5 | 0.36 | 1.20 | 18.10 | 48.31 | 2.77 | 9.88 | 0.76 | 16.18 | 0.20 | 0.07 | 97.85 |
| | 1σ | 0.14 | 0.03 | 0.98 | 0.84 | | 0.12 | 0.03 | 0.21 | 0.07 | 0.01 | |
| RKD-3 | 4 | 0.28 | 1.22 | 18.65 | 48.04 | 1.95 | 10.60 | 0.77 | 15.53 | 0.22 | 0.07 | 97.45 |
| | 1σ | 0.04 | 0.03 | 0.41 | 0.56 | | 0.10 | 0.05 | 0.14 | 0.03 | 0.05 | |
| RKD-4 | 5 | 0.37 | 1.21 | 18.92 | 48.07 | 1.63 | 10.83 | 0.76 | 15.65 | 0.21 | 0.04 | 97.69 |
| | 1σ | 0.04 | 0.02 | 0.12 | 0.39 | | 0.11 | 0.03 | 0.14 | 0.04 | 0.03 | |
| RKD-5 | 5 | 0.38 | 1.18 | 18.98 | 47.93 | 1.93 | 11.34 | 0.74 | 15.30 | 0.23 | 0.16 | 98.19 |
| | 1σ | 0.09 | 0.01 | 0.47 | 0.91 | | 0.06 | 0.03 | 0.19 | 0.04 | 0.03 | |
| RKD-6 | 5 | 0.45 | 1.29 | 20.45 | 45.33 | 1.87 | 12.78 | 0.81 | 14.48 | 0.25 | 0.27 | 97.99 |
| | 1σ | 0.12 | 0.03 | 0.70 | 0.81 | | 0.17 | 0.01 | 0.22 | 0.02 | 0.04 | |
| RKD-7 | 5 | 0.32 | 1.10 | 17.82 | 50.28 | 1.68 | 10.39 | 0.71 | 15.86 | 0.20 | 0.09 | 98.47 |
| | 1σ | 0.03 | 0.03 | 0.67 | 0.72 | | 0.12 | 0.04 | 0.24 | 0.04 | 0.02 | |
| RKD-26 | 5 | 0.50 | 1.29 | 19.23 | 47.16 | 1.80 | 12.58 | 0.81 | 14.64 | 0.29 | 0.23 | 98.55 |
| | 1σ | 0.06 | 0.03 | 0.22 | 0.35 | | 0.05 | 0.01 | 0.14 | 0.05 | 0.02 | |
| SOCrAl | 5 | 0.22 | 1.11 | 16.26 | 43.96 | 9.34 | 11.03 | 0.76 | 14.79 | 0.20 | 0.45 | 98.14 |
| 1d-2 | 1σ | 0.02 | 0.03 | 0.09 | 0.28 | | 0.10 | 0.02 | 0.12 | 0.03 | 0.03 | |
| SOCrAl | 5 | 0.22 | 1.09 | 16.35 | 44.23 | 9.12 | 11.11 | 0.77 | 14.82 | 0.20 | 0.41 | 98.34 |
| 1c-2 | 1σ | 0.02 | 0.02 | 0.09 | 0.13 | | 0.18 | 0.02 | 0.14 | 0.03 | 0.04 | |

## Pt-Fe Blebs

| Name | Fe | Pt | Re | Ni | Mn | Cr | Al | Elem. Totals | Pt/Fe Molar | $X_{Fe}$ Molar |
|---|---|---|---|---|---|---|---|---|---|---|
| RKD-13 | 16.92 | 64.87 | bdl | 0.38 | bdl | bdl | 0.31 | 82.88 | 1.10 | 46.18 |
| RKD-14 | 17.77 | 73.08 | bdl | 0.35 | bdl | bdl | bdl | 91.70 | 1.18 | 45.47 |
| RKD-15 | 18.69 | 75.13 | bdl | 0.10 | bdl | bdl | bdl | 94.46 | 1.15 | 46.34 |
| RKD-16 | 21.10 | 72.47 | bdl | 0.10 | bdl | bdl | bdl | 93.62 | 0.98 | 50.53 |
| RKD-17 | 21.33 | 73.87 | bdl | 0.09 | bdl | bdl | bdl | 95.24 | 0.99 | 50.41 |
| RKD-21 | 21.75 | 70.67 | bdl | 0.12 | bdl | bdl | bdl | 93.11 | 0.93 | 51.75 |
| RKD-22 | 24.30 | 70.84 | bdl | bdl | bdl | bdl | bdl | 95.79 | 0.83 | 54.55 |
| RKD-23 | 24.11 | 70.19 | bdl | bdl | bdl | bdl | bdl | 94.65 | 0.83 | 54.76 |
| RKD-24 | 24.71 | 68.59 | bdl | bdl | 0.06 | bdl | 0.15 | 94.01 | 0.79 | 55.04 |
| RKD-28 | 22.29 | 63.00 | bdl | 1.37 | 0.06 | bdl | 0.61 | 87.93 | 0.81 | 51.71 |
| RKD-30 | 22.32 | 71.47 | bdl | 0.79 | bdl | bdl | bdl | 94.98 | 0.92 | 51.45 |
| RKD-32 | 40.03 | 53.35 | bdl | 0.12 | bdl | bdl | bdl | 93.99 | 0.38 | 72.20 |
| RKD-34 | 40.86 | 52.85 | bdl | 0.08 | bdl | bdl | bdl | 93.92 | 0.37 | 73.05 |
| RKD-35 | 39.18 | 51.95 | bdl | 0.18 | bdl | bdl | 0.15 | 92.05 | 0.38 | 71.59 |

**Supplementary Table 2 – Results of mass balance calculation (section 4.2.2) for the RKD experiments.**

| Experiment Name | $\chi^2$ | Pass/Fail | Liquid | Olivine | Spinel | Plagioclase | Pyroxene | FeO | MnO | $Na_2O$ | $K_2O$ |
|---|---|---|---|---|---|---|---|---|---|---|---|
| RKD-1 | 0.328 | pass | 0.693 | 0.294 | 0.013 | 0.000 | 0.000 | -1.88 | 0.92 | 0.501842 | 0.025044 |
| RKD-2 | 0.222 | pass | 0.692 | 0.297 | 0.011 | 0.000 | 0.000 | -10.80 | -1.27 | 0.79382 | 0.047839 |
| RKD-3 | 2.889 | pass | 0.666 | 0.322 | 0.012 | 0.000 | 0.000 | -13.17 | -2.16 | 0.704382 | 0.04579 |
| RKD-4 | 4.151 | pass | 0.667 | 0.322 | 0.011 | 0.000 | 0.000 | -13.71 | -0.85 | 0.472041 | 0.043225 |
| RKD-5 | 2.664 | pass | 0.674 | 0.317 | 0.009 | 0.000 | 0.000 | -6.12 | 0.56 | 0.329662 | 0.028901 |
| RKD-6 | 2.419 | pass | 0.612 | 0.379 | 0.009 | 0.000 | 0.000 | -2.16 | 1.00 | 0.217286 | 0.019603 |
| RKD-7 | 2.771 | pass | 0.741 | 0.254 | 0.005 | 0.000 | 0.000 | -6.93 | 0.00 | 0.218603 | 0.031028 |
| RKD-8 | 2.838 | pass | 0.892 | 0.108 | 0.000 | 0.000 | 0.000 | -1.23 | 0.00 | -25.5917 | -6.36098 |
| RKD-9 | 4.426 | pass | 0.902 | 0.098 | 0.000 | 0.000 | 0.000 | -7.32 | -2.23 | -51.8034 | -18.5034 |
| RKD-12 | 1.825 | pass | 0.904 | 0.096 | 0.000 | 0.000 | 0.000 | -4.04 | 0.00 | -35.8495 | -11.5403 |
| RKD-13 | 2.178 | pass | 0.928 | 0.072 | 0.000 | 0.000 | 0.000 | -3.60 | -4.95 | 0 | 0 |
| RKD-14 | 1.288 | pass | 0.930 | 0.070 | 0.000 | 0.000 | 0.000 | -4.10 | -3.06 | 0 | 0 |
| RKD-15 | 0.004 | pass | 0.673 | 0.122 | 0.000 | 0.105 | 0.100 | -1.85 | -5.51 | 0 | 0 |
| RKD-16 | 1.681 | pass | 0.936 | 0.064 | 0.000 | 0.000 | 0.000 | -3.61 | 0.00 | 0 | 0 |
| RKD-17 | 0.709 | pass | 0.933 | 0.067 | 0.000 | 0.000 | 0.000 | -2.88 | 0.00 | 0 | 0 |
| RKD-19 | 0.134 | pass | 0.514 | 0.247 | 0.000 | 0.238 | 0.000 | -5.80 | -0.78 | -36.3818 | -23.6278 |
| RKD-20 | 0.006 | pass | 0.551 | 0.236 | 0.000 | 0.213 | 0.000 | -6.43 | 1.26 | -40.0743 | -27.188 |
| RKD-21 | 1.293 | pass | 0.464 | 0.068 | 0.000 | 0.258 | 0.210 | -0.50 | 2.41 | 0 | 0 |
| RKD-22 | 2.657 | pass | 0.784 | 0.161 | 0.000 | 0.055 | 0.000 | 0.87 | 2.39 | 0 | 0 |
| RKD-23 | 1.269 | pass | 0.788 | 0.155 | 0.000 | 0.056 | 0.000 | -0.80 | 0.00 | 0 | 0 |
| RKD-24 | 0.395 | pass | 0.790 | 0.155 | 0.000 | 0.054 | 0.000 | -0.18 | 3.63 | 0 | 0 |
| RKD-25 | 13.24 | pass | 0.658 | 0.342 | 0.000 | 0.000 | 0.000 | -8.75 | 0.00 | 0 | 0 |
| RKD-26 | 3.213 | pass | 0.623 | 0.365 | 0.000 | 0.012 | 0.000 | -5.71 | -0.62 | 0 | 0 |
| RKD-27 | 0.718 | pass | 0.677 | 0.323 | 0.000 | 0.000 | 0.000 | -0.10 | -11.24 | 0 | 0 |

Note for RKD-1 through RKD-7 with initially no Na or K, this value represents the bulk wt% of $Na_2O$ and $K_2O$ gained

| Experiment Name | $\chi^2$ | Pass/Fail | Liquid | Olivine | Spinel | Plagioclase | Pyroxene | FeO | MnO | $Na_2O$ | $K_2O$ |
|---|---|---|---|---|---|---|---|---|---|---|---|
| RKD-28 | 3.295 | pass | 0.923 | 0.077 | 0.000 | 0.000 | 0.000 | -5.25 | -2.45 | 0 | 0 |
| RKD-29 | 1.624 | pass | 0.933 | 0.067 | 0.000 | 0.000 | 0.000 | -5.69 | -3.83 | 0 | 0 |
| RKD-30 | 1.457 | pass | 0.950 | 0.050 | 0.000 | 0.000 | 0.000 | -5.18 | -2.60 | 0 | 0 |
| RKD-31 | 0.501 | pass | 0.858 | 0.125 | 0.000 | 0.017 | 0.000 | -0.84 | 4.91 | 0 | 0 |
| RKD-32 | 1.259 | pass | 0.877 | 0.118 | 0.000 | 0.006 | 0.000 | -1.27 | 3.79 | 0 | 0 |
| RKD-33 | 1.986 | pass | 0.878 | 0.117 | 0.000 | 0.005 | 0.000 | -1.58 | 4.78 | 0 | 0 |
| RKD-34 | 0.363 | pass | 0.850 | 0.129 | 0.000 | 0.021 | 0.000 | -0.84 | 4.01 | 0 | 0 |
| RKD-35 | 1.12 | pass | 0.883 | 0.116 | 0.000 | 0.000 | 0.000 | -1.22 | 3.90 | 0 | 0 |
| SOCrAl-1c | 2.988 | pass | 0.684 | 0.300 | 0.016 | 0.000 | 0.000 | -1.99 | -0.62 | 0 | 0 |
| SOCrAl-1d | 2.376 | pass | 0.683 | 0.302 | 0.015 | 0.000 | 0.000 | -1.62 | 0.00 | 0 | 0 |

# *Appendix 1*

## Reassessing the thermal history of martian meteorite Shergotty and Apollo mare basalt 15555 using kinetic isotope fractionation of zoned minerals

Frank Richter [a*]

**Lee M. Saper [b]**

Johan Villeneuve [c]

Marc Chaussidon [d]

E. Bruce Watson [e]

Andrew M. Davis [a]

Ruslan A. Mendybaev [a]

Steven B. Simon [f]

[a] *The University of Chicago, 5734 South Ellis Avenue, Chicago, IL 60637, USA*
[b] *California Institute of Technology, Pasadena, CA, USA*
[c] *CRPG, Universite' de Lorraine, Nancy, France*
[d] *Institut de Physique du Globe de Paris, Paris, France*
[e] *Rensselaer Polytechnic Institute, Troy, NY, USA*
[f] *University of New Mexico, Albuquerque, NM, USA*

## 1. Abstract

Elemental abundance and isotopic fractionation profiles across zoned minerals from a martian meteorite (Shergotty) and from a lunar olivine-normative mare basalt (Apollo 15555) were used to place constraints on the thermal evolution of their host rocks. The isotopic measurements were used to determine the extent to which diffusion was responsible for, or modified, the zoning. The key concept is that mineral zoning that is the result of diffusion, or that was significantly affected by diffusion, will have an associated diagnostic isotopic fractionation that can quantify the extent of mass transfer by diffusion. Once the extent of diffusion was determined, the mineral zoning was used to constrain the thermal history. An isotopic and chemical profile measured across a large zoned pigeonite grain from Shergotty showed no significant isotopic fractionation of either magnesium or lithium, which is evidence that the chemical zoning was dominantly the result of crystallization from an evolving melt and that the crystallization must have taken place at a sufficiently fast rate that there was not time for any significant mass transfer by diffusion. Model calculations for the evolution of the fast-diffusing lithium showed that this would have required a cooling at a rate of about ~ 150˚C/h or more. Measurable isotopic fractionation across a zoned olivine grain from lunar mare basalt 15555 indicated that the chemical zoning was mainly due to crystallization that was modified by a small but quantifiable amount of diffusion. The results of a diffusion calculation that was able to account for the amplitude and spatial scale of the isotopic fractionation across the olivine grain yielded an estimate of 0.2˚C/h for the cooling rate of 15555. The results of an earlier study of zoned augite and olivine grains from martian nakhlite meteorite NWA 817 were reviewed for comparison with the results from Shergotty. The isotopic fractionations near the edges of grains from NWA 817 showed that, in contrast to Shergotty, the lithium zoning in augite and of magnesium in olivine

was due entirely to diffusion. The isotopic fractionation data across zoned minerals from the martian meteorites and from the lunar basalt were key for documenting and quantifying the extent of mass transfer by diffusion, which was a crucial step for validating the use of diffusion modeling to estimate their cooling rates.

## 2. Introduction

Compositional zoning, which is a common feature of many igneous minerals, can develop when crystallization proceeds at a sufficiently fast rate that the mineral cannot maintain bulk equilibrium with the evolving melt from which it is crystallizing. Here, such zoning will be referred to as crystallization zoning. Mineral zoning can also arise from, or be modified by, diffusion during or after crystallization. Establishing the extent to which diffusion caused or modified a given instance of mineral zoning is critical when zoning is used to constrain the thermal history and chemical evolution of a mineral grain. A number of approaches have been developed to determine the role of diffusion in connection with igneous mineral zoning. An often applied method involves comparing the zoning of two or more elements with significantly different diffusion rates with the expectation of how their initial profiles would evolve to different degrees if diffusion was the operative process (for examples, discussion, and mathematical formulation, see Costa et al., 2008 and Watson and Cherniak, 2015). In the case of minerals such as olivine, where the diffusion rate of major and trace elements depends on crystallographic orientation, the ratio of the length scale of the zoned portions in different directions can be used to test whether the profiles are consistent with having been produced by diffusion (see, for example, Costa and Dungan, 2005). The work presented here takes a different approach by determining the extent of diffusion in a zoned mineral based on two key concepts: (1) crystallization in igneous systems occurs at a sufficiently high temperature that equilibrium isotope fractionation between minerals and melts can be regarded as

negligible (Tomascak et al., 1999; Teng et al., 2008); and (2) mass transport by diffusion in silicate systems produces diagnostic kinetic isotopic fractionations that can be used to quantify the extent of diffusion (Richter et al., 2003). Laboratory experiments by Richter et al. (2014, 2017) and by Sio et al. (2018) demonstrated and quantified isotope fractionations by diffusion in pyroxene and olivine that serve as "fingerprints" of the extent of diffusion in these igneous minerals. It is, of course, possible that a given instance of isotopic zoning of an igneous mineral can arise by crystallization from a melt that was itself evolving in isotopic composition, for example, by crustal contamination. However, such zoning is unlikely to have the diagnostic spatial correspondence between elemental and isotopic zoning documented by the laboratory experiments. Once the degree to which diffusion caused or affected mineral zoning is determined, it can be used to constrain the timescales of magmatic processes and cooling. In what follows, we review the results of laboratory experiments that documented isotopic fractionation by diffusion in minerals and use the results to specify parameters used to model the isotopic fractionation by diffusion of pigeonite from the basaltic martian meteorite Shergotty and from an olivine grain from the lunar low-Ti mare basalt 15555. The extent that diffusion affected the zoning of these minerals was used to constrain their thermal history. In a final section, the zoned pyroxenes from Shergotty are compared to those from an earlier similar study by Richter et al. (2016) of the martian nakhlite meteorite Northwest Africa 817 (NWA 817). While the magnesium elemental zoning of pyroxenes from these two meteorites is very similar their distinctly different isotopic fractionation provides a clear indication that the zoning resulted from different processes: fractional crystallization of pyroxene in Shergotty and diffusion out of initially homogeneous pyroxene grains in the case of NWA 817.

## 3. Laboratory Experiments and Model Calculations of Isotope Fractionation by Diffusion

Laboratory experiments that quantify the rate of diffusion and the associated kinetic isotopic fractionation provide the foundation for modeling diffusive transport in pyroxene and in olivine. Diffusion experiments involving minerals often focus on lithium because it is a very fast diffuser and the expectation that the large mass ratio of $^{7}Li/^{6}Li$ (1.17) would result in measurable kinetic isotope fractionation. The results of laboratory experiments involving diffusion of lithium in olivine (Dohmen et al., 2010) and in pyroxene (Richter et al., 2014) are surprisingly complicated. For example, many of the experiments by Richter et al. (2014) in which lithium diffused into augite and diopside resulted in remarkable concentration profiles in which lithium propagated into the pyroxenes as a steep-fronted step rather than the usual smoothly declining profile. Panel (a) in Fig. 1 shows an example of such a stepped profile along with the associated lithium isotopic fractionation (panel b) reported in the usual permil notation $\delta^{7}Li\ (‰) = 1000 \times [(^{7}Li/^{6}Li)_{sample}/(^{7}Li/^{6}Li)_{standard} - 1]$. Dohmen et al. (2010) had previously reported similar step-like propagation of lithium in olivine and interpreted it as being the result of lithium occurring in two different sites: fast-diffusing interstitial lithium and slow-diffusing lithium in metal sites. The lithium in the two sites is assumed to be subject to an exchange reaction involving vacancies written as $Li^{*} + V \leftrightarrow Li_M$ where $Li^{*}$, $V$, and $Li_M$ represent the abundance of interstitial lithium, of vacancies, and of lithium in metal sites, respectively. The exchange is governed by an equilibrium constant, $K = [Li_M]/([Li^{*}] \times [V])$, with the square brackets indicating concentration. Dohmen et al. (2010) showed that lithium will propagate into the mineral as a step when there are a sufficiently large number of vacancies and the equilibrium constant $K$ is sufficiently large. The reason for this is that when the fast-diffusing interstitial lithium encounters a vacancy, it will “jump” into a

slow-diffusing metal site and lithium does not penetrate further into the grain until all the vacancies at a given distance from the grain edge are filled. Figure 1b shows that a negative lithium isotopic fractionation develops in that portion of the grain with elevated lithium as a result of $^{6}$Li having diffused into the grain faster than $^{7}$Li. Further into the grain interior the isotopic composition jumps abruptly back to unfractionated values because an insignificant amount of lithium diffused into the grain beyond the abrupt concentration step. The relative diffusion of $^{6}$Li compared to $^{7}$Li used to fit the isotopic fractionation data in Fig. 1b was calculated using a mass dependence of the interstitial lithium diffusion coefficients parameterized as $D6_{Li}/D7_{Li} = (7/6)^{\beta}$ with $\beta = 0.27$. For a detailed discussion of the two-site lithium diffusion model for olivine, see Dohmen et al. (2010), and for its application to account for the concentration and isotopic fractionation profiles of lithium diffused in pyroxene, see Richter et al. (2014, 2016).

Richter et al. (2014) found that in some experiments lithium diffused into pyroxene along a smoothly declining profile rather than as a step. An example of this is shown in panels (c) and (d) of Fig.1 from an experiment run under more reducing conditions (log $fO_2 = -15$) than the experiment shown in panels (a) and (b) that was run with log $fO_2 = -12$. A point worth noting is that lithium-zoned pyroxene grains from both terrestrial (Parkinson et al., 2007, Jeffcoate et al., 2007) and martian rocks (Beck et al., 2006; Richter et al., 2016) all have smoothly varying profiles of lithium concentration and isotopic fractionation, not step-like profiles.

The model curves shown in panels (a) and (b) of Fig. 1 were calculated assuming the initial concentration of vacancies in the interior is the same as the lithium in metal sites at the boundary but with the interstitial lithium at the boundary being very much less. Profiles such as the ones shown in panels (c) and (d) in Fig. 1 result when the interstitial lithium concentration at the grain edge is comparable to or greater than the

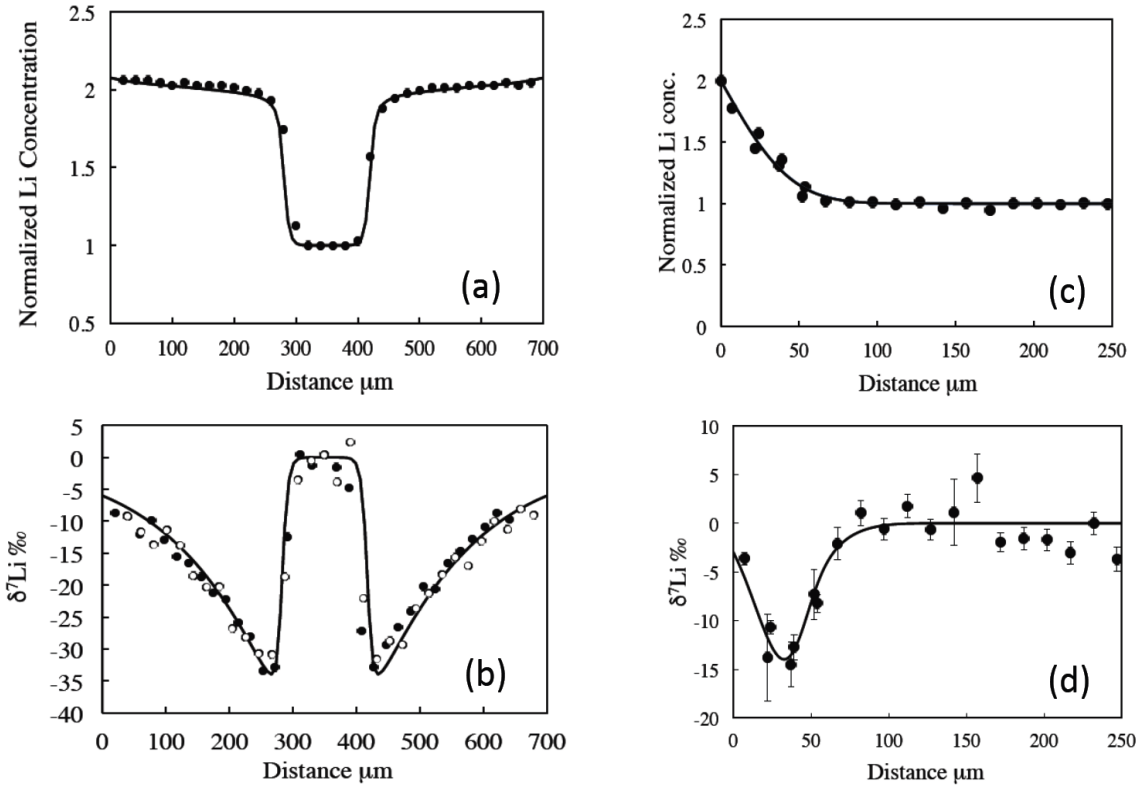


**Figure 1.** Panel (a) shows the lithium concentration normalized by the average value in the interior across a 700 µm wide Templeton augite grain from experiment LiPx8 by Richter et al. (2014). Panel (b) uses filled and unfilled circles to show the measured lithium isotopic fractionation relative to the unfractionated interior measured along two parallel transects across the same grain as in (a). Comparing the isotopic fractionation from the two transects provides a realistic measure of the uncertainty of the isotopic measurements. The panels on the right show the normalized lithium concentration (c) and isotopic fractionation (d) from one edge to the interior of an augite grain from experiment LiPx20 by Richter et al. (2014). The calculated profiles shown as continuous black curves that fit the lithium concentration and isotopic data were calculated using a two-species lithium model (see text for details). Figure 1 is a modified version of Figs. 4 and 7 of Richter et al. (2014).

vacancy concentration in the grain interior. The profiles in panels (c) and (d) were calculated assuming that the initial vacancy concentration was equal to the lithium concentration at the grain edge (V=Li*). The same value of $\beta$ = 0.27 was able to fit the isotopic fractionation data from the two experiments shown in Fig 1 despite their very different profiles. However, when the concentration of vacancies in the model calculation is negligible (i.e. V<<Li*) lithium is effectively in only one type of site and a fit similar to that shown in panel (d) of Fig. 1 required a larger value of $\beta$ = 0.44 (see Fig. 7 and discussion in Richter et al., 2014). Estimates of $\beta$ for lithium diffusing in pyroxenes can also be obtained from natural zoned samples. Richter et al. (2014) were able to fit the lithium isotopic fractionation data from terrestrial clinopyroxenes reported by Parkinson et al. (2007) using $\beta$ = 0.25, and data from Jeffcoate et al. (2007) with $\beta$ = 0.30. Richter et al. (2014) also derived an estimate of $\beta$ = 0.27 for lithium diffusing in augite from martian nakhlite MIL 03346 using data reported by Beck et al. (2006). Subsequently, Richter et al. (2016) measured and fit the lithium isotopic fractionation of ten additional augite grains from nakhlites MIL 03346 and NWA 817 using values of □ from 0.28 to 0.40. The overall conclusion based on these estimates is that when the measured isotopic fractionation of lithium in natural pyroxenes can be fit using $\beta = 0.35 \pm 0.10$ it can be taken as evidence of lithium transport having been dominantly by diffusion. The uncertainty as to the value of $\beta$ one should expect for the relative diffusion of lithium isotopes in a given pyroxene grain is a reflection of the complex multisite diffusion of lithium in pyroxene. While the uncertainly in the choice of $\beta$ translates into a similar uncertainty in the calculated amplitude of isotopic fractionations, the spatial distribution of the isotopic fractionations in relation to the concentration profile of their parent element is an equally important indicator of whether diffusion was the cause of the fractionations.

To our knowledge, there have not yet been experiments directly quantifying

magnesium isotopic fractionation by diffusion in pyroxene minerals. There is no reason to assume that the value of $\beta_{Mg}$ should be similar to $\beta_{Li}$, in fact, in the case of diffusion in a silicate liquid, $\beta_{Li}$ is about four times larger than $\beta_{Mg}$ (Richter et al., 2003, 2008). The same is true for lithium diffusion in olivine where Richter et al. (2017) reported $\beta_{Li}$ =0.4±0.1 compared to $\beta_{Mg}$ =0.09±0.05 estimated by Sio et al. (2018). For lack of more direct evidence, we will assume that this difference between $\beta_{Mg}$ and $\beta_{Li}$ also applies to pyroxenes, yielding an estimate of $\beta_{Mg} \sim \beta_{Li}/4 \sim 0.1$.

The only laboratory study to date of isotopic fractionation associated with Fe-Mg interdiffusion in olivine is by Sio et al. (2018) who reported a value of $\beta_{Fe}$ = 0.16±0.09. The diffusion couple used in their experiment juxtaposed olivine with a magnesium number mg# = 83.4 (mg# = Mg/(Mg+Fe) atomic) with olivine with mg# = 88.8. The high magnesium content diluted the kinetic isotope fractionation of magnesium to the extent that they were not able to directly resolve $\beta_{Mg}$. They did however make an estimate of $\beta_{Mg}$ using the anticorrelation of the isotopic fractionation of magnesium and iron in olivine of $\beta_{Mg} \sim \beta_{Fe}/2$ derived from earlier studies of natural samples (Sio et al., 2013; Oeser et al., 2015) to estimate a value of $\beta_{Mg}$ = 0.09±0.05. These values of $\beta_{Fe}$ and $\beta_{Mg}$ are reasonably consistent with values reported by Oeser et al. (2015) based on the iron and magnesium isotopic fractionation of seven zoned terrestrial olivine grains that gave an average estimate of $\beta_{Fe}$ = 0.161±0.071 and $\beta_{Mg}$ = 0.084±0.019 (uncertainty of 1σ calculated from data in their Table 1). Given these results, we will use $\beta_{Mg}$ = 0.1 to calculate the relative mobility of magnesium isotopes in olivine.

## 4. Parameters for Calculating the Diffusion Rate in Pyroxene and Olivine

The one-dimensional mass conservation equation for calculating transport by diffusion in a mineral grain can be written as

$$\frac{\partial \rho}{\partial t} = \left(\frac{1}{r^n}\right)\frac{\partial}{\partial r}\left(r^n D_{(T,X)}\frac{\partial \rho}{\partial r}\right) \quad (1)$$

where is ρ molar density, $D_{(T,X)}$ is the diffusion coefficient that depends on temperature $T$ and composition $X$, $n = 0$ makes it applicable to a slab, $n = 1$ for a cylinder, and $n = 2$ for a sphere. The complete mathematical problem requires initial and boundary conditions, a temperature history $T(t)$, and a constitutive equation for the dependence of the diffusion coefficient on mineral composition and thermodynamic state. The diffusion coefficients in the various applications of Eqn. (1) are specified using the following parameterizations. For the magnesium diffusion coefficient in pyroxene we use $D_{Mg} = 2.77\times10^{-3}\, e^{-E/RT}$ $cm^2s^{-1}$ with $E = 320$ kJ, the gas constant $R = 8.314$ J $mol^{-1}$ $K^{-1}$ and $T$ the absolute temperature (Muller et al., 2013). The diffusion coefficient in olivine is calculated as $\log[D_{Fe-Mg}] = -5.21 - 201000/2.303RT + 3(X_{Fa} - 0.1) + (1/6)\log(fO_2/10^{-7})$, taken from Dohmen and Chakraborty (2007b,c) where $D_{Fe-Mg}$ is in units of $cm^2$ $s^{-1}$, $R$ and $T$ as above, $X_{Fa}$ is the mole fraction fayalite, and $fO_2$ is the oxygen fugacity in Pascals. This parameterization is for magnesium diffusing along the c-axis of olivine. The diffusion coefficients along the a- and b-axes are equal and smaller than along the c-axis by a factor of about six (Dohmen et al., 2007a). The lithium diffusion coefficient in pyroxene minerals is calculated using $D_{Li} = 2.4\times10^5\, e^{-E/RT}$ $cm^2$ $s^{-1}$ with $E$=330 kJ and $R$ and $T$ as above. This parameterization was derived from experiments run at $\log fO_2 \sim -12$ with $fO_2$ in bars (for details see Richter et al. 2014). Figure 2 shows the diffusion coefficients for lithium and magnesium in pyroxene as a function of temperature calculated using these parameterizations and that of magnesium in olivine for three choices of the mole fraction fayalite. The lithium diffusion coefficient as a function of temperature plotted in Fig. 2 is for an oxygen fugacity of $10^{-12}$ bars.

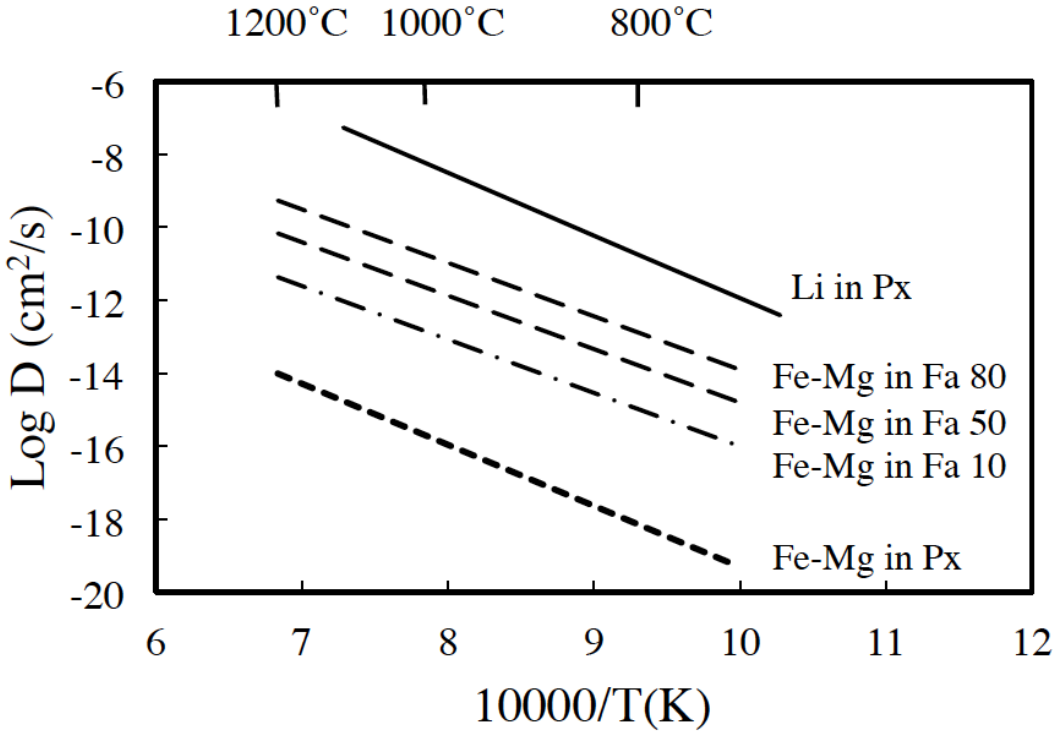


**Figure 2.** Summary of diffusion coefficients of lithium in pyroxene and of magnesium (i.e., Fe-Mg exchange) in pyroxene and olivine as a function of temperature. The line representing the diffusion coefficient of lithium in pyroxene is a best fit to the combined data from experiments by Coogan et al. (2005) and Richter et al. (2014) run at log $fO_2$ = –12 and experiments by Caciagli-Warman (2010) run at log $fO_2$ = –10.3. The diffusion coefficient of magnesium in pyroxene was calculated using the parameterization given by Muller et al. (2013). The magnesium diffusion coefficient along the c-axis of olivine as a function of temperature for three different fayalite contents was calculated using the parameterization given by Dohmen and Chakraborty (2007b,c) with the oxygen fugacity corresponding to the FMQ buffer.

## 5. Analytical Methods

A variety of methods were used to analyze the major element and lithium composition, along with the magnesium and lithium isotopic fractionation across pigeonite grains from Shergotty and the magnesium isotopic fractionation across a large olivine grain from Apollo sample 15555.

A backscattered electron (BSE) image of a large pigeonite grain (SH3) from Shergotty and quantitative color maps of MgO, FeO, and $Na_2O$ concentration were obtained with a TESCAN LYRA3 scanning electron microscope equipped with two Oxford 80 $mm^2$ silicon drift x-ray detectors. A 256×256 quantitative map was made using Oxford AZtec software and exported to Wavemetrics Igor software for further processing. In the case of the MgO and FeO maps only data from pyroxene points were plotted. In order to reduce noise, smoothing was done by averaging each pixel with the surrounding eight pixels. Major element profiles across pigeonite grains from Shergotty were also measured with a Zeiss Evo 60 SEM operated at 20kV and equipped with an Oxford Instruments Aztec XMax 50 silicon drift detector. The data were reduced with AZtec software and have a precision of 1% relative.

The lithium abundance along with the lithium and magnesium isotopic composition was measured along traverses across a number of pigeonite grains from Shergotty using the CAMECA 1270 ion probe at the Centre de Recherches Pétrographiques et Géochimiques, Nancy, France. The analytical methods used for these ion probe measurements are the same as described in Richter et al. (2016). Lithium and magnesium isotopic compositions measured by secondary ion mass spectrometry can have significant instrumental mass fractionation (IMF) effects that depend on composition. The IMF of lithium and magnesium as a function of pyroxene composition (Figs. B1 and B2 in Appendix B) was determined by measuring the isotopic composition

of a set of pyroxenes that were synthesized for this purpose as described in Appendix B. In the case of lithium the uncertainty of the IMF correction as a function of composition is much the same as the 2□ error of the individual isotopic measurements (see Fig. B1 in Appendix B) and therefore no IMF correction other than subtracting a constant 36.9 ‰ (i.e., the average of measured lithium isotopic composition of the synthetic pyroxenes). Subtracting 38.1‰ from the measured □$^{7}$Li at spots across Shergotty pyroxene grains makes average of the data set close to zero. Because we are only interested in changes in the isotopic composition along a transect (i.e., the isotopic fractionation) we are free to shift the data set by any fixed amount for convenience of presentation. When we report the 2σ uncertainty of lithium isotopic measurements across Shergotty pyroxene grains we use 2σ error of 50 repeated measurements made at each spot. In the case of the magnesium isotopes there is a resolved slope to the IMF as a function of the enstatite fraction of pyroxene (see Fig. B2 in Appendix B). The 2σ uncertainty bounds around the regression line is a function of the enstatite fraction and much larger than the uncertainty of the individual measurements. Accordingly, when we report the uncertainty of IMF-corrected $\delta^{26}$Mg data measured across pyroxene grains from Shergotty we use the 2σ uncertainty bound of the IMF as a function of the enstatite fraction at the spot where the magnesium isotopic composition is measured.

A FeK$_\alpha$ map of the large zoned olivine grain and surrounding minerals from lunar basalt 15555 was made by Larry Taylor at the University of Tennessee using a CAMECA SX-50 electron microprobe (EMP). The olivine composition was measured along a transect across the large olivine grain using a JEOL JSM-5800LV scanning electron microscope equipped with an Oxford Link ISIS-300 energy dispersive X-ray microanalysis system (EDS) that gives a precision of better than 1% relative for the forsterite content. The magnesium isotopic composition was measured along the same

transect using the CAMECA 1270 ion microprobe at Centre de Recherches Pétrographiques et Géochimiques in Nancy, France using analytical methods described in Chaussidon et al., (2017). The IMF of magnesium as a function of forsterite composition of olivine was determined by measuring the isotopic composition of a set of olivine grain that were synthesized specifically for this purpose as described in Appendix B. The slope and uncertainty of the magnesium IMF correction for the $^{26}Mg/^{24}Mg$ data as a function of the forsterite fraction of olivine is shown in Fig. B3. The uncertainty of the IMF correction is much larger than uncertainty of the individual isotopic measurements and therefore we use the 2□ uncertainty of the IMF correction as a function of the forsterite fraction of olivine as the measure of the uncertainty of the IMF-corrected $\delta^{26}Mg$ measured across the olivine grain from lunar basalt 15555.

## 6. Lithium and Magnesium-Zoned Pyroxene (Pigeonite) Grains from Shergotty

### 6.1. Previous studies of Shergotty

Shergotty is a basaltic meteorite from Mars described by Stolper and McSween (1979) as a pyroxene-rich cumulate (~70% pyroxene) with a foliated texture of preferentially oriented large pyroxene prisms with an average grain size of about 450 μm. It has a crystallization age of 165±4 Ma (Nyquist et al., 2001). A number of previous studies of Shergotty (see for example Laul et al.,1986; Udry et al., 2016) have focused on zoned pyroxene grains such as the one shown in Fig. 3. Stolper and McSween (1979) used laboratory experiments to interpret the major element zoning in terms of Mg-rich pyroxene cores that began to crystallize at about 1240˚C and then developed zoned rims as the temperature dropped below about 1140˚C. The cooling responsible for the Fe-Mg zoning could have been associated with shallow intrusion or extrusion (Lentz et al., 2001; McSween et al. 2001). These two papers noted an additional important aspect of the zoning of Shergotty pyroxenes: the lithium concentration measured in the rims was

significantly lower than that in the cores. The lower lithium concentration in the rims is opposite of what one would expect for crystallization zoning given that lithium is generally assumed to be somewhat incompatible in pyroxene and thus in a closed system the concentration in the melt should increase as crystallization proceeds. Lentz et al. (2001) and McSween et al. (2001) suggested that the low lithium concentration in the rims might be the result of crystallization from a melt with initially about 2% water that lost lithium by partitioning into a water-rich fluid that exsolved from the melt during ascent and decompression. This required them to assume that lithium has a strong tendency to partition into aqueous fluids but they made no quantitative assessment of the partition coefficient that would be required. The general idea of lithium having been lost by fractionation into an aqueous fluid has also been suggested to explain lithium zoning of minerals from several other martian meteorites (see, for example, Udry et al., 2016) despite Treiman et al. (2006) having pointed out that in order for the required large amount of lithium to have been lost to an aqueous phase derived from a melt with 2% initial water, the partitioning of lithium from the melt into the aqueous phase would have to be thirty times larger than the experimentally constrained value. The inadequacy of even much larger initial amounts of water to account for the large loss of lithium from shergottite melts led Treiman et al. (2006) to suggest that the lithium zoning in pyroxenes in Shergotty very likely involved intracrystalline diffusion. Udry et al. (2016) also argued that post-crystallization diffusion played a role in producing the zoning of pyroxenes from Shergotty. These propositions that diffusion was responsible for some of the lithium zoning in pyroxene grains in Shergotty can be tested quantitatively, as shown below, by measuring the variation of the lithium isotopic composition across the grains.

There have been several estimates of the time scales involved in the cooling and crystallization of Shergotty using a variety of approaches. Muller (1993) used

clinopyroxene microstructure to infer a cooling rate for Shergotty of $2\times10^{-3}$°C/h. Lentz and McSween (2000) compared crystal size distributions from Shergotty with those from experiments by McCoy and Lofgren (1999) to infer that the system cooled at a rate between 0.1 and 0.5 ˚C/h with the cores having grown between 11 and 53 days and the entire grain between 19 and 93 days (see their Table 2). Even a simple back-of-the-envelope calculation would show that these cooling rates are all much too slow for any lithium zoning to have been preserved.

### 6.2. Elemental and isotopic zoning of a pigeonite grain from Shergotty

A backscattered electron (BSE) image of a large pigeonite grain (SH3) from Shergotty and quantitative color maps of MgO, FeO, and $Na_2O$ concentration are shown in Fig 3. The BSE image also shows the ion probe spots where magnesium isotopes were measured (the larger spots) and where both the lithium abundance and isotopic compositions were measured (the smaller spots). The $Na_2O$ map allows one to see the distribution of maskelynite (transformed from plagioclase by shock) and devitrified glass around the pyroxene grain. Small areas of maskelynite and glass were also trapped within the large pyroxene grain. The extent of what was late-crystallizing plagioclase and melt suggests that the section of grain SH3 shown in Fig. 3 was surrounded by melt during its crystallization except for two small portions along the edge. The MgO and FeO maps show the continuity of the zoning along the entire edge of the grain. The FeO map includes two lines along which the major element data shown in Fig. 4 was measured. Similar data across other pyroxene grains from Shergotty are given in Appendix A.

The lithium abundance and both the lithium and magnesium isotopic composition was measured along traverses across a number of pigeonite grains from Shergotty using the CAMECA 1270 ion probe at the Centre de Recherches Pétrographiques et

Géochimiques, Nancy, France. The analytical methods and instrumental mass fractionation are discussed in Section 4. The MgO concentration along line 3.1 of grain SH3 together with the magnesium isotopic fractionation, and the Li concentration and isotopic fractionation measured at the spots running from the top left to lower right in the BSE image in Fig. 3 are shown in Fig. 5.

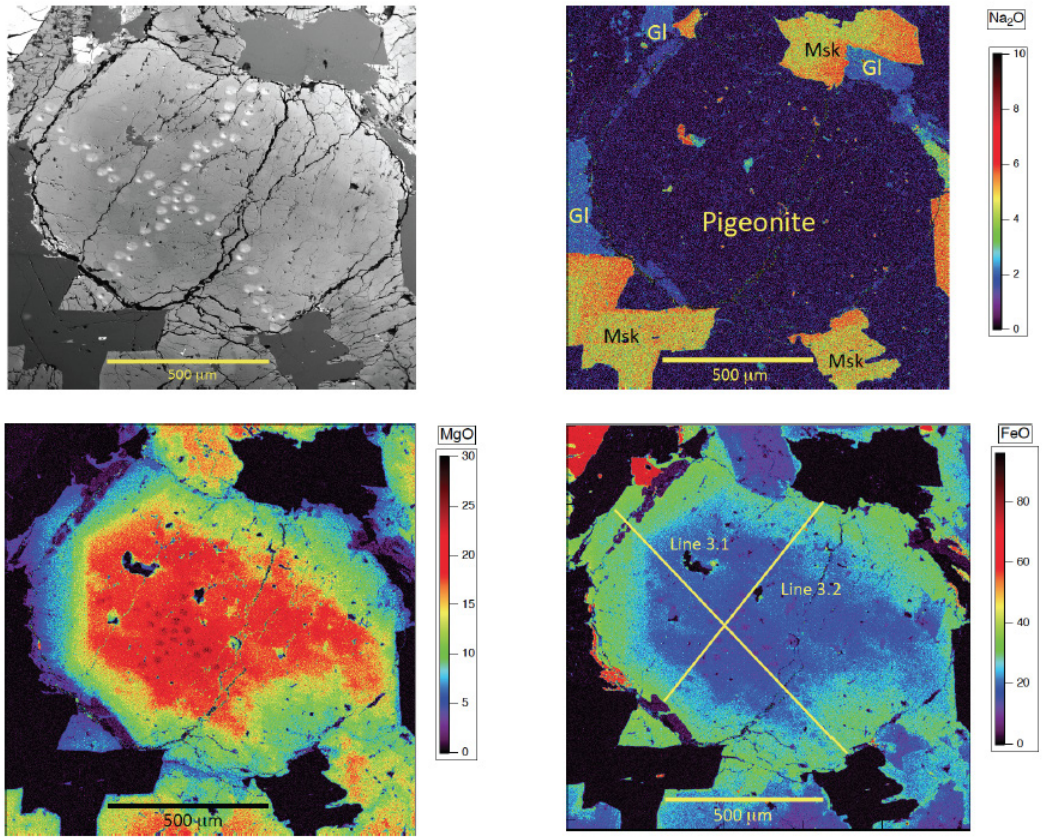


**Figure 3.** Top left: Backscattered electron image of Shergotty pigeonite grain SH3 and false color maps of $Na_2O$, MgO, and FeO with color scales in wt%. The larger light-colored spots in the backscattered electron image are ion probe spots from the magnesium isotopic measurements; the smaller spots are from the lithium abundance and isotopic measurements.

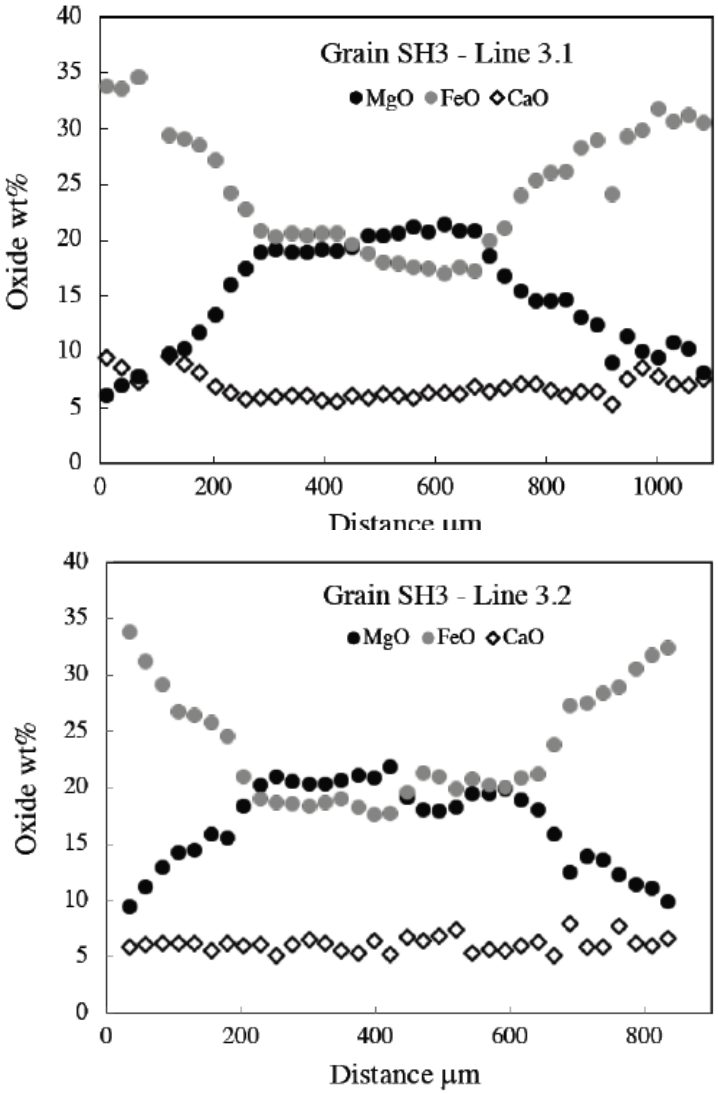


**Figure 4.** The two panels show the wt% FeO (grey circles), MgO (black circles), and CaO (diamonds) measured along lines 3.1 and 3.2 across Shergotty pigeonite grain SH3 shown in the FeO map in Fig. 3.

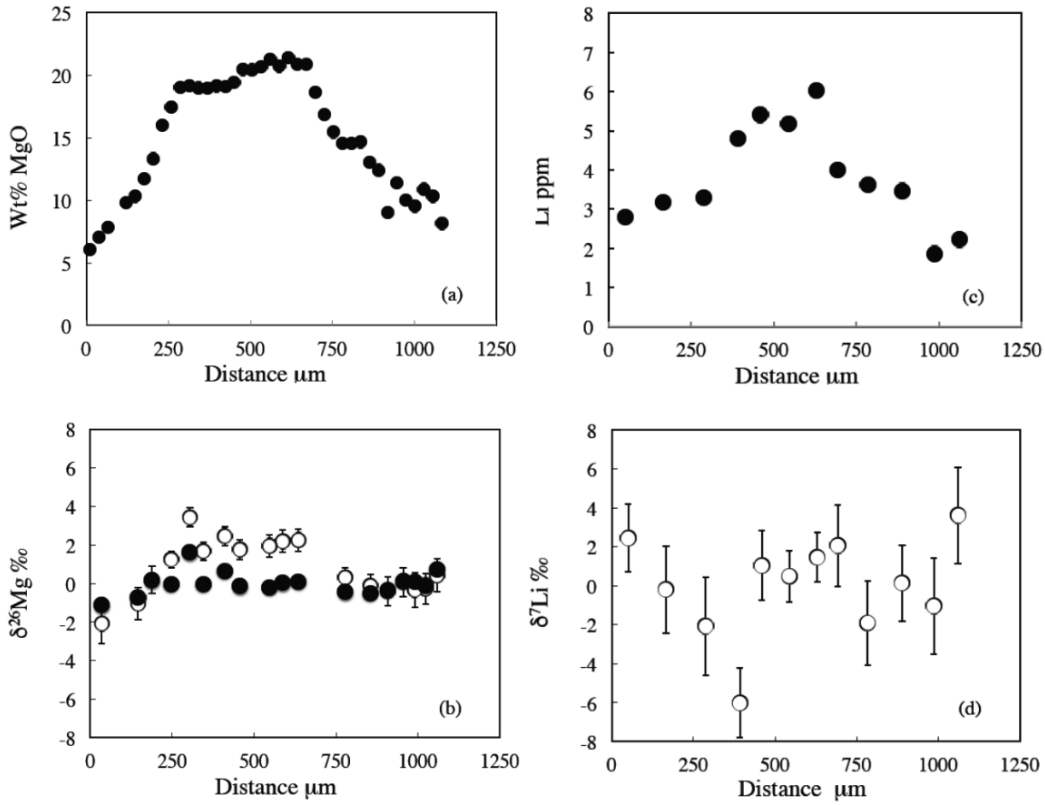


**Figure 5.** MgO and Li concentration and isotopic fractionation data measured across Shergotty pigeonite grain SH3 shown in Fig.3. The MgO concentration was measured along line 3.1 and the Li concentration along with the lithium and magnesium isotopic composition was measured at the ion probe spots that more or less follow line 3.1. The magnesium isotopic data shown as unfilled circles with error bars was corrected for the IMF as a function of the local enstatite fraction of the pigeonite whereas the black circles show the uncorrected values. The 2σ error of the $\delta^{26}$Mg IMF-corrected data reflects the uncertainty of the matrix corrections for the IMF (see Fig. B2 in Appendix B). The lithium isotopic fractionation did not require IMF correction (see Fig. B1 in Appendix B). The errors bars of the lithium isotopic data points are ±2σ, derived from the statistics of 50 repeated measurements at spot.

One might be inclined to argue that the Li and MgO concentration data shown in Fig. 5 already imply that the zoning of this pyroxene grain must be mainly the result of crystallization from an evolving melt with little or no diffusion. The argument would be based on the similar length scale of the Li and MgO zoning despite the orders of magnitude faster diffusion of lithium in pyroxene compared to magnesium (see Fig. 2) and therefore, had diffusion been important in causing the magnesium zoning, the faster diffusing lithium would have become uniform long before the iron-magnesium exchange had affected the outer 400 μm of the grain. There are several potential flaws in this line of reasoning. It could be that the lithium had in fact become uniform in terms of chemical potential and that the lithium zoning is due to the dependence of the activity coefficient of lithium on the major element zoning of pyroxene. This, however, can be ruled out based on experimental partitioning data (see Appendix C) that show that for the Li chemical potential to be uniform the Li concentration would increase with decreasing MgO in pyroxene, which is opposite to what is observed. Another possibility is that the lithium and magnesium zoning might be due to processes during different stages in the evolution of the system. For example, the elemental data on its own cannot rule out a two-stage evolution: Stage 1 with crystallization and/or diffusion producing the magnesium zoning on a time scale that was sufficiently long to have homogenized the much faster-diffusing lithium, followed by Stage 2 with a short duration sufficient to allow for the diffusive zoning of lithium but too short to have significantly affected the prior zoning of magnesium. The discussion in the next section shows how isotopic measurements are used to distinguish between otherwise possible scenarios for the thermal evolution of Shergotty.

## 6.3 Constraints on the thermal evolution of Shergotty from magnesium zoning and isotopic fractionation of pigeonite grain SH3

Crystallization calculations using the alphaMELTS 1.8 front-end (Smith and Asimow, 2005) for the MELTS thermodynamic model (Ghiorso and Sack, 1995) hereafter referred to as "MELTS calculations" were used to explore the implications of pigeonite grain SH3 having a relative homogeneous core with similar ~20 wt% FeO and MgO. The initial melt composition used for the calculation is the bulk composition of Shergotty that Stolper and McSween (1979) used in their equilibrium crystallization experiments. The validity of the MELTS calculations was tested by comparing the minerals in equilibrium with the melt as a function of temperature predicted by MELTS with experimental data reported by Stolper and McSween (1979). The panel on the left of Fig. 6 shows the result of the calculation along with the temperature at which Stolper and McSween (1979) reported the first appearance of each major mineral. The MELTS calculation is in excellent agreement with the experimental data for the temperature of first appearance of the two pyroxenes (pigeonite and augite) and close to that for plagioclase.

The black lines in the panel on the right of Fig. 6 shows the results of a MELTS batch crystallization calculation for the composition of pigeonite in equilibrium with melt at temperatures from T = 1235 to 1055˚C. Perfect batch melting, by definition, assumes that the bulk composition of all minerals are continuously in equilibrium with the melt and thus perfectly homogeneous. While this can account for the core of a grain like SH3, it cannot account for the zoned portion of the grain. For this reason, a second set of pigeonite compositions versus temperature was calculated using MELTS assuming batch melting down to T = 1135˚C, which can explain the homogeneous core of grain SH3 with FeO = MgO ~ 20 wt%, followed by perfect fractional crystallization (dashed lines) to

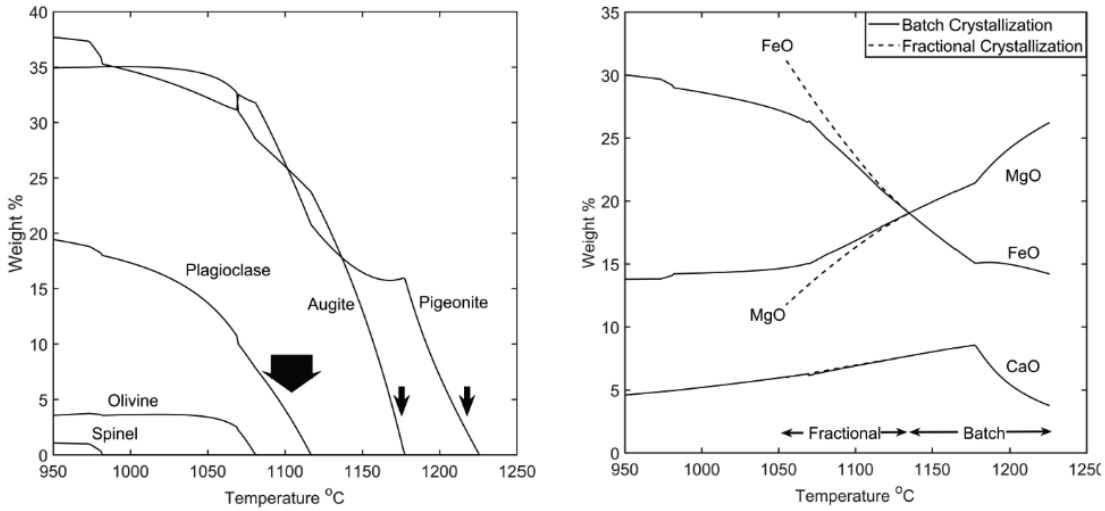


**Figure 6.** The panel on the left shows the cumulative wt% of minerals in equilibrium with melt as a function of temperature calculated using MELTS assuming batch crystallization of a system with the same bulk composition used by Stolper and McSween (1979) in their equilibrium crystallization experiments. The temperature of first appearance of these minerals in the experiments quenched at different temperatures is shown by the arrows, which from right to left show the highest temperature at which pigeonite, augite, and plagioclase were found in the quenched material from the Stolper and McSween (1979) experiments (see their Table 4). The broad arrow for the first appearance of feldspar reflects that a range of temperatures rather than a specific temperature was reported. The panel on the right shows the results of a MELTS calculation for the evolution of the major oxide concentration in pigeonite assuming batch crystallization (black lines) of a system with same bulk composition as used for the results shown in the panel on the left. At T=1135˚C the concentration of FeO and MgO are both about 20 wt%, which is a good approximation to the measured composition of the core of pigeonite grain SH3 (see Fig. 5). The dashed lines show how the pigeonite composition evolves when MELTS is used to calculate perfect fractional crystallization for T<1135˚C.

account for the increase of FeO and decrease of MgO in the outer portions of SH3. Batch crystallization requires that the system evolve sufficiently slowly in order for diffusion to continuously homogenize both the melt and the minerals and to maintain equilibrium between the pigeonite and the melt. Fractional crystallization, on the other hand, requires the system to evolve sufficiently fast that mass transport by diffusion within the mineral grains is negligible so that each increment of crystallization is isolated from any further exchange with the melt. The MELTS batch crystallizatiuon calculation shown in the right hand panel of Fig. 6 is interpreted as implying that pigeonite grain SH3 was in equilibrium with the melt at T = 1135˚C with FeO = MgO ~ 20 wt% and then fractionally crystallized as it rapidly cooled to develop the zoned rims with increasing FeO and decreasing. The mass fraction of melt at T = 1135˚C when the fast cooling begun is still large, about 65%.

A lower bound for the duration of the slow crystallization or post-crystallization homogenization of the pigeonite core of grain SH3 can be estimated by the time $t > r^2/D$ required to homogenize a cylinder or a sphere of radius $r$ given a value for the diffusion coefficient $D$ (see Figs. 5.3 and 6.1 in Crank, 1975). Using $r$=200 □m (0.02 cm) as the radius of the core of grain SH3 and $D = 3.7\times10^{-15}$ cm$^2$ s$^{-1}$ at T=1135˚C (from Muller et al., 2013) yields an estimate that the core of SH3 would be homogenized if it had been at T=1135˚C for more than $10^{11}$ seconds (~3200 years). This calculation shows that the Lentz and McSween (2000) estimate that the core of Shergotty pyroxene grains grew for between 11 and 53 days is far too short a time to have produced even roughly homogeneous cores.

The question of how the zoned portion of pigeonite grain SH3 might have been produced is explored using a numerical calculation to solve the mass conservation equation for the evolution of the magnesium concentration and isotopic fractionation.

The conservation Eqn. (1) with n = 2 for a sphere written in terms of nondimensional variables is

$$\frac{\partial \rho_i}{\partial t'} = D'_{(t')}\left(\frac{\partial^2 \rho_i}{\partial r'^2} + \frac{2}{r'}\frac{\partial \rho_i}{\partial r'}\right) \tag{2}$$

where $\rho_i$ is a measure of the concentration of an element or isotope $i$, $t'=(D_{To}/r_{gr}^2)t$ with $t$ the dimensional time in seconds, $r'=r/r_{gr}$ with $r_{gr}$ the final radius of the grain in centimeters, $D'_{(t')}=D_{(t')}/D_{To}$ with $D_{To}$ the diffusion coefficient in units of $cm^2\ s^{-1}$ at the temperature $T_o$ when diffusion begins. $D_{(t')}$ is the diffusion coefficient at time $t'$ determined by the temperature $T(t')$ for the assumed cooling rate. When Eqn. (2) is used for the magnesium isotopes it is assumed that the diffusion coefficient of $^{24}Mg$ is larger than that of $^{26}Mg$ by a factor of $(26/24)^{\beta}$ with $\beta = 0.1$. Nondimensional variables are used here and in subsequent sections in order that the results of a given calculation can be used for the evolution of grains of different size $r_{gr}$, and different reference diffusion coefficients $D_{To}$ corresponding to the temperature $T_o$ when diffusion is assumed to have begun. One can calculate the dimensional cooling rate for any particular grain by redimensionalizing time as $t=t'(r_{gr}^2/D_{To})$ where $t'$ is the nondimensional time it took to fit zoning of the grain measured in units $r'$.

An issue that can be explored using the numerical model for the magnesium evolution of a pyroxene grain is whether the zoned rim of grain SH3 could be explained by diffusion of magnesium out of an initially homogeneous grain of fixed size. Such a case is specified by $r' = 1$ for all $t'$, an initial condition $\rho_{Mg}$ = 20 wt% MgO (i.e., approximately the measured wt% MgO in the core of the grain) from $r' = 0$ to 1 at $t'=0$ and $\rho_{Mg}$ = 5 wt% MgO (i.e., the approximate wt% MgO at the grain edge) at $r' = 0$ and1 for $t'>0$. The magnesium isotopic composition of the grain is assumed to be uniform ($\delta^{26}Mg = 0$ ‰) at $r'$ from 0 to 1 and subject a boundary condition $\delta^{26}Mg = 0$‰ at $r' = 0$

and 1 for all $t' > 0$. This boundary condition assumes that there is no significant equilibrium isotopic fractionation of magnesium between pyroxene and melt and that the there is a sufficiently large amount of melt that the isotopic composition of the melt is not significantly altered by the flux of isotopically fractionated magnesium out of the grain. The results of such a calculation run to $t' = 0.01$ with the temperature decreasing linearly by 100˚C over the course of the calculation are shown in Fig. 7. The calculated magnesium isotopic fractionation is locally positive in the boundary layers, as a result of $^{24}Mg$ having diffused out of the grain faster than $^{26}Mg$. The issue here is not so much the time scale but rather that a large isotopic fractionation has developed, which when

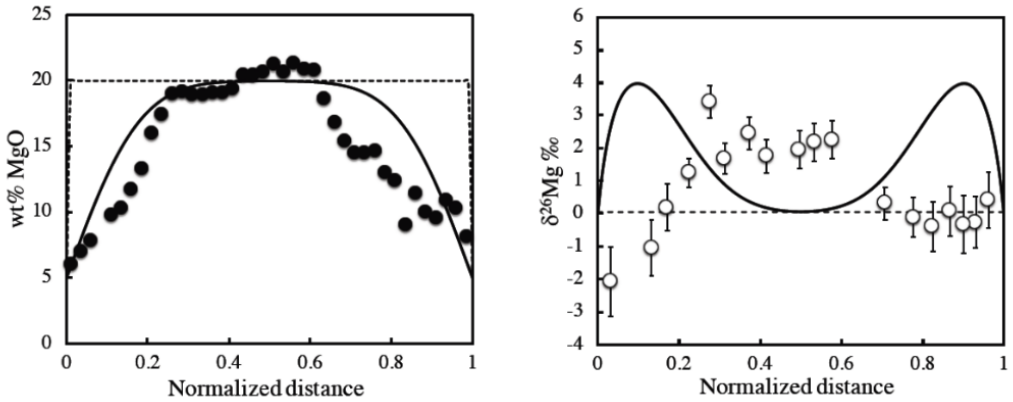


**Figure 7.** Results of a numerical calculation for the diffusive evolution of magnesium after a nondimensional time t' = 0.01 starting from a uniform grain with 20 wt % MgO (dashed line in the panel on the left) subject to a boundary condition of 5 wt% MgO at each edge of the grain. The measured wt% MgO along line 3.1 of Shergotty grain SH3 is shown by the black circles. The panel on the right shows the calculated magnesium isotopic fractionation associated with the diffusion of magnesium out of the grain calculated using ß=0.1. The open circles show the matrix-corrected magnesium isotopic fractionation across line 3.1. The initial isotopic ratio of magnesium in the grain was taken as $\delta^{26}Mg = 0$ ‰, which was also used as the boundary condition at r' = 1.

compared to the measured data, makes it obvious that the magnesium zoning of the rim of grain SH3 could not have been the result of any significant amount of diffusion after the grain had grown to its present size.

A numerical calculation was also used to model a case where diffusion takes place while the zoned portion of a spherical grain is growing. The grain growth in the model starts with the grain already having a homogeneous core at $t' = 0$ with a radius $r' = 0.4$ (i.e., 40% of the final radius) and that for $t'$ between 0 and $t_{xtl}$ the grain grows from $r' =$ 0.4 to 1 with the volume increasing linearly with time as shown in Fig. 8. Grain growth ends at $t' = t_{xtl}$, with diffusion continuing until $t' = 4t_{xtl}$, by which time the temperature is sufficiently low that diffusion has become negligible. The temperature is assumed to decrease linearly with time as $T(t') = T_0 - \Delta T t'$ where $T_0 = 1135$˚C and $\Delta T = 100$˚C is the temperature change over each nondimensional time interval $t_{xtl}$. Figure 8 shows the dimensional temperature as a function of time $t'$ used to calculate $D'_{(t')}$ in the Muller et al. (2013) parameterization of the magnesium diffusion coefficient in pyroxene (see Fig. 2). The initial conditions at $t' = 0$ assumes uniform concentrations of $^{24}$Mg and $^{26}$Mg between $r' = 0$ and 0.4 and $\delta^{26}$Mg = 0‰. The magnesium concentration ($^{24}$Mg +$^{26}$Mg) applied at the growing edge of the grain is assumed to decrease linearly as $C(r') = C_o - \Delta C\ t'$ with $C_o$=20 and $\Delta$C is such that the concentration is reduced to 5 during the period of grain growth ($t' = 0$ to $t_{xtl}$) and C = 5 at $r' = 1$ for $t' > t_{xtl}$. The decrease of the magnesium concentration imposed at the growing edge of the grain is meant to reflect the decreasing magnesium concentration of material added to the grain during fractional crystallization as shown in Fig. 6. The isotopic composition at the grain edge is assumed to be the same as the initial value in the core (i.e., $\delta^{26}$Mg = 0 ‰ at $r'(t')$ for all $t'$ from 0 to $4t_{xtl}$).

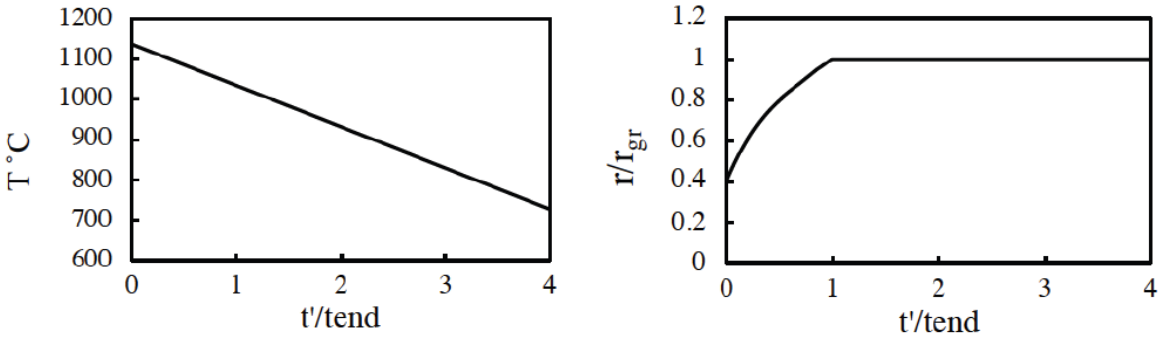


**Figure 8.** The panel on the left shows the linear cooling assumed in the magnesium evolution calculations of a growing spherical grain as a function of the nondimensional time t' measured in units $t_{xtl}$. $t_{xtl}$ is the nondimensional time over which the grain grew to its final size. The panel on the right shows the growth the fractional radius r/ $r_{gr}$ ($r_{gr}$ is the final radius of the model grain) as a function of time. The grain growth corresponds to equal amounts of volume added per unit time. The portion of the grain from $r/r_{gr}$= 0 to 0.4 (not shown) is assumed to be the core with an initially uniform elemental and isotopic composition.

The model of a growing grain was used to explore how fast the system must have cooled to account for the magnitude of magnesium isotopic fractionations measured in the rim of grain SH3. Figure 9 shows the calculated wt% MgO and the magnesium isotopic fractionation across a model grain that grew a rim with decreasing wt% MgO for the interval $t'$ = 0 to 0.08 while the temperature decreased and the grain grew as shown in Fig. 8 for a nondimensional time $t'$ = 0.08. The cooling and diffusion continuing until $t'$ = 0.24.

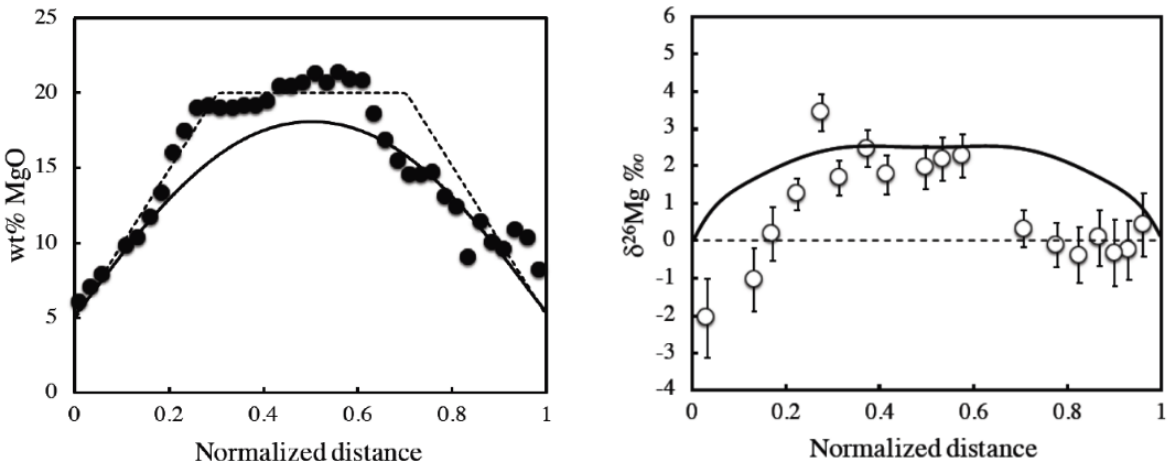


**Figure 9.** Panel on the left shows the calculated evolution of the wt% MgO (solid black curve) starting from a core having the extent and wt% MgO shown by the horizontal portion of the dashed line. The slopping dashed lines show the wt% MgO the grain would have if there had been no diffusion. The black circles show the wt% MgO measured along line 3.1 across Shergotty grain SH3. The panel on the right shows the calculated magnesium isotopic fractionation along with the matrix-corrected fractionation shown as open circles. The model grain crystallized over a nondimensional time t' = 0.08 with the temperature decreasing and the radius evolving as shown in Fig. 8. Diffusion continued to t' = 0.24 by which time the system had cooled to the point that diffusion had become negligible. The isotopic fractionation was calculated using ß = 0.1 for an initially unfractionated grain.

The wt% MgO and isotopic fractionation profiles shown in Fig. 9 were calculated for a nondimensional time $t' = (D_{To}/r_{gr}^2)t = 0.08$ where $t$ is the dimensional time, $D_{To} = 3.7\times10^{-15}$ cm$^2$ s$^{-1}$ is the magnesium diffusion coefficient from Muller et al. (2013) for $T$ = 1135˚C, the temperature $To$ when diffusion was assumed to have begun, and $r_{gr} = 0.05$ cm is the final radius of the grain. The dimensional time $t$ corresponding to $t' = 0.08$ is then $t = 0.08\ (r_{gr}^2/D_{To}) = 5.4\times10^{10}$ seconds (~1700 years). Given that Fig. 9 shows that

the core is no longer homogeneous and that the magnesium isotopic fractionation is as large as the measured data would allow, it follows that the grain must have grown the rim in less than about 1700 years and that the cooling rate must have been faster than 0.05˚C $y^{-1}$.

Because lithium diffuses in pyroxenes many orders of magnitude faster than magnesium, one can anticipate that modeling the lithium zoning of grain SH3 in the same way as done for magnesium will result in a much shorter bound on the duration for the crystallization of the rim and a correspondingly faster cooling rate. However, it is precisely the sluggishness of magnesium diffusion in pyroxene that led to the conclusion that a very long time at high temperature was required for grain SH3 to have a homogeneous core.

### 6.4 Constraints on the thermal evolution of Shergotty from lithium zoning and isotopic fractionation of pigeonite grain SH3

Lithium diffuses much faster than magnesium or any other major element in pyroxene, therefore the fact that the core of grain SH3 is relatively uniform in major element abundances (see Fig. 4) implies that it must have also been uniform in lithium. While the major element zoning of the pigeonite rim of SH3 can be explained by fractional crystallization of a closed system (see Fig. 6), the same cannot be the case for lithium, which being somewhat incompatible in pyroxene (Brenan et al., 1998 and data in Appendix C) would in a closed system increase rather than decrease toward the edge of the grain. Even accepting that the lithium budget of Shergotty was an open system, the fact that grain SH3 is zoned in lithium already implies sufficiently rapid cooling that there was not time for lithium to have become homogenized by diffusion. An explicit estimate of how fast the parent rock must have cooled can be derived by modeling the effect of lithium diffusion in pigeonite grain SH3 compared to the measured isotopic fractionation.

The numerical model used in the previous section to calculate the evolution of magnesium was modified by using the kinetic properties of lithium diffusion in pyroxene. A model calculation was first used to explore whether the lithium zoning could be due to lithium having diffused out of a grain that was initially uniform in lithium concentration and isotopic composition. As already noted, such a situation could have arisen if the growth of the grain had been sufficiently slow for lithium to have been first homogenized and the lithium zoning developing subsequently during rapid cooling by diffusion of lithium out of the fully-grown grain. Figure 10 shows the results of a model calculation for the lithium zoning after a nondimensional time $t' = 0.04$ of a grain with initially 6 ppm lithium and 1 ppm lithium at the boundary. If one only focused on modeling the lithium abundance data, it would seem that diffusion could be viable explanation of the zoning. The fact that the measured lithium concentration data are somewhat scattered around a smooth curve (i.e., the calculated profile in Fig. 10) is not particularly troubling because it is commonly observed that lithium measurements in minerals from martian meteorites tend to be quite "noisy" (see Figure 7 in Richter et al., 2016). The important point, however, is that the calculated lithium isotopic fractionation of the grain, modeled assuming an initial and boundary value of $\delta^7\text{Li} = 0‰$ and $\beta = 0.35$ clearly shows that by $t' = 0.04$ the calculated isotopic fractionation is obviously inconsistent with the measured data. The point to emphasize is that the lithium isotope measurements provide the key evidence that diffusion of lithium out of an initially uniform grain cannot be the process responsible for the lithium zoning of grain SH3.

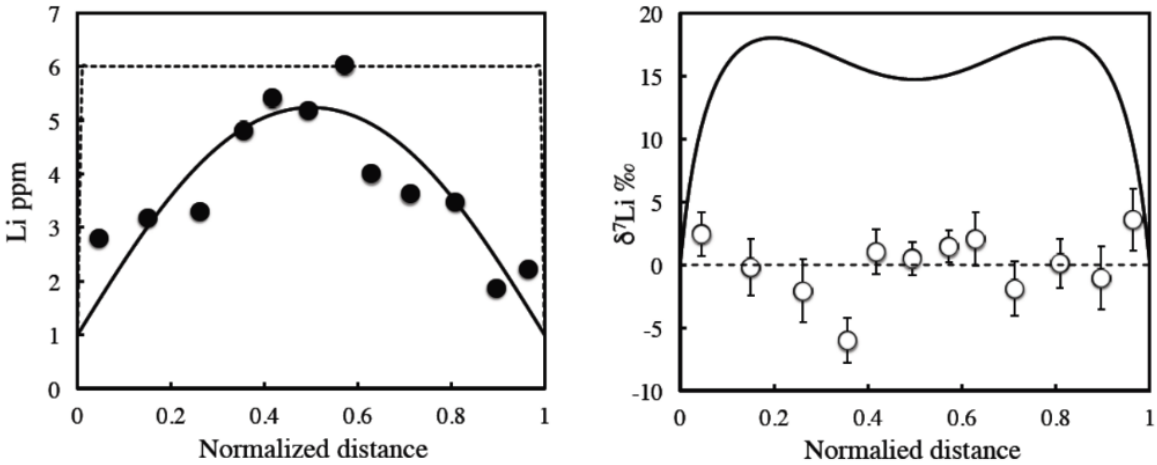


**Figure 10.** Results of a numerical calculation for the lithium abundance and isotopic fractionation due to diffusion after a nondimensional time t' = 0.04 starting from initially uniform grain interior with 6 ppm Li (dashed line) subject to a boundary condition of 1 ppm at each edge of the model grain. Distance across the grain is normalized by the grain size (i.e., r' = $r/r_{gr}$). The panel on the left shows the calculated lithium concentration profile along with black circles showing the measured lithium concentration in Shergotty grain SH3 along line SH3.1. The panel on the right shows the lithium isotopic fractionation calculated for a grain with $\delta^7$Li = 0‰ for both the initial and boundary conditions, and using ß = 0.35 to calculate the relative diffusion coefficient of the lithium isotopes. The calculated positive $^7$Li ‰ in the grain interior is due to about 50% of the lithium having diffused out of the grain with $^6$Li having been lost faster than $^7$Li.

Having shown that very little, if any, of the lithium zoning of pigeonite grain SH3 can have been the result of diffusive loss from a fully-grown grain that was initially uniform in lithium, new calculations were used to model situations where a grain was assumed to simultaneously cool and grow as shown in Fig. 8. For this calculation, the nondimensional time $t'$ is defined as $t' = (D_{To}/r_{gr}^2)t$, where $t$ is the dimensional time, $D_{To}$ is the lithium diffusion coefficient corresponding to the temperature $To$ = 1135˚C at the

time ($t' = 0$) when the rim growth began and $r_{gr}$ is the final radius of the grain. The lithium abundance at the growing edge of the grain was assumed to decrease linearly with time from an initial 5.5 ppm to 1 ppm over the period of grain growth and remaining constant thereafter. A value of $\beta = 0.35$ was used to calculate the relative diffusivity of the lithium isotopes. Figure 11 shows the results of a calculation run to $t' = 0.05$. Had the grain cooled for longer than $t' = 0.05$ the calculated lithium isotopic fractionation would have become unacceptably large. The conclusion is that the lithium isotopic fractionation measured across grain SH3 implies that the grain rim must have grown in less than about $t' = 0.1$. Using a radius of 0.05 cm for pigeonite grain SH3 and $D_{To} = 1\times10^{-7}$ cm$^2$ s$^{-1}$ for the diffusion coefficient of lithium at $T = 1135$˚C (see Fig. 2) when diffusion began, the rim of grain SH3 must have grown on a timescale of less than 2500 seconds (~40 minutes). Assuming that the temperature drop during the crystallization of the rim was of the order of 100˚C, the cooling rate must have been faster than 150˚C/h (~2˚C per minute). Because lithium diffusion in clinopyroxene depends on $f$O$_2$ (see Fig. 11 in Richter et al., 2016) an important point is that the value of the diffusion coefficient of lithium used here to dimensionalize time comes from diffusion experiments run at log $f$O$_2$ between –10.3 and –12, which is comparable to the estimates of the $f$O$_2$ of Shergotty at magmatic temperatures of log $f$O$_2$ ~ –11 by Papike (2000) and log $f$O$_2$ ~ –12 by Wadhwa (2001).

It follows from the modeling and discussion above that the both the magnesium and lithium zoning of the pigeonite grain SH3 from Shergotty was dominantly due to crystallization. The lack of isotopic evidence for any significant diffusion of lithium provides the more stringent lower bound on the rate of cooling rate of grain SH3.

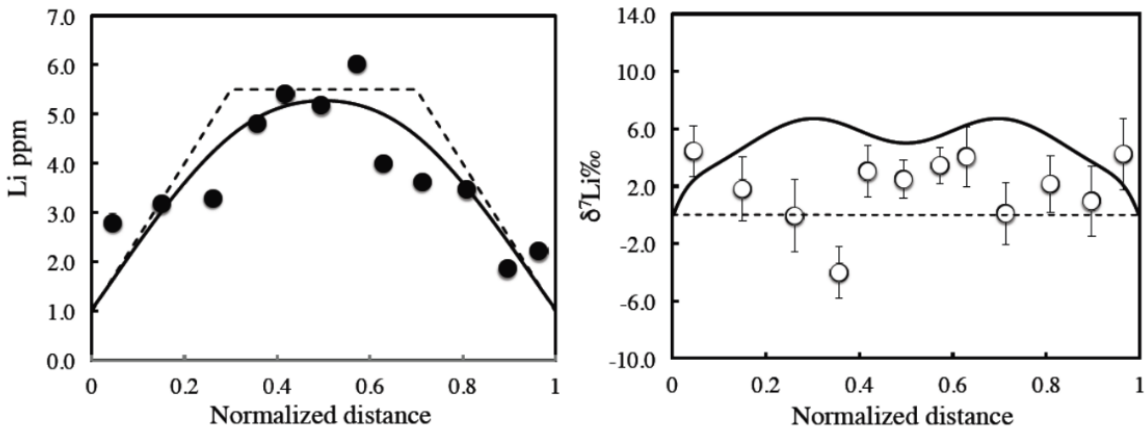


**Figure 11.** Calculated diffusive evolution as function of nondimensional time of the lithium concentration (left-hand panel) and the isotopic fractionation (right-hand panel) of an idealized spherical pyroxene grain with an initially homogeneous core (horizontal portion of the dashed lines) with subsequent growth of the rim from t' = 0 to 0.05 as the temperature dropped by 100˚C as shown in Fig. 8. The slopping dashed lines are the zoning due to the decreasing boundary concentration had there been no diffusion. The lithium isotopic fractionation was calculated assuming a value of □ = 0.35. The black circles show the measured lithium concentration and the open circles the lithium isotopic fractionation across Shergotty grain SH3, which for comparison with the calculated profile was increased by 2‰ from the values plotted in Figs. 5 and 10.

## 7. Constraints on the evolution of Mare Basalt 15555 from magnesium zoning and isotopic fractionation of olivine

### 7.1 Previous studies

The Apollo 15 mission returned a 3.3-billion-year-old olivine-normative mare basalt (15555) that because of its large size is often referred to as Great Scott (named after astronaut David Scott, who collected it). Bulk chemical analyses of Apollo 15 olivine-normative basalts were reported by Ryder and Schuraytz (2001). Basalt 15555 is a coarse-grained, porphryritic rock with about 12% rounded olivine phenocrysts, about 50% subhedral zoned pyroxene phenocrysts and a matrix dominated by poikilitic plagioclase. Schnare et al (2008) made a detailed study of the mineral modes, major-element and trace-element composition of olivine grains in the polished section 15555,257. Several early studies reported experimental data on the crystallization of a plausible parental melt of 15555 (Kesson, 1975; Walker et al., 1977). Taylor et al. (1977) modeled the Fe-Mg zoning of olivine grains as being due to diffusive exchange of iron and magnesium across an initial sharp composition contrast and estimated a cooling rate of 5°C/day. There was not, however, any independent evidence for the assumption that the Fe-Mg zoning was due to diffusion, which motivated the present study of the magnesium isotopic fractionation across the same olivine grain from 15555 as a way of determining the degree, if any, to which the zoning can be attributed to diffusion.

### 7.2. Magnesium zoning and isotopic fractionation of an olivine grain from 15555

A false color iron abundance image of zoned olivine grains from polished section 15555,172 is shown in Fig. 12. The variation of MgO and FeO measured along the white line segments across the grain on the left in Fig. 12 is shown in Fig. 13.

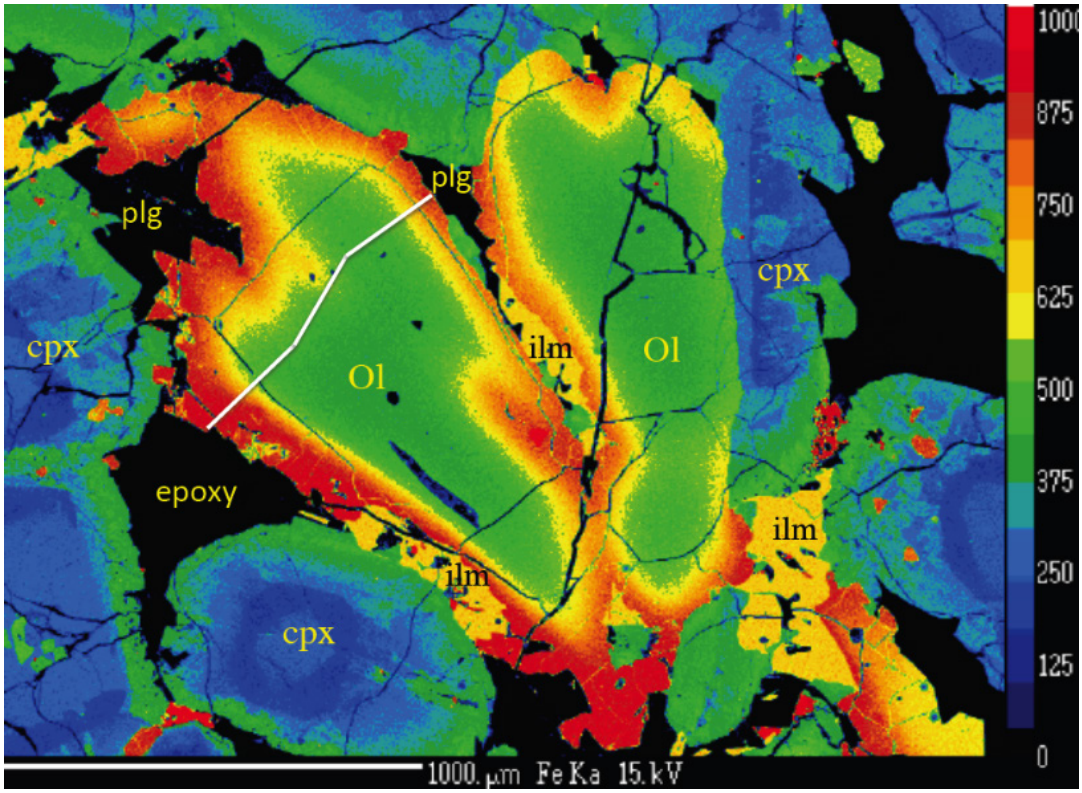


**Figure 12.** Fe Kα image of a large zoned olivine grain from mare basalt 15555 and surrounding minerals labeled as cpx for clinopyroxene, plag for plagioclase, and ilm for ilmenite. The yellow to red colors surrounding the olivine's green core reflect increasing amounts of iron. The white line segments across the grain on the left show the transect along which the major element composition and magnesium isotopic composition was measured.

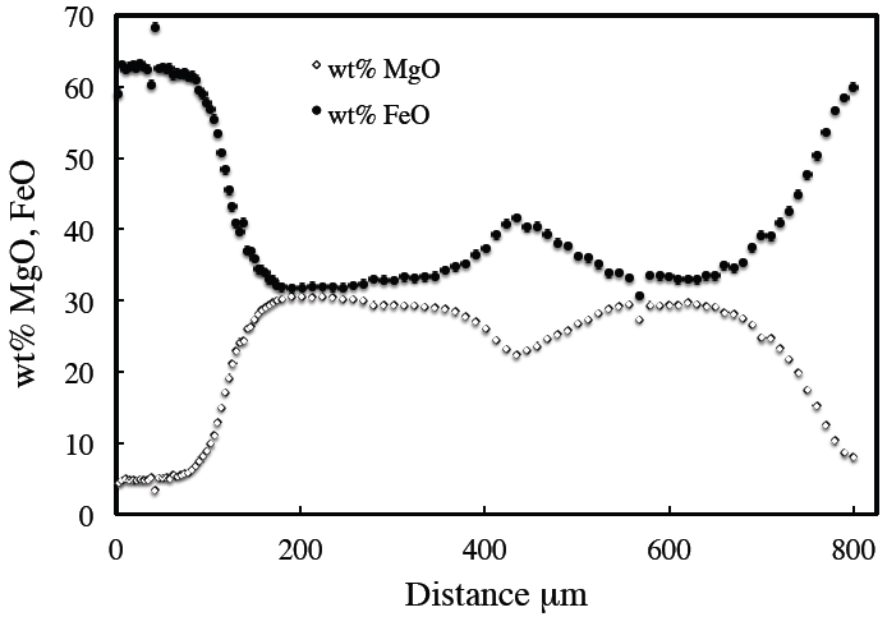


**Figure 13.** Weight percent MgO and FeO along the transect shown by the white line segments in Fig. 12. The local increase (decrease) of FeO (MgO) around 450 μm suggests that two initially separate olivine grains grew into each other while the iron-rich outer portions of the grains were still developing.

MELTS was used to calculate both batch and fractional crystallization of olivine from a parental melt composition for 15555 suggested by Ryder (2001). Figure 14 compares the results of the MELTS batch crystallization calculation for the fayalite fraction of olivine as function of temperature to that found in the equilibrium experiments by Walker et al. (1977). The good agreement validates our MELTS calculation. The measured core composition of olivine has about 30 wt% each of MgO and FeO, which corresponds to a fayalite fraction Fe/(Fe+Mg) atomic ≈ 0.36, which according to Fig. 14 requires that the entire core and melt were in equilibrium down to a temperature of about 1175˚C. This implies that the initial crystallization of the olivine was sufficiently slow, or that the system was at 1175˚C for a sufficiently long time for the olivine to be or become homogeneous and in equilibrium with the evolved melt. The time $t = r^2/D$ required for homogenizing magnesium in a 200 μm core is about 3 years using $D = 4\times10^{-}$

$^{12}$ cm$^2$ s$^{-1}$ for magnesium diffusion along the a-axis of olivine at T=1175˚C. This value for the diffusion coefficient of magnesium was calculated using the Dohmen and Chakraborty (2007b,c) parameterization for a fayalite fraction of 0.36, with log $fO_2$ for lunar basalt corresponding to the iron-wüstite buffer minus one log unit (Jones, 2004) and taking into account that the diffusion coefficient along the a-axis of olivine is a factor of six smaller than along the c-axis. The zoned portions of the olivine grains must have resulted from a second stage of evolution where the temperature decreased from 1175˚C sufficiently rapidly such that equilibrium could no longer be maintained between the melt and the interior of the grain. The transition from batch to fractional crystallization was further explored with MELTS calculations. Figure 15 shows the results of two MELTS calculations for the evolution of the olivine composition as a function of temperature with one assuming batch crystallization continuing to a temperature of 1050˚C and a second one with fractional crystallization from 1175˚C to 1020˚C. Both calculations showed that there was there was an interval from ~1175˚C to 1100˚C with no net olivine crystallization but that in the batch crystallization case the composition of the olivine continued to change by maintaining equilibrium with the melt that was changing in composition due the crystallization of other minerals (mostly pigeonite). When the MELTS calculation is switched from batch to perfect fractional crystallization for T<1175˚C the hiatus in crystallization results in a gap in the olivine composition of FeO and MgO from about 30 wt% in the core to the much higher (lower) FeO (MgO) once fractional crystallization resumes. No such gap, which would appear as an abrupt drop (increase) in the MgO (FeO) concentration, is seen in the actual zoning of the olivine grain. Diffusion could have smoothed such an abrupt change in olivine composition, which can be tested by comparing the magnesium and/or iron isotopic fractionation across the grain with the results of a model calculation for the isotopic fractionation

associated with the amount of smoothing by diffusion that would be required. One should keep in mind the results shown in Fig. 15 are for an idealized situation where perfect batch crystallization changes instantaneously to perfect fractional crystallization at T=1175˚C. In reality, the transition from a homogeneous core to a zoned rim would most likely not have been an instantaneous change from bulk to perfect fractional crystallization, but rather something intermediate involving partial exchange between the outer portion of the grain and melt. Be this as it may, Fig. 14 shows that the core of the olivine grain with a fayalite fraction of 0.36 would have been in equilibrium with the surrounding melt at T~1175˚C and that the zoning developed after the temperature cooled below 1175˚C.

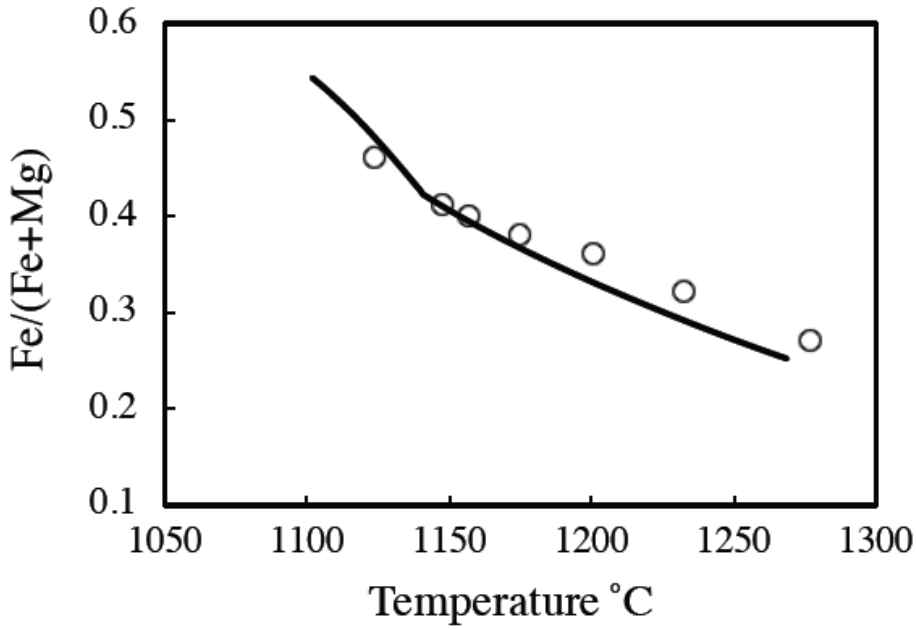


**Figure 14.** The black line shows the evolution of the atom ratio Fe/(Fe+Mg) (i.e., the fayalite fraction) of olivine calculated using the MELTS code assuming continuous equilibrium between olivine and melt (i.e. batch crystallization). The unfilled circles show the fayalite fraction as a function of temperature from olivine recovered from the equilibrium experiments reported by Walker et al. (1977). The agreement between the

calculated and observed fayalite fraction of olivine as a function of temperature gives us confidence that the MELTS calculation is a realistic representation of the early high-temperature stage of the evolution of olivine in 15555.

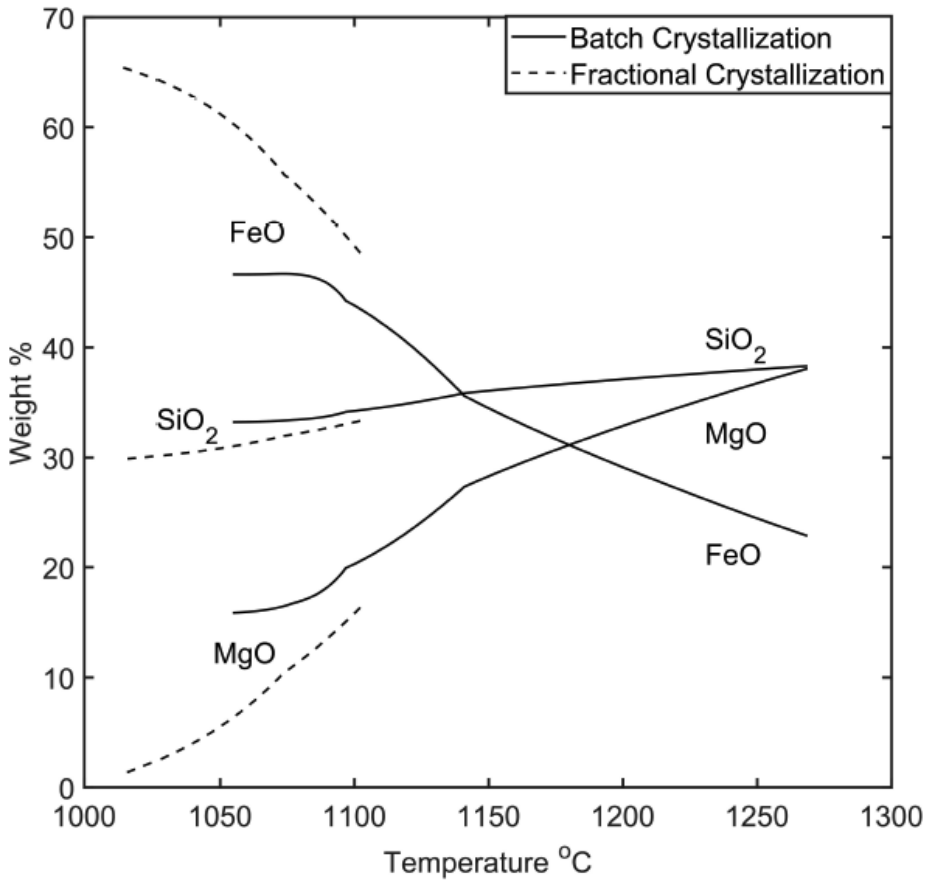


**Figure 15.** Results from MELTS calculations for the evolution of the oxide concentrations in olivine assuming batch crystallization (solid lines) of a system with the bulk composition of 15555 given by Ryder (2001). The dashed lines for T < 1100˚C show how the composition evolves when MELTS is used to calculate perfect fractional crystallization with decreasing temperature starting from 1175˚C. There is a gap in the crystallization of olivine between 1175˚C and 1100˚C, which is why there is no composition of fractionally crystallized olivine until T = 1100˚C.

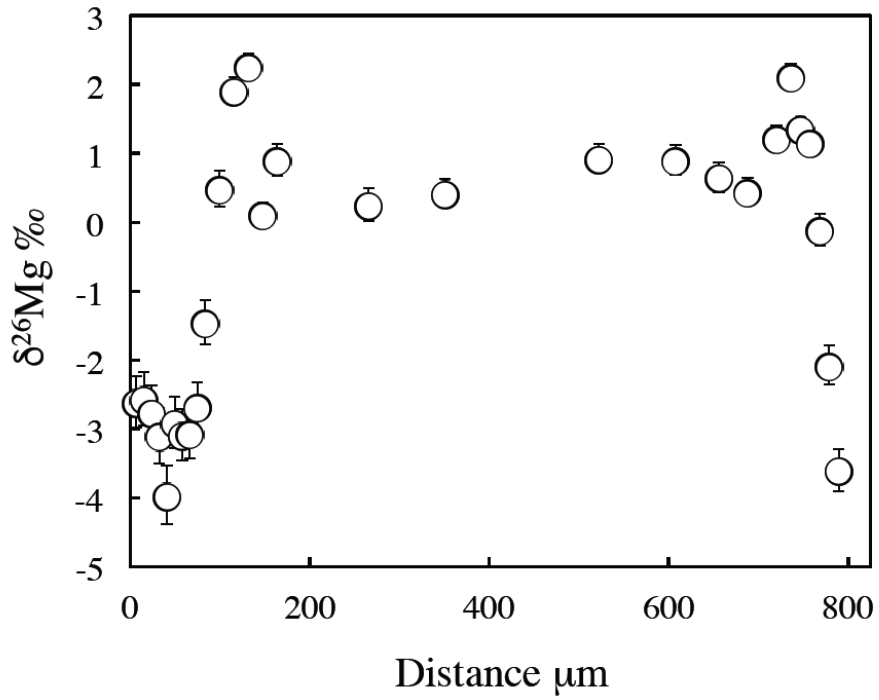


**Figure 16.** Matrix-corrected magnesium isotopic composition of olivine measured at spots along the white line segments in Fig. 12 plotted against distance from the left edge of the grain. The error bars reflect the overall uncertainty of the IMF matrix corrections for the instrumental mass fractionation as a function of olivine composition (see Fig. B3 in Appendix B).

Figure 15 suggests that the rapid decrease (increase) in the MgO (FeO) towards the rim of the olivine grain from lunar rock 15555 involved some degree of fractional crystallization. Determining the role, if any, that diffusion had in affecting the zoning of the olivine grain can be done by measuring the isotopic composition of magnesium (and/or iron) across the olivine grain. Figure 16 shows the IMF-corrected magnesium isotopic composition at spots along the white line segments shown in Fig. 12 measured with a CAMECA 1270 ion microprobe. The data show the interior of the grain to be quite

uniform in magnesium isotopic composition and that there are well-resolved isotopic fractionations of +2‰ to about –4‰ close to both edges of the grain.

The isotopic data in Fig. 16 shows that the interior of the grain was relatively homogeneous in isotopic composition at the time diffusion began and that the isotopic fractionation due to diffusion was restricted to boundary layers near each edge of the grain. The fact that the isotopic composition at the grain edge is significantly lower than in the interior may at first sight seem surprising given that it has been shown that the isotopic fractionation of magnesium during crystallization of olivine from a basaltic liquid is negligible (Teng et al., 2008). This implies that the isotopic composition of melt at the grain boundary would be same as that in the grain core, not negative by several ‰. However, if the boundary condition at the grain edge were no-flux, then the isotopic fractionation at the grain edge would become negative once the diffusion flux from the interior reaches the edge (for an example see Fig. 7 in Richter et al., 2003). The reason for the negative fractionation is that when diffusion down a concentration gradient impinges on a no-flux boundary the faster diffusing lighter isotope ‘piles up’ there causing the isotopic fractionation to become increasingly negative. The most likely cause of an effectively no-flux boundary condition at the edge of the olivine grain is that pyroxene, in which magnesium diffuses orders of magnitude more slowly than in olivine (see Fig. 2), had already crystallized and had become juxtaposed with olivine. The conclusion regarding the nature of the boundary condition at the olivine grain edge is another instance where isotopes point to something that would not have been obvious from the parent element concentration profiles.

### 7.3 Magnesium isotopic constraints on the cause of major element zoning of olivine and implications for the thermal history of 15555

Given the limited extent of the lithium zoning, a conservation of mass equation in Cartesian coordinates for total magnesium or its isotopes (Eqn. 3) was used.

$$\frac{\partial C_i}{\partial t'} = \frac{\partial}{\partial x'}\left( D'_{i(T,\, X_{FA},\, fO_2} \frac{\partial C_i}{\partial x'} \right) \tag{3}$$

$C_i$ is a measure of the abundance of species $i$, $x'$ is distance measured in units $l$ (the length of the modeled segment), $t'$ is time measured in units $l^2/D_{To}$ and $D'_i = D^*_{i(T,X_{Fa},fO_2)} / D_{To}$ where $D^*_{i(T,X_{Fa},fO_2)}$ is the dimensional diffusion coefficient of magnesium species $i$ calculated using the parameterization by Dohmen and Chakraborty (2007b,c). $D_{To}$ is the value of the diffusion coefficient in the grain interior when diffusion began at T = 1050˚C with $X_{Fa}$ = 0.36 and log $fO_2$ corresponding to the iron-wüstite buffer minus one log unit (IW–1). The diffusion coefficient for $^{24}$Mg can considered to be indistinguishable from that of the total magnesium and the diffusion coefficient of $^{26}$Mg relative to that of $^{24}$Mg calculated as $D_{^{26}Mg} / D_{^{24}Mg} = (24/26)^{\beta}$, with the value for $\beta$ to be determined by fitting the measured data.

A remarkable coincidence arises when model calculations are used to test the proposition by Taylor et al. (1977) that the zoning of olivine grain from 15555 was due entirely to diffusion starting from an initial step in concentration. Figure 17 shows that such a calculation for the diffusive evolution of a step assuming a constant value for the Fe-Mg interdiffusion coefficient results in a very good fit to the measured Mg concentration data (thin black line in Fig. 17). But several things are wrong with this. To begin with, it ignores the well-documented dependence of the rate of Fe-Mg interdiffusion on the olivine composition, which when taken into account results in the profile becoming distinctly asymmetrical and no longer fits the measured data (heavy

black curve in Fig. 17). The difference in the diffusion coefficient between the low fayalite interior and the higher fayalite composition at the grain edge is about a factor of 100, which accounts for asymmetry of the diffusion profile. The panel on the right of Fig. 17 shows a second flaw in that the Mg isotopic fractionation calculated assuming a fixed Fe-Mg interdiffusion coefficient results in a very poor fit to the measured isotopic fractionation data. Having used a no-flux boundary condition would not have changed this because the diffusive flux and associated isotopic fractionation in the constant diffusion coefficient model had not yet reached the edge of the grain.

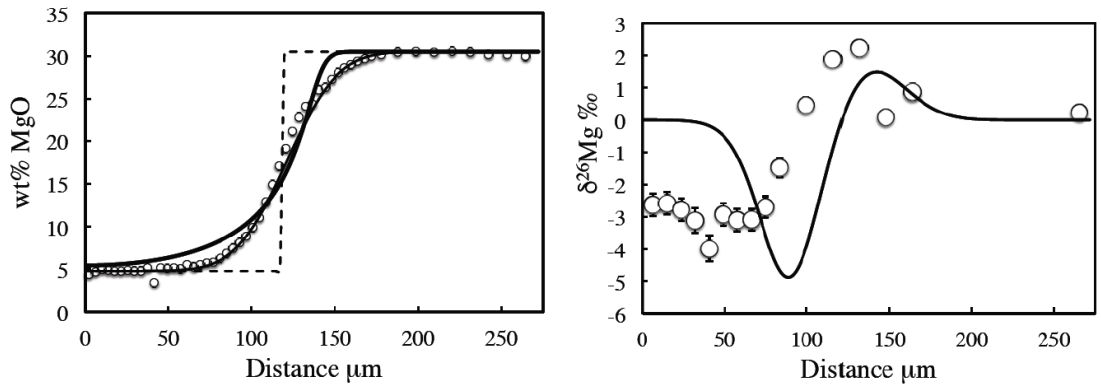


**Figure 17.** The panel on the left shows wt% MgO (small circles) measured along the left portion of the transect across the 15555 olivine grain shown in Fig. 12 compared to a model calculation of the diffusive evolution of an initial step (dashed line) for a constant Mg diffusion coefficient (thin black line) and for the diffusion coefficient depending on the local composition of the olivine concentration (heavy black line) as parameterized by Dohmen and Chakraborty (2007b,c). The panel on the right compares the measured Mg isotopic fractionation to the fractionation calculated using ß = 0.15 for the case with constant Mg diffusion coefficient.

Once one realizes that there was measurable diffusive Fe-Mg exchange in the olivine 15555, the task becomes one of finding by trial and error the zoning due to crystallization that evolves by diffusion to fit both the magnesium zoning and isotopic fractionation. The simplest model for this assumes that diffusion began after the olivine grain had grown to its present size and was bounded by pyroxene to account for the no-flux boundary condition required by the negative magnesium isotopic fractionation at the edge of the grain. The effectively no-flux boundary condition is due to the diffusion of magnesium in pyroxene being very much slower than in olivine and thus when olivine is juxtaposed with pyroxene the flux of magnesium across the contact would be negligible while diffusion was taking place in the olivine grain. The diffusion coefficient of magnesium in olivine used in the calculations depends on temperature and the local fayalite composition of olivine as given by Dohmen and Chakraborty (2007b,c). Figure 18 shows the results of a calculation in which an initial zoning was prescribed such that the system evolves by diffusion to give a good fit to both the wt% MgO and the magnesium isotopic fractionation data. The calculations that yielded the fits to the data shown in Fig. 19 for the left and right edge of the olivine grain were run for nondimensional times of $t' = 0.0015$ and 0.0008 over which the temperature dropped 200˚C staring from 1050˚C (the temperature corresponding to 5 wt% MgO in Fig. 15). The dimensional times $t = (l^2/D_{To})t'$ are 65 and 35 days for $l = 0.03$ cm and $D_{To} = 2.4\times10^{-13}$ cm$^2$ s$^{-1}$ calculated using T = 1050˚C, a fayalite fraction of 0.36, and $fO_2 = 1.5\times10^{-15}$ bars (IW–1) in the Dohmen and Chakraborty (2007b,c) parameterization for the magnesium diffusion coefficient along the c-axis of olivine reduced by a factor of 6 to account for the diffusion being along the slower a-axis. These times result in estimates for the cooling rate of lunar rock 15555 of 3 and 6˚C per day, which are much the same as that given more than 40 years ago by Taylor at al. (1977) but now with the added

confidence provided by the magnesium isotopic fractionation across the olivine grain determining the extent of magnesium diffusion.

The magnesium isotopic fractionation in panel (b) of Fig. 18 was fit with $\beta_{Mg}$ = 0.14 and that in panel (d) with $\beta_{Mg}$ = 0.16. That somewhat different run durations and $\beta_{Mg}$ values had to be used to fit the boundary layer at each edge of the olivine grain provides a measure of the uncertainty inherent in using necessarily simplified assumptions regarding the initial and boundary conditions to model the diffusive evolution of an olivine grain from a natural setting. The $\beta_{Mg}$ values (0.14 and 0.16) used to fit the isotopic fractionation data shown in Fig. 18 are somewhat larger than the average $\beta_{Mg}$ = 0.084 reported by Oeser et al. (2015) based on modeling the magnesium isotopic fractionation of a set of eight terrestrial olivines. This difference may be due to the fact that the terrestrial olivines are much more magnesium rich than the lunar olivine studied here.

## 8. Results and Discussion

Lithium and magnesium isotopic measurements across zoned pigeonite grains from Shergotty showed little isotopic fractionation in either the relatively homogeneous core of the grains or in the zoned rims (see Fig. 5 and additional data in Appendix A). The lack of significant isotopic fractionation is evidence that the lithium and magnesium concentration variations of the zoned portions of the grains was not caused by, or significantly affected by, diffusion. Therefore, the dominant process that determined the distribution of lithium and magnesium in the grains must have been crystallization from a melt of evolving composition. MELTS calculations were used model the major element evolution of pigeonite crystallized from a plausible Shergotty parental melt (Fig. 6), leading to the conclusion that the uniform core of the pigeonite grains with approximately equal amounts of FeO and MgO can be explained by batch crystallization down to a temperature of 1135˚C. Batch crystallization implies that the crystallizing grains are

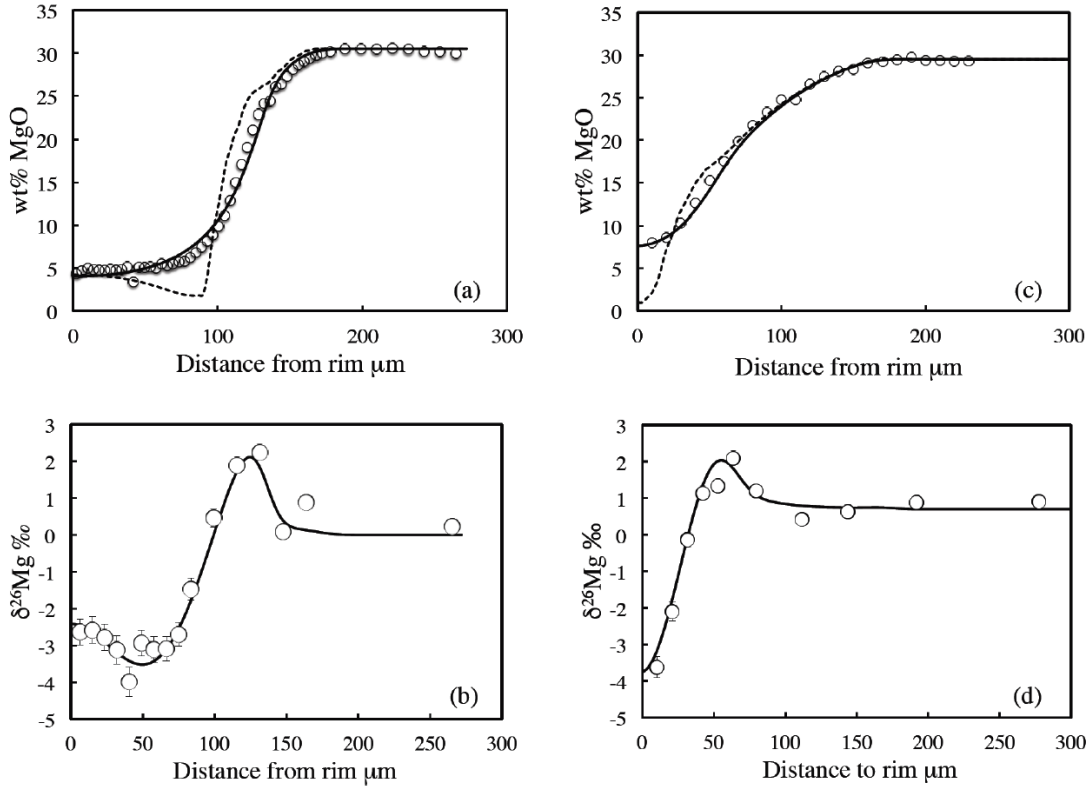


**Figure 18.** Panels (a) and (b) compare model calculations with the measured wt% MgO (unfilled circles) and magnesium isotopic fractionation (circles with error bars) in 15555 olivine from the edge to 300 µm along the left side of white line segment shown in Fig. 12. Panels (c) and (d) are for data as a function of distance from the edge along the white line segment ending at the right edge of the grain. The initial condition for these calculations is shown by the dotted line in panel (a) and (c) with a no-flux boundary condition at the edge of the grain. The temperature at the start of the calculation was 1050˚C and then cooled linearly by 200˚C over the course of the calculation. The isotopic fractionation was modeled assuming that it was initially uniform and evolved with a mass-dependence of the magnesium diffusion coefficients given by ß = 0.14 for the calculated fractionation shown in panel (b) and with ß = 0.16 for the fractionation shown in panel (d). The nondimensional run time t' for the results shown in panel (a) and (b) is 0.0015 and 0.0008 for that in panel (c) and (d).

uniform and in equilibrium with the evolving melt composition as the system cools. For this to be the case, the crystallization must have been sufficiently slow for diffusion to have sufficient time to homogenize the grains. This line of reasoning leads to an estimate that the core of the pigeonite grain SH3 from Shergotty would maintain equilibrium with the evolved melt if it had been at T=1135˚C for more than 3200 years. Batch crystallization, however, does not produce zoned minerals, thus at about T=1135˚C grain SH3 must have begun to cool sufficiently rapidly that it grew by fractional crystallization sufficiently fast that there was not enough time for there to have been any significant mass transport by diffusion as evidenced by the limited isotopic fractionation. Bounds on the cooling rate of this second stage of the thermal evolution of grain SH3 were determined by numerical calculations of the magnesium isotopic fractionation of a cooling grain growing a rim around an initial core as a function of the cooling rate. Comparing the calculated magnesium isotopic fractionation with the measured data (see Fig. 9) required that the rim must have grown in less than 1700 years. When the same approach was used to model much faster diffusing lithium in grain SH3 (see Fig. 11), the lack of significant lithium isotopic fractionation associated with the lithium concentration gradient led to an estimate of time over which the rim must have grown for only 40 minutes corresponding to a cooling rate of about 150˚C/h.

The major element and magnesium isotopic zoning of a large olivine grain (Figs. 13 and 16) from mare basalt 15555 was used to document a two-stage thermal history. The core composition of the olivine grain has a composition with a fayalite fraction of 0.36 (Fig. 13), which is consistent with a MELTS batch crystallization calculation down to T=1175˚C (Fig. 15), suggests that it must have cooled sufficiently slowly for it to be uniform in composition and in equilibrium with the evolved melt composition at T=1175˚C. The local increase in FeO and decrease in MgO in the center of the grain is

interpreted to be the result of two partially crystallized olivine grains growing into each other. The homogenization time of the olivine of the 200 μm grain cores at T=1175˚C was estimated to be about three years. The zoned edges of the grain, where the MgO concentration decreases to ~5 wt% and FeO increases to ~60 wt%, implies that the cooling rate must have increased sufficiently for the crystal to grow by fractional crystallization. The magnesium isotopic composition across the olivine grain (Fig. 16) shows well-resolved fractionations at the edges that indicated that a small but resolvable amount of diffusion modified the zoning. The locally heavy $\delta^{26}$Mg (~ +2‰) in the zoned part of the grain is the result of the faster diffusion of $^{24}$Mg down the magnesium concentration gradient leaving behind magnesium slightly enriched in $^{26}$Mg. The light $\delta^{26}$Mg (~ –4‰) at the edges of the grain was interpreted as being due to the faster $^{24}$Mg that diffused down the concentration gradient "piling up" at an effective no-flux boundary due to the olivine being bounded by pyroxene. Pyroxene provides a no-flux boundary because the rate of diffusion of magnesium in the pyroxene is many orders of magnitude slower than in olivine (Fig. 2). The duration of the fast cooling stage of lunar rock 15555 (~45 days at about 0.2˚C/h) was estimated based on the time required to diffuse an amount of magnesium indicated by the isotopic fractionation in the zoned portions of the olivine grain.

Table 1 lists the estimates of the durations, and corresponding cooling rates where applicable, of two distinct stages of the crystallization of Shergotty and of mare basalt 15555. The estimated second-stage cooling rate of Shergotty of greater than 150˚C/h is certainly extraordinarily fast but not unprecedented. First and Hammer (2016), for example, recently proposed a multistage thermal history for another shergottite, Yamato 980459, with a final cooling rate of 100˚C/h. Saper and Stolper (2020) used diffusion modeling of MgO gradients in glassy inclusions in olivine from Yamato 980459 to

estimate a cooling rate of 383±43 °C/hr. The 150˚C/h cooling rate of Shergotty inferred in the present study is, however, much faster than what was proposed in previous studies such as that by Lentz and McSween (2000), who argued that the total time of pigeonite growth was between 19 and 93 days. Had this been the case diffusion would have had more than enough time to erase any lithium zoning of the pyroxene grains. Lentz and McSween (2000) also estimated that the pyroxene cores grew for a time between 11 and 53 days. This is orders of magnitude too short a time to homogenize pigeonite cores, which because of the very slow diffusion of magnesium in pyroxene, we estimated would have required several thousand years.

Table 1 also lists for comparison with Shergotty the two-stage thermal history of another martian meteorite, NWA 817, that was studied by Richter et al. (2016) using the same isotope-based methods as used here. NWA 817 is similar to Shergotty in that it is a pyroxene-rich cumulate (~70% augite), however it is much older than of Shergotty being a nakhlite, a class of martian meteorites that have a common crystallization age of 1340±40 Ma (Udry and Day, 2018) while Shergotty has an age of 165±4 Ma. There are several other significant differences between these two martian meteorites. The augite grains from NWA 817 are zoned, with the lithium abundance increasing towards the grain edge, which is expected for closed system crystallization, given that lithium is somewhat incompatible in pyroxene (see lithium partitioning data in Appendix A). The lithium zoning of the pigeonite grains in Shergotty, on the other hand, have the lithium decreasing towards the edges of the grains (Fig. 5). Another significant difference is that while the zoning of pyroxene grains in Shergotty was shown here to be dominantly due to fractional crystallization, the zoning of NWA 817 was shown by Richter et al. (2016) to be explicable entirely by diffusion from initially homogeneous grains.

**Table 1**. Summary of results derived from modeling the zoning and isotopic fractionation of minerals from Shergotty, nakhlite NWA 817, and from mare basalt 15555. The temperature of Stage 1 is derived from MELTS batch crystallization calculations that match the proportions and composition of minerals in the grain cores. The duration and cooling rates for Stage 2 were derived from model calculation related to the zoned portion of the mineral grains. The depth below the cold surface of a partially molten layer corresponding to the reported cooling rates is taken from in Fig. 19.

| | **Stage 1** | ← | **Stage 2** | → | |
|---|---|---|---|---|---|
| **Sample** | **Temperature and duration** | **Duration** | **Cooling rate** | **Growth rate** | **Burial depth** |
| **Shergotty** | 1135˚C for >3200 y | < 1 h | >150˚C/h | >200 μm/h | <10 cm |
| constraint: | homogeneous pigeonite cores | no lithium isotope fractionation | | zoning extent and duration | |
| **15555** | 1175˚C for > 3 y | ~1000 h | ~ 0.2˚C/h | ~0.2 μm/h | ~400 cm |
| constraint: | homogeneous Mg olivine cores | extent of Mg isotopic fractionation | extent of Mg isotopic fractionation | zoning extent and duration | |
| **NWA 817** | 1100˚C for > 2000 y | ~1000 h | ~ 0.2˚C/h | | ~ 400 cm |
| constraint: | homogeneous Mg augite cores | Mg zoning and isotope fractionation | Mg zoning and isotope fractionation | not constrained | |

Table 1 includes values for the distance from a cold surface at –50˚C (close to average surface temperature of the Moon and Mars) that can account for the estimated cooling rates for each of the three rocks listed. The distance estimates were made using the cooling curve shown in Fig. 19 calculated with the error function solution to the heat equation given by $T(t,z) = -50 + 1150 erf\left(\frac{z}{2\sqrt{kt}}\right)$ with $T$ in ˚C, $z$ in cm, $t$ in seconds, and with a thermal diffusion coefficient $k$ = 0.006 cm$^2$ s$^{-1}$ as used by Peck et al. (1977) to model the measured temperature versus depth in a Hawaiian lava lake. The curve in Fig. 19 corresponds to the temperature change with time *T(t)* at a distance $z$ = 10 cm from the cold surface, but it can be used for *T(t)* at any other distance by expanding or contracting the time scale by $(z/10)^2$. Note that the cooling has an initial period of constant temperature when the cooling from the cold surface has not yet arrived at the distance $z$.

The most obvious interpretation of the distance of a sample from cold surface listed in Table 1 is that it represents an emplacement depth below the surface. In the case of 15555, which comes from basalt erupted onto the lunar surface, such an interpretation is not particularly problematic. Recall however that 15555 was already highly crystalline at the time cooling began and that in order for any partially molten material silicate material to flow onto the surface it must not have had much more than 40% crystals. At crystal fractions higher than this the effective bulk viscosity of the crystal-laden melt increases very rapidly and the mixture develops yield strength (see Saar et al., 2001, and Mueller et al., 2010) that inhibits flow. It seems likely that the originally erupted material had a crystal fraction of no more than about 40% and that the crystallinity at a depth of 400 cm increased by a

combination of crystal settling during the relatively isothermal portion of the cooling curve and further crystallization during subsequent cooling. For a sample at about 400 cm below the surface the isothermal portion of the cooling curve would have lasted for about 500 hours with subsequent crystallization of pigeonite continuing for an additional 1000 hours as the temperature decreased by about 100˚C.

The remarkably fast cooling of highly crystalline Shergotty (>150˚C/h) and the implied emplacement within 10 cm of a very cold surface requires a special setting for the last stage of the thermal evolution of this meteorite. First and Hammer (2016) suggested that their inferred final cooling rate of 100˚C/h of a similar shergottite, Yamato 980459, could be explained by a breakout from a pahoehoe-like flow erupted onto the surface of Mars. In the case of Shergotty there is not a problem transporting the melt plus the homogeneous cores of pigeonite and augite grains because as the MELTS batch crystallization calculation shows, the melt volume fraction would have been about 65% when the pigeonite had equal wt% MgO and FeO. The rims of the pigeonite grains would have had to have grown to their final size and the melt fraction reduced to about 20% in a matter of minutes, perhaps in a thin pahoehoe flow as proposed by First and Hammer (2016). This, however, does not account for the large crystal fraction of Shergotty or for the foliated texture with large preferentially oriented pyroxene grains described by Stolper and McSween (1979). A slightly different setting that could have produced both the high crystal fraction and the foliated texture along with the final very rapid cooling is a thicker pahoehoe flow with perhaps up to 40% crystals, which then had the melt break out rapidly, leading to deflation and rapid cooling of the crystals that were left behind. While this scenario could account for both the texture and very

rapid cooling of Shergotty, it does not explain the open system behavior of lithium evidenced by the decrease in lithium concentration between the pigeonite cores and rims. The open system behavior of lithium during the crystallization of Shergotty remains, as far as we are concerned, an unsolved puzzle.

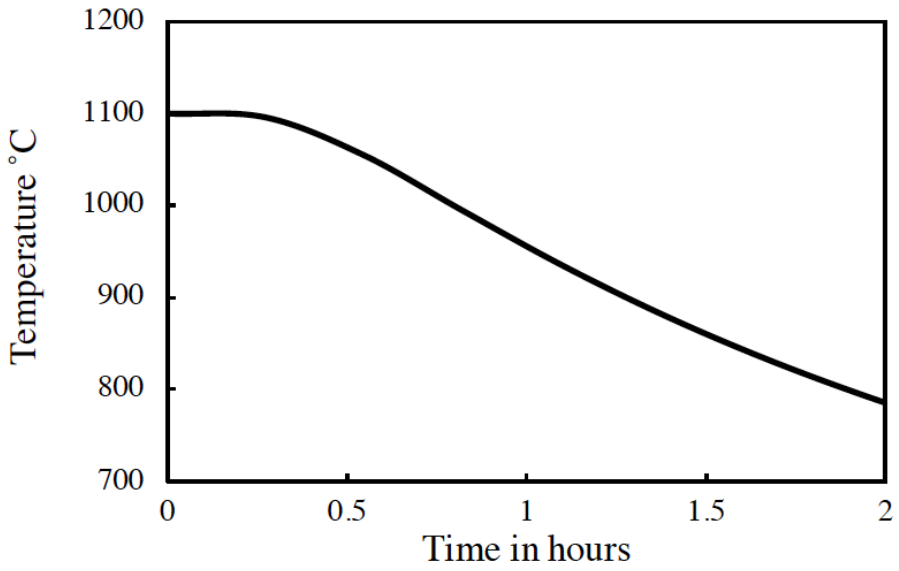


**Figure 19.** Thermal evolution of a sample at a depth z in a partially molten silicate layer based on parameters derived from the cooling with depth at Kīlauea Iki lava lake, Hawai‘i. The curve in the figure corresponds to the thermal evolution at a depth z = 10 cm. For the cooling curve at any other depth, the time scale is stretched or shortened by a factor $(z/10)^2$ with z centimeters.

The work presented here along with the earlier results by Richter et al. (2016) for NWA 817 show three distinct types of zoning: pyroxene grains from Shergotty with no

significant evidence of diffusion, zoned olivine from mare basalt 15555 showing limited but resolvable post-crystallization mass transport by diffusion, and pyroxene grains from nakhlite NWA 817 where the zoning can be explained in terms of diffusion from an initially homogenous grain. In each of these cases, the isotopic fractionation data allowed for quantifying the extent of mass transport by diffusion, which in turn was key for constraining their thermal history. Figure 20 illustrates the importance of the isotopic fractionation data by comparing magnesium abundance and isotopic fractionation profiles from Shergotty and NWA 817. Aside from different spatial scales, the magnesium abundance profiles are remarkably similar, which could have led one to assume that they were the result of the same process. However, the isotopic fractionation data clearly shows that this was not the case. The isotopic fractionation measured across the pigeonite grain SH3 from Shergotty is opposite to what it would be if there had been significant diffusion down the magnesium concentration gradient. It is possible that the magnesium isotopic differences across SH3 are due to inadequate correction of matrix effects. The fractionation across the augite grain 11 from NWA 817, on the other hand, was almost perfectly modeled by Richter et al. (2016) as having been caused by the diffusive loss of magnesium from a grain initially uniform in magnesium abundance and isotopic composition. In the case of the olivine grain from the 15555, the isotopic fractionations document and quantify the limited but resolvable extent that diffusion modified the distribution of magnesium and that it must have taken place after pyroxene had crystallized. The process or processes responsible for the zoning of Shergotty, NWA 817, and 15555 would have been hard to document and quantify without the isotopic fractionation data.

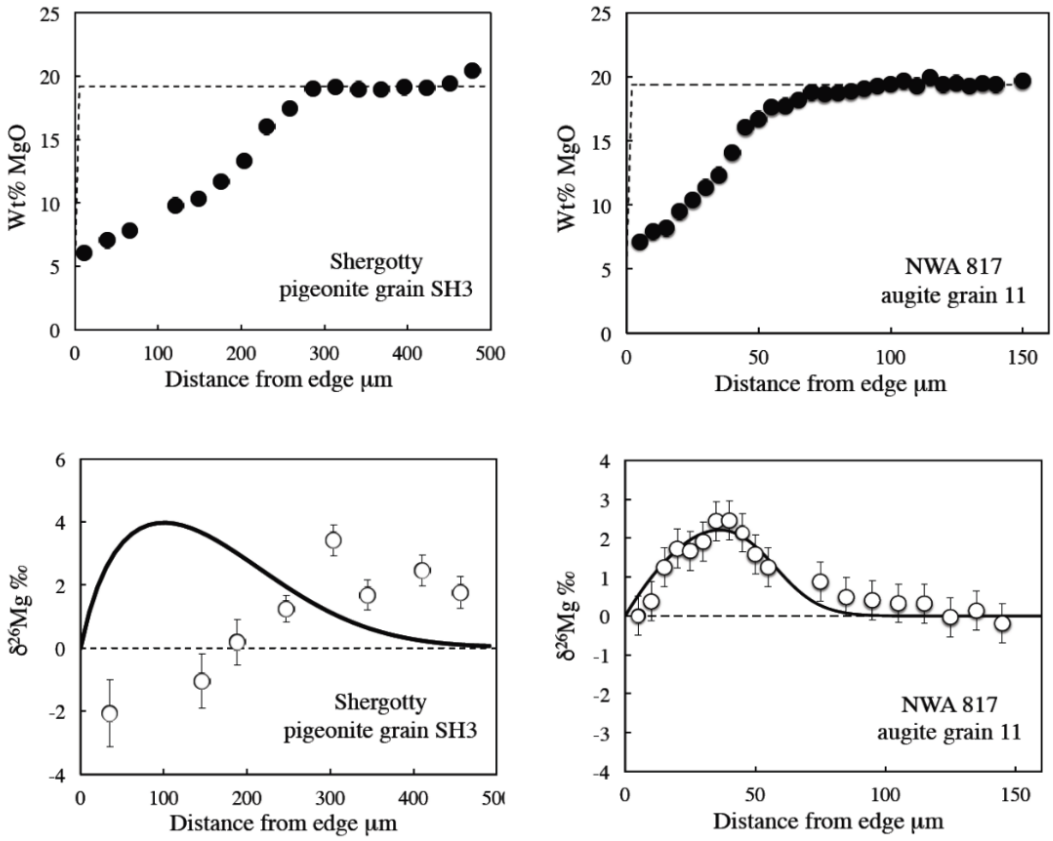


**Figure 20.** Comparison of the magnesium zoning and isotopic fractionation at the edge of pigeonite grain SH3 from Shergotty and that at the edge of an augite grain from nakhlite NWA 817 reported Richter et al. (2016). The calculated isotopic fractionation of lithium in SH3 calculated assuming that the lithium zoning was due to diffusion out of an initially homogeneous grain is shown by the solid curve and is clearly inconsistent with the measured fractionations shown by the open circles. This is in marked contrast to the magnesium evolution of the augite grain from NWA 817 where the measured data is reproduced by a calculation in which both the wt% MgO profile and the magnesium isotopic fractionation are

due entirely to diffusion of magnesium out of an initially homogeneous grain. The dashed lines in these figures show the initial conditions assumed for the diffusion calculations.

## 9. Acknowledgments

The work reported here was supported by NASA grants NNX13AH09G S01 (FMR), 80NSSC17K0251 (AMD), NNX16AI26G and NNX17AI43G (SBS), and NNX17AE84G (RAM). Support from Europlanet 2020 Project 16-EPN2-014 (FMR) and Programme National de Planétologie from INSU-CNRS and l'Agence Nationale de la Recherche grant ANR-18-CE31-0010-01 (JV) is also gratefully acknowledged. We thank Yan Liang of Brown University for helping us find the published data we list in Appendix C and Thomas Stephan of the University of Chicago for implementing the Mahon (1996) data analysis algorithm. We also thank three anonymous reviewers and the associate editor for their many suggestions that improved the manuscript.

## 10. References

Beck P., Barrat J. A., Chaussidon M., Gillet Ph., and Bohn M. (2004) Li isotopic variations in a single pyroxene from Northwest Africa 480 shergottite (NWA 480): a record of degassing of Martian magmas? *Geochim. Cosmochim. Acta* **68,** 2925–2933.

Brenan J. M., Neroda C. C., Lundstrom H. F., Shaw H. F., Ryerson F. J., and Phinney D. L. (1998) Behaviour of boron, beryllium, and lithium during melting and crystallization: Constraints from mineral-melt partitioning experiments. *Geochim. Cosmochim. Acta* **62**, 2129–2141.

Caciagli-Warman N. (2010) Experimental constraints on lithium exchange between clinopyroxene, olivine and aqueous fluid at high pressures and temperatures (Ph.D. thesis). Univ. Toronto, Toronto, Canada.

Chaussidon M., Deng Z., Villeneuve J., Moureau J., Watson B., Richter F., and Moynier F. (2017) In situ analysis of non-traditional isotopes by SIMS and L-MC-ICP-MS: key aspects and the example of Mg isotopes in olivines and silicate glasses. *Rev. Mineral. Geochem*. **82**, 127–163.

Coogan L. A., Kasemann S. A. and Chakraborty S. (2005) Rates of hydrothermal cooling of new oceanic upper crust derived from lithium-geospeedometry. *Earth Planet. Sci. Lett.* **240**, 415– 424.

Costa F. and Dungan M. (2005) Short time scales of magmatic assimilation from diffusion modeling of multiple elements in olivine. *Geology* **33**, 837–840

Costa F., Dohmen R. and Chakraborty S. (2008) Time scales of magmatic processes from modeling the zoning patterns of crystals. *Rev. Mineral. Geochem*. **69**, 545–594.

Dohmen R. and Chakraborty S. (2007a) Fe–Mg diffusion in olivine I: experimental determination between 700 and 1200˚C as a function of composition, crystal orientation and oxygen fugacity. *Phys. Chem. Mineral.* **34**, 389-409.

Dohmen R. and Chakraborty S. (2007b) Fe–Mg diffusion in olivine II: point defect chemistry, change of diffusion mechanisms and a model for calculation of diffusion coefficients in natural olivine. *Phys. Chem. Mineral.* **34**, 409-430.

Dohmen R. and Chakraborty S. (2007c) Erratum to: Fe–Mg diffusion in olivine II: point defect chemistry, change of diffusion mechanisms and a model for calculation of diffusion coefficients in natural olivine. *Phys. Chem. Mineral.* **34**, 597–598.

Dohmen R., Kasemann S. A., Coogan L. A. and Chakraborty S. (2010) Diffusion of Li in olivine. Part 1: Experimental observations and a multiple species diffusion model. *Geochim. Cosmochim. Acta* **74**, 274–292.

First E. and Hammer J. (2016) Igneous cooling history of olivine-phyric shergottite Yamato 980459 constrained by dynamic crystallization experiments. *Meteorit. Planet. Sci.* **51**,1233–1255.

Ghiorso M. S., and Sack R. O. (1995), Chemical mass-transfer in magmatic processes IV. A revised and internally consistent thermodynamic model for the interpolation and extrapolation of liquid-solid equilibria in magmatic systems at elevated temperatures and pressures. *Contrib. Mineral, Petrol.* **119**, 197–212.

Herd C. D. K. and Papike J. J. (2000) Oxygen fugacity of the martian basalts from analysis of iron–titanium oxides: Implications for mantle–crust interaction on Mars. *Meteor. Planet. Sci.* **35,** A70.

Jeffcoate A. B., Elliott T., Kasemann S. A., Ionov D., Cooper K. and Brooker R. (2007) Li isotope fractionation in peridotites and mafic melts. *Geochim. Cosmochim. Acta* **71**, 202–218.

Jones J.H. (2004) Redox conditions among the terrestrial planets. *Lunar Planet. Sci.* **35**, #1264.

Kesson S. (1975) Melting experiments of synthetic Mare basalts and their petrogenetic implications. *Proc. Lunar Sci. Conf.* **6**, 476-477.

Lentz R. C. F and McSween H. Y. Jr. (2000) Crystallization of the basaltic shergottites: Insights from crystal size distribution (CSD) analysis of pyroxenes. *Meteorit. Planet. Sci.* **35,** 919–927.

Lentz R.C.F., McSween H. Y. Jr., Ryan J., and Riciputi L.R. (2001) Water in martian magmas: Clues from light lithophile elements in shergottite and nakhlite pyroxenes. *Geochim. Cosmochim. Acta* **65**, 4551–4565.

Mahon K.I. (1996) The new "York" regression: Application of improved statistical method to geochemistry. *Int. Geol. Rev.* **38**, 293-303.

McCoy T. J. and Lofgren G. **(**1999**)** Crystallization of the Zagami shergottite: An experimental study. *Earth Planet. Sci. Lett.* **173,** 397–411.

McSween H. Y. Jr., Grove T. L., Lentz R. C. F., Dann J. C., Holzheid A. H., Riciputi L. R., and Ryan J. G. (2001) Geochemical evidence of magmatic water within Mars from pyroxenes in the Shergotty meteorite. *Science* **409**, 487–489.

Muller T., Dohmen R., Becker H.W. ter Heege Jan H., and Chakraborty S. (2013) Fe-Mg interdiffusion rates in clinopyroxene: experimental data and implications for Fe-Mg exchange geothermometers. *Contrib. Mineral. Petrol.* **166**, 1563–1576.

Nyquist L.E., Bogard D.D., Shih C.-Y., Greshake A., Stoffler D., and Eugster O. (2001) Ages and geologic histories of Martian meteorites. *Chronology and Evolution of Mars* **96**, 105–164.

Oeser M., Dohmen R., Horn I., Schuth S. and Weyer S. (2015) Processes and time scales of magmatic evolution revealed by Fe–Mg chemical and isotopic zoning in natural olivines. *Geochim. Cosmochim. Acta* **154**, 130–150.

Parkinson I. J., Hammond S. J., James R. H. and Rogers N. W. (2007) High-temperature lithium isotope fractionation: Insights from lithium isotope diffusion in magmatic systems. *Earth Planet. Sci. Lett.* **257**, 609–621.

Peck D. L., Hamilton S. H. and Shaw H. R. (1977) Numerical analysis of lava lake cooling models: part II, application to Alae lava lake, Hawai‘i. *Amer. J. Sci.* **227**, 415–437

Richter F. M., Davis A. M., DePaolo D. J., and Watson E. B. (2003) Isotope fractionation between molten basalt and rhyolite. *Geochim. Cosmochim. Acta* **67**, 3905–3923.

Richter F. M., Watson E. B., Mendybaev R. A., Teng F.-Z., and Janney P. E. (2008) Magnesium isotope fractionation in silicate melts by chemical and thermal diffusion. *Geochim. Cosmochim. Acta* **72**, 206–220.

Richter F., Watson B., Chaussidon M., Mendybaev R., and Ruscitto D. (2014) Lithium Isotope fractionation by diffusion in minerals. Part 1: Pyroxenes. *Geochim. Cosmochim. Acta.* **126**, 352–370.

Richter F., Chaussidon M., Mendybaev R., and Kite E. (2016) Reassessing the cooling rate and geologic setting of Martian meteorites MIL 03346 and NWA 817. *Geochim. Cosmochim. Acta* **182**, 1–23.

Richter F. M., Chaussidon M., Watson E. B., Mendybaev R. and Homolova V. (2017) Lithium isotopic fractionation in minerals Part 2: Olivine. *Geochim. Cosmochim. Acta* **219**, 124–142.

Righter K., Yang Y., Costin G. and Downs R. T. (2008) Oxygen fugacity in the Martian mantle controlled by carbon: new constraints from nakhlite MIL 03346. *Meteorit. Planet. Sci.* **43**, 1709–1723.

Ryder G. and Schuraytz B.C. (2001) Chemical variations of the large Apollo 15 olivine-normative mare basalt rock samples. *J. Geophys. Res.* **106**, 1435-1451.

Saar M. O., Manga M., Cashman K. V. and Fremouw S. (2001) Numerical models of the onset of yield strength in crystal-melt suspensions. *Earth Planet. Sci. Lett.* **187**, 367–379.

Saper L. M. and Stolper E. M. (2020) Controlled cooling rate experiments on olivine-hosted melt inclusions: chemical diffusion and quantification of eruptive cooling rates on Hawai‘i and Mars. *Geochem. Geophys. Geosyst.* **21**, #2019GC008772 (40 pp).

Schnare D. W., Day J. M. D., Norman M. D., Liu Y. and Taylor L. A. (2008) A laser-ablation ICP-MS study of Apollo 15 low-titanium olivine-normative and quartz-normative mare basalts. *Geochim. Cosmochim. Acta* **72**, 2556–2572.

Sio C. K., Dauphas N., Teng F.-Z., Chaussidon M., Helz R. T. and Roskosz M. (2013) Discerning crystal growth from diffusion profiles in zoned olivine by in situ Mg–Fe isotopic analyses. *Geochim. Cosmochim. Acta* **123**, 302–321.

Sio C. K., Roskosz M., Dauphas N., Bennett N.R., Mock T., and Shahar A. (2018) The isotope effect for Mg-Fe interdiffusion in olivine and its dependence on crystal orientation, composition and temperature. *Geochim. Cosmochim. Acta.* **239**, 463–480.

Smith, P. M., and P. D. Asimow (2005), Adiabat_1ph: A new public front-end to the MELTS, MELTS, and pHMELTS models, *Geochem. Geophys. Geosyst.* **6**, #Q02004.

Stolper E. and McSween H. Y. Jr. (1979) Petrology and origin of the shergottite meteorites. *Geochim. Cosmochim. Acta* **43,** 1475–1498.

Taylor L. A., Onorato P. I. K., and Uhlmann D. R. (1977) Cooling rate estimates based on kinetic modelling of Fe-Mg diffusion in olivine. *Proc. Lunar Sci. Conf.* **8**, 1581–1592.

Teng, F.-Z., Dauphas, N., and Helz, R. T. (2008). Iron isotope fractionation during magmatic differentiation in Kīlauea Iki lava lake. *Science* **320**, 1620–1622.

Tomascak P. B., Tera F., Helz R. T. and Walker R. J. (1999) The absence of lithium isotope fractionation during basalt differentiation: New measurements by multi-collector sector ICP-MS. *Geochim. Cosmochim. Acta* **63**, 907–910.

Treiman A. H., Musselwhite D. S., Herd C. D. K., and Shearer C. K. Jr. (2006) Light lithophile elements in pyroxenes from Northwest Africa (NWA) 817 and other Martian meteorites: Implications for water in Martian magmas. *Geochim. Cosmochim. Acta* **70,** 2919–2934.

Udry A., and Day J. M. D. (2018) 1.34 billion-year-old magmatism on Mars evaluated from the co-genetic nakhlite and chassignite meteorites. *Geochim. Cosmochim. Acta*, **238**, 292–315.

Udry A., McSween H. Y. Jr., Hervig R. L., and Taylor L. A. (2016) Lithium isotopes and light lithophile element abundances in shergottites: Evidence for both magmatic degassing and subsolidus diffusion. *Meteoritics* **51**, 80–104.

Wadhwa M. (2001) Redox state of Mars upper mantle and crust from Eu anomalies in shergottite pyroxenes. *Science* **291,** 1527–1530.

Walker D., Longhi J., Stolper E. M., Grove T. L., and Hays J. F. (1977) Slowly cooled microgabbros 15065 and 15555. *Proc. Lunar Sci. Conf.* **8**, 1521–1547.

Watson E. B. and Cherniak D. J. (2015) Quantitative cooling histories of stranded diffusion profiles. *Contrib. Mineral. Petrol.* **169**, 1–30.

## 11. Supplementary Material

For complete supplementary data, the reader is referred to the published on-line version of the article: https://doi.org/10.1016/j.gca.2020.11.002.

**Appendix A**

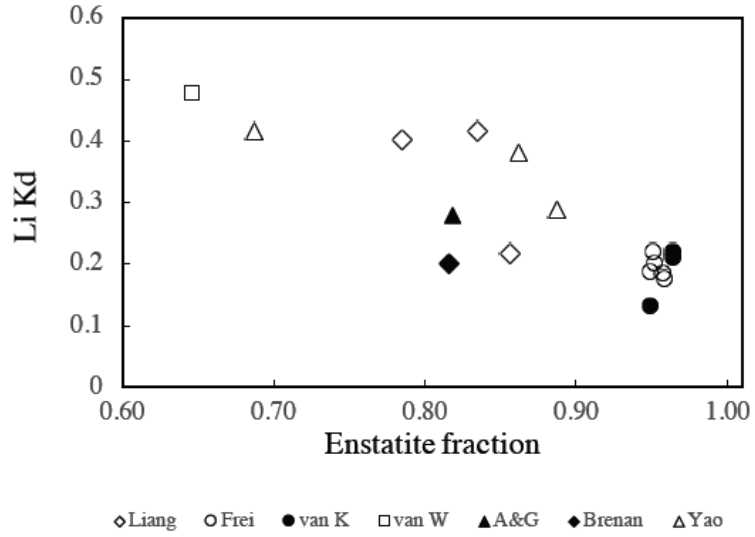


The compilation of Li partitioning data used to construct this figure was provided byYan Liang (Brown University). The diamond data points labeled "Liang" are unpublished data. The other data comes from the references below.

Van Kan Parker M., Mason P.R.D., and van Westrenen M. (2011) Experimental study of trace element partitioning between lunar orthopyroxene and anhydrous silicate melt: Effects of lithium and iron. *Chem. Geol.* 285, 1-14.

Yao L., Sun C., and Liang Y. (2012) A parameterized model for REE distribution between low-Ca pyroxene and basaltic melts with applications to REE partitioning. *Contrib. Mineral Petrol.* 164, 261-280.

Adam J. and Green T. (2006) Trace element partitioning between mica- and amphibole-bearing garnet lherzolite and hydrous basanitic melt: 1. Experimental results and the investigation of controls on partitioning behaviour. *Contrib. Mineral Petrol.* 152, 1-17.

Frei D., Liebscher A., Franz G., Wunder B., Klemme S., and Blundy J. (2009). Trace element partitioning between orthopyroxene and anhydrous silicate melt on the lherzolite solidus from 1.1 to 3.2 GPa and 1,230to 1,535C in the model system Na2O–CaO–MgO–Al2O3–SiO2. *Contrib. Mineral Petro*l**. 157,** 473-490**.**

van Westrenen W., Blundy J.D., and Wood B.J. (2000) Effect of $Fe^{2+}$ on garnet–melt trace element partitioning: experiments in FCMAS and quantification of crystal-chemical controls in natural systems. *Lithos* **53**, 189-201.

## Appendix B

## Instrumental mass fractionation (IMF) of magnesium and lithium measured with a CAMECA 1270 HR Secondary Ion Mass Spectrometer

The pyroxenes used to determine instrumental mass fractionation of lithium (Fig. B1) and magnesium (Fig. B2) when measured with a CAMECA 1270 SIMS were synthesized using six different starting materials. The components were added as oxides ($SiO_2$, $TiO_2$, $Al_2O_3$, FeO, MgO, MnO, CaO) except for Li, which was introduced in the form of natural spodumene (see Richter et al. 2014). The sum of FeO and MgO was maintained constant in the 5 pyroxene mixes at 40wt%, with FeO varying from 35 to 15 wt% and MgO in a reverse sense from 5 to 25wt%. The sixth starting composition was similar to the bulk Shergotty meteorite used by Stolper and McSween (1979) to crystallize zoned pyroxenes. The mixtures were packed in high-purity graphite capsules, pressurized to ~1 GPa and held at a desired temperature (1180-1500°C, depending on Mg/Fe) for a few hours to a few days in a piston cylinder apparatus. The run products turned out to be mixtures of glass and pyroxene crystals with 100% dense mats of quench crystals in some cases and blocky pigeonite in others. The Shergotty meteorite composition was ramped from 1280 to 1000°C at 1°/min, which produced large, zoned pyroxenes sometimes exceeding 1 mm in size. This experiment, combined with the run products of the five pyroxene compositions, produced a wide variety of Li-doped pyroxenes, with MgO ranging from 2.1 to 20.3 wt% and FeO from 30.3 to 6.3 wt%. Because of the very fast diffusion of lithium it had sufficient time to come to equilibrium with the local major element composition of the large zoned pyroxene grains. The instrumental mass fractionation of magnesium and lithium in these pyroxenes as a

function of enstatite fraction was used for matrix corrections of the magnesium isotopic data from Shergotty.

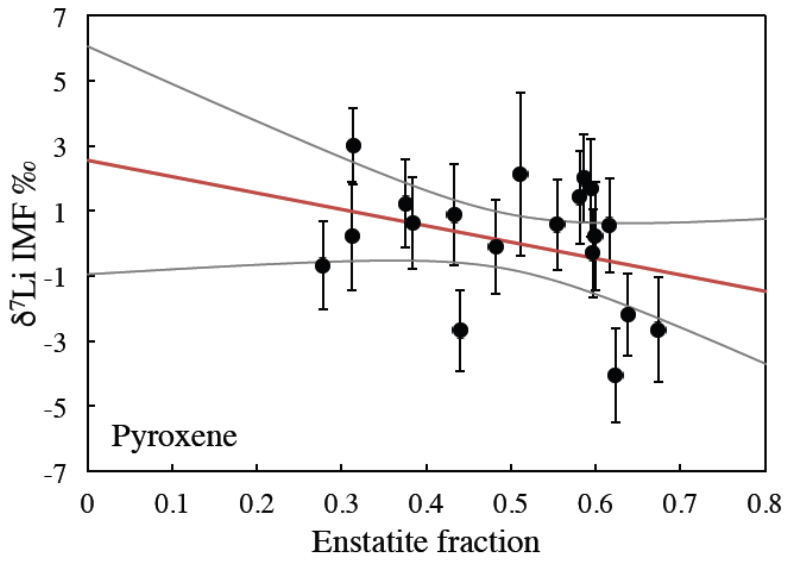


**Figure B1.** Lithium IMF as a function of enstatite fraction of pyroxene (□$^{7}$Li IMF ‰ =2.55-5.02×En). Here and in the two figures below, the red line is the regression through the data weighted by the 2□ error of each data point and the enveloped defined by the black lines are the 2□ uncertainty of the of the IMF as a function of the enstatite fraction (forsterite fraction in the case of olivine). The weighted regression and the IMF□uncertainty are calculated as given by Mahon (1996). The 2□ uncertainty of the individual lithium isotopic measurements is much the same as the 2□ uncertainty of the lithium IMF. Because of this we do not IMF correct the □$^{7}$Li measured across pyroxene grains from Shergotty and use the 2□ error of the individual measurement as the measure of the uncertainty.

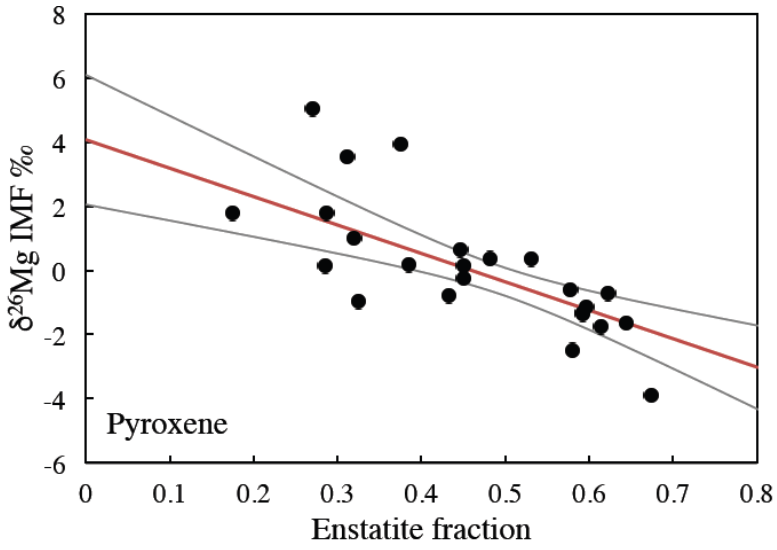


**Figure B2.** Magnesium IMF as a function of enstatite fraction of pyroxene. The red line is the regression through the data weighted by the 2□ error of each data point (□$^{26}$Mg IMF ‰ = 4.08-8.87×En). The 2□ uncertainty of the IMF shown by the two black lines is much larger than the uncertainty of the individual measurements and therefor we use the uncertainty of the IMF as a function of the enstatite fraction as the uncertainty of the IMF-corrected □$^{26}$Mg data measured across pyroxene grains from Shergotty.

The olivine samples used to determine the instrumental mass fractionation of magnesium in olivine consist of 7 synthetic olivine grains shown as black circles with 2□□error bars. These synthetic olivines ranging from $Fo_{12}$ to $Fo_{77}$ were produced at the Rensselaer Polytechnic Institute as described in Chaussidon et al. (2017). The magnesium

isotopic composition of the synthetic was measured with a CAMECA 1270 ion probe in the same session as the olivine grains from lunar rock 15555. The regression line through the data with Fo<0.8 was used for matrix correcting the measured magnesium isotopic composition across the olivine grain from lunar rock 15555.

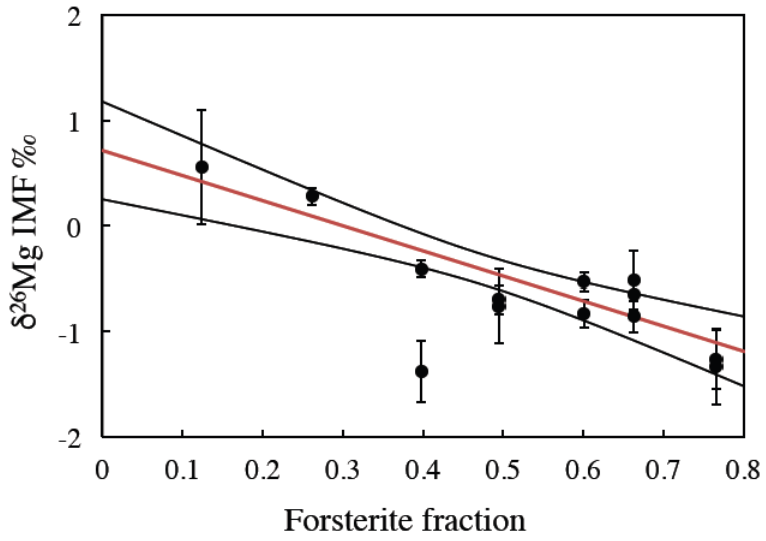


**Figure B3.** The red line is the uncertainty-weighted regression of the IMF as a function of the forsterite fraction of olivine (□$^{26}$Mg IMF ‰ =-0.71-2.38×Fo). The 2□ uncertainty of the magnesium IMF (black lines) is much larger the uncertainly of the individual magnesium isotopic measurements and we use the uncertainty of the IMF as the measure of the uncertainty of the □$^{26}$Mg measure across the olivine grain from lunar basalt 15555.

**Appendix B References**

Chaussidon M., Deng Z., Villeneuve J., Moureau J., Watson B., Richter F., and Moynier, F. (2017) In situ analysis of non-traditional isotopes by SIMS and LA-MC-ICP-MS: key aspects and the example of Mg isotopes in olivines and silicate glasses. *Rev. Mineralogy and Geochemistry* **82**, 127-163.

Mahon K.I. (1996) The new "York" regression: Application of improved statistical method to geochemistry. *Int. Geol. Rev.* **38**, 293-303.